EVALUATION OF TRANSVERSE BEHAVIOR OF GEOSYNTHETICS WHEN USED FOR SUBGRADE STABILIZATION

by

Zachary Lee Morris

A thesis submitted in partial fulfillment
of the requirements for the degree

of

Master of Science

in

Civil Engineering

MONTANA STATE UNIVERSITY
Bozeman, Montana

November, 2013

©COPYRIGHT

by

Zachary Lee Morris

2013

All Rights Reserved

APPROVAL

of a thesis submitted by

Zachary Lee Morris

This thesis has been read by each member of the thesis committee and has been found to be satisfactory regarding content, English usage, format, citation, bibliographic style, and consistency and is ready for submission to The Graduate School.

Dr. Steven Perkins

Approved for the Department of Civil Engineering

Dr. Jerry Stephens

Approved for The Graduate School

Dr. Ronald W. Larsen

STATEMENT OF PERMISSION TO USE

In presenting this thesis in partial fulfillment of the requirements for a master's degree at Montana State University, I agree that the Library shall make it available to borrowers under rules of the Library.

If I have indicated my intention to copyright this thesis by including a copyright notice page, copying is allowable only for scholarly purposes, consistent with "fair use" as prescribed in the U.S. Copyright Law. Requests for permission for extended quotation from or reproduction of this thesis in whole or in parts may be granted only by the copyright holder.

Zachary Lee Morris

November 2013

ACKNOWLEDGEMENTS

First, I give much deserved appreciation to my wife, Elise Morris, for her support, patience, willingness to accommodate a very hectic schedule, and always be there for me. I express my sincere gratitude to Mr. Eli Cuelho and Dr. Steve Perkins for their continued guidance, support, availability, and eagerness to help in all aspects of this paper.

I would like to thank the Western Transportation Institute and the Department of Civil Engineering at Montana State University for access to labs, tools, and materials. I am very thankful to the Montana Department of Transportation for being the project sponsor, and the following State Departments of Transportation that participated in this research project: Idaho, New York, Ohio, Oklahoma, Oregon, South Dakota, Texas, and Wyoming.

Last, but certainly not least, I would like to thank the Lord for always being there for me in time of need. I thank His disciple Pastor Brett LaShelle for the spiritual leadership that he provides to me and the love of family and friends who have always been there for me and have helped me through the difficult times in my life; especially my mother and father.

TABLE OF CONTENTS

1. INTRODUCTION 1

Background and Problem 1
Geosynthetics 2
Field Study 5
Organization of Thesis 7

2. LITERATURE REVIEW 8

Subgrade Stabilization 8
Field Studies 11
Fannin and Sigurdsson (1996) 11
Tingle and Webster (2003) 18
Hufenus et al. (2006) 20
Cuelho and Perkins (2009) 24
Instrumentation and Equipment 27
Strain Gage 27
Photogrammetry 40
LVDT 41
Summary 43
Contribution to Body of Knowledge 46

3. EXPERIMENTAL PROGRAM 48

Field Study 48
Construction 49
Subgrade 50
Base Course 52
Rut Measurements 53
Data Acquisition and Instrumentation 54
Strain Gage Instrumentation 55
Strain Gage Calibration 62
Strain Gage Survivability 70
Strain Gage Noise, Zero-Shift, and Temperature Effects 72
LVDT Instrumentation 73
LVDT Temperature Effects 75
Mechanical Properties of Geosynthetics 76
Wide Width Tensile Strength 77
Cyclic Tensile Modulus 79
Resilient Interface Shear Stiffness 81
Junction Strength 84
Aperture Stability Modulus 86

TABLE OF CONTENTS - CONTINUED

4. RESULTS AND ANALYSIS 89

Field Measurements 91
Subgrade Strength, Base Course Thickness, and Empirical Correction 92
Transverse Rut Profiles 96
Strain Gage Measurements 99
LVDT Measurements 102
Synthesis 110

5. SUMMARY, CONCLUSIONS, AND RECOMMENDATIONS 121

Summary 121
Conclusions 122
Lessons Learned 123
Recommendations for Future Work 125

REFERENCES CITED 128

APPENDICES 132

APPENDIX A: Strain Gage Instrumentation Procedures 133
APPENDIX B: Strain Gage Calibration Plots 159
APPENDIX C: Wide-Width Tensile Strength Load-Displacement Plots 166
APPENDIX D: Cyclic Tensile Modulus Load-Displacement Plots 173
APPENDIX E: Resilient Interface Shear Stiffness Plots 180
APPENDIX F: Junction Strength Plots (lb/junction) 187
APPENDIX G: Junction Strength Plots (lb/in) 193
APPENDIX H: Aperture Stability Modulus Plots 199
APPENDIX I: Transverse Rut Profiles 205
APPENDIX J: Strain Gage Dynamic Strain Plots 223
APPENDIX K: Strain Gage Static Strain Plots 231
APPENDIX L: LVDT Dynamic Displacement Plots 239
APPENDIX M: LVDT Static Displacement Plots 254
APPENDIX N: LVDT Dynamic Strain Plots 269
APPENDIX O: LVDT Static Strain Plots 284

LIST OF TABLES

Table Page

1: Summary of Geosynthetic Test Sections 4

2: Summary of Geosynthetic Material Properties Published by Manufacturers 5

3: Geosynthetic Properties Used in Field Study (modified after Hufenus et al., 2006). 21

4: Approximate Tensile Strength Induced by Fill Installation and Loading (modified after Hufenus et al., 2006) 24

5: General Properties of Subgrade 52

6: General Properties of Base Course Aggregate 53

7: Cyclic Strain Gage Calibration Procedure 63

8: Strain Gage Calibration Factors 65

9: Strain Gage Survivability 71

10: XMD Wide-Width Tensile Strength Test Results 78

11: Resilient Interface Shear Stiffness Test Results 84

12: XMD Junction Strength and Stiffness Test Results 86

13: Summary of Aperture Stability Modulus Test Results 88

14: Subgrade Strength and Base Course Thickness at Instrumented Locations 93

15: Select Mechanical Properties of Geogrids 114

16: Minimum Recommended Requirements for Geogrids in Subgrade Stabilization Applications 123

LIST OF FIGURES

Figure Page

1: Possible reinforcement functions provided by geosynthetics in subgrade stabilization applications (after Haliburton et al., 1981). 10

2: Base course layout of field study (after Fannin and Sigurdsson, 1996). 12

3: Surface profiles of test sections at base course thickness of 25 cm (after Fannin and Sigurdsson, 1996). 13

4: Surface profiles of test sections at base course thickness of 50 cm (after Fannin and Sigurdsson, 1996). 14

5: Average rut depth vs. base course thickness for test sections: a) unreinforced, b) geotextile 1, c) geotextile 2, d) geogrid, and e) geotextile 3 (modified after Fannin and Sigurdsson, 1996). 16

6: Relationship between average rut depth and number of passes at base course thicknesses of: a) 0.25 m, b) 0.3 m, c) 0.35 m, d) 0.40 m, and e) 0.50 m (modified after Fannin and Sigurdsson, 1996). 17

7: Layout of test sections: (a) plan, and (b) profile (after Tingle and Webster, 2003). 19

8: Typical post-trafficking DCP results for Item 4 (after Tingle and Webster, 2003). 19

9: Strain of geosynthetics during compaction and trafficking (after Hufenus et al., 2006). 23

10: Relationship between geosynthetic tensile strength in XMD and N_{add} at 75 mm of mean rut depth (after Cuelho and Perkins, 2009). 26

11: a) calibration results of a woven geotextile, b) wide-width tensile test results of a woven geotextile, c) calibration results for punched/drawn geogrid (after Warren and Howard, 2010). 29

12: Global and local response of geogrid (after Perkins et al., 1997). 31

LIST OF FIGURES - CONTINUED

Figure Page

13: Global and local response of geogrid in an unloading-reloading cycle (after Perkins et al., 1997). 31

14: Coefficient of variation for strain gages (after Bathurst et al., 2002). 34

15: Results from monotonic, in-air tension tests on a) a geogrid, and b) a geotextile (after Cuelho et al., 2008). 38

16: Results from cyclic tension tests on a) a geogrid, and b) a geotextile (after Cuelho et al., 2008)..... 39

17: Leadwire connection onto a) a geotextile and b) a geogrid (after Cuelho et al., 2008). 43

18: Design and layout of test sections..... 49

19: In-situ testing plan. 51

20: Grain-size distribution of subgrade..... 52

21: Grain-size distribution of base course aggregate. 53

22: Elevation rut compared to apparent rut..... 54

23: Mobile lab. 55

24: Instrumentation arrangement within a single test section. 56

25: Location of strain gages and LVDT sensors. 56

26: Jumper wires attached to strain gages..... 58

27: Completed placement and wiring of a strain gage on a woven geogrid..... 59

28: Completed strain gage installation on a welded geogrid with protective coating..... 60

29: Completed strain gage installation on a woven geotextile. 61

30: Strain gage calibration setup - local view. 68

LIST OF FIGURES - CONTINUED

Figure Page

31: Strain gage calibration setup – global view. 68

32: Strain gage calibration verification – Enkagrid Max 30. 69

33: Placement of LVDT leadwires and strain gages on a woven geotextile. 75

34: Wide-width tensile strength test setup. 78

35: XMD cyclic tensile modulus test results. 80

36: Resilient interface shear stiffness apparatus (from ASTM D7499). 81

37: Illustrated calculation of resilient interface shear stiffness (from ASTM D7499). 82

38: Typical junction strength test specimen setup (from ASTM D7737). 85

39: Aperture stability modulus testing device (image courtesy of Tensar International, Inc.). 87

40: Possible reinforcement functions provided by geosynthetics in subgrade stabilization applications: a) lateral confinement, and b) membrane support (modified after Haliburton et al., 1981). 91

41: Trafficking log and dynamic field measurements. 92

42: Uncorrected longitudinal rut versus truck pass for Test Sections 1, 2, and 3.. 94

43: Corrected longitudinal rut versus truck pass for Test Sections 1, 2, and 3. 95

44: Correction factor for subgrade strength variations (based on longitudinal data). 96

45: Transverse profile - Test Section 3-South. 98

46: Transverse profile - Test Section 7-North. 98

LIST OF FIGURES - CONTINUED

Figure Page

47: Strain gage dynamic results – Test Section 3. 100

48: Strain gage dynamic results – Test Section 10. 100

49: Strain gage static results – Test Section 3..... 101

50: Strain gage static results – Test Section 10..... 101

51: LVDT dynamic displacement results – Test Section 3-South. 103

52: LVDT dynamic displacement results – Test Section 7-North. 104

53: LVDT static displacement results – Test Section 3-South. 104

54: LVDT static displacement results – Test Section 7-North. 105

55: LVDT positions in west wheel path. 107

56: LVDT dynamic strain results – Test Section 3-South. 108

57: LVDT dynamic strain results – Test Section 7-North. 108

58: LVDT static strain results – Test Section 3-South. 109

59: LVDT static strain results – Test Section 7-North. 109

60: LVDT 2 to 3 strain compared to strain gage strain at truck pass 40. 110

61: Truck pass at transition to membrane support and at failure for all reinforced test sections. 112

62: LVDT dynamic displacement results of Test Section: a) 13-North, b) 13-South, c) 14-North, and d) 14-South. 119

NOMENCLATURE

CBR	California Bearing Ratio
DCP	Dynamic Cone Penetrometer
HDPE	High-Density Polyethylene
LVDT	Linear Variable Differential Transformer
LWD	Light Weight Deflectometer
MD	Machine Direction
PET	Polyester
PMY	Polyester Multifilament Yarn
PP	Polypropylene
PPF	Polypropylene Fiber
PVC	Polyvinyl Chloride
XMD	Cross-Machine Direction

ABSTRACT

State departments of transportation (DOTs) routinely use geogrids and geotextiles for subgrade stabilization. There is a general consensus between state DOTs concerning the effectiveness of these geosynthetics for this application; however, there is a lack of understanding and agreement with respect to the material properties of the geosynthetics that most directly relate to performance.

A full-scale field study using geosynthetics as subgrade stabilization was conducted to analyze the performance and transverse behavior of 14 reinforced test sections under vehicular loads. Insight into the mechanisms of support that geosynthetics provide was determined based on strain gage and LVDT measurements, and transverse rut profiles. Mechanical properties of geosynthetics were compared to truck passes at the transition from lateral confinement to membrane support as well as at failure to evaluate which properties best predicted field performance. The properties evaluated included wide-width tensile strength, cyclic tensile modulus, resilient interface shear stiffness, junction strength, and aperture stability modulus.

The behavior of geosynthetics was primarily characterized by when they started to transition from lateral confinement to membrane support. The results indicate that in general, the geosynthetics transitioned between truck pass 80 to 300 at a corresponding average elevation rut of about 1.7 inches, or between 1.7 to 3.1 inches of apparent rut. Failure was defined as 3 inches of elevation rut, and in general, the geosynthetics that transitioned to membrane support before truck pass 80 to 300 failed early.

The results from the field study indicate that junction strength and stiffness, and wide-width tensile strength at 2% and 5% strain may be the most pertinent mechanical properties of geogrids, and surface friction may be the most pertinent property of geotextiles, for estimating field performance when used for subgrade stabilization applications with 10 to 12 inches of base aggregate, CBR strength values between 1.5 to 2.2, and elevation ruts less than 3.0 inches (or less than 5.4 inches of apparent rut).

CHAPTER ONE

INTRODUCTION

Background and Problem

The use of fabric for soil reinforcement in the United States dates back to 1926 when the South Carolina Highway Department used cotton fabric as a reinforcement for bituminous surface treatment (Beckham and Mills, 1935). The success from this creative reinforcement application has grown tremendously and now synthetic materials called geosynthetics are used in a variety of geotechnical applications to facilitate compaction, improve bearing capacity, extend service life, reduce fill thickness, diminish deformations, and delay rut formation (Hufenus et al., 2006). Two specific lines of products, geogrids and geotextiles, are commonly used in transportation applications to benefit roadways through three possible mechanisms: 1) lateral restraint of the base and subgrade through friction and interlock between the aggregate, soil, and geosynthetic; 2) increase in system bearing capacity by reducing the stress on the subgrade; and 3) membrane support of wheel loads (Holtz et al., 2008).

State departments of transportation (DOTs) routinely use geogrids and geotextiles for subgrade stabilization. In subgrade stabilization applications, the geosynthetic is placed on top of a weak subgrade (having a California Bearing Ratio (CBR) of three or less), which is then topped with base course aggregate. The geosynthetic reduces stresses on the subgrade by providing lateral restraint, improving the system's bearing capacity, and/or providing membrane support of the wheel loads through tension in the

geosynthetic. Between DOTs, there is a general consensus concerning the effectiveness of geosynthetics in subgrade stabilization; however, there is a lack of understanding and agreement on the material properties of the geosynthetic that are most directly related to performance.

The primary objectives of this thesis are to describe the transverse behavior of various geosynthetics when used for subgrade stabilization, and to provide insight into which material properties are most closely related to field performance. Full-scale field test sections were constructed and trafficked during the summer of 2012. Analysis of data from displacement sensors, strain gages, and rut measurements was used to determine the behavior and field performance of 14 geosynthetic reinforced test sections. The material properties of the geosynthetics were characterized by their physical attributes (thickness, aperture size or apparent opening size), and their mechanical properties (wide-width tensile strength, cyclic tensile modulus, resilient interface shear stiffness, junction strength, and aperture stability modulus).

Geosynthetics

The geosynthetic types used in the field study were geogrids and geotextiles. Geogrids are relatively stiff polymeric materials which are typically composed of relatively high-strength interconnecting ribs that form an open grid structure. There are a variety of processes used to manufacture these products such as integrally-formed, vibratory-welded, laser-welded, extruded, knitted, and woven. The knitted and woven geogrids are often times coated with PVC or polymer to protect them from damage. Grid openings (i.e., apertures) are typically rectangular; however, some products are

triangular. Apertures allow soil particles on either side of the geogrid to come into direct contact with one another. As traffic loads are applied, the base course aggregate interlocks with the geogrid which reduces lateral spreading and therefore increases the roadway's bearing capacity. Under higher surface deformations, the geogrid begins to act like a membrane to provide structural support. The geogrids used in this study are listed in Table 1, and their general material properties are listed in Table 2.

Geotextiles are permeable fabrics and are available in a variety of structures and polymer compositions designed to meet a wide range of applications, and can be classified as nonwoven, woven, and knitted. Nonwoven geotextile manufacturing methods are needle-punched, thermally-spun, bonded, and knitted. Woven geotextiles typically exhibit higher strength than nonwoven geotextiles and are manufactured using a weaving process to form a monofilament, multifilament, or silt-film tape structure. As traffic loads are applied, the base course interacts with the surface of the geotextile which provides lateral confinement to the base course. Similar to geogrids, geotextiles can also support traffic loads as a membrane under higher surface deformations. In addition, geotextiles function as a separator between the base course and subgrade, and in certain situations can also function as a drainage path for water. The geotextiles used in this study are listed in Table 1, and their general material properties are listed in Table 2.

Table 1: Summary of Geosynthetic Test Sections

Geosynthetic Test Section	Manufacturer - Product	Abbreviation	Structure
1, 2, 3	Tensar - BX Type 2	BX Type 2	integrally formed, geogrid
4	NAUE - Secugrid 30/30 Q1	Secugrid 30/30 Q1	vibratory welded, geogrid
5	Colbond - Enkagrid Max 30	Enkagrid Max 30	laser welded, geogrid
6	Synteen - SF 11	SF 11	PVC coated, woven geogrid
7	Synteen - SF 12	SF 12	PVC coated, woven geogrid
8	TenCate - Mirafi BXG 11	BXG 11	PVC coated, woven geogrid
9	Huesker - Fornit 30	Fornit 30	polymer coated, knitted woven geogrid
10	SynTec - Tenax MS330	Tenax MS330	extruded, triple layer, geogrid
11	Tensar - TX 140	TX 140	integrally formed, triaxial, geogrid
12	Tensar - TX 160	TX 160	integrally formed, triaxial, geogrid
13	TenCate - Mirafi RS580i	RS580i	multifilament, woven geotextile
14	Propex - Geotex 801	Geotex 801	needle punched, nonwoven geotextile

Table 2: Summary of Geosynthetic Material Properties Published by Manufacturers

Geosynthetic Test Section	Polymer[a]	Roll Width (in)	Mass per unit area (oz/yd^2)	Aperture Size (in) MD x XMD[a]
BX Type 2	PP	160	NP	1.0 x 1.3
Secugrid 30/30 Q1	PP	186	5.9	1.3 x 1.3
Enkagrid Max 30	PP	197	6	1.7 x 1.6
SF 11	PMY	186	NP	1.0 x 1.0
SF 12	PMY	183	NP	1.0 x 1.0
BXG 11	PMY	158	9.1	1.0 x 1.0
Fornit 30	PP	206	6.5	0.6 x 0.6
Tenax MS330	PP	156	9.7	1.7 x 2.0[b]
TX 140	PP	160	NP	1.6 x 1.6[c]
TX 160	PP	160	NP	1.6 x 1.6[c]
RS580i	PPF	204	NP	40[d]
Geotex 801	PP	186	8	80[d]

[a] acronym meanings: PP = polypropylene, PMY = polyester multifilament yarn, PPF = polypropylene fiber
MD = machine direction, XMD = cross-machine direction
[b] for a single layer; apparent opening size is reduced when three layers are stacked on top of one another
[c] reported as "rib pitch" in manufacturer's specification sheet
[d] Apparent Opening Size (AOS) in U.S. Standard sieve size (ASTM D4751)
NP = information was not provided by the manufacturer

Note that the TX 140 and TX 160 materials have equilateral triangular apertures, and therefore "rib pitch" stands for the distance from node to node. Because the triangular apertures have legs perpendicular to the machine direction, the XMD distance from node to node is 1.6 inches.

Field Study

A field study was conducted in the summer of 2012 to analyze the behavior and performance of geosynthetics used as subgrade stabilization. Test sections were built at TRANSCEND, a transportation research facility located in Lewistown, Montana. By conducting the research project at TRANSCEND rather than on a typical jobsite, three

important aspects of the project were able to be controlled: 1) the strength of the roadbed subgrade, 2) the cross-sectional design of the road, and 3) traffic.

Construction of the test site consisted of excavation of a trench, placement and compaction of subgrade, installation of geosynthetics and instrumentation, and placement and compaction of base course. A trench 3 ft deep by 16 ft wide by 860 ft long was excavated and lined with plastic sheeting. Subgrade material with known and consistent material properties was then placed in the trench and compacted in layers up to the top of the trench. The subgrade's strength was mainly controlled by water content and measured using a hand-held vane shear device. The target subgrade strength for most of the test sections was a CBR of 1.70, which was correlated to vane shear strength through extensive laboratory testing. A light weight deflectometer, nuclear densometer, dynamic cone penetrometer, and in-field CBR were also used to characterize the subgrade during construction. On top of the subgrade, instrumented geosynthetics were placed. Each geosynthetic reinforced test section was 50 ft long and had two instrumented locations. The base course material was placed and compacted on top of the geosynthetics.

The behavior and performance of the test sections was measured using installed instrumentation and rut measurements throughout trafficking. The instrumentation used in the field study mainly consisted of displacement sensors and strain gages. Linear variable differential transformers (LVDTs) were used to measure displacement. Strain gages were carefully attached to the surface of transverse load bearing members of the geosynthetics, and were calibrated under in-air cyclic loading representative of the field study loading conditions. The instrumentation from the test sections was wired to a

mobile lab office located near the center of the project site. Inside the mobile lab, data loggers and computers were installed and dynamic and long-term static field data was collected regularly to assess the behavior of the geosynthetics throughout trafficking.

Trafficking was carried out using a fully loaded three-axle dump truck that weighed 45,420 lb. The truck passed over the test sections in only one direction with a speed of approximately 5 mph to reduce dynamic loads due to unevenness in the gravel surface. Periodic rut measurements were made using a robotic total station. The rut was measured approximately every 3 ft in the longitudinal wheel paths, and approximately every 8 inches in the transverse direction where the geosynthetic was instrumented.

Organization of Thesis

This thesis consists of five chapters. Chapter two is a literature review of subgrade stabilization field studies and instrumentation techniques that are applicable to this thesis. The third chapter describes the design and construction of the test sections, methods used to characterize the geosynthetics, both in-lab and in-field, and also the installation and calibration procedures for the strain gages. Chapter four presents, analyzes, and synthesizes the results from the methods described in chapter three. Chapter five summarizes the results, presents conclusions, and makes recommendations for future work.

CHAPTER TWO

LITERATURE REVIEW

The literature review consists of four sections. A brief overview of subgrade stabilization is given in Section 1. In Section 2, field studies that used geosynthetics for subgrade stabilization applications are presented. The relevant instrumentation and equipment used in similar studies, with an emphasis on strain gages and calibration procedures, is reviewed in Section 3. Lastly, a summary of the literature and how this thesis contributes to the body of knowledge is presented in Section 4.

Subgrade Stabilization

Subgrade stabilization techniques can be explained as methods used to increase the allowable capacity of the roadway by reducing stresses on the subgrade induced by vehicular loading. Geosynthetics used in subgrade stabilization applications are most beneficial when the subgrade CBR strength is less than 3 (Holtz et al., 2008), and the geosynthetic provides the most benefit when placed on top of the subgrade and covered by base course aggregate. Other methods that are commonly used for subgrade improvements include chemical stabilization (e.g., lime, cement), stabilization using industrial by-products (e.g., foundry slag, fly ash), and mechanical stabilization (e.g., scarifying, drying, and compacting). The location, soil type, economics, availability of materials, and availability of equipment will determine which method is best to use.

The main applications of geosynthetics for subgrade stabilization are temporary roads, working platforms, unpaved roads, and permanent roads. In temporary roads,

geosynthetics reduce rutting of the gravel surface and/or decrease the amount of gravel required to support the anticipated traffic (Holtz et al., 2008). They are often times used to create working platforms when the existing soils are too weak to support heavy equipment. In addition, for unpaved and permanent paved roads, the temporary working platform can be used to provide an improved roadbed (Holtz et al., 2008). The primary reasons why geosynthetics decrease rutting is because they prevent lateral spreading of the base course, increase bearing capacity, and under severe rutting, may provide membrane support to the wheel loads (Holtz et al., 2008), as illustrated in Figure 1.

Subgrade stabilization using geosynthetics for both temporary and permanent roadways on soft subgrades has numerous benefits. Some of the benefits include reduction of stress on the subgrade, separation of subgrade and base course, filtration of water, reduction of excavation depth and/or base course thickness, reduction of disturbance to soft or sensitive subgrades during construction, increase in subgrade strength with time through filtration, reduction of differential settlements caused by variation in subgrade strength, reducing roadway maintenance, and extending the life of the pavement (Holtz et al., 2008).

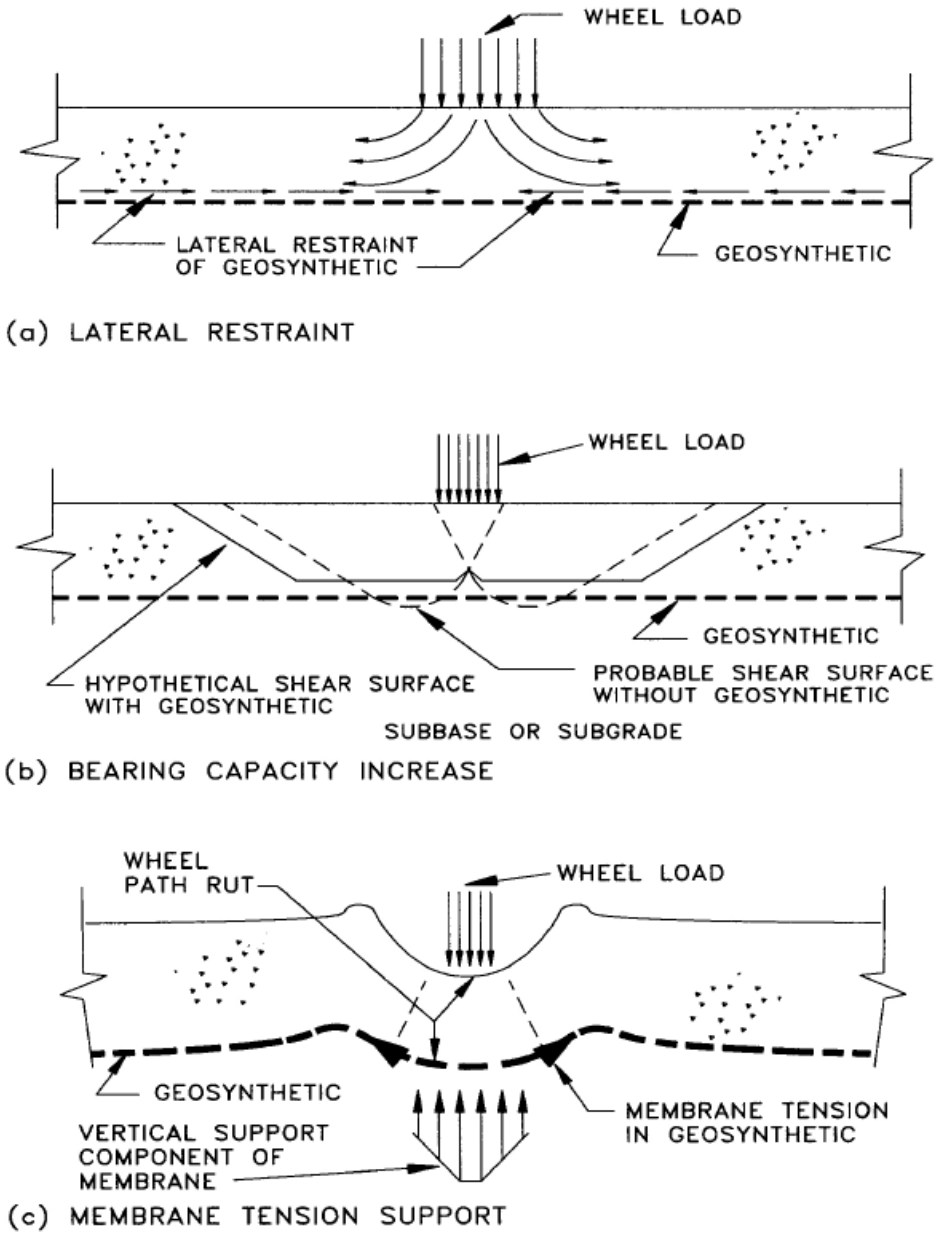


Figure 1: Possible reinforcement functions provided by geosynthetics in subgrade stabilization applications (after Haliburton et al., 1981).

Field Studies

Full-scale field studies on unpaved roads with weak subgrades using geosynthetics were reviewed. The studies evaluated the benefits that various geosynthetics provide with respect to subgrade strength, base course thickness, and surface deformation. The behavior of the geosynthetics and the primary support mechanisms that they can provide (i.e., lateral confinement, bearing capacity increase, and/or membrane support) were discussed in most of the field studies.

Fannin and Sigurdsson (1996)

Fannin and Sigurdsson (1996) performed a field study on an unpaved road underlain by soft subgrade on the right-of-way of Highway 91/91A near New Westminster, B.C. The field study consisted of five test sections which were each 4.5 m wide by 16 m long. Two test sections had nonwoven geotextiles, one had a scrim reinforced nonwoven geotextile (scrim = woven + nonwoven and is used for rough soil conditions or steep slope applications (Herlin, 2008)), one had a biaxial high-junction-strength geogrid, and one was a control section with no reinforcement. The subgrade was an organic, very clayey silt with some fine sand, and the base course aggregate was a very sandy gravel (19 mm minus). The base course for each test section was formed into a double wedge shape which varied the base course thickness from 50 cm to 25 cm and back up to 50 cm throughout each test section as illustrated in Figure 2.

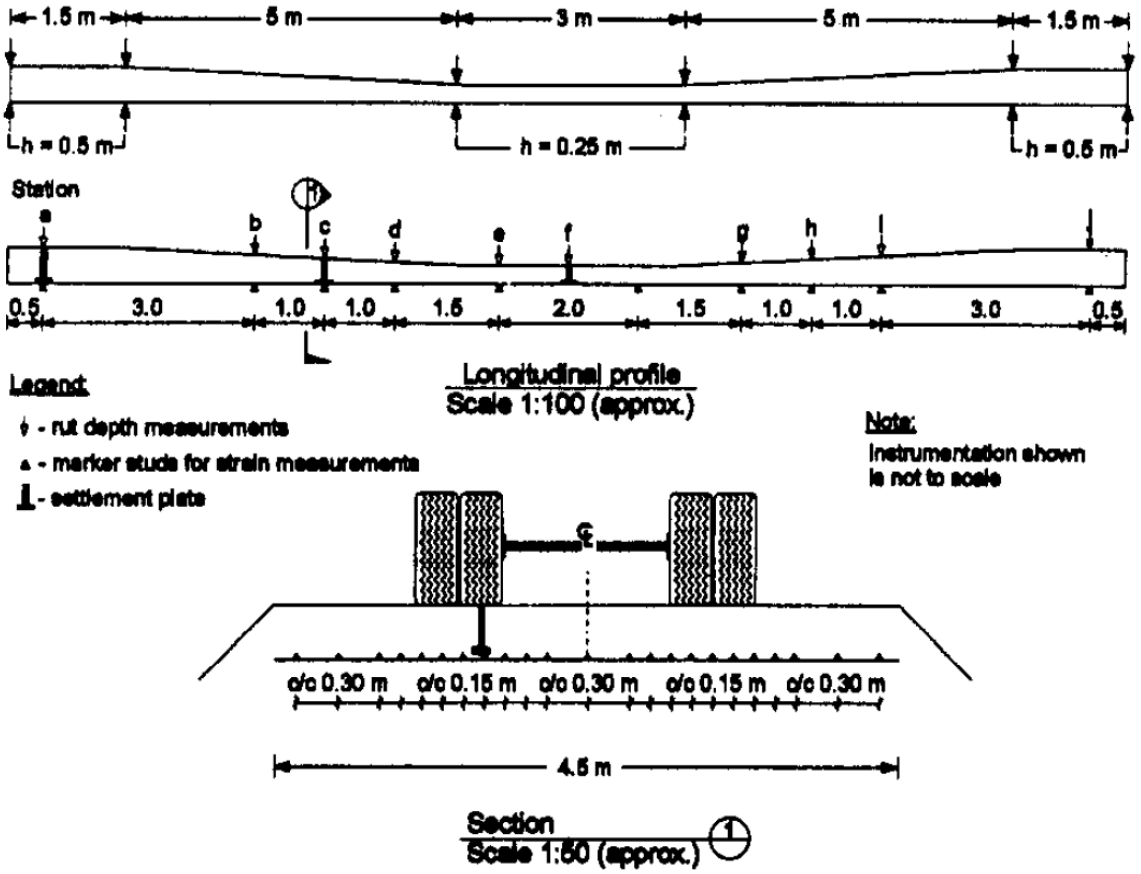


Figure 2: Base course layout of field study
(after Fannin and Sigurdsson, 1996).

The reason for the double wedge longitudinal profile was to allow for repeatability of measurements at various layer thicknesses and to study the effects of base thickness on performance. A two-axle truck with tire pressures of 620 kPa and a total weight of 110 kN, was used to traffic the test sections. The truck was driven in both directions at 7 km/hr across the test sections. Measurements were stopped after elevation ruts exceeded 20 cm; after which the ruts were filled in with additional base course.

Transverse surface profiles of the base course surface were taken throughout trafficking. Heave of the base course material was observed in all of the test sections

with a base course thickness of 25 cm as illustrated in Figure 3, and was not observed for a base course thickness of 50 cm as illustrated in Figure 4. Transverse profiles helped verify the behavior of the geosynthetics used in their field study.

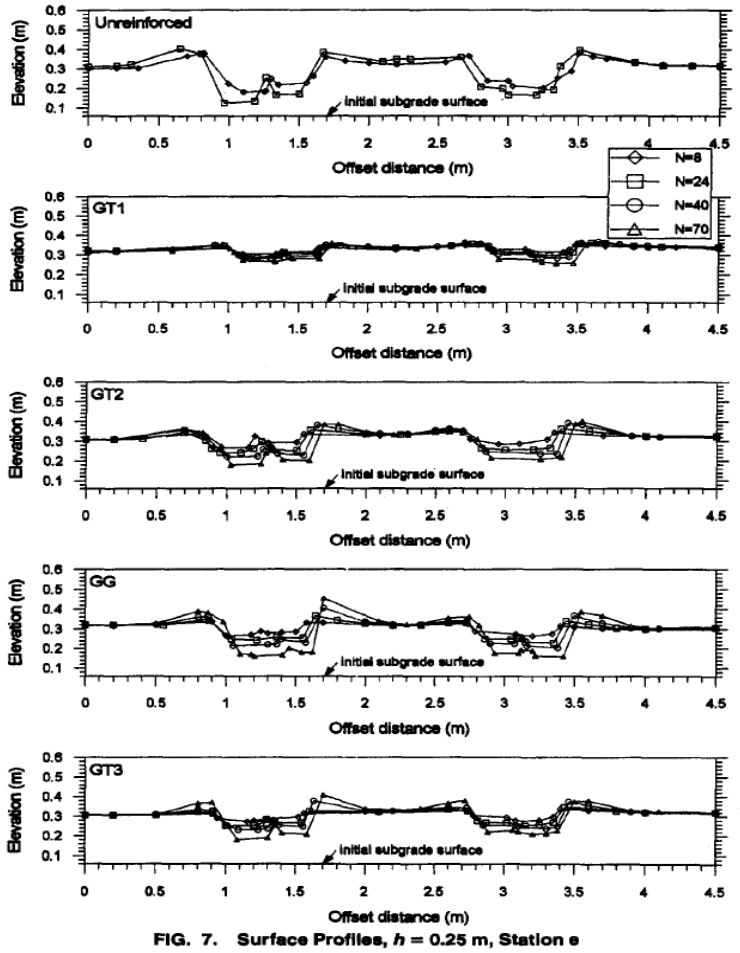


Figure 3: Surface profiles of test sections at base course thickness of 25 cm (after Fannin and Sigurdsson, 1996).

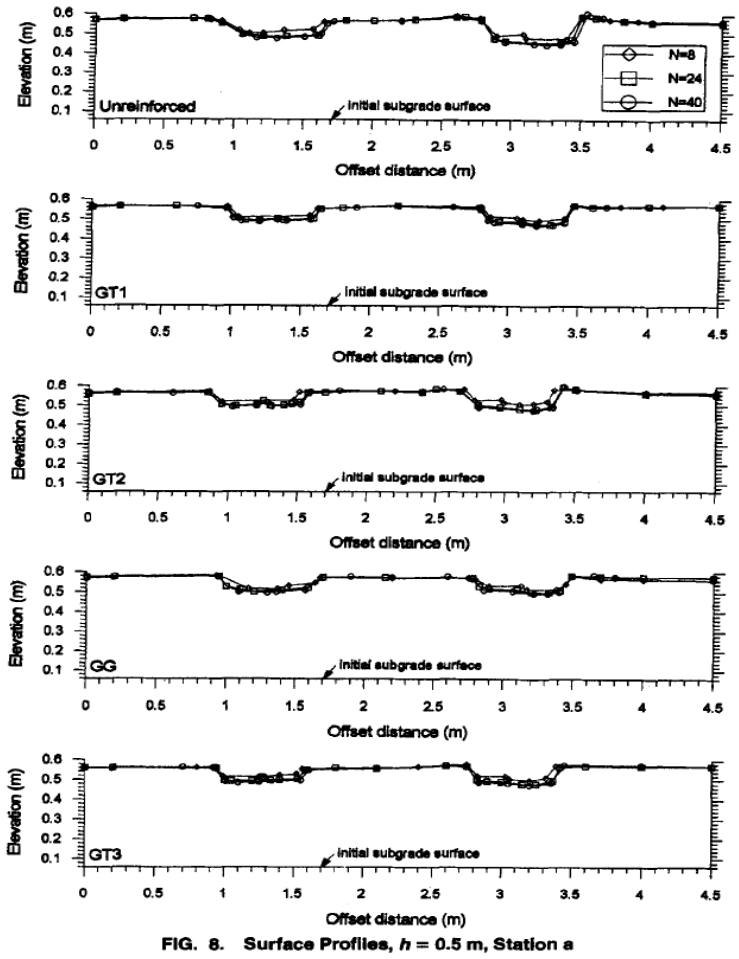


FIG. 8. Surface Profiles, $h = 0.5$ m, Station a

Figure 4: Surface profiles of test sections at base course thickness of 50 cm (after Fannin and Sigurdsson, 1996).

Fannin and Sigurdsson made several important conclusions based on their research. First, the analytical approach of Giroud and Noiray (1981) significantly over predicted the number of vehicle passes to develop 5 cm of rut likely due to compaction of the base course aggregate, and in contrast, the relationship between base course thickness and vehicle loading was more appropriate for 15 cm of rut using Giroud and Noiray's analytical approach. Fannin and Sigurdsson concluded that to maximize the potential benefit of a geosynthetic on thin gravel layers over soft soils, adequate separation of the

base course aggregate and subgrade is important. This conclusion is illustrated in Figure 5, where the strongest geotextile (GT1) outperformed the geogrid at base course thicknesses of 25 cm and 30 cm. The relative deterioration of the geogrid section was in part attributed to some intrusion of the subgrade soil through apertures of the grid leading to a loss of interlock between the grid and base course material. Lastly, the authors concluded that the benefit of using geosynthetics diminishes with increasing base course thickness, as illustrated in Figure 5. Note that "N" in Figure 5 denotes the number of truck passes.

The authors observed that on thin gravel layers over soft subgrades, if adequate separation of the base course aggregate and subgrade is provided by the geosynthetic, then the tensile stiffness of the geosynthetic may act to increase the contribution of a tensioned-membrane effect, and improve trafficability. Figure 6 verifies this conclusion by observing that at around 10 cm of average rut (averaged rut depth of inner and outer wheel paths), the curves of the geosynthetic reinforced sections tend to shift towards a constant average rut depth.

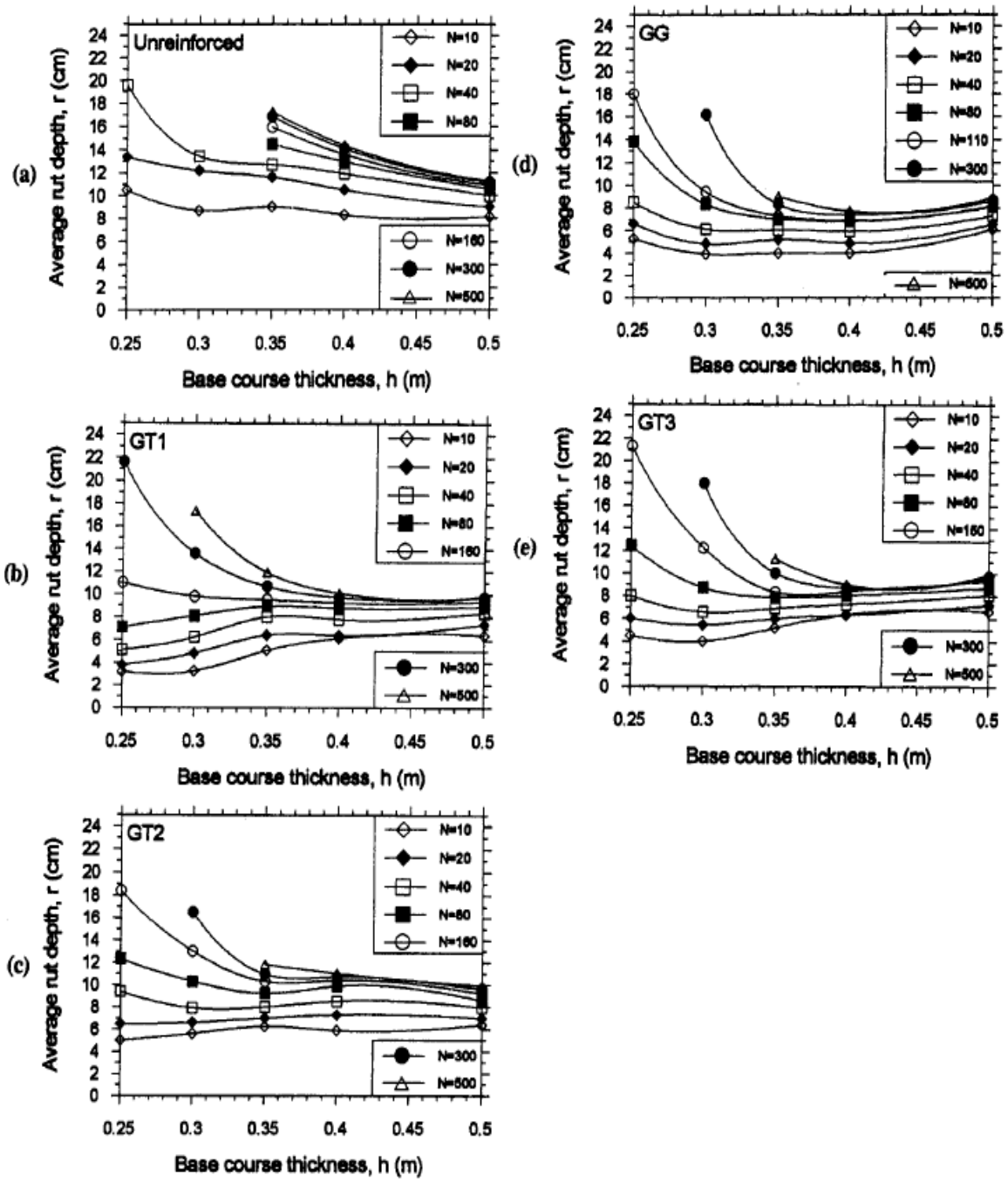


Figure 5: Average rut depth vs. base course thickness for test sections:
a) unreinforced, b) geotextile 1, c) geotextile 2, d) geogrid, and e) geotextile 3
(modified after Fannin and Sigurdsson, 1996).

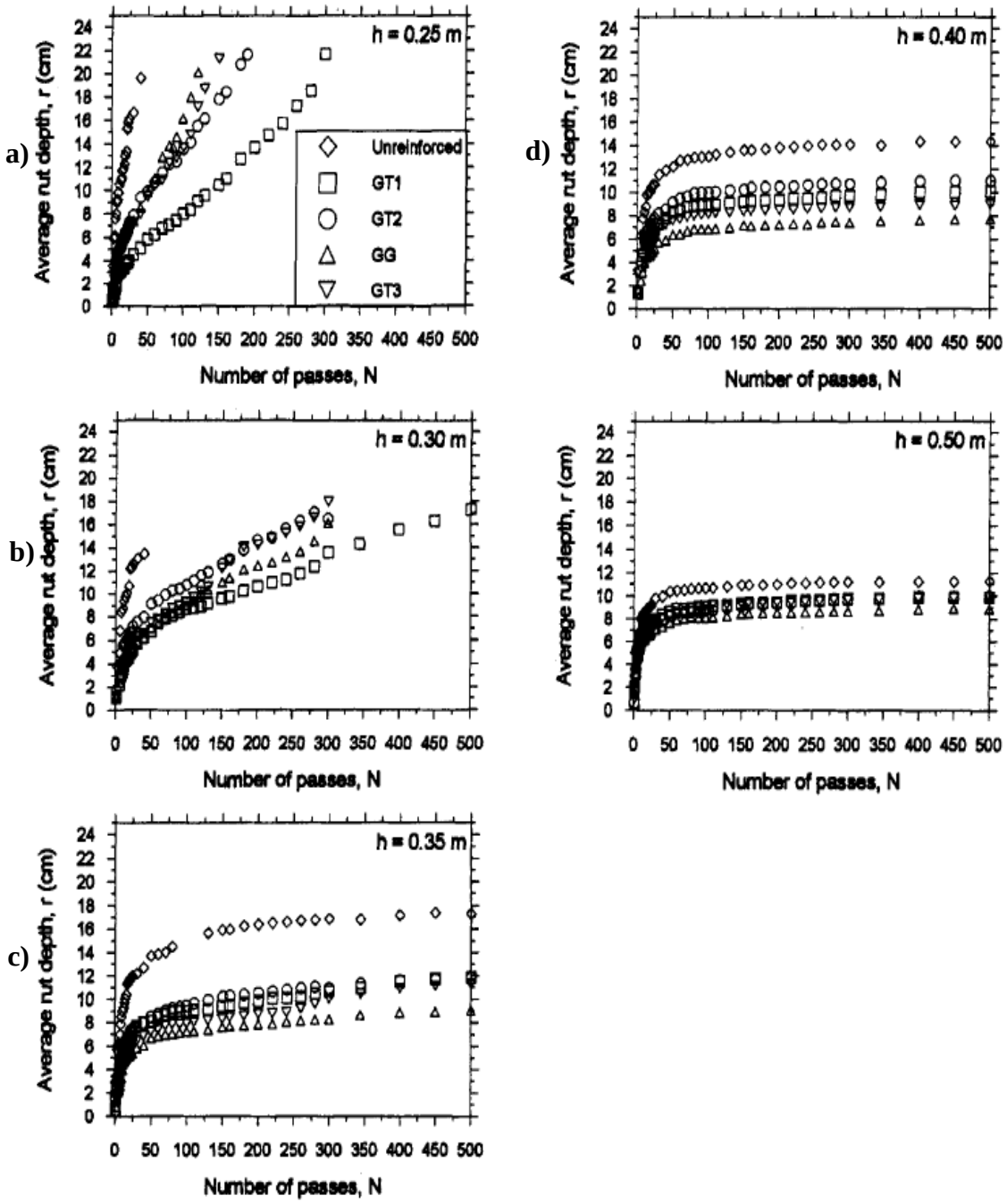


Figure 6: Relationship between average rut depth and number of passes at base course thicknesses of: a) 0.25 m, b) 0.3 m, c) 0.35 m, d) 0.40 m, and e) 0.50 m (modified after Fannin and Sigurdsson, 1996).

Tingle and Webster (2003)

Tingle and Webster (2003) discuss a full-scale geosynthetic-reinforced unpaved field study that the Corps of Engineers performed in Vicksburg, Mississippi in 1995. The objective of the study was to validate the existing criteria for geotextile-reinforced unpaved roads and to modify the criteria for the addition of stiff biaxial geogrids underlain by nonwoven geotextiles. The subgrade at the test site was a high-plasticity clay (CH) known as Vicksburg Buckshot constructed to a CBR value of 0.7 to 1.0. The base course thickness design varied over the test sections. Section 1 was a control and consisted of 20 inches of well-graded crushed limestone. Sections 2 and 3 consisted of 15 inches of crushed limestone over a woven and nonwoven geotextile, respectively, and section 4 consisted of 10 inches of crushed limestone over a stiff biaxial geogrid overlaying a nonwoven geotextile.

Each test section was 20 ft wide by 150 ft long. The existing subgrade was excavated to a depth of approximately 46 inches and new subgrade material was placed in 6-inch lifts to a total thickness of 36 inches at a CBR near 2. To decrease the subgrade strength to the design CBR of 0.7 to 1.0, the subgrade was pulverized with a high-speed rotary mixer and flooded with water before installation of the next lift. After the final lift, the subgrade was inundated with water for 3 weeks to allow the moisture to equilibrate. It is important to note that post-trafficking investigations indicated an increase in subgrade strength had occurred throughout all of the test sections, although the amount of increase and the duration of trafficking were not specified. Regardless, the increase in strength over time demonstrated the effect of overburden pressure and consolidation on

the very soft subgrade. The layout of the test sections and typical post-trafficking dynamic cone penetrometer (DCP) results for Item 4 (i.e., Test Section 4) are shown in Figure 7 and Figure 8, respectively.

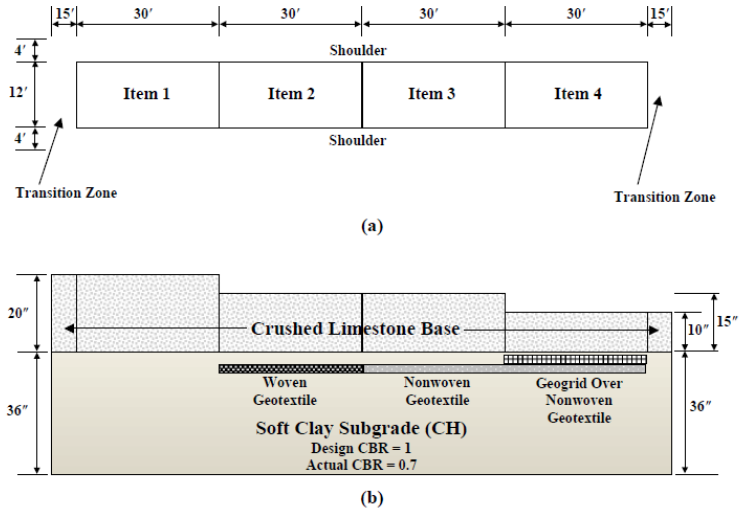


Figure 7: Layout of test sections: (a) plan, and (b) profile (after Tingle and Webster, 2003).

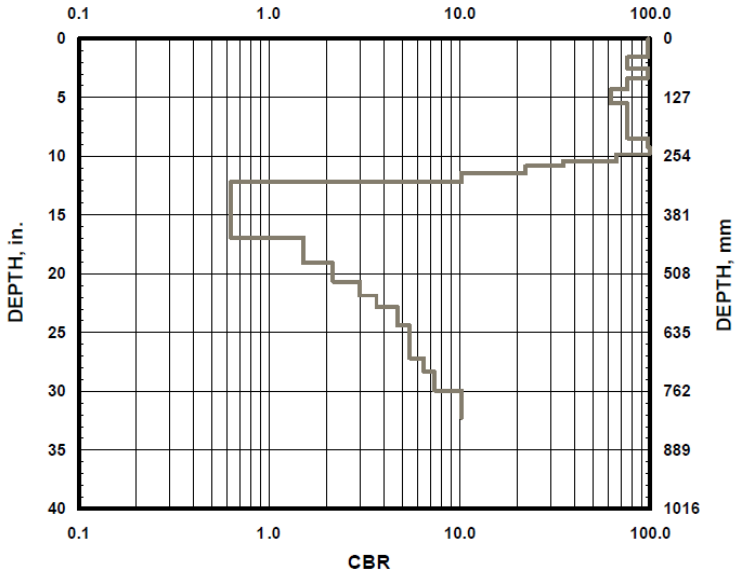


Figure 8: Typical post-trafficking DCP results for Item 4 (after Tingle and Webster, 2003).

The test sections were trafficked using a M923 5-ton military truck loaded to a gross weight of 43.5 kips. The tire pressure was 75 psi and the truck passed over the test sections at approximately 10 mph. Similar to Fannin and Sigurdsson (1996), the truck passed over the test sections moving forward, and then went in reverse back over the test sections in the same wheel path.

Rut was measured using a 10 ft metal straightedge across the traffic lane and recording the maximum rut depth. The measured rut depth included both the permanent deformation and the upheaval within the traffic lane. In addition, cross-section measurements were taken with a rod and level at the same locations to verify permanent surface deformation.

The results of the analyses performed by the authors supported the existing design procedure used by the Corps of Engineers for unreinforced sections, but concluded that the bearing-capacity factor for geotextile-reinforced unpaved roads appears to be unconservative for the conditions of the full-scale field study analyzed. Lastly, the authors proposed a temporary bearing-capacity factor for the use of a geogrid and geotextile combination.

Hufenus et al. (2006)

Hufenus et al. (2006) conducted a full-scale field study to evaluate subgrade stabilization with geosynthetics on unpaved roads in Dissenhofen, Switzerland. Fourteen test sections (2 of which were controls, one with a separator and one without) measuring 8 m in length were constructed. The main purpose of the field study was to investigate how the geosynthetics affected the bearing capacity of the test sections. The subgrade

was classified as a medium-plasticity silty clay. The CBR strength values along the test site varied from about 0.5 to greater than 12 because of the differences in the in-situ soil. Three lifts of base course layers were used, each 20 cm thick after compaction. The first two layers consisted of particle sizes from 8 to 64 mm of crushed concrete and brickwork scrap. The third layer was classified as a GP (poorly graded sandy gravel) with particle sizes as large as 32 mm. The main function of the third and final layer of base course was to improve the density of the base course and to increase interlocking of the material by minimizing the particle movement in the voids while trafficking.

Seven different geosynthetics were used to represent the various types of reinforcement, and three weaker materials, a nonwoven separating geotextile (field V1) and two woven slit tape geotextile (fields 1 and 10), were also included. The geosynthetics used are listed in Table 3.

Table 3: Geosynthetic Properties Used in Field Study
(modified after Hufenus et al., 2006).

Field	Type of geosynthetic	Apertures (mm)	Tensile strength at (kN/m)			
			2%		5%	
			MD	XMD	MD	XMD
1	PP slit tape woven	-	2	2	8	8
2	PVC-coated knitted PET grid	20 x 20	9	9	14	14
3/4	PVC-coated knitted PVA grid	40 x 40	12	12	32	32
5/6	PET flat rib grid	32 x 32	10	10	20	20
7/8	Biaxial extruded PP grid	65 x 65	11	12	22	25
9	Biaxial extruded PP grid in 5 layers	60 x 60	6	10	14	20
10	PP slit tape woven	-	12	12	30	30
11	PET yarn reinforced PP nonwoven	8.5 x 8.5	7.5	7.5	22	22
12	PP nonwoven (reinforcement)	-	0.4	0.3	0.6	0.4
V1	PP nonwoven (separation)	-	0.2	0.1	0.3	0.2

The geosynthetics were instrumented with strain gages to measure short and long-term strain, and the ongoing formation of ruts was assessed from profile measurements using a cross-bar device designed for the project with an accuracy of ±5 mm. The test sections were trafficked after each base course layer. After the first layer of base aggregate was placed and compacted with a 25 kN static roller, it was trafficked. A three-axle truck was used for trafficking with a tire pressure of 8.5 bar, and additional weight was added to the truck to increase the load throughout trafficking. The first layer was trafficked with a truck weight of 130 kN. A second layer of base aggregate was then placed and compacted with a 80 kN vibratory roller. The second layer was trafficked for 10 passes with a truck weight of 220 kN, and then for 10 passes at 280 kN. The third and final base course layer was also placed and compacted with a 80 kN vibratory roller, and trafficked with a truck weight of 280 kN for 61 passes. Measurements were taken throughout trafficking to relate the performance of the geosynthetics.

The static strain measurements beneath the right wheel track showed that the strain deformation of the geosynthetics during compaction and trafficking was below 1% as illustrated in Figure 9.

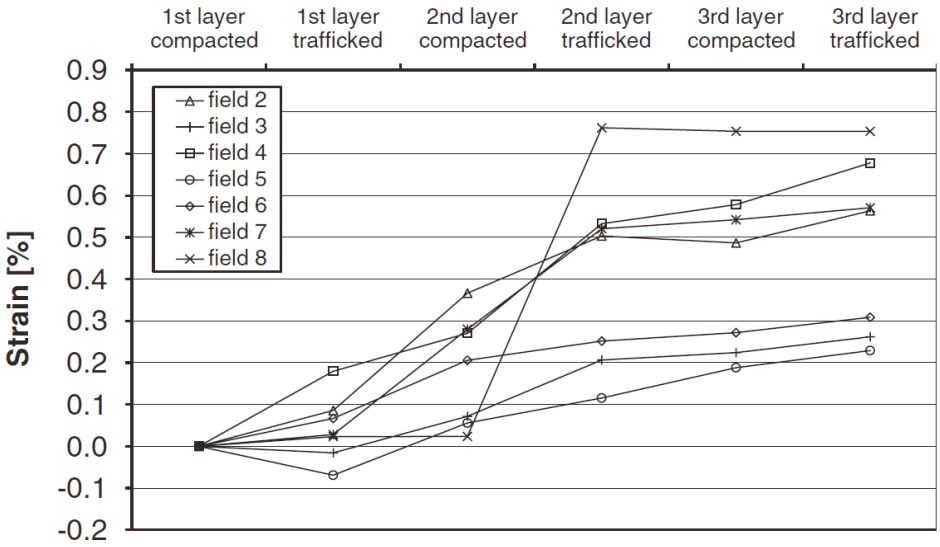


Figure 9: Strain of geosynthetics during compaction and trafficking (after Hufenus et al., 2006).

Based on CBR and static plate load tests, the authors concluded that a significant improvement in the bearing capacity of the fill layers reinforced by geosynthetics was found to be true only for thin layers ($h \leq 0.5$ m) on very weak subgrade (CBR ≤ 2); however, reinforcement is effective for CBR ≤ 3 when $h \leq 0.5$ m. Analysis of the results showed that the use of stiffer geosynthetics under strains of 1 to 3% increased the bearing capacity and compactability of a fill layer on soft ground and that geosynthetic tensile strength requirements at 2% strain, both in longitudinal and transverse directions, should be greater than or equal to 8 kN/m. The additional mobilized permanent strength, which results from installation and loading of layers 2 and 3, is listed in Table 4.

Table 4: Approximate Tensile Strength Induced by Fill Installation and Loading (modified after Hufenus et al., 2006)

Field	Subgrade	Geosynthetic	Nonwoven Underlay	Additionally Mobilized Permanent Strength (kN/m)		Permanent Strength (kN/m)	Maximum Strength (kN/m)
				2nd Layer	3rd Layer		
2, 3	Relatively firm	Knitted grid	With	3	1	7	11
4	Soft	Knitted grid	Without	6	3	9	17
5/6	Soft	Flat rib grid	Without/With	1	1	5	9
7	Soft	Extruded grid	Without	3	1	6	10
8	Soft	Extruded grid	With	8	1	10	18

The results show that the effectiveness of geogrids was reduced when used in direct combination with a separating layer because the separating layer prevented optimal interlocking with the geogrid and the reduced friction between the two materials caused them to slide with respect to one another. Thus, it was recommended that to prevent mixing between the subsoil and the fill material, a separating layer should still be used, but the geogrid should be laid 5 cm above it within the granular layer, to improve both shear interaction and the bearing capacity. The authors concluded that the base course layer can be reduced by about 30% for their specified compaction values and bearing capacities, although they recommend a minimum fill thickness of 30 cm. Lastly, the performance of the test sections showed that geosynthetics helped reduce rut formations as a function of trafficking, which increased the service life of the road.

Cuelho and Perkins (2009)

Cuelho and Perkins (2009) conducted a full-scale field study using geosynthetics for subgrade stabilization on an unpaved road. The field study consisted of 12 test sections and was constructed at TRANSCEND, a large scale transportation research facility

located in Lewistown, Montana. By conducting the research project at TRANSCEND, three important aspects of construction were able to be controlled: 1) the strength of the roadbed subgrade, 2) the cross-sectional design of the road, and 3) traffic.

Construction of the test sections involved excavating a trench 4 m wide by 1 m deep, and then lining the trench with plastic sheeting. A weak subgrade was purchased, hauled to the test site, and prepared to a CBR target strength of 1.70. The base course aggregate was prepared and compacted in a single 20 cm lift.

Ten of the 12 test sections were constructed using geosynthetics, and the remaining two test sections were controls which had no geosynthetics. A three-axle fully loaded dump truck weighing approximately 205 kN, with a tire pressure of 690 kPa, was used to traffic the test sections. Failure of the test sections was defined as 100 mm of elevation rut measured using surveying equipment, which occurred for all test sections within 40 truck passes.

Using data from linear variable differential transformers (LVDTs), transverse strain in the geosynthetics was determined at a single location within each test section. The dynamic strains during trafficking were relatively small (about 2%). On average, static strain measurements were around 3 to 5% in most materials, but greatest in the nonwoven geotextile which had over 14% strain. From the results, the authors observed that tensile stiffness appears to be the most pertinent geosynthetic material property when used in subgrade stabilization. Their study indicated that tensile strength at 2% axial strain correlated to performance for the majority of the geosynthetics used as illustrated

in Figure 10, where N_{add} is the additional number of truck passes that reinforced test sections had compared to control test sections which had no geosynthetic reinforcement.

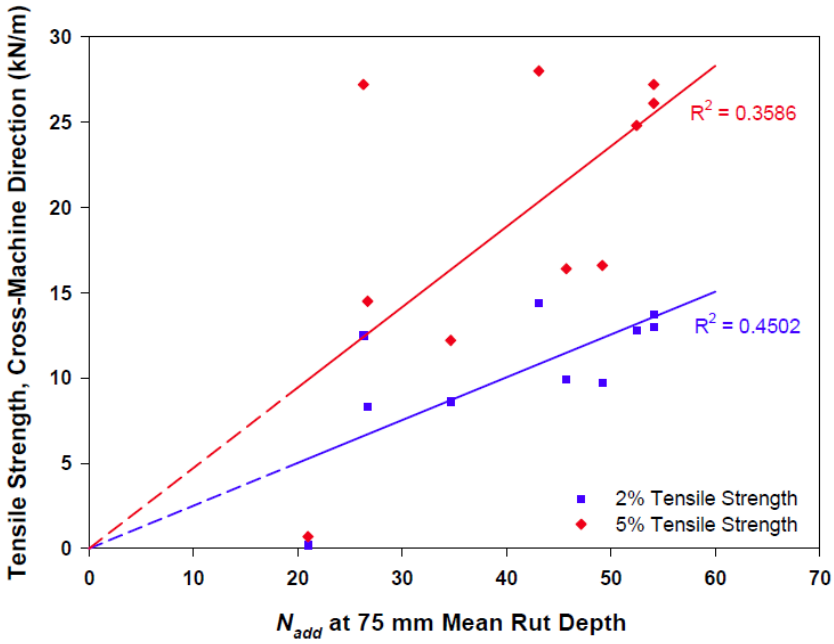


Figure 10: Relationship between geosynthetic tensile strength in XMD and N_{add} at 75 mm of mean rut depth (after Cuelho and Perkins, 2009).

The geotechnical design methods (FHWA, 1995; Giroud and Han, 2004; Steward et al., 1977) all underestimated the necessary base course thickness which lead to a maximum of 40 truck passes until all of the test sections failed. The authors designed the test sections, based on the design methods, to last 455 design truck passes for the geosynthetic-stabilized sections. This means that it took about 8% of the designed truck passes to fail all of the test sections.

From their field study, the authors observed, using LVDT displacement measurements, that initially the wheel loads pushed the geosynthetic away from the side of the vehicle toward the outer edge of the test sections (i.e., lateral confinement). As the

rut bowl began to form, the LVDT measurements showed that the geosynthetic began to move in the opposite direction (i.e., toward the rutted area). Therefore, using these displacement measurements, it was possible to measure movements and observe the geosynthetics shift from lateral restraint as the primary reinforcement mechanism to membrane support.

Instrumentation and Equipment

The instrumentation and equipment reviewed focused on strain gages, photogrammetry, and LVDTs. Strain gage installation procedures on geosynthetics, survivability rates in field applications, and calibration procedures will be discussed, with an emphasis on calibration procedures involving photogrammetry. Lastly, LVDT installation procedures on geosynthetics will be presented.

Strain Gage

Since 1982, bonded resistance strain gages have been used to quantify the strain response of geosynthetics (Brooks, 2009; Perkins et al., 1997; Sluimer and Risseeuw, 1982; Warren et al., 2010; Warren and Howard, 2007). Strain gages are well-suited to measure strain because they are bonded directly to the material being tested and provide a direct measurement of strain. Strain gages have been used to measure strain in a variety of materials and special methods have been developed over the past three decades to effectively use strain gages on geosynthetics.

To ensure accuracy in measurements, the strain gages must be calibrated against the true global strain in the geosynthetic. In addition, if strain gages are to be installed in

a field application, the use of environmental protection is needed. It is recommended to calibrate the strain gages with their environmental protection because some types of environmental protection may stiffen the gage location and affect the strain gage readings (Oglesby et al., 1992; Perkins and Lapeyre, 1997).

The calibration factor for a particular combination of gage, bonding technique, reinforcement type, and location of gage is typically established from constant-rate-of-strain, wide-width tensile testing (Bathurst et al., 2002). Warren et al. (2010) discuss calibrating strain gages using two digital single-lens reflex (SLR) cameras and image processing software. The authors used Micro-Measurements strain gages EP-08-19CDZ-350 for geotextiles and EP-08-230DS-120 for geogrids. In an earlier publication by Warren and Howard (2007), sensor selection, installation, and survivability was discussed with respect to a full-scale field study constructed in 2005. To better protect the strain gages, the authors placed a neoprene pad over the gage locations on the geotextiles and a piece of strip drain over the gage locations on the geogrids, which resulted in approximately 81% of the gages surviving the construction phase. However, because the trafficking occurred during an uncharacteristically dry season, the subgrade was stronger than anticipated and the strain gages did not show any appreciable strain.

To calibrate their strain gages, Warren and Howard performed monotonic wide-width tensile tests on instrumented geosynthetic samples. The local strains were determined using images from a camera focused on the strain gage, and global strains and slippage were determined using images from a second camera focused on the entire sample; however, results from their testing indicated that slippage did not occur

throughout the testing. Output from the strain gage was plotted with respect to the strain determined by the camera, and a linear calibration equation was obtained to convert the raw field data in voltage to strain. The calibration factors were determined by dividing the global strains by the local strains. illustrates the calibration and wide-width tensile results for a woven geotextile, and the calibration results for a punched/drawn geogrid.

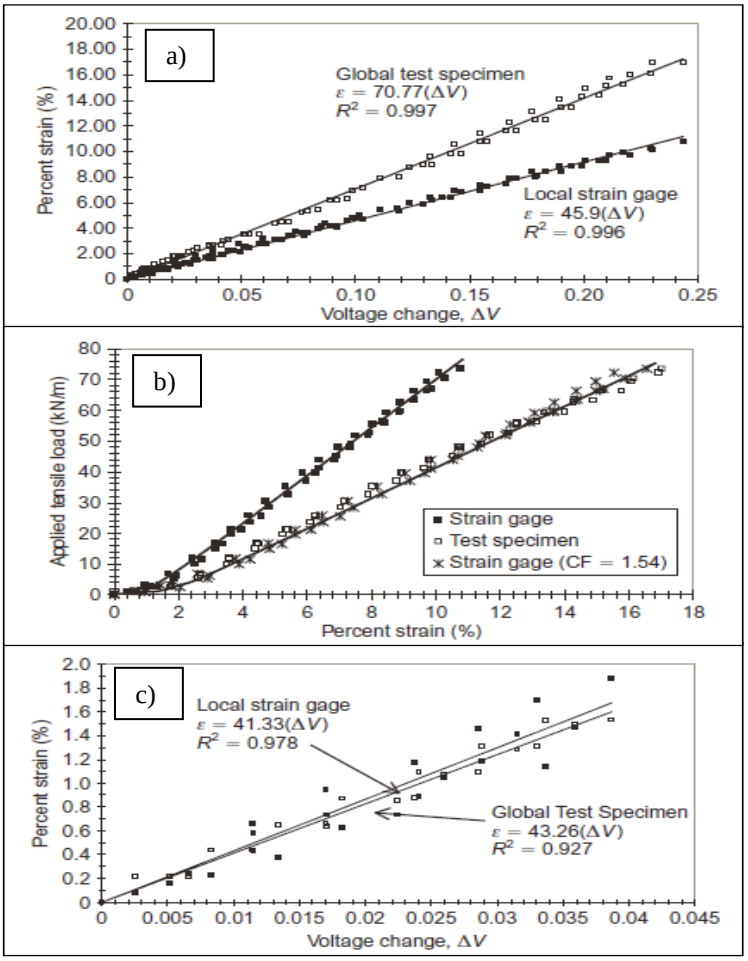


Figure 11: a) calibration results of a woven geotextile, b) wide-width tensile test results of a woven geotextile, c) calibration results for punched/drawn geogrid (after Warren and Howard, 2010).

The authors placed gages on one side of the geosynthetic, which is appropriate because local bending is generally negligible in uniaxial tension tests (Perkins et al., 1997); however, the strain gages were not calibrated with environmental protection, which may affect the strain readings. Further, the authors calibrated the strain gages in uniaxial tension, but used them in a cyclic manner. To assess the response of strain gages used in field applications, it is necessary to duplicate the types of loads anticipated in the field, in the laboratory (Perkins and Lapeyre, 1997).

Perkins et al. (1997) analyzed resistance strain gages on a polymeric geogrid material. The authors evaluated methods of gage installation, calibration, and field performance. Their work showed that strain gages were suitable for relatively short-term dynamic measurements, but performed poorly in long-term static measurements. The strain gages used were Kyowa high elongation KFE-5-120-C1 (manufactured by Soltec Corporation, San Fernando, California). The poor performance of long-term static measurements was assumed to be due to drift of the gages. The authors tested samples in the laboratory with strain gages on both sides of the geosynthetic, and also with strain gages on only one side. The tests yielded similar results which imply that local bending was not a significant factor in uniaxial tension tests. Because the geogrid used in the tests was very stiff, it was concluded that potential stiffening due to the bonding adhesive used for the strain gage was not significant. The authors also tested an instrumented geogrid in cyclic tension. From their results, it was concluded that the calibration of strain gages to match a global response depends on the load application anticipated. Figure 12 presents

their results in cyclic tension with a calibration factor of 1.6, and Figure 13 presents a single cyclic load applied with no calibration factor necessary.

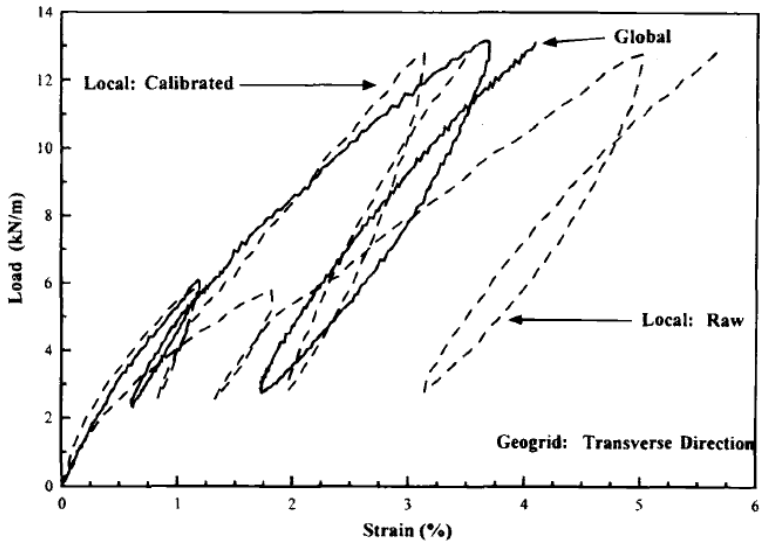


Figure 12: Global and local response of geogrid (after Perkins et al., 1997).

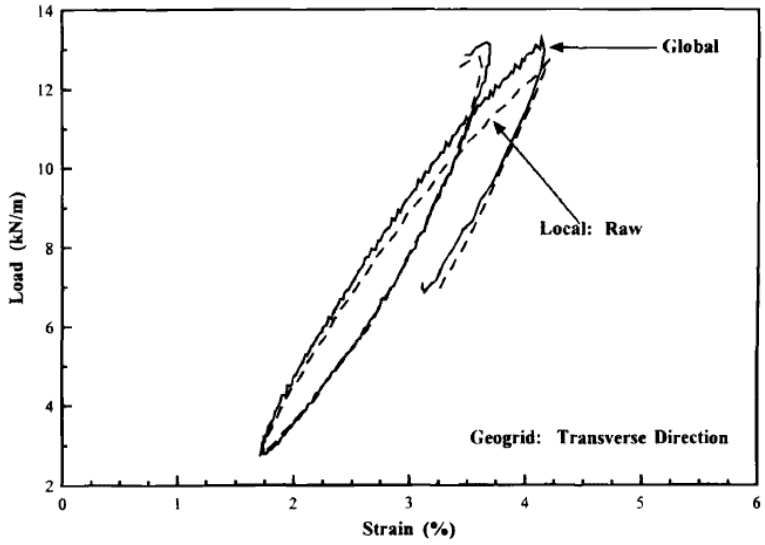


Figure 13: Global and local response of geogrid in an unloading-reloading cycle (after Perkins et al., 1997).

Perkins and Lapeyre (1997) also published a paper on in-isolation strain measurement of geosynthetics. The paper focused on a comparison of vibrating wire displacement gages, vibrating wire strain gages, linear variable differential transformers, and bonded resistance foil strain gages. The results from their experiments revealed that environmental protection provides some stiffening to the area of the gage, or acts to distribute the strain around the area of the gage, and that under-registration of gages generally increases with global strain level.

Derakhshandeh and Chou (1990) reported on the use of geosynthetics in landfills. The authors installed 41 strain gages onto four different geosynthetics, and calibrated the strain gages using calibration curves from laboratory testing. Their results indicated that the stress-strain relationships could be obtained only based on the assumption that the stiffness of the geogrids and the strain gages were equivalent (that is, had a calibration factor of 1.0). The strain gages were calibrated in uniaxial tension, and the gages used were CP-08-250BG-120, EA-06-031DE-120, and EA-06-500BH-120 (manufactured by Micro-Measurements, Denver, Colorado). The authors reported that out of the 41 strain gages installed, 40 were in good working condition after 9 months in the field, and that the strains registered throughout the project's duration were from -0.3 to 0.9%.

Short-term strain and deformation behavior of geosynthetic walls was analyzed using strain gages by Bathurst et al. (2002). Their paper showed that properly calibrated strain gages were useful to estimate reinforcement strains at low strain levels (0.02 to 2%), and that the strain gages must be calibrated against the "true" global strain in the reinforcement because strain gages bonded to woven geogrids or geotextiles typically

generate a local hard spot causing under-registration of global tensile strains. Similar to Perkins and Lapeyre (1997), Bathurst et al. (2002) concluded that, in general, under-registration of strain gages increases with global strain level. The bonded strain gages used in the field typically gave a nonlinear response or failed at strains greater than 3%, and the authors concluded that, based on their instrumentation used, extensometers provided the only practical means of estimating reinforcement strains at large strain levels. At lower strain levels (0.2 to 1%), the coefficient of variation (COV) for extensometers was between 29 to 56%, whereas for strain gages it was around 13 to 14%. Note that the COV values were based on a 95% prediction level by comparing the average strain of two strain gages to each individual strain gage's strain. The COV was calculated as the standard deviation of the ratio of gage strain to average strain divided by the mean of the ratio of gage strain to average strain. This procedure is illustrated for strain gages in Figure 14. The authors concluded that at low strains (0.02 to 2%), strain gages provided accurate estimates, and at large strains (greater than 2%), extensometers provided more reliable estimates because the COV improves to approximately 9% at strains greater than 2%.

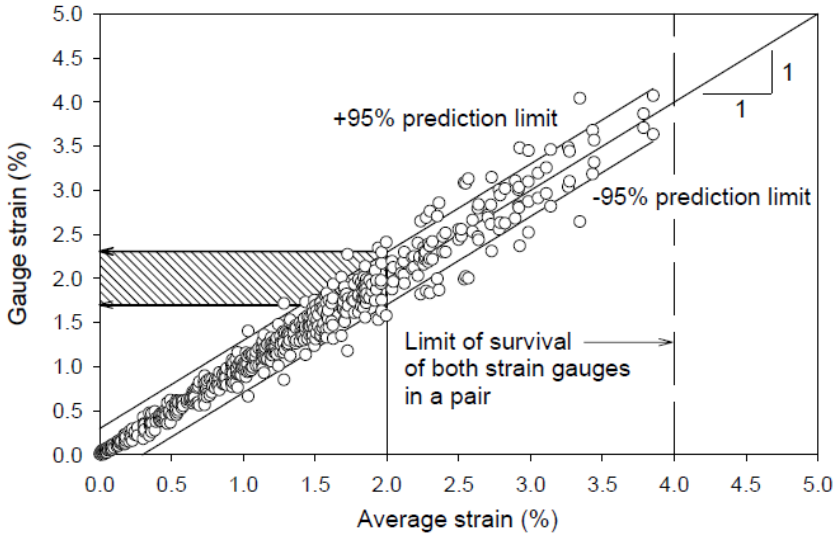


Figure 14: Coefficient of variation for strain gages (after Bathurst et al., 2002).

In his master's thesis, Cuelho (1998) discussed procedures for installing and testing strain gages. The author used EP-08-500GB-120 gages for the geogrids and EP-08-40CBY-120 gages for geotextiles (manufactured by Micro-Measurements, Raleigh, North Carolina), and thoroughly documented the installation procedures of the strain gages. The results from the strain gages were compared to strains calculated using extensometers. The strain gages that were subjected to cyclic loading tended to slightly overestimate the strain in the geogrids. Strain gages bonded to the geotextiles had less consistent results, particularly at higher strains, which is likely due to the adhesive/sealant lacking the necessary stiffness to transfer strain through its thickness from the geotextile into the strain gage. Similar to Cuelho (1998), Brooks (2009) and Oglesby et al. (1992) also thoroughly documented procedures for installing strain gages on geosynthetics.

Oglesby et al. (1992) attached strain gages to geogrids for high elongation measurements. The authors used EP-08-250BG-120 strain gages (manufactured by Micro-Measurements) and recommended bonding the strain gages with Micro-

Measurement's M-Bond A-12 high elongation epoxy. 120-ohm gages were selected because they have higher elongation capabilities (i.e., the higher the strain gage's resistance is, the lower its elongation limit typically is). Practical and repeatable procedures were described, and an extensive lab study was performed to determine the effects of submergence in water on the strain gage readings. The authors concluded that water submergence was not an issue for high-density polyethylene (HDPE) geogrids. However, based on their observations, it was concluded that the strain gage readings on the woven PVC coated polyester geogrid were affected by submergence and that further research was needed to investigate the feasibility of protecting the gage from the effects of water.

The two geogrids analyzed in their study were tested in uniaxial extension tests at 1% strain per minute. The integrally formed HDPE geogrid had a near linear relationship between the strain gage and crosshead strain up to approximately 10% crosshead strain (at which the gage strain was approximately 7.5%). The woven PVC coated polyester geogrid had a near linear relationship up to approximately 15% crosshead strain (at which the gage strain was approximately 11%). The authors tested the HDPE geogrid with and without protective coating, and the results showed that the ratio of strain gage reading to overall strain was 0.7 with protective coating and 0.8 without. Thus, the authors concluded that protective coatings applied to the strain gage affect its readings.

The reliability of strain gages in geogrid reinforcement was analyzed by Gnanendran and Selvadurai (2001). Their study indicated that strain gages installed on the top and bottom of geogrids provide more reliable results because they minimize the

influence from bending. The strain gages used were Showa N11-FA-5-120-11 foil strain gages. The strain gages were installed on a stiff geogrid and were calibrated in-air using weights carefully applied to the geogrid. Approximately 1 kN of force was added to the geogrid specimen which was 74 cm long by 87 cm wide, and the calibration factors were determined from the elongation that the geosynthetic experienced under the applied hanging weight. It is important to note that the applied weight results in a strain of roughly less than or equal to 0.25%, and that while their method provided reasonable results and conclusive evidence that local bending affects strain measurements, the validity of their calibration at higher strain values is unknown.

Hufenus et al. (2006) had unprecedented strain gage survivability rates in a full-scale field study on a geosynthetic reinforced unpaved road on soft subgrade. 32 strain gages were installed with no failures throughout their field study due to the protective measures taken, which consisted of applying a kneadable putty to the strain gage and surrounding area, and loosely attaching a rubber foil around the strain gage for additional protection without hindering the strain gage's elongation. The kneadable putty adheres to nearly every material and is called AK 22 (manufactured by Hottinger Baldwin Messtechnik GmbH, Darmstadt, Germany). The putty is an adhesive compound which is supplied ready for use and gives effective protection immediately after application. The putty does not contain any solvents, cannot dry out, and is resistant to aging (Messtechnik-GmbH, 2008). However, caution should be asserted regarding AK 22 because the putty is directly applied on top of the strain gage, is only fully waterproof for about 100 days, and may alter the strain measurement readings.

The strain gages were calibrated using one gage on top of the geosynthetic under using wide-width tensile (uniaxial) testing at a constant rate of 3 mm/min. In their field study, the loading conditions were cyclic and strain gages were only installed on top of the geosynthetics, even though considerable rut formation occurred while trafficking. The gages used in their study consisted of foil strain gages with a constantan grid on a polyimide film. The authors designed for a maximum of 5% strain in the geosynthetics, but had less than 3% strain in their field study.

Cuelho et al. (2008) described the use of strain gages to make monotonic and cyclic measurements. The authors provided guidelines and emphasized the importance of selecting the appropriate strain gage, proper installation, installing gages on both sides of the geosynthetic to mitigate bending effects, and the need to calibrate the gages in a laboratory. Monotonic and cyclic calibration tensile tests were performed with strain gages and LVDTs attached to the geosynthetic. The monotonic tensile tests were run at a constant load rate of 2 mm per minute. The correlations between the strain gages and the LVDTs on the geogrid were excellent and repeatable. Strain gages installed on geotextile showed larger differences, with the strain gage providing an under-registration of strain above 2%. The primary reason for the difference is because at higher strain levels the bedding material used to bond the stain gage to the geosynthetic lacked the necessary stiffness to transfer strain through its thickness from the geosynthetic into the gage. The monotonic tensile test results are shown in Figure 15.

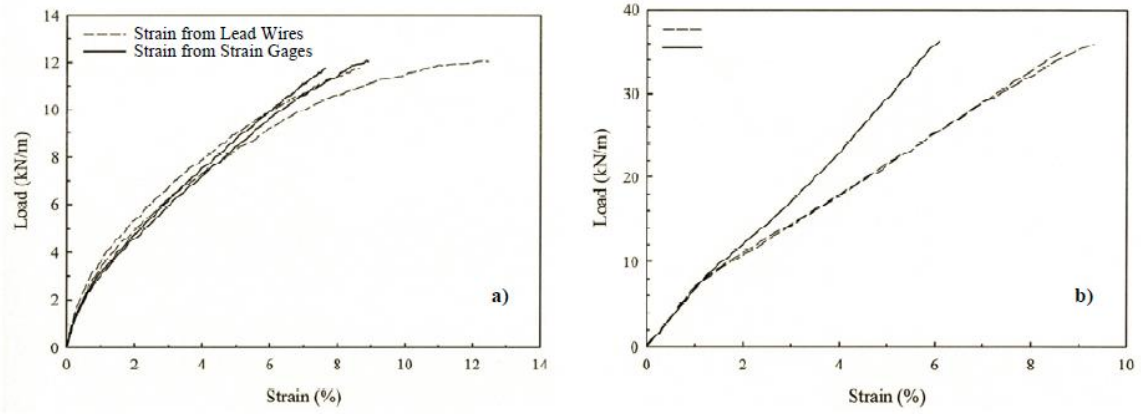


Figure 15: Results from monotonic, in-air tension tests on a) a geogrid, and b) a geotextile (after Cuelho et al., 2008).

The cyclic tensile tests performed by Cuelho et al. (2008) showed similar results. The tests were conducted by applying 14 individual load pulses to the material in relatively rapid succession at incrementally increasing load levels as shown in Figure 16. Both the geogrid and geotextile materials exhibited greater stiffness under cyclic loads when compared to slow monotonic loads, which is mainly due to kinematic loading effects inherent with plastics. The strain gage readings were nearly identical to the LVDT readings for strains under approximately 1.5%; however, as was the case in the monotonic tensile tests, above 2% strain the strain gages under-estimated the strain in the geotextile.

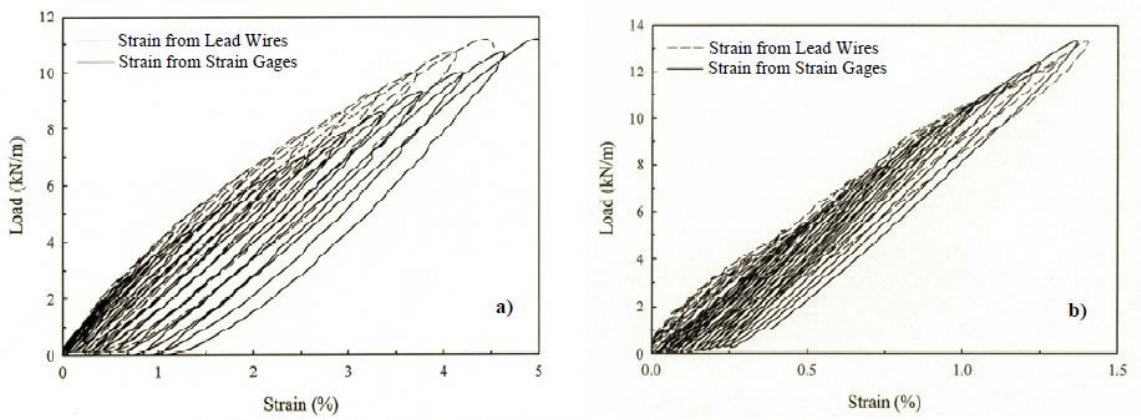


Figure 16: Results from cyclic tension tests on a) a geogrid, and b) a geotextile (after Cuelho et al., 2008).

The initial results from a full-scale field study near Virginia Polytechnic Institute and State University were published by Brandon et al. (1996). The authors installed N2A-06-40CBY-120 (manufactured by Micro-Measurements) foil strain gages on geogrid test sections, and FLK-6-1L (manufactured by Texas Measurements) on geotextile test sections. The strain gages were only mounted on the bottom of the geosynthetics and were protected by digging out a small hole beneath the strain gage location and filling it with fine sand. Unfortunately, wet conditions during testing decreased the strain gage survivability. Strain gages do not operate properly when wet, and infiltration of water past the protective coating is one of the main reasons why strain gages stop working in wet conditions. Eight months after the geosynthetics were installation in the field, only 5 out of 18 (28%) of the geogrid strain gages were still functional, and only 1 out of 18 (6%) of the geotextile strain gages were still functional.

The authors calibrated the strain gages using the calibration factors provided by the manufacturer. The calibration factors were verified through tensile strength testing

(presumably uniaxial) of instrumented geosynthetic samples; however, the loading conditions experienced in the field were cyclic.

These studies illustrate the measurement of strain in geosynthetics using bonded resistance strain gages. The studies emphasize the need for calibrating strain gages on geosynthetics, potential difficulties of applying strain gages on geosynthetics, the use of strain gages in field applications, and special precautions regarding protection of strain gages on geosynthetics.

Photogrammetry

There are many methods and techniques for measuring strain and calibrating strain gages on geosynthetics. The methods discussed here include video-extensometer and digital images. The first reported use of a video-extensometer for measuring geosynthetic strain was performed by Shinoda and Bathurst (2004). The authors performed wide-width strip tensile loading under constant rate-of-strain, constant load (creep), and stress relaxation load paths. On the geosynthetics tested, small targets were painted on the surface, and these targets were tracked using a commercially available charge-coupled device camera with ancillary hardware and software. The authors had consistent and repeatable results, and estimated the accuracy of the video-extensometer technique as approximately ±0.005%, ±0.01%, and ±0.02% of the measured strain value for strain levels of 10%, 20%, and 30%, respectively.

Thomas and Cantré (2009) presented the use of low-budget photogrammetry for measurements requiring high accuracy. The authors discuss two studies at the University of Rostock (Rostock, Germany), with an emphasis on three-dimensional measurements.

The authors describe adjustments that can be made to most digital cameras that increase the quality of images; however, Australis 5.07 and 6.0 (made by Photometrix, Victoria, Australia) was used to calculate displacements and strains. Australis is not a low-cost solution, but was readily available at the University of Rostock. The first study, which focused on analyzing a clay beam, had an accuracy of ±0.01%. For the second study, which focused on analyzing a geosynthetic tube, an accuracy of approximately ±0.002% was acquired.

Warren et al. (2010) describe the use of two digital single-lens reflex (SLR) cameras for calibrating strain gages on geosynthetics. The authors performed constant rate of strain wide-width tensile tests on various geosynthetic products. One camera was focused on the local strain gage area, and the other was focused on global displacement. The images were analyzed in National Instruments^{TM} Vision Development Module, an image processing software which has sub-pixel accuracy (down to 1/10th of a pixel). The images were used to compare strain from a strain gage to the strain calculated by the local camera. The procedure had reasonable accuracy (estimated based on at ±0.3% strain). To increase the accuracy, the authors evaluated each image three times, and used the average.

LVDT

Perkins and Lapeyre (1997) used linear variable differential transformers (LVDTs) to measure displacement on geotextiles and geogrids, and then used these measurements to calculate strain. The authors placed RDP Electronics (Pottstown, Pennsylvania) LVDTs with a range of ±5.1 mm and a sensitivity of ±0.015 mm, which

corresponds to a nominal strain range of ±10% and a sensitivity of ±0.03%. The gages were mounted to the geosynthetic using small rectangular mounting plates measuring 30 mm by 12 mm. The axis of the gage was approximately 14 mm above the surface of the geosynthetic specimen, while the length of the unclamped geosynthetic between the mounting plates was 39 mm, and the nominal gage length was 50 mm. This technique of applying LVDTs, while very effective in the lab, is not practical in field applications because the LVDTs would be destroyed by the base course.

Cuelho et al. (2008) discussed methods of using LVDTs for small strain and displacement measurements under monotonic and cyclic loading. The authors described leadwire requirements, how to attach the leadwire to geosynthetics, and how to run the leadwire to the LVDT sensors. The three main properties of the leadwire that the authors emphasize are: 1) should be stainless steel to prevent corrosion; 2) should have a "bright" finish to reduce friction; and 3) should have a spring temper so it does not easily kink.

To attach the leadwire to the geosynthetic, a small hole, slightly larger than the diameter of the leadwire, can be hand-drilled into the geosynthetic. For some geotextiles, the leadwire can be pushed or weaved through the material; however, depending on the material, an adhesive may be necessary to reduce local distortion when loaded. The adhesive should have stiffness properties similar to the geotextile. After the leadwire is through the geosynthetic, it is bent 180 degrees at its point of application, and is secured in place by a plastic coating tube such as that on 22 gauge solid core wire. An example of leadwire installation on a geotextile and geogrid is shown in Figure 17.

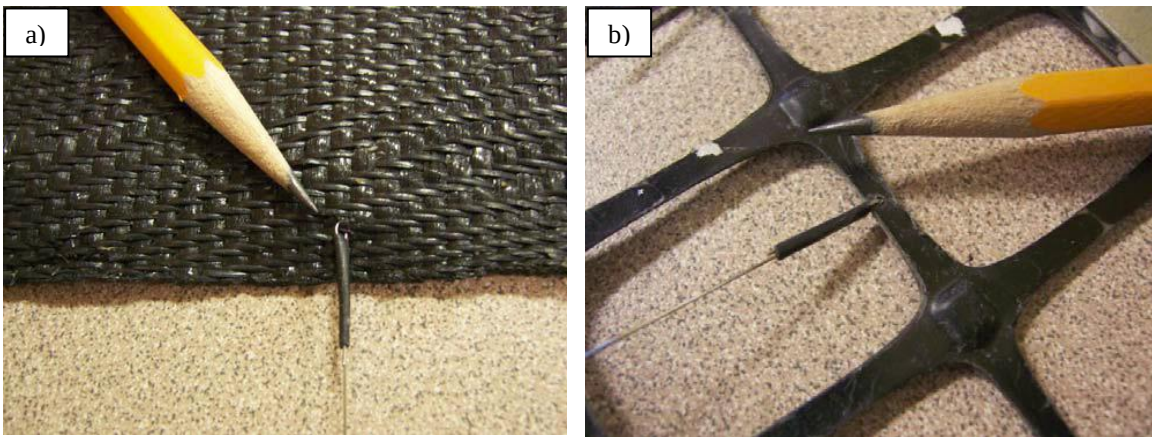


Figure 17: Leadwire connection onto a) a geotextile and b) a geogrid (after Cuelho et al., 2008).

The leadwire should then be threaded through protective tubing to protect it from soil which would restrict its ability to move freely. The protective tube should be sufficiently stiff (brass or PVC) to resist bending or crushing during loading, and should have an inner diameter of about 2 mm.

Brass tubing was used by Cuelho and Perkins (2009) to protect LVDT leadwires in a full-scale field study. The LVDT leadwires were run from the geosynthetic to a box outside the test section which housed the LVDT sensors, and the method described by Cuelho et al. (2008) was implemented. The authors were able to measure the dynamic and long-term static displacement of the geosynthetics throughout trafficking, and also calculated the dynamic and long-term static strain from the displacement measurements.

Summary

Subgrade stabilization using geosynthetics is recommended for soils having CBR values less than 3, where the geosynthetic is placed between the subgrade and base course. The main applications of subgrade stabilization are temporary roads, working

platforms, permanent roads, and unpaved roads. The primary reasons why geosynthetics decrease rutting is because they provide the base course with lateral restraint, increased bearing capacity, and/or membrane support of the wheel loads (Holtz et al., 2008).

The field studies that were reviewed focused on subgrade stabilization using geosynthetics on unpaved roads. The studies demonstrated that geosynthetics improve the bearing capacity of the subgrade and can reduce base course thickness by, in general, up to 30% with respect to rutting and/or bearing capacity. The geosynthetics provided the greatest subgrade stabilization benefit at base course thicknesses around 10 to 12 inches, and the benefit of using geosynthetics decreased with increasing base course thickness. The tensile strength of the geosynthetic at 2% strain is important because it acts to increase the contribution of a tensioned-membrane effect. The separation of the subgrade and base course can be very important in subgrade stabilization applications because the migration of subgrade through apertures of geogrids can result in a reduction of interlock between geogrids and can weaken the base course aggregate.

The measurement of the static and dynamic response of geosynthetics under vehicular loads is challenging. Strain gages and LVDTs are two types of instrumentation that have been used to characterize tensile behaviors and movement of geosynthetics in field applications with satisfactory results. Strain gages are particularly challenging due to each geosynthetic having its own unique structure and composition, stiffening effects from adhesives, and the harsh environments which the strain gages must endure. The strain gages primarily used on geosynthetics in high-strain environments, such as subgrade stabilization applications, are high-elongation gages with a polyimide backing.

The EP series gage by Micro-Measurements (Raleigh, North Carolina) is typically selected because the gage can accommodate large strain measurements.

Installation of strain gages on both sides of the geosynthetic can eliminate the strains induced by bending, and protection of strain gages is essential to increase the strain gage survivability in the field. In subgrade stabilization applications, strain gages should be mounted on the top and bottom of the geosynthetic, and to protect strain gages from damage due to compaction, trafficking, and water infiltration, adhesives or silicones are commonly used. Other methods have also been used to further protect the strain gages such as neoprene mats (e.g., mouse pads), PVC, wick drains, rubber foil (such as foil/butyl rubber tape), and sand layers. From the literature reviewed, neoprene mats and rubber foil seem to provide the best results (Brooks, 2009; Hufenus et al., 2006; Warren and Howard, 2007).

Strain gages should be calibrated according to their anticipated loads; however, from the literature reviewed, several authors calibrated their strain gages in uniaxial tension even though cyclic loading was anticipated. Perkins et al. (1997) determined that it was necessary to duplicate the types of loads anticipated in the field for proper calibration purposes. The use of environmental protection during calibration is also important to account for the effects it has on behavior (Oglesby et al., 1992; Perkins et al., 1997). Several publications reviewed, however, did not apply environmental protection to their strain gages when calibrating.

Photogrammetry is a relatively new method used in the laboratory to calibrate strain gages on geosynthetics in the laboratory. Video-extensometers provide excellent

information but are often cost prohibitive. Alternative options such as digital cameras are emerging as a new and affordable method for precision measurements, and the images taken by the digital cameras can be analyzed using low-cost or free software.

Linear variable differential transformers (LVDTs) are often used to measure geosynthetic displacement in the field, and from these measurements strain can be calculated. LVDTs are relatively simple to use and provide accurate displacement measurements on geosynthetics without affecting the behavior of the gaged area. Leadwires are often used to bring the point of measurement from the geosynthetic to the LVDT which is housed outside the testing area. The leadwire should be able to resist corrosion, have minimal frictional resistance, and have a spring temper (Cuelho et al., 2008).

Contribution to Body of Knowledge

The primary objectives of this thesis are to describe the transverse behavior of various geosynthetics when used for subgrade stabilization, and to provide insight into which material properties are most closely related to field performance. Analysis of data from displacement sensors, strain gages, and rut measurements were used to determine the behavior and field performance of 14 geosynthetic reinforced test sections and 3 control test sections. The material properties of the geosynthetics were characterized by their physical attributes (thickness, aperture size or apparent opening size), and their mechanical properties (wide-width tensile strength, cyclic tensile modulus, resilient interface shear stiffness, junction strength, and aperture stability modulus). Insight will be provided into which mechanical properties best estimate the field performance of

geosynthetics. Also, a detailed description of the instrumentation of strain gages and LVDTs, and calibration of strain gages will be described.

CHAPTER THREE

EXPERIMENTAL PROGRAM

Field Study

Fourteen reinforced test sections with various geosynthetics and three control test sections were constructed and trafficked during the summer of 2012. Three of the reinforced test sections had the same geosynthetic (BX Type 2) and varying subgrade strengths so that subgrade strength variations in all of the test sections could be corrected empirically. Similarly, Control Sections 1 to 3 had varying base course thicknesses so that differences in base course thicknesses between all of the test sections could be corrected empirically.

Measurements from instrumentation and transverse rut profiles were taken to analyze the transverse behavior of the geosynthetics, and the mechanical properties of the geosynthetics were compared with the field measurements and transverse rut profiles to determine the performance of the geosynthetics. Field measurements consisted of strain gages and linear variable differential transformers (LVDTs). The material properties of the geosynthetics were characterized by their physical attributes (thickness, aperture size or apparent opening size), and select mechanical properties (wide-width tensile strength, cyclic tensile modulus, resilient interface shear stiffness, junction strength, and aperture stability modulus).

Construction

Construction consisted of excavating a 3 ft deep by 16 ft wide by 860 ft long trench to build 17 test sections (14 with geosynthetics and 3 without). The trench bottom was leveled, compacted, and lined with plastic sheeting. A subgrade (hauled to the site) with known material properties was mixed with water to achieve the desired CBR strength of 1.70. The subgrade was placed and compacted in six lifts of about 6 inches thick each, and each lift was tested to ensure material uniformity. The subgrade was leveled after the last lift and pre-instrumented geosynthetics were placed and pulled taut to remove wrinkles and undulations in the material. The instrumentation was connected to the data acquisition circuitry and the base course aggregate was placed and compacted in approximately two 6-inch lifts for the geosynthetic reinforced test sections. The layout of the test sections is shown in Figure 18.

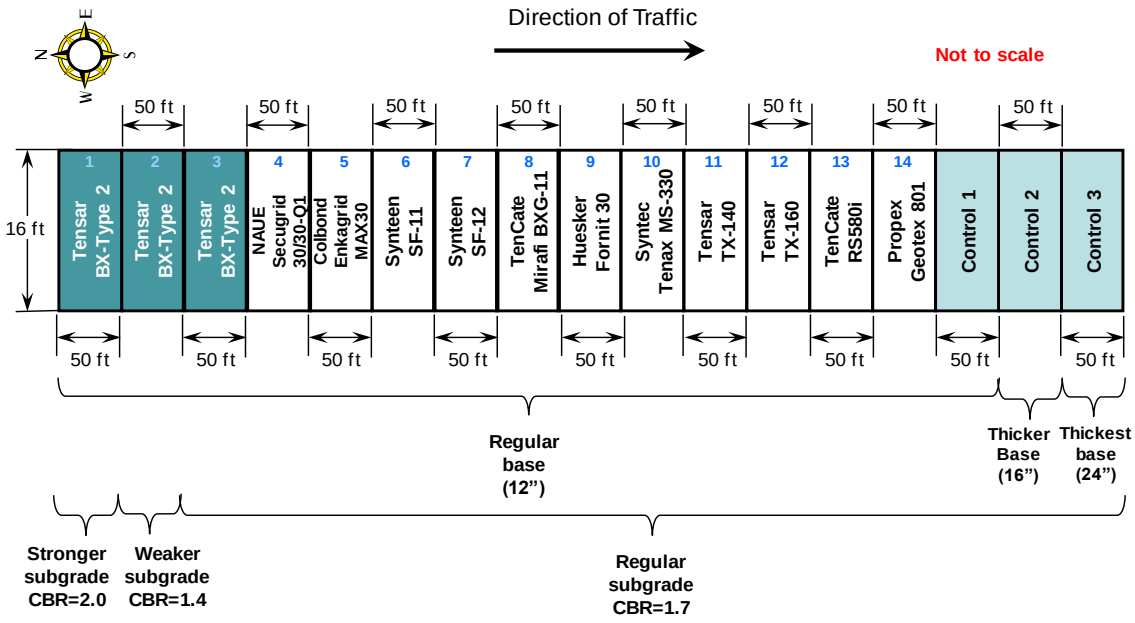
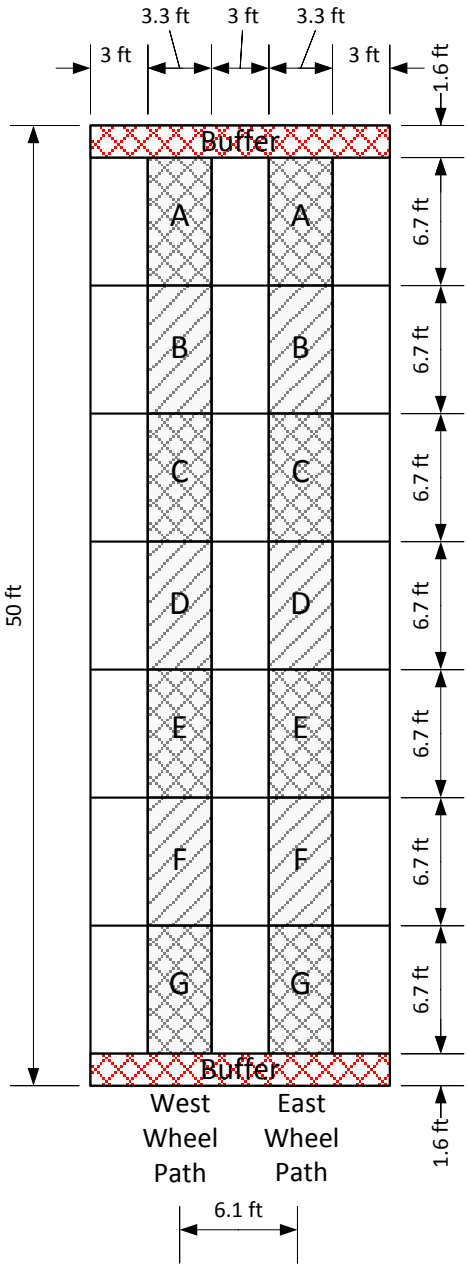


Figure 18: Design and layout of test sections.

Proper strength and consistency of the subgrade and base course was monitored during construction. Measurements were made using a hand-held vane shear, light weight deflectometer (LWD), nuclear densometer, dynamic cone penetrometer (DCP), in-field CBR, and water contents as illustrated in Figure 19. All of the testing was performed in the anticipated wheel paths to measure the subgrade strength and base course thickness. A robotic total station was used to survey the final elevation of the subgrade and base course. Longitudinal rutting from trafficking and transverse profiles of the two instrument locations ("C" and "E") in each test section were also measured using the robotic total station.

Subgrade

The subgrade soil was obtained from a nearby source, and consisted of natural overburden material that had been cleared and stockpiled to provide access to underlying gravel sources. The material was dried and screened to remove particles greater than one-inch in diameter and also to help blend the stockpile together to ensure uniformity. The subgrade was delivered to the test site and stockpiled adjacent to the excavated trench. The material properties and gradation of the subgrade are shown in Table 5 and Figure 20, respectively.



Subgrade			
Measurement Device	**Layers**	**Measurements per Layer**	**Location of Measurement**
Vane Shear	all	14	A,B,C,D,E,F,G
Light Weight Deflectometer	all	6	B,D,F
Dynamic Cone Penetrometer	final	6	A,D,G
In-Field CBR	final	2	D
Nuclear Density Gage	final	2	D

Base Course Aggregate			
Measurement Device	**Layers**	**Measurements per Layer**	**Location of Measurement**
Light Weight Deflectometer	first	12	B,D,F
Light Weight Deflectometer	final	6	B,D,F
Dynamic Cone Penetrometer	final	6	A,D,G
In-Field CBR	final	2	D
Nuclear Density Gage	final	2	D

Figure 19: In-situ testing plan.

Table 5: General Properties of Subgrade

Property	
Liquid Limit	34
Plastic Limit	17
Plasticity Index	17
% passing #200 sieve	55%
Max. dry unit weight†	112 lb/ft^3
Optimum moisture content†	16%

† using standard Proctor procedure (ASTM D698)

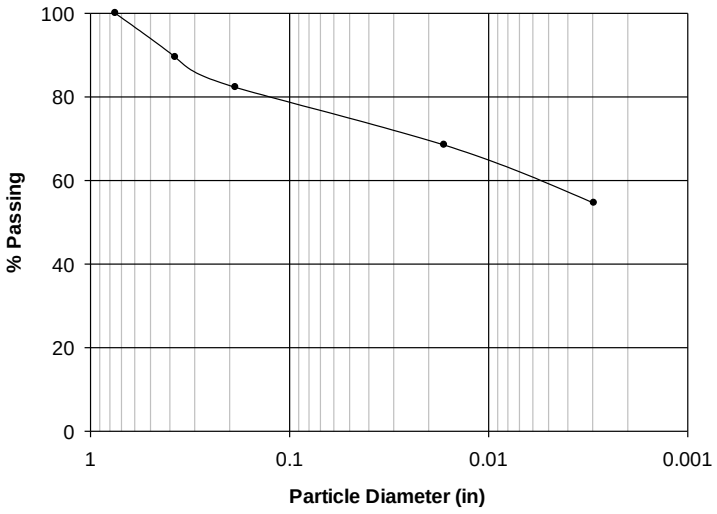


Figure 20: Grain-size distribution of subgrade.

Base Course

The base course aggregate was obtained from a nearby gravel pit and had material properties and gradation shown in Table 6 and Figure 21, respectively. The base aggregate was compacted using a vibratory roller to 95% of optimum dry unit weight based on the modified Proctor procedure.

Table 6: General Properties of Base Course Aggregate

Property	
Liquid Limit of fines	23
Plastic Limit of fines	15
Plasticity Index of fines	8
% passing #200 sieve	10%
Max. dry unit weight†	139 lb/ft^3
Optimum moisture content†	6.0%
% fractured faces	55%
CBR† (at ρ_{dry} = 140 lb/ft^3)	>100

† using modified Proctor procedure (ASTM D1557)

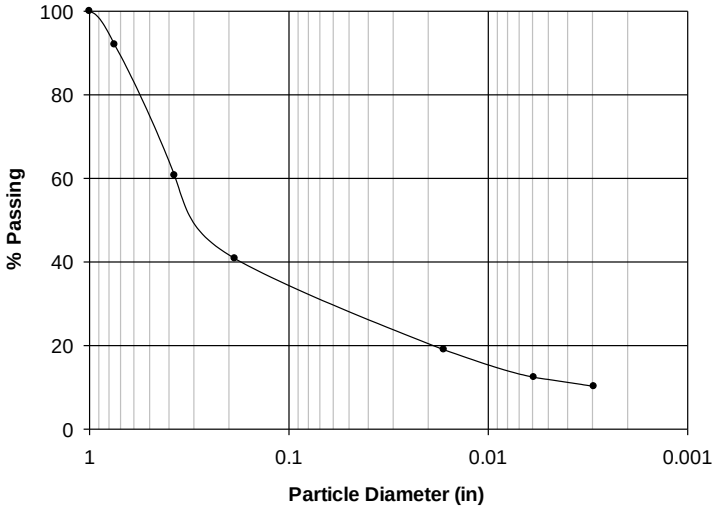


Figure 21: Grain-size distribution of base course aggregate.

Rut Measurements

Rut measurements were taken during trafficking along the two longitudinal wheel paths and two transverse instrumented locations in each test section. A robotic total station (Leica TPS1205+ series with a GRZ4 360° prism) was selected to measure rut, and had an accuracy of ±3.0 mm ±1.5 ppm (5 second accuracy in general). Measurements were taken periodically throughout trafficking to monitor the rut depth as

determined by elevation. Failure of the test sections was defined as when the rut reached 3 inches. Note that elevation rut is different than apparent rut, as illustrated in Figure 22, where heave is the difference between the two.

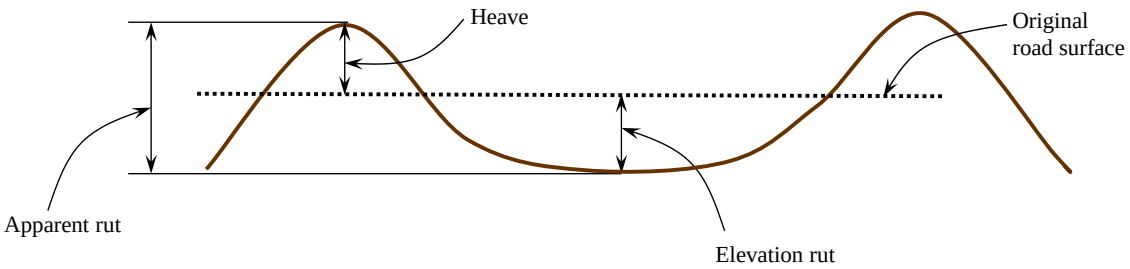


Figure 22: Elevation rut compared to apparent rut.

Data Acquisition and Instrumentation

Instrumentation measurements were recorded by two Campbell Scientific (Logan, Utah) CR9000X data loggers. Each CR9000X collected dynamic data from all of the instrumentation at 25 Hz. While 25 Hz produced satisfactory data, a faster sampling rate, such as at least 100 Hz as recommended by Pilson et al.(1995), is desirable. This faster sampling rate was not able to be acquired due to the high level of instrumentation in the project. Long-term static data was sampled every half hour throughout trafficking.

A picture of the mobile lab which housed the data loggers is shown in Figure 23. Note that the box in front of the mobile lab housed the LVDTs and pore water pressure sensors. Although pore water pressure sensors were part of the field study, they were not analyzed in this thesis.



Figure 23: Mobile lab.

Strain Gage Instrumentation. Strain gages were used to measure the local strain of the geosynthetics during trafficking. Strain gages were bonded directly to the geosynthetics to provide a direct measurement of local strain at two separate locations within each test section. The strain gages and other instrumentation were positioned near the outside of the wheel path on the west side of each test section as illustrated in Figure 24 and Figure 25.

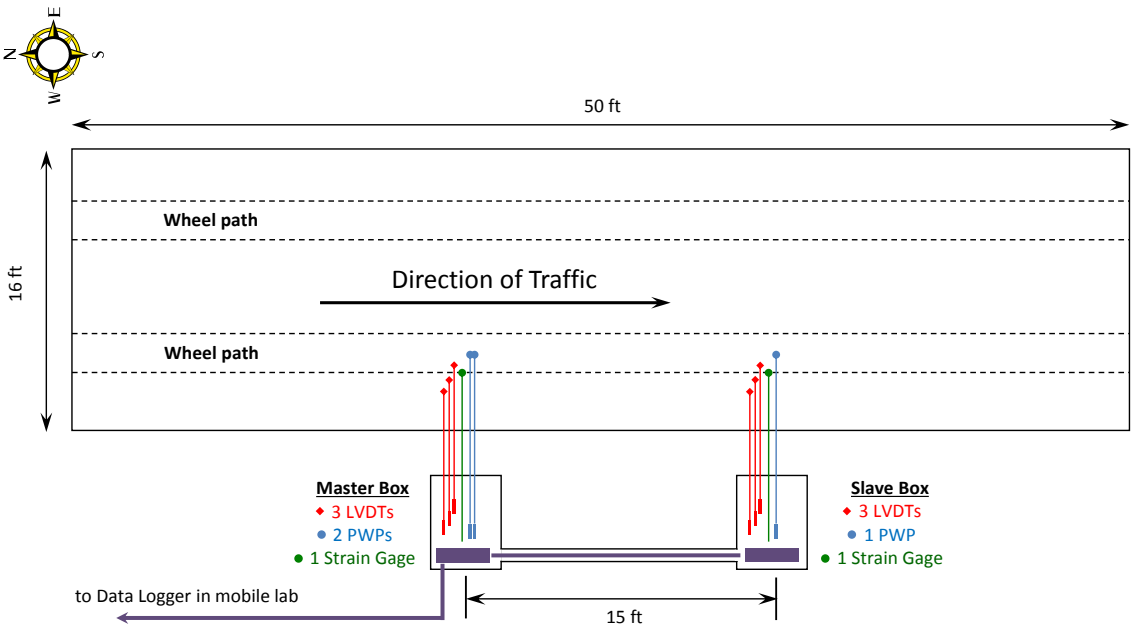


Figure 24: Instrumentation arrangement within a single test section.

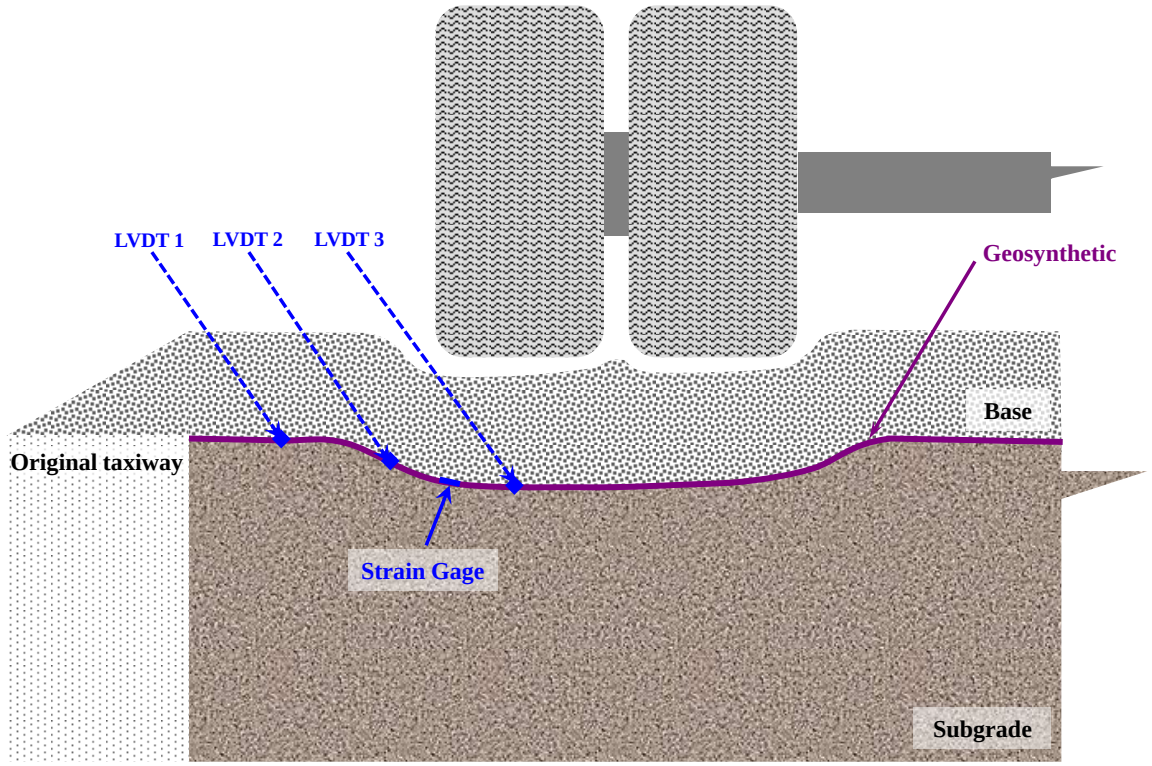


Figure 25: Location of strain gages and LVDT sensors.

Strain gage sizes were selected primarily based on their size in relation to the size of the elements they needed to be mounted on. The EP series of strain gage (Micro-Measurements, Raleigh, North Carolina) was selected because it accommodates large strain measurements (±20% in some cases). A detailed explanation of the strain gages, circuitry, and formulas used, as well as the strain gage instrumentation procedures is provided in Appendix A.

Instrumenting strain gages on geogrids consists of six main steps: 1) preparing the strain gages, 2) preparing the geogrid surface, 3) attaching the strain gages to the geosynthetic, 4) curing the adhesive, 5) attaching the leadwires, and 6) applying and curing the protective coating. The adhesive used was M-Bond A-12 (Micro-Measurements) because it accommodates high strains (±20% in some cases). Strain gaging took place in an enclosed building at the TRANSCEND research facility in Lewistown to minimize influences from wind, sun, water, and airborne contaminants.

Preparation of the strain gages consisted of attaching wires from the strain gage to bondable terminals. The reason for this step was to prevent potential forces transmitted along the leadwire from damaging the strain gage or affecting its performance during installation and trafficking. Examples of a typical setup of the gages with jumper wires attached are shown in Figure 26. Special solvents were used to clean the strain gages after this step to remove any foreign matter or solder residues prior to bonding.

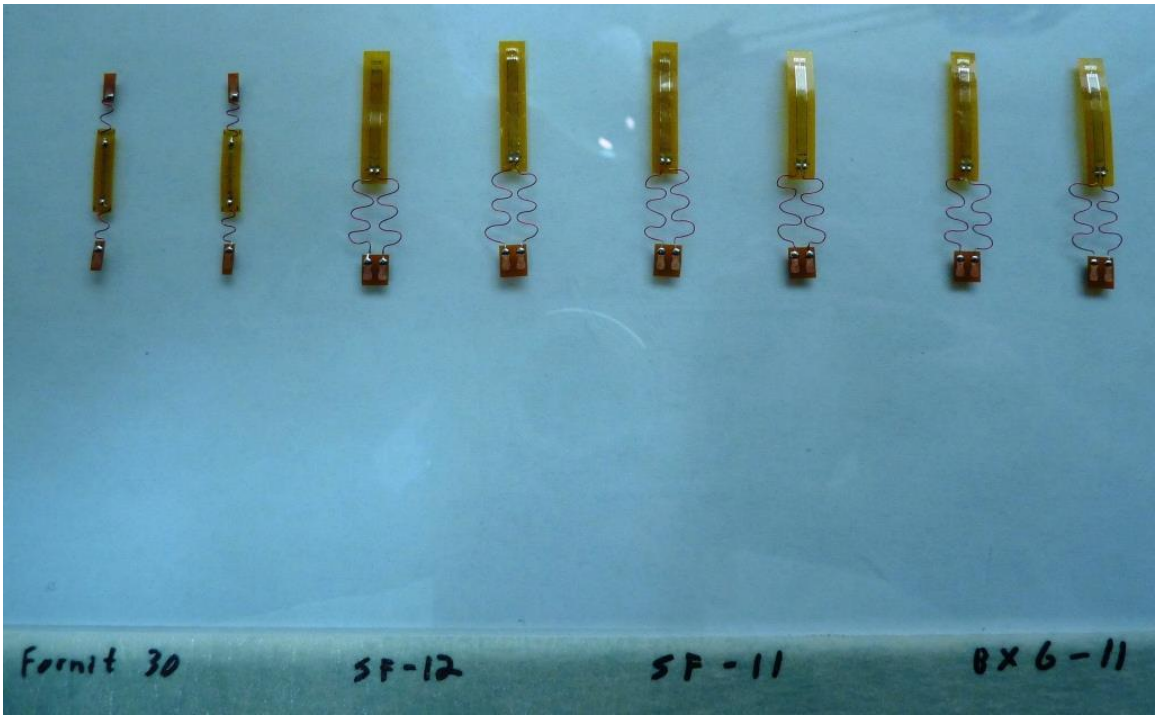


Figure 26: Jumper wires attached to strain gages.

The surface of the geogrid was thoroughly cleaned before applying the adhesive and attaching the strain gage. Preparation of the surface consists of degreasing the surface using a solvent, lightly abrading the surface with sandpaper, and applying chemical conditioning and neutralizing agents. For the woven geogrid products, the protective PVC or polymer coating, applied by the manufacturers to protect the woven grid structure, was removed prior to the cleaning and prepping process. The solvent degreaser removes oils, greases, organic contaminants, and soluble chemical residues. Abrading the surface removes any surface defects of the geogrid, and lightly roughens the surface to facilitate bonding of the adhesive. The conditioning and neutralizing solutions bring the surface to an optimum pH of 7.0 to 7.5.

The strain gages were positioned on the material, the adhesive was applied, and then pressure was applied to the gages to create an optimum bond. Two gages were attached to the material at a single location (one on the top of the geosynthetic and one on the bottom) to negate the effects of local bending of the gaged area. Strain gages were attached to the transverse ribs of the geogrids, or in the transverse direction of the geotextile to measure strain in the transverse direction during trafficking. Curing of the adhesive was achieved by elevating the temperature to 150 °F for 6 hours in the gage area. Excess glue was carefully removed using a dremel tool and the leadwires were attached. A strain gage bonded to a woven geogrid is shown in Figure 27.

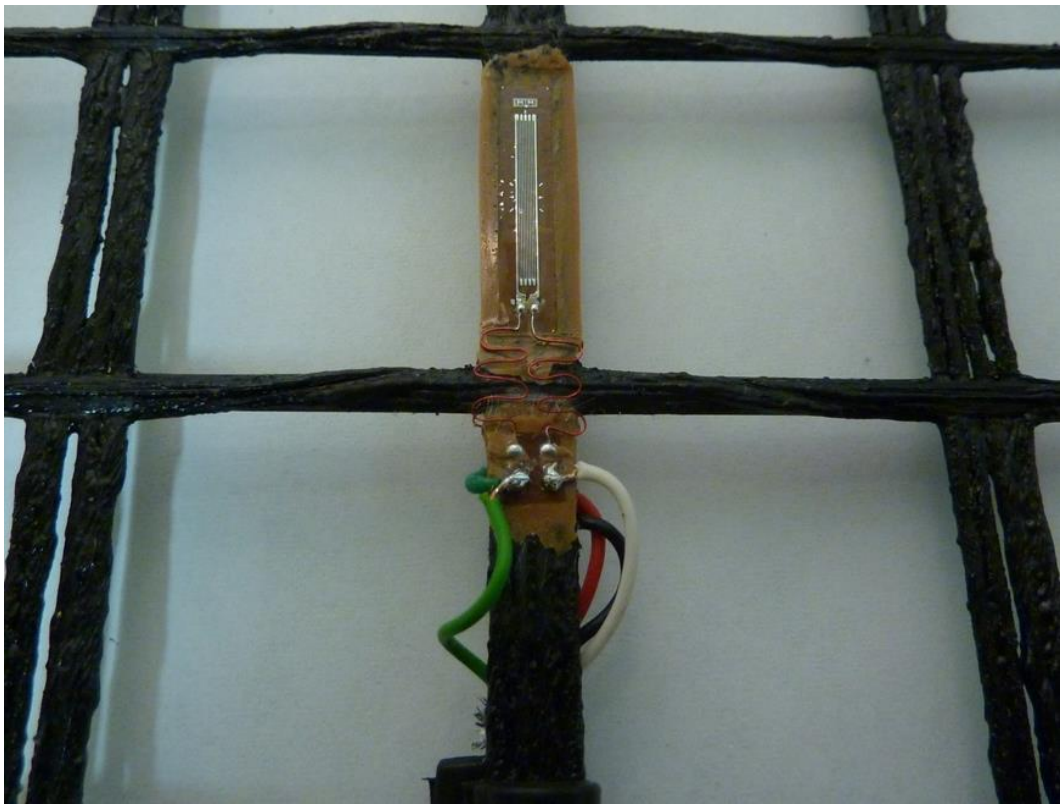


Figure 27: Completed placement and wiring of a strain gage on a woven geogrid.

A protective coating is then applied to keep water from entering the gaged area and to protect it from physical damage during construction and trafficking. M-Coat J from Micro-Measurements was used for this purpose. A thin piece of Teflon™ adhesive was used to separate the exposed gage surface from the coating material, as recommended by the manufacturers. Curing of the protective coating was accelerated by heating the gage area to 125 °F for 2.5 hours. A finished strain gage installation on a welded geogrid is shown in Figure 28.



Figure 28: Completed strain gage installation on a welded geogrid with protective coating.

The procedure used to bond strain gages to geotextiles was similar, but modified slightly to accommodate the unique surface structure of the materials. To minimize stiffening of the gaged area, RTV-3145 (a non-conducting silicone manufactured by Dow Corning, Midland, Michigan) was used to bond the strain gages to the geotextiles and also act as the protective coating. A completed strain gage installation on a woven geotextile is shown in Figure 29.

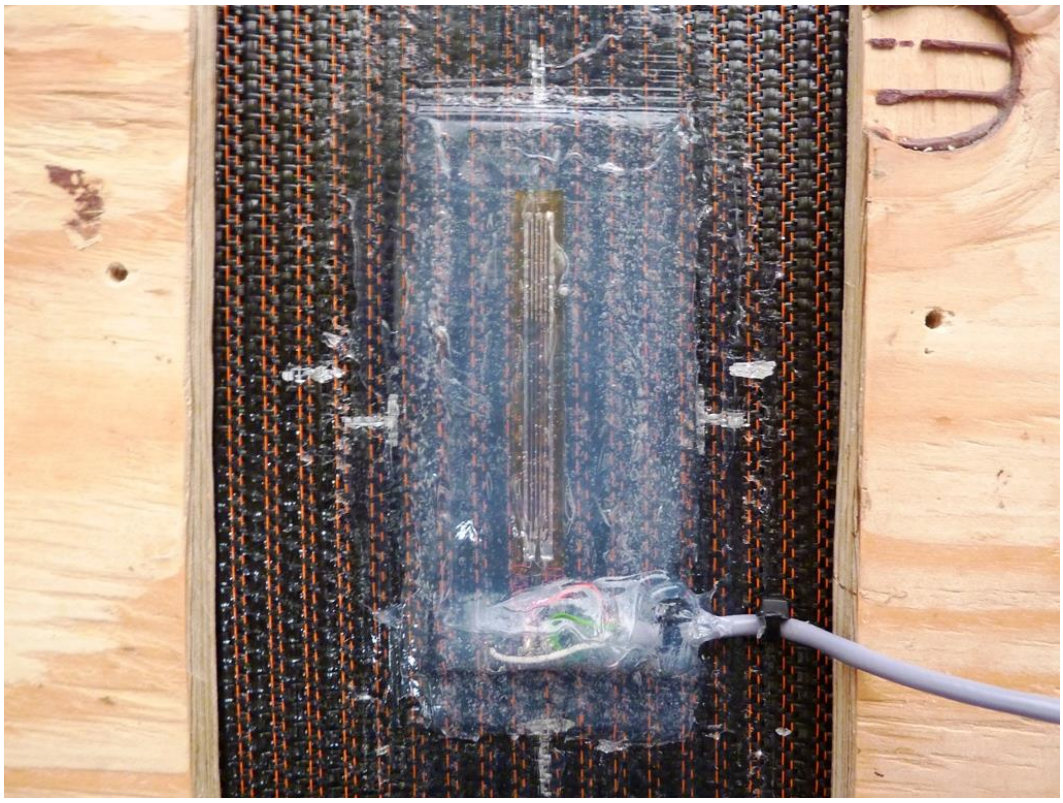


Figure 29: Completed strain gage installation on a woven geotextile.

A three-wire circuit was used to negate influence from long leadwires between the strain gage area and the Wheatstone bridge circuitry (see Appendix A). Shunt calibration of the strain gage was done to ensure proper operation and determine the baseline measurement for the gages prior to installation of the base course aggregate.

Strain Gage Calibration. Strain gage calibration for each geosynthetic was required to develop correction factors that convert local strains to global strains. The calibration takes into account the effects from the bonding adhesive and environmental protection, which can stiffen and alter the strain of the geosynthetics, and the strain registered by the strain gage. Cyclic in-air tensile calibration was selected instead of the typical constant-rate-of-strain wide-width tensile testing because it has been proven that the correction factors may differ depending upon the loading conditions.

In-air cyclic tensile calibration at 1 Hz cycles was performed for the twelve different geosynthetics used in the field study. Because of the significant delay in receiving the strain gages (up to four months past guaranteed date), the lab calibrations were not performed until after the field study was completed. However, this provided the opportunity to analyze the raw field data and determine the uncalibrated strains in the field. Thus, by being able to analyze the field data first, the optimum lab calibration procedure was able to be performed because the cyclic strains experienced in the field were able to be duplicated in the lab.

The maximum strains and averaged dynamic strains experienced by the strain gages throughout trafficking were approximately 4.0% and 0.16%, respectively. Note that calibration factors were not applied to these values. Also, because the dynamic measurements was sampled at 25 Hz and the averaged dynamic strains were based on averaging measurements over a period of one second, the non-averaged dynamic strains were slightly greater.

At the end of trafficking, the strain varied from 0.2 to 4.0% between all of the geosynthetic, and therefore a wide range of strain cycles had to be incorporated into the lab calibrations. From the literature reviewed, it was determined that typical calibration factors for converting local strains to global strains are generally less than two (i.e., global strain ≤ 2 * local strain), which would result in a maximum strain value of close to 8.0% in the field. Because of the possibility of having calibration factors greater than 2.0, the strain gages were calibrated from 0 to 10% of global permanent strain with 50 cyclic strain cycles of ±0.10% (±1000με) at each permanent strain value. The strain gage calibration procedure applied a total of 750 cycles at increasing permanent strain values as shown in Table 7.

Table 7: Cyclic Strain Gage Calibration Procedure

Permanent Strain (%)	**Cyclic Strain Cycle (%)**	**Number of Cycles**
0.25	0.15 - 0.35	50
0.50	0.40 - 0.60	50
0.75	0.65 - 0.85	50
1.00	0.90 - 1.10	50
1.50	1.40 - 1.60	50
2.00	1.90 - 2.10	50
2.50	2.40 - 2.60	50
3.00	2.90 - 3.10	50
4.00	3.90 - 4.10	50
5.00	4.90 - 5.10	50
6.00	5.90 - 6.10	50
7.00	6.90 - 7.10	50
8.00	7.90 - 8.10	50
9.00	8.90 - 9.10	50
10.00	9.90 - 10.10	50

The procedure used to determine the strain gage calibration factors consisted of a MTS servo-hydraulic load frame with Curtis Sure-Grip Geosynthetic Grips (see Figure 34), a high-quality digital camera, and a CR-1000 data logger (Campbell Scientific, Logan, Utah). The CR-1000 data logger was connected to the strain gage (using the same quarter Wheatstone bridge circuit as used in the field) and MTS load frame. Global displacements were obtained from the MTS load frame and then global strain was calculated. It is important to note that shunt calibration was performed before calibration to determine the adjusted gage factor for the strain gages. The camera used was a 15.1 megapixel Canon EOS 50D digital single-lens reflex (SLR) (model number DS126211) with Canon EFS 17-85 mm ultrasonic lens with macro. The camera was triggered by a Canon remote switch (model number RS-80N3), and focused on the rib adjacent and parallel to the strain gage. Images were used to provide supplemental information on local strains in case the strain gage failed early or had drastically different readings than the global strain. The images were processed using ImageJ, a public domain Java image processing and analysis program inspired by NIH Image (Ferreira and Rasband, 2012). ImageJ is easy to use and has the ability to process images at sub-pixel resolution.

The calibration factors were determined based on the highest calibrated field strain for each geosynthetic. For example, if a geosynthetic experienced a maximum uncorrected strain of 1.8% in the field, and had a calibration factor of 1.40, then the strain gage would be analyzed in the lab from 0 to 2.52% corrected strain. The integrally formed, extruded, and welded geogrids (i.e., BX Type 2, Secugrid 30/30 Q1, Enkagrid Max 30, Tenax MS330, TX 140, and TX 160) had calibration factors from 0.80 to 1.00.

The woven geogrids (i.e., SF 11, SF 12, BXG 11, and Fornit 30) had calibration factors from 1.16 to 1.46, and the woven (RS580i) and nonwoven (Geotex 801) geotextiles had calibration factors of 1.75 and 1.80, respectively. The calibration factors for each geosynthetic are shown in Table 8.

Table 8: Strain Gage Calibration Factors

Geosynthetic Test Section	Highest Raw Field Dynamic Strain Value (%)	Calibration Factor	Corrected Highest Field Dynamic Strain Value (%)
BX Type 2	3.20	**0.94**	3.01
Secugrid 30/30 Q1	0.64	**0.85**	0.54
Enkagrid Max 30	1.34	**1.00**	1.34
SF 11	0.74	**1.40**	1.04
SF 12	0.36	**1.46**	0.53
BXG 11	0.92	**1.16**	1.07
Fornit 30	0.54	**1.43**	0.77
Tenax MS330	1.40	**0.94**	1.32
TX 140	4.00	**0.80**	3.20
TX 160	3.72	**0.84**	3.11
RS580i	0.84	**1.75**	1.47
Geotex 801	4.22	**1.80**	7.60

Calibration factors less than 1.00 mean that strain values from the strain gage over-registered the strain applied to the geosynthetic; that is, the strain gage had strains greater than the global strains. The reason for this is likely due to the placement of the strain gage on the geosynthetic. The BX Type 2, Tenax MS330, TX 140, and TX 160 geogrids are manufactured using a punched and drawn process, which results in variations in material stiffness along individual members. Thus, it is likely that by placing the strain gage in the center of the transverse rib, the geogrid strained more in the strain gage location and therefore a calibration factor less than 1.00 is reasonable. The

Secugrid 30/30 Q1 and Enkagrid Max 30 geogrids are vibratory-welded when manufactured. Similar to the punched and drawn process, variations in material stiffness along individual members may result because of the welding of the nodes.

Under-registration occurs when the strain gage has a lower strain reading than global reading (i.e., when the calibration factor is greater than 1.00). The primary reason for this is caused by localized stiffening from the bonding adhesive. The adhesive stiffens the strain gage area, and therefore the strain gage registers less strain than the global strain as was the case in the SF 11, SF 12, BXG 11, and Fornit 30 woven geogrids; and the RS580i and Geotex 801 geotextiles. In addition, there is a second mechanism which creates under-registration primarily for the geotextiles which is related to the ability of the adhesive to transfer load to the strain gage. RTV-3145 silicone was used for the geotextiles instead of M-Bond A-12 because it is more flexible and therefore does not stiffen the gaged area as much. A thin bedding from the adhesive was created to prevent wrinkles and undulations of the strain gage on the uneven surface of the geotextiles. Because the bedding positions the strain gage slightly above the geotextile and RTV-3145 silicone is flexible, the strain gage did not register the true amount of strain in the geotextiles.

Grip slippage was monitored visually, and equal loading of the instrumented and adjacent parallel non-instrumented rib was applied. Visual observation of grip slippage was performed using a permanent marker, and marking the top and bottom of the geosynthetic in the grips. It should be noted that all of the geosynthetics had been tested previously in wide-width tensile strength to failure and grip slippage only occurred in the

SF 11 and SF 12 woven geogrids at high strains (greater than 10%). To ensure equal loading on the strain gage rib and the adjacent parallel non-instrumented rib, the geogrid's aperture between the instrumented and non-instrumented ribs was centered in the grips. This ensured that any localized necking that occurred was equal on both sides.

To process the images in ImageJ with increased accuracy, the settings of the camera were adjusted. Exposure was reduced and the aperture was widened to decrease the time it took to capture an image. Focus and focal length were manually set so that the image was taken at the exact same distance each time and therefore a global pixel correction could be made when processing the images in ImageJ. Also, having sufficient lighting increased the quality of the images.

The most difficult part of processing the images was determining two reference points to measure from. The most accurate method determined was by placing thin pieces of blue painter's tape on the adjacent parallel rib to the strain gage as shown in Figure 30. The blue painter's tape was cut with small precision scissors and the pieces of tape were positioned to be approximately the same gage length as the strain gage. Permanent markers were used as well, but the ink from the markers spread beyond the line that was drawn and when looking at the images down to the nearest ten-thousandths of an inch, it became evident that the painter's tape was the more reliable measurement method. The local and global views of the calibration setup are shown in Figure 30 and Figure 31, respectively.

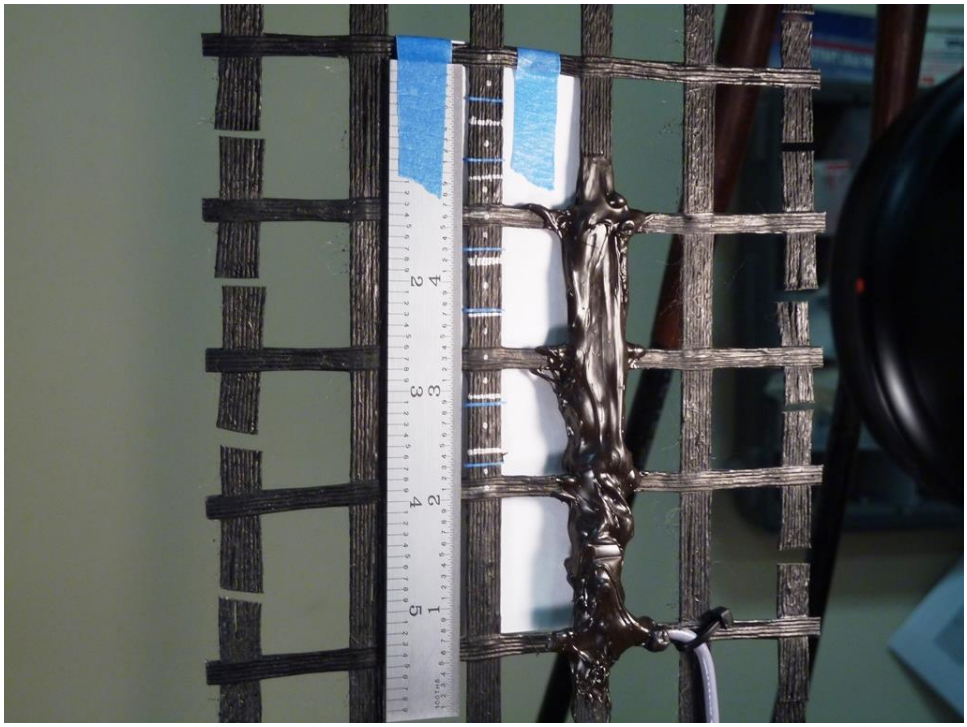


Figure 30: Strain gage calibration setup - local view.

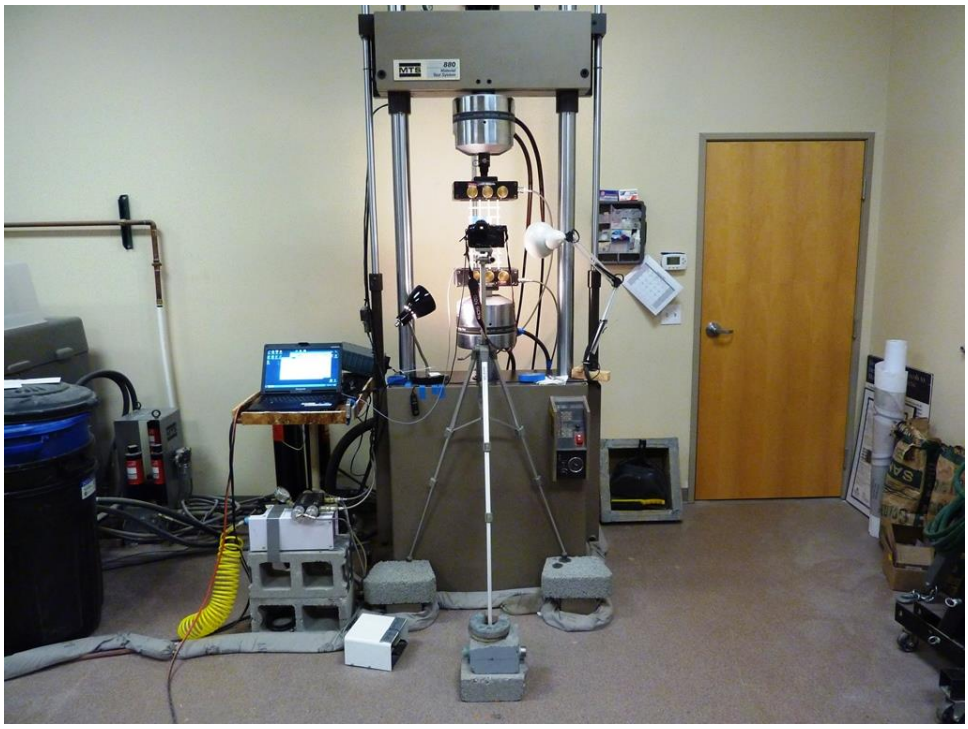


Figure 31: Strain gage calibration setup – global view.

The strain gages did not fail during calibration and because the calibration factors were appropriate, only a verification of the local strains of the non-instrumented rib was performed to check the accuracy of the camera technique. This verification was performed on the Enkagrid Max 30 material. The local strain determined by the images was manually analyzed three times for each image in ImageJ, averaged, and then compared to the strain gage readings. Manual analysis is typically not as accurate as methods involving software and hardware such as video extensometer, but it provided accurate and repeatable results as illustrated in Figure 32. Lastly, note that the strain gage on the Enkagrid Max 30 material begins to shown over-registration at higher strain values. The calibration factor is still 1.00 because in the field, the strain gage never reached strains above approximately 1.34%.

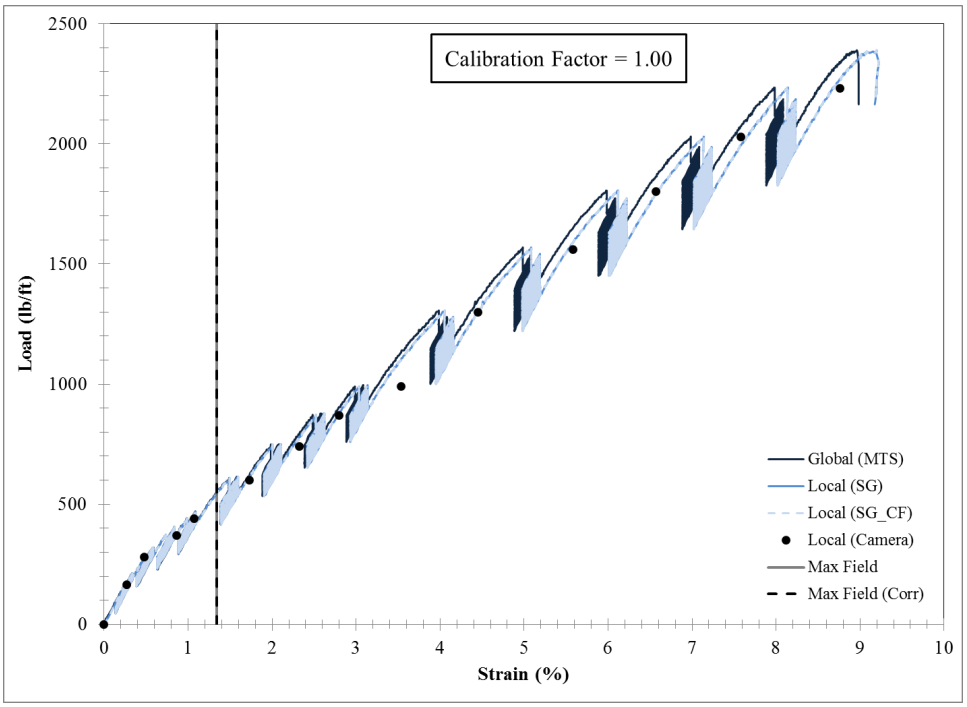


Figure 32: Strain gage calibration verification – Enkagrid Max 30.

The local strains measured by the camera and ImageJ for the Enkagrid Max 30 geogrid were useful in verifying the material's local behavior, and provided a redundant measurement in case the strain gage failed or produced significantly different results than the global strain. In general, the camera slightly over-estimated the global strain and local strain from the strain gage, but did so very consistently (approximately 10% on average). This may be a factor of the strain gage adhesive or environmental protection stiffening the strain gage area which could affect the adjacent parallel rib's strain. Another possibility is that the thin pieces of blue painter's tape which were used to measure the strain by the camera and ImageJ were moving enough to alter the strain readings. Further, the differences in the individual ribs can also lead to differences in strain. Although the Enkagrid Max 30 geogrid has near identical transverse ribs, any small differences in the ribs can lead to differences in strain. Lastly, the manual processing of the images can introduce errors. Although ImageJ was able to measure the images to the nearest ±0.0001 to 0.0003 inches (±0.02 to 0.06%) for the Enkagrid Max 30 geogrid, and three separate strain measurements were made at each point and then averaged, the exact start and finish points on the painter's tape were not always easy to distinguish which slightly decreased the accuracy of the measurements. Individual strain gage calibration plots are shown in Appendix B.

Strain Gage Survivability. Out of the 28 strain gage locations, 100% survived construction, but only 36% (10 strain gage locations) survived all of trafficking. Of those 10 instrument locations, one provided erratic data between truck passes 556 to 665 (i.e., the gage appeared to have failed at truck pass 556, but at truck pass 665 it provided

reliable strain readings again). The strain gage survivability during trafficking in the field study is listed in Table 9.

Table 9: Strain Gage Survivability

Geosynthetic Test Section	Truck Passes at Failure	
	North Gage Location	South Gage Location
BX Type 2 (CBR=2.15)[a]	556[b]	DNF
BX Type 2 (CBR=1.61)[a]	303	20
BX Type 2 (CBR=1.78)[a]	DNF	DNF
Secugrid 30/30 Q1	303	175
Enkagrid Max 30	405	405
SF 11	303	175
SF 12	1	10
BXG 11	251	40
Fornit 30	40	40
Tenax MS330	DNF	DNF
TX 140	405	303
TX 160	140	175
RS580i	DNF	DNF
Geotex 801	DNF	DNF

[a] values in parenthesis denote average values from longitudinal survey measurements
[b] strain gage signal was somewhat erratic from truck pass 556 to 665
DNF = did not fail

From post-trafficking investigations that were performed in the summer of 2013, it became evident that the primary reason for gage failure was due to water infiltration. The M-Coat J environmental protection used on the geogrids was able to protect the gages very well from the base course aggregate during construction and trafficking; however, it was not able to prevent the infiltration of water on all of the geogrids. The geotextiles did not have strain gage failures most likely because the RTV-3145 silicone that was used to protect the gages sealed the gage locations more thoroughly. If RTV-

3145 silicone or AK 22 putty had been used as environmental protection instead of M-Coat J on the geogrids, the strain gage survivability rates would likely have improved. Lastly, additional protection of the strain gages prior to the installation of base course aggregate is recommended. Inexpensive neoprene pads or rubber foil may have further increased the strain gage survivability.

From the field study, the highest uncorrected strain measured by the strain gages was approximately 4%, which means that the EP series gage and M-Bond A-12 adhesive were not essential. Because of the limited availability and cost in purchasing EP series gages, it is recommended that EA series gages be used in future full scale field or laboratory studies because they have better fatigue life characteristics, are typically in stock, come in a variety of resistances, and can measure strains up to ±5% which is sufficient for most field applications. M-Bond A-12 adhesive works well for the EP series gage because it accommodates large strains; however, it requires elevated cure temperatures and can also become gritty unless carefully used. For the EA series gages, AE-10 is ideal because it provides 6 to 10% elongation when cured at room temperature for 24 to 48 hours. Nevertheless, if very high strains are anticipated, then the EP series gage and M-Bond A-12 adhesive is the best option.

Strain Gage Noise, Zero-Shift, and Temperature Effects. Noise in the strain gages was likely a result of using low resistance strain gages in certain test sections and/or not using signal conditioners. Test Section 3 (BX Type 2) used 350-ohm resistance strain gages and had excellent results without signal conditioners. Some test sections, such as Test Section 9 (Fornit 30) in particular, used 120-ohm resistance gages and had a

significant amount of noise in the strain gage readings. Also, the data loggers may have introduced noise into the measurements.

To reduce noise, three-wire circuits were used with 350-ohm resistance strain gages (when possible). A three-wire circuit accounts for leadwire resistance and is described in Appendix A in this thesis. A minimum of 350-ohm resistance strain gages is recommended for future full-scale studies to help reduce noise. If less than 350-ohm strain gages are to be used, then alternative methods to reduce noise in measurements should be considered, such as the use of signal conditioners.

The long-term behavior of the strain gages did not show signs of zero-shift or changes in strain due to temperature. Zero-shift was a concern because of the poor fatigue life of the EP series gage, and temperature was a concern because the stiffness of the environmental protection used on the strain gages could have increased when the temperature decreased. The effect of temperature on the strain gage readings was analyzed using thermocouples that were installed at the subgrade-base course interface in Test Section 9. Temperature measured by the thermocouples varied from approximately 41.0 to 73.5 °F throughout trafficking. Using Micro-Measurements Tech Note TN-504, the thermal output for this range of temperatures is approximately 0 to +100 με (0 to +0.01% strain) for the EP series gage. Because the effect from temperature was within the noise of the measurements, temperature effects were not applied to the strain measurements in the field.

LVDT Instrumentation. Linear variable differential transformers (LVDTs) were used in the field study to measure displacement of the geosynthetics near the outside west

wheel path (see Figure 24 and Figure 25). The method of installing LVDTs on geosynthetics outlined by Cuelho et al. (2008) was implemented in the field study. In brief, this method consists of attaching leadwires to the geosynthetic, running the wires through protective tubing, and attaching the leadwires to the LVDT sensor which is housed in a box outside of the test section.

Model HR 1000 LVDTs (manufactured by Measurement Specialties, Hampton, Virginia) having a stroke range of ±1.0 inch were used in this study. Three LVDTs were used at each of the two instrumented locations in each test section. Stainless steel leadwires were used to bring the point of measurement from the geosynthetic to the LVDTs which were housed inside weatherproof boxes. Leadwires were 0.4 mm in diameter and had a spring temper and bright finish. High strength PVC tubing, with an inner diameter of approximately 2 mm, was used to protect the leadwire from the base course aggregate and allow free movement during trafficking. It is important to note that only 1 out of 84 of the LVDT leadwire connections failed throughout trafficking (no LVDTs failed during construction).

The furthest west leadwire (as connected to the geosynthetic) was labeled LVDT 1, the middle leadwire LVDT 2, and the furthest east leadwire LVDT 3 as illustrated in Figure 25. The distance between LVDT 1 and 2 was approximately six inches, and between LVDT 2 and 3 was approximately eight inches. LVDT 1, 2, and 3 were all on the same transverse rib for the geogrids, and were in the same transverse line for the geotextiles as illustrated in Figure 33.

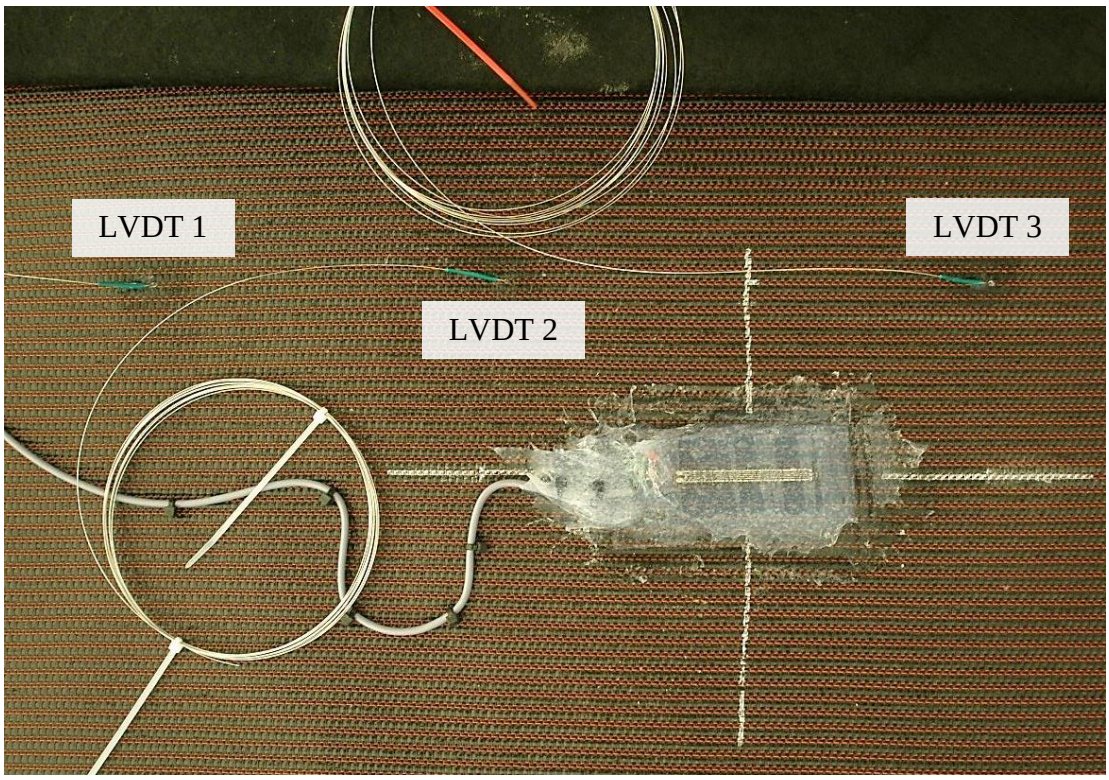


Figure 33: Placement of LVDT leadwires and strain gages on a woven geotextile.

Knowing the original distance between each displacement measurement point allowed the global strain between measurement points to be determined during trafficking. It is important to note that the strain gages were installed on a parallel adjacent rib to the LVDTs, and were centered between LVDT 2 and 3 to provide redundancy in measurements and to compare local versus global strains.

LVDT Temperature Effects: The temperature effects on the LVDT displacement measurements were evaluated. The LVDTs were housed inside boxes just outside of the test sections as illustrated in Figure 25, and because the LVDT sensors were inside the boxes which were exposed to the environment, increases in temperature throughout the day affected the sensor readings. The LVDT long-term static displacement data showed

that the temperature can affect the displacements as much as 0.025 inches, with the peak displacement occurring during the day when the temperatures of the LVDT sensors were at their highest due to the environment. Because trafficking was only performed during the day, the displacements caused by temperature were only about half of the 0.025 inches. Thus, the temperature influences on LVDT displacement measurements throughout trafficking were approximately 0.0125 inches, or ±0.00625 inches. Because the displacements introduced by temperature effects were relatively small, temperature effects were not accounted for in the LVDT displacement measurements.

The temperature effects were also analyzed on the calculated strain from the LVDT displacement measurements. The LVDT long-term static data showed that the temperature can affect the strains as much as 0.2%, and because trafficking was only performed during the day, the strain caused by temperature was approximately 0.1%, or ±0.05%. Similar to the displacement measurements, strains introduced by temperature effects were relatively small, and were not accounted for in the LVDT strain calculations.

Mechanical Properties of Geosynthetics

Mechanical properties of geosynthetics were characterized using five standard laboratory tests. Wide-width tensile strength, cyclic tensile modulus, and resilient interface shear stiffness tests were performed in the geosynthetic's cross-machine direction (XMD), which is transverse to the direction of traffic. The tests were performed in the XMD so that the transverse behavior of the geosynthetics could be related to field performance based on the mechanical properties of the geosynthetics. Junction strength in the XMD and aperture stability modulus tests were performed by SGI Testing Services

(Norcross, Georgia), an independent geosynthetic testing lab. In addition, SGI also tested the Geotex 801 geotextile in the XMD for grab breaking load.

Wide Width Tensile Strength

Wide-width tensile strength tests (ASTM D4595 and ASTM D6637) were used to determine the force-elongation properties of the geosynthetics in their XMD. A MTS servo-hydraulic load frame was used to conduct the wide-width tensile strength tests. The geosynthetics were held on both ends by Curtis Sure-Grip Geosynthetic Grips which apply pressure to the geosynthetics using a pneumatically driven hydraulic system. The grips can accommodate a sample up to eight inches wide and have a capacity of 10,000 lbs. The setup for a typical wide-width tensile strength test is shown in Figure 34.

The geogrids tested were approximately eight inches wide and had a gage length of approximately twelve inches long, while the geotextiles had a width of eight inches and gage length of four inches. Tension was applied at a constant rate of strain of 10% per minute based on the initial gage length of the geosynthetic. At least three samples, but no more than six, were tested in the XMD. The number of samples tested is based upon a statistical formula within the ASTM standard test method to ensure uniformity of results between samples. A summary of the wide-width tensile strength test results are listed in Table 10. The wide-width tensile strength load-displacement plots are provided in Appendix C.

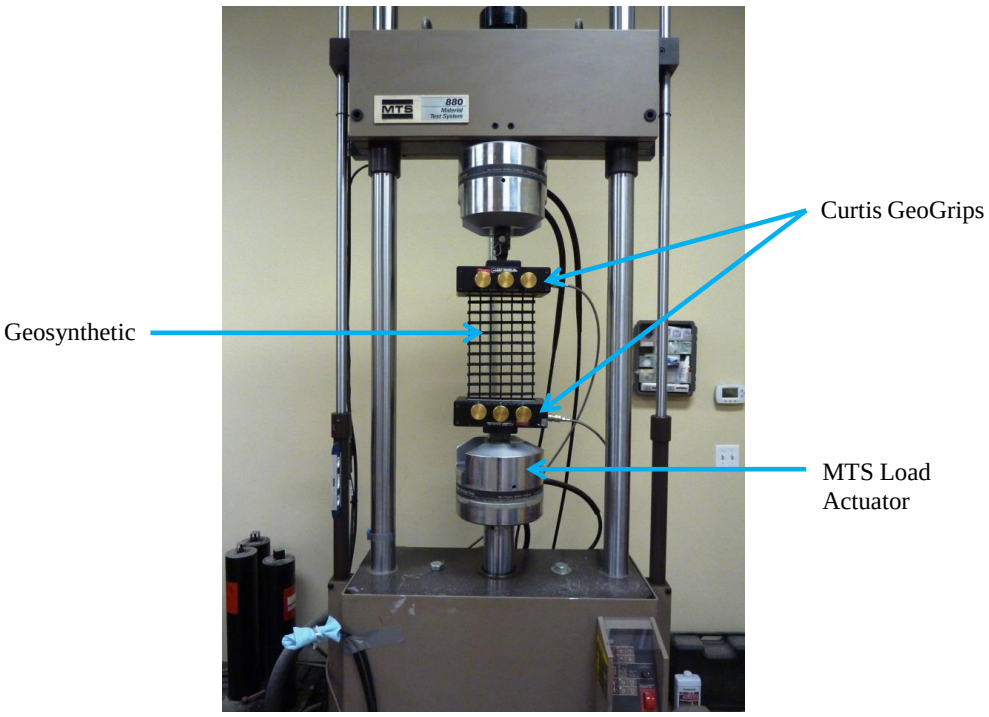


Figure 34: Wide-width tensile strength test setup.

Table 10: XMD Wide-Width Tensile Strength Test Results

Geosynthetic Test Section	Strength[a] @ 2% (lb/ft)	Strength[a] @ 5% (lb/ft)	Ultimate[a] Strength (lb/ft)
BX Type 2	822	1,494	1,946
Secugrid 30/30 Q1	946	1,830	2,713
Enkagrid Max 30	857	1,775	2,378
SF 11	617	925	3,782[b]
SF 12	987	1,446	5,818[b]
BXG 11	740	1,281	3,221
Fornit 30	946	1,939	2,618
Tenax MS330[c]	692	1,343	2,248
TX 140	322	665	843
TX 160	391	747	884
RS580i	1,501	3,440	6,112
Geotex 801	[d]	[d]	255[e]

[a] ASTM D4595 and ASTM D6637
[b] SF 11 and SF 12 experienced grip slippage at their ultimate strength values
[c] tested by WTI as a composite, i.e., not separately
[d] data was difficult to interpret at low strain values
[e] grab tensile strength (ASTM D-4632) in Pounds as tested by SGI Testing Services, LLC

Cyclic Tensile Modulus

Cyclic tensile modulus tests were performed to evaluate the tensile modulus of geosynthetics under small-strain cyclic loading (representative of traffic loads) according to ASTM D7556. 1000 load cycles were applied at 1 Hz between axial strain limits of ±0.1% at six permanent strain values: 0.5, 1.0, 1.5, 2.0, 3.0, and 4.0%. The total number of tests is determined using the same statistical equation as the wide-width tensile strength test, and also used the same testing setup as illustrated in Figure 34.

The cyclic tensile modulus (J_{cyclic}) is calculated using the following equations:

$$J_{cyclic} = \frac{(\alpha_f * 100)}{(\varepsilon_2 - \varepsilon_1)} \qquad \text{Equation 1}$$

where α_f = equivalent force per unit width (lb/ft), as determined using the following equation,

$$\alpha_f = \frac{(P_2 - P_1)}{W_s} \qquad \text{Equation 2}$$

ε_2 = percent strain corresponding to the cycle's highest strain value,
ε_1 = percent strain corresponding to the cycle's lowest strain value,
P_2 = maximum tensile load for the cycle (lb),
P_1 = minimum tensile load at the end of the cycle (lb), and
W_s = specimen width (ft).

The equivalent force per unit width was calculated for the last 10 cycles of each cyclic load step and averaged together to determine a single cyclic tensile modulus for

each load step. The Propex Geotex 801 material was not tested because it has low strength at small stains and would not yield a representative cyclic tensile modulus.

The results from the cyclic tensile modulus tests are summarized in Figure 35. In general, the cyclic modulus went down slightly for the BX Type 2, Secugrid 30/30 Q1, Enkagrid Max 30, BXG 11, and Tenax MS330 geogrids. The SF 11, SF 12, TX 140, and TX 160 geogrids all had increasing cyclic moduli, while the Fornit 30 geogrid went down at low cyclic modulus values, then increased, and at the highest cyclic modulus value decreased. The RS580i geotextile had a significantly higher cyclic modulus and was always increasing. Representative load-displacement results in the XMD are shown in Appendix D.

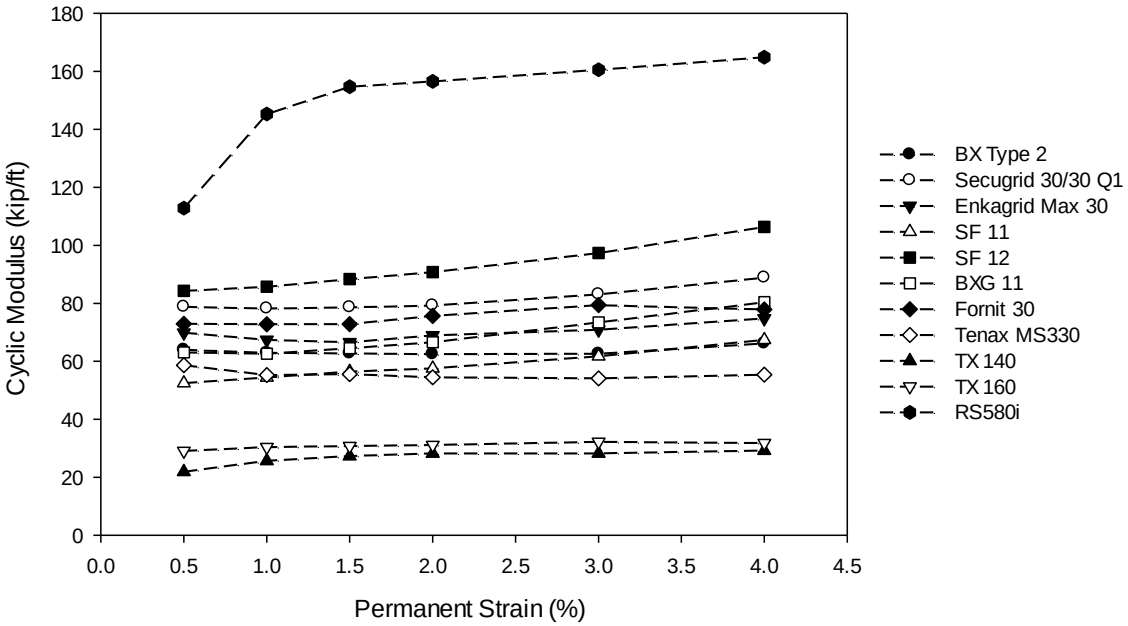


Figure 35: XMD cyclic tensile modulus test results.

Resilient Interface Shear Stiffness

Resilient interface shear stiffness tests (ASTM D7499) were used to measure the stiffness of the interface between the geosynthetic and the surrounding soil under small cyclic loads. The test is conducted by embedding a short sample of geosynthetic in soil and applying cyclic loads at various levels of confinement and load. Applied load and displacement along the front and rear of the embedded sample are recorded. An annotated illustration of the testing device is shown in Figure 36.

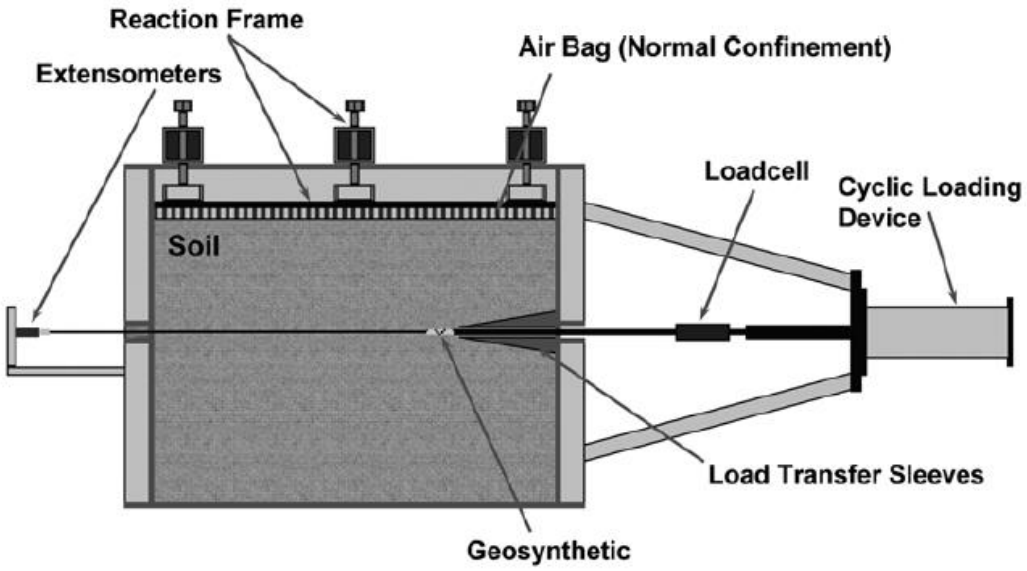


Figure 36: Resilient interface shear stiffness apparatus (from ASTM D7499).

The length of the embedded geosynthetic is specified to be 2 to 4 inches long and contain at least two full grid apertures; the width should be at least 12 inches. The sample length is relatively short when compared to traditional pullout tests to ensure that strain and shear stress along the length of the geosynthetic are generally uniform when loaded.

A total of six prescribed levels of horizontal cyclic force are applied to the geosynthetic at five specified levels of normal stress confinement. Resilient interface shear stiffness (G_I) is calculated from the last 10 cycles and averaged to yield a value for each step using the illustration in Figure 37, which relates the shear along the geosynthetic as it is displaced. Up to 30 values of G_I can be obtained from each test using this method (corresponding to the various levels of applied load and confinement). A regression equation based on the general equation that describes the resilient modulus of unbound granular soils (Equation 3), can be used to predict G_I. A single value for the interface normal stress (σ_I = 5.076 psi) and the interface shear stress (τ_I = 0.725 psi) were used in this analysis, based on the work conducted by Perkins and Christopher (2010).

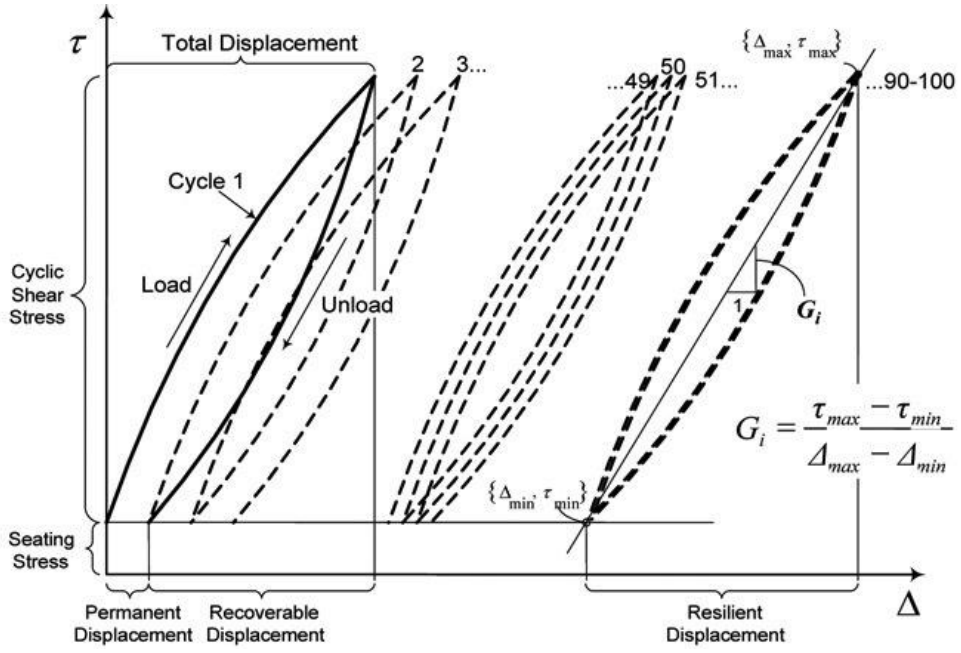


Figure 37: Illustrated calculation of resilient interface shear stiffness (from ASTM D7499).

$$G_I = k_1 P_a \left(\frac{\sigma_I}{p_a}\right)^{k_2} \left(\frac{\tau_I}{p_a} + 1\right)^{k_3} \quad \text{Equation 3}$$

where,

G_I = resilient interface shear stiffness (psi/in),

p_a = atmospheric pressure (14.69 psi),

P_a = atmospheric pressure divided by a unit length of 1 inch (14.69 lb/in^3),

σ_I = interface normal stress (psi),

τ_I = interface shear stress (psi), and

k_1, k_2, and k_3 are material parameters determined from the test results.

A summary of the k_1, k_2, and k_3 material parameters and resilient interface shear stiffness (G_I) is provided in Table 11. The standard G_I (i.e., all data from the test is used to calculate G_I) varied from 88 to 329 ksi with the TX 140 geogrid having the lowest G_I, and the RS580i geotextile having the highest G_I. Individual plots of the measured versus predicted standard resilient interface shear stiffness are provided in Appendix E for each of the geosynthetics. The select data used to calculate G_I consisted of low confinement and high shear stress to relate the test most closely to subgrade stabilization applications. The confinement analyzed was at 31.0 kPa (approximately 650 psf) at the fourth prescribed load level (i.e., high shear stress).

Table 11: Resilient Interface Shear Stiffness Test Results

Geosynthetic Test Section	k_1	k_2	k_3	Standard G_I (ksi)[a]	Select G_I (ksi)[a,b]
BX Type 2	84,611	0.92	-8.9	305	199
Secugrid 30/30 Q1	62,815	0.82	-15.2	186	229
Enkagrid Max 30	156,570	1.18	-41.0	91	256
SF 11	173,469	1.52	-21.7	178	281
SF 12	104,984	1.14	-9.4	292	469
BXG 11	108,376	1.21	-12.6	240	333
Fornit 30	44,194	0.94	-12.9	129	187
Tenax MS330[c]	100,343	1.17	-16.8	190	264
TX 140	44,176	0.62	-27.8	88	82
TX 160	103,015	1.12	-13.4	242	282
RS580i	59,303	0.81	-2.3	329	683
Geotex 801	46,413	0.88	-12.4	147	194

[a] interface normal stress σ_I = 5.076 psi and Interface shear stress τ_I = 0.725 psi used for all calculations
[b] confinement = 650 psf at fourth prescribed load level
[c] tested as a composite, i.e., not separately

Junction Strength

Junction strength tests (ASTM D7737) are generally used to verify that the junctions of a particular geogrid have sufficient strength to undergo construction stresses, but can also be used to evaluate the transfer of stresses between the base course aggregate and geosynthetic. The junction strength tests generally involve cutting specimens in the shape of a "T" with at least one transverse member protruding from either side of the junction being tested. The specimen is gripped on both sides of the "T" and the orthogonal rib is pulled until failure of the junction occurs. A typical junction strength test setup is shown in Figure 38.

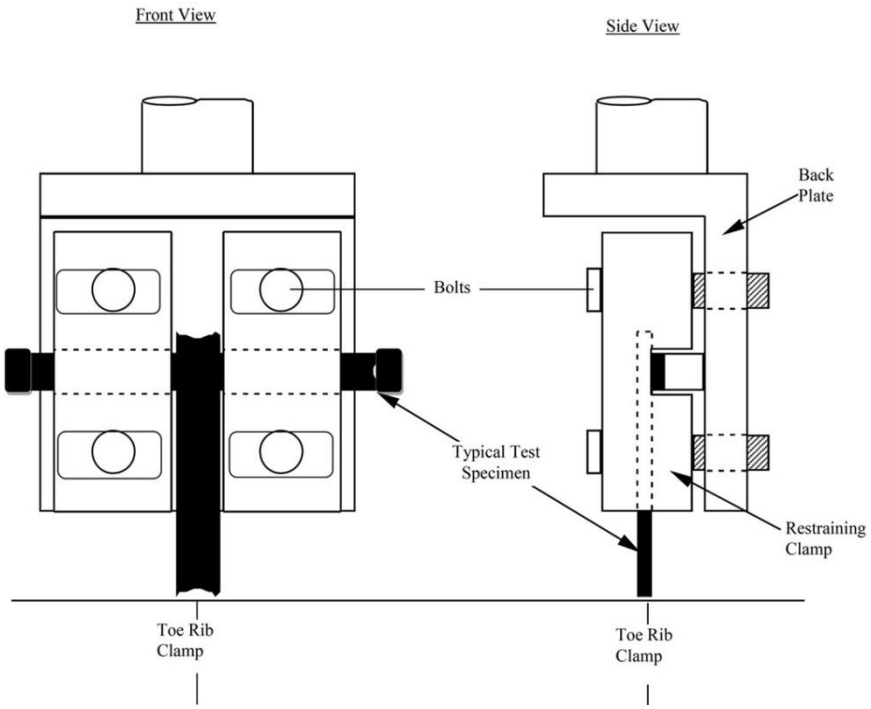


Figure 38: Typical junction strength test specimen setup (from ASTM D7737).

The junction strength and stiffness results are summarized in Table 12. It is important to note that the junction strength of the SF 11 geogrid was greater than the junction strength of the SF 12 geogrid even though the SF 12 geogrid is designed to have higher junction strength than the SF 11 geogrid. Also, the linear portion of the junction strength (lb/in) versus displacement curves between 0 to 0.10 inches of displacement was used to determine junction stiffness, which is reported in units of lb/in per inch of displacement. Note that the junction stiffness of the TX 140 geogrid was greater than the junction stiffness of the TX 160 geogrid even though the TX 160 geogrid had greater junction strength. Plots of the junction strength in lb/junction versus displacement are shown for each geogrid in Appendix F, and plots of the junction strength in lb/in versus displacement are shown for each geogrid in Appendix G.

Table 12: XMD Junction Strength and Stiffness Test Results

Geosynthetic Test Section	Tested by SGI		
	Junction Strength (lb/junction)	Junction Strength (lb/in)	Junction Stiffness (lb/in per in)
BX Type 2	206.7	171.6	785.3
Secugrid 30/30 Q1	90.6	57.6	773.9
Enkagrid Max 30	106.6	49.5	537.4
SF 11	46.1	37.1	355.5
SF 12	34.4	28.6	274.5
BXG 11	42.5	35.8	711.4
Fornit 30	8.9	10.5	130.3
Tenax MS330	103.6[a]	65.5[a]	170.5[a]
TX 140	111.8	72.4	342.5
TX 160	123.4	75.1	268.0
RS580i	NA	NA	NA
Geotex 801	NA	NA	NA

[a] for a single layer (three layer material)
NA = Not Applicable

Aperture Stability Modulus

Aperture stability modulus tests are used to quantify the dimensional stiffness of a geogrid under a torsional load, and were performed based on the method developed by Kinney (2000). The test is conducted by confining a square sample of a geogrid in a stiff stationary square clamp, where the interior 9 inch by 9 inch portion of the material is not clamped, as shown in Figure 39. A moment is then applied to the center of the geogrid at five load increments and the degree of rotation is measured. The aperture stability modulus (*ASM*) is defined as the torque (17.70 in-lb), divided by the rotation at that torque (Equation 4). According to the draft standard, the test is stopped if the rotation reaches 20 degrees. In this case, the highest torque should be used in the equation, and

the report should state that the aperture stability modulus is less than the calculated value (Kinney, 2000).

$$ASM = \frac{Torque\ (17.70\ in{-}lb)}{Rotation\ (deg.)} \qquad \text{Equation 4}$$

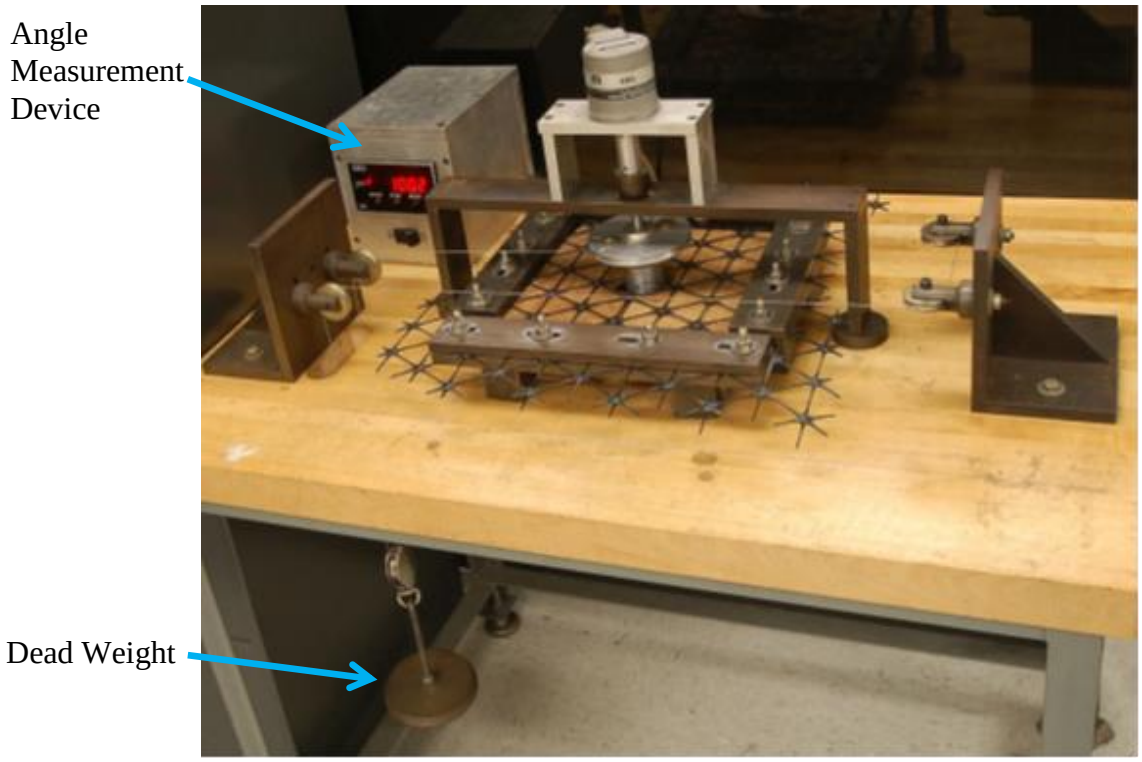


Figure 39: Aperture stability modulus testing device (image courtesy of Tensar International, Inc.).

The results for the aperture stability modulus tests are listed in Table 13. The Fornit 30 geogrid has aperture sizes of approximately 0.6 inch x 0.6 inch, and because of this, the torsional loads applied were approximately at the junctions on the geogrid which means that the aperture stability modulus reported may be higher than the true value for the Fornit 30 material. Individual aperture stability modulus plots for each geogrid are provided in Appendix H.

Table 13: Summary of Aperture Stability Modulus Test Results

Geosynthetic Test Section	Tested by SGI Aperture Stability Modulus (lb-in/deg)
BX Type 2	6.9
Secugrid 30/30 Q1	10.2
Enkagrid Max 30	13.9
SF 11	2.2
SF 12	2.4
BXG 11	3.1
Fornit 30	9.6
Tenax MS330	1.1[a]
TX 140	2.5
TX 160	4.9
RS580i	NA
Geotex 801	NA

[a] for a single layer (three layer material)
NA = Not Applicable

CHAPTER FOUR

RESULTS AND ANALYSIS

The transverse behavior of geosynthetics was evaluated by analyzing the strain gage and LVDT long-term static and dynamic measurements, and the transverse rut profiles from the field test during trafficking. The transition from lateral confinement to membrane support was analyzed primarily based on the transverse rut profiles and the LVDT measurements. Subgrade strength variations were accounted for by correcting rut response, and field performance of the geosynthetic test sections was evaluated based on the mechanical properties of the geosynthetic compared to the truck passes at failure, and the transition from lateral confinement to membrane support. Note that only the transverse locations were analyzed because the focus of this thesis is on the transverse behavior of geosynthetics.

The transition from lateral confinement to membrane support in subgrade stabilization applications is directly related to rutting. In general, wheel path rutting (in excess of 4 inches of apparent rut) is required to develop membrane-type support (Holtz et al., 2008). After analyzing the transverse rut profiles, it was determined that apparent rut is generally between 1.0 to 1.8 times greater than elevation rut, and so membrane-type support is likely to develop around 2.2 to 4.0 inches of elevation with respect to Holtz et al. (2008). Recall that elevation rut is different than apparent rut (see Figure 22). Because of the rut expected in the field (i.e., 3 inches of elevation rut), displacement and strain of the geosynthetic materials, and transverse rut profiles, were expected to indicate the transition from lateral confinement to membrane support. However, because strain

gages measure local strains, it was difficult to determine when the geosynthetics transitioned from lateral confinement to membrane support using solely strain gage data. On the other hand, displacement measurements from the LVDTs were positioned to analyze a larger range of the transverse behavior of the geosynthetics, thereby helping determine the transition point more easily. Conceptually, as the geosynthetic is pushed laterally away from the applied wheel load, the primary reinforcement function is lateral confinement; however, when the geosynthetic begins to be drawn toward the rutted area directly beneath the applied wheel load, the primary reinforcement function becomes membrane support as illustrated in Figure 40. Similarly, as heave begins to occur, the geosynthetic is beginning to transition from lateral confinement to membrane support as is also shown in Figure 40. It is important to note that heave is a direct result of bearing capacity failure.

In general, a roadway is permanently stabilized when heave is minimized and/or is no longer increasing. Based on this understanding, it was assumed that the strains and displacement in the geosynthetics would begin to converge to constant values as the reinforced test sections began to permanently stabilize.

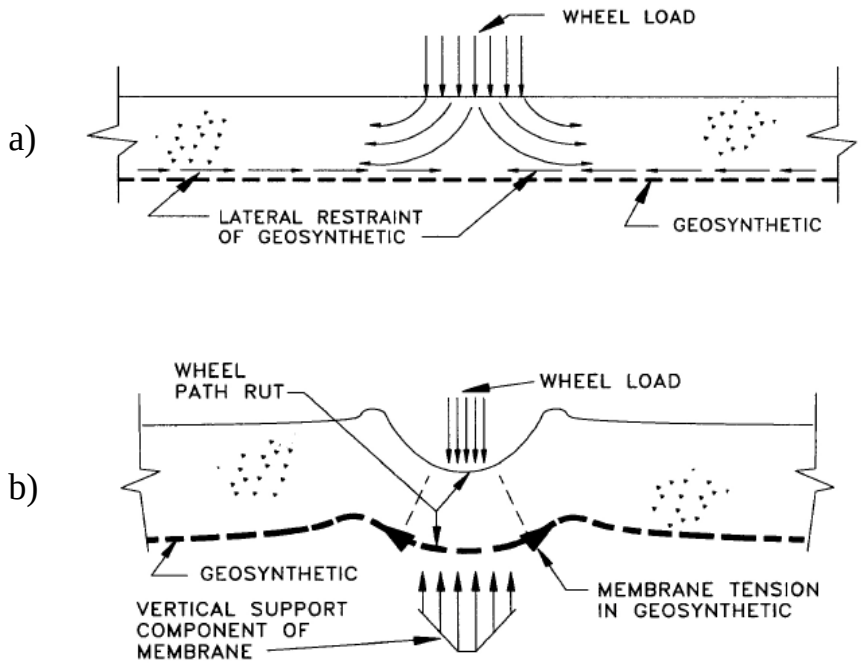


Figure 40: Possible reinforcement functions provided by geosynthetics in subgrade stabilization applications: a) lateral confinement, and b) membrane support (modified after Haliburton et al., 1981).

Field Measurements

The transverse behavior of geosynthetics was characterized using transverse rut profiles generated from survey data collected during trafficking of the test sections, and strain gage and LVDT measurements. The transverse rut profiles were used to evaluate the heave characteristics of the test sections and estimate the geosynthetic's transition from lateral confinement to membrane support by analyzing the rut bowl formation. The strain gage and LVDT measurements were used to further understand this transition and provided the strains and displacements of the geosynthetics.

Trafficking of the test sections began on September 13, 2012 and ended on November 7, 2012. Long-term static measurements were recorded every half hour and

dynamic measurements were recorded during selected truck passes. The trafficking log along with the times when dynamic measurements were recorded is provided in Figure 41. A total of 740 truck passes were applied during trafficking.

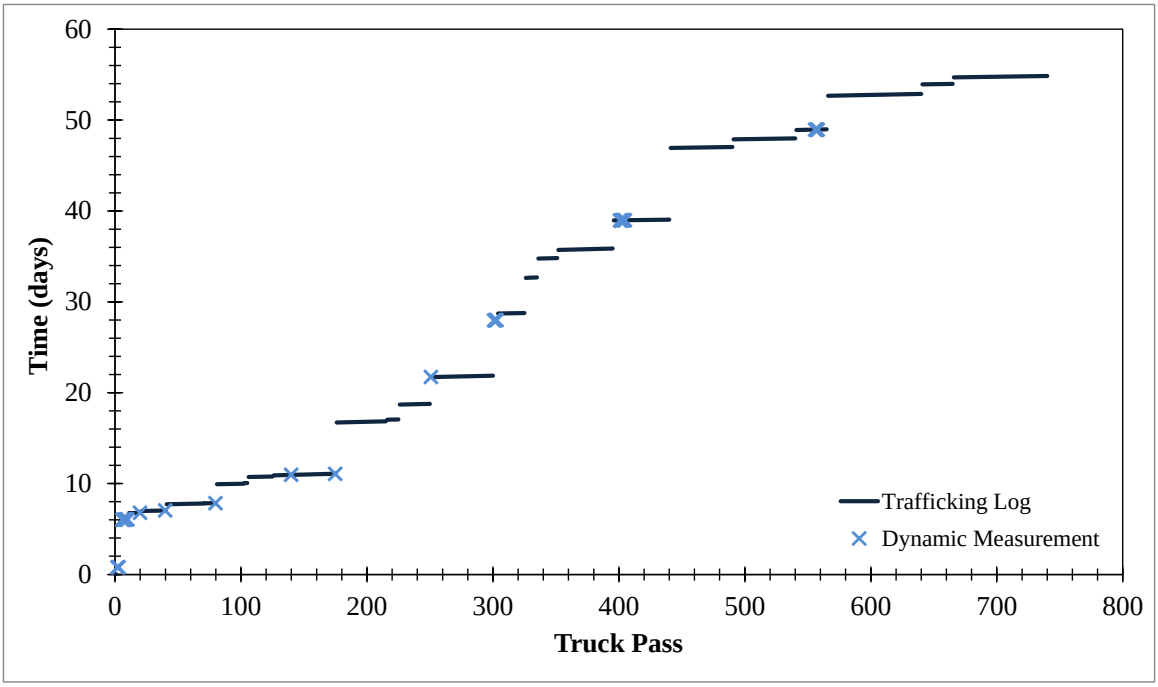


Figure 41: Trafficking log and dynamic field measurements.

Subgrade Strength, Base Course
Thickness, and Empirical Correction

The subgrade strength and base course thickness for both the north and south transverse locations are listed in Table 14. The base course thickness was determined by surveying the top of the subgrade and the base course aggregate in the longitudinal direction prior to trafficking. Because the transverse profile of the subgrade was not taken at the instrumented locations, base thickness in the wheel path was determined using linear interpolation of the longitudinal measurement points closest to the transverse profiles.

Table 14: Subgrade Strength and Base Course Thickness at Instrumented Locations

Test Section	Subgrade Strength (CBR) at Transverse Location[a]		Base Course Thickness (in) at Transverse Location[a]	
	North	South	North	South
1 - BX Type 2 (CBR=2.15)[b]	2.13	2.16	11.1	11.4
2 - BX Type 2 (CBR=1.61)[b]	1.69	1.56	10.5	10.8
3 - BX Type 2 (CBR=1.78)[b]	1.84	1.85	11.3	11.5
4 - Secugrid 30/30 Q1	1.76	1.74	12.1	11.7
5 - Enkagrid Max 30	1.79	1.76	9.3	9.3
6 - SF 11	1.74	1.72	10.8	9.5
7 - SF 12	1.80	1.81	10.4	9.8
8 - BXG 11	1.88	1.76	10.3	10.8
9 - Fornit 30	1.80	1.75	10.9	12.0
10 - Tenax MS330	1.78	1.81	10.6	10.5
11 - TX 140	1.79	1.78	10.5	11.3
12 - TX 160	1.69	1.82	10.4	9.8
13 - RS580i	1.63	1.71	12.5	10.6
14 - Geotex 801	1.63	1.66	11.4	11.7
Control 1 (Base=11.3")[b]	1.80	1.77	11.6	11.2
Control 2 (Base=16.3")[b]	1.88	1.90	16.8	17.7
Control 3 (Base=24.9")[b]	1.70	1.81	26.0	24.1

[a] from west wheel path only
[b] values in parenthesis denote average values from longitudinal survey measurements

An empirical correction for subgrade strength was determined to account for differences in subgrade strength at various locations in the test sections. Test Sections 1, 2, and 3 were used to determine the correction factors because they had the same geosynthetic, but purposely varied in subgrade strength. Longitudinal rut data was used to determine the correction factors because of the significantly higher number of measurement points (28 measurements in each test section). Points which had approximately the same base course thickness and CBR values of the test section's average value ±0.05 CBR were used. The average subgrade strength values for Test

Sections 1, 2, and 3 were 2.15, 1.61, and 1.78, respectively. The uncorrected longitudinal rut versus truck pass is shown in Figure 42.

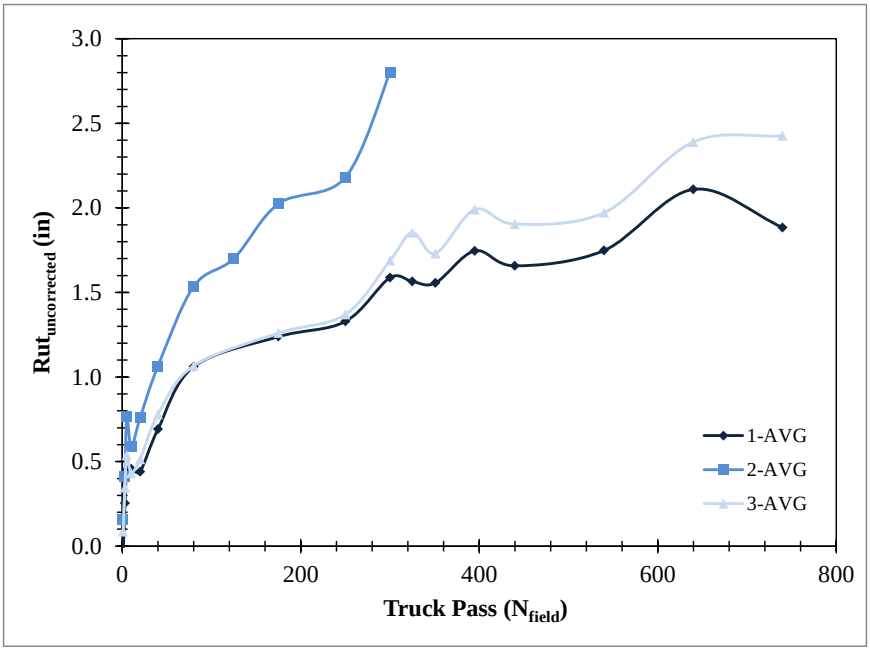


Figure 42: Uncorrected longitudinal rut versus truck pass for Test Sections 1, 2, and 3.

Because Test Section 3 had a subgrade CBR strength representative of Test Sections 4 to 14, Test Sections 1 and 2 were adjusted to match Test Section 3 by applying a multiplicative factor of 1.15 and 0.66, respectively. The corrected longitudinal rut versus truck pass is shown in Figure 43.

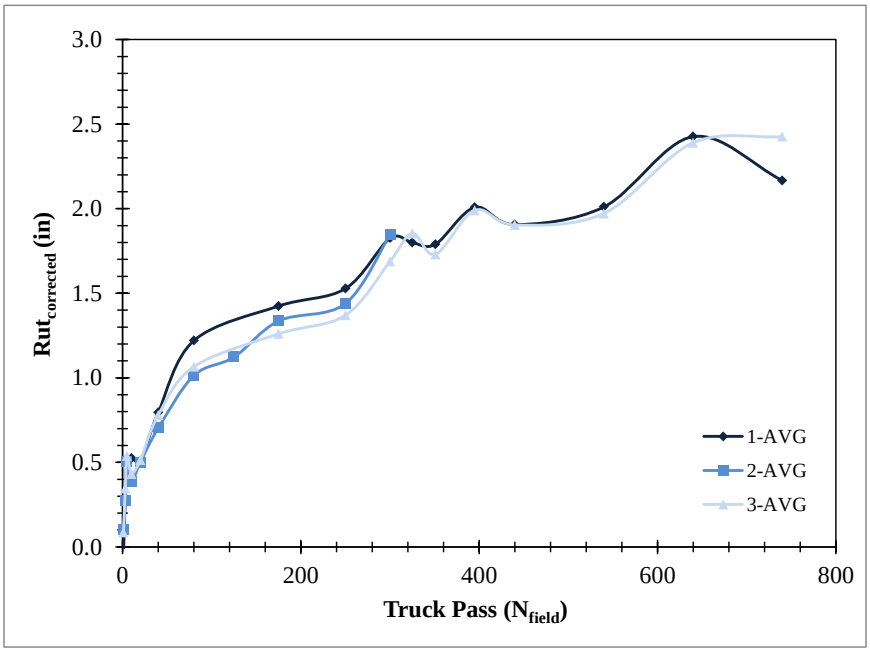


Figure 43: Corrected longitudinal rut versus truck pass for Test Sections 1, 2, and 3.

The subgrade adjustments were applied to all of the transverse rut measurements using linear interpolation between these multiplicative factors based on subgrade strength. The linear interpolation was performed using the bi-linear line illustrated in Figure 44. Recall that there are only two transverse instrumentation locations in each test section. Also, because this thesis focuses on the transverse behavior of geosynthetics and instrumentation was located in the west wheel path, the correction factors were only used in the west wheel path of the instrumented locations. Lastly, the subgrade strength correction factor was not applied to the transverse rut profiles, and because of the uncertainty in the effect that base aggregate less than 12 inches thick has on performance in reinforced test sections, the variations in base course thickness were not accounted for.

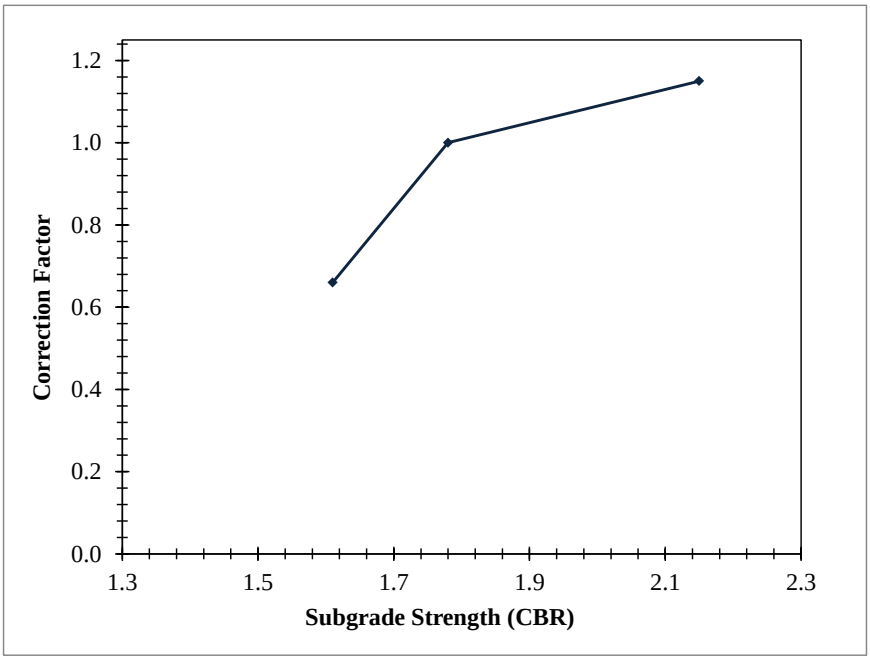


Figure 44: Correction factor for subgrade strength variations (based on longitudinal data).

Transverse Rut Profiles

The transverse profiles of the base course at the two instrumented locations in each test section were surveyed in the transverse direction before and during trafficking to generate profiles which were used to analyze rut formation throughout trafficking. Representative results of the transverse behavior of test sections are shown for the south instrumented location of Test Section 3 and north instrumented location of Test Section 7 in Figure 45 and Figure 46, respectively.

Failure of a test section was defined as when rut depths, measured by changes in elevation, exceeded 3 inches. When failure was reached, the ruts were filled in so trafficking of the remaining test sections could continue. A thick solid line was used in Figure 45 and Figure 46 to indicate when a test section failed, and if a test section did not fail before the end of trafficking (i.e., truck pass 740), then no thick solid line was used.

Note how in Test Section 3-South (Figure 45), the ruts were not repaired and trafficking continued to truck pass 740, whereas for Test Section 7-North (Figure 46), the rut bowl developed rapidly and the ruts were filled in at truck pass 300. Also, note the amount of base aggregate heave in Test Section 7-North. Dotted vertical lines indicate generally where the three LVDT leadwires were originally attached to the geosynthetic, and dashed vertical lines represent the anticipated wheel paths of the truck. The LVDT and wheel path lines are only for a conceptual view. The original LVDT leadwire locations slightly varied because each geosynthetic had its own unique structure which dictated the position of the LVDT measurements. Further, movement of the LVDTs is based on how the rut bowl forms during trafficking. Note that the truck's wheel path slightly wandered at truck pass 250. The transverse rut profiles for all of the test sections are shown in Appendix I.

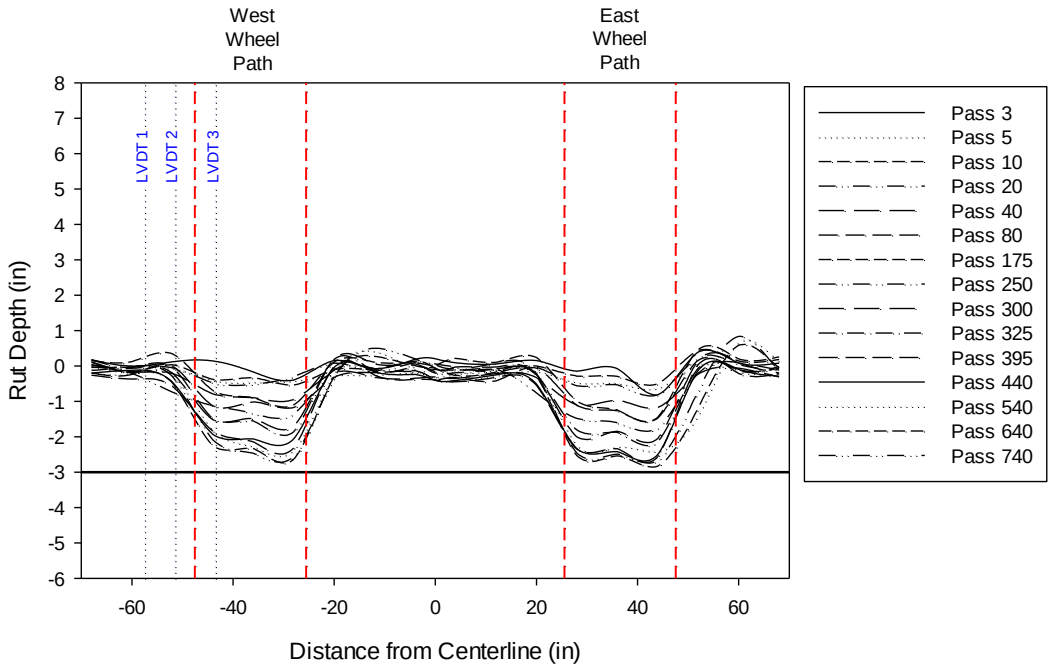


Figure 45: Transverse profile - Test Section 3-South.

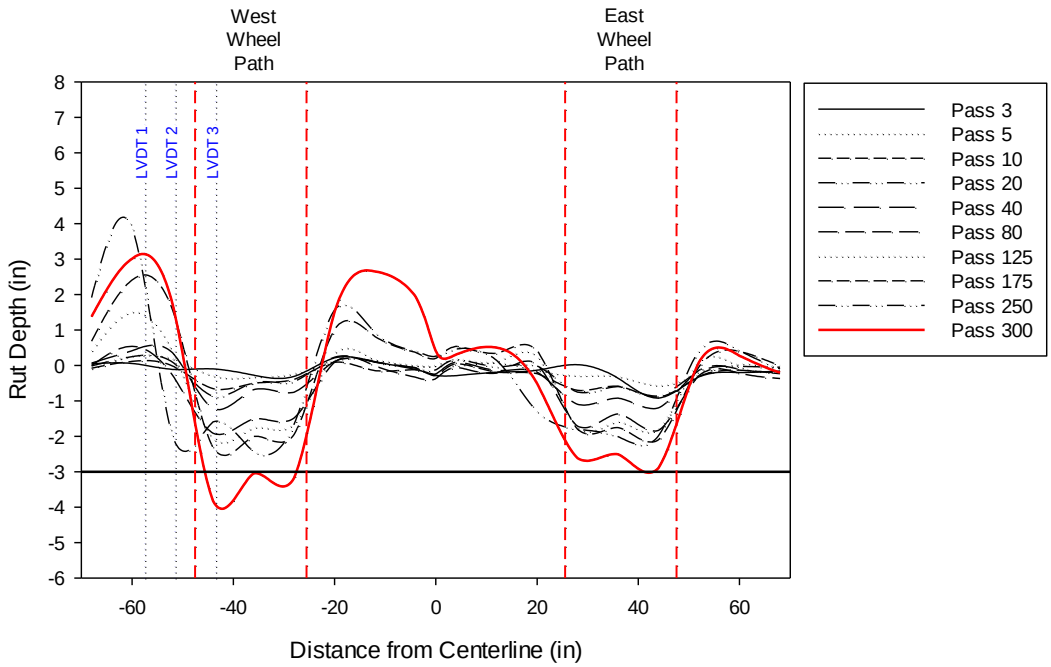


Figure 46: Transverse profile - Test Section 7-North.

Heave in the transverse rut profiles indicated that the geosynthetic was beginning to transition from lateral confinement towards membrane support. Heave began to occur at different levels of trafficking for each test section, but in general occurred between truck pass 80 to 300. The test sections where heave began to occur before truck pass 80 typically reached three inches of elevation rut faster; that is, the test sections failed faster. For example, the west wheel path in Test Section 3-South had negligible heave, and Test Section 3-South did not fail in the field study (i.e., all 740 truck passes were applied before reaching 3 inches of rut), whereas Test Section 7-North began to shown signs of heave around truck pass 40, and failed at truck pass 300.

Strain Gage Measurements

Dynamic and long-term static strain gage readings were plotted to analyze the local strain in the geosynthetics throughout trafficking. Figure 47 and Figure 48 illustrate the dynamic strain gage results for Test Section 3 and 10, respectively, and Figure 49 and Figure 50 display the long-term static strain gage results for Test section 3 and 10, respectively. Note that as the strains begin to converge to a constant value, the roadway is beginning to permanently stabilize. Also, missing data from a strain gage plot indicates that the gage was not functioning properly. Lastly, dynamic strain is shown for individual truck passes, which were compiled into a single plot. The dynamic and static strain gage plots for all of the test sections are shown in Appendix J and Appendix K, respectively.

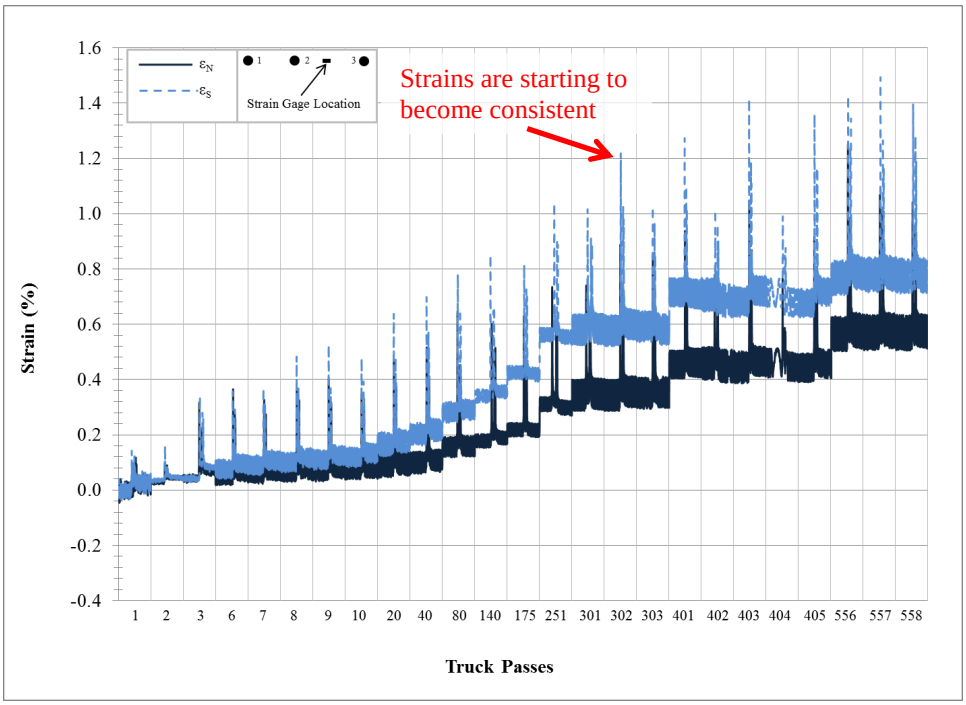


Figure 47: Strain gage dynamic results – Test Section 3.

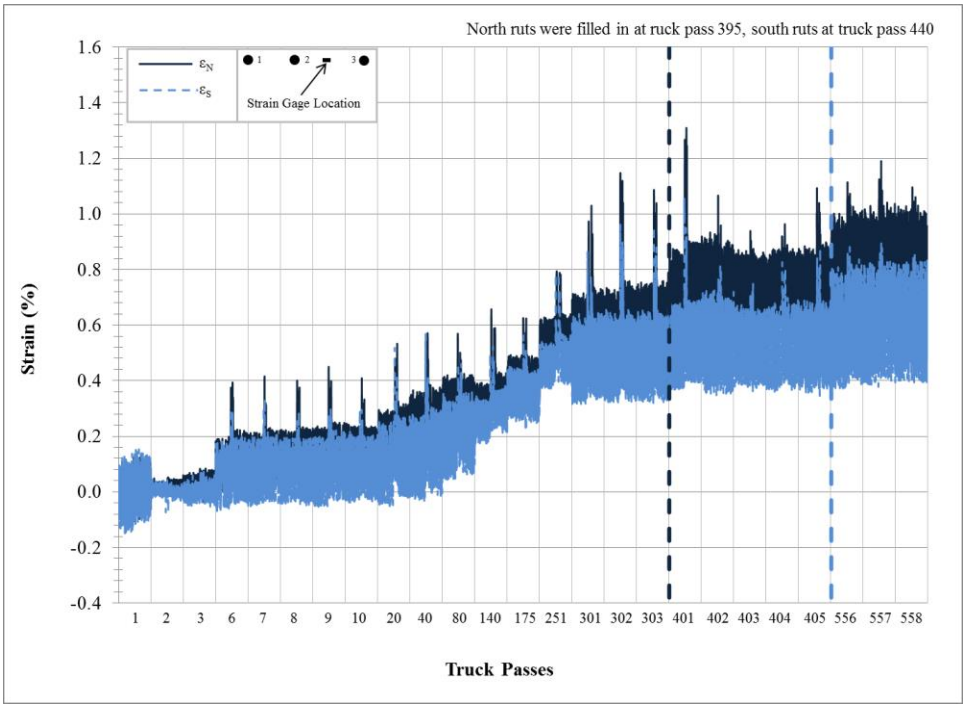


Figure 48: Strain gage dynamic results – Test Section 10.

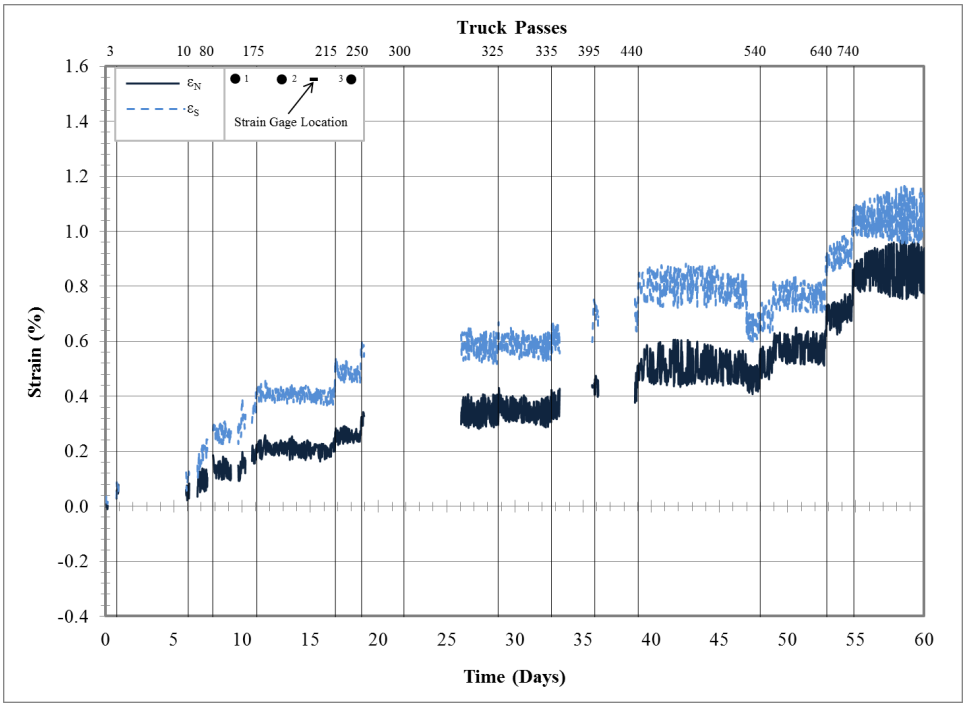


Figure 49: Strain gage static results – Test Section 3.

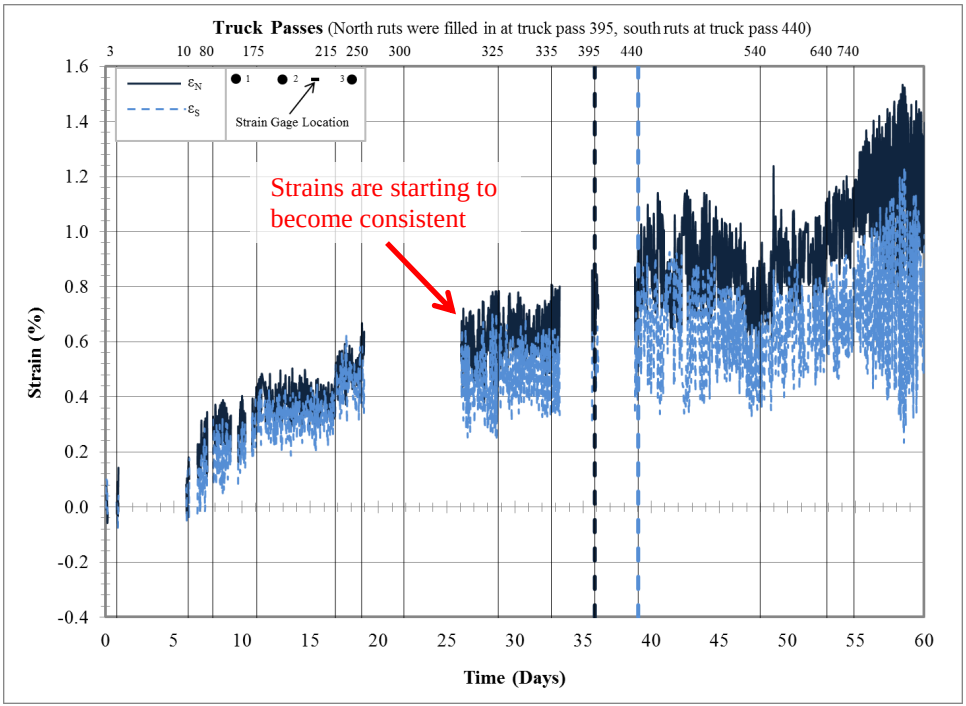


Figure 50: Strain gage static results – Test Section 10.

In general, from truck passes 1 to 300, the strains measured from the strain gages increased steadily which indicates that the geosynthetics were providing lateral confinement to the base course aggregate and/or membrane support of the wheel loads as depicted in Figure 40. Because the dynamic strains are generally moving towards a consistent pattern from truck passes 301 to 558, the roadway is beginning to permanently stabilize as illustrated in Figure 47. Thus, although the strain gage plots provide valuable information regarding the strain in the geosynthetics, the transition from lateral confinement to membrane support is not well-defined in the strain gage data, but the approximate truck pass when the geosynthetic permanently stabilizes the roadway can be estimated (i.e., when no further deformation of the test section occurs).

The long-term static strain gage plots illustrated the permanent strain in the test sections and also the long-term behavior of the strain gages. The long-term static strain matched well with the dynamic strain, and provided data from truck passes 559 to 740 which generally followed the same strain pattern as the dynamic data from truck passes 556 to 558. For example, if the dynamic strains from truck pass 556 to 558 were increasing, then the long-term static strains from truck pass 559 to 740 were also increasing. In addition, the long-term static strains also showed the approximate truck pass when the geosynthetic permanently stabilized the roadway as illustrated in Figure 50.

LVDT Measurements

LVDTs measured dynamic and long-term static displacements which were also used to evaluate the transition from lateral confinement to membrane support of the

geosynthetics throughout trafficking, and to verify when the geosynthetics began to permanently stabilize the roadway. Figure 51 and Figure 52 illustrate the dynamic LVDT displacement results for Test Section 3-South and 7-North, respectively, and Figure 53 and Figure 54 illustrate the long-term static LVDT displacement results for Test Section 3-South and 7-North, respectively. The dynamic and static LVDT plots for all of the test sections are shown in Appendix L and Appendix M, respectively.

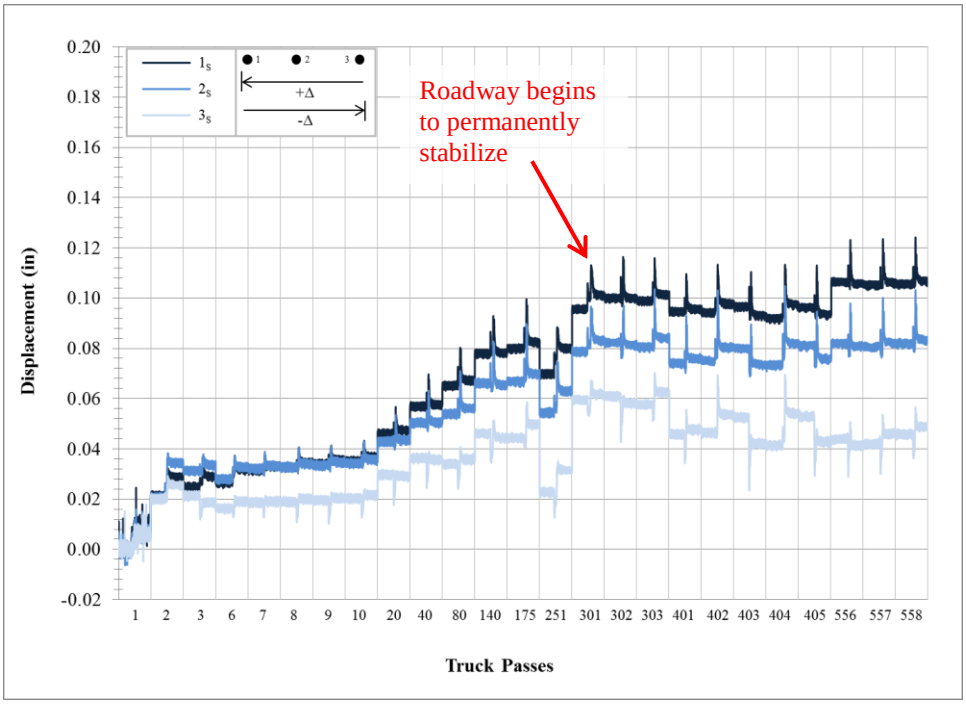


Figure 51: LVDT dynamic displacement results – Test Section 3-South.

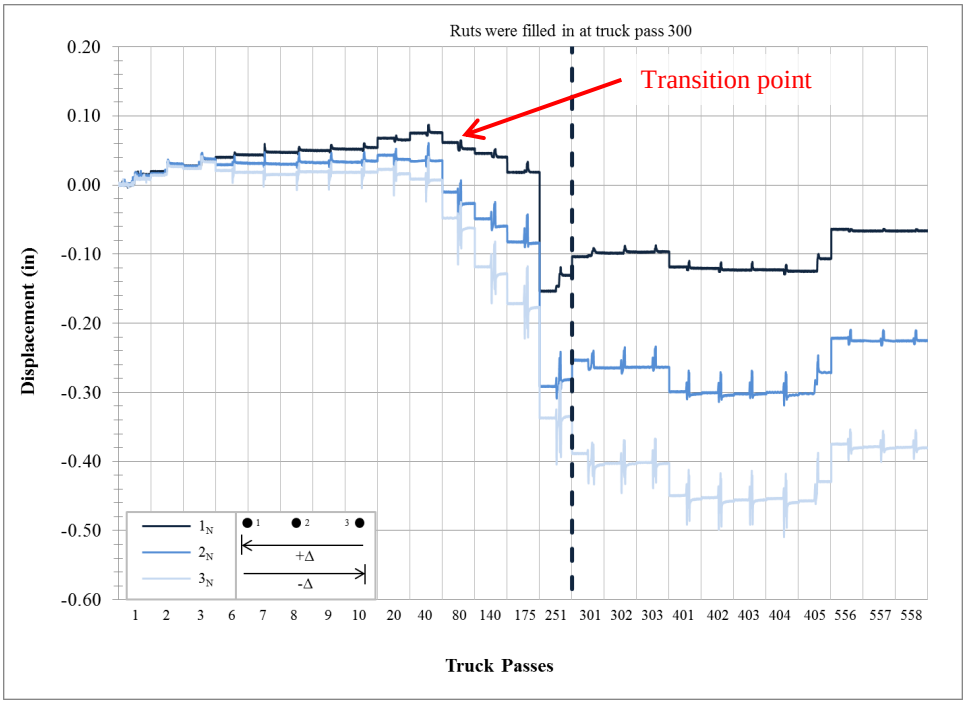


Figure 52: LVDT dynamic displacement results – Test Section 7-North.

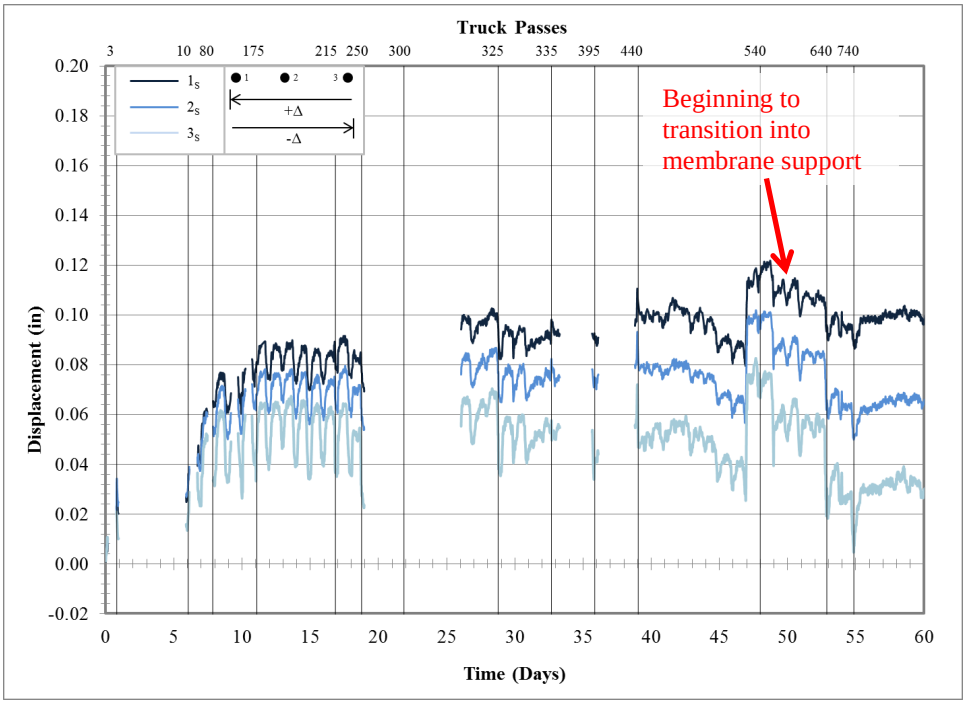


Figure 53: LVDT static displacement results – Test Section 3-South.

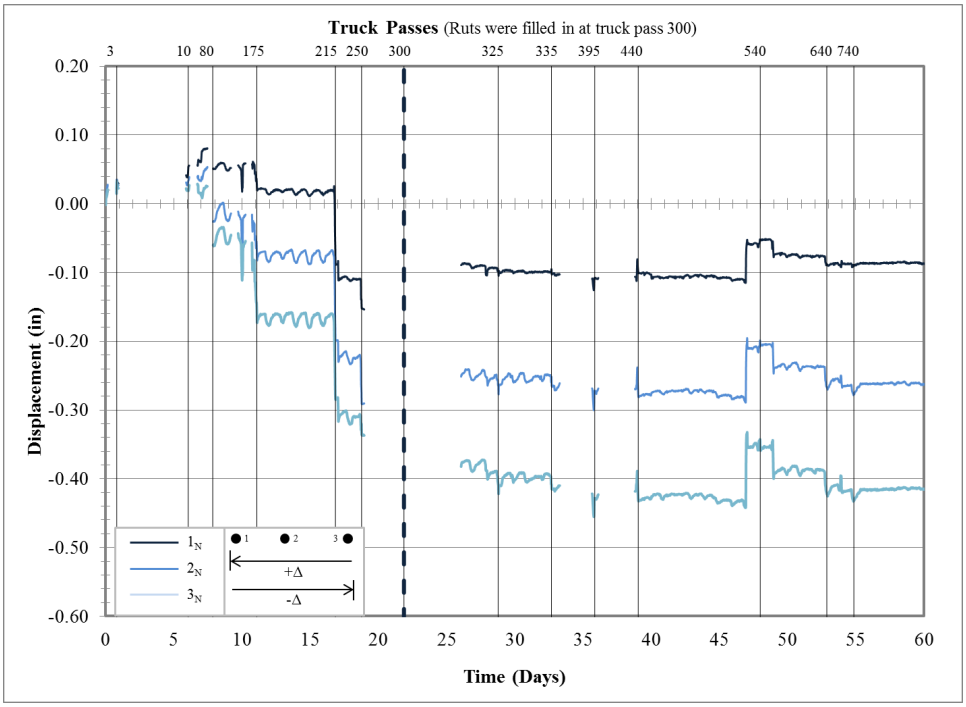


Figure 54: LVDT static displacement results – Test Section 7-North.

In general, if all of the displacements were positive (i.e., they were moving laterally away from the rut bowl), then the geosynthetic was primarily providing lateral confinement to the base course, but when all of the displacements began to move toward the rut bowl, then the geosynthetic started to provide membrane support to the wheel loads as illustrated in Figure 52. Test sections that showed signs of permanent stabilization performed significantly better in the field study as indicated in Figure 51.

The transition from lateral confinement to membrane support, as determined by the LVDT displacement measurements, occurred at different truck passes for each test section, but in general occurred between truck pass 175 to 300. Referring to Figure 52, Test Section 7-North transitioned between truck pass 40 to 80 and did not shows signs that it was becoming permanently stabilized prior to failure. Similar to the transverse rut

profiles, the earlier a geosynthetic transitioned from lateral confinement to membrane support, the quicker the ruts in that test section developed, and therefore the quicker the test section failed. In general, the test sections that transitioned before truck pass 175 reached 3 inches of elevation rut faster; that is, the test sections failed faster. For example, Test Section 3-South transitioned between truck pass 540 to 565 using the LVDT long-term static displacement results in Figure 53 and the trafficking log in Figure 41 (trafficking log was used because the static long-term plots do not have an arithmetic scale with respect to truck passes), and did not fail; whereas Test Section 7-North transitioned between truck pass 40 to 80 and failed at truck pass 300.

The long-term static LVDT displacement plots were used to evaluate the long-term behavior of the geosynthetics and also provided data from truck passes 559 to 740 (note that the dynamic data was only recorded up to truck pass 558). In general, the long-term static displacements matched well with the dynamic displacements, and from truck passes 559 to 740, the geosynthetics were typically beginning or continuing to transition into membrane support as illustrated in Figure 53.

LVDT displacement data also provided a means of calculating strain in the geosynthetics, and provided a redundant measurement of the strain experienced by the strain gage. The strain from LVDT positions 1 to 2, positions 2 to 3, and positions 1 to 3 were calculated using the displacement data from the LVDTs. Recall that the location of the LVDTs is only in the west wheel path, and the LVDT spacing is about 6 inches from LVDT 1 to 2, and about 8 inches from LVDT 2 to 3, as depicted in Figure 55. Figure 56 and Figure 57 illustrate the LVDT dynamic strains in Test Section 3-South and 7-North,

respectively, and Figure 58 and Figure 59 illustrate the LVDT long-term static strains in Test Section 3-South and 7-North, respectively. The dynamic and static LVDT strain plots for all of the test sections are shown in Appendix N and Appendix O, respectively.

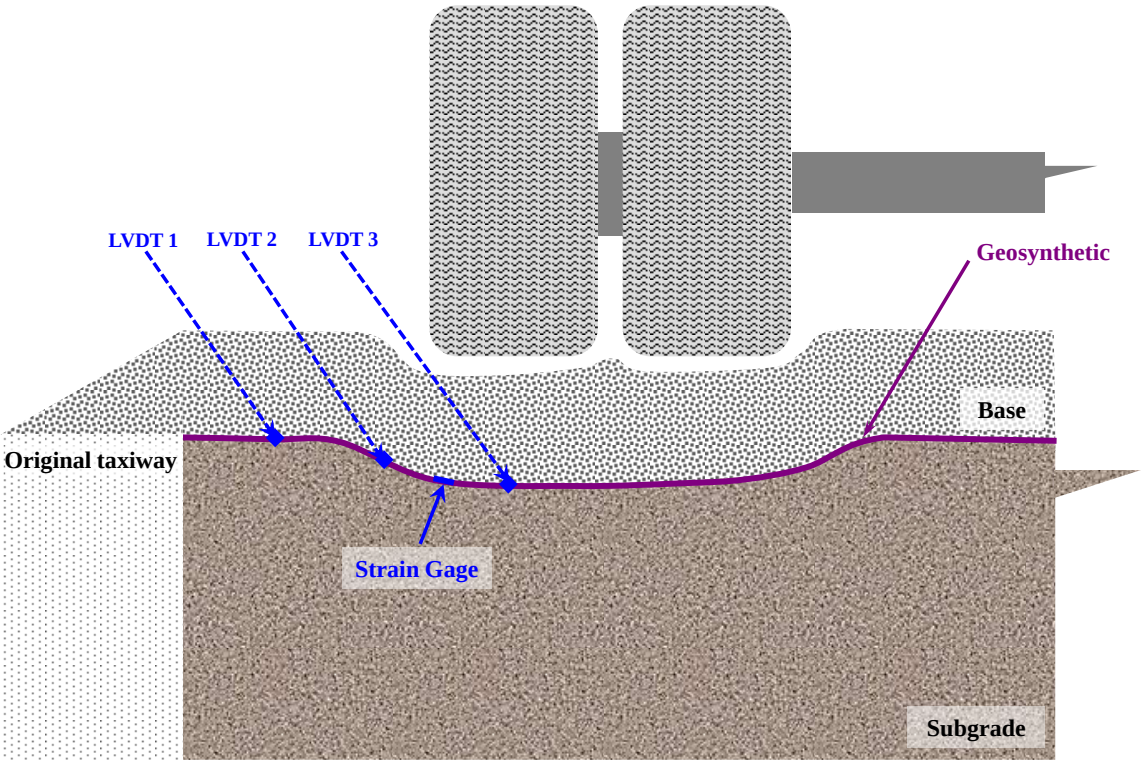


Figure 55: LVDT positions in west wheel path.

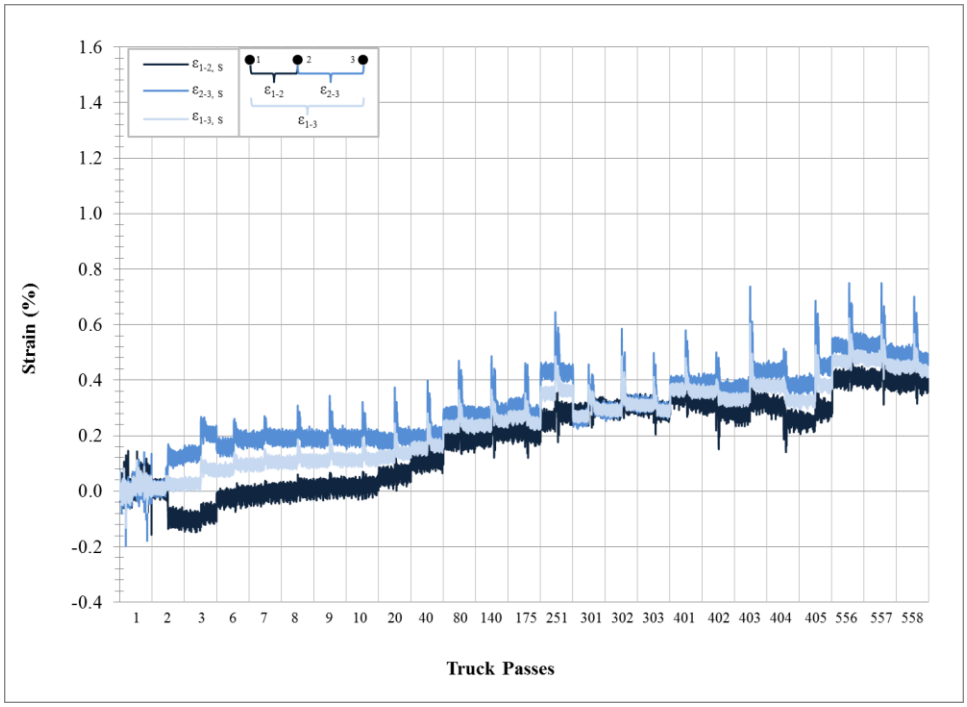


Figure 56: LVDT dynamic strain results – Test Section 3-South.

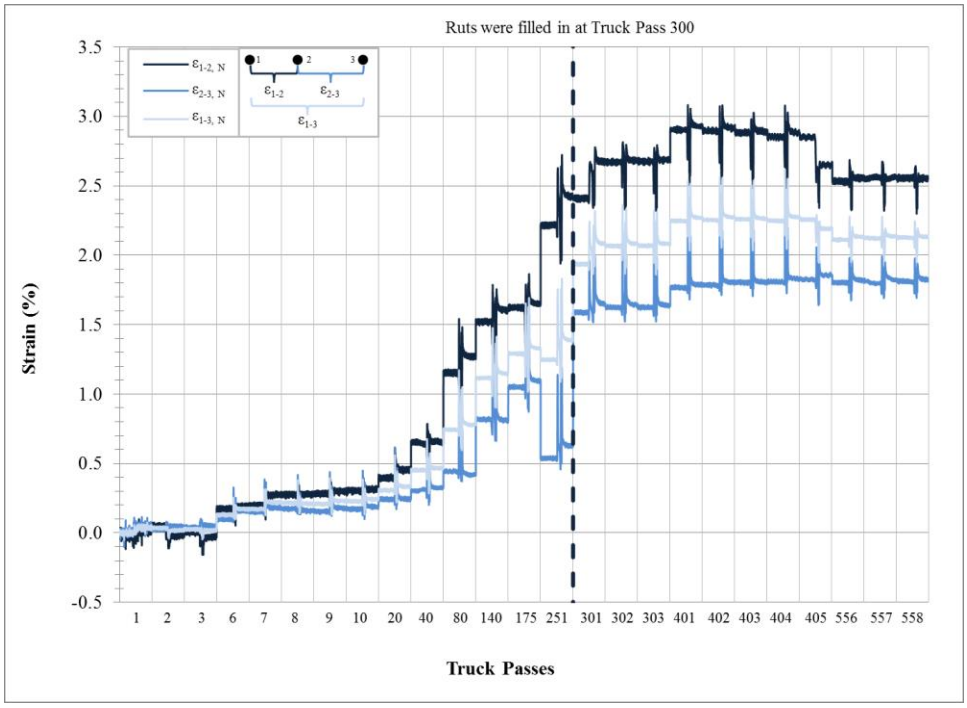


Figure 57: LVDT dynamic strain results – Test Section 7-North.

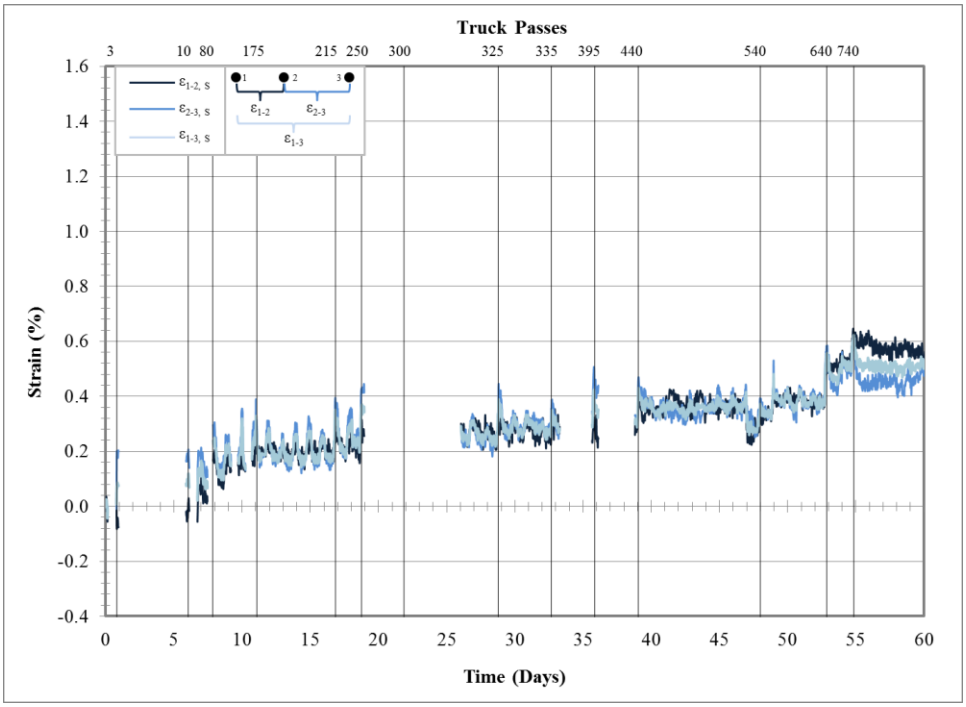


Figure 58: LVDT static strain results – Test Section 3-South.

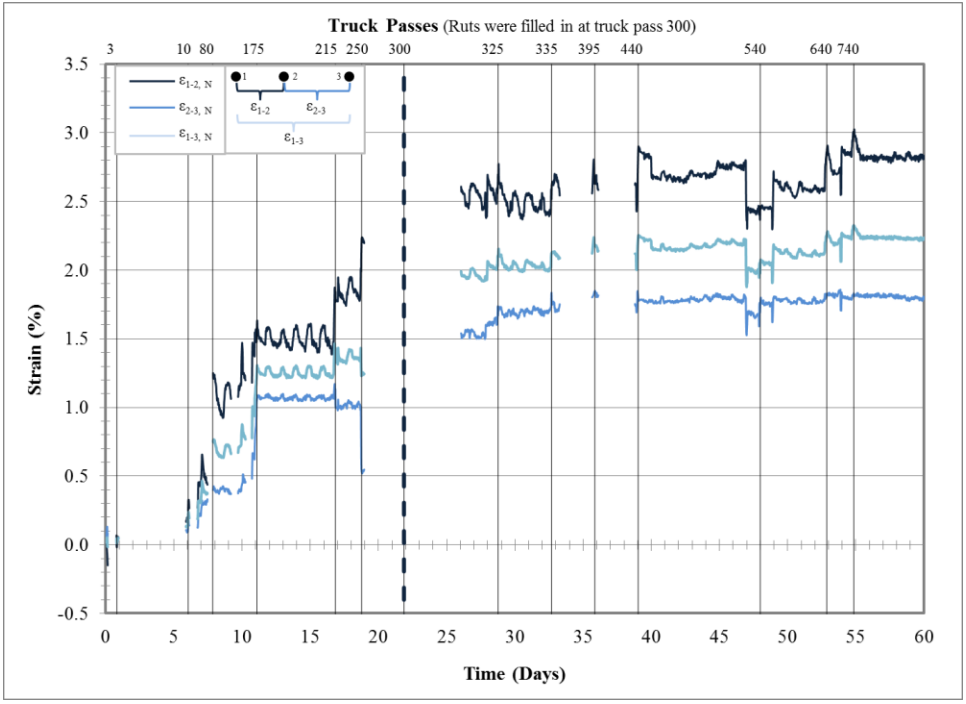


Figure 59: LVDT static strain results – Test Section 7-North.

The truck pass where the test sections began to permanently stabilize was less clear with the LVDT strain data; however, the strains from LVDT 2 to 3 provided a redundant measurement to the strain gages and typically matched closely to the strain gage strains as shown for truck pass 40 in Figure 60. The reason for the differences in Test Section 14 (Geotex 801) may be due to an increased stiffening of the strain gage area when embedded in soil; however, this was not verified in the field study and further research is needed on this concept.

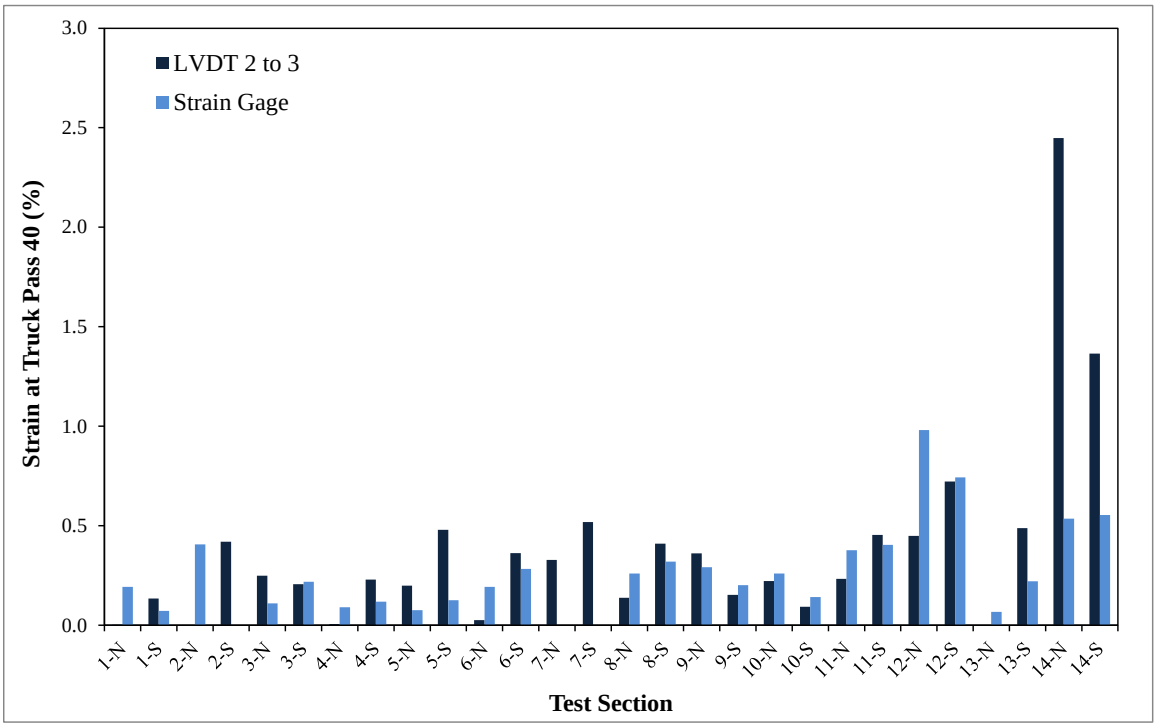


Figure 60: LVDT 2 to 3 strain compared to strain gage strain at truck pass 40.

Synthesis

The strain gage and LVDT long-term static and dynamic measurements, and the transverse rut profiles from the field test during trafficking were analyzed to determine

the transition from lateral confinement to membrane support for each instrumented location and also the field performance of the geosynthetics. The transition was primarily based on the transverse rut profiles and the LVDT measurements, and field performance of the geosynthetic test sections was evaluated based on the mechanical properties of the geosynthetic compared to the truck passes at failure and at the transition. Note that only the transverse instrumented locations were analyzed (i.e., west wheel path), and also that lateral confinement and membrane support are not independent of one another; rather, they are typically acting together in a subgrade stabilization application to support the traffic loads, which reduces the stress on the subgrade and increases bearing capacity.

The truck pass at which the geosynthetic transitioned from lateral confinement to membrane support is summarized for all test sections in Figure 61. Note that because the truck driver got off the wheel path sometime between truck pass 176 to 250 and power supply issues resulted in missing data between truck pass 251 to 300, the data between truck pass 176 to 300 was not used and/or available. Further, because some ruts were filled in at truck pass 300, several of the transitions are missing (e.g., Test Section 6-North in particular). Also, Test Sections 1 and 2 are not shown in Figure 61 because they had different subgrade strengths than Test Sections 3 to 14.

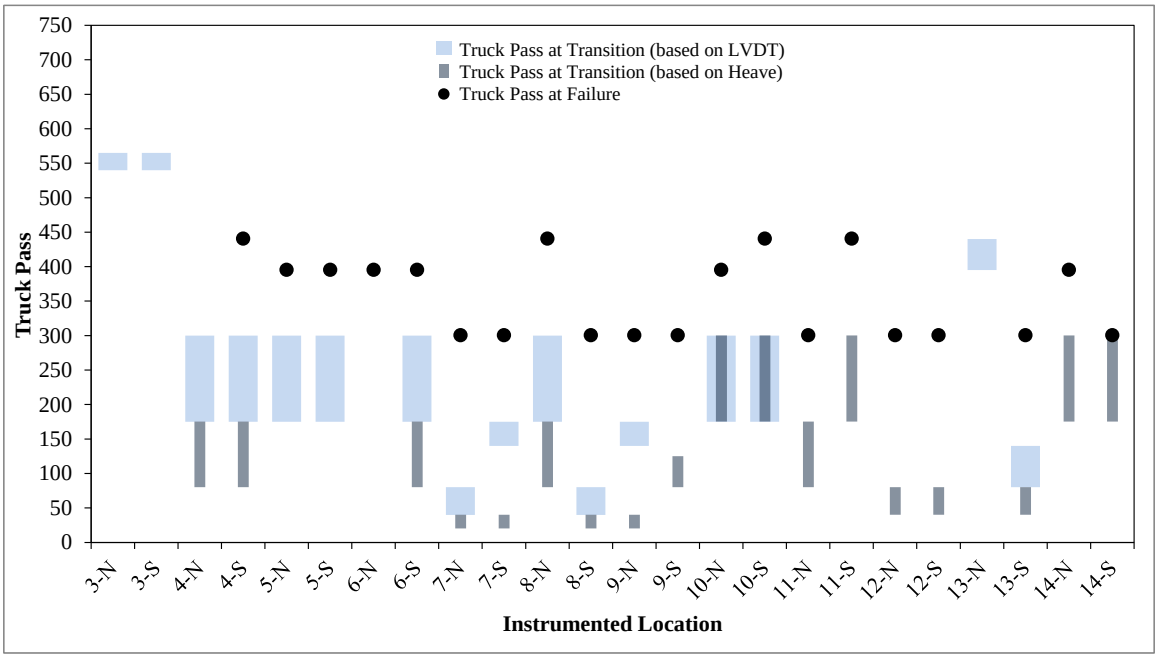


Figure 61: Truck pass at transition to membrane support and at failure for all reinforced test sections.

The transition from lateral confinement to membrane support is very important in the behavior and performance of geosynthetics when used for subgrade stabilization because it indicates a bearing capacity failure, especially with respect to heave. From Figure 61, the geosynthetics were primarily providing lateral confinement for truck passes 1 to between 80 to 300, and membrane support for truck passes 81 to 301 up to failure, or until the end of trafficking (i.e., truck pass 740). If a test section transitioned early (i.e., before truck pass 80 to 300 based on heave, or truck pass 175 to 300 based on LVDT displacement data), it typically failed early. This behavior is verified by both the transverse rut profiles and LVDT displacement measurements based on when heave began to occur and when the LVDTs began to move toward the rut bowl, respectively. On average, the transition from lateral confinement to membrane support (using both the transverse rut profile and LVDT displacement data in Figure 61) occurred around 1.7

inches of elevation rut (around 1.7 to 3.1 inches of apparent rut), with the lowest and highest elevation rut at these transitions being 0.7 and 2.6 inches, respectively. However, it is important to note that the LVDTs only measure displacement in one direction and therefore, as trafficking progressed, movement of the subgrade and base course aggregate soils may have slightly altered the LVDT measurements. Regardless of this, the transition from lateral confinement to membrane support was still generally well-pronounced using the LVDT displacement data and therefore the analyses that follow will incorporate the transition using both the transverse rut profiles and the LVDT displacement measurements.

Analyses between selected mechanical properties of the geosynthetics versus the number of truck passes at transition and failure were performed. Note that in addition to the standard mechanical properties of the geosynthetics, junction stiffness and select data from the resilient interface shear stiffness test results were analyzed. Junction stiffness was determined based on the linear portion of the junction strength (lb/in) versus displacement curves between 0 to 0.10 inches of displacement as described in chapter 3. The select data used for the resilient interface shear stiffness tests consisted of low confinement and high shear stress to relate the test most closely to subgrade stabilization applications. The confinement analyzed was 650 psf (31.0 kPa) at the fourth prescribed load level (i.e., high shear stress), which is also described in chapter 3.

A test section was assumed to perform well if both of its instrumented locations did not transition early and also did not fail at truck pass 300, and to perform poorly if either of its instrumented locations did transition early and also failed at truck pass 300,

as illustrated in Figure 61. The geogrids that transitioned early and failed early were SF 12, BXG 11, Fornit 30, TX 140, and TX 160 (highlighted in Table 15). Because these geogrids transitioned early and in general failed at truck pass 300, their mechanical properties were analyzed and compared to test sections that did not transition early and also that did not fail until after truck pass 300. Select mechanical properties of all of the geogrids are listed in Table 15. Note that the Tenax MS330 is a triple-layer geogrid and was not included in the analyses comparing junction strength (JS), junction stiffness (JST), or aperture stability modulus (ASM) because those tests were performed using only one layer of material, and simply multiplying the results by three is likely not truly representative of the actual properties of the composite (e.g., the junctions and apertures for all three layers may not be loaded equally).

Table 15: Select Mechanical Properties of Geogrids

Geosynthetic Test Section	WWT[a] (lb/ft) @			CM[a] @ 2% (kip/ft)	G_I[a] (ksi)		JS[a] (lb/in)	JST[a] (lb/in per in)	ASM[a] (lb-in/deg)
	2%	5%	Ult.		Std.	Select Data			
BX Type 2	822	1,494	1,946	62.4	305	199	171.6	785.3	6.9
Secugrid 30/30 Q1	946	1,830	2,713	79.3	186	229	57.6	773.9	10.2
Enkagrid Max 30	857	1,775	2,378	68.9	91	256	49.5	537.4	13.9
SF 11	617	925	3,782	57.5	178	281	37.1	355.5	2.2
SF 12	987	1,446	5,818	90.8	292	469	28.6	274.5	2.4
BXG 11	740	1,281	3,221	66.5	240	333	35.8	711.4	3.1
Fornit 30	946	1,939	2,618	75.6	129	187	10.5	130.3	9.6
Tenax MS330	692	1,343	2,248	54.4	190	264			
TX 140	322	665	843	28.2	88	82	72.4	342.5	2.5
TX 160	391	747	884	31.1	242	282	75.1	268.0	4.9

[a] acronym meanings: WWT = wide-width tensile, CM = cyclic modulus, G_I = resilient interface shear stiffness, JS = junction strength, JST = junction stiffness, ASM = aperture stability modulus

Table 15 was used to analyze the mechanical properties that were most directly related to field performance. The WWT (wide-width tensile) strength showed that the

TX 140 and TX 160 geogrids at 2%, 5%, and at ultimate strength were lower than all of the other geogrids. Because of the lower strength values, these geogrids may not have sufficient strength and stiffness for subgrade stabilization applications. The SF 11 geogrid had the next lowest values of WWT strength which were 617 and 925 lb/ft at 2 and 5% strain (see Table 15), respectively. Because the SF 11 geogrid did not fail until truck pass 395 (i.e., it performed well), specifying minimum WWT strengths of 600 and 900 lb/ft at 2 and 5% strain, respectively, is a conservative approach. Similarly, the cyclic tensile modulus of the Tenax MS330 material at 2% strain was 54.4 kip/ft, which is just above the TX 140 and TX 160 materials. Because the Tenax MS330 material performed well, the cyclic tensile modulus could be specified at a minimum value of 50 kip/ft (see Table 15); however, it should be noted that the cyclic tensile modulus test is more appropriate for base reinforcement applications where repetitive cyclic loads are applied at the same level of strain, and is therefore cautioned for predicting performance in subgrade stabilization applications.

The resilient interface shear stiffness (G_I) did not relate very well to field performance in this application. The SF 12 geogrid had a G_I almost equal to the BX Type 2 geogrid even though the BX Type 2 test section did not fail and the SF 12 test section failed at truck pass 300. Because of this, the testing data was analyzed further and the best relationship was found when the data was analyzed at low confinement and high shear. However, although the relationship increased slightly overall with respect to all of the geogrids, it showed that the SF 12 geogrid had a higher G_I than the BX Type 2 geogrid and therefore did not seem to predict field performance well.

The junction strength and stiffness provided invaluable information into why certain test sections likely performed better than others. The reason that geogrids transitioned to membrane support early related most directly to their junction strength and junction stiffness, which were generally weaker than test sections that did not transition early. Further, from post-trafficking investigations performed in the summer of 2013, the geogrids that transitioned early showed signs that the junctions were loose, broken, or that the machine direction rib had shifted out of its original position. This observation was confirmed with the SF 12 material, which was stronger than the SF 11 material in all of the laboratory tests performed except for junction strength and stiffness, and is possibly the reason why the SF 11 geogrid performed well, and the SF 12 geogrid performed poorly, as illustrated in Figure 61. Also, the BX Type 2 geogrid (Test Section 3 specifically) had the strongest junction strength and stiffness, and it outperformed all of the other test sections; while the Fornit 30 geogrid had the weakest junction strength and stiffness, and consequently performed the poorest of all the test sections (using Figure 61 and the transverse rut profiles). Because the geogrids that performed poorly in general had junction strength values less than 35 lb/in (see Table 15), a minimum junction strength value of 35 lb/in is appropriate. Also, junction stiffness by itself may be an important property in geogrids. The TX 160 geogrid was stronger than the TX 140 geogrid in all of the laboratory tests performed, including junction strength; however, junction stiffness was greater in the TX 140 geogrid than the TX 160 geogrid (342.5 and 268.0 lb/in per inch, respectively). This may be why the TX 140 geogrid performed slightly better than the TX 160 geogrid, as illustrated in Figure 61. Similar to the

junction strength, the SF 11 geogrid's junction stiffness was typically just slightly greater than the geogrids that performed poorly, and because the SF 11 geogrid's junction stiffness was 355.5 lb/in per inch, an appropriate minimum junction stiffness is about 350 lb/in per inch.

The aperture stability modulus tests did not relate very well to field performance. The SF 11 geogrid had the lowest aperture stability modulus, yet it performed better than the SF 12, BXG 11, Fornit 30, TX 140, and TX 160 geogrids. This relationship suggests that the aperture stability modulus did not seem to predict field performance well.

The ability of a geosynthetic to provide lateral confinement, reduce the stress on the subgrade, and provide membrane support of the wheel loads is highly dependent on the mechanical properties of the geosynthetic. In particular, the analyses illustrate that junction strength and stiffness, and wide-width tensile strength may play an important role in estimating the performance of geogrids when used for subgrade stabilization. The minimum requirements of the most pertinent mechanical properties of geogrids are recommended based on the transverse behavior and performance of the geogrids in this field study. The recommendations are based on limited data, which consists of base course aggregate thicknesses between approximately 9.5 to 12.5 inches, CBR strength values between 1.5 to 2.2, and rut depths up to about 3.0 inches of elevation rut (up to about 5.4 inches of apparent rut). A geogrid should have a wide-width tensile strength of 600 lb/ft and 900 lb/ft at 2% and 5% strain, respectively, and a junction strength and stiffness of 35 lb/in and 350 lb/in per inch, respectively. The ultimate WWT strength was not able to be determined using the data presented in this thesis because ultimate

strengths were never reached in the field; however, Holtz et al. (2008) recommend a minimum ultimate strength of 1,230 lb/ft for survivability requirements of geogrids installed in harsh conditions, and this seems appropriate.

The nonwoven and woven geotextiles performed well in the field study, but because of the limited testing on the mechanical properties of the geotextiles, only limited conclusions from this field study can be drawn. The nonwoven geotextile (Geotex 801) was only tested for resilient interface shear stiffness and grab breaking load. The nonwoven geotextile has low tensile capacity when compared to the geogrids; however, it outperformed several geogrid reinforced test sections. The woven geotextile (RS580i) is a high-strength geotextile which also performed very well in the field study. The RS580i geotextile was tested in WWT strength, cyclic tensile modulus, and resilient interface shear stiffness. Because both geotextiles performed well and had significant differences in material and mechanical properties, one of the primary reasons why they performed well is likely because of their surface structure. Both of the geotextiles had frictional surfaces which were sufficient to provide lateral confinement and membrane support to the base course aggregate. However, it is likely that after geotextiles, and geosynthetics in general, fully transition to membrane support, the tensile strength begins to govern performance. This concept was not verified from the geotextiles used in the field study because sufficient membrane support was not reached at 3 inches of elevation rut as can generally be seen in the dynamic LVDT displacements measurements for Test Sections 13 (RS580i) and 14 (Geotex 801) in Figure 62.

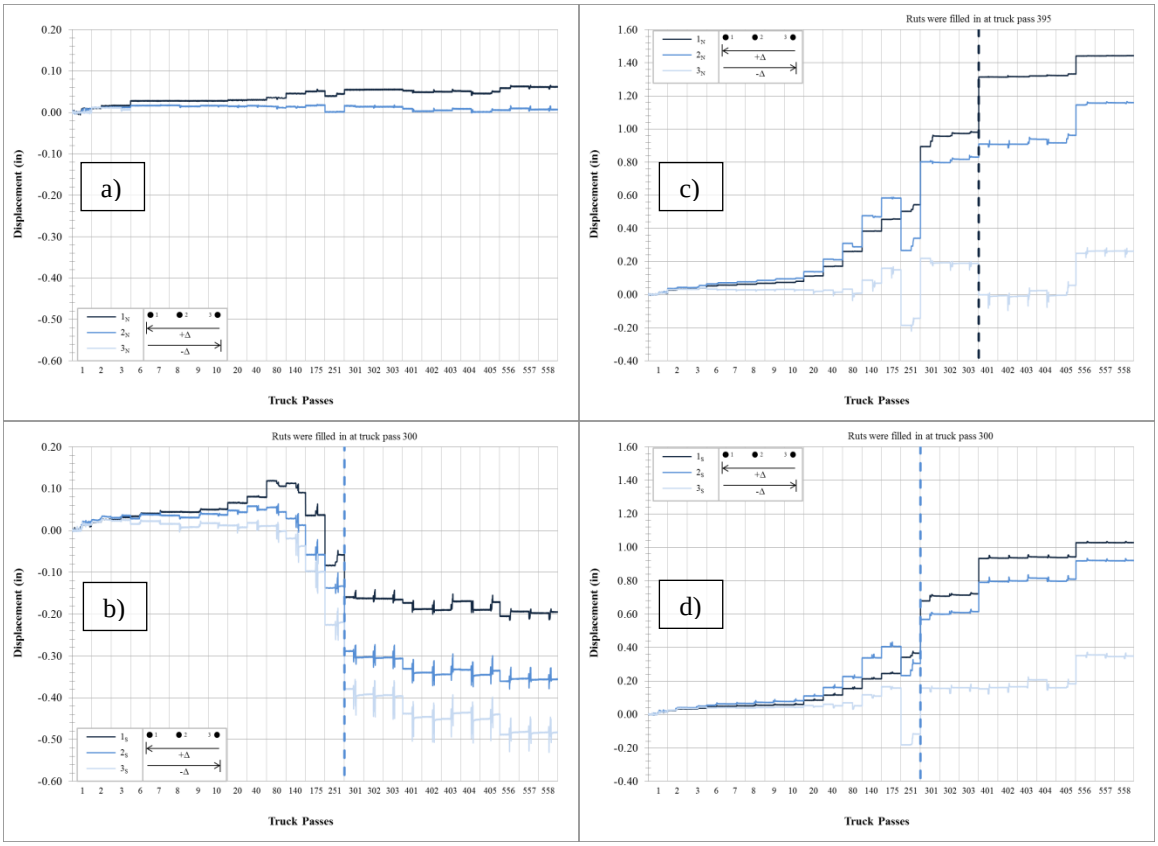


Figure 62: LVDT dynamic displacement results of Test Section:
a) 13-North, b) 13-South, c) 14-North, and d) 14-South.

Note the drastic difference in performance between Test Section 13-North and 13-South. From Table 14, the base course thickness for Test Section 13-North and 13-South was 12.5 and 10.6 inches, respectively. This was the most drastic variation in base course thicknesses within a single test section for the transverse instrumented locations. Thus, because of the significant variation, it is possible that the base course aggregate was not able to interlock sufficiently at the south location of the woven geotextile; however, this has not been verified and is therefore only speculative.

One of the generally agreed upon reasons why geotextiles perform well in subgrade stabilization applications is that they separate the subgrade from the base

aggregate. Thus, the fines from the subgrade are prevented from migrating into, and weakening, the base aggregate. Geogrids, on the other hand, are open structures that allow intrusion of the subgrade soil through their apertures, which as a result weakens the base aggregate and may also reduce the interlock between the geogrid and base aggregate. This observation was made by Fannin and Sigurdsson (1996), in which the authors suggested that the mixing of subgrade soil with base aggregate likely compromises the mechanism of lateral restraint, and therefore contamination of base aggregate is a very important function on thin gravel layers over soft subgrade soils.

CHAPTER FIVE

SUMMARY, CONCLUSIONS, AND RECOMMENDATIONS

Summary

State departments of transportation routinely use geogrids and geotextiles for subgrade stabilization. There is a general consensus between state DOTs concerning the effectiveness of these geosynthetics in subgrade stabilization; however, there is a lack of understanding and agreement with respect to the material properties of the geosynthetic that most directly relate to performance.

A full-scale field study using geosynthetics as subgrade stabilization was conducted to analyze the performance and transverse behavior of 14 reinforced test sections under vehicular loads. Insight into the mechanisms of support that geosynthetics provide was determined based on strain gage and LVDT measurements, and transverse rut profiles. Mechanical properties of the geosynthetics were compared to the truck passes at transition as well as at failure to evaluate which properties best predicted field performance. The properties that were analyzed were wide-width tensile strength, cyclic tensile modulus, resilient interface shear stiffness, junction strength, and aperture stability modulus. Lastly, correction factors were used to correct rut depths for subgrade strength variations across the test sections and determine the rut depth at transition for the geosynthetics.

Conclusions

In general, the geosynthetics provided lateral confinement for the first 80 to 300 truck passes and transitioned to membrane support for truck passes beyond 80 to 300 as determined using strain gage and LVDT measurements, and transverse rut profiles. The transition from lateral confinement to membrane support occurred around 1.7 inches of elevation rut (between 1.7 to 3.1 inches of apparent rut) on average, with a variation from 0.7 to 2.6 inches of elevation rut. The transverse rut profiles and LVDT displacement data was most useful in determining this transition.

Analyses between the mechanical properties of the geosynthetics and the truck pass at transition and failure were used to evaluate the performance of the test sections. From the analyses, the junction strength and stiffness, and wide-width tensile strength related well with the performance of the test sections up to 3.0 inches of elevation rut (or up to 5.4 inches of apparent rut). In the geosynthetic design and construction guidelines reference manual (Holtz et al., 2008), the recommended geogrid survivability requirements for subgrade stabilization applications consist of an ultimate wide-width tensile strength between 820 and 1,230 lb/ft, and junction strength between 8 and 25 lb/junction, depending on the geogrid class. Holtz et al. (2008) note that junction strength requirements have not been fully supported by data, and therefore recommend that manufacturers submit data from full-scale installation damage tests in accordance with ASTM D5818 to evaluate the integrity of the junctions for survivability requirements. With the field study presented in this thesis, data now exists that verifies the importance of junction strength, and also adds to the body of knowledge concerning

the ability of other mechanical properties of geogrids to predict field performance. The minimum recommended requirements for geogrids in subgrade stabilization applications are listed in Table 16.

Table 16: Minimum Recommended Requirements for Geogrids in Subgrade Stabilization Applications

Mechanical Property	Minimum Requirement[a]
Ultimate Junction Strength (lb/in)	35
Junction Stiffness (lb/in per inch)	350
Wide-Width Tensile Strength at 2% Strain (lb/ft)	600
Wide-Width Tensile Strength at 5% Strain (lb/ft)	900
Ultimate Wide-Width Tensile Strength (lb/ft)	1,230

[a] for multiple layer geogrids, the minimum requirements should be per layer unless verification testing is performed

Geotextiles used in subgrade stabilization should be able to serve as a separator between the subgrade and base aggregate, have a frictional surface that provides sufficient interaction with the base aggregate, and also meet the geotextile survivability requirements specified by Holtz et al. (2008). The geotextile surface must have sufficient friction to laterally confine the base course. The degree of friction required can be verified using pull-out tests or direct shear tests instead of resilient interface shear stiffness tests, although more research is needed to verify the correlations of these tests to field performance.

Lessons Learned

The LVDT installation technique proposed by Cuelho et al. (2008) was verified and is recommended for future full-scale field studies. The procedure worked well and

only one LVDT leadwire connection failed during trafficking out of the 84 that were installed. Further, the LVDTs were more reliable than the strain gages, and if local displacements and measurements are desired, then LVDT leadwires can be spaced closer together to provide those measurements which can then be used to calculate the local strain. This proposed method would eliminate the need for strain gages and would have significantly improved the instrumentation survivability in the field study.

Strain gages may be used on geosynthetics when the use of LVDTs is not practical. Truly, strain gages are well-suited because they bond directly to the geosynthetic; however, they can be expensive, involve many installation materials that expire quickly, and also require a skilled technician to install and calibrate the gages. Further, the survivability of strain gages in subgrade stabilization applications is generally low when compared to other types of instrumentation. Regardless, if strain gages are to be used, then the following recommendations are proposed.

- Use EA series gage (or equivalent) unless strains greater than 5% are expected.
- Use M-Bond AE-10 (or equivalent) on geogrids for a bonding adhesive unless strains greater than 6 to 10% are expected, and use RTV-3145 clear silicone as the bonding adhesive on geotextiles.
- Use RTV-3145 for environmental protection on both the geogrids and geotextiles (AK 22 may be a viable alternative).
- Place rubber foil or neoprene pads over the strain gages prior to construction.
- If leadwire lengths are long, then the gages should have at least 350-ohms of resistance.

Resilient interface shear stiffness tests should be performed with the same subgrade and base course soils as to be used in the field study. If the test is performed only in the base course aggregate, then it is more applicable to a base reinforcement application. Also, for a subgrade stabilization application, it may be more applicable to perform pull-out tests or direct shear tests instead of resilient interface shear stiffness tests to evaluate the performance of geosynthetics.

Transverse profiles of the top of the subgrade should be taken so that the exact transverse profiles of the base course during trafficking are known. Fortunately, even though the transverse profiles were not taken on top of the subgrade in the field study, the base course thicknesses at the wheel paths were known and were used to determine the approximate base course thicknesses of the transverse profiles.

LVDTs are temperature sensitive devices, and should be kept in a controlled environment to obtain the highest level of accuracy. Because the LVDTs were housed inside a box just outside the test sections and were exposed to the environment, there were displacements due to temperature effects which were carried into the strain calculations. Although the temperature effects were minor, if increased accuracy is desired, then LVDTs should either be housed in a controlled environment, or temperatures should be measured inside the box.

Recommendations for Future Work

In subgrade stabilization applications such as temporary roads, working platforms, unpaved roads, and permanent roads, the addition of base course aggregate to ruts that develop is essential. As the ruts near a serviceability failure, construction

equipment is used to repair the ruts so that work can continue. The field study described in this thesis defined failure as three inches of elevation rut. After failure occurred, the ruts were filled in with an unknown amount of non-compacted base course aggregate and data was not analyzed from that point forward. While this allowed the truck to continue trafficking and provided a direct comparison between test sections, it does not truly represent what happens in the field; that is, the amount of gravel added is important, and the formation of ruts (i.e., behavior and performance of the geosynthetic) after they are repaired is critical.

A subgrade stabilization field study that evaluates the behavior and performance of geosynthetics with the addition of known base course aggregate thickness at increased rut depths should be conducted. The objectives of the field study should be to evaluate the pertinent material properties of the geosynthetics at greater rut depths, and to analyze the behavior and performance of the geosynthetics, before and after base course aggregate is used to repair ruts. The repair of the increased elevation rut depth should be around 5 to 6 inches. This way, the harsh conditions which some construction projects experience can be accounted for.

The recommended work would result in a more robust analysis because the transition from lateral confinement to membrane support would be more distinct, and at 5 to 6 inches of elevation rut the geosynthetics would be primarily providing membrane support to the traffic loads. It is recommended that more geotextile products be analyzed so that the pertinent material and mechanical properties of the geotextiles can be determined for subgrade stabilization applications. Also, with the recommended work, a

comprehensive subgrade stabilization design manual may be written which specifies the material and mechanical property requirements for geosynthetics to perform well at all levels of rut. Lastly, the proposed work could result in a new design equation(s) which more accurately predicts the formation of rut using any type of geogrid or geotextile in subgrade stabilization applications.

REFERENCES CITED

Bathurst, R.J., Allen, T.M., and Walters, D.L., 2002, Short-term strain and deformation behavior of geosynthetic walls at working stress conditions: Geosynthetics International, v. 9, p. 451-482.

Beckham, W.K., and Mills, W.H., 1935, Cotton-fabric reinforced roads : W. K. Beckham and W. H. Millls. (Engineering News Record, Vol. 115 No. 14.): Journal of the Franklin Institute, v. 220, p. 816.

Brandon, T., Al-Qadi, I., Lacina, B., and Bhutta, S., 1996, Construction and Instrumentation of Geosynthetically Stabilized Secondary Road Test Sections: Transportation research record, v. 1534, p. 50-57.

Brooks, J.A., 2009, Strain gage installation and survivability on geosynthetics used in flexible pavements [M.S.C.E. thesis]: Ann Arbor, University of Arkansas.

Cuelho, Christopher, B.R., and Perkins, S.W., 2008, Small Strain and Displacement Monitoring Methods for Geosynthetics under Monotonic and Cyclic Loading, Geoamericas 2008: Cancun, Mexico, Industrial Fabrics Association international.

Cuelho, and Perkins, S.W., 2009, Field Investigation of Geosynthetics Used for Subgrade Stabilization: U.S. Department of Transportation, Report No. FHWA/MT-09-003/8193, Washington, DC, Federal Highway Administration.

Cuelho, E.V., 1998, Determination of Geosynthetic Constitutive Parameters and Soil/Geosynthetic Interaction by In-Air and In-Soil Experiments [M.S.C.E. thesis]: Bozeman, Montana State University.

Derakhshandeh, M., and Chou, N., 1990, Geotextiles in Landfills: Colorado Department of Highways, Report No. CDOH-DTD-R-90-5, Denver.

Fannin, R., and Sigurdsson, O., 1996, Field Observations on Stabilization of Unpaved Roads with Geosynthetics: Journal of Geotechnical Engineering, v. 122, p. 544-553.

Ferreira, T., and Rasband, W., 2012, ImageJ User Guide.

FHWA, 1995, Geosynthetic Design and Construction Guidelines: Federal Highway Administration, Report No. FHWA HI-95-038.

Giroud, J., and Han, J., 2004, Design Method for Geogrid-Reinforced Unpaved Roads. I. Development of Design Method: Journal of Geotechnical and Geoenvironmental Engineering, v. 130, p. 775-786.

Gnanendran, C.T., and Selvadurai, A.P.S., 2001, Strain measurement and interpretation of stabilising force in geogrid reinforcement: Geotextiles and Geomembranes, v. 19, p. 177-194.

Herlin, B., 2008, Geocomposite cover for sulfide tailings at mine site in Ontario, Geosynthetics, Volume 26: Roseville, Industrial Fabrics Association International, p. 32-36.

Holtz, R.D., Christopher, B.R., and Berg, R.R., 2008, Geosynthetic Design and Construction Guidelines: Report No. FHWA-NHI-07-092, Washington, D.C., National Highway Institute.

Hufenus, R., Rueegger, R., Banjac, R., Mayor, P., Springman, S.M., and Brönnimann, R., 2006, Full-scale field tests on geosynthetic reinforced unpaved roads on soft subgrade: Geotextiles and Geomembranes, v. 24, p. 21-37.

Messtechnik-GmbH, H.B., 2008, Instructions for use. Covering putty AK 22: Darmstadt, Hottinger Baldwin Messtechnik GmbH.

Micro-Measurements, V.P.G.-. 2010, Precision Strain Gages and Sensors: Raleigh, Vishay Precision Group - Micro-measurements.

Oglesby, J., Mahmoodzadegan, B., and Griffin, P., 1992, Evaluation of Methods and materials Used to Attach Strain Gages to Polymer Grids for High Strain Conditions: Louisiana Transportation Research, Report No. FHWA/LA-92/265: Baton Rouge.

Perkins, and Lapeyre, J.A., 1997, In-isolation strain measurement of geosynthetics in wide-width strip tension test: Geosynthetics International, v. 4, p. 11-32.

Perkins, Schulz, J.L., and Lapeyre, J.A., 1997, Local Versus Global Strain Measurement of a Polymeric Geogrid: Journal of testing and evaluation, v. 25, p. 576.

Perkins, S.W., and Christopher, B., 2010, Development of Design Charts for Unpaved Roads Using NAUE Geosynthetics: Phases I, II & III: Espelkamp-Fiestel.

Pilson, C.C., Hudson, W.R., and Anderson, V., 1995, Experimental Design, Planning, and Analysis of Pavement Test Sections for the Texas Mobile Load Simulator: Texas Department of Transportation, Report No. TX-96/2921-1F: Austin.

Shinoda, M., and Bathurst, R.J., 2004, Strain Measurement of Geogrids Using a Video-Extensometer Technique: Geotechnical Testing Journal, v. 27.

Sluimer, G., and Risseeuw, P., 1982, A strain-gage technique for measuring deformation in geotextiles., 2nd International Conference on Geotextiles: Las Vegas, NV, p. 835-838.

Steward, J.E., Mohney, J., and Williamson, R., 1977, Guidelines for use of fabrics in construction and maintenance of low-volume roads: Report No. FHWA-TS-78-205, Portland, U.S. Forest Service.

Thomas, H., and Cantre, S., 2009, Applications of Low-Budget Photogrammetry in the Geotechnical Laboratory: Photogrammetric record, v. 24, p. 332-350.

Tingle, J.S., and Webster, S.L., 2003, Corps of engineers design of geosynthetic-reinforced unpaved roads: Transportation research record, p. 193-201.

Warren, Christopher, B., and Howard, I.L., 2010, Geosynthetic strain gage installation procedures and alternative strain measurement methods for roadway applications: Geosynthetics International, v. 17, p. 403-430.

Warren, and Howard, I.L., 2007, Sensor selection, installation, and survivability in a geosynthetic-reinforced flexible pavement: Geosynthetics International, v. 14, p. 298-315.

APPENDICES

APPENDIX A:

STRAIN GAGE INSTRUMENTATION PROCEDURES

Background

Strain gages were used to measure the local strain of the geosynthetics during trafficking. Strain gages were bonded directly to the geosynthetics to provide a direct measurement of local strain at locations within each test section. The process of applying strain gages to geosynthetics is challenging because adhesives can stiffen the material and alter the strain of the geosynthetics and the strain registered by the strain gage. Geosynthetics are made of a variety of plastic materials such as polypropylene and polyester, and are also manufactured in various processes such as integrally-formed, welded, woven, knitted, extruded, and nonwoven; which also means that rib and/or weave dimensions can vary significantly. Because of the variety of geosynthetics, adhesive technology is still evolving and standardized methods of applying strain gages are limited.

Before the procedures are described, the understanding of strain gages and the circuitry used in the field study will be discussed. A brief overview of what strain and strain gages are will be presented followed by a discussion of the circuitry required to measure the strain. Lastly, the equations used to determine strain in the field study will be presented.

Strain is the amount of deformation of a body due to an applied force. It is defined as the ratio of the change in length (ΔL) of an object to the object's original length (L). The relationship is expressed in Equation A-1.

$$\varepsilon = \frac{\Delta L}{L} \qquad \text{Equation A-1}$$

Strain can be positive or negative, which typically corresponds to tension or compression, respectively.

A strain gage is a device that measures strain by a change in electrical resistance. When a strain gage is integrally attached to an object, the change in resistance can be caused by force, pressure, temperature, noise, etc. The three strain gages used for this study (EP-08-500GC-350, EP-08-230DS-120, and EP-08-20CBW-120, manufactured by Micro-Measurements, Raleigh, North Carolina) are shown in Figure A-1. Generally, the higher the resistance of the strain gage the less signal loss when long leadwire lengths are used. In this study the 350-ohm gages were not available for some of the gage geometries selected; therefore, 120-ohm gages were used instead. To mitigate signal loss and noise, a three-wire circuit was used for all test sections, regardless of resistance. The EP series gages that were selected are specifically designed for use in the measurement of large strains (greater than 3 to 5%) (Micro-Measurements, 2010). The gages, however, are not recommended for cyclic strains, but were used because large strain accumulations were expected in the field and the EP series gage accommodates larger strains (up to 20% in some cases).

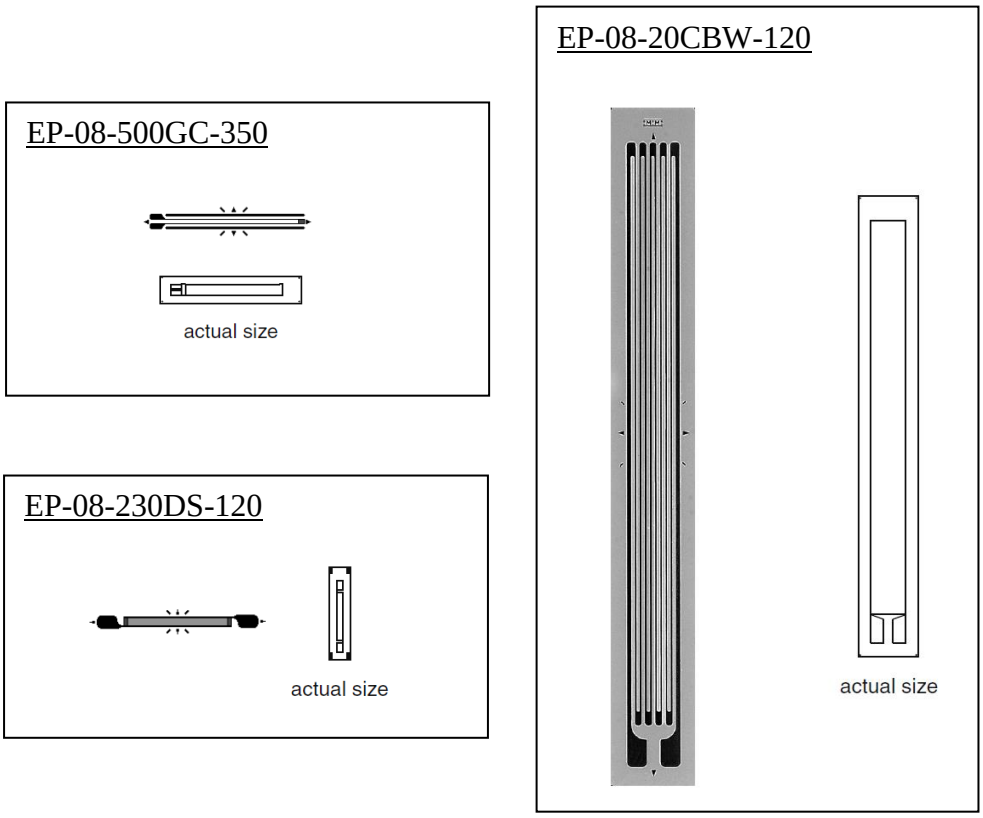


Figure A-1: Strain gages used:
EP-08-500GC-350, EP-08-230DS-120, and EP-08-20CBW-120.

A quarter Wheatstone bridge circuit was used to convert the resistance changes into voltage changes so that the strain gages could be monitored by a data logger. The quarter Wheatstone bridge circuit that was used in this study is shown in Figure A-2 for a strain gage with 350 ohms of resistance. The circuit is ideal because the two gages are connected in series and will negate the effects of bending when placed on opposite sides of the geosynthetic. The actual circuit boards used in the field study are shown in Figure A-3.

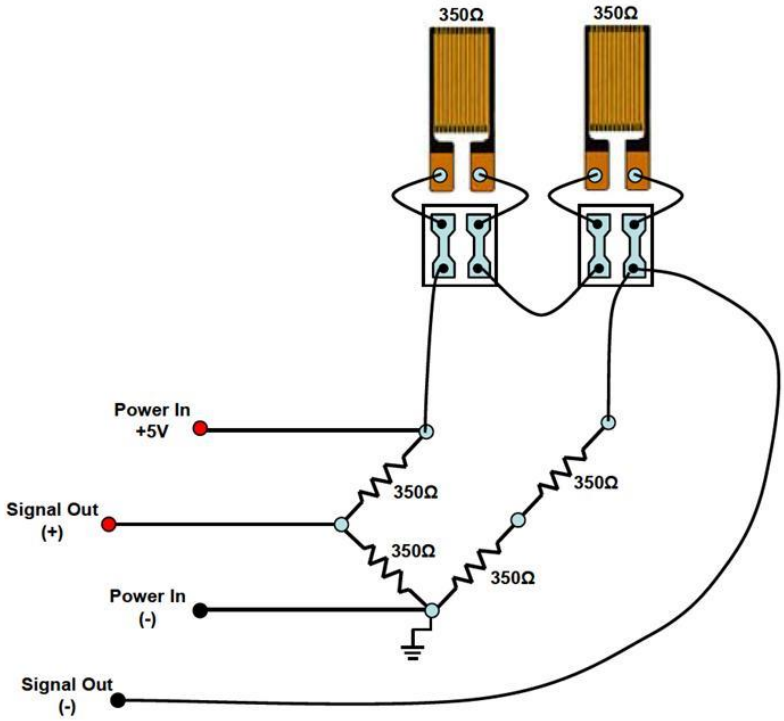


Figure A-2: Quarter Wheatstone bridge circuit
(image courtesy of Eli Cuelho).

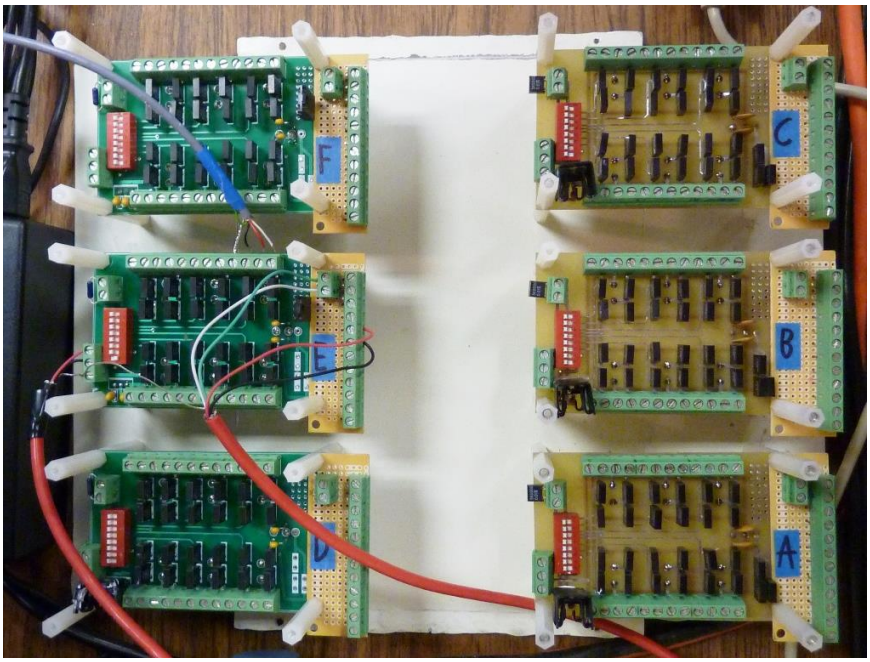


Figure A-3: Quarter Wheatstone bridge circuit boards used in field study.

The leadwire used to connect the strain gages from the geosynthetic to the boxes located just outside the test section was 426-BSV (manufactured by Micro-Measurements). The leadwire had 4 conductors and was 26-gauge stranded copper wire. The wires were twisted and shielded with a jacket, and had vinyl (PVC) insulation. This leadwire was selected because it had small conductors which made soldering the leadwires to the terminals near the strain gages much easier. The leadwire also has a very low profile which minimized the potential damage that may have been caused by construction of the base course material and trafficking.

An excitation voltage of 5V was used for the EP-08-500GC-350 and EP-08-20CBW-120 gages, and an excitation voltage of 1.8V was used for the EP-08-230DS-120 gages. The excitation voltages were determined using Micro-Measurements Tech Note TN-502. Strain from the strain gages was determined using the excitation and output voltages, and equations from Micro-Measurement's Tech Notes. After the strain gages were instrumented on the geosynthetics and placed in the field, they were shunt calibrated to adjust their gage factors, which were provided by the manufacturers. Shunt calibration consisted of increasing the resistance of one arm of the Wheatstone bridge using a precision shunt resistor and comparing the theoretical strain to the actual strain. In this sense, the gage factor of the strain gage is adjusted to account for the differences in the circuitry as well as the changes to the strain gage during installation. Although simple in concept, shunt calibration is difficult and a detailed reference for shunt calibration is Micro-Measurement's Tech Note TN-514.

Equation A-2 was used to determine the theoretical strain as shown below. The equation was obtained from Micro-Measurements Tech Note TN-514. Note that because a three-wire (i.e., three leadwires) circuit is being used, leadwire resistance is accounted for and is not needed in the calculations.

$$\varepsilon_{theoretical} = \frac{R_G}{F_G * R_C} \qquad \text{Equation A-2}$$

where,

$\varepsilon_{theoretical}$ = theoretical strain,

R_G = combined resistance of strain gages (ohms),

F_G = gage factor of the strain gages provided by the manufacturer (not combined), and

R_C = precision calibration resistor's resistance (ohms).

The equation used to determine the uncorrected strain (i.e., no correction factors applied from strain gage lab calibration) is shown in Equation A-3. The equation has been re-arranged, but was originally obtained from Micro-Measurements Tech Note TN-507.

$$\varepsilon_{uncorrected} = \frac{E_{out}}{E_{in} * F_G} * \left(\frac{4}{10^3 - 2 * \frac{E_{out}}{E_{in}}} \right) \qquad \text{Equation A-3}$$

where,

$\varepsilon_{uncorrected}$ = uncorrected strain,

E_{out} = voltage output (mV), and

E_{in} = voltage input (V).

For shunt calibration, the gage factor (F_G) was adjusted in the uncorrected strain equation to match the theoretical strain. The adjusted gage factor was the gage factor used in all of the succeeding measurements.

The strain was corrected after the field study was performed, which is described in greater detail in chapter 3 of this thesis. Equation A-4 was used to correct the strain gage field readings as shown below.

$$\varepsilon_{corrected} = \varepsilon_{uncorrected} * CF \qquad \text{Equation A-4}$$

where,

$\varepsilon_{corrected}$ = corrected strain, and

CF = calibration factor.

In most strain gage applications, signal conditioners are desirable because they reduce noise associated with instrumentation and long leadwire lengths, and make calculating strain more straight forward. However, in this study, signal conditioners were not selected due to budget constraints. Equations A-2, A-3, and A-4 were the equations used to determine the true field strain in the geosynthetics, and for subgrade stabilization applications, this is appropriate because of the large strains involved.

Geogrids

Every geogrid used in this thesis had its own unique procedure for strain gage installation. Each procedure is unique because of the variation in rib dimensions, manufacturing processes, and materials used. Therefore, strain gages were selected primarily based on their size in relation to the size of the ribs that they were mounted on.

The EP series (Micro-Measurements) of strain gage was selected because it accommodates large strain measurements, which were anticipated in the field study. The strain gages used on each of the geogrids are listed in Table A-1.

Table A-1: Strain Gages Used for Geosynthetics

Geosynthetic	**Strain Gage**
BX Type 2	EP-08-500GC-350
Secugrid 30/30 Q1	EP-08-500GC-350
Enkagrid Max 30	EP-08-500GC-350
SF 11	EP-08-500GC-350
SF 12	EP-08-500GC-350
BXG 11	EP-08-500GC-350
Fornit 30	EP-08-230DS-120
Tenax MS330	EP-08-230DS-120
TX 140	EP-08-230DS-120
TX 160	EP-08-230DS-120
RS580i	EP-08-20CBW-120
Geotex 801	EP-08-20CBW-120

In general, the instrumentation of strain gages on geogrids consisted of six main steps: 1) preparing the strain gages, 2) preparing the geogrid surface, 3) attaching the strain gages to the geogrid, 4) curing the adhesive, 5) attaching the leadwires, and 6) applying and curing the protective coating. In the field, all of the strain gages were installed on the full width geogrids inside a closed building to minimize the influences from wind, sun, water, and airborne contaminants. To ease in the process of applying the strain gages, platforms were created to elevate the geogrids. An example of one of the platforms is illustrated in Figure A-4.



Figure A-4: Platform used for elevating geosynthetics.

Preparation of the strain gages consisted of attaching jumper wires from the strain gage to bondable terminals. The reason for this step is to prevent potential forces transmitted along the leadwire from damaging the strain gage or affecting its performance during installation and trafficking. To prepare the jumper wires, a template for bending the jumper wires was made, and the jumper wire ends were tinned. Prior to soldering the jumper wires to the strain gages, PDT-1 drafting tape (Micro-Measurements) was placed over the gage area to protect it from solder fluxes, and then the strain gage tabs and terminals were tinned. Small strips of drafting tape were used to secure the terminals and jumper wires as shown in Figure A-5 and an example of a typical setup of the gage with jumper wires attached is shown in Figure A-6.

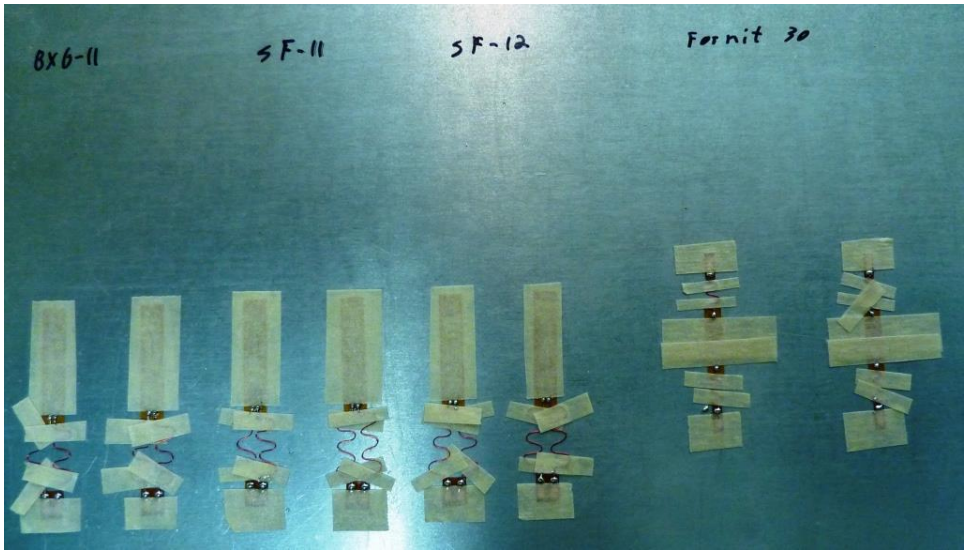


Figure A-5: Strain gage preparation.

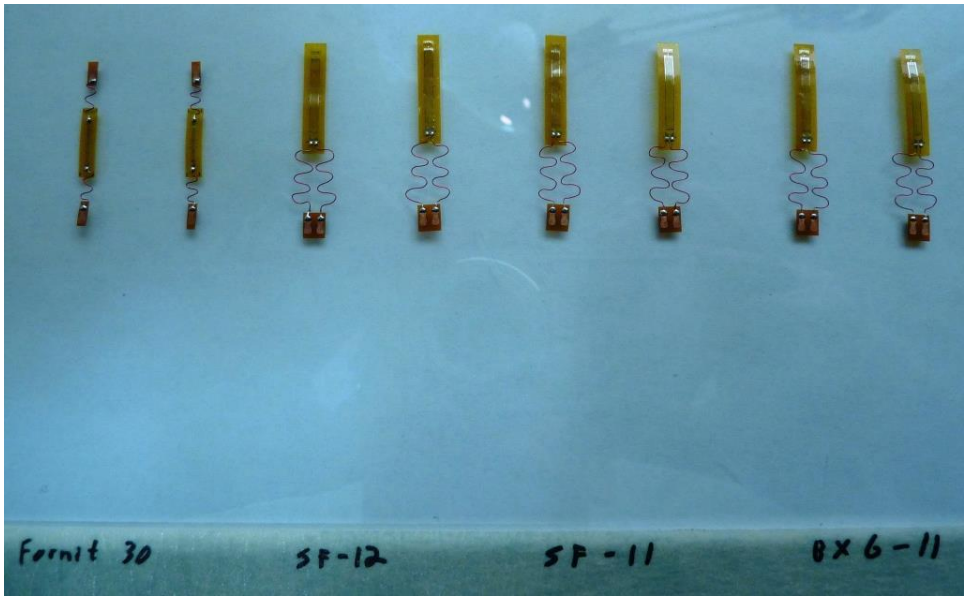


Figure A-6: Jumper wires attached to strain gages.

It is important to note that the gages were soldered prior to placement on the geosynthetic to reduce the risk of debonding the gage which can occur when strain gages are placed on geosynthetics, and then soldered in place. After soldering was complete, the drafting tape was removed using M-Line Rosin Solvent (Micro-Measurements). M-

Line Rosin Solvent deteriorates the adhesive, removes any foreign matter or solder residues, and cleans/sterilizes the gage prior to bonding. Additional preparation was required for the geogrids which had thin ribs (i.e., Tenax MS330, TX 140, and TX 160). The strain gages used had a wider matrix width (i.e., total width) than the rib width. Therefore, a razor blade was used to trim the strain gage to just wider than its gage width (i.e., the part of the strain gage which has the foil on it) by pushing straight down. An example of this trimming is shown in Figure A-7.

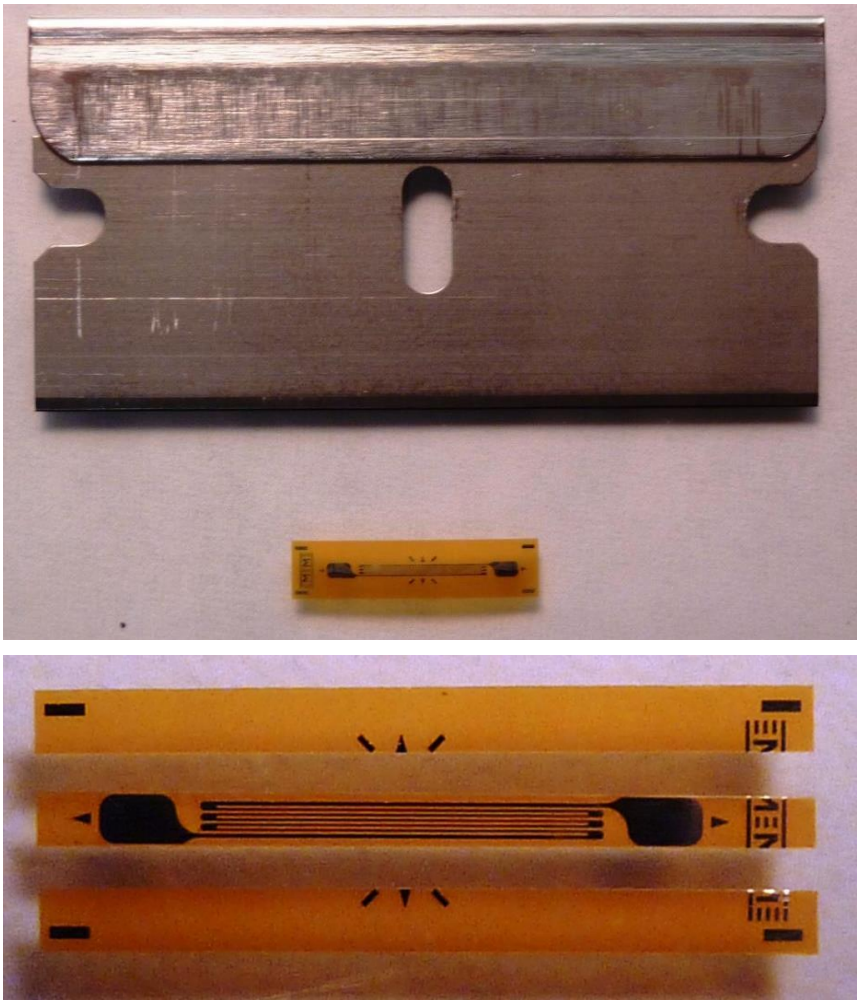


Figure A-7: Preparation of strain gages for thin-rib geogrids.

The surface of the geogrid was thoroughly cleaned before applying the adhesive and attaching the strain gage. The integrally formed, extruded, and welded geogrids (i.e., BX Type 2, Secugrid 30/30 Q1, Enkagrid Max 30, Tenax MS330, TX 140, and TX 160) had different surface preparation procedures than the woven geogrids (i.e., SF 11, SF 12, BXG 11, and Fornit 30). The integrally formed, extruded, and welded geogrids procedure in general consisted of degreasing the surface using CSM-2 degreaser (Micro-Measurements), wet abrading the surface with waterproof sandpaper (240-400 grit, depending on the geogrid) and M-Prep Conditioner A (Micro-Measurements), wiping clean with gauze pads, applying M-Prep Neutralizer 5A (Micro-Measurements) with cotton-tipped applicators, and wiping clean with gauze pads. The solvent degreaser removes oils, greases, organic contaminants, and soluble chemical residues while abrading the surface removes any surface defects of the geogrid, and lightly roughens the surface to facilitate bonding of the adhesive. The conditioning and neutralizing solutions bring the surface to an optimum pH of 7.0 to 7.5. The Secugrid 30/30 Q1 geogrid had an additional step; after spraying the surface with CSM-2 degreaser, the material was gently etched with a scalpel inside of its ‘diamonds’ as shown in Figure A-8.

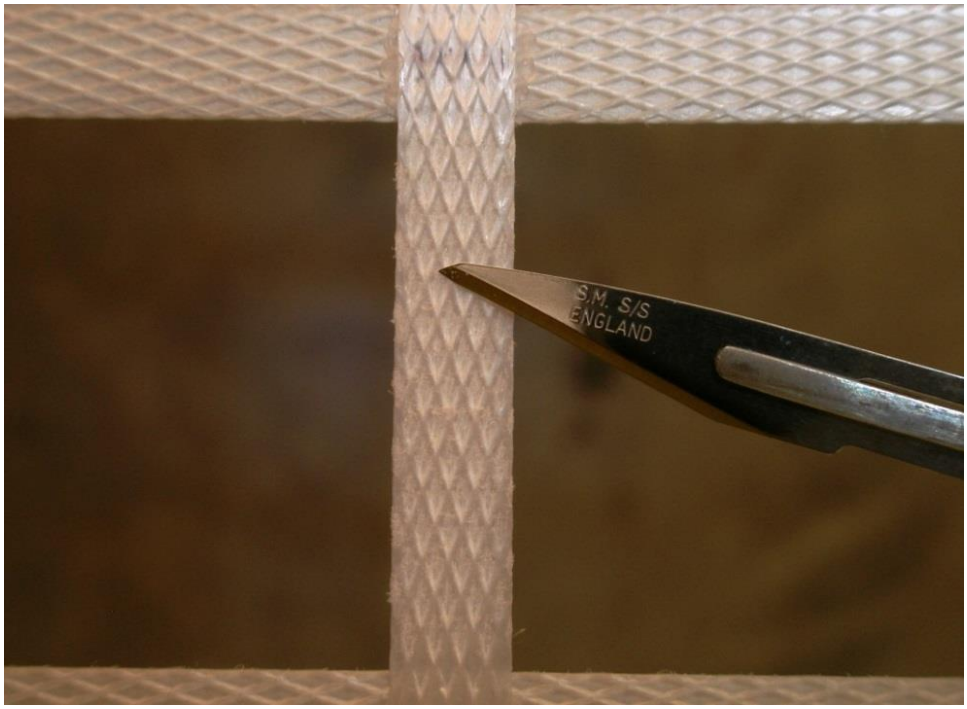


Figure A-8: Secugrid 30/30 Q1 surface preparation.

For the woven geogrid products, the protective PVC or polymer coating, applied by the manufacturers to protect the woven grid structure, was removed using a precision probe with a hook tip (Moody Tools, Warwick, Rhode Island) and clear PVC cleaner. The Fornit 30 geogrid was an exception because it had a coating that could be removed with CSM-2 degreaser. After the coating was removed for all of the woven geogrids, the area was sprayed with CSM-2 degreaser. The area was not conditioned and neutralized because of how the fibers act like a sponge and could potentially absorb too much conditioner which might lead to a lower pH level.

On the Secugrid 30/30 Q1, SF 11, SF 12, BXG 11, and Fornit 30 geogrids, creating a bedding for the strain gages using the same adhesive as used to place the strain gages was required. A bedding was created to prevent wrinkles and deformations in the

strain gage caused by the uneven surface of the geogrid. To create the bedding, the adhesive (M-Bond A-12) was applied conservatively and worked into the material (if applicable). A layer of thin Teflon was then placed on the top and bottom, followed by a rubber and aluminum piece approximately the same size as shown in Figure A-9. Pre-determined weights were placed on top of the aluminum pieces and an adjacent rib to obtain the desired pressure (about 15 psi) applied to the strain gage as shown in Figure A-10.

The adhesive was heat cured at 150 °F for 6 hours using a heat box. The heat boxes were constructed using 2 inch thick foil-faced insulation foam sheets. A box 16 inches wide by 16 inches long by 12 inches tall was created with the foil facing inwards. A 60-watt light bulb was placed on the top with a dimmer switch to control the temperature, and thermocouples were placed on the geogrid to monitor the temperature. An example of the heat box setup used in lab is shown in Figure A-11.

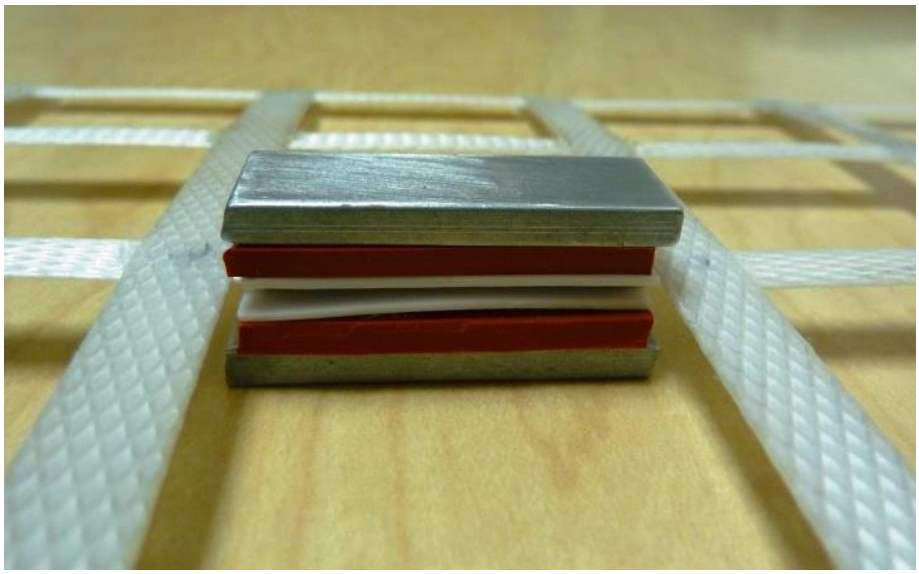


Figure A-9: Geogrid bedding material procedure.



Figure A-10: Example of pressure applied to geogrid.



Figure A-11: Heat box setup used for curing.

After curing, the bedding material was wet abraded with 400 grit sandpaper and M-Prep Conditioner A, wiped clean, and neutralized with M-Prep Neutralizer 5A. Cellophane or Mylar tape (Mylar tape is ideal for heat curing) was placed over the strain gage assembly (i.e., strain gage, jumper wires, and terminals), and a small piece of Teflon film was placed on the backside of the jumper wires to provide true strain relief. Note that if the jumper wires are not covered with Teflon film on one side and tape on the other, then they will become part of the M-Bond A-12 adhesive and will not provide strain relief.

The strain gages were carefully positioned on the geogrids. The tape was "curled over" itself for proper strain gage alignment, and the tape touching the geogrid was pushed down on the top and bottom so that it touched, which fixed the strain gages into their desired position. The proper positioning of the strain gages is a critical step because when the adhesive is placed, the tape with the strain gages can then be laid down onto the adhesive and proper alignment is guaranteed. An example of strain gage alignment on a woven geogrid is shown in Figure A-12.

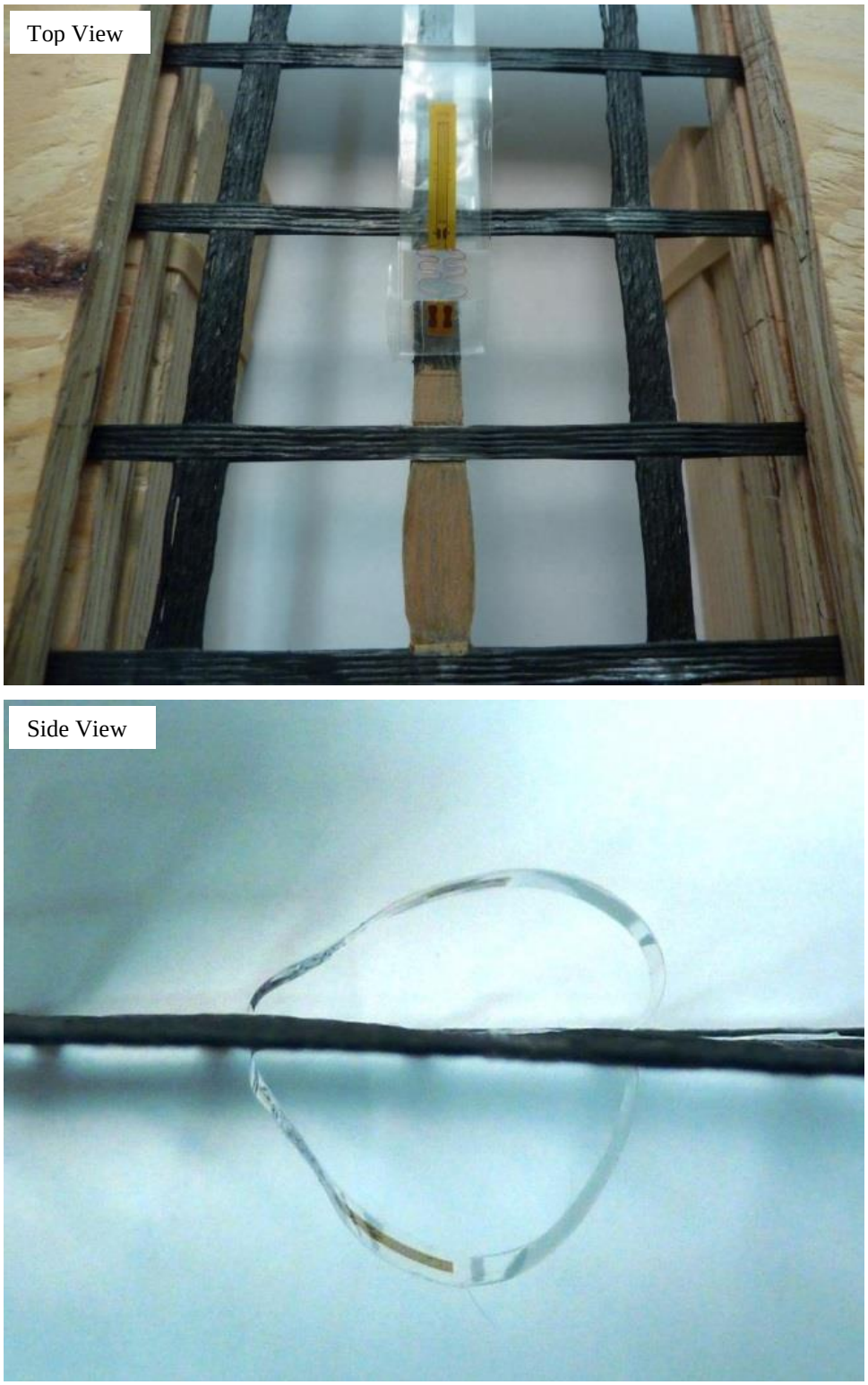


Figure A-12: Strain gage placement on a woven geogrid (top and side views).

Adhesive was applied to the geogrid rib and on the backside of the strain gages, and the gages were laid down onto the rib. Pressure was applied to the gages using calculated weights (see Figure A-10) to create an optimum bond (about 15 psi) using the same setup as shown in Figure A-9, except for the Teflon strips were removed. The adhesive was cured at 150 °F for 6 hours in the heat box as shown in Figure A-11.

The tape was removed from the strain gage by peeling it back over itself (starting from the terminals) at an angle of approximately 150 degrees. The strain gage was covered with drafting tape, and the excessive adhesive that "flowed out" beyond the rib width was removed. A combination of a dremel tool, scalpel, and sand paper were used to remove the excess adhesive. Figure A-13 shows the dremel tool that was used.



Figure A-13: Dremel tool used to remove excess adhesive.

The leadwires were attached in a quarter Wheatstone bridge circuit as previously described. Then, the drafting tape was sprayed with CSM-2 degreaser, removed, and the gage and surrounding area was sprayed with CSM-2 degreaser. A strain gage bonded to a woven and integrally formed geogrid is shown in Figure A-14.

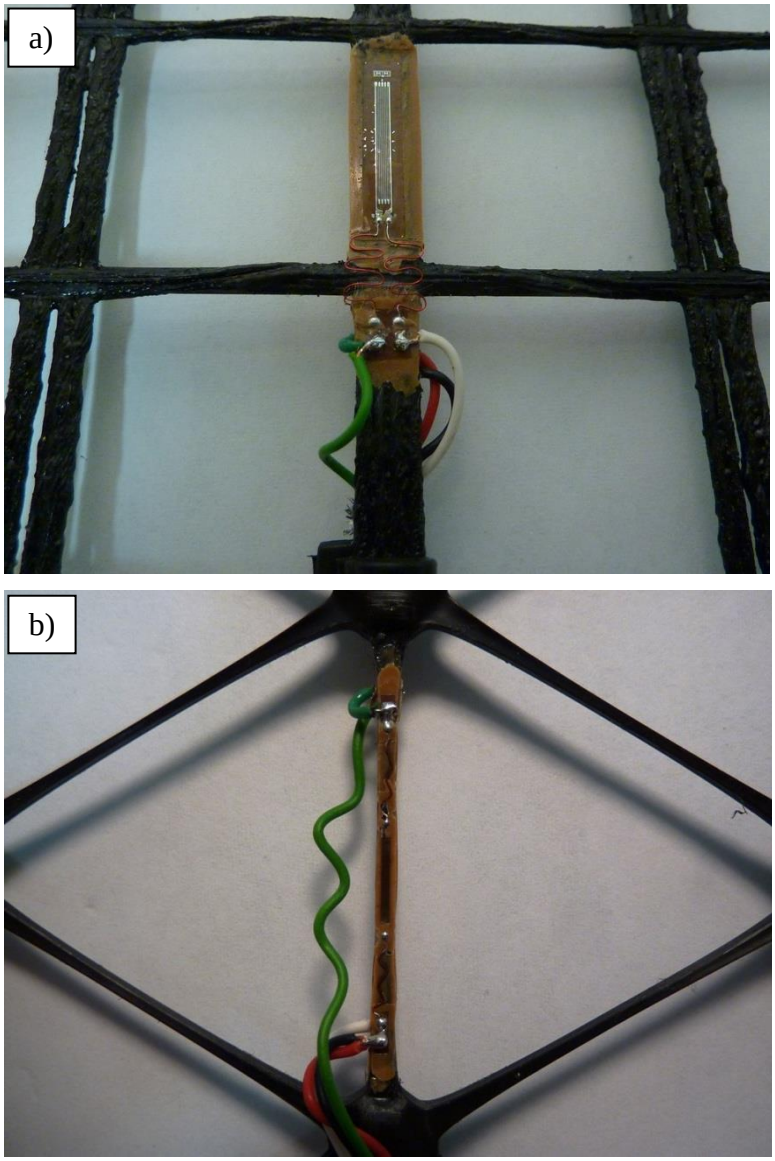


Figure A-14: Strain gages after soldering on a a) woven geogrid and an b) integrally formed geogrid.

A protective coating was applied to keep water from entering the gaged area and to protect it from physical damage during construction and trafficking. M-Coat J from Micro-Measurements was used for this purpose. To apply M-Coat J, a thin piece of Teflon adhesive (supplied with M-Coat J) was used to separate the exposed gage surface from the coating material, as recommended by the manufacturers and shown in Figure A-15. M-Coat J was applied carefully to ensure that all of the wires and sides were covered with at least 2 mm of protection, and that the M-Coat J adhesive extended at least 25 mm beyond the edges of the Teflon adhesive. Curing of the protective coating was accelerated by heating the gage area to 125 °F for 2.5 hours, which also increased the moisture resistance of the coating. A finished strain gage location on a welded geogrid is shown in Figure A-16.

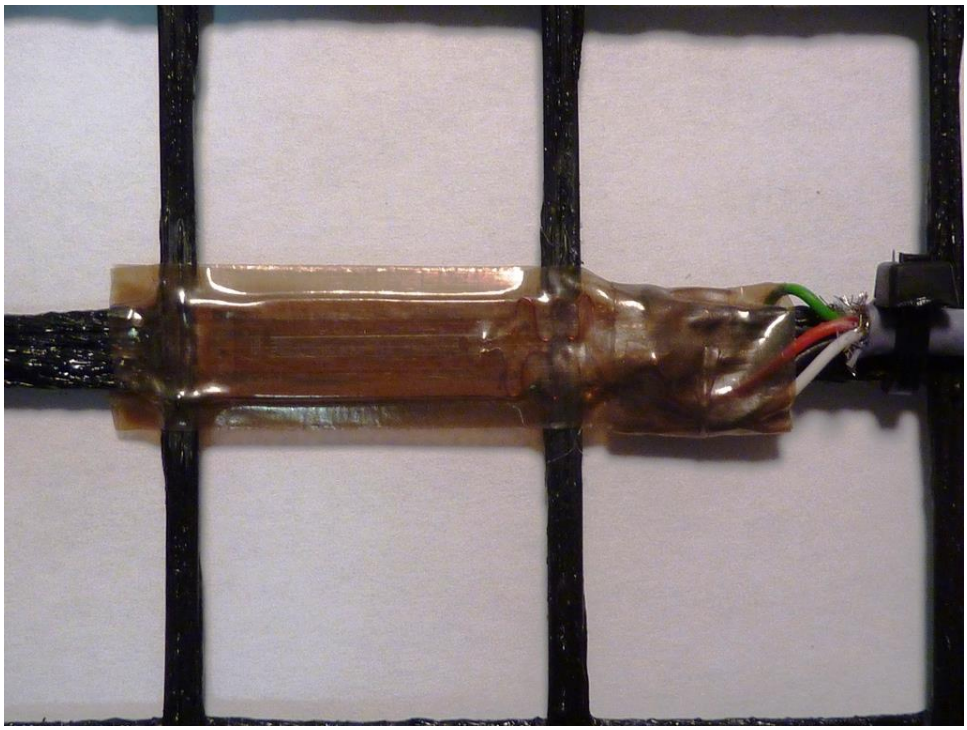


Figure A-15: Teflon adhesive on strain gage.



Figure A-16: Finished strain gage installation on a welded geogrid.

Geotextiles

The procedure used to bond strain gages to geotextiles was similar, but modified slightly to accommodate the unique surface structure of the materials. The desired gage area was marked, sprayed with CSM-2 degreaser, allowed to dry, and a non-conducting clear silicone, RTV-3145 (Dow Corning, Midland, Michigan) was worked into the material. Marking and aligning the desired gage area consisted of using the selvage edge of the geotextile, forming a 90 degree angle, and marking the area with a permanent marker. In the field, this process was performed on top of the geotextile, and then small

wires were pushed or weaved through the geotextile for aligning and marking the bottom gage properly. Similar to the woven geogrids, M-Prep Conditioner A and Neutralizer 5A was not used because the geotextiles also behave like a sponge, which could bring the pH level below optimum.

The RTV-3145 clear silicone was used to minimize stiffening of the gaged area, and also serves as a waterproof and protective coating. The M-Bond A-12 adhesive used on the geogrids was too stiff of a material to apply to the geotextiles used in this thesis, especially the Geotex 801. Therefore, RTV-3145 clear silicone was selected because of its successful use in previous strain gage instrumentation studies on geotextiles. Working the silicone into the geotextile was critical to waterproof the gages. A clean glass plate was placed on the bottom of the geotextile and an area roughly 2 inches wide by 5 inches long was massaged through the material onto the glass; the glass plate was then placed on top and the procedure was repeated from the bottom of the geotextile. The glass was removed and additional silicone was carefully applied (to avoid introducing air bubbles) to the top and bottom locations so that sufficient silicone was available to create a level bedding surface. A clean utility knife razor blade was then used to level the bedding material. Because the RS580i geotextile is a woven geotextile, it required a slightly thicker bedding material than the nonwoven Geotex 801 geotextile so that the strain gage did not have wrinkles in it. An example of the bedding material on the woven geotextile is shown in Figure A-17.

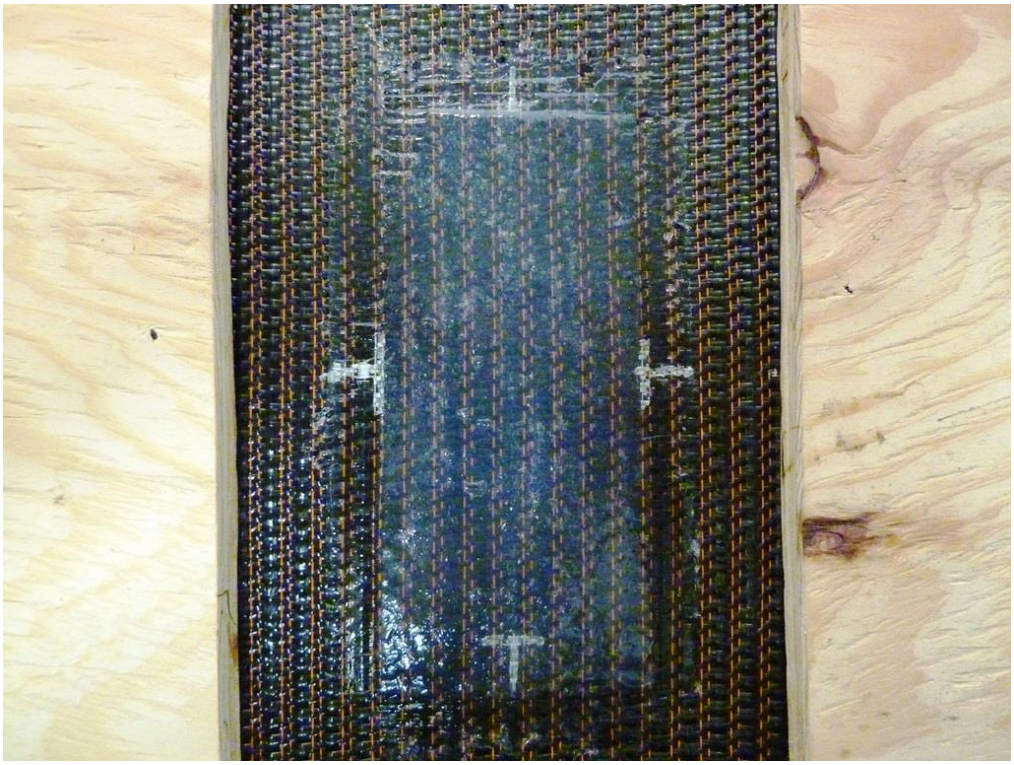


Figure A-17: Woven geotextile bedding material.

Approximately one day after the bedding material was placed, a thin layer of additional silicone was placed over the air cured bedding material and the strain gages were applied. The strain gages used for the geotextiles were EP-08-20CBW-120 (Micro-Measurements) as listed in Table A-1. Tape was not used to place the strain gages. Instead, tweezers were used and the strain gages were carefully positioned and placed.

Teflon film strips were laid over the gage and silicone areas, and pressure was applied (about 15 psi) to the strain gages using wood blocks just slightly larger than the strain gages with weights placed on top and a solid surface on the bottom to react to. Figure A-18 shows the application of the Teflon strips. The silicone was air cured for approximately 1 to 2 hours and then the bottom parts (i.e., starting at the terminals) of the Teflon strips were removed. The reason for this is so that solder fluxes do not ruin and/or

contaminate the strain gage and surrounding silicone. The strain gages were wired on the top and bottom with two of the leadwires going through the geotextile to connect the two gages in the quarter Wheatstone bridge circuit. The remaining Teflon strips were removed and the strain gages and leadwires were encapsulated in the RTV-3145 silicone and air cured for one day. The final installed strain gage location of the woven geotextile is shown in Figure A-19.

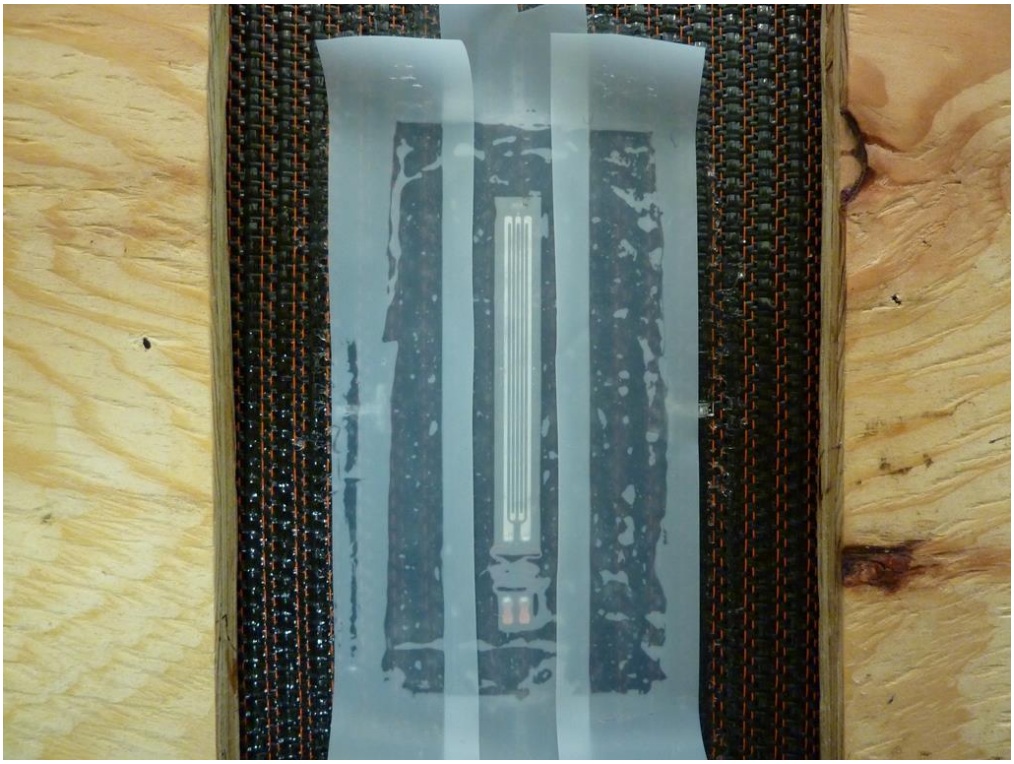


Figure A-18: Teflon strips applied to strain gage on a woven geotextile.

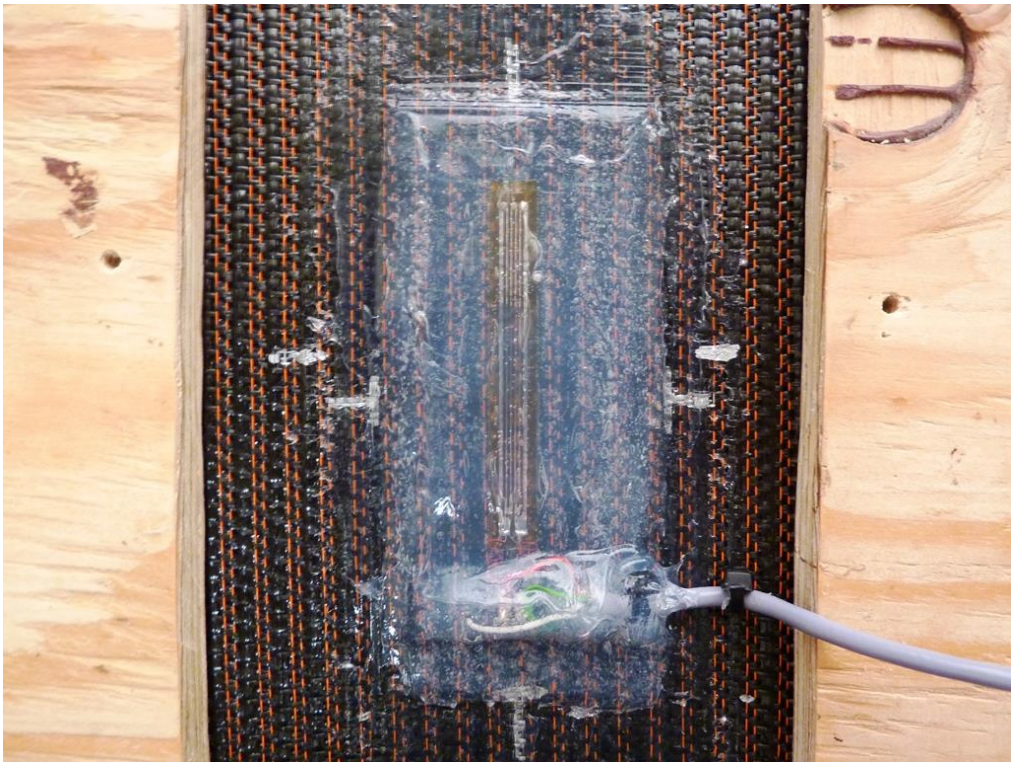


Figure A-19: Installed strain gages on a woven geotextile.

APPENDIX B:

STRAIN GAGE CALIBRATION PLOTS

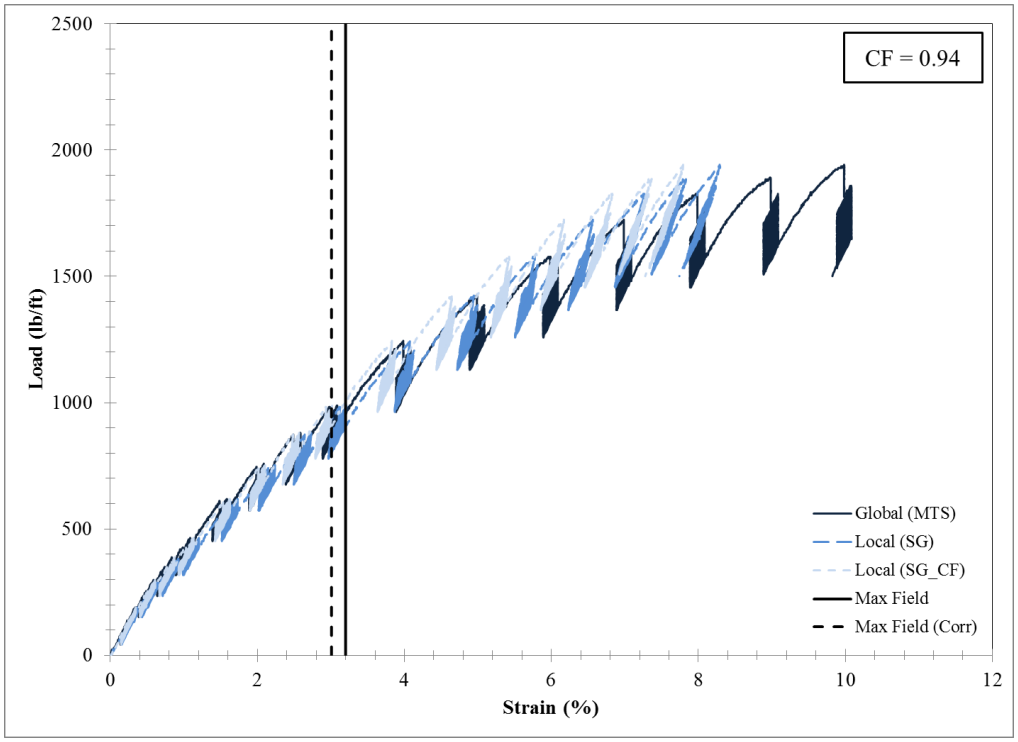


Figure B-1: Tensar BX Type 2.

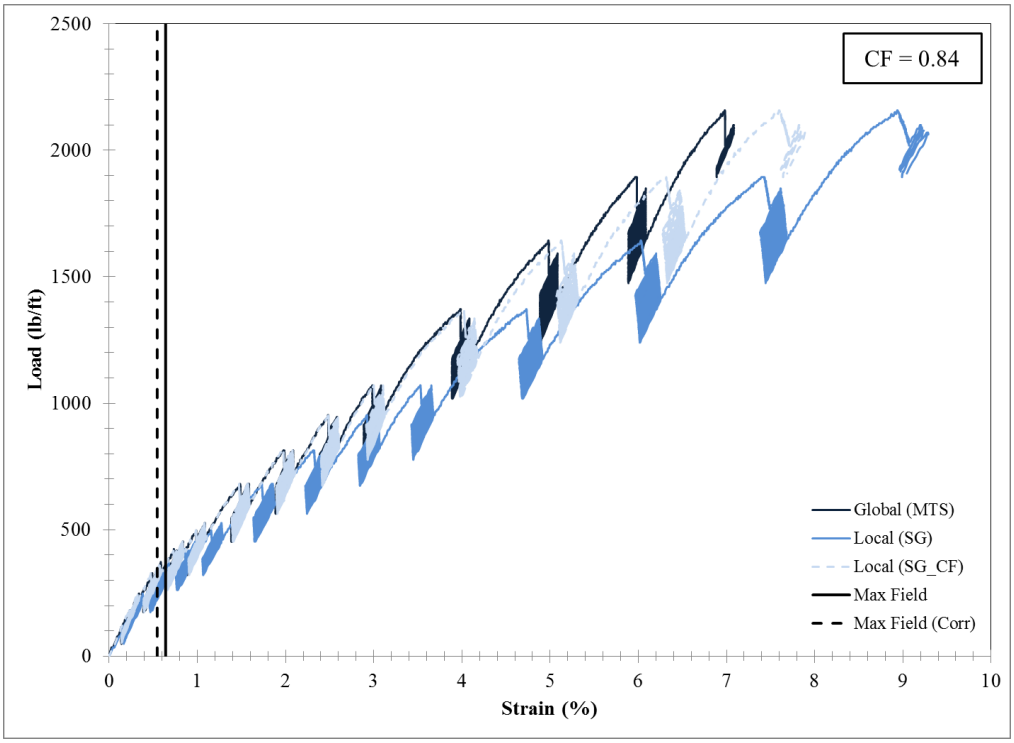


Figure B-2: NAUE Secugrid 30/30 Q1.

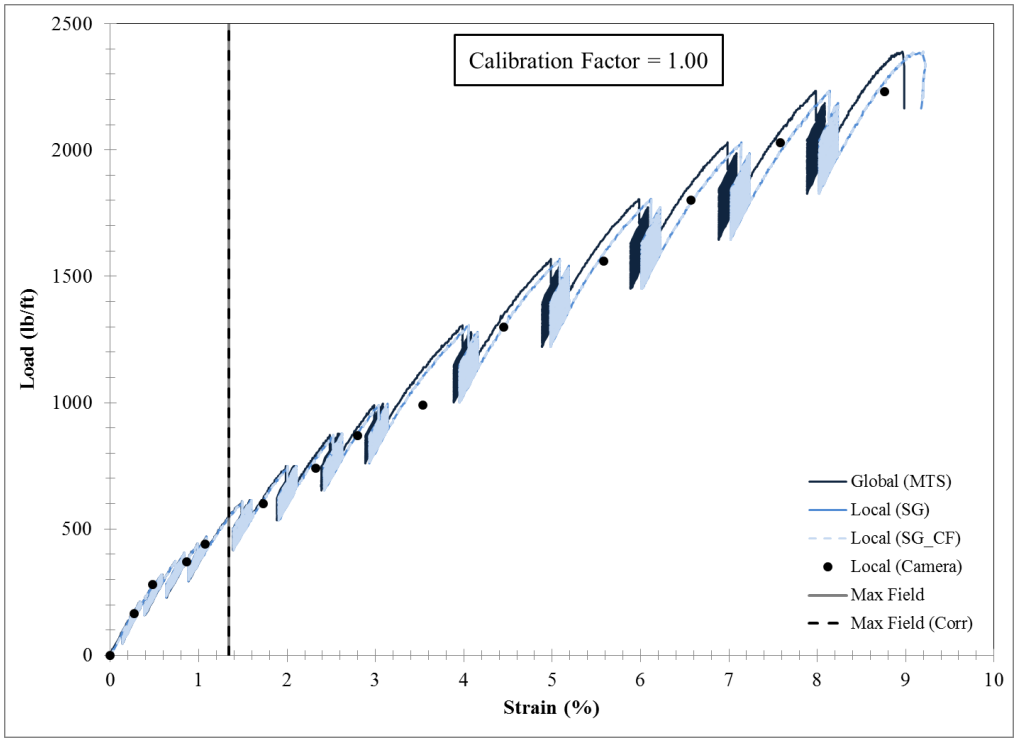


Figure B-3: Colbond Enkagrid Max 30.

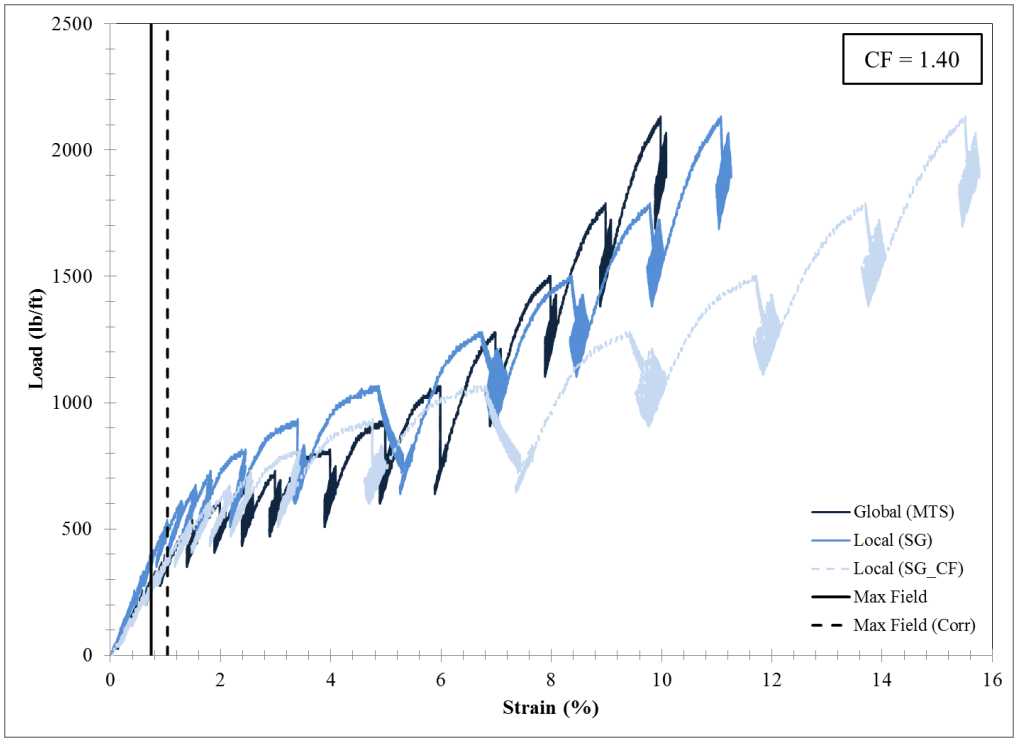


Figure B-4: Synteen SF 11.

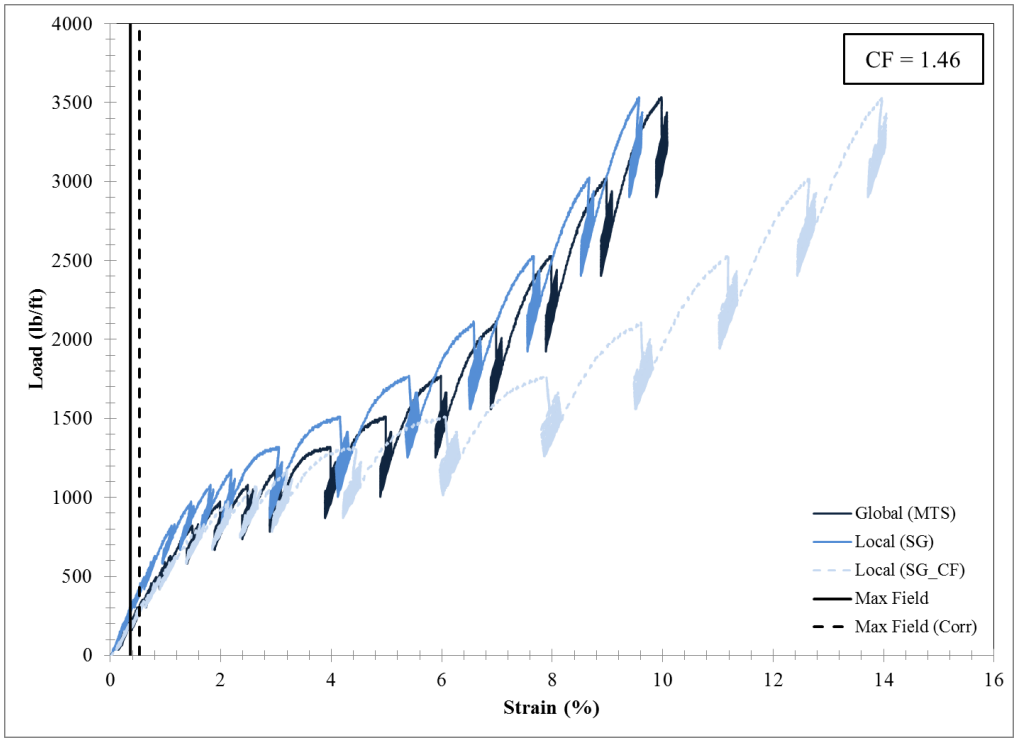


Figure B-5: Synteen SF 12.

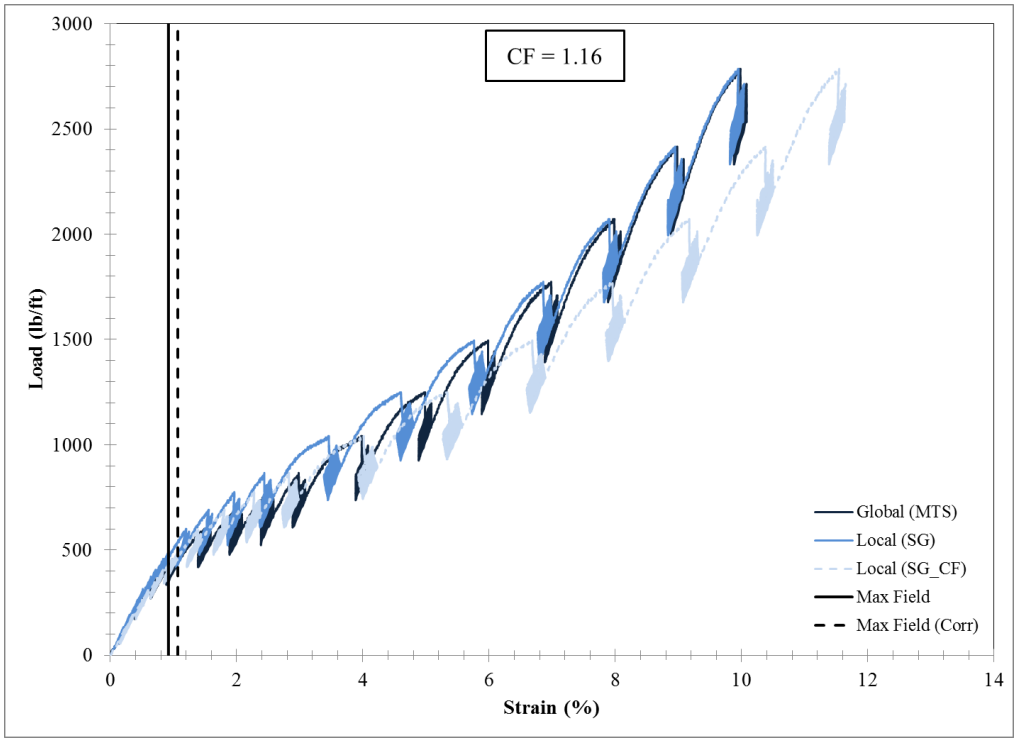


Figure B-6: TenCate Mirafi BXG 11.

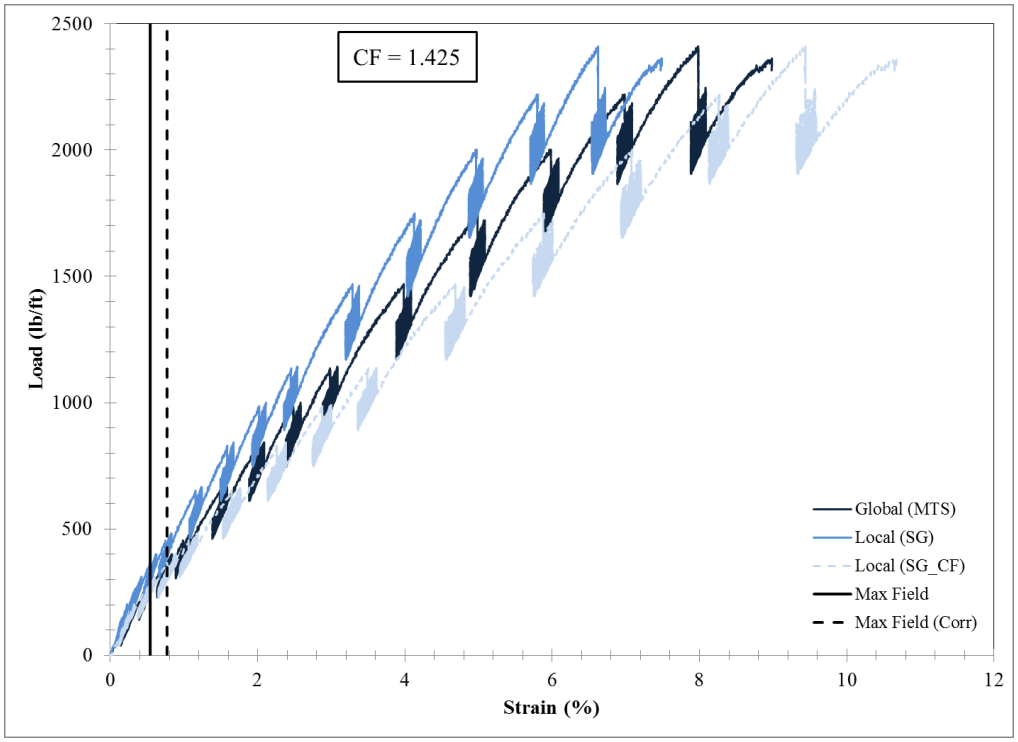


Figure B-7: Huesker Fornit 30.

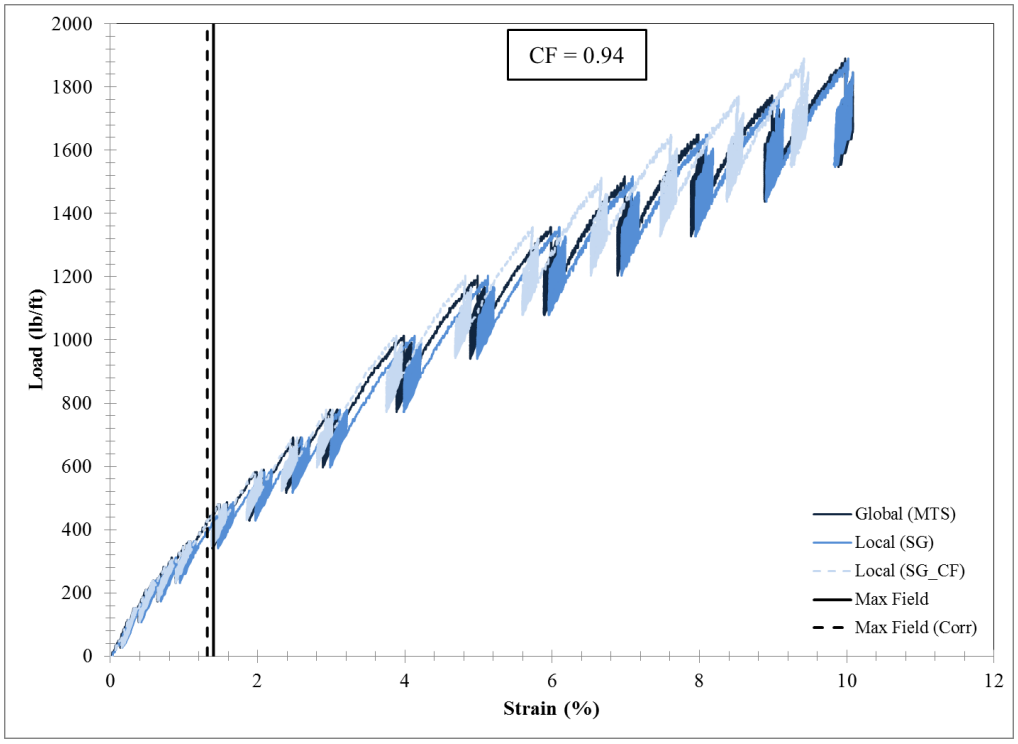


Figure B-8: SynTec Tenax MS330.

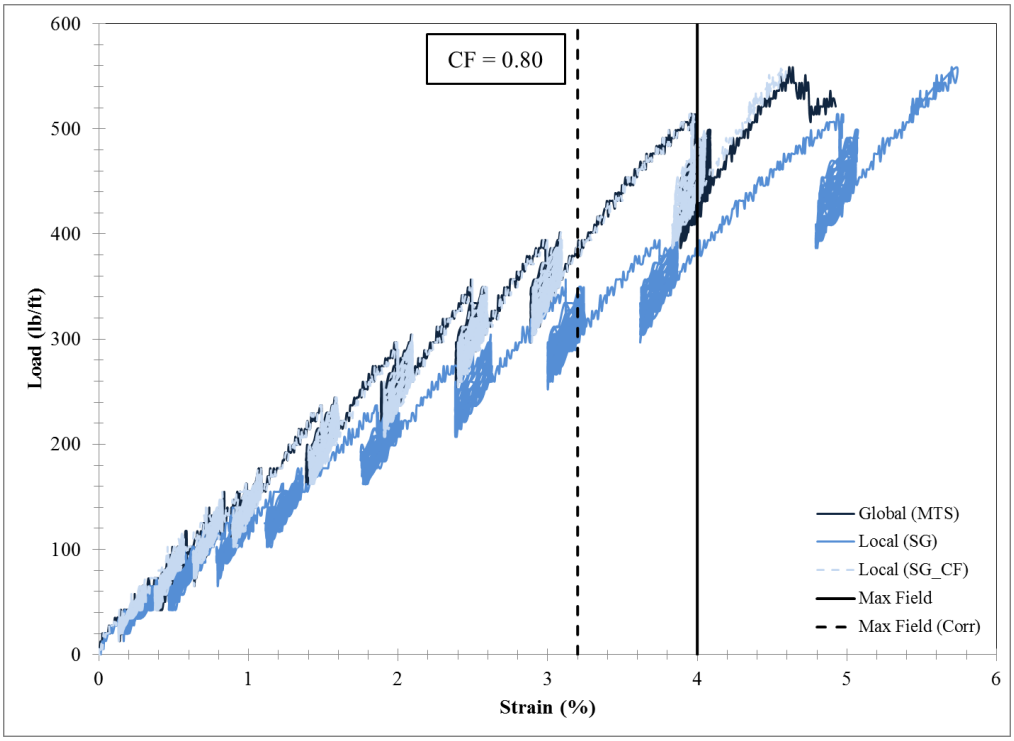


Figure B-9: Tensar TX 140.

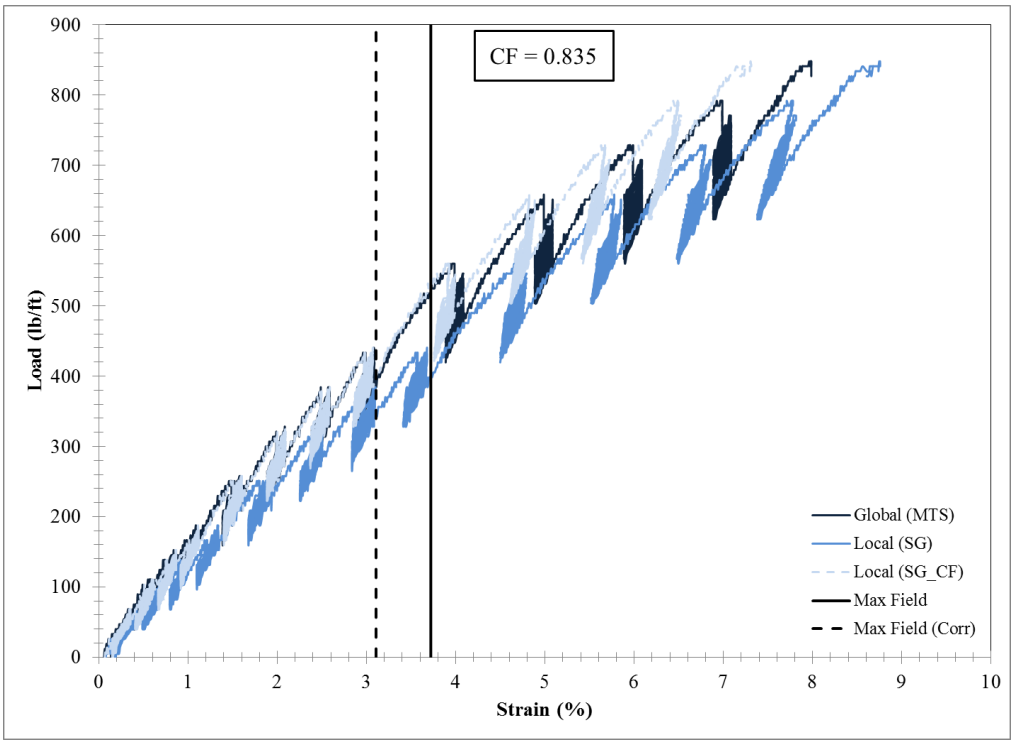


Figure B-10: Tensar TX 160.

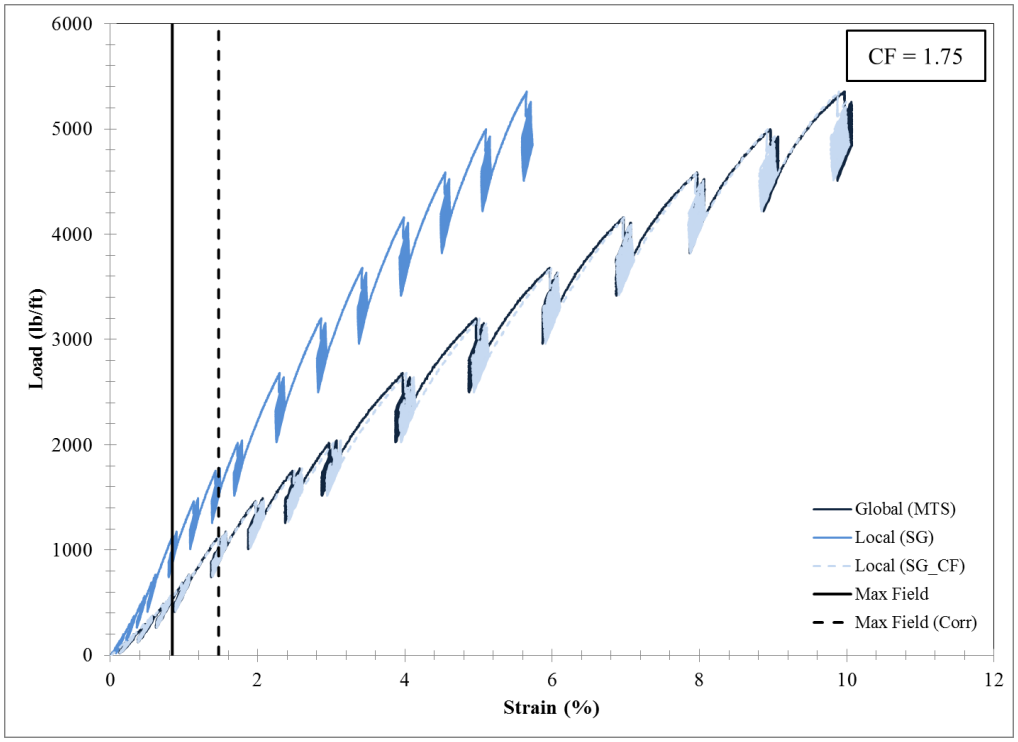


Figure B-11: TenCate Mirafi RS580i.

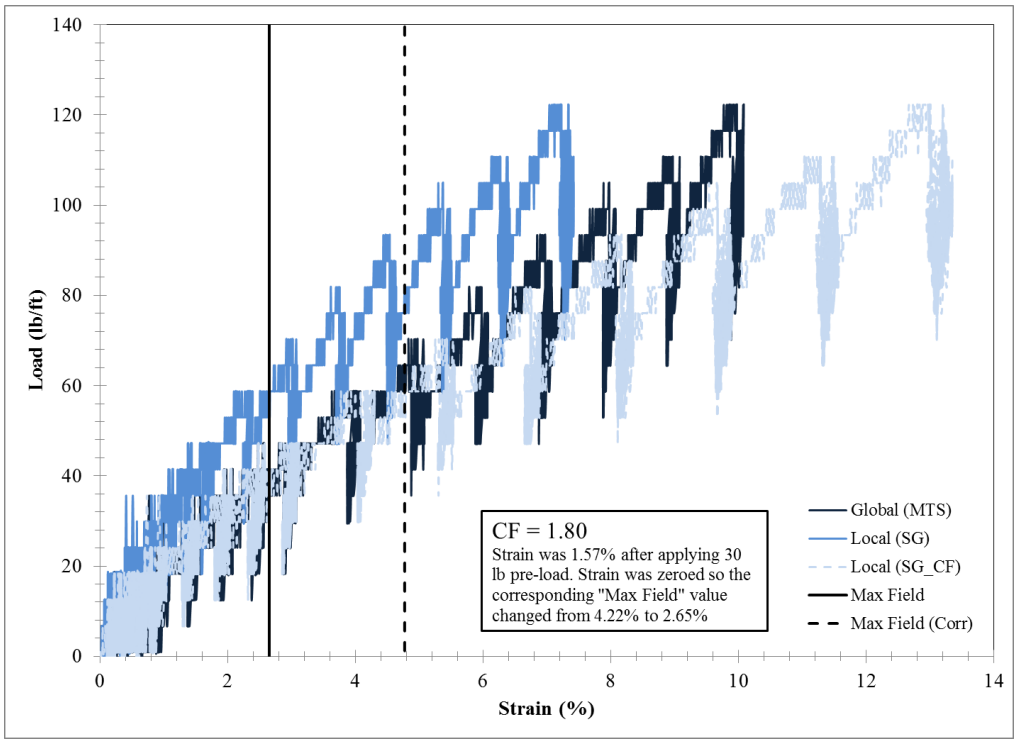


Figure B-12: Propex Geotex 801.

APPENDIX C:

WIDE-WIDTH TENSILE STRENGTH LOAD-DISPLACEMENT PLOTS

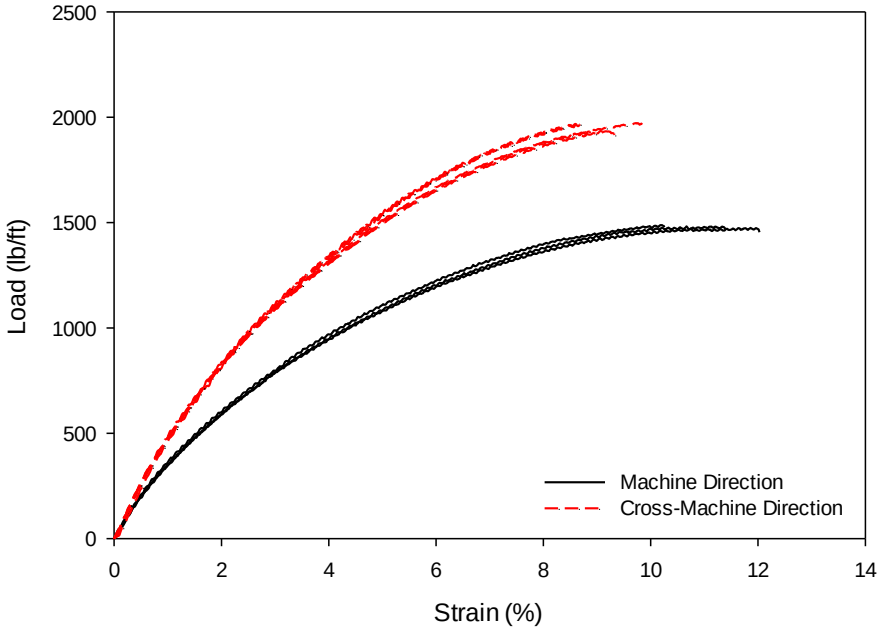


Figure C-1: Tensar BX Type 2.

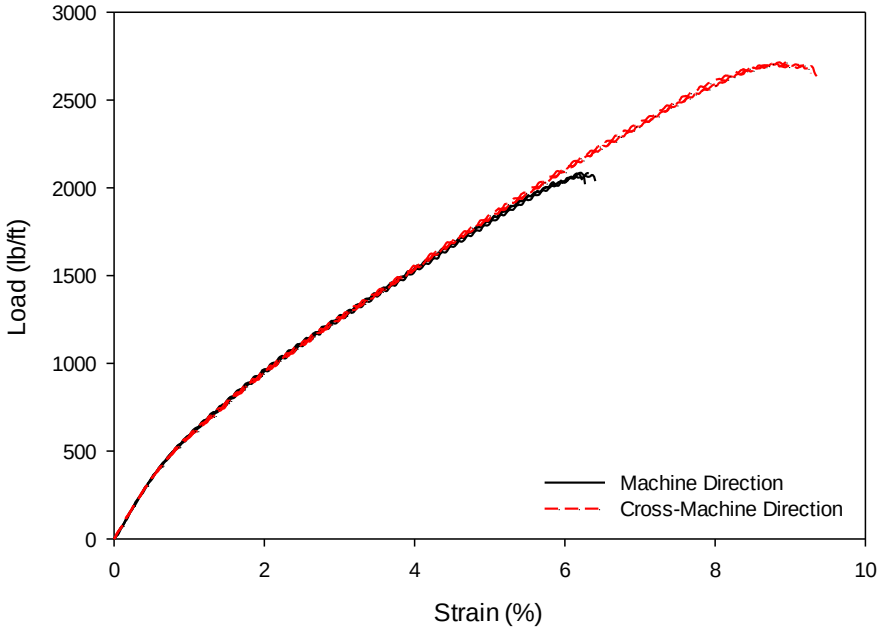


Figure C-2: NAUE Secugrid 30/30 Q1.

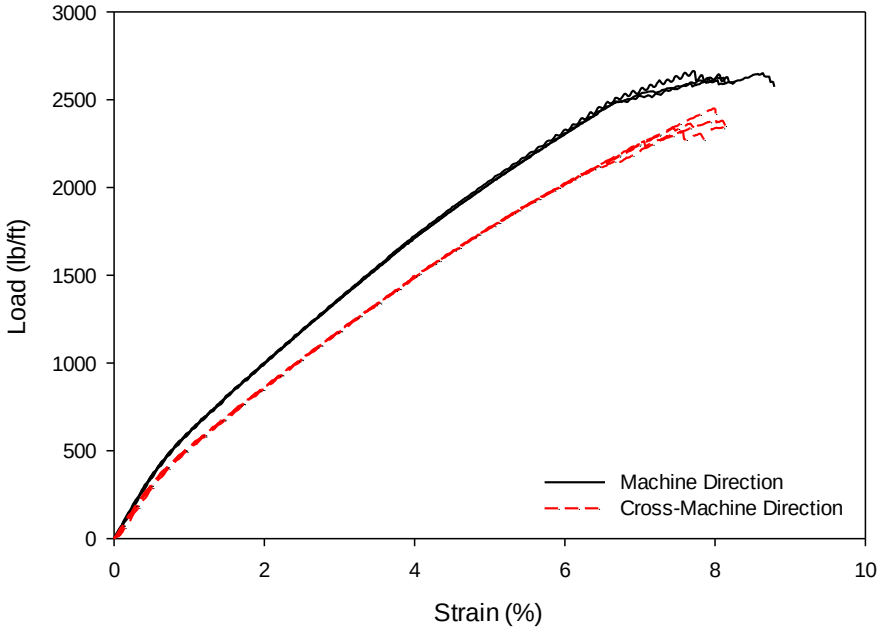


Figure C-3: Colbond Enkagrid Max 30.

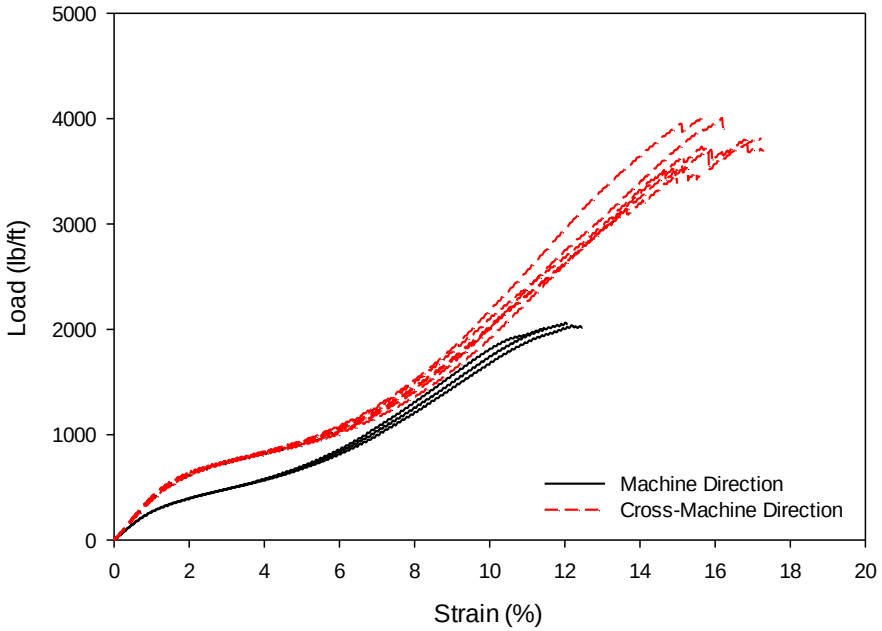


Figure C-4: Synteen SF 11.

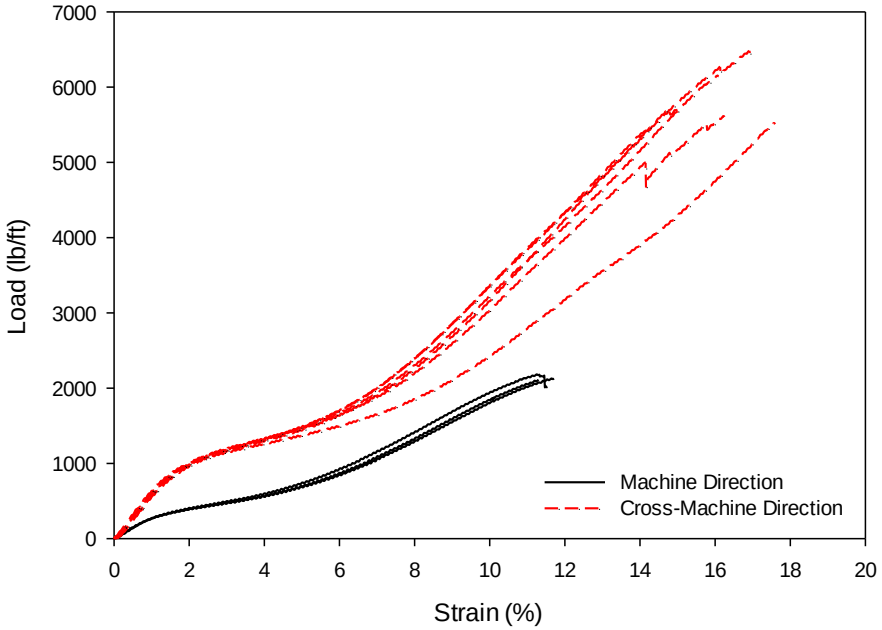


Figure C-5: Synteen SF 12.

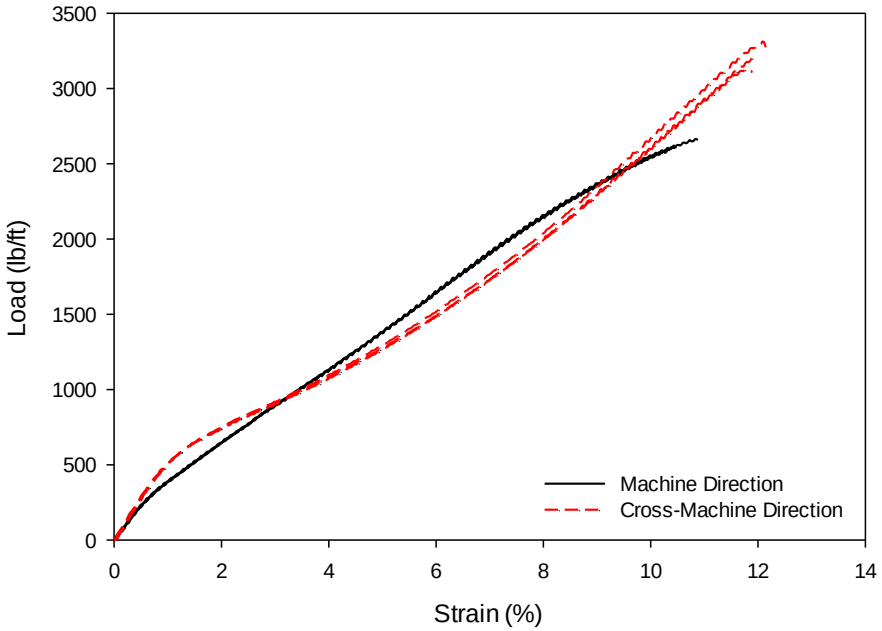


Figure C-6: TenCate Mirafi BXG 11.

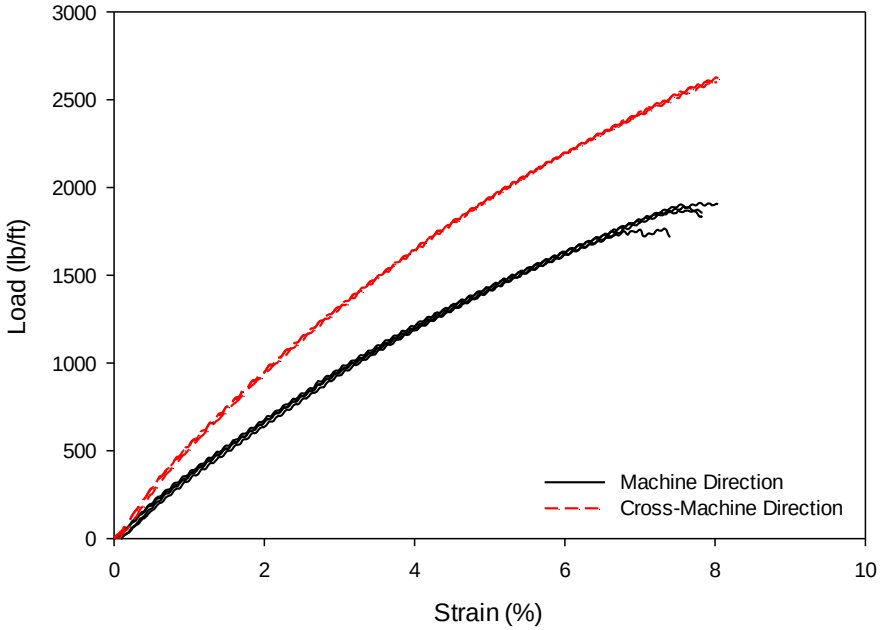


Figure C-7: Huesker Fornit 30.

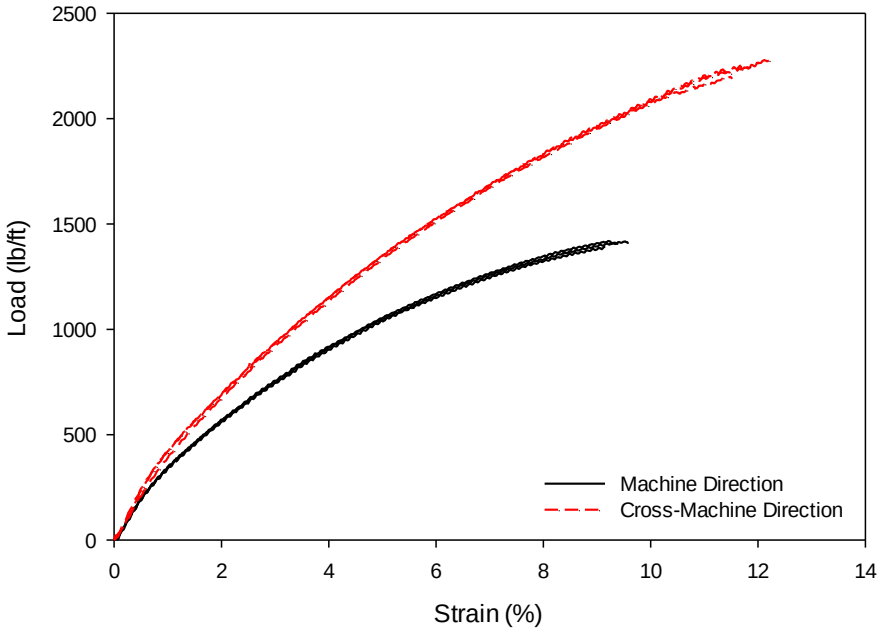


Figure C-8: SynTec Tenax MS330.

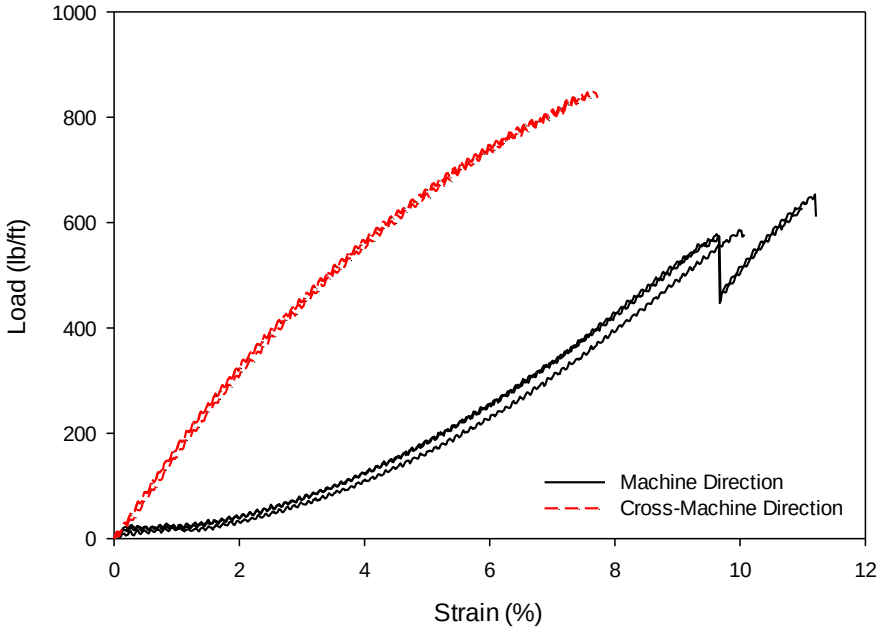


Figure C-9: Tensar TX 140.

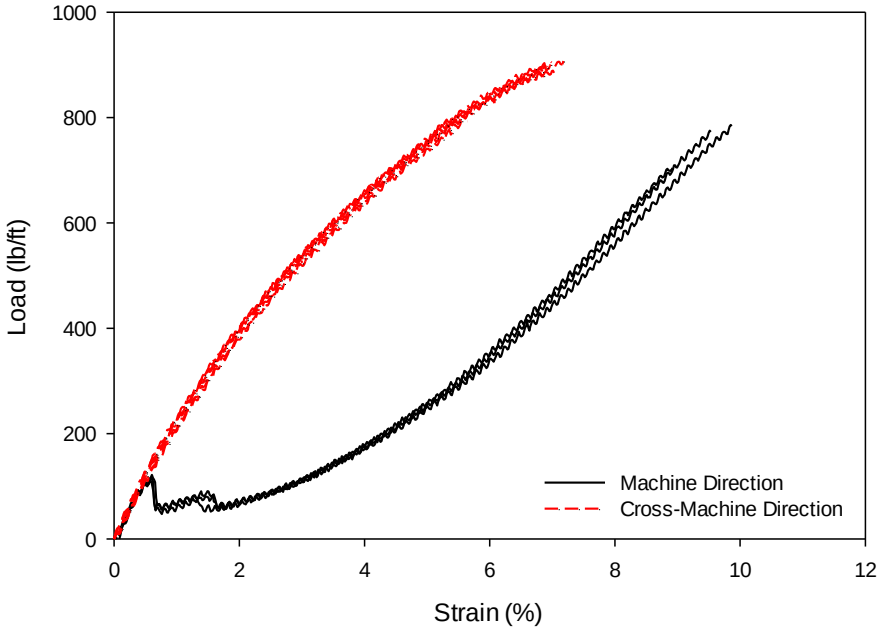


Figure C-10: Tensar TX 160.

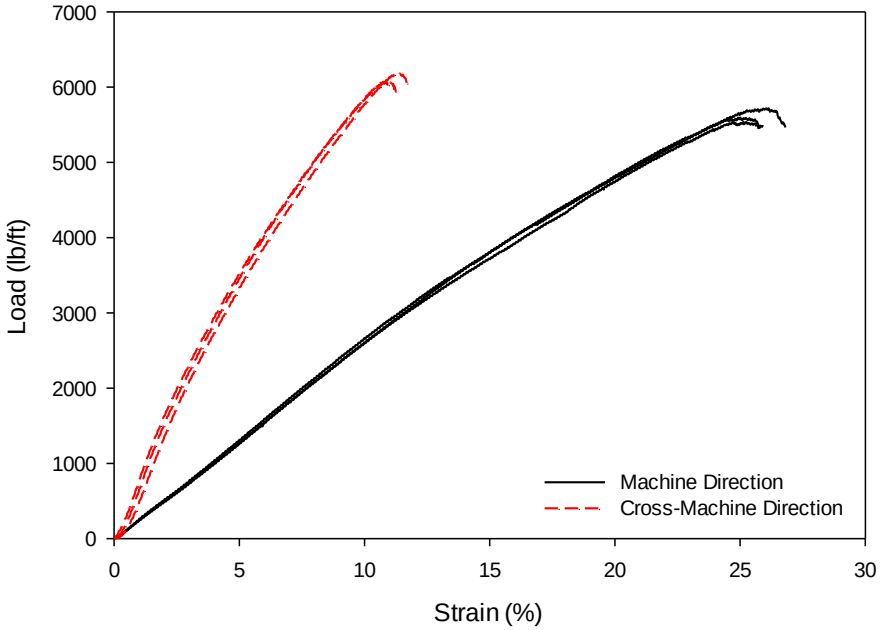


Figure C-11: TenCate Mirafi RS580i.

APPENDIX D:

CYCLIC TENSILE MODULUS LOAD-DISPLACEMENT PLOTS

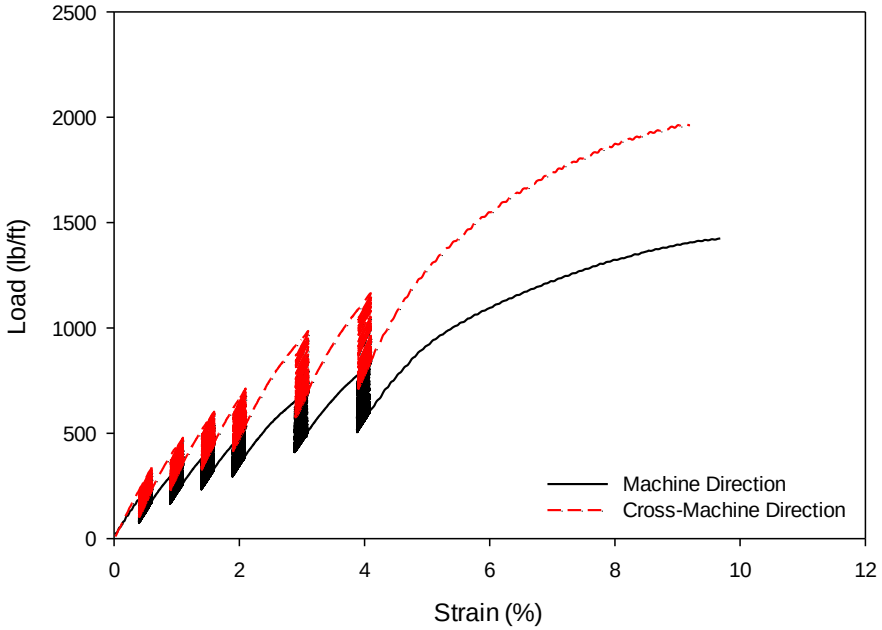


Figure D-1: Tensar BX Type 2.

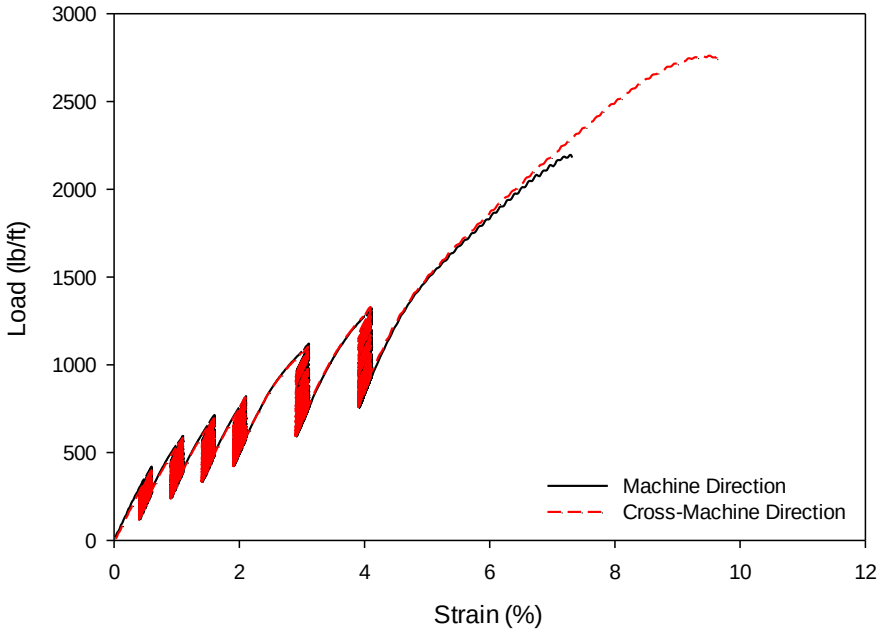


Figure D-2: NAUE Secugrid 30/30 Q1.

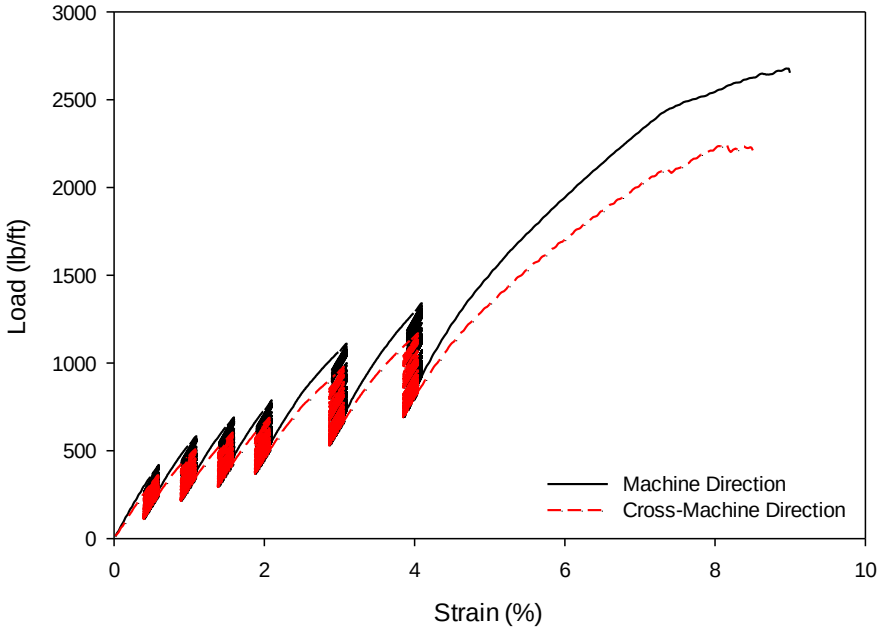


Figure D-3: Colbond Enkagrid Max 30.

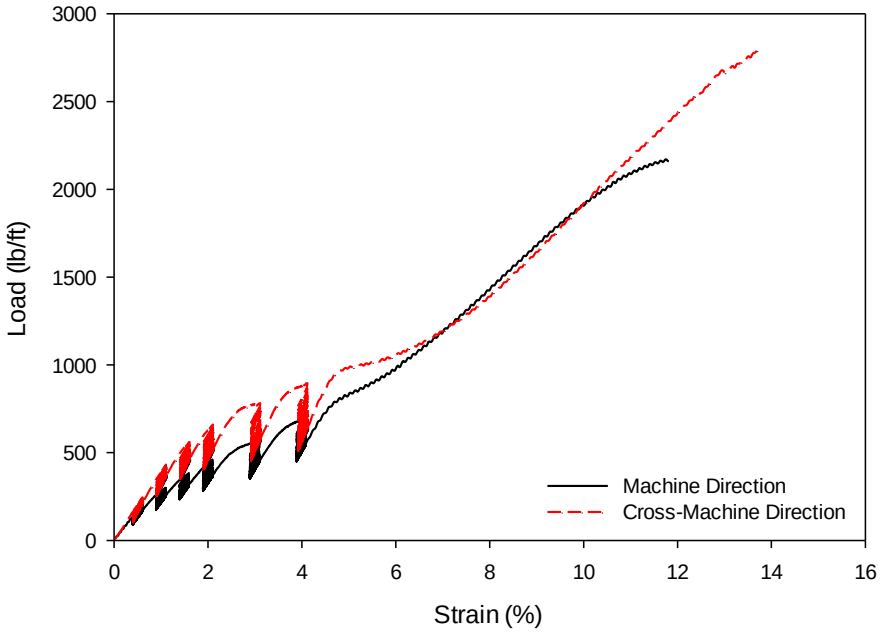


Figure D-4: Synteen SF 11.

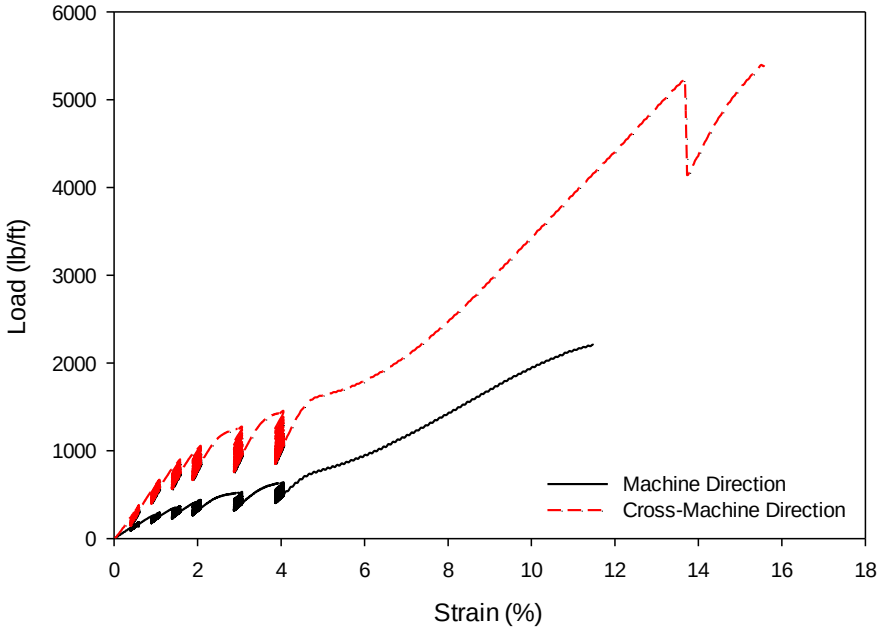


Figure D-5: Synteen SF 12.

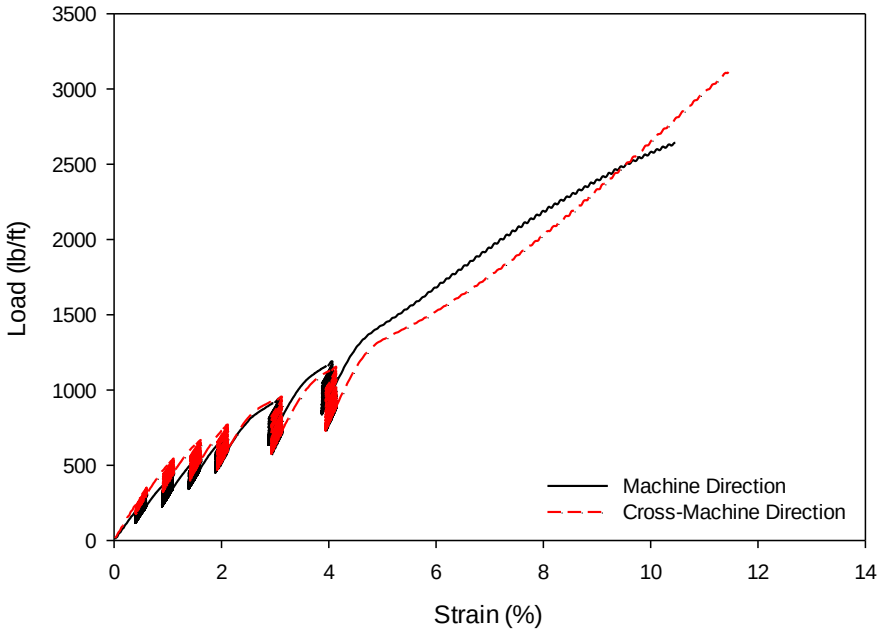


Figure D-6: TenCate Mirafi BXG 11.

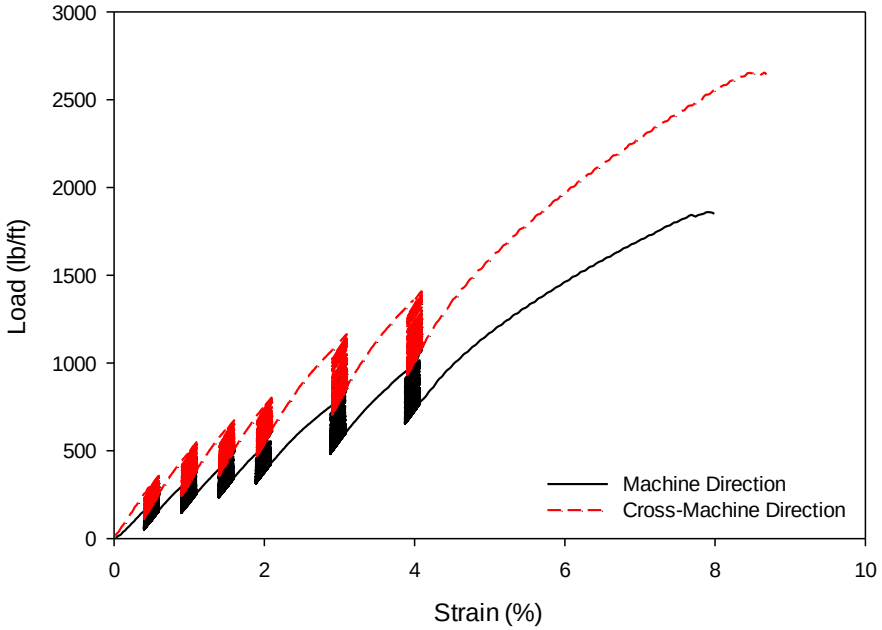


Figure D-7: Huesker Fornit 30.

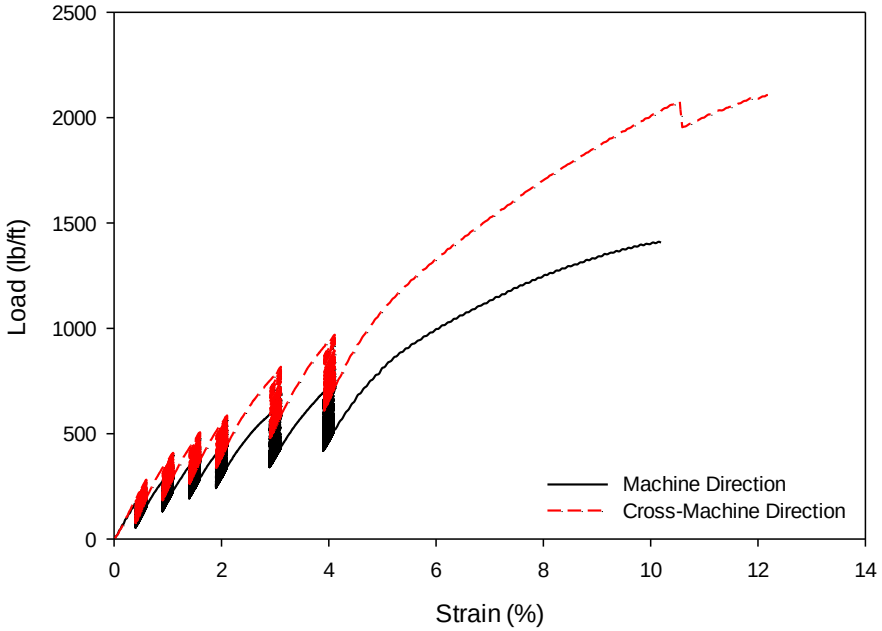


Figure D-8: SynTec Tenax MS330.

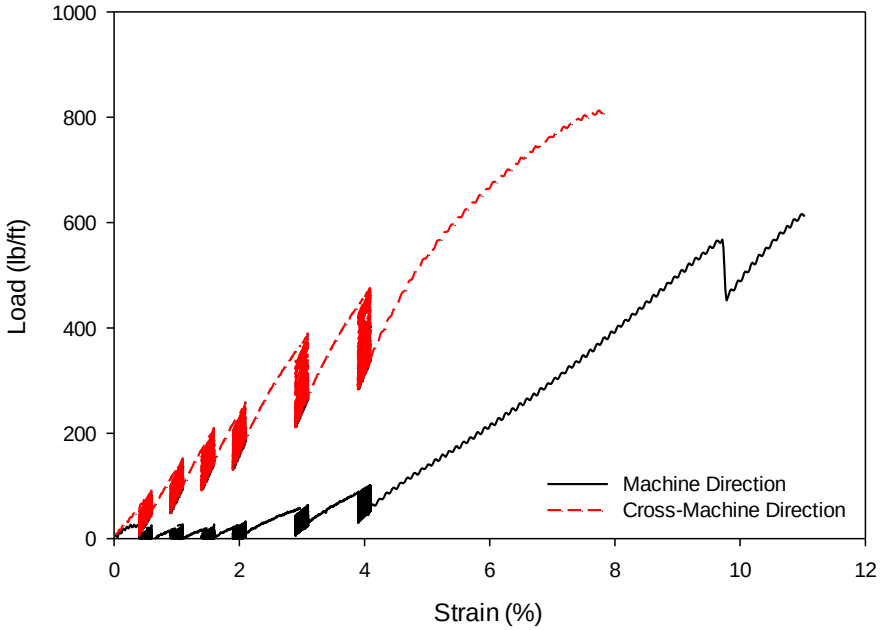


Figure D-9: Tensar TX 140.

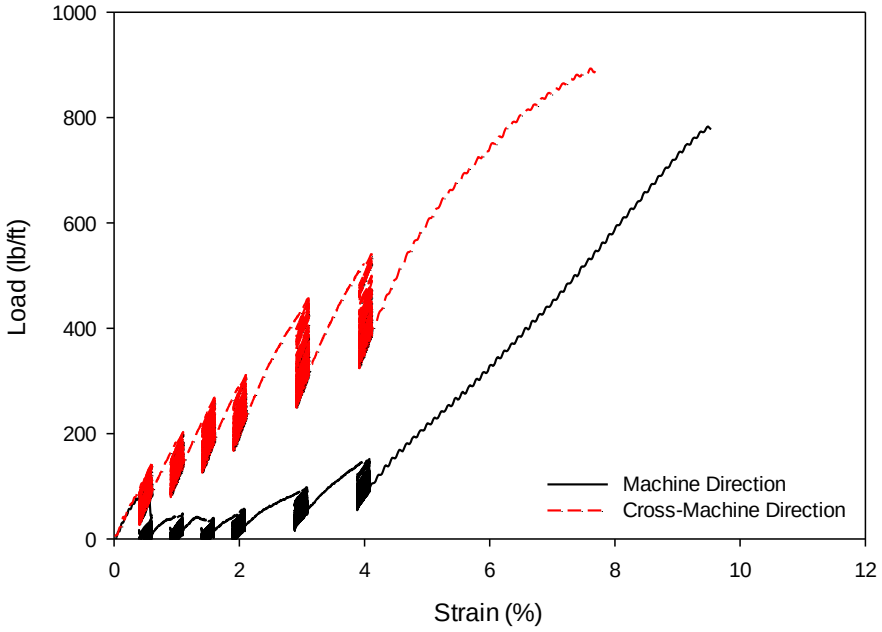


Figure D-10: Tensar TX 160.

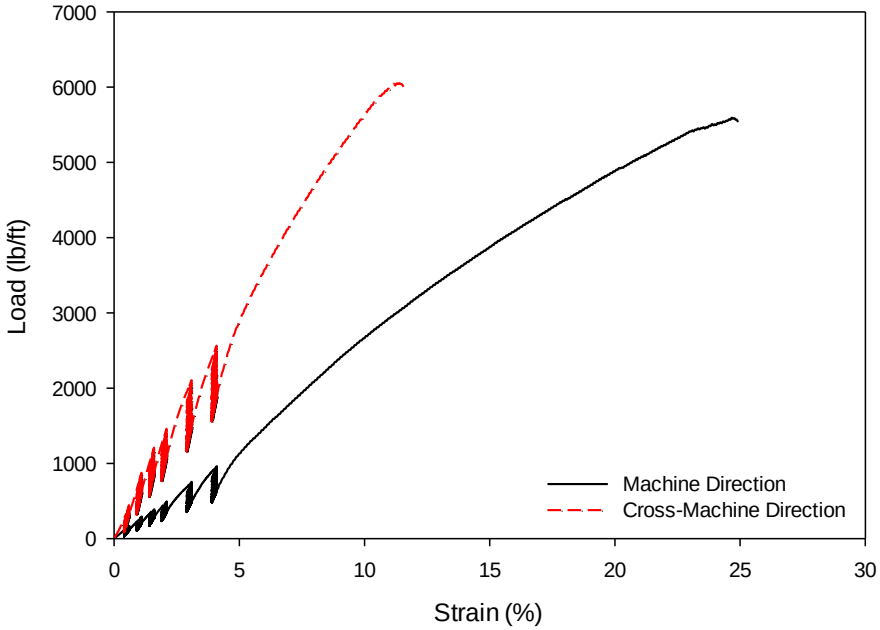


Figure D-11: TenCate Mirafi RS580i.

APPENDIX E:

RESILIENT INTERFACE SHEAR STIFFNESS PLOTS

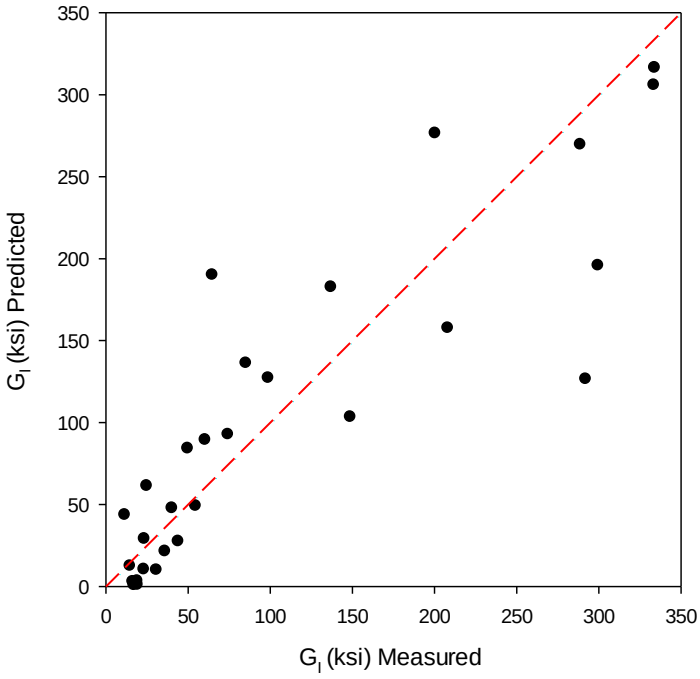


Figure E-1: Tensar BX Type 2.

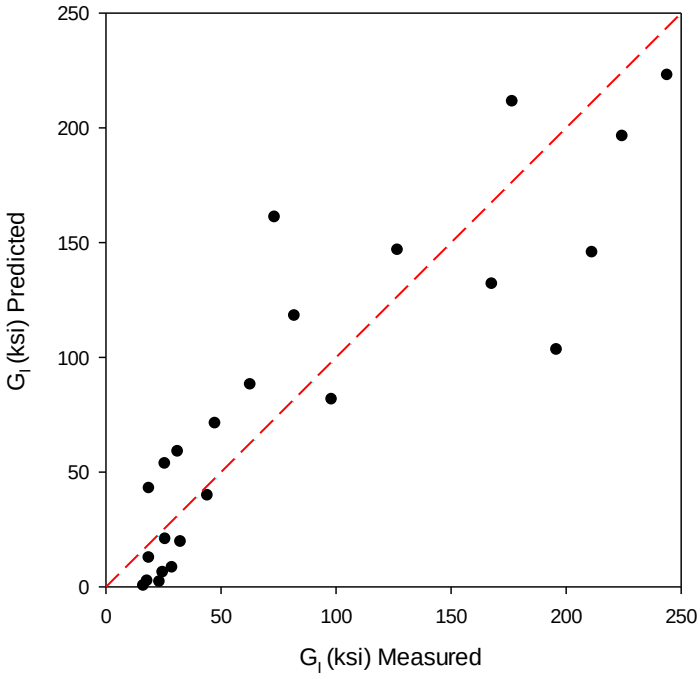


Figure E-2: NAUE Secugrid 30/30 Q1.

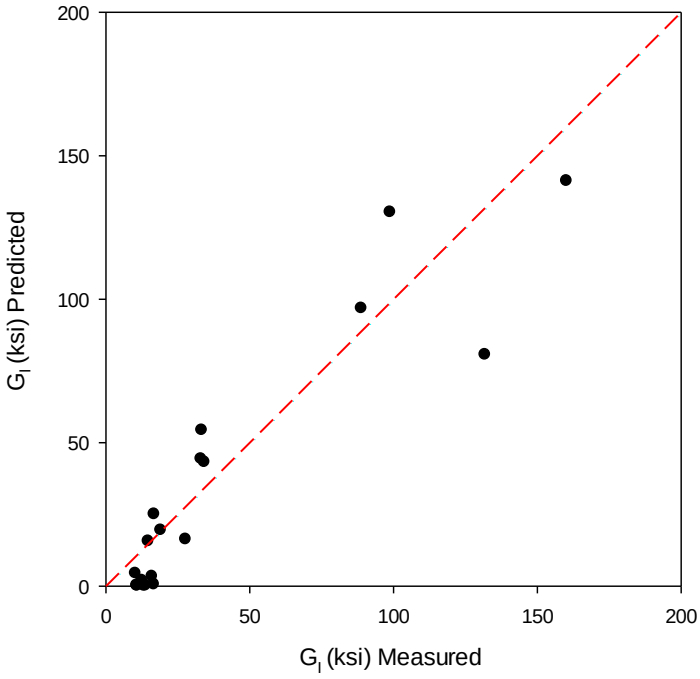


Figure E-3: Colbond Enkagrid Max 30.

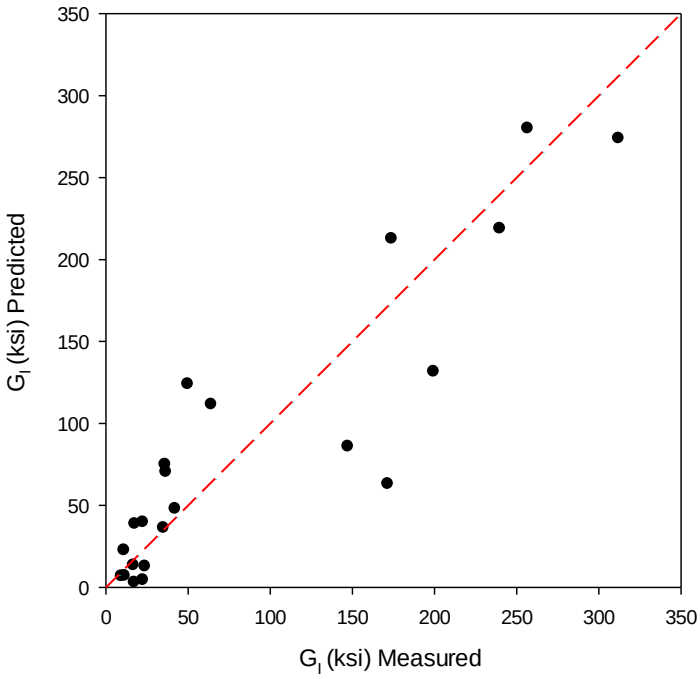


Figure E-4: Synteen SF 11.

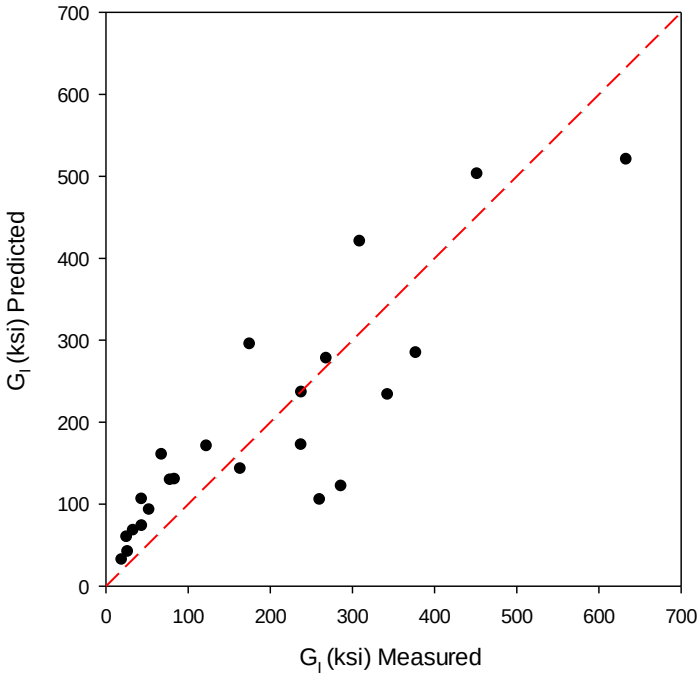


Figure E-5: Synteen SF 12.

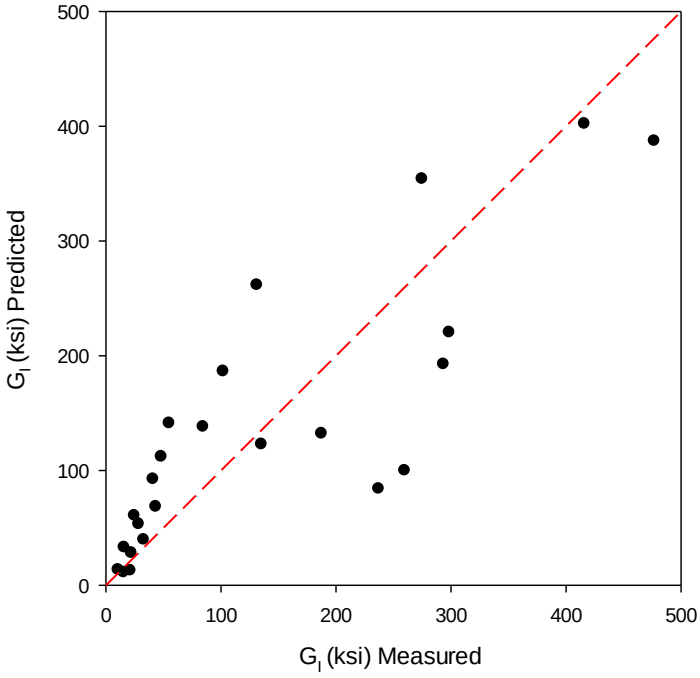


Figure E-6: TenCate Mirafi BXG 11.

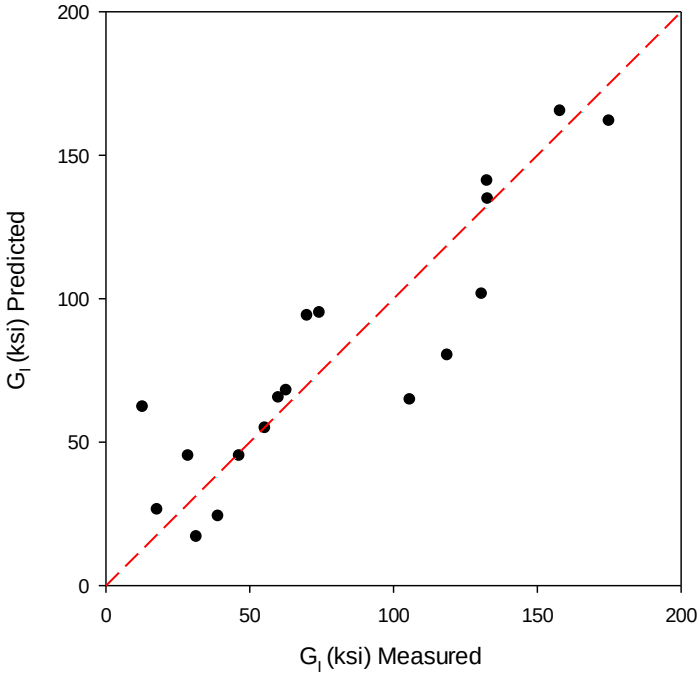


Figure E-7: Huesker Fornit 30.

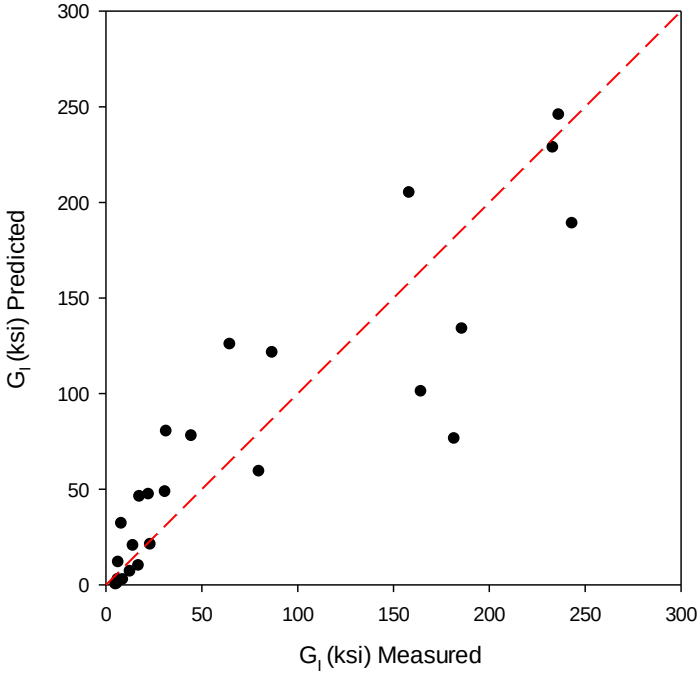


Figure E-8: SynTec Tenax MS330.

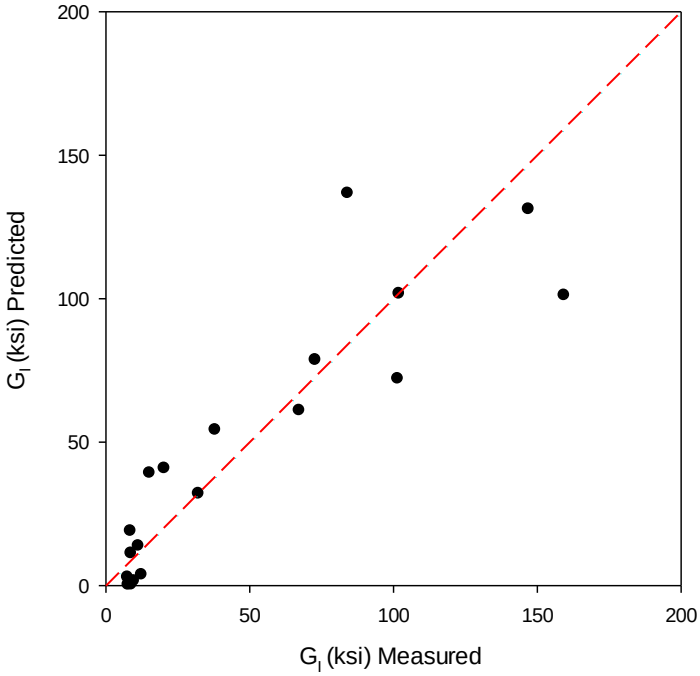


Figure E-9: Tensar TX 140.

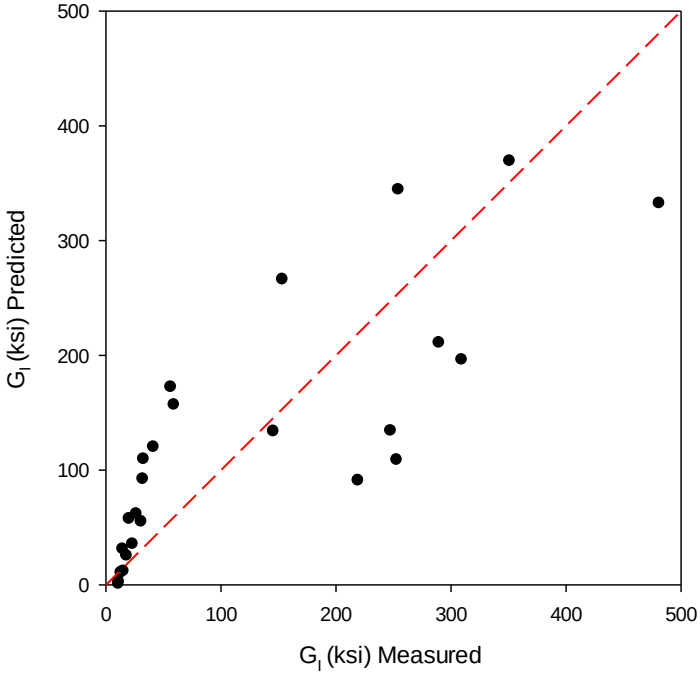


Figure E-10: Tensar TX 160.

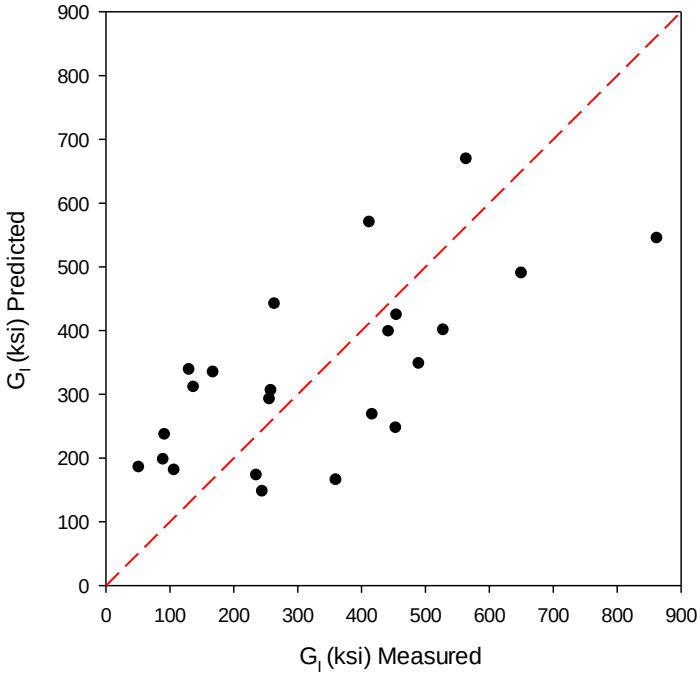


Figure E-11: TenCate Mirafi RS580i.

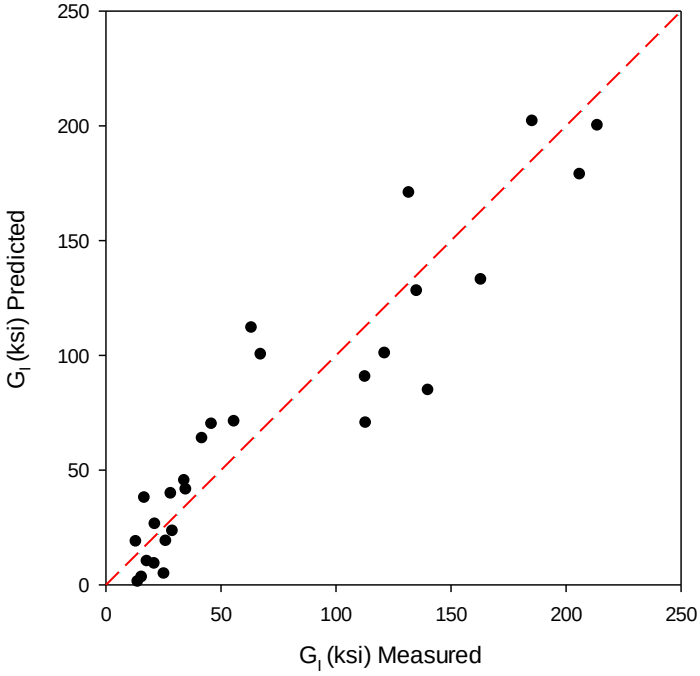


Figure E-12: Propex Geotex 801.

APPENDIX F:

JUNCTION STRENGTH PLOTS (LB/JUNCTION)

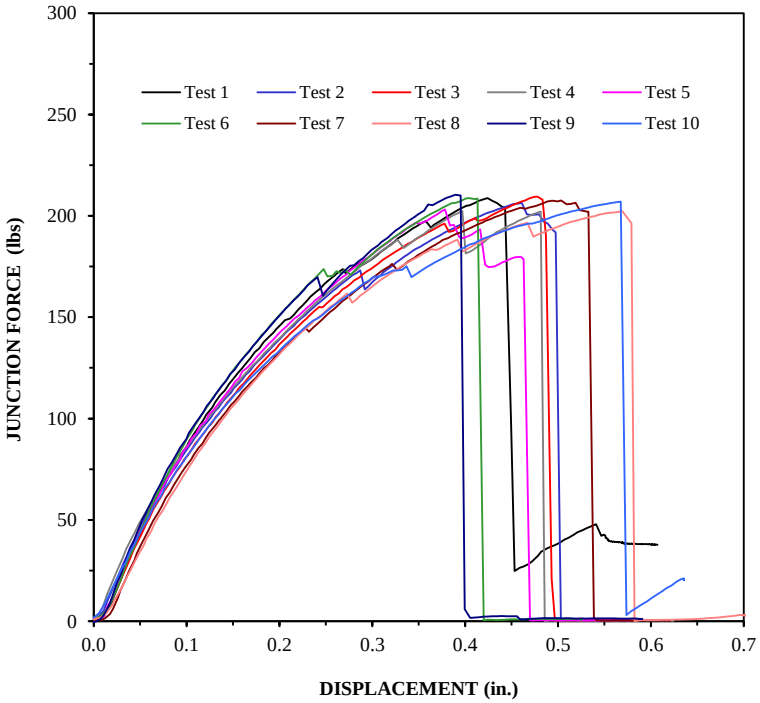


Figure F-1: Tensar BX Type 2.

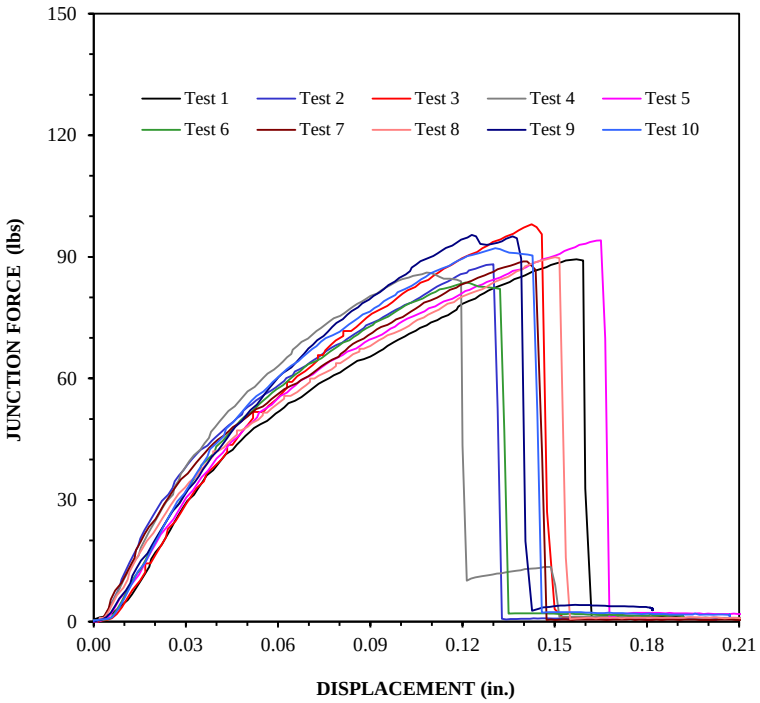


Figure F-2: NAUE Secugrid 30/30 Q1.

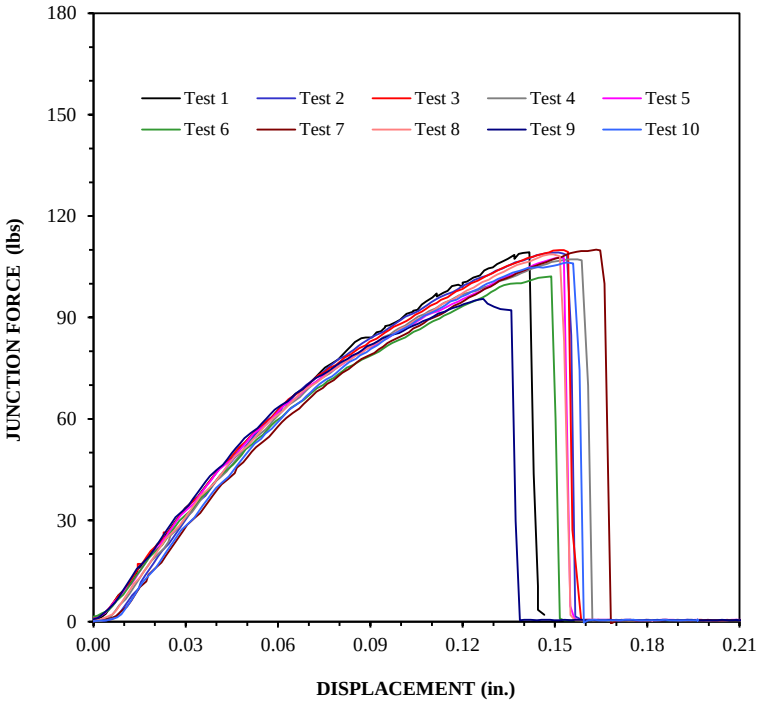


Figure F-3: Colbond Enkagrid Max 30.

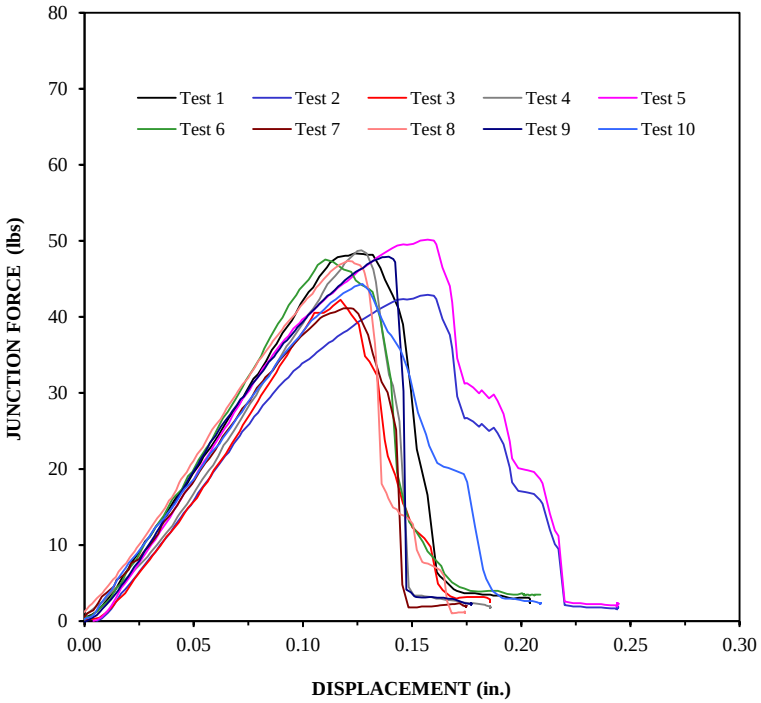


Figure F-4: Synteen SF 11.

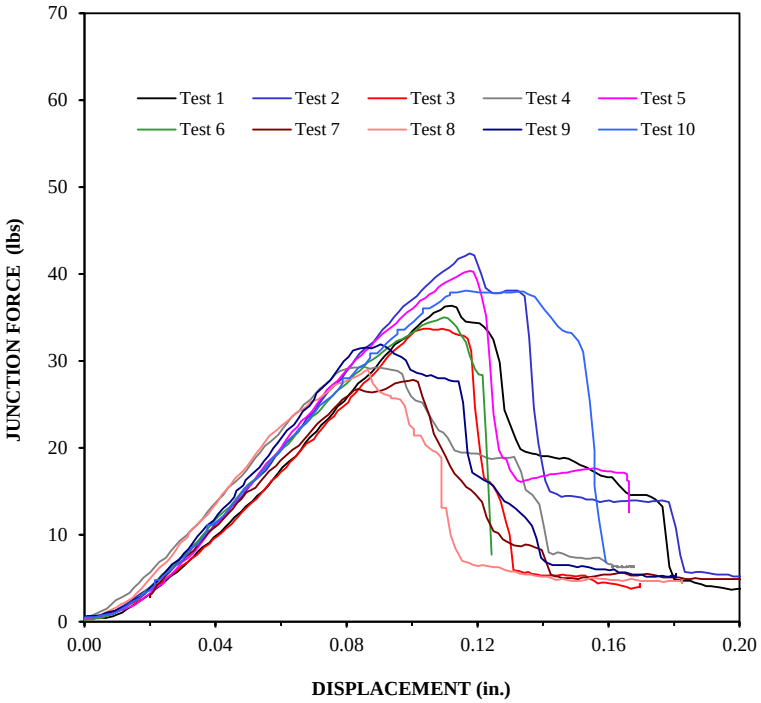


Figure F-5: Synteen SF 12.

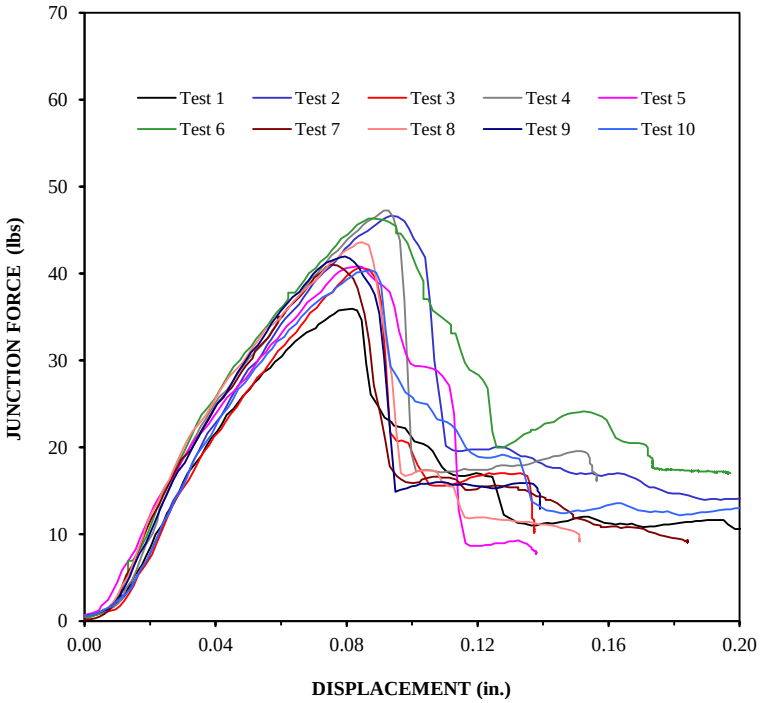


Figure F-6: TenCate Mirafi BXG 11.

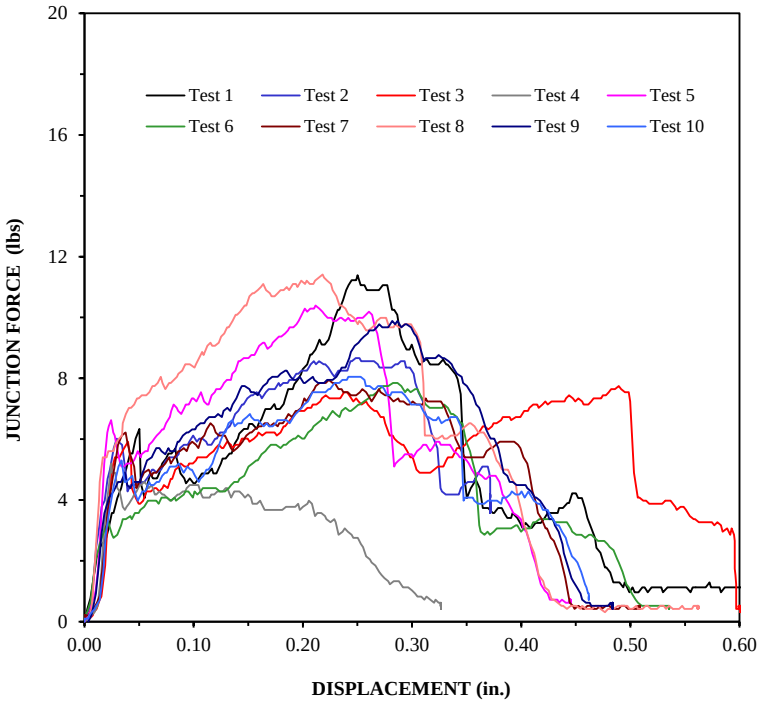


Figure F-7: Huesker Fornit 30.

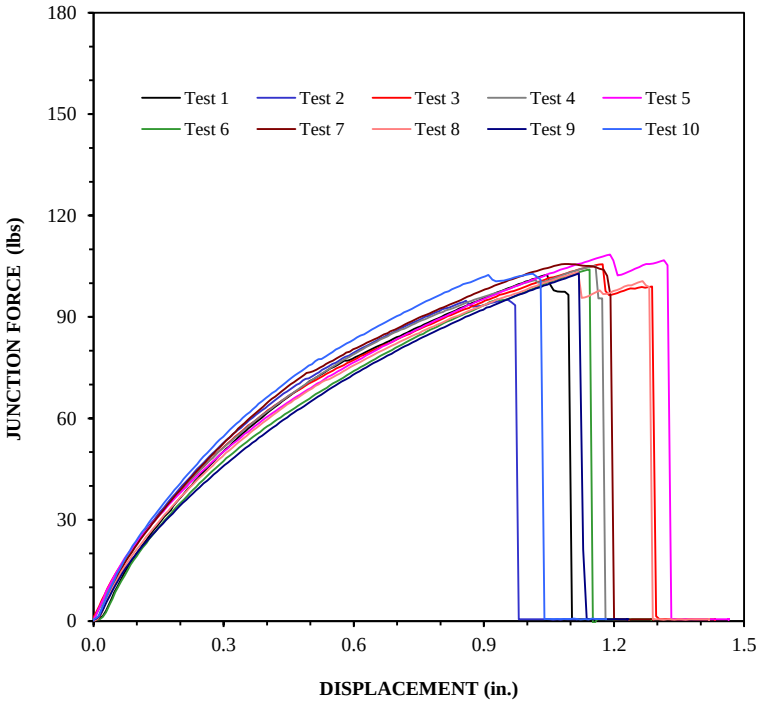


Figure F-8: SynTec Tenax MS330 (single layer).

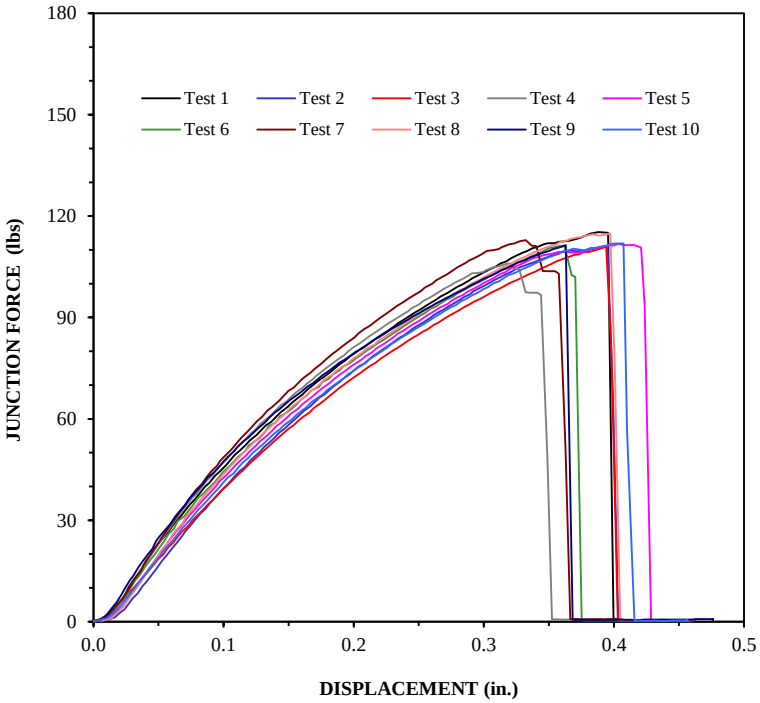


Figure F-9: Tensar TX 140.

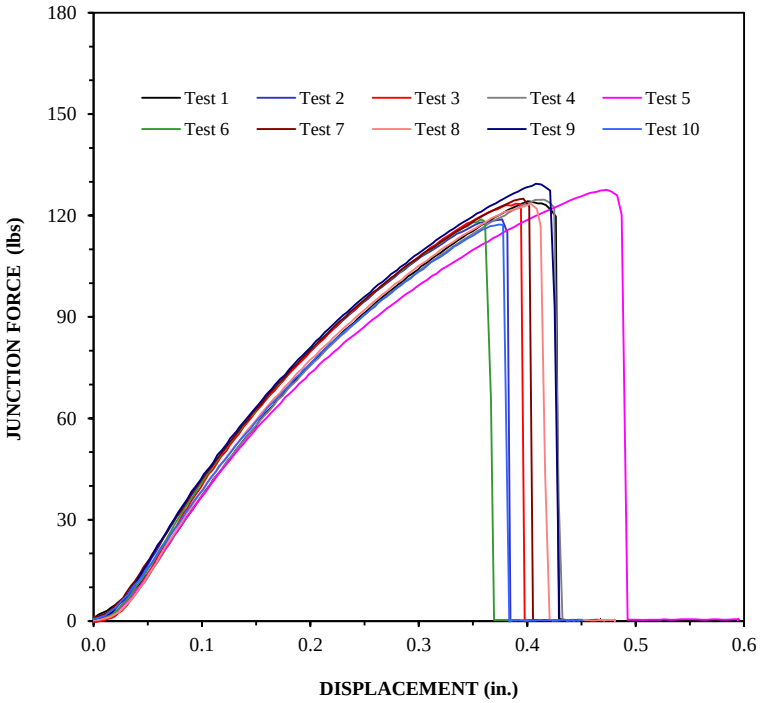


Figure F-10: Tensar TX 160.

APPENDIX G:

JUNCTION STRENGTH PLOTS (LB/IN)

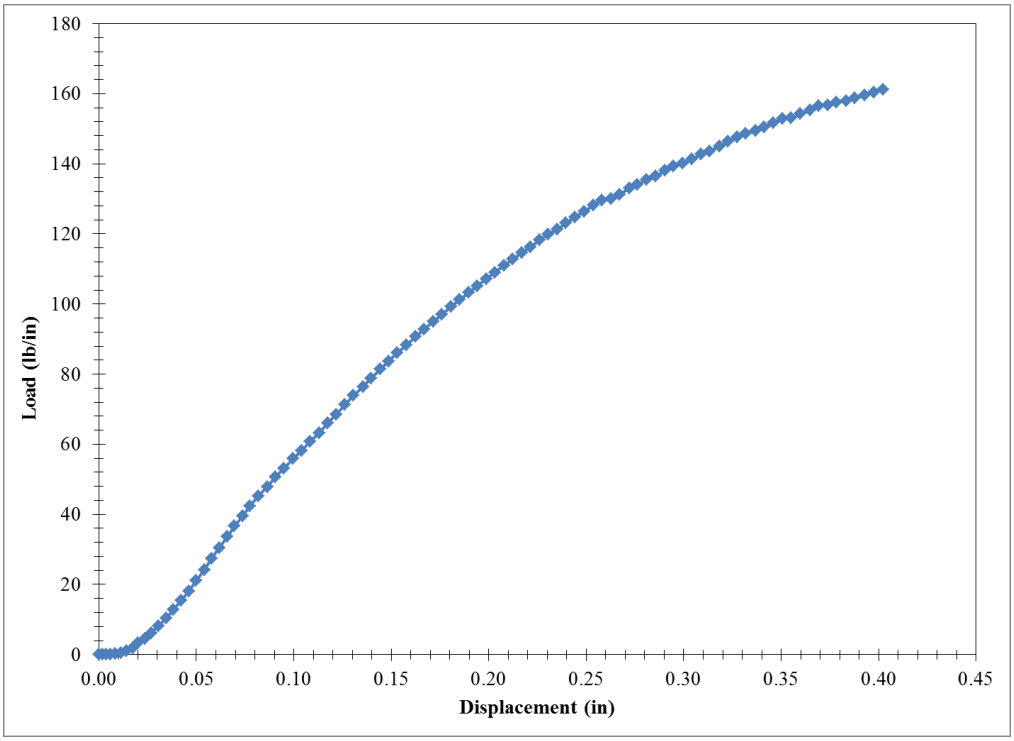


Figure G-1: Tensar BX Type 2.

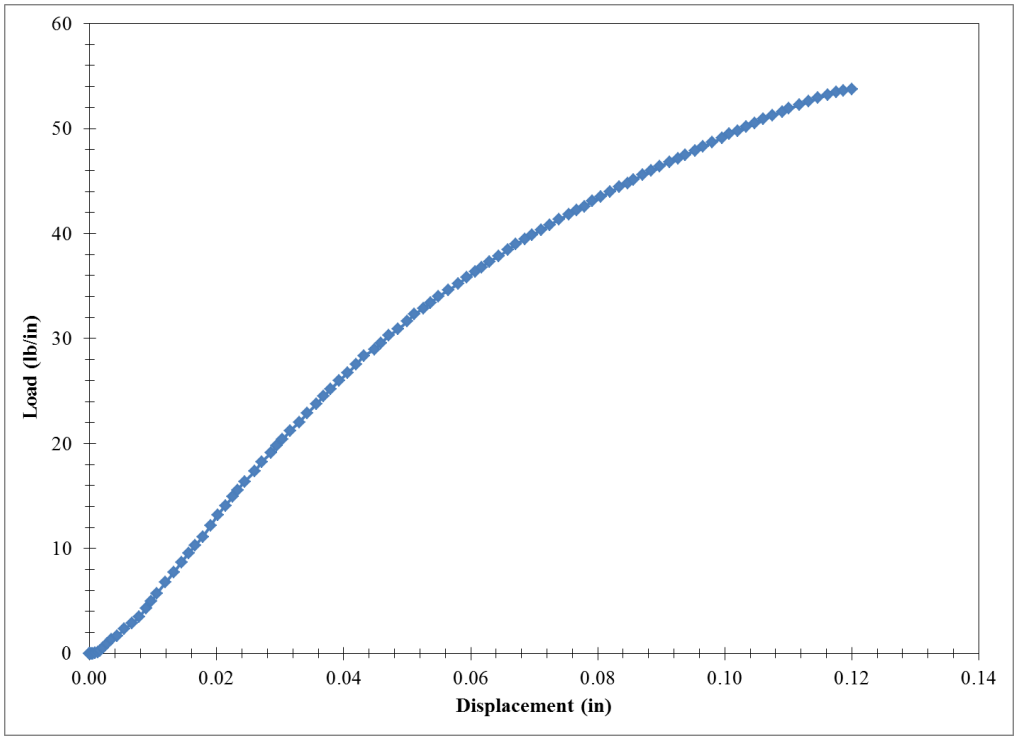


Figure G-2: NAUE Secugrid 30/30 Q1.

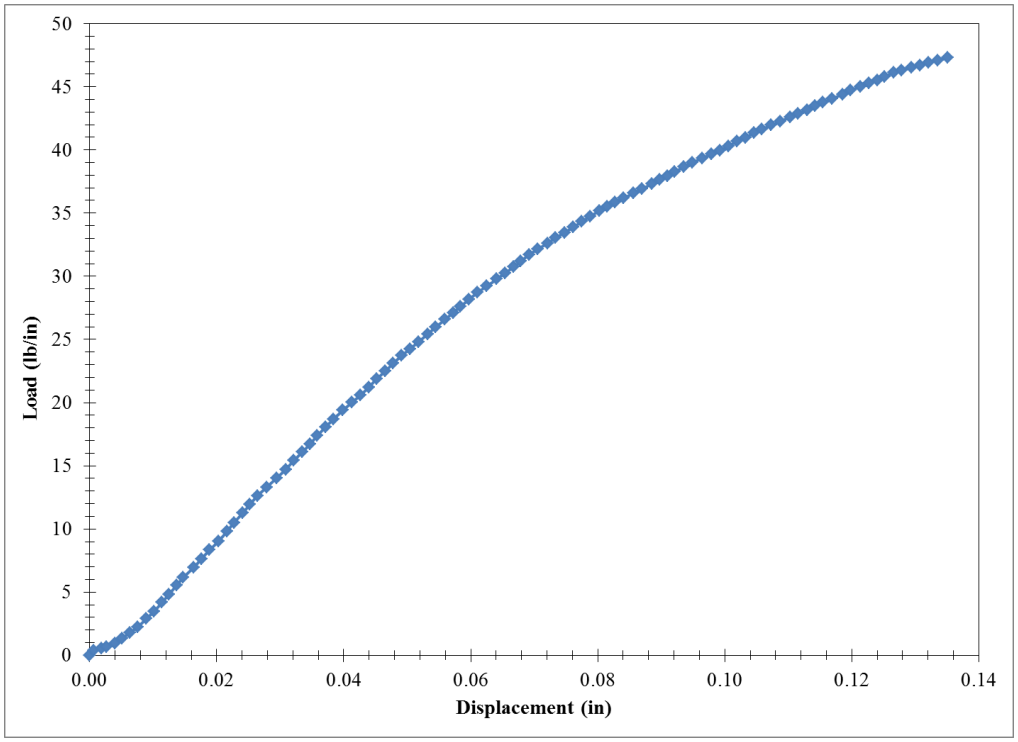


Figure G-3: Colbond Enkagrid Max 30.

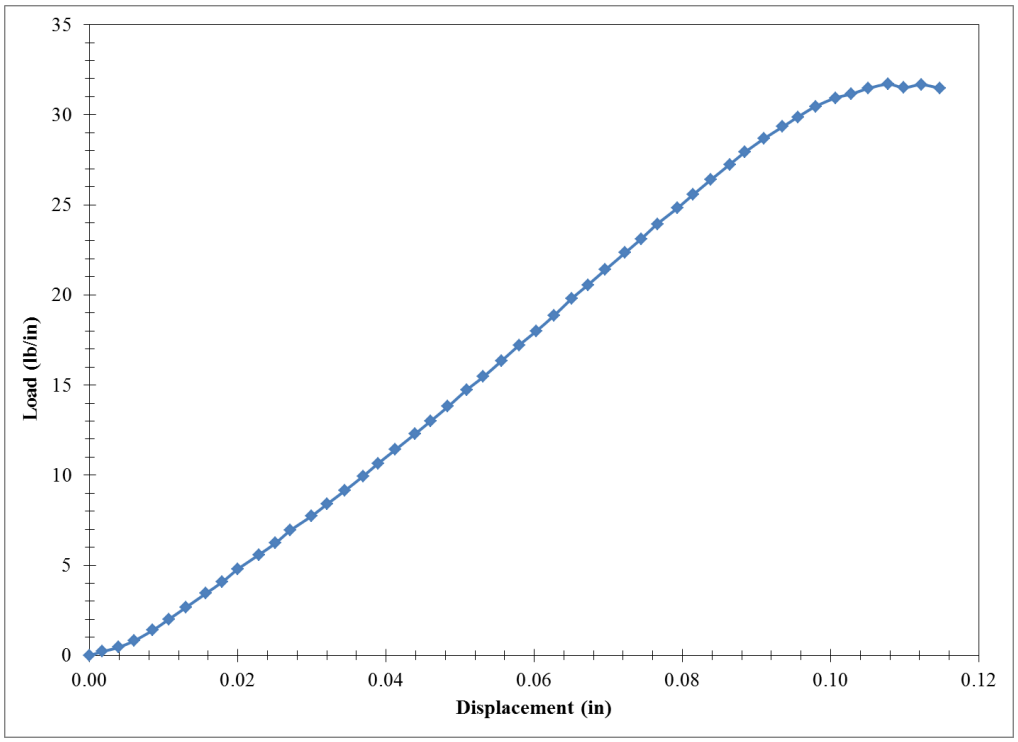


Figure G-4: Synteen SF 11.

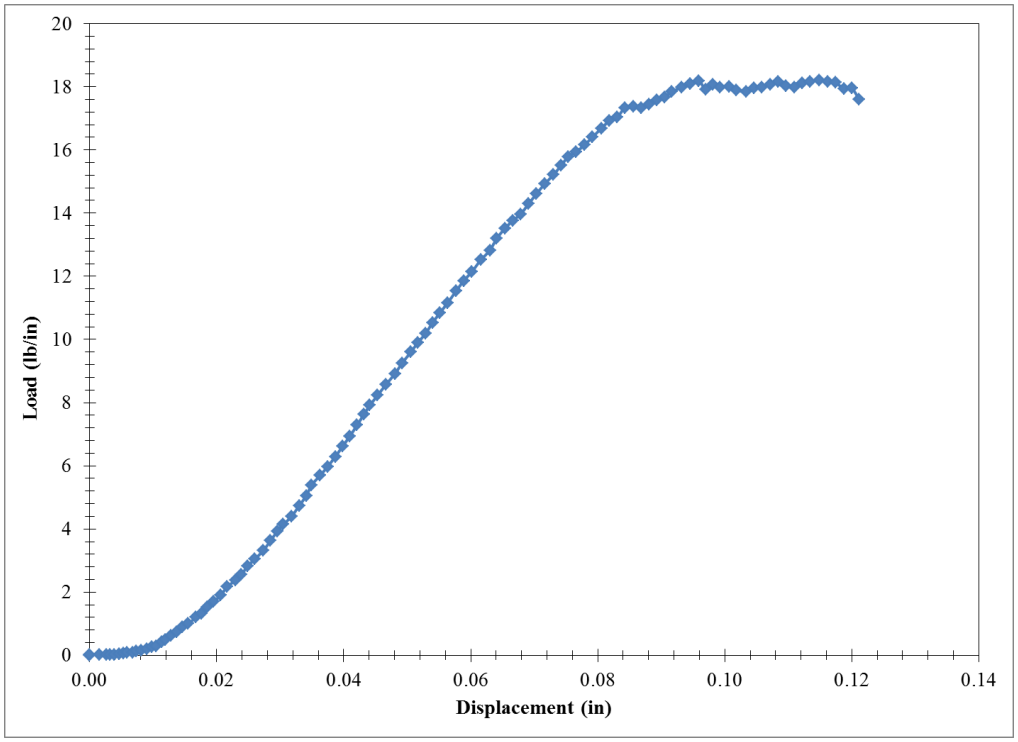


Figure G-5: Synteen SF 12.

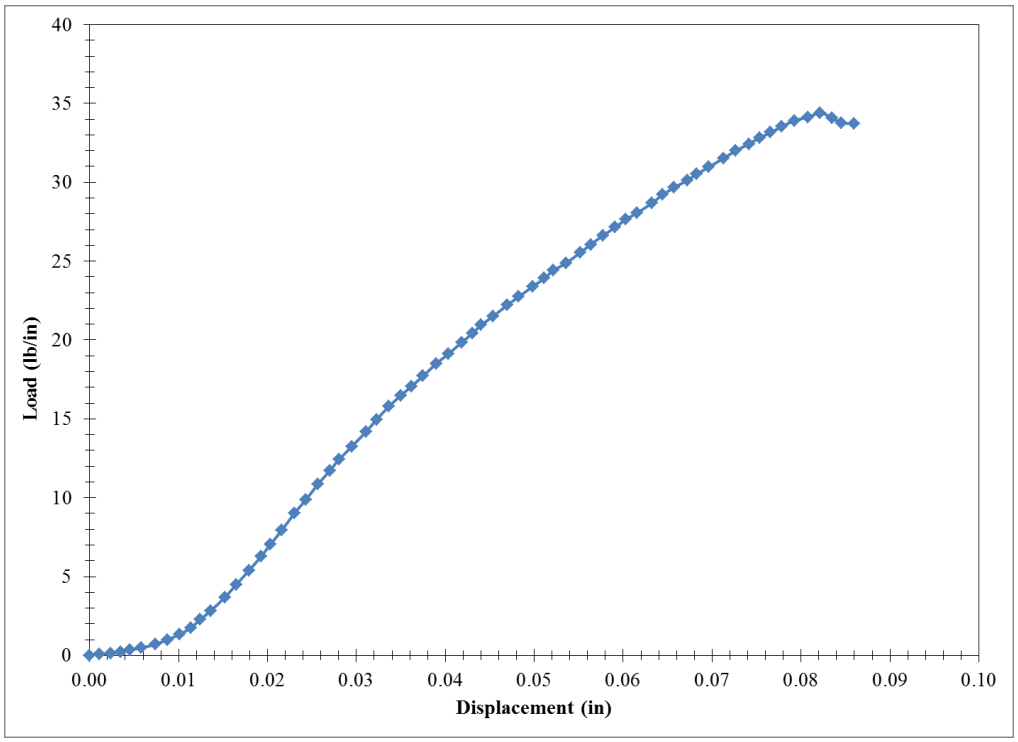


Figure G-6: TenCate Mirafi BXG 11.

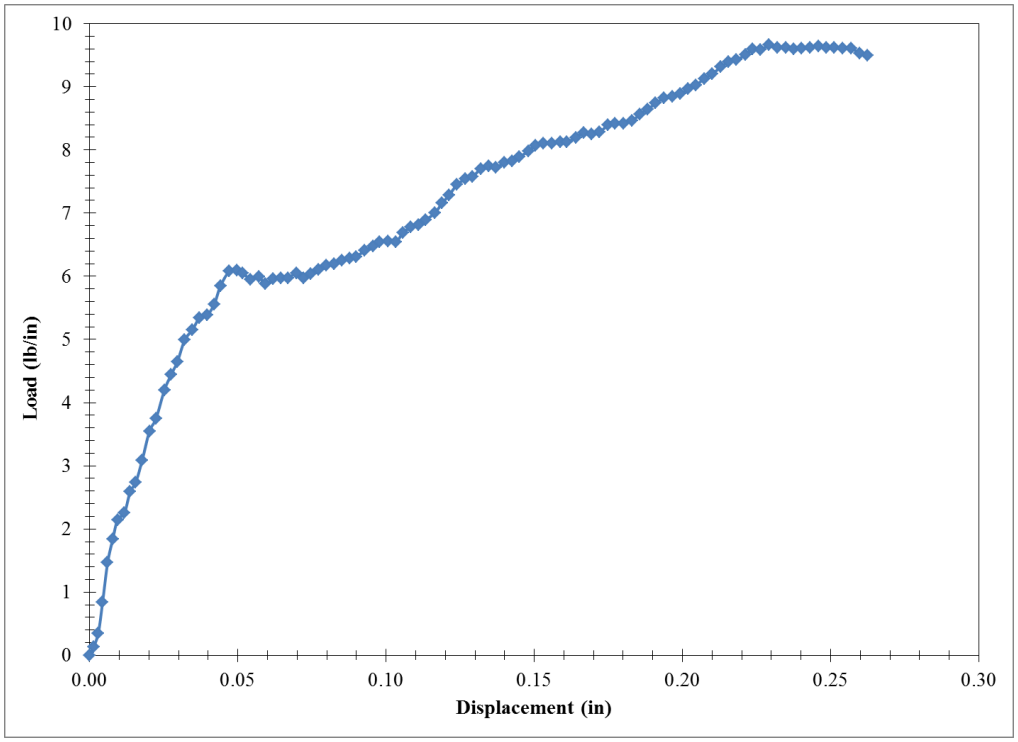


Figure G-7: Huesker Fornit 30.

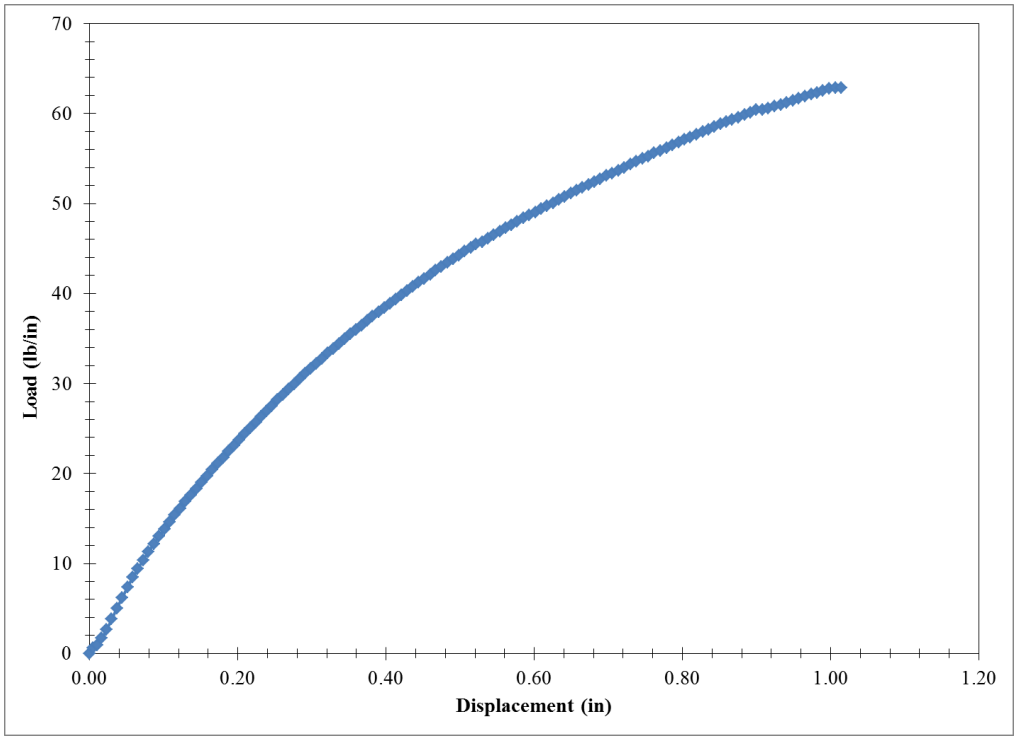


Figure G-8: SynTec Tenax MS330 (single layer).

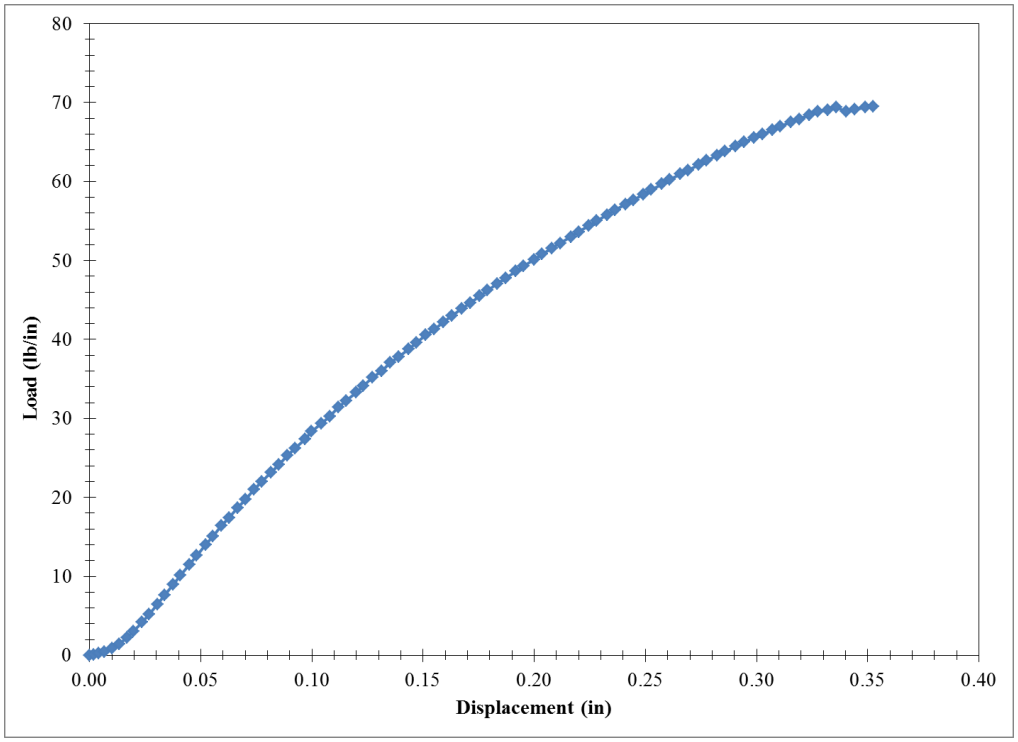


Figure G-9: Tensar TX 140.

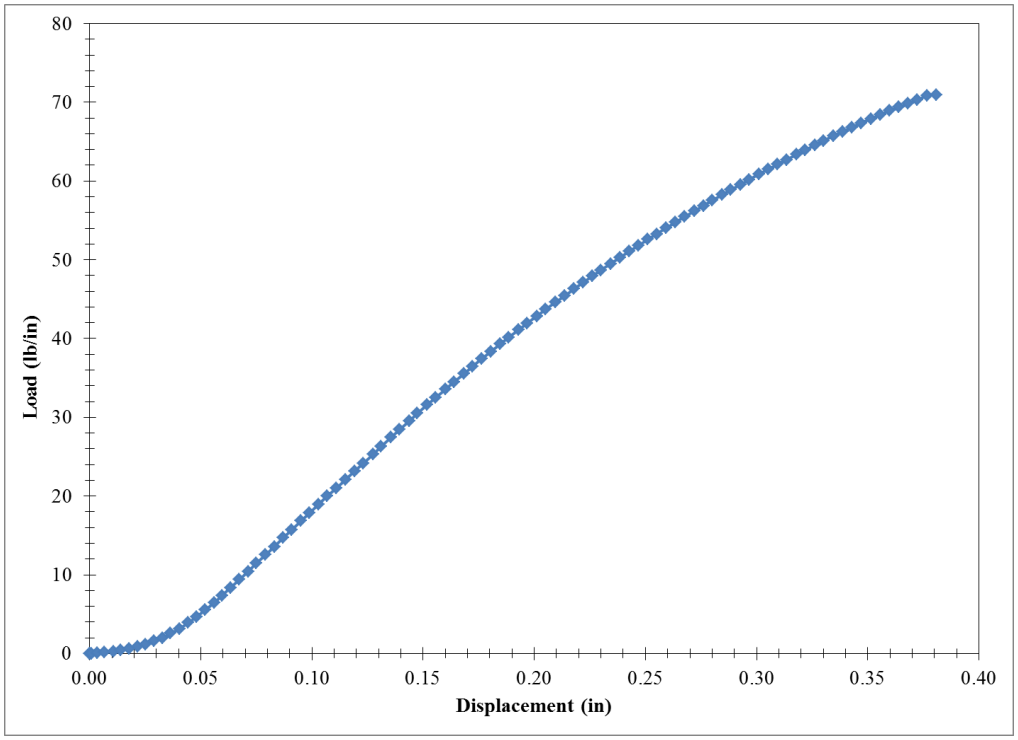


Figure G-10: Tensar TX 160.

APPENDIX H:

APERTURE STABILITY MODULUS PLOTS

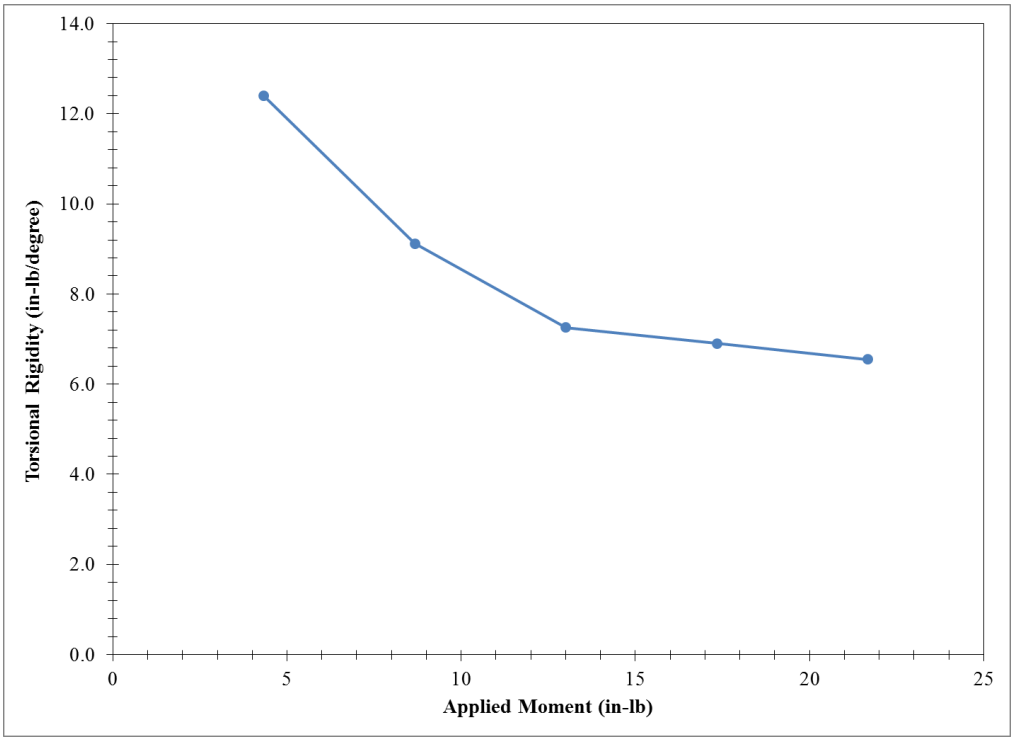


Figure H-1: Tensar BX Type 2.

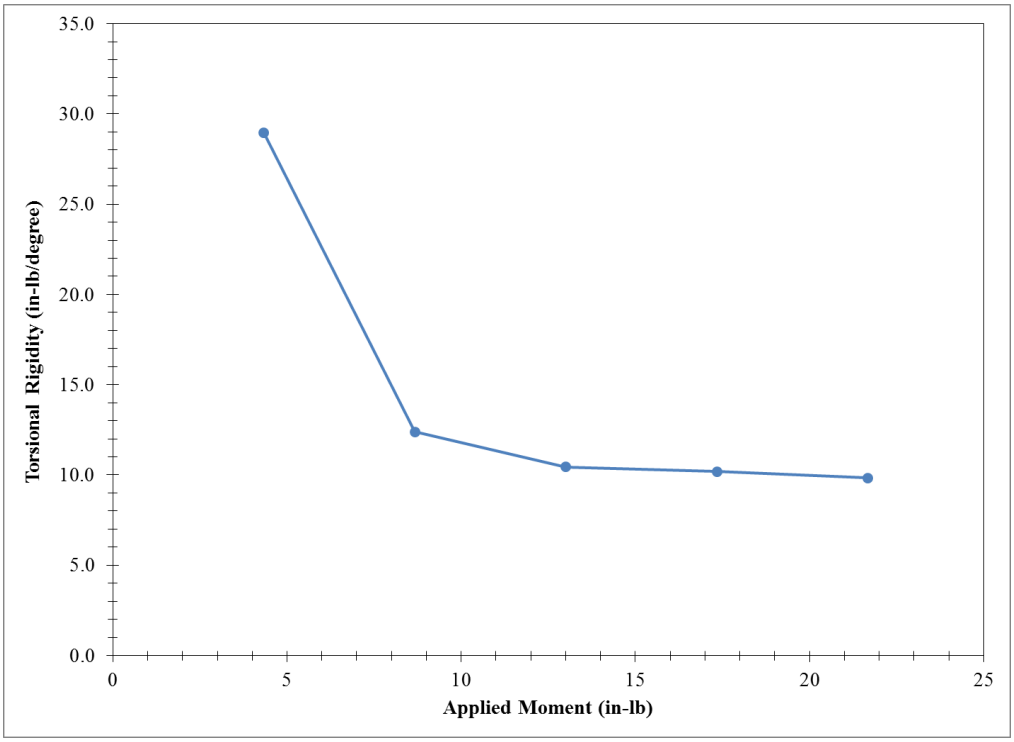


Figure H-2: NAUE Secugrid 30/30 Q1.

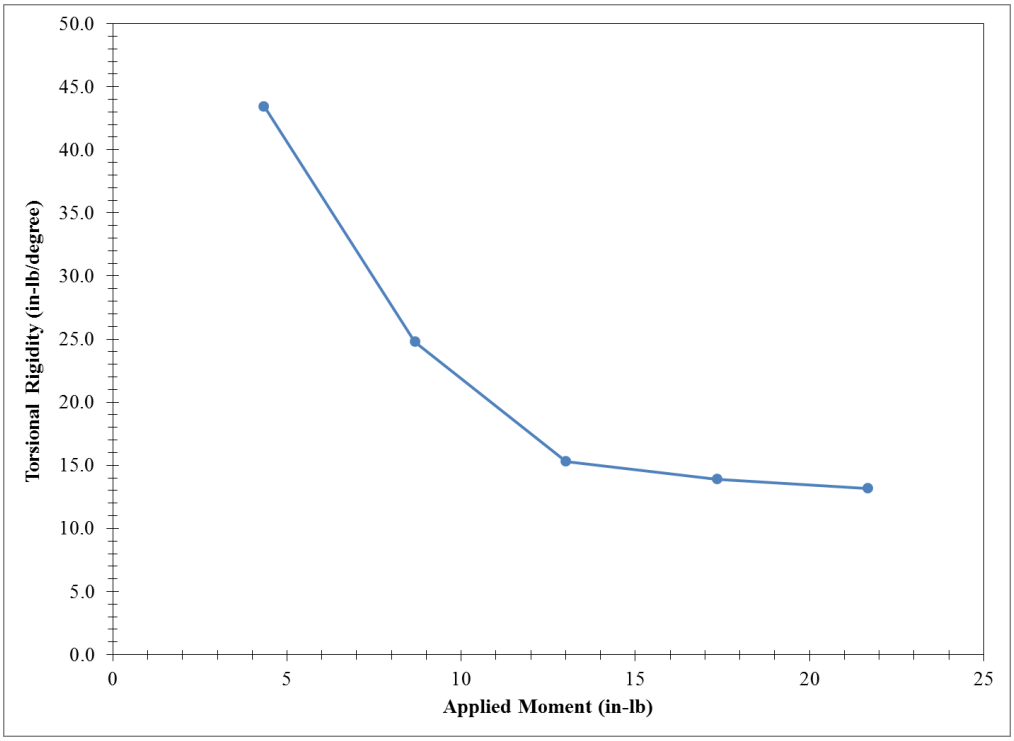


Figure H-3: Colbond Enkagrid Max 30.

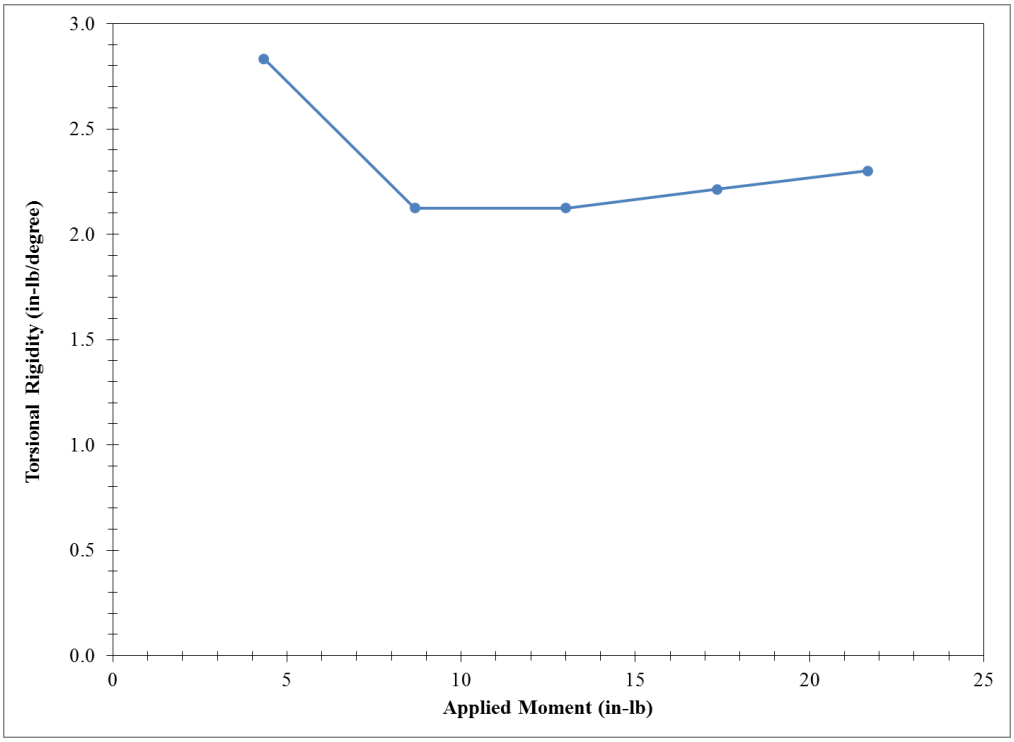


Figure H-4: Synteen SF 11.

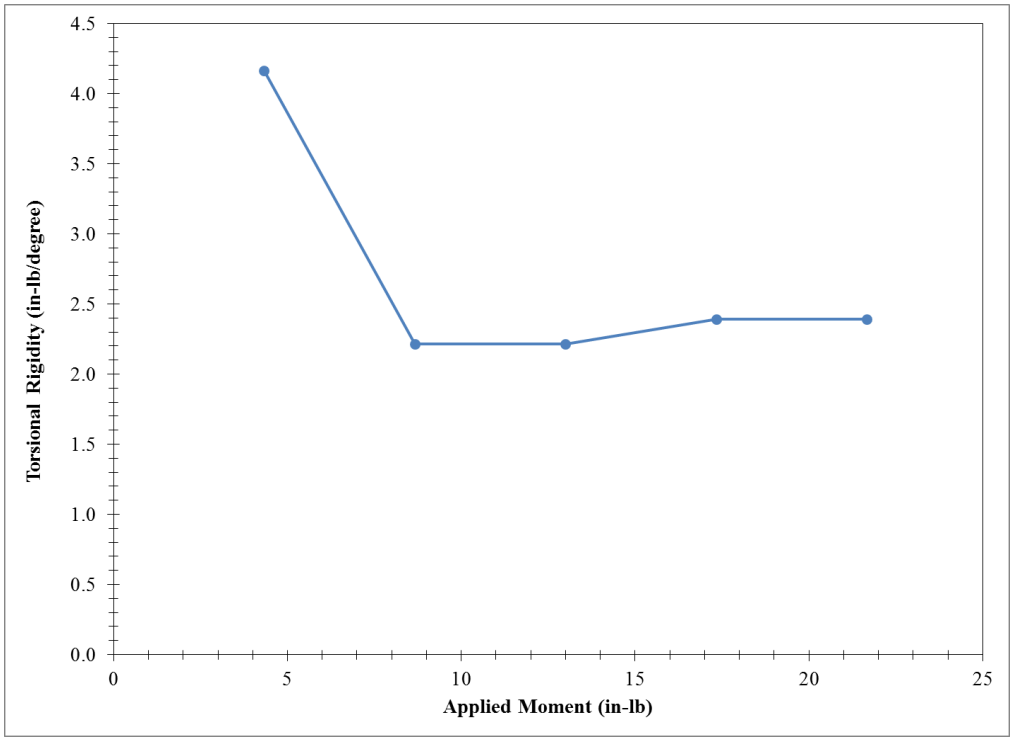


Figure H-5: Synteen SF 12.

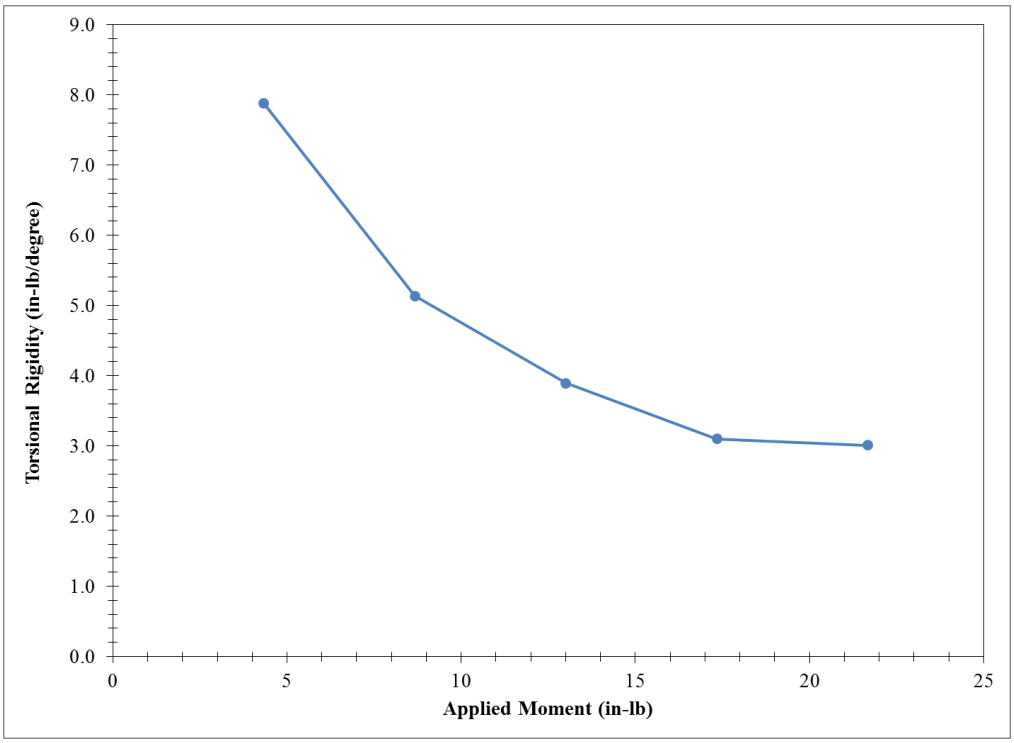


Figure H-6: TenCate Mirafi BXG 11.

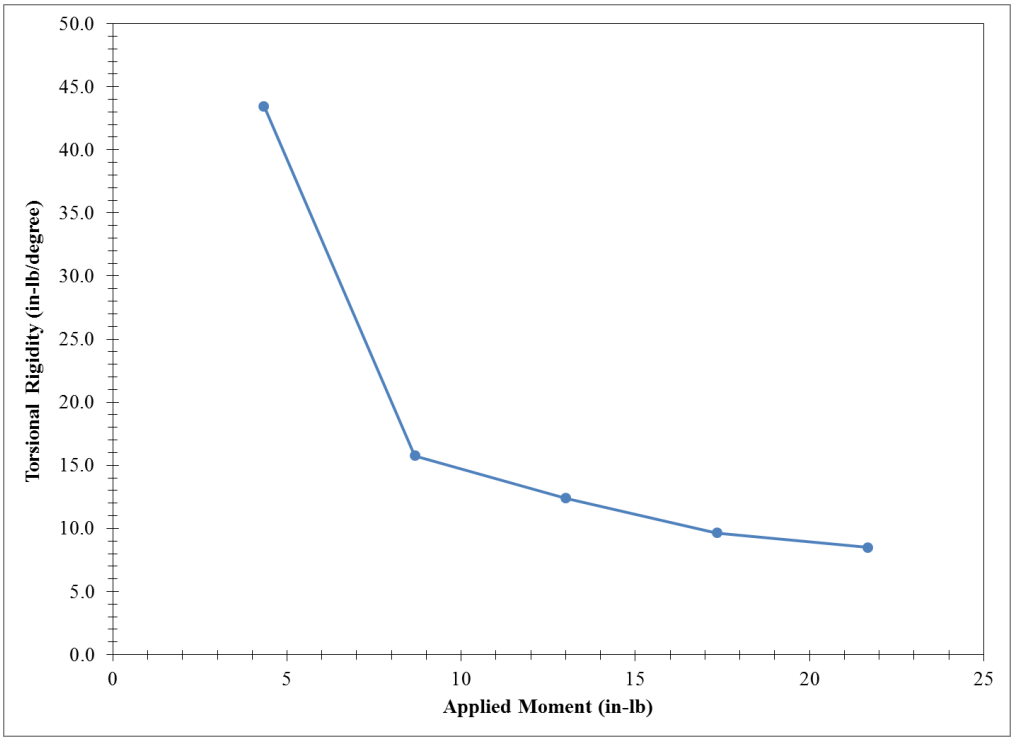


Figure H-7: Huesker Fornit 30.

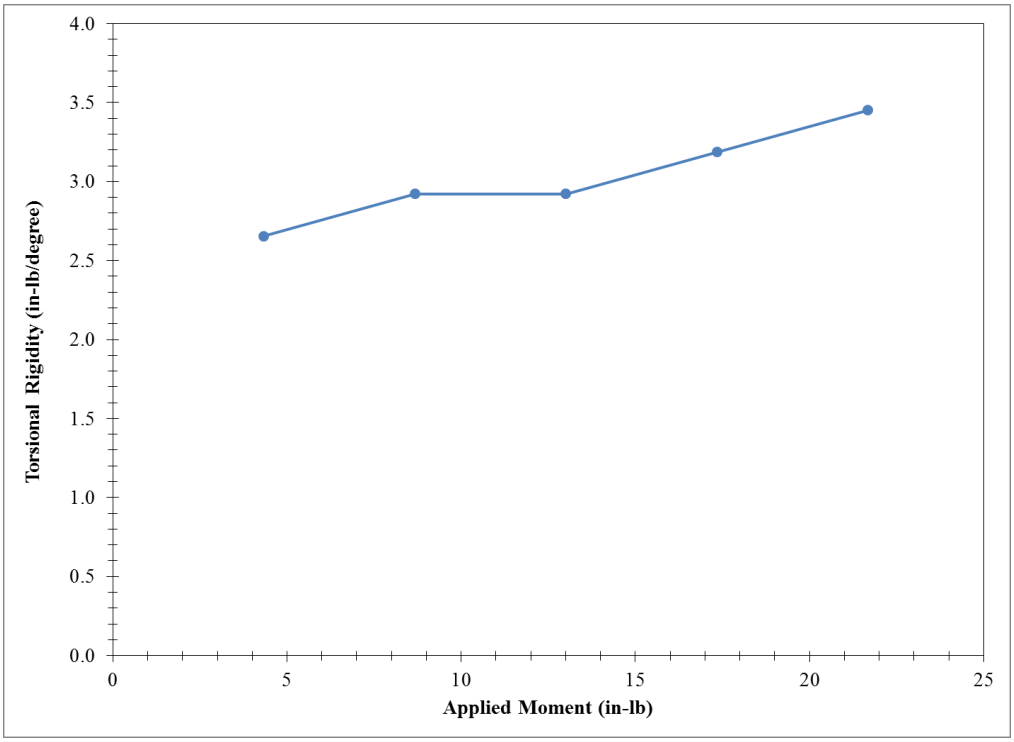


Figure H-8: SynTec Tenax MS330 (single layer).

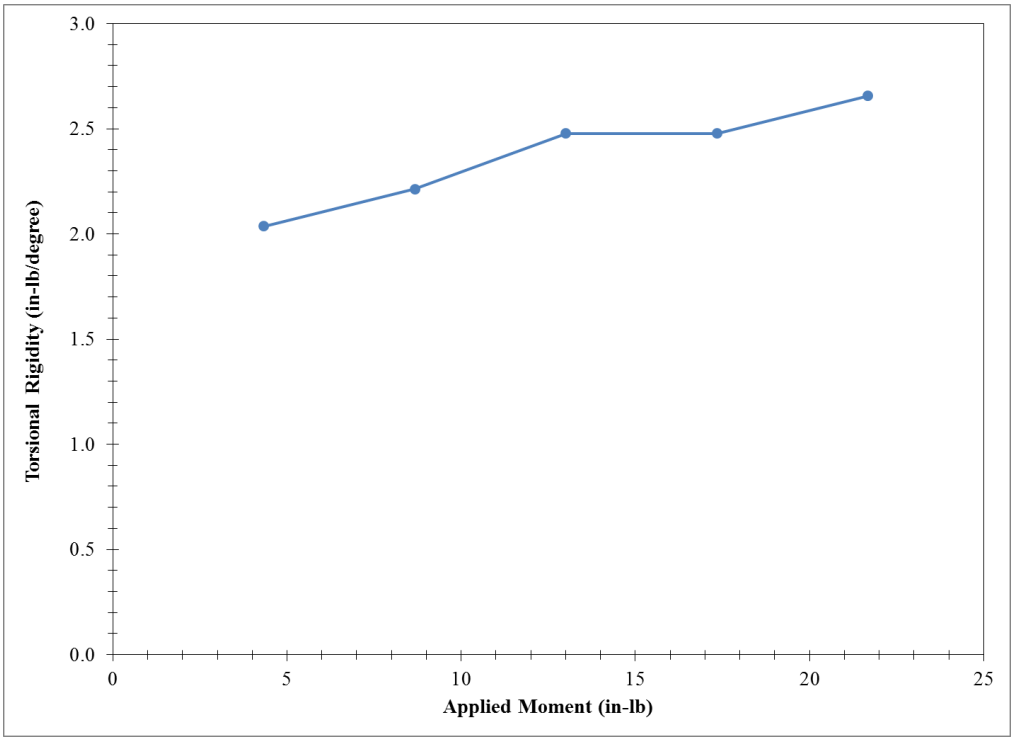


Figure H-9: Tensar TX 140.

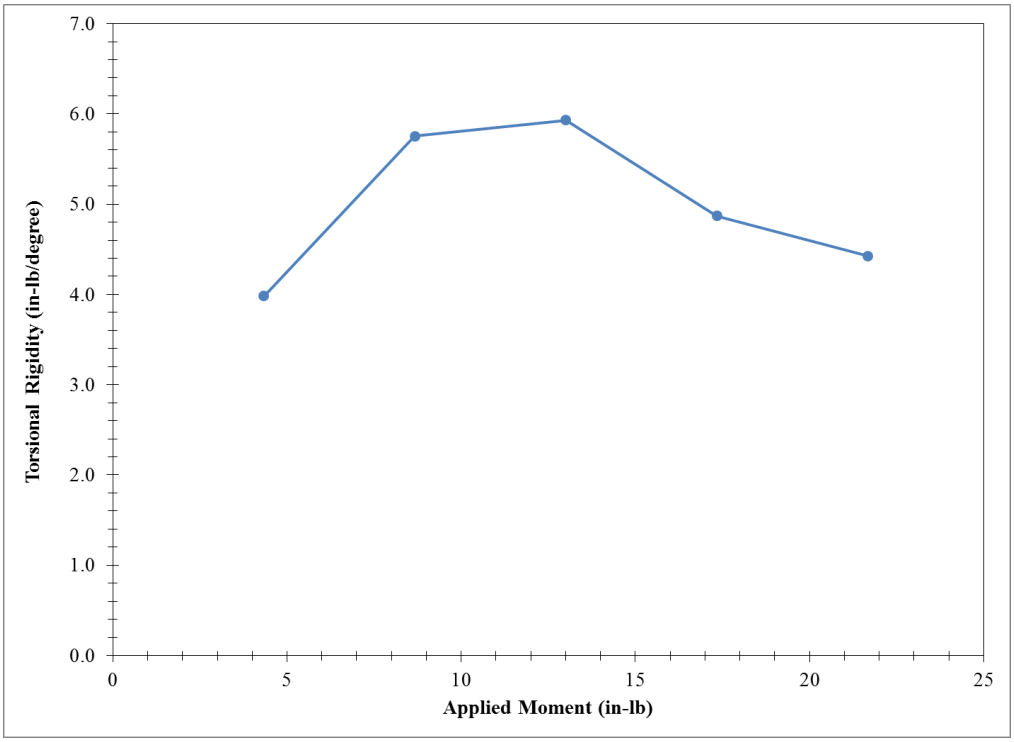


Figure H-10: Tensar TX 160.

APPENDIX I:

TRANSVERSE RUT PROFILES

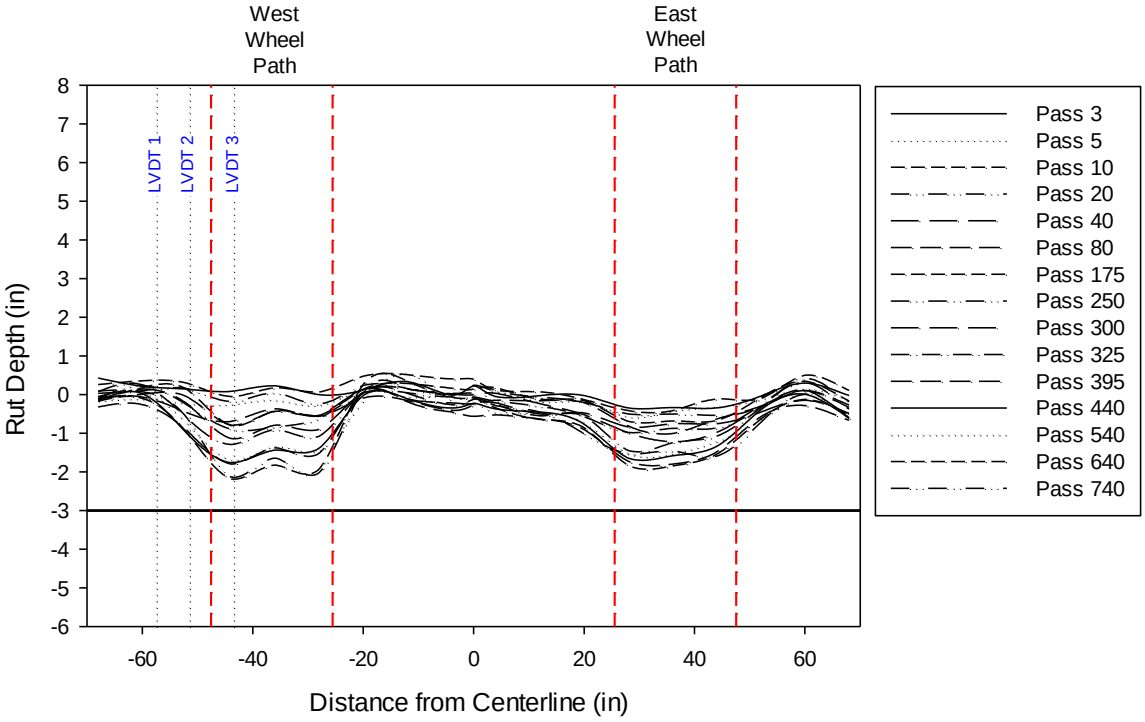


Figure I-1: Tensar BX Type 2 (1-North) (CBR = 2.15).

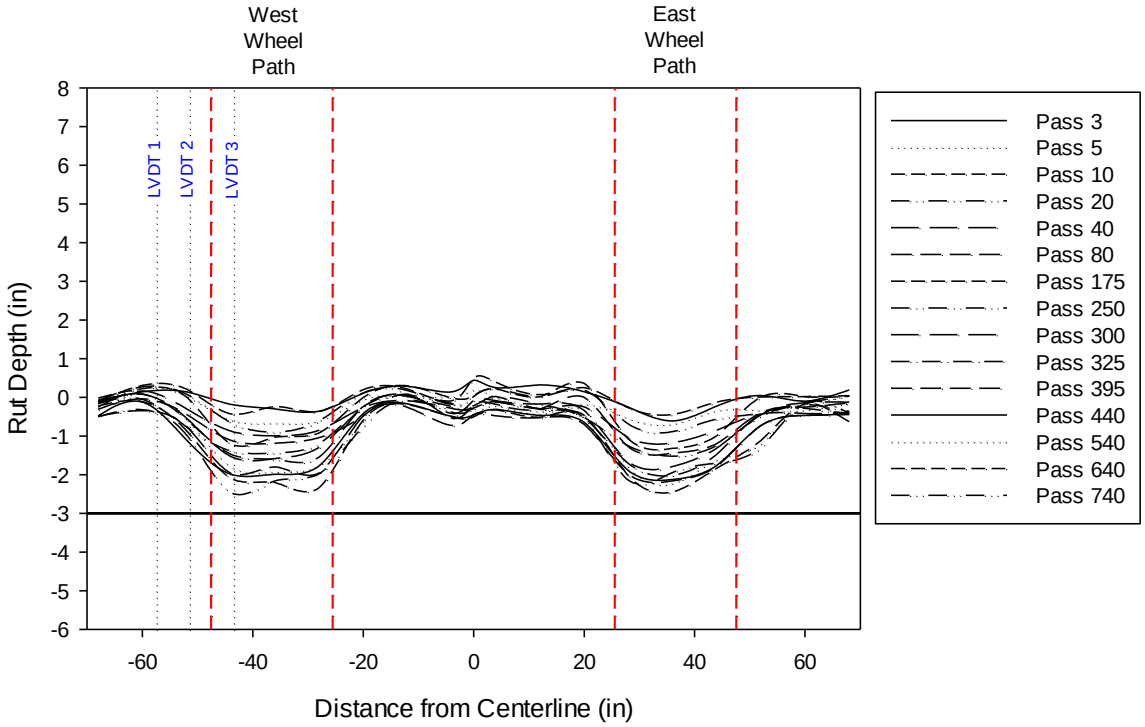


Figure I-2: Tensar BX Type 2 (1-South) (CBR = 2.15).

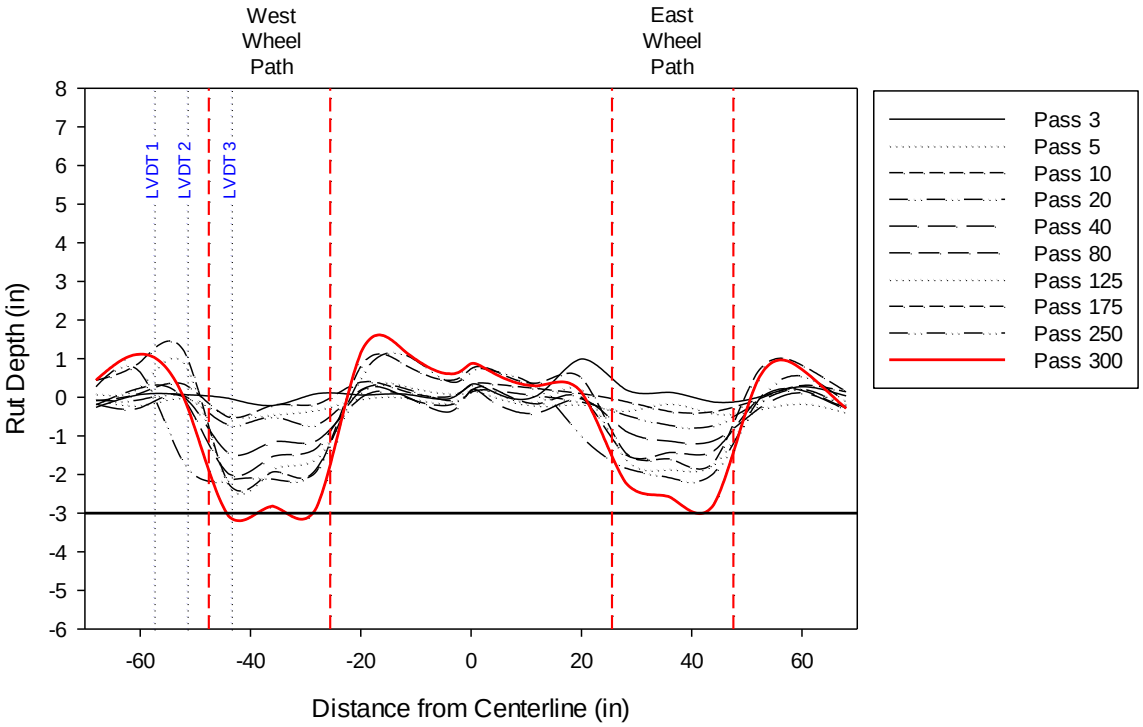


Figure I-3: Tensar BX Type 2 (2-North) (CBR = 1.61).

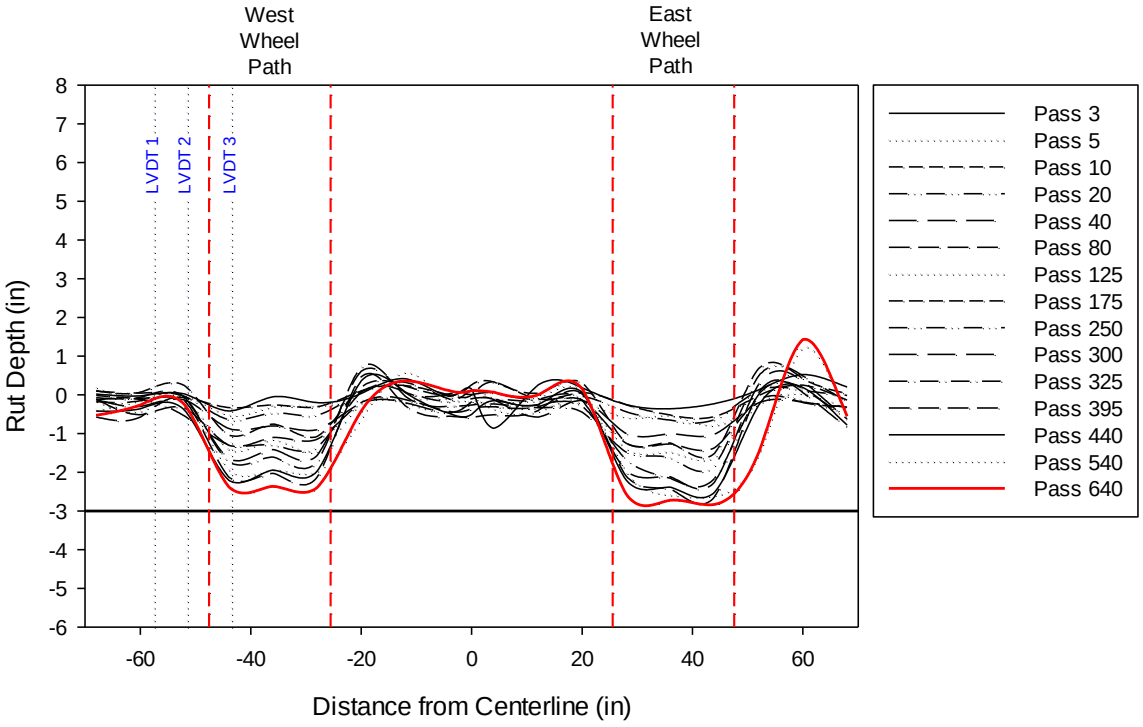


Figure I-4: Tensar BX Type 2 (2-South) (CBR = 1.61).

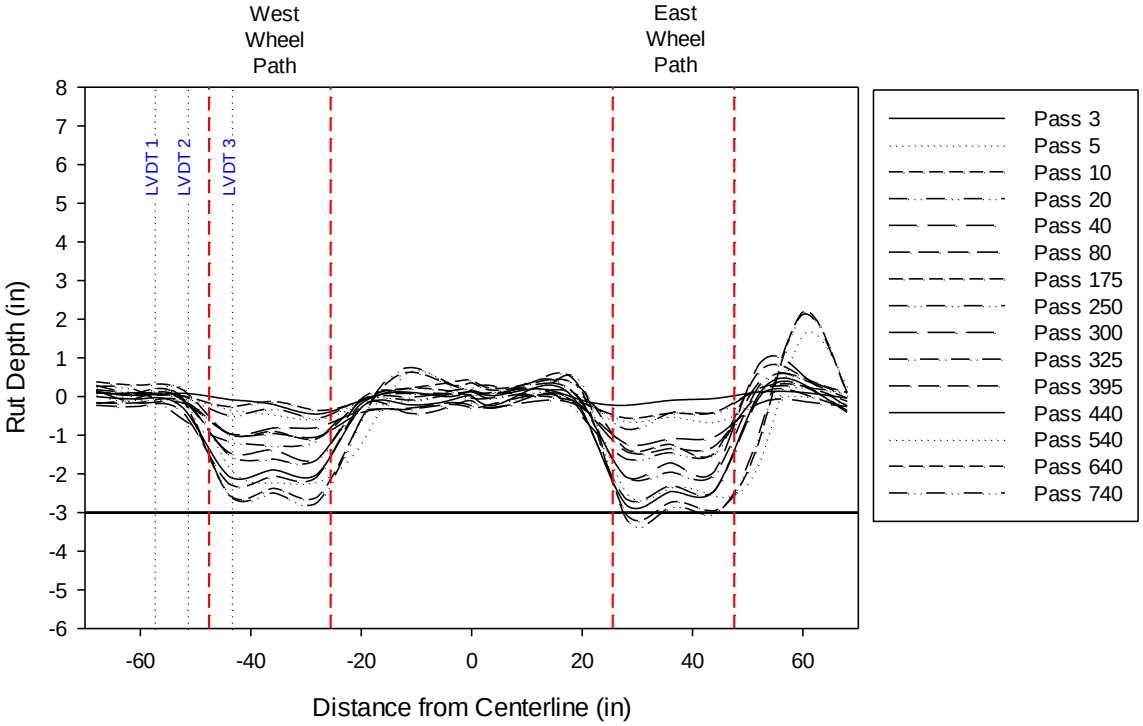


Figure I-5: Tensar BX Type 2 (3-North) (CBR = 1.78).

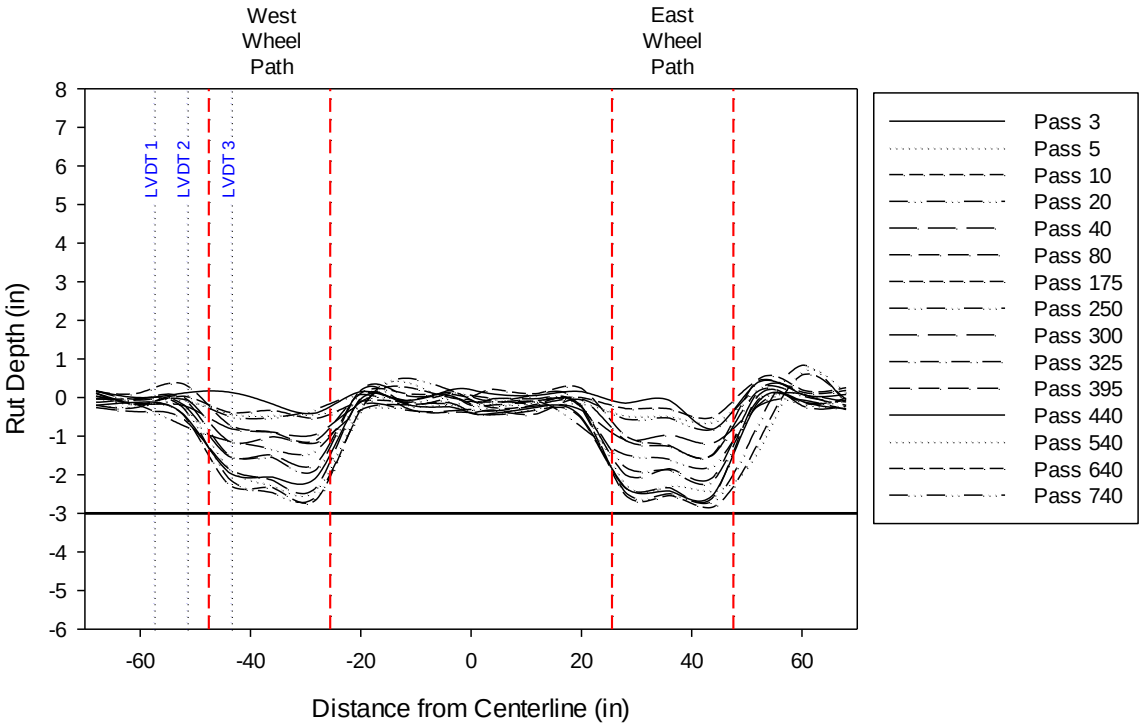


Figure I-6: Tensar BX Type 2 (3-South) (CBR = 1.78).

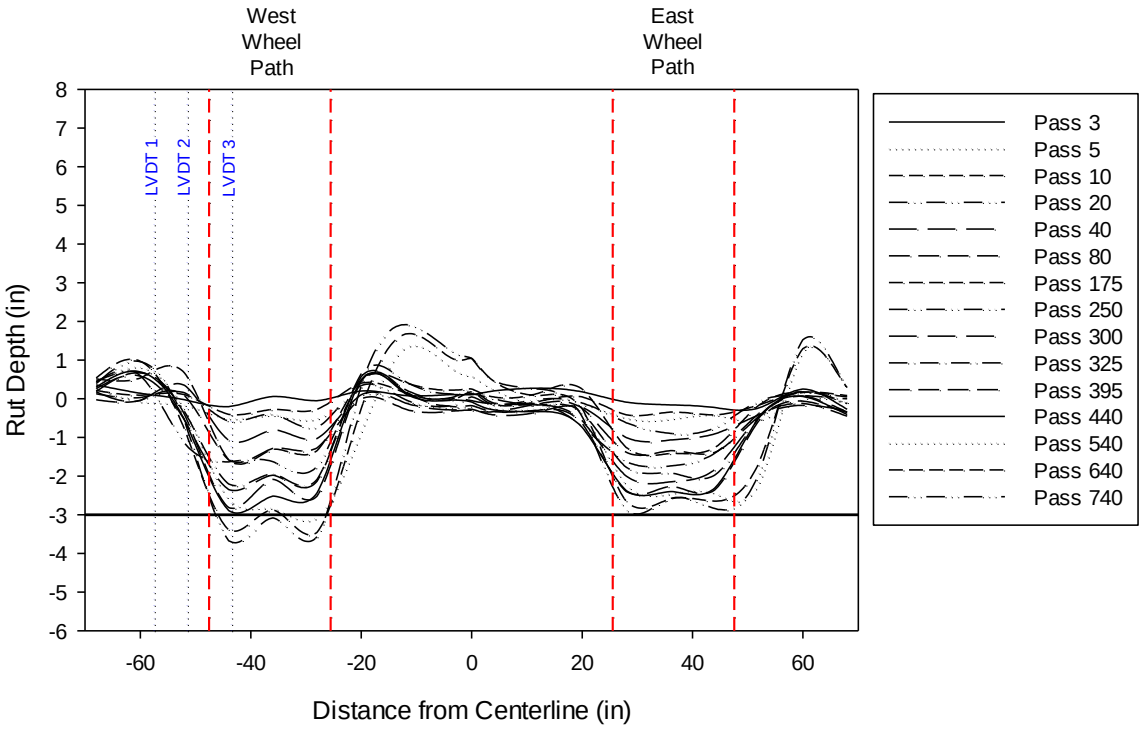


Figure I-7: NAUE Secugrid 30/30 Q1 (4-North).

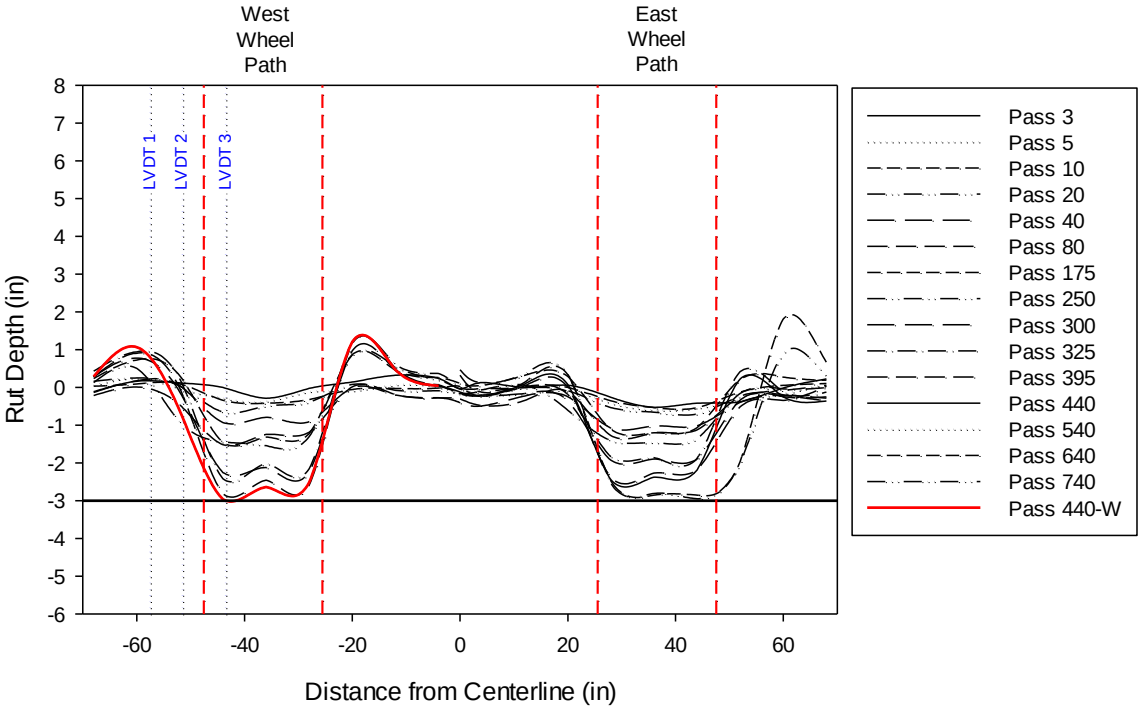


Figure I-8: NAUE Secugrid 30/30 Q1 (4-South).

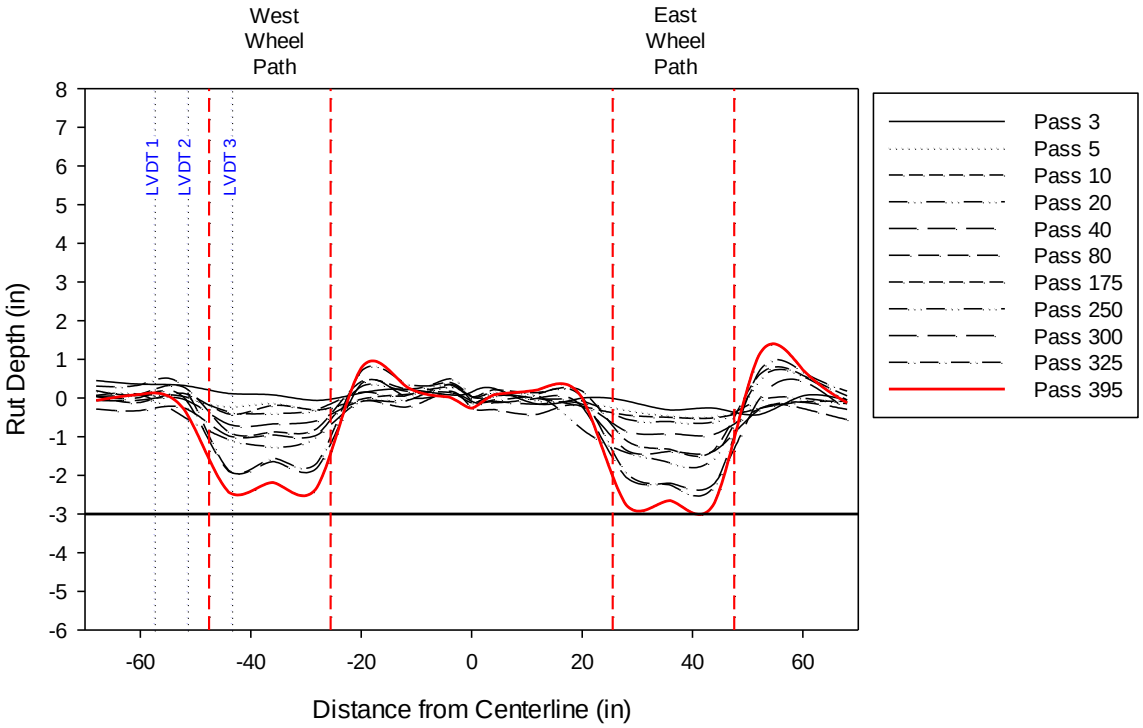


Figure I-9: Colbond Enkagrid Max 30 (5-North).

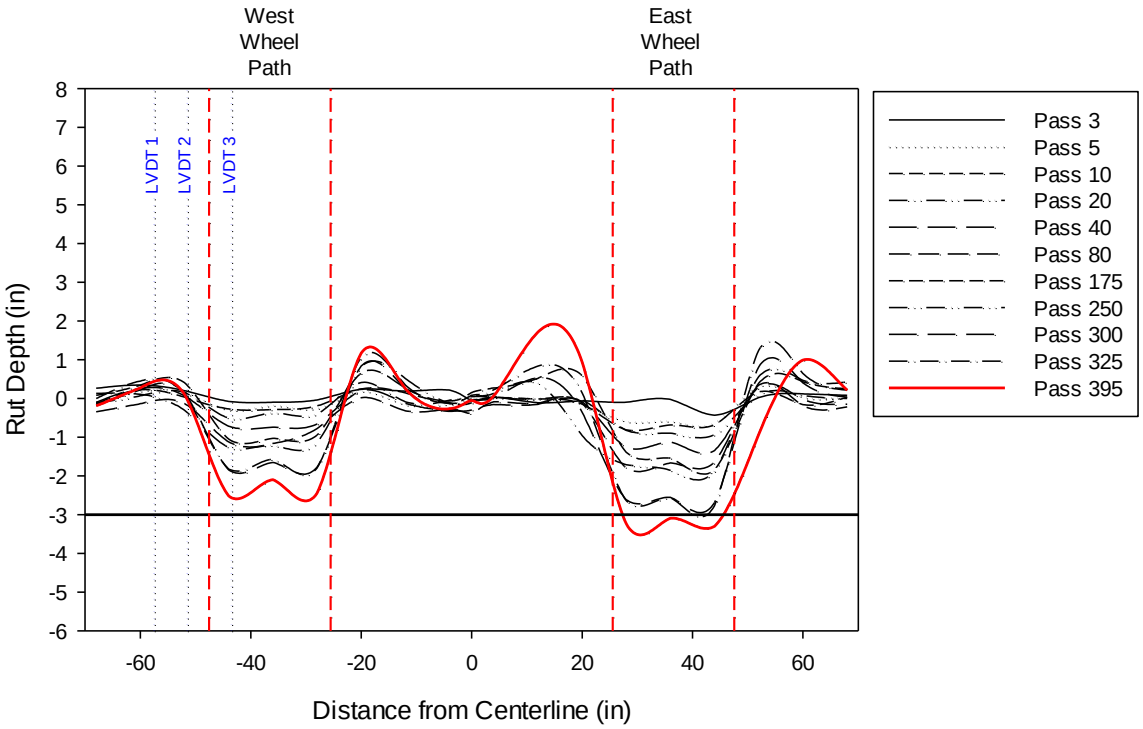


Figure I-10: Colbond Enkagrid Max 30 (5-South).

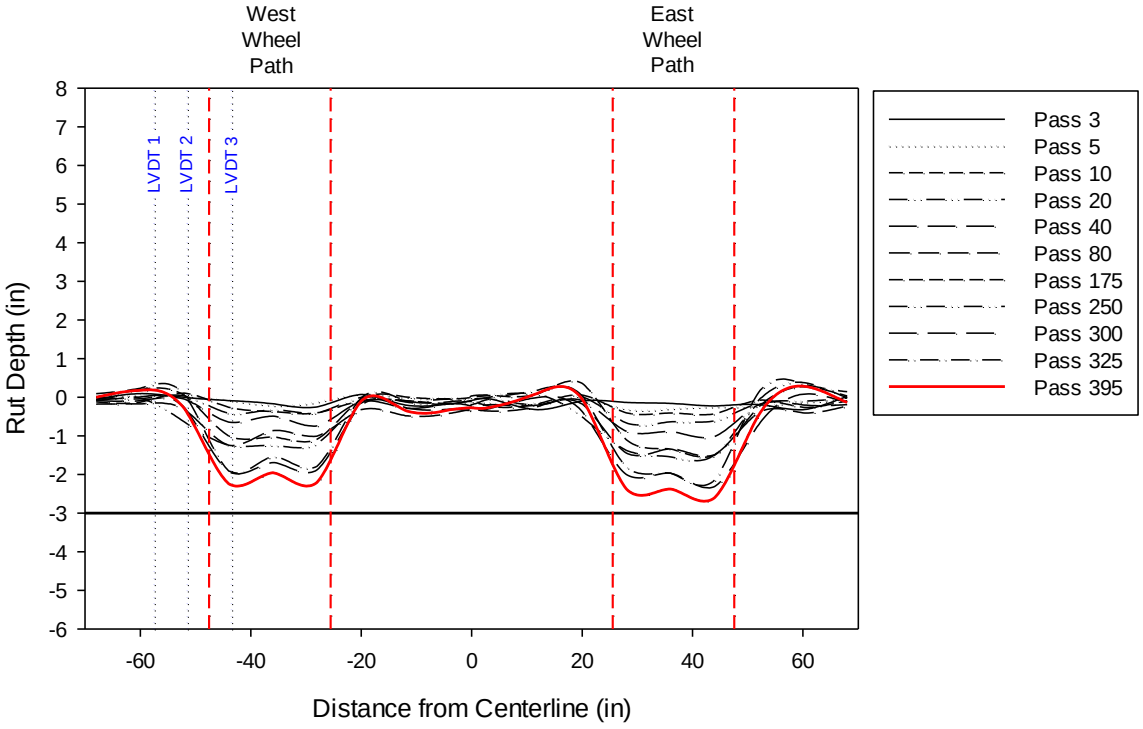


Figure I-11: Synteen SF 11 (6-North).

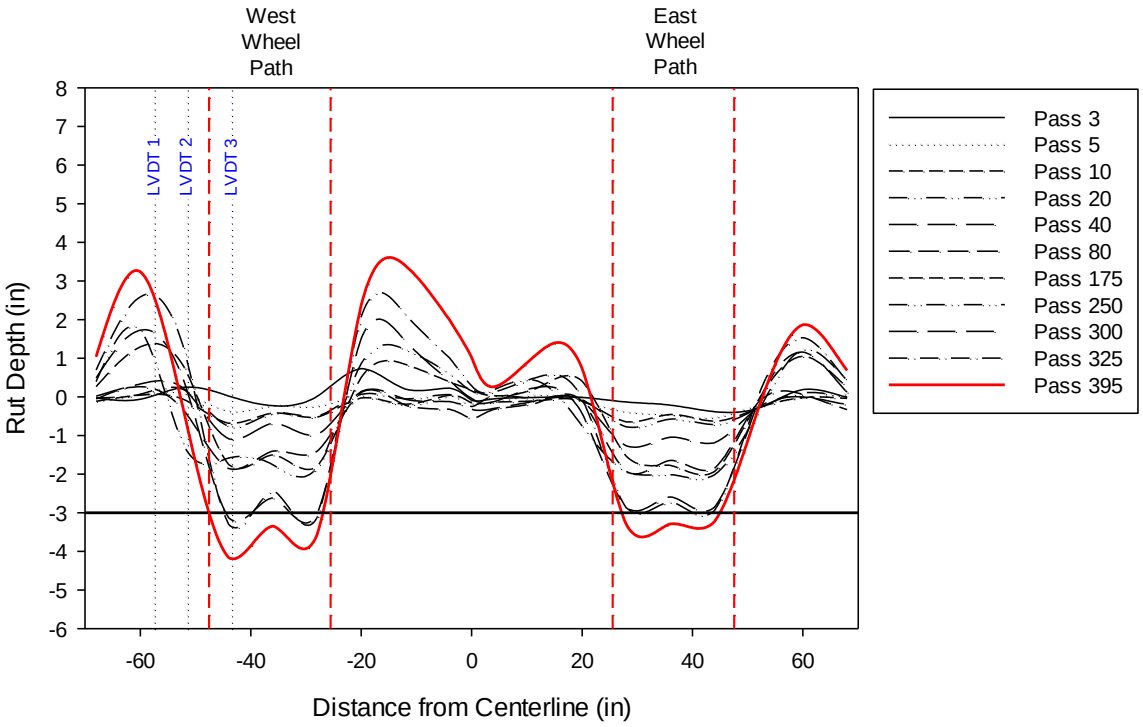


Figure I-12: Synteen SF 11 (6-South).

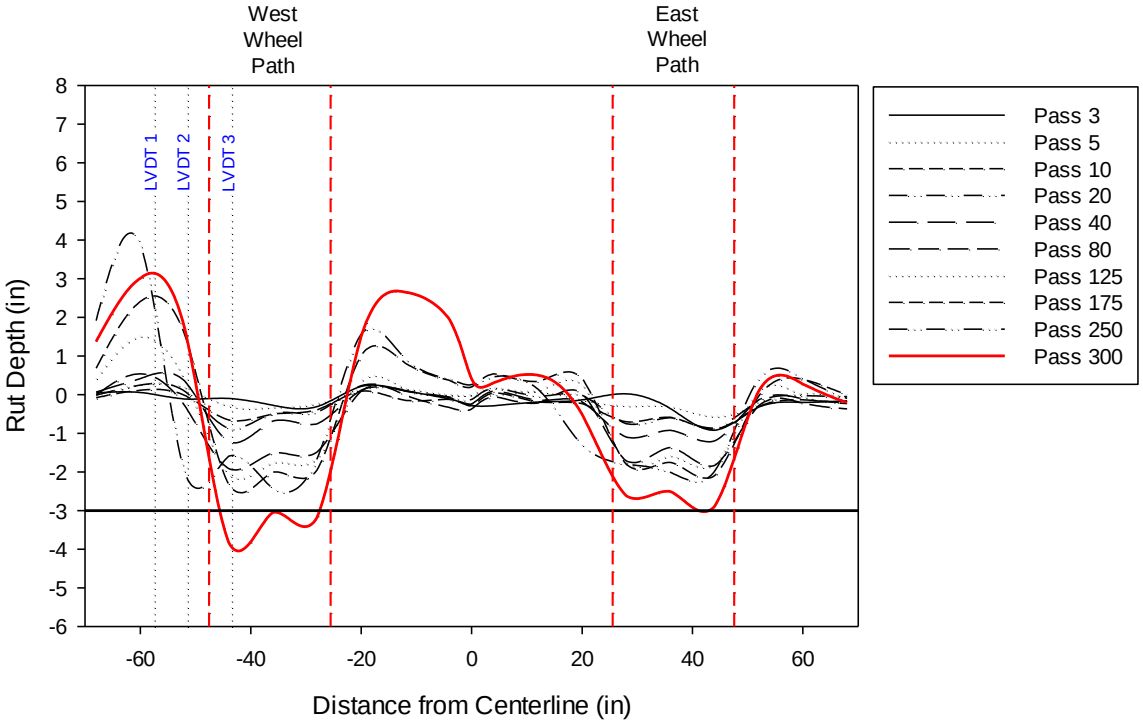


Figure I-13: Synteen SF 12 (7-North).

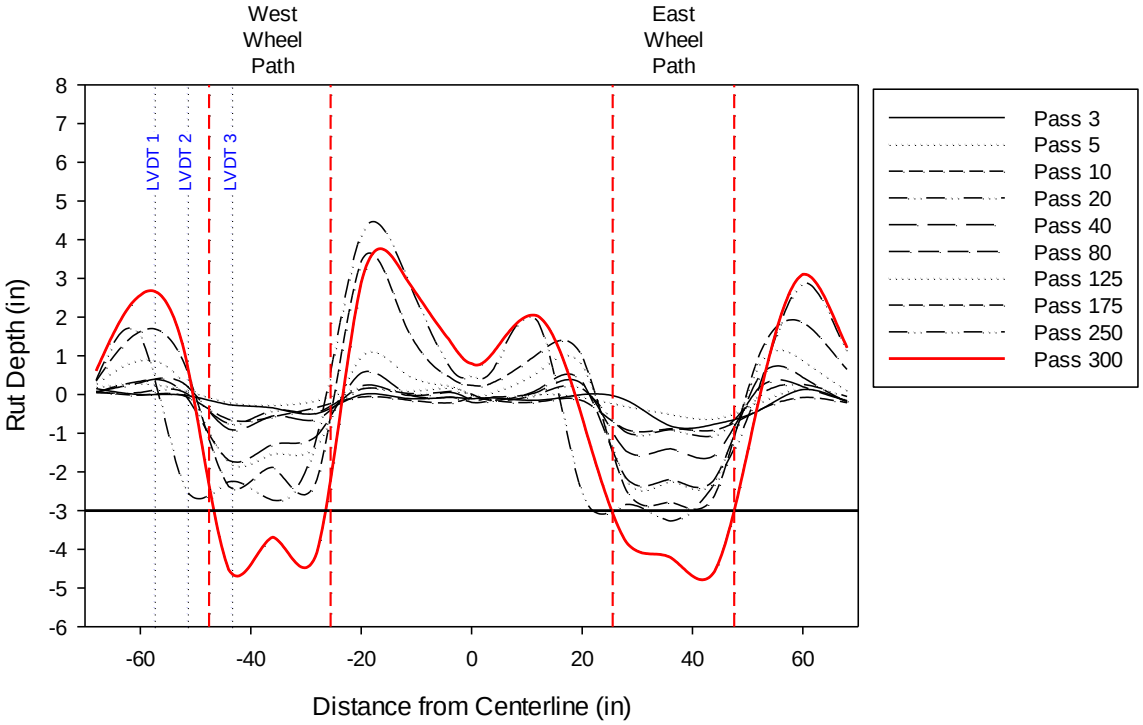


Figure I-14: Synteen SF 12 (7-South).

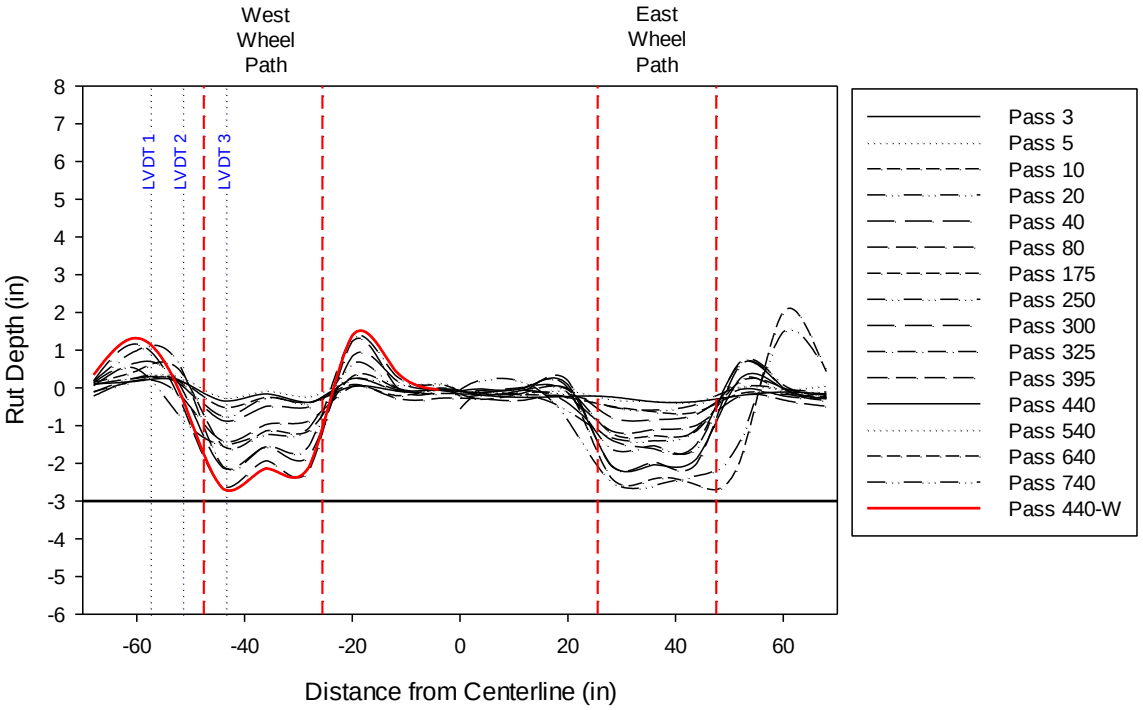


Figure I-15: TenCate Mirafi BXG 11 (8-North).

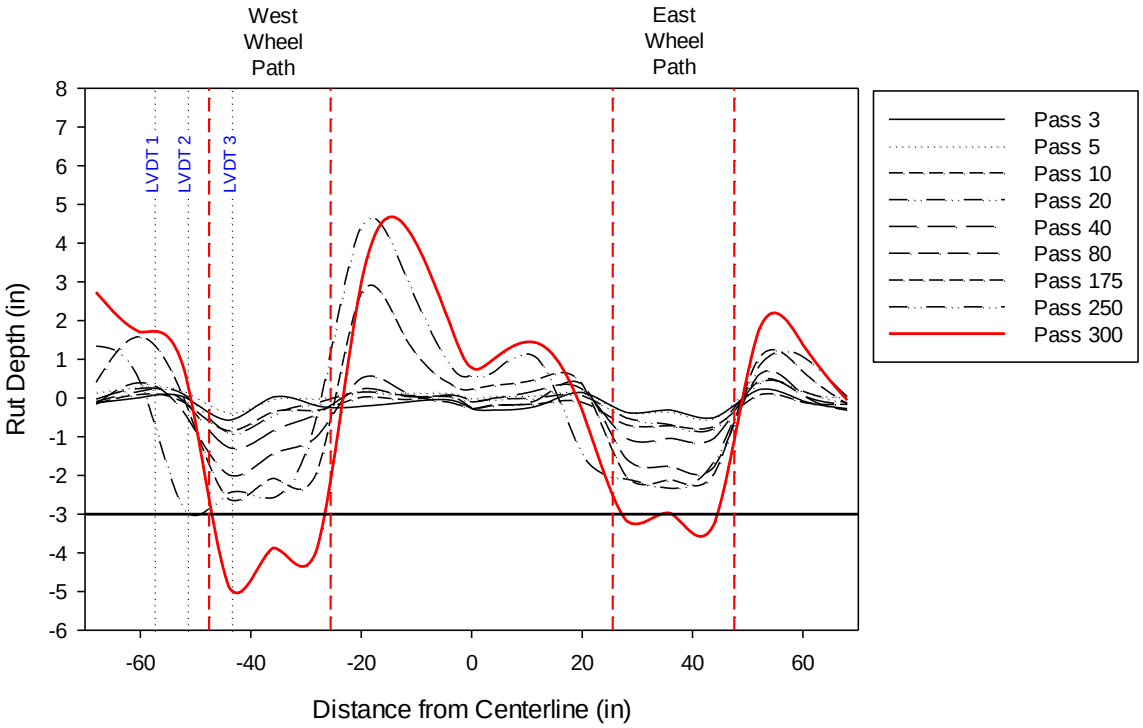


Figure I-16: TenCate Mirafi BXG 11 (8-South).

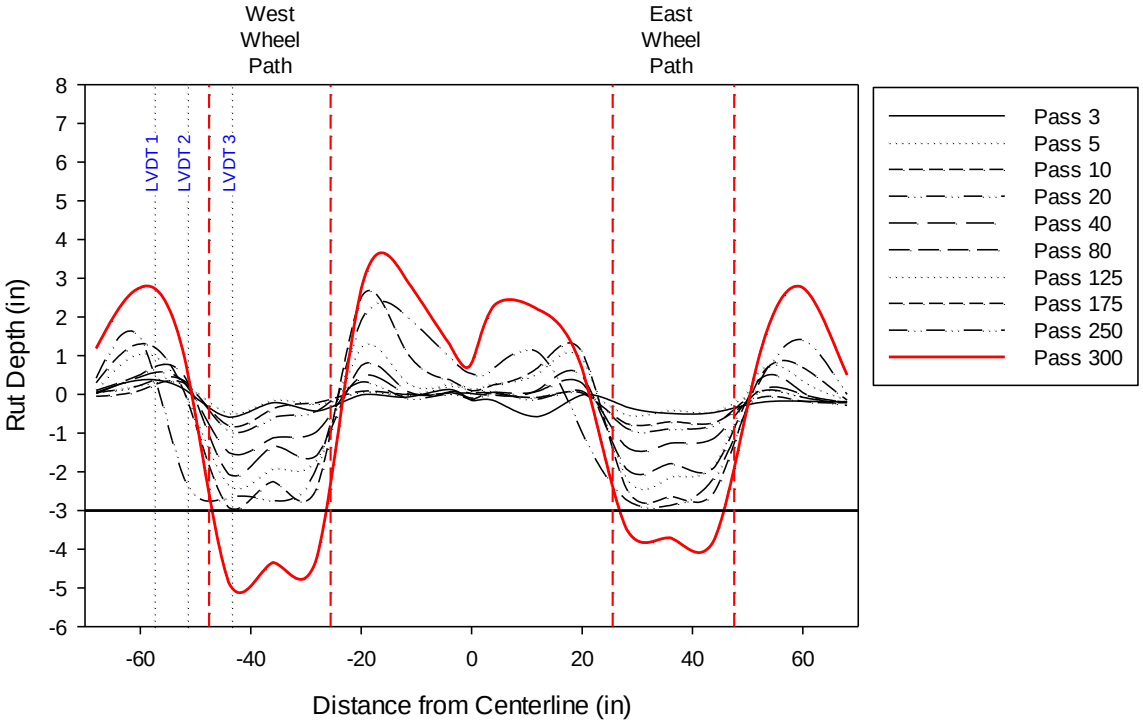


Figure I-17: Huesker Fornit 30 (9-North).

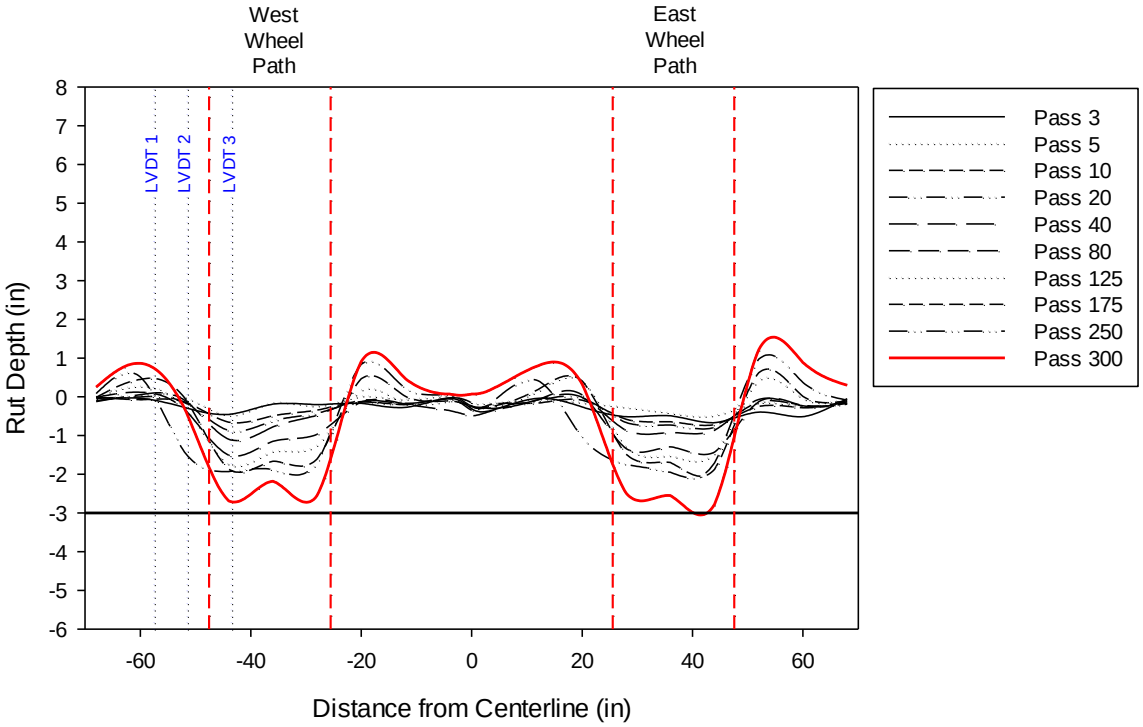


Figure I-18: Huesker Fornit 30 (9-South).

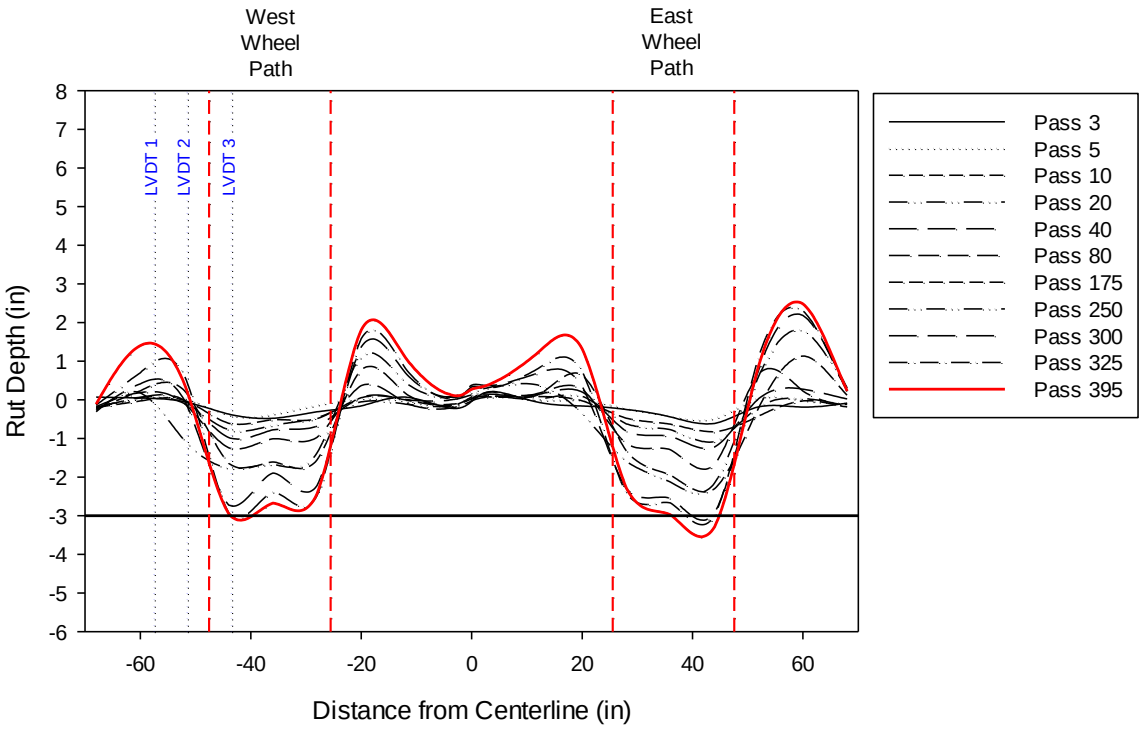


Figure I-19: SynTec Tenax MS330 (10-North).

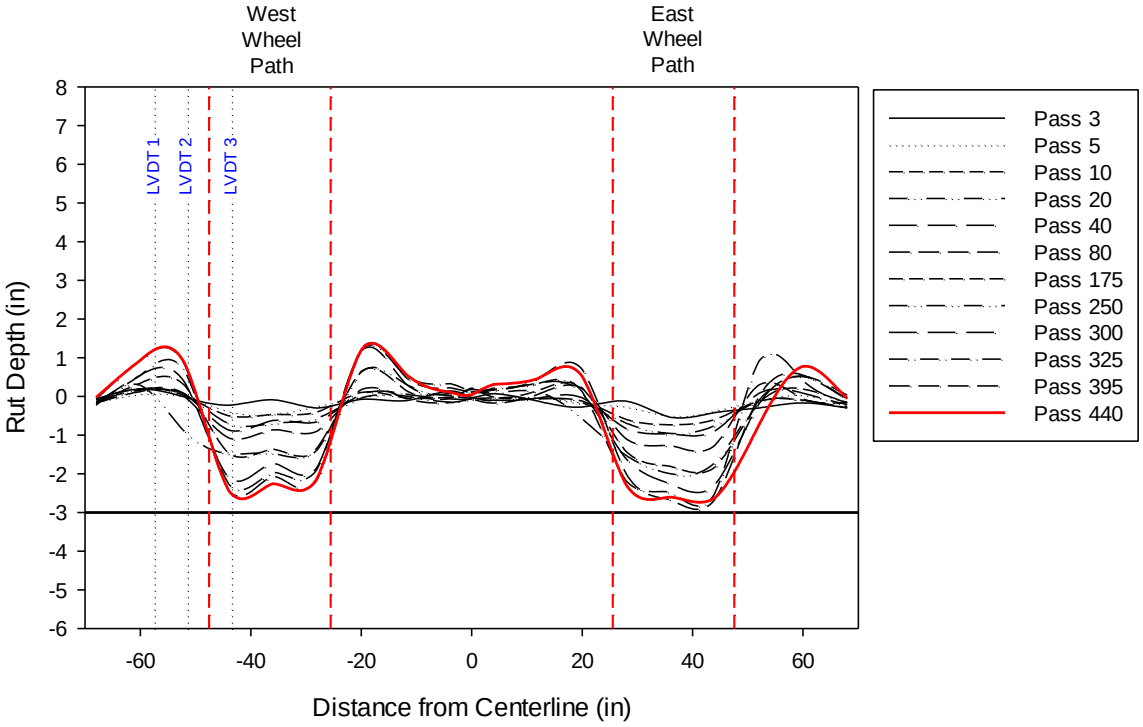


Figure I-20: SynTec Tenax MS330 (10-South).

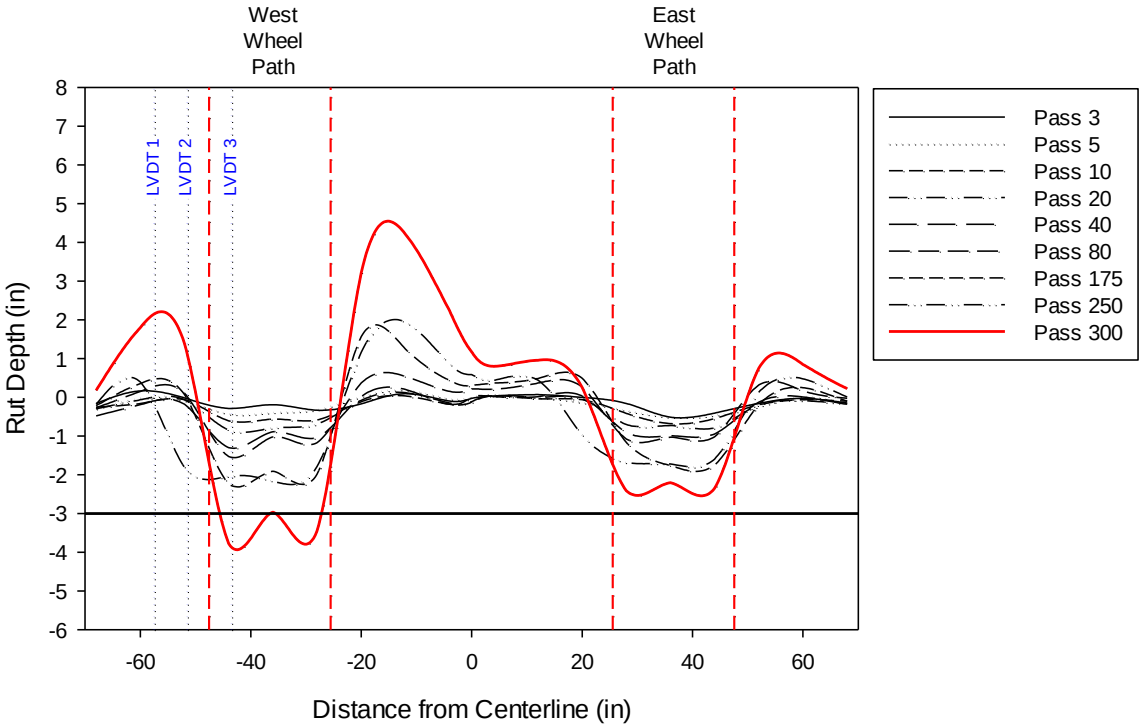


Figure I-21: Tensar TX 140 (11-North).

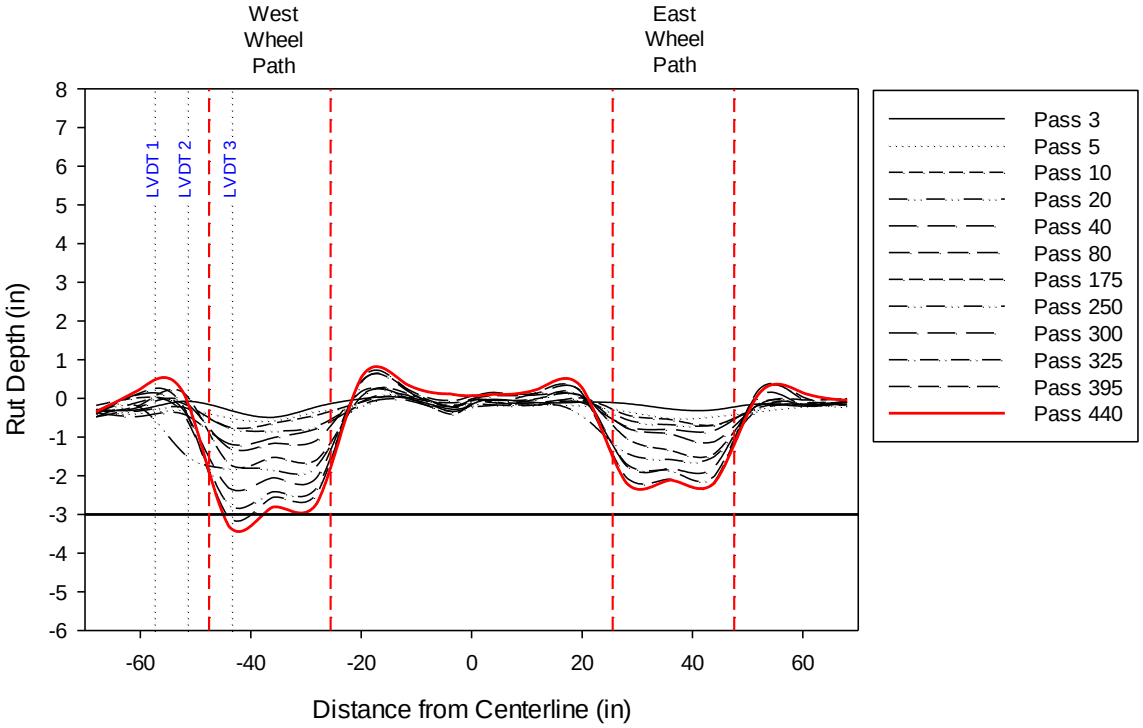


Figure I-22: Tensar TX 140 (11-South).

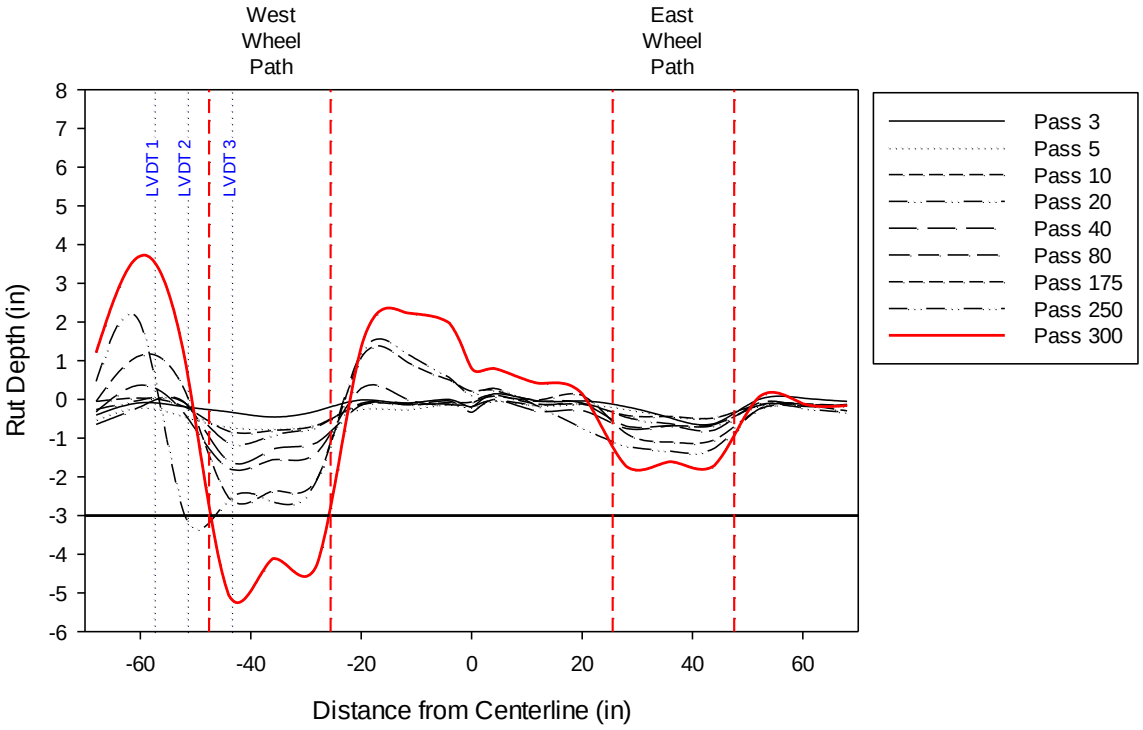


Figure I-23: Tensar TX 160 (12-North).

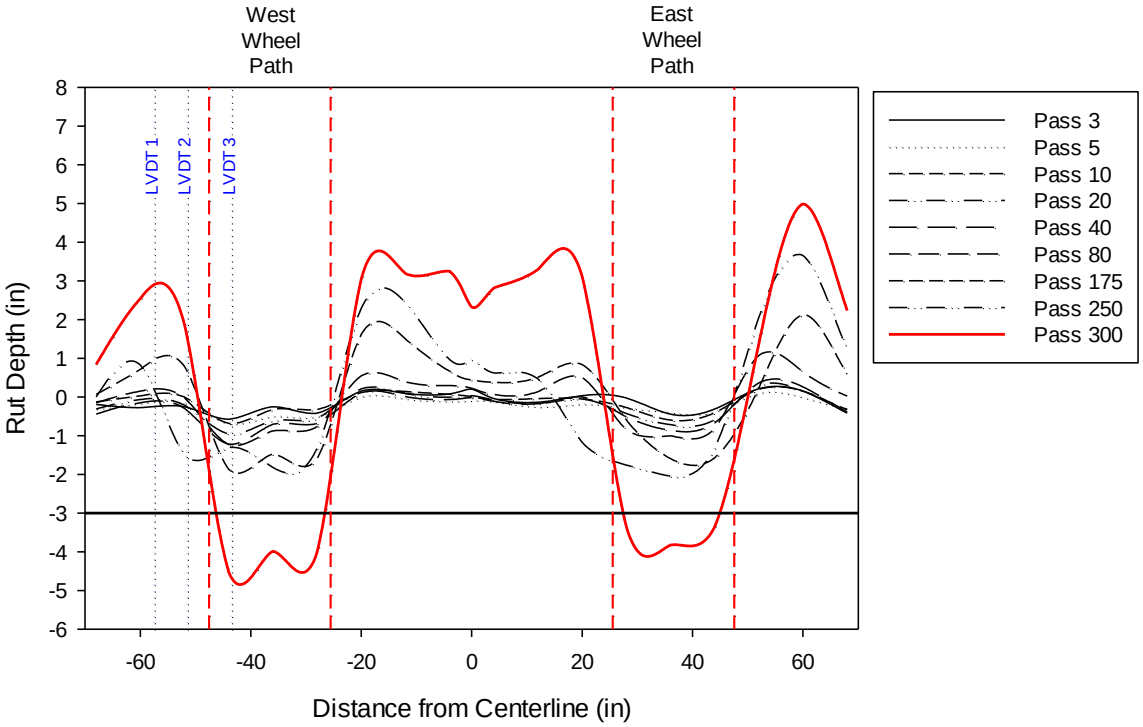


Figure I-24: Tensar TX 160 (12-South).

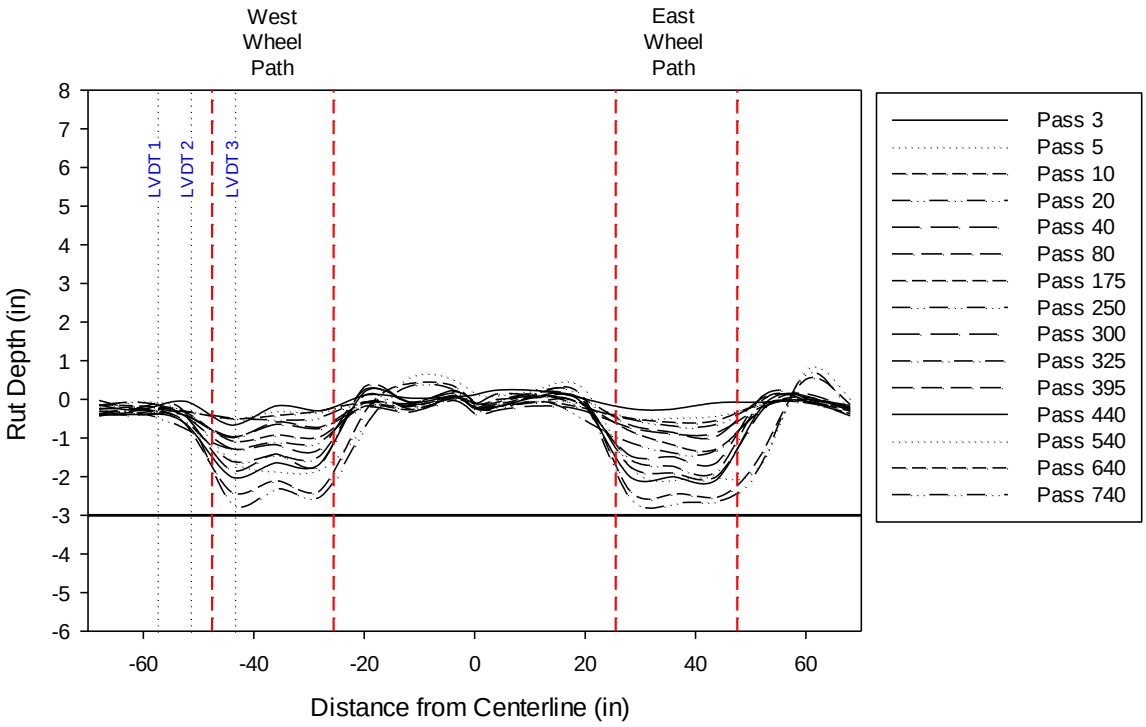


Figure I-25: TenCate Mirafi RS580i (13-North).

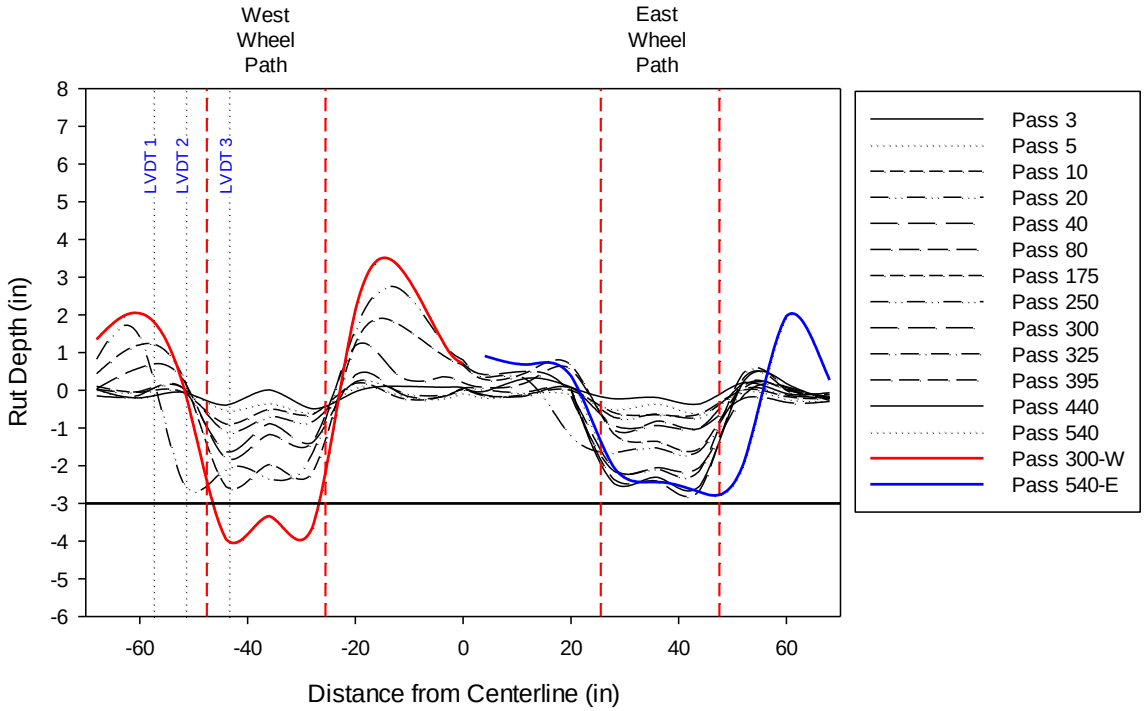


Figure I-26: TenCate Mirafi RS580i (13-South).

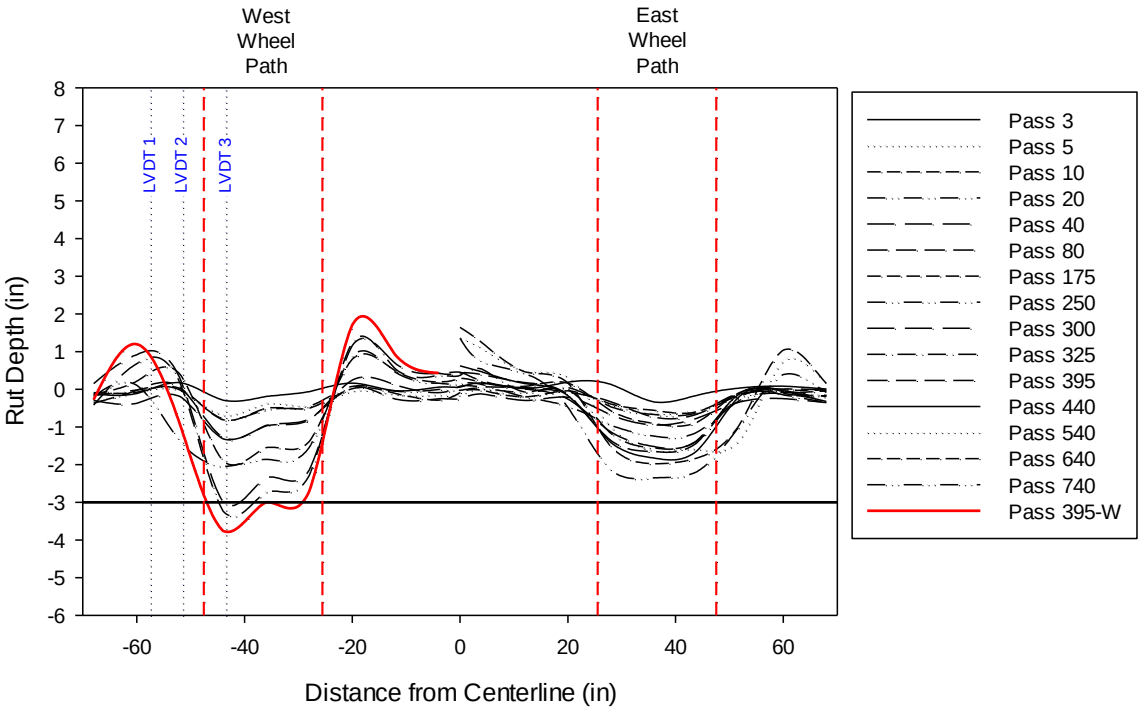


Figure I-27: Propex Geotex 801 (14-North).

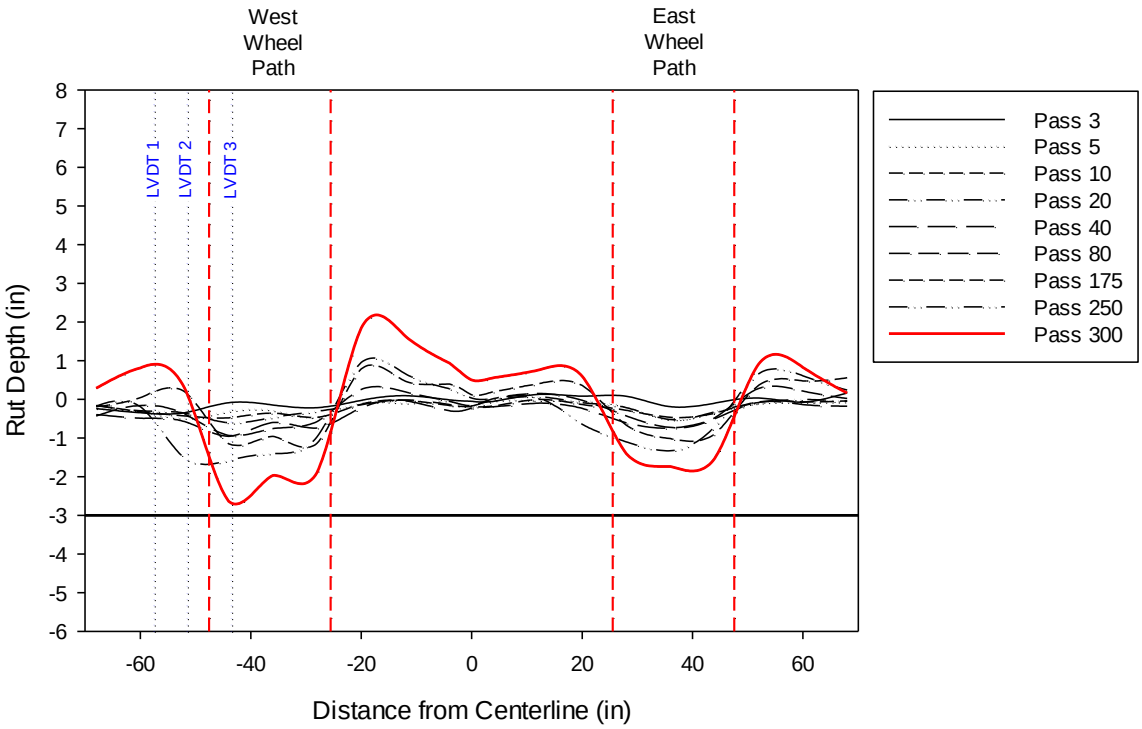


Figure I-28: Propex Geotex 801 (14-South).

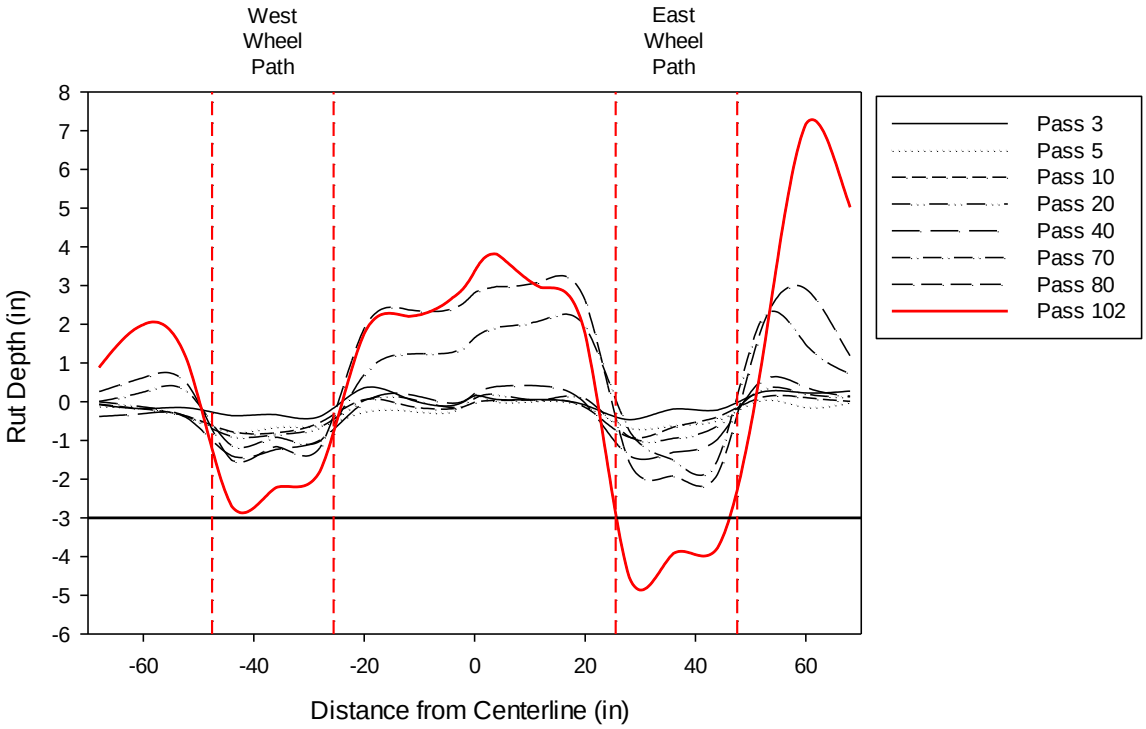


Figure I-29: Control 1-North (Base = 11.3”).

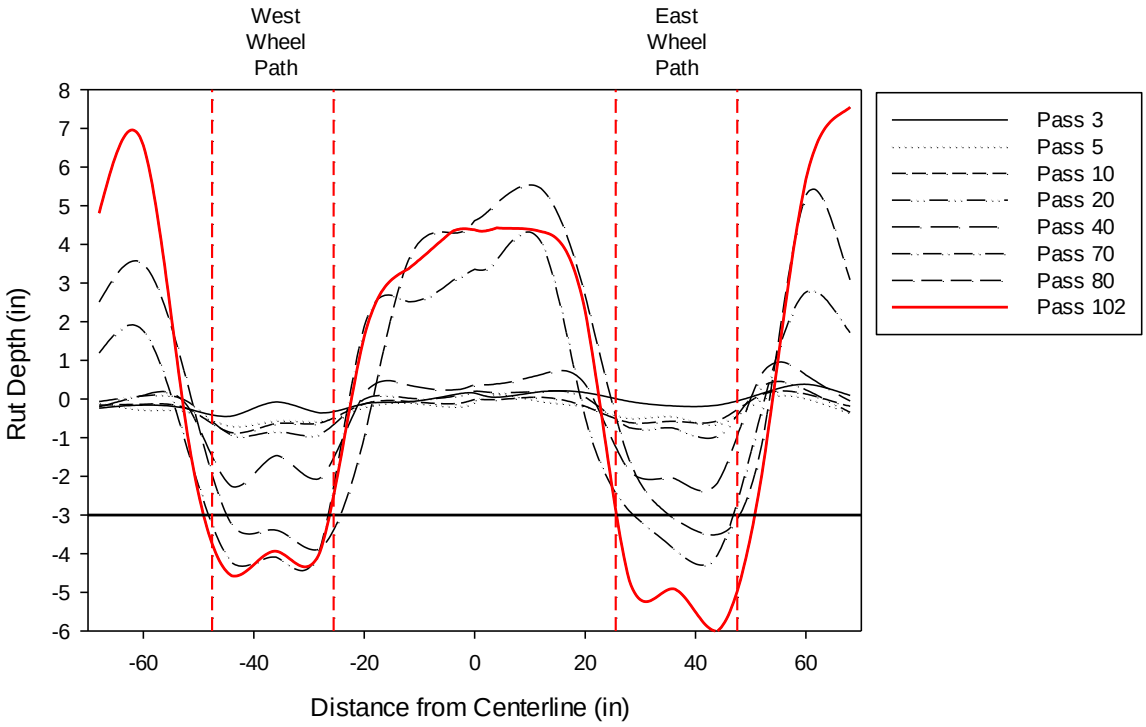


Figure I-30: Control 1-South (Base = 11.3”).

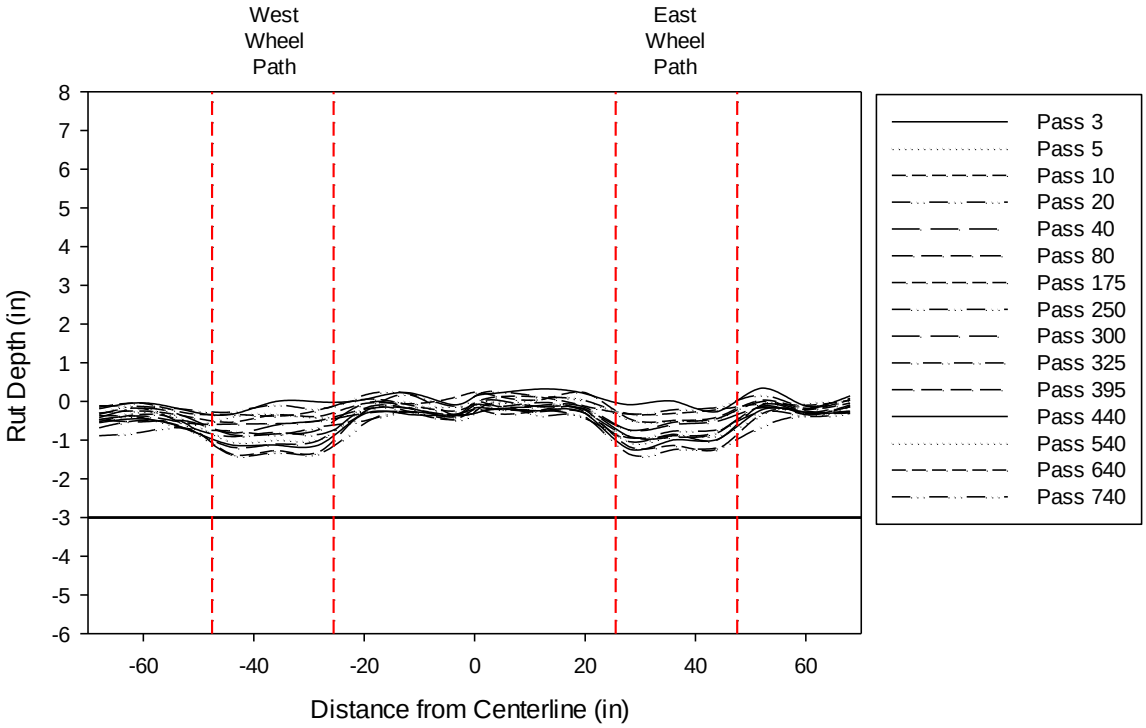


Figure I-31: Control 2-North (Base = 16.3”).

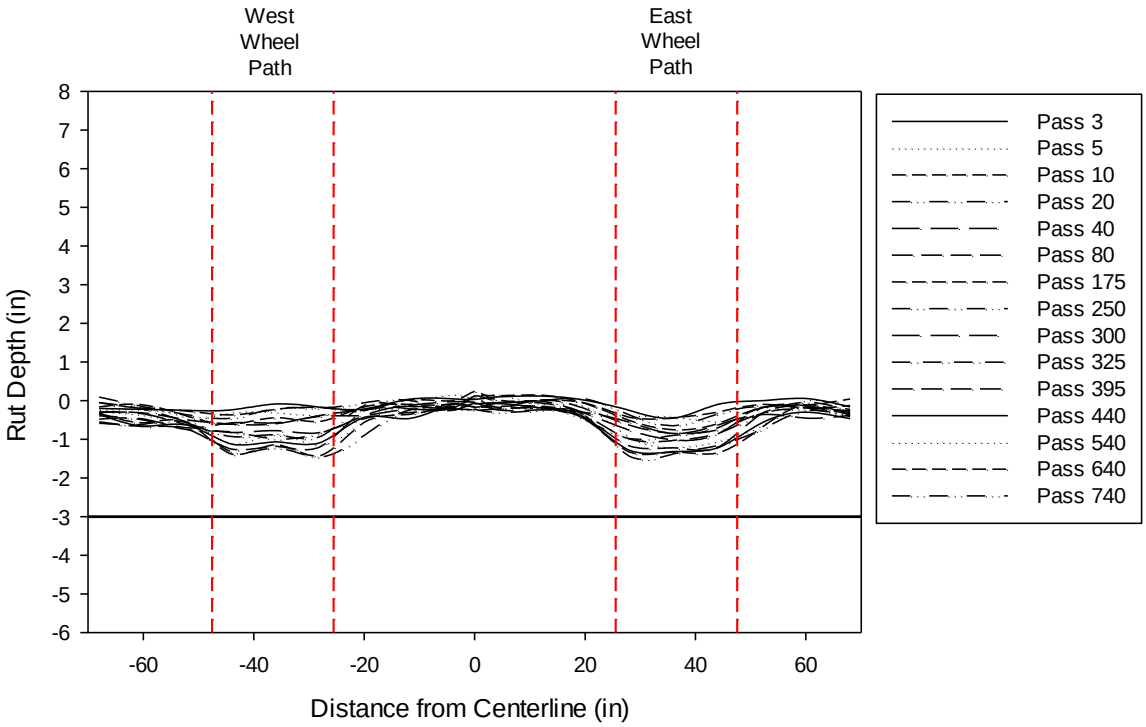


Figure I-32: Control 2-South (Base = 16.3”).

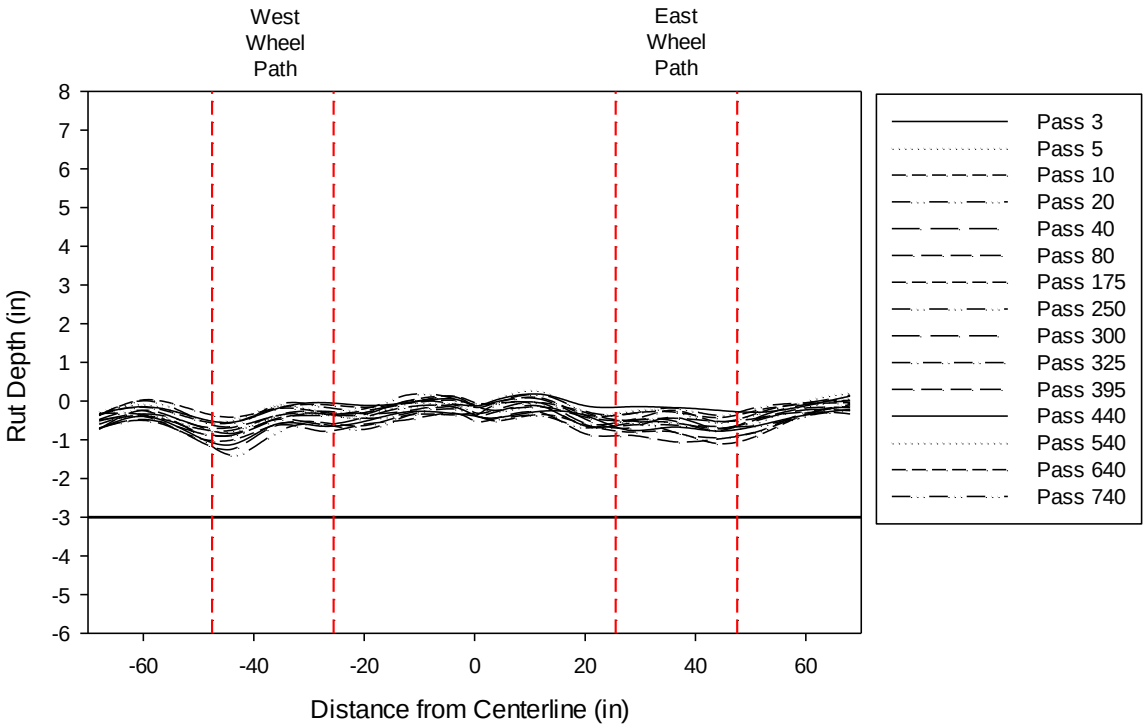


Figure I-33: Control 3-North (Base = 24.9”).

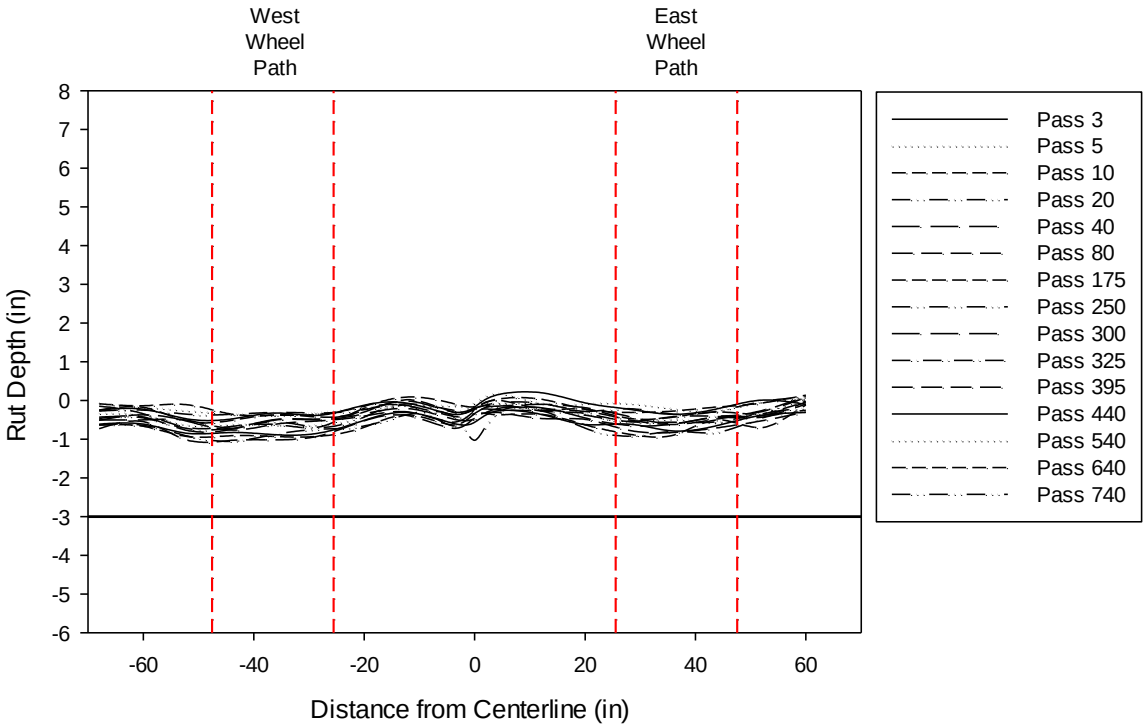


Figure I-34: Control 3-South (Base = 24.9”).

APPENDIX J:

STRAIN GAGE DYNAMIC STRAIN PLOTS

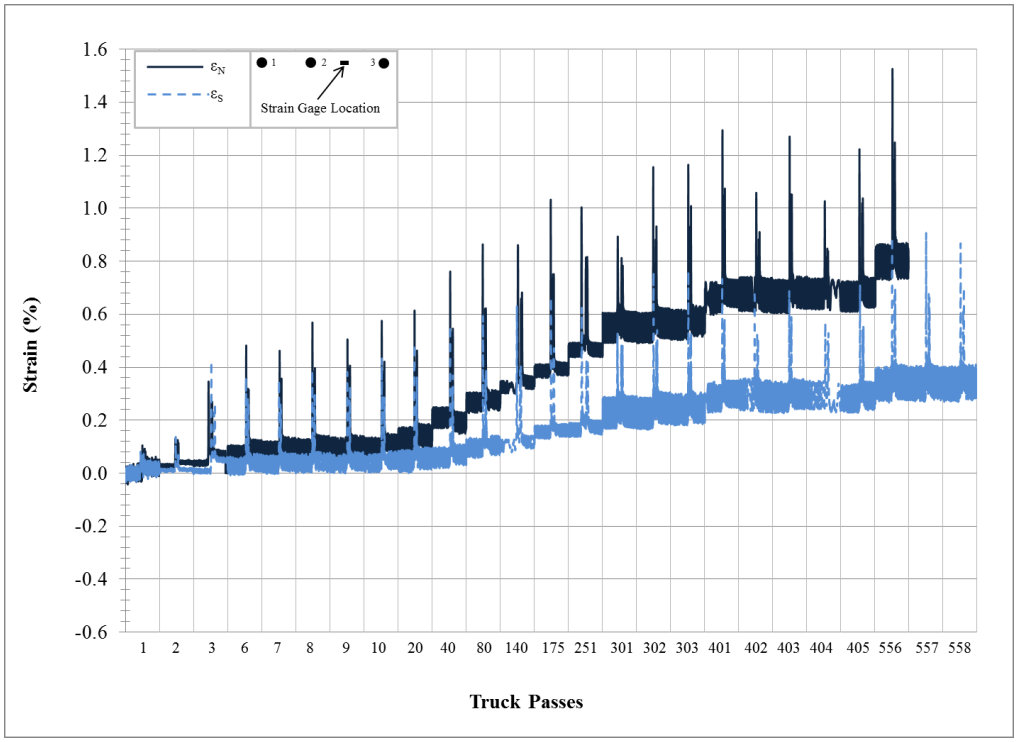


Figure J-1: Tensar BX Type 2 (CBR = 2.15).

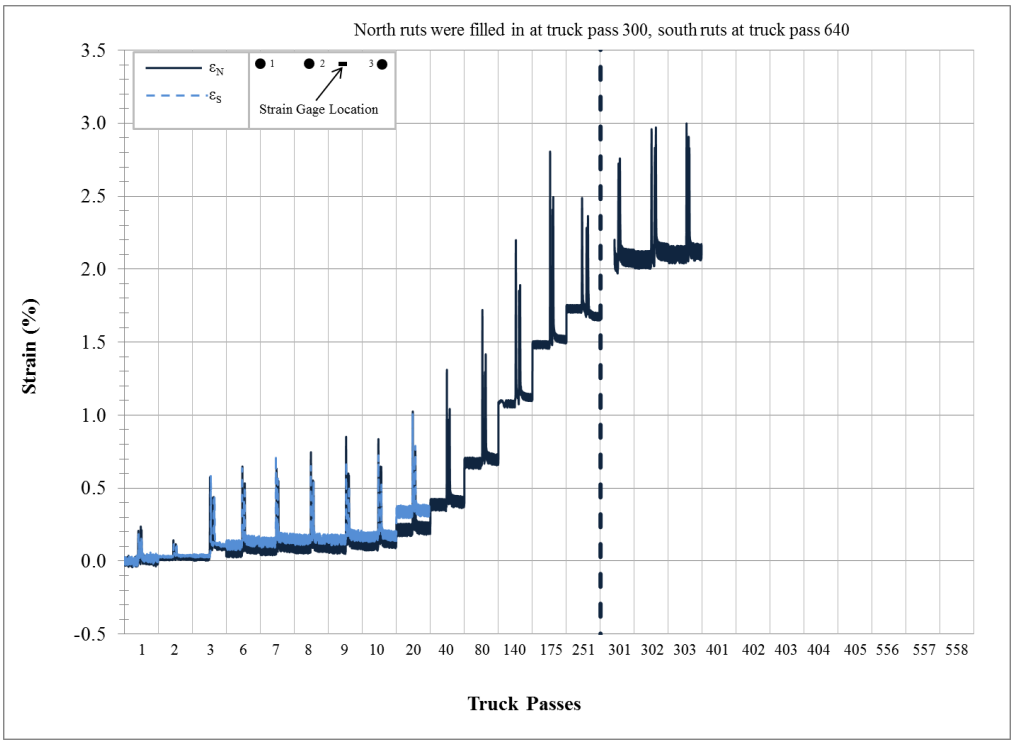


Figure J-2: Tensar BX Type 2 (CBR = 1.61).

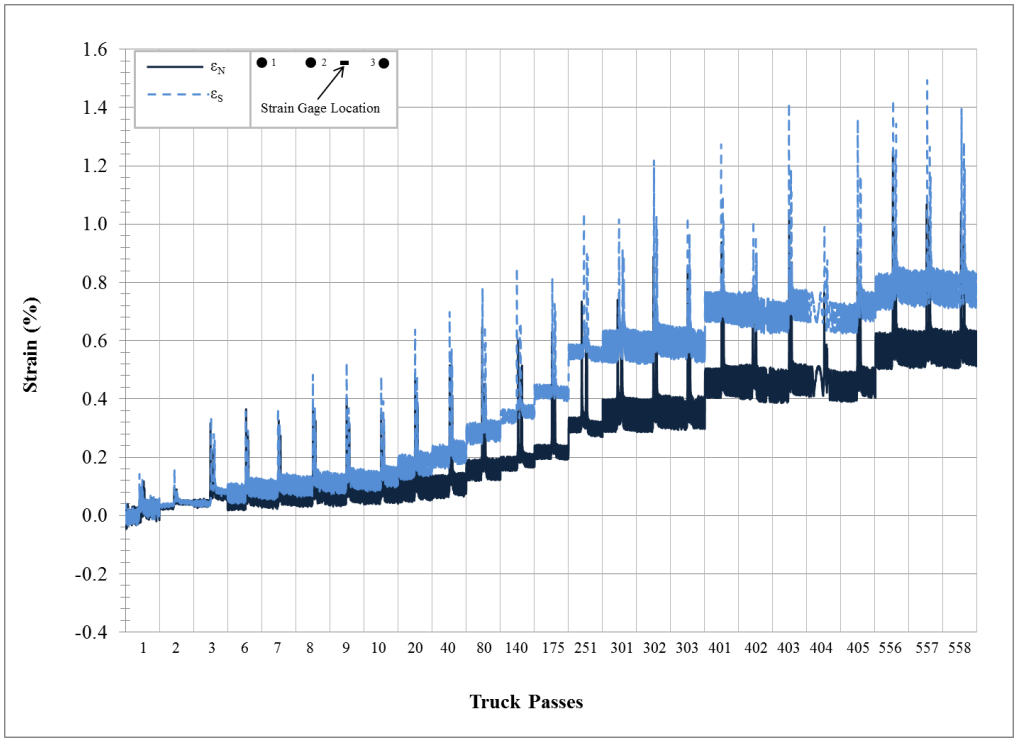


Figure J-3: Tensar BX Type 2 (CBR = 1.78).

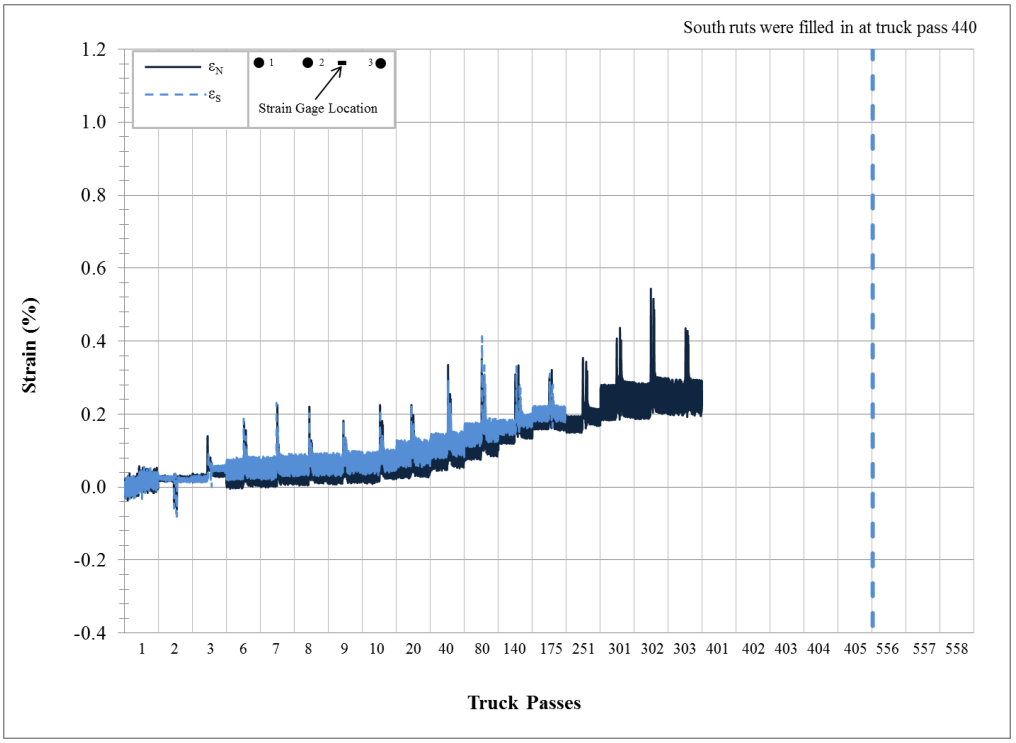


Figure J-4: NAUE Secugrid 30/30 Q1.

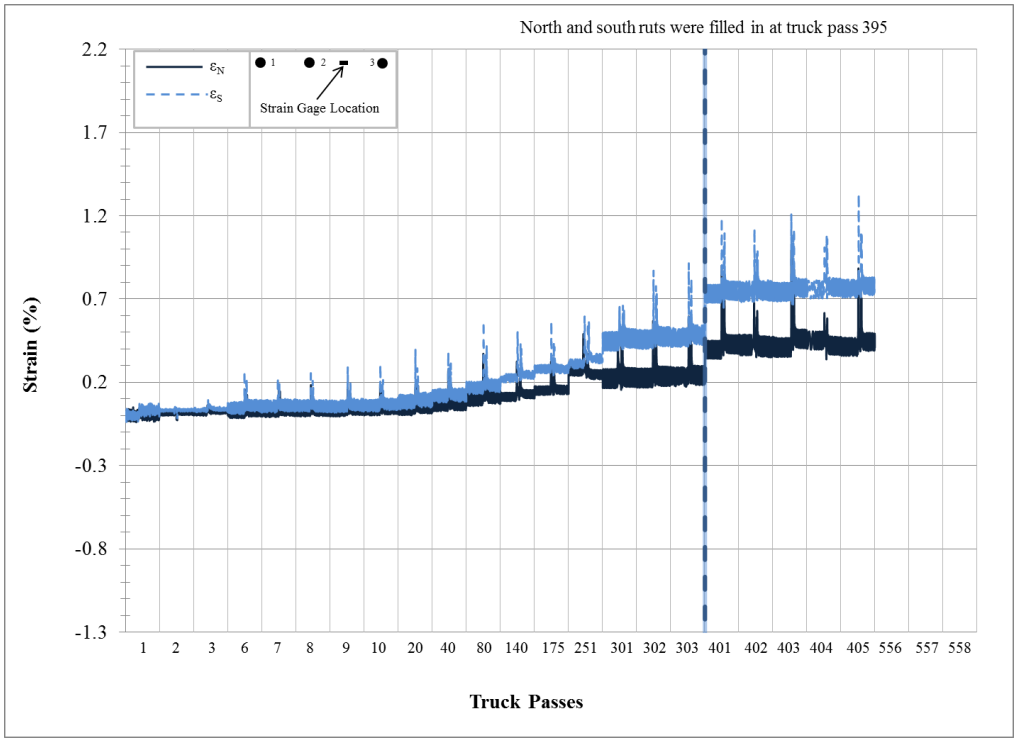


Figure J-5: Colbond Enkagrid Max 30.

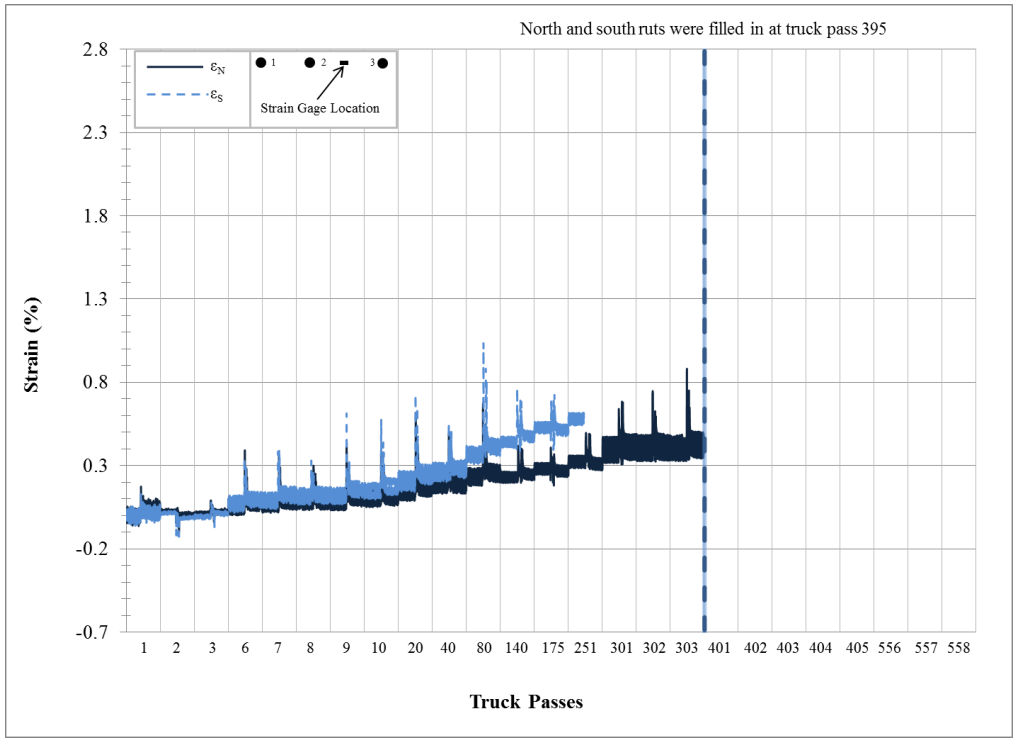


Figure J-6: Synteen SF 11.

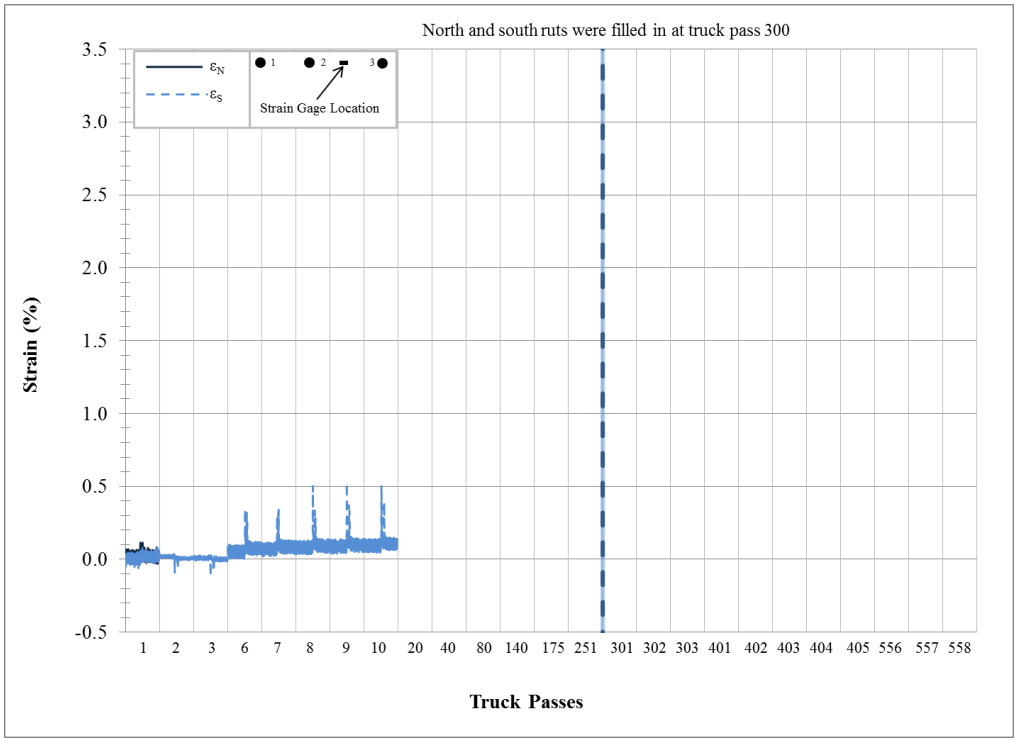


Figure J-7: Synteen SF 12.

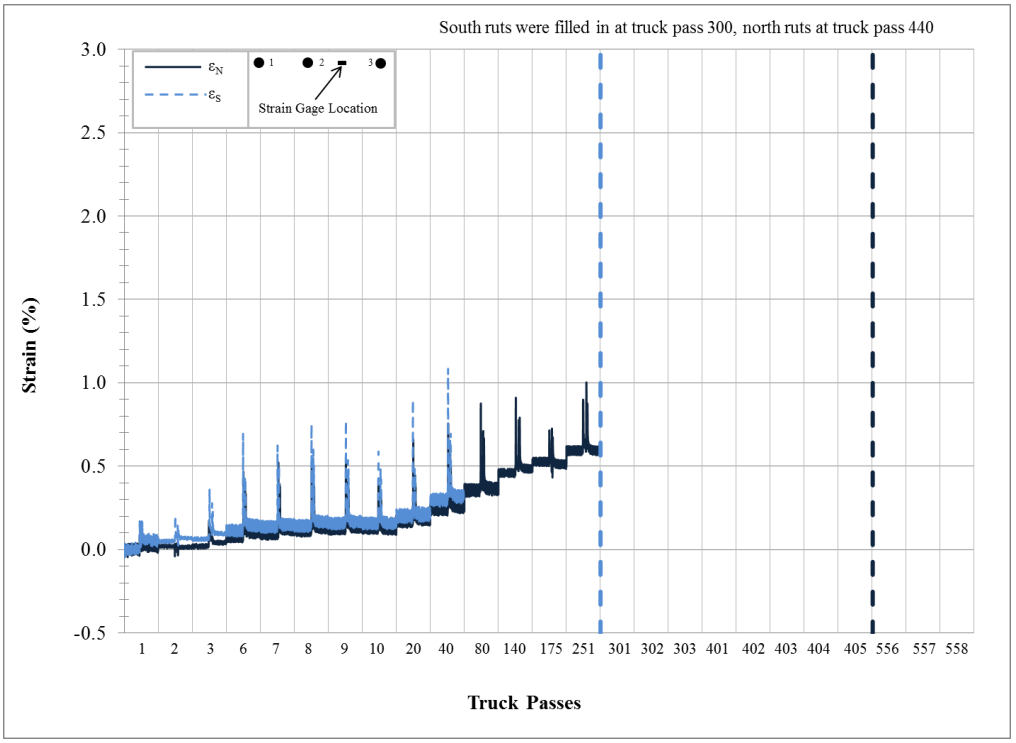


Figure J-8: TenCate Mirafi BXG 11.

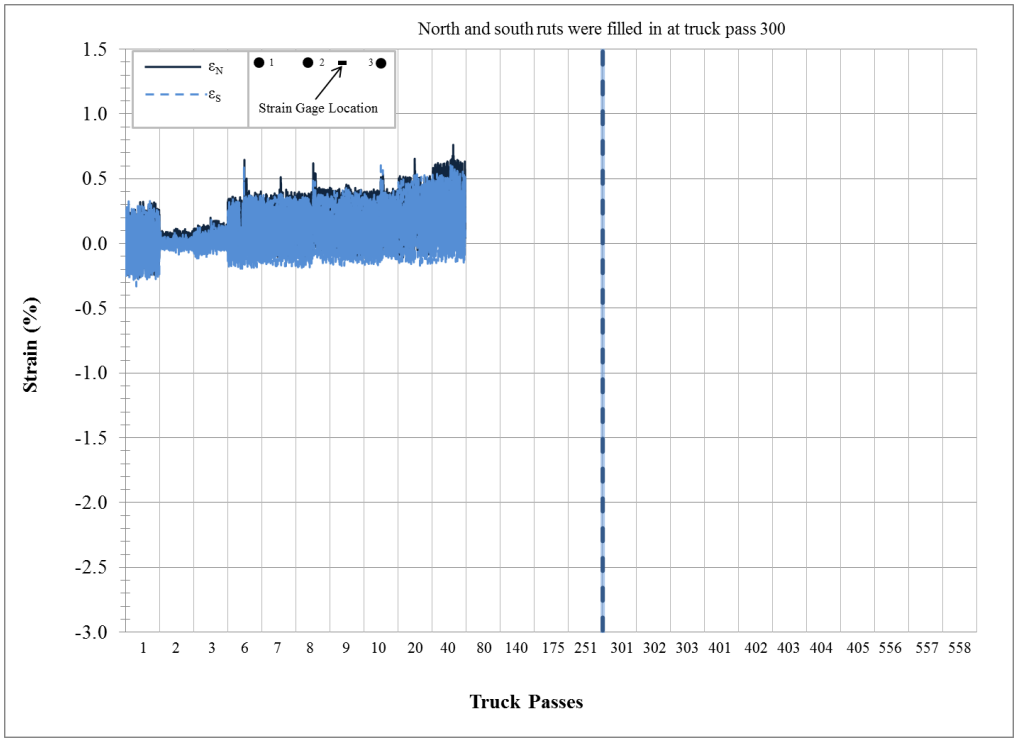


Figure J-9: Huesker Fornit 30.

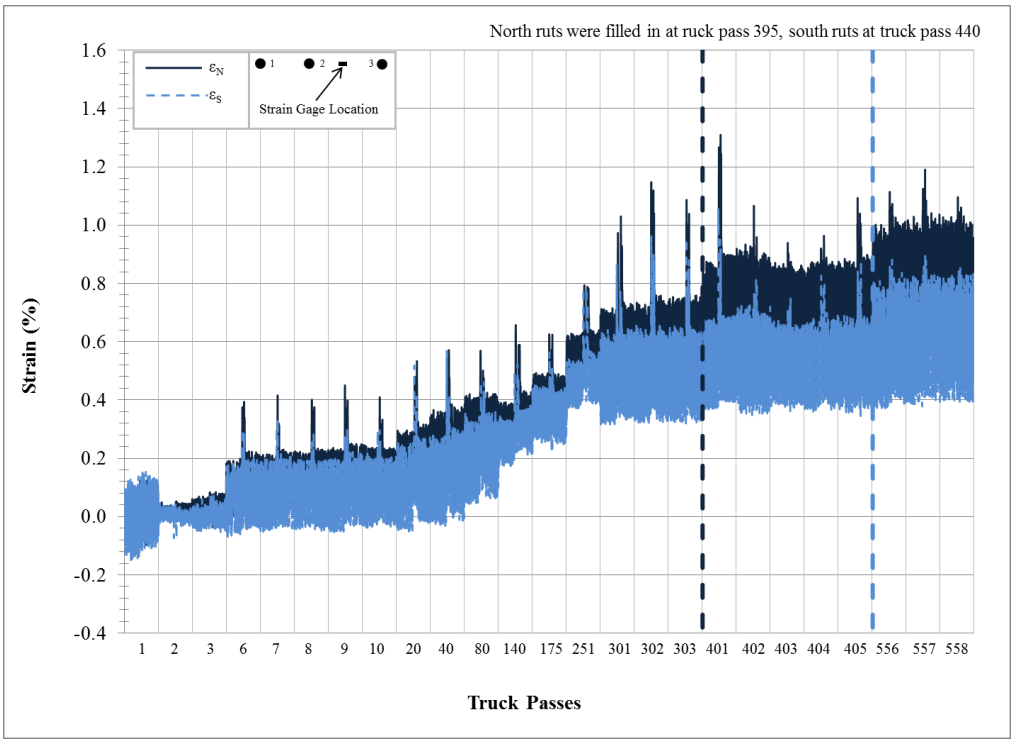


Figure J-10: SynTec Tenax MS330.

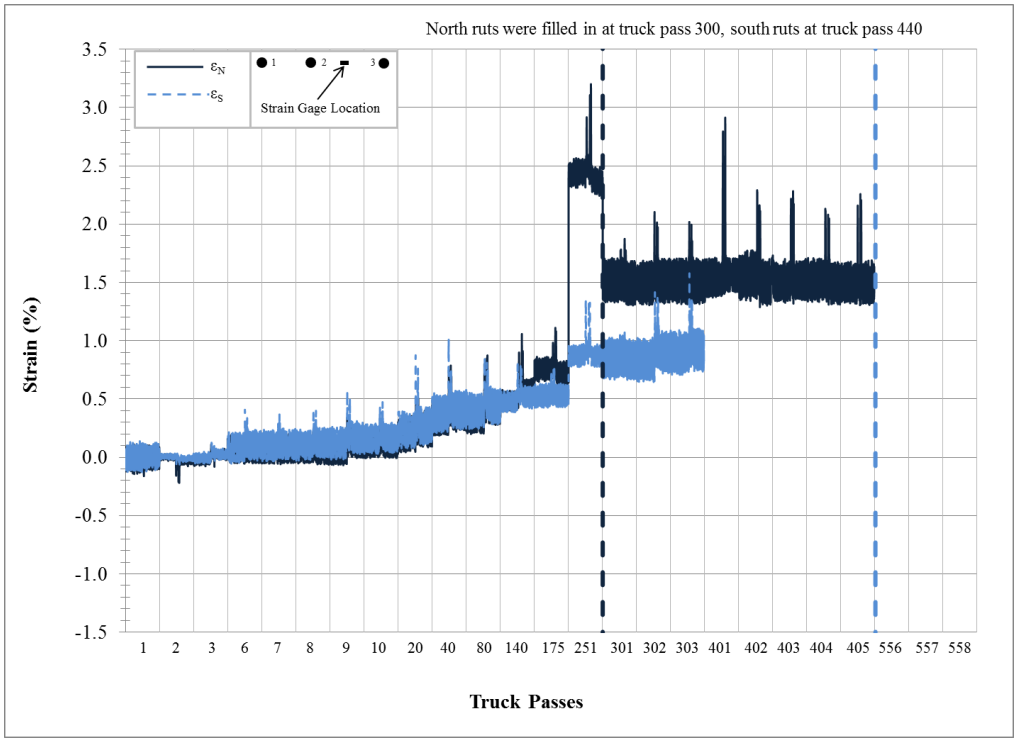


Figure J-11: Tensar TX 140.

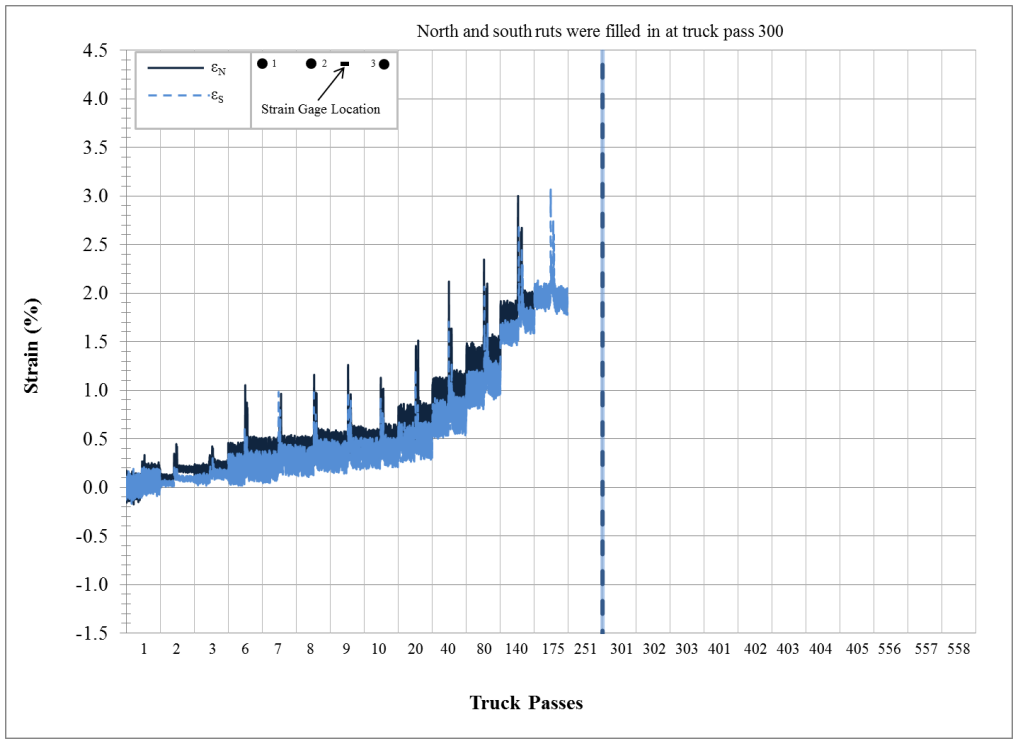


Figure J-12: Tensar TX 160.

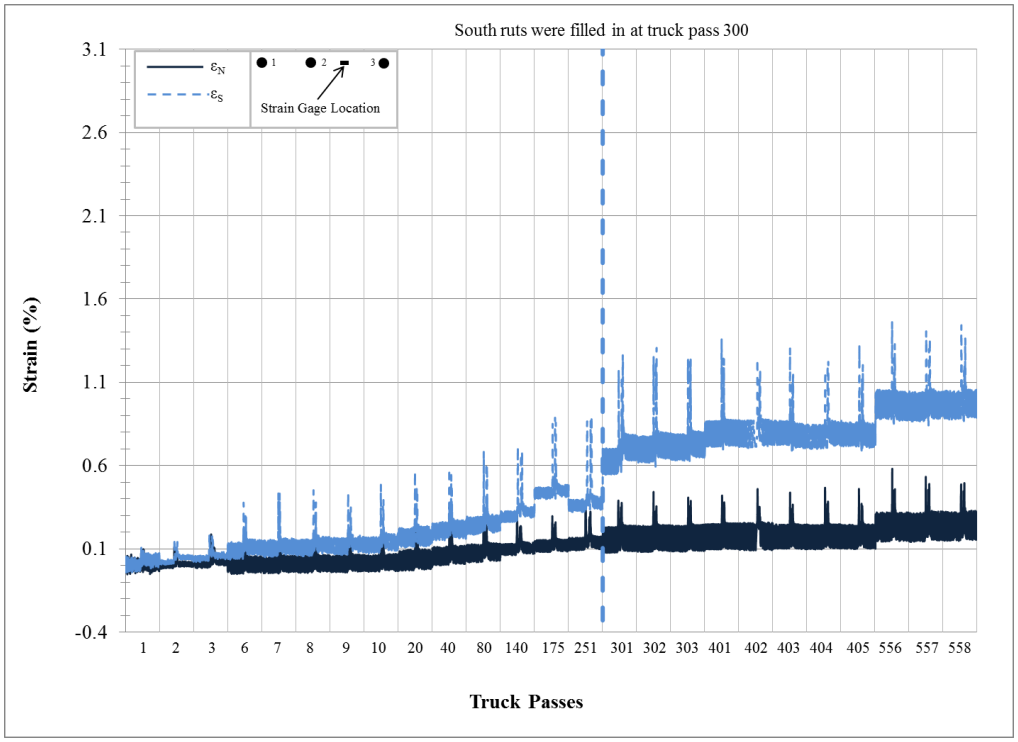


Figure J-13: TenCate Mirafi RS580i.

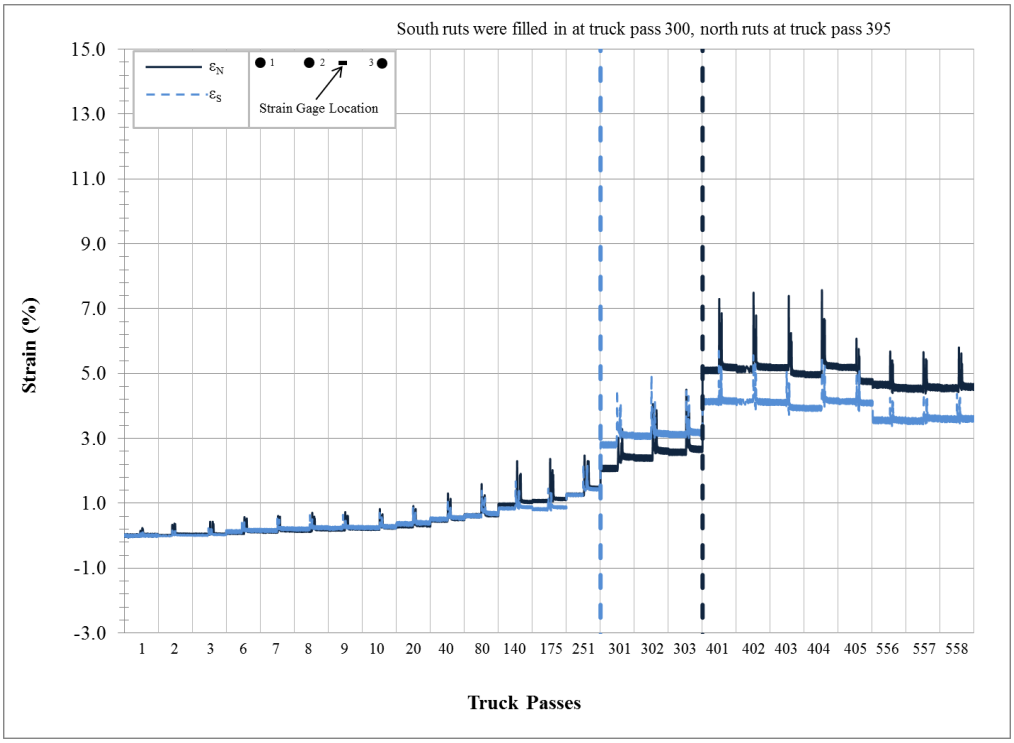


Figure J-14: Propex Geotex 801.

APPENDI K:

STRAIN GAGE STATIC STRAIN PLOTS

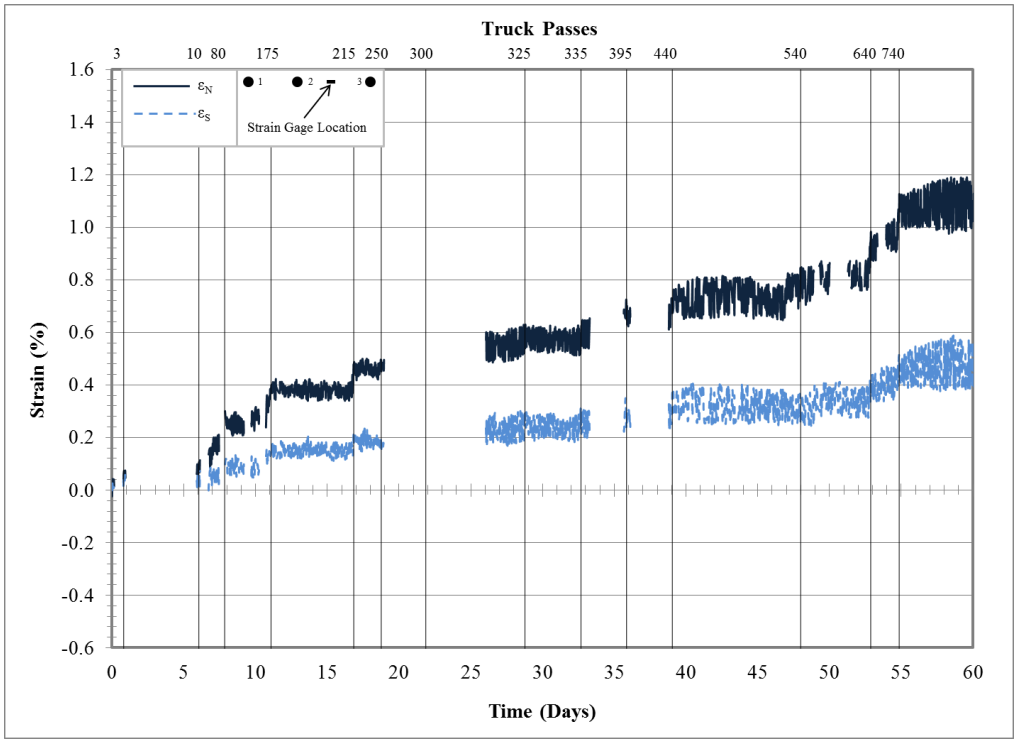


Figure K-1: Tensar BX Type 2 (CBR = 2.15).

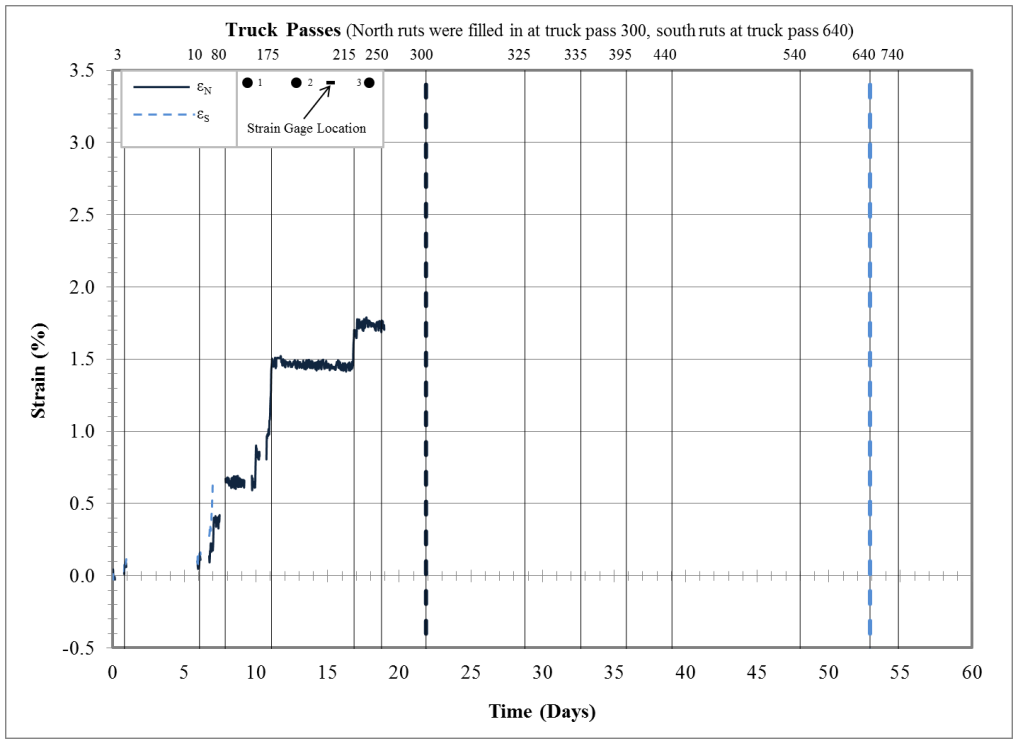


Figure K-2: Tensar BX Type 2 (CBR = 1.61).

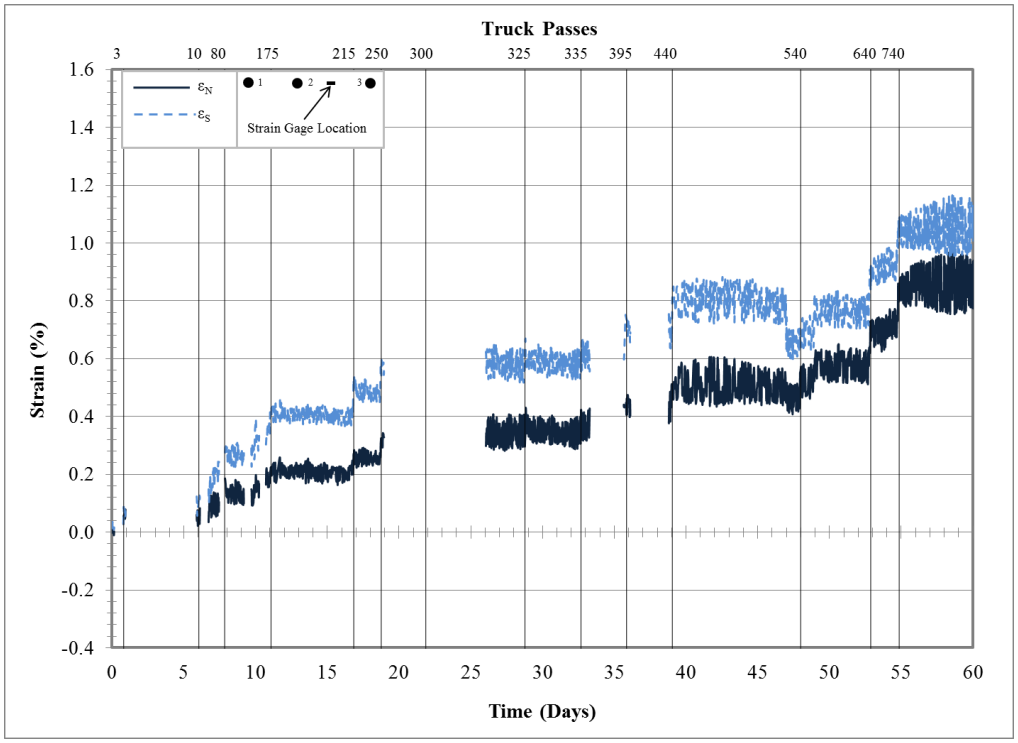


Figure K-3: Tensar BX Type 2 (CBR = 1.78).

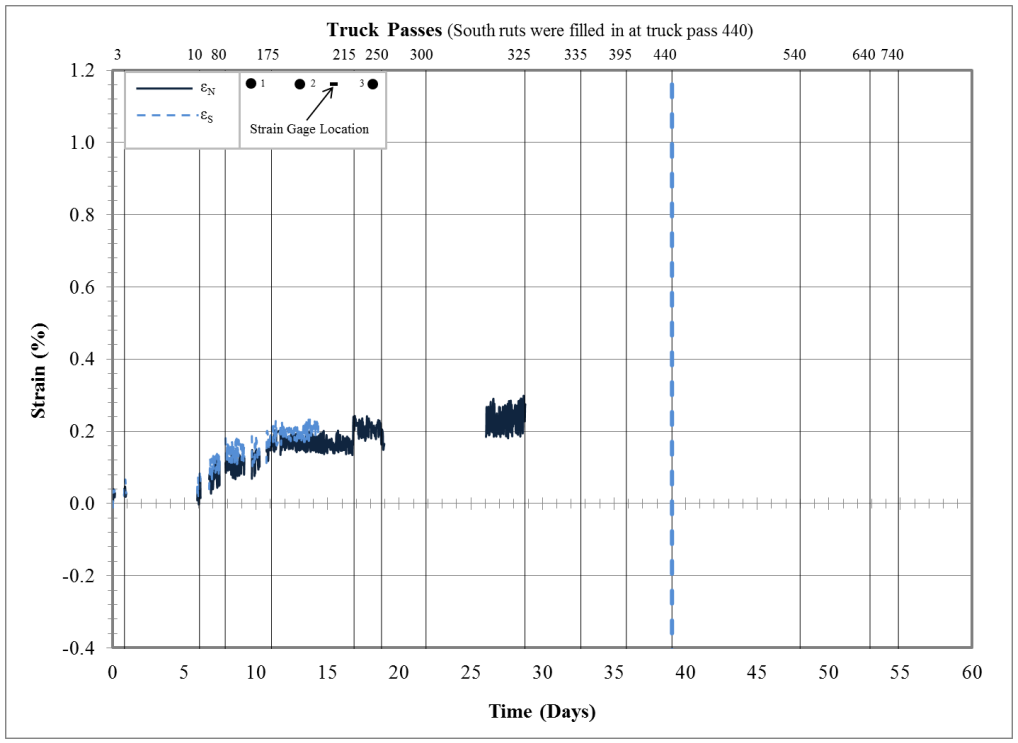


Figure K-4: NAUE Secugrid 30/30 Q1.

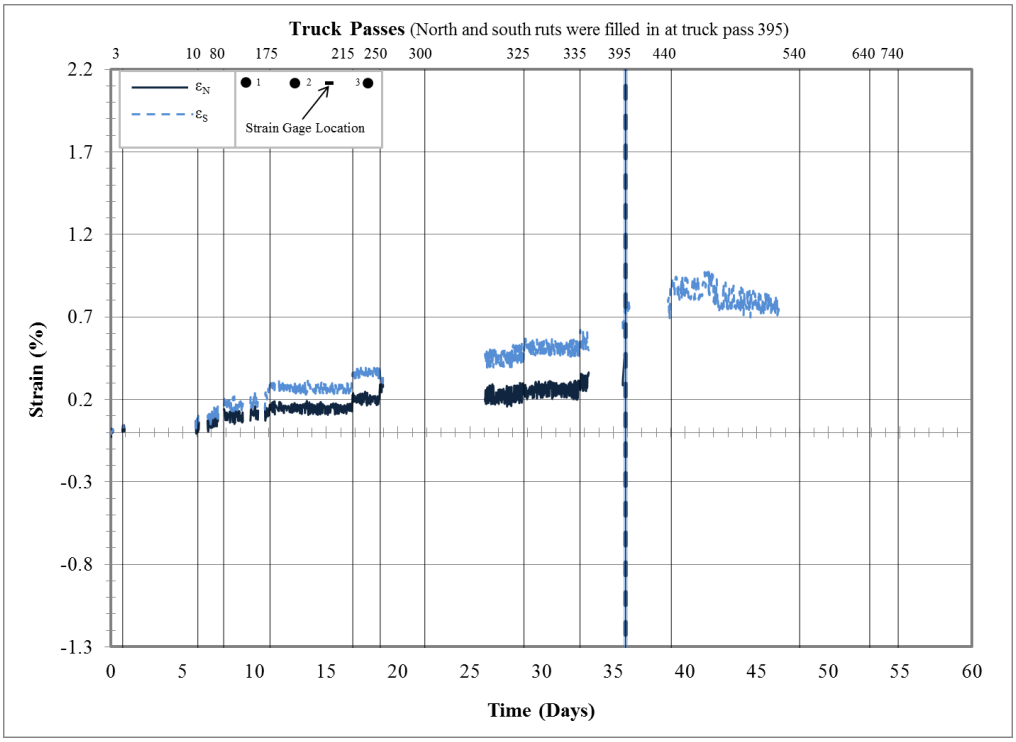


Figure K-5: Colbond Enkagrid Max 30.

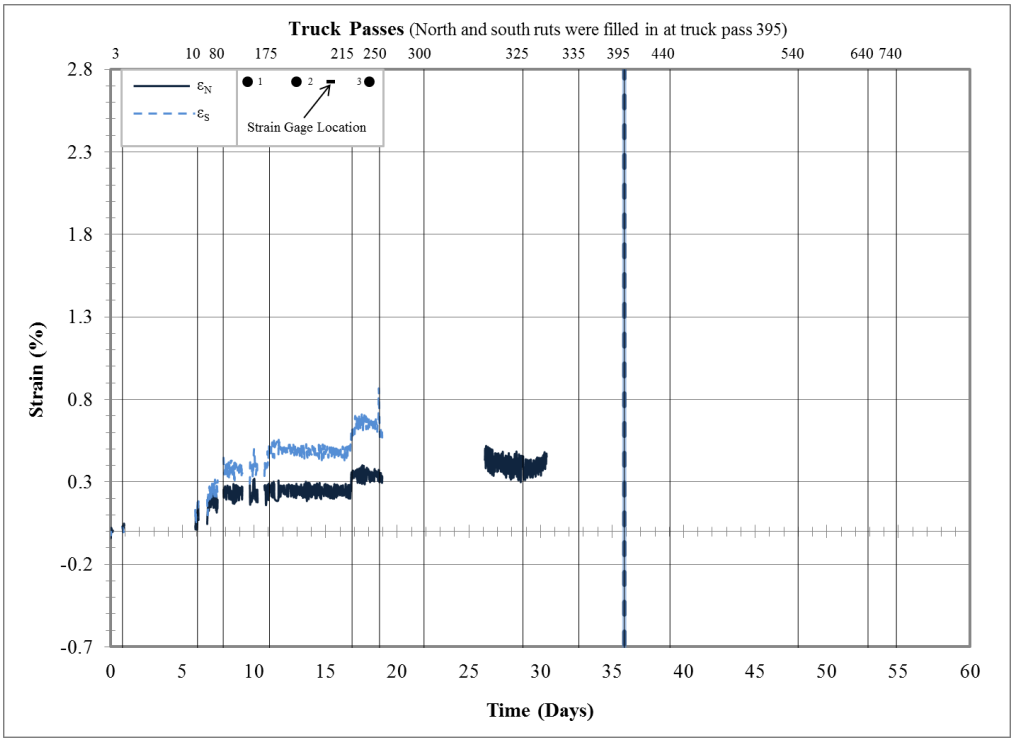


Figure K-6: Synteen SF 11.

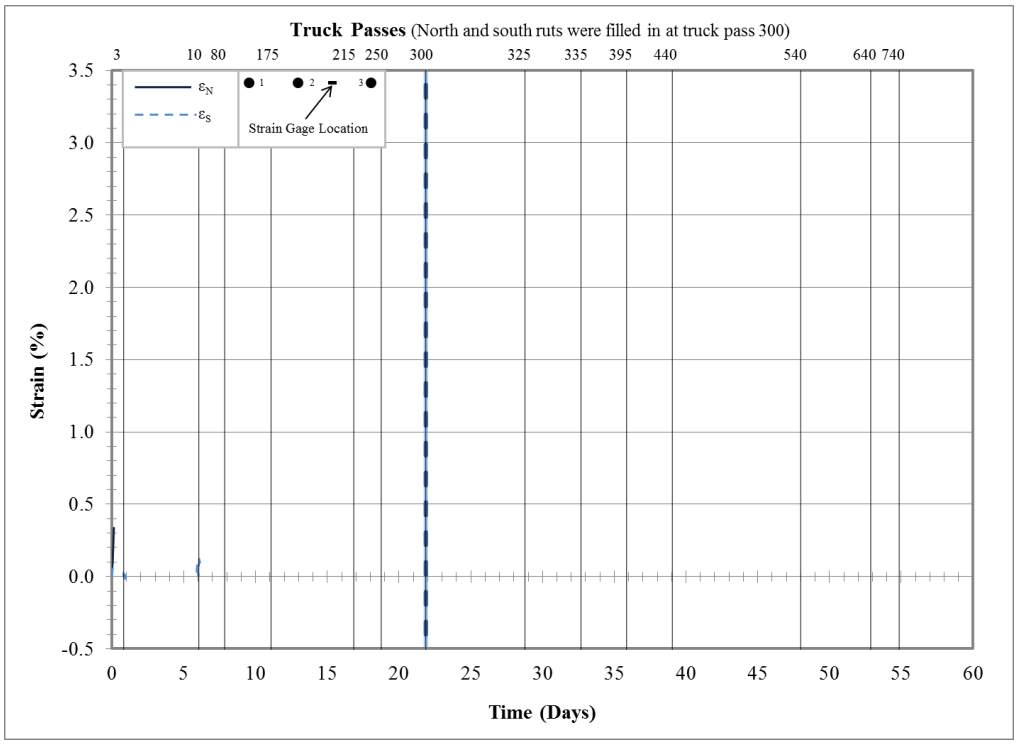


Figure K-7: Synteen SF 12.

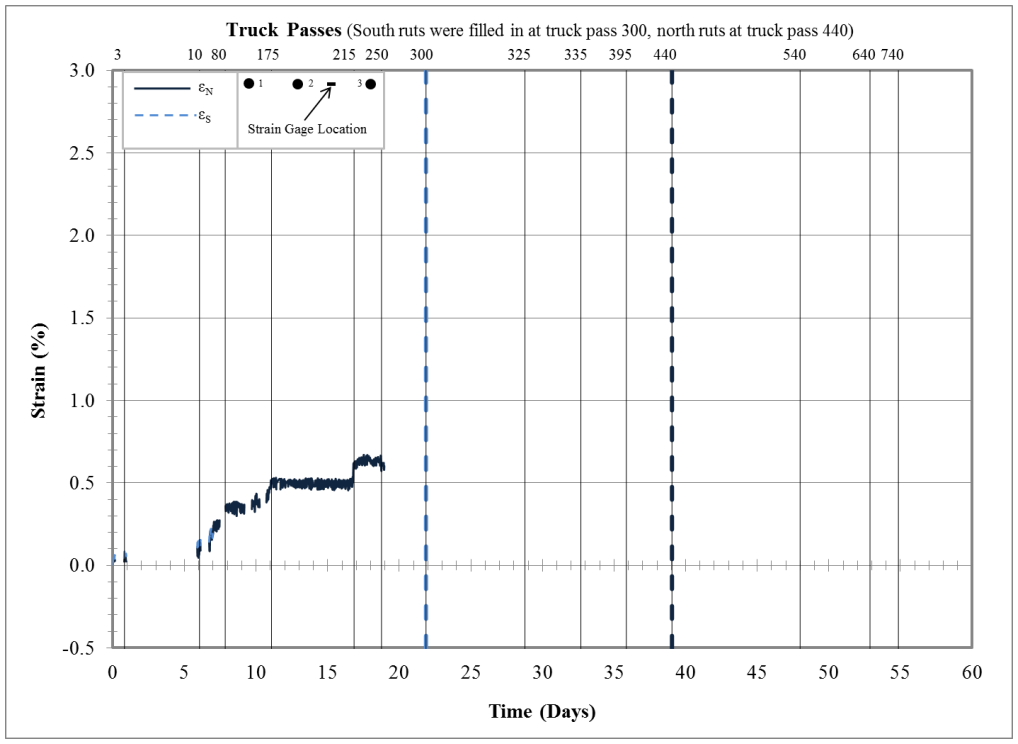


Figure K-8: TenCate Mirafi BXG 11.

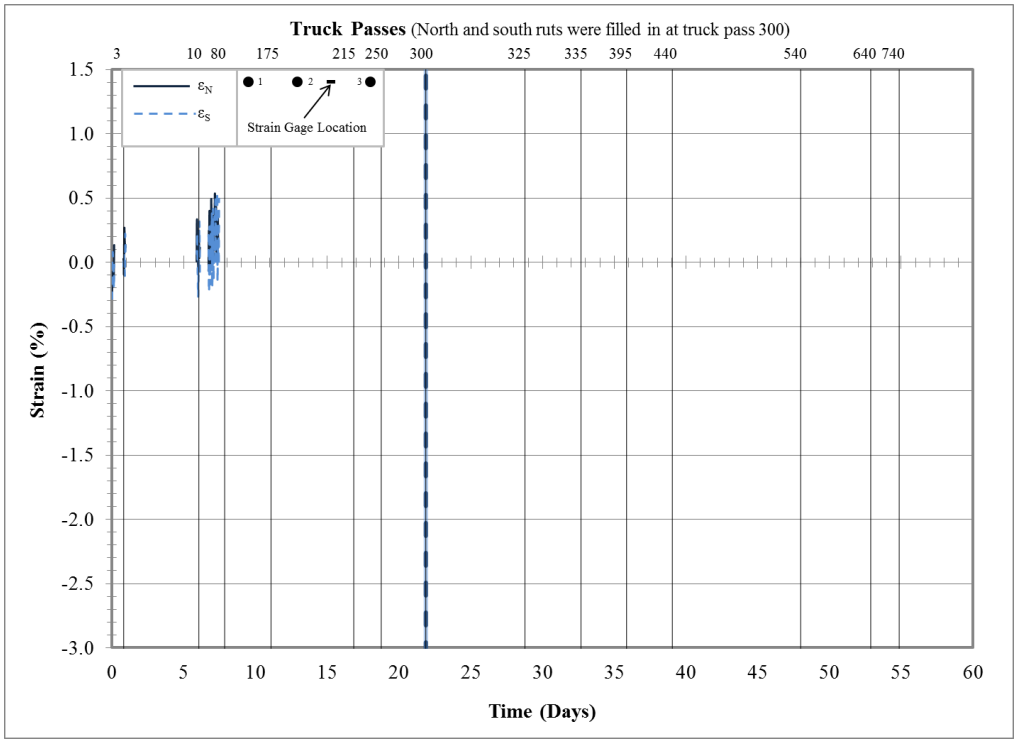


Figure K-9: Huesker Fornit 30.

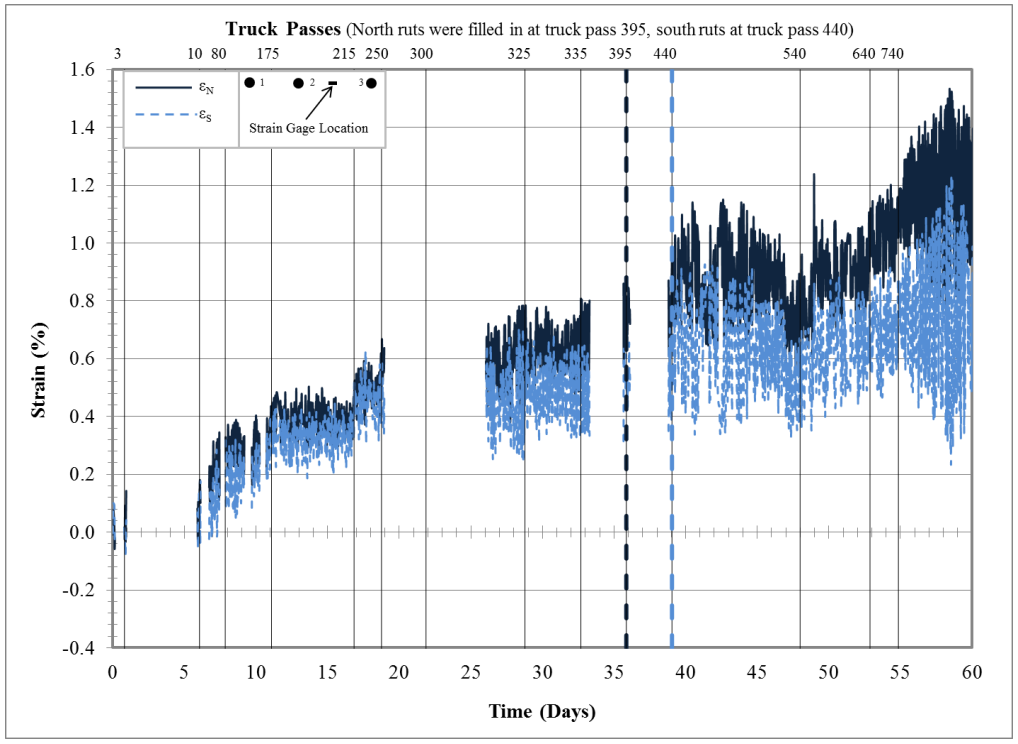


Figure K-10: SynTec Tenax MS330.

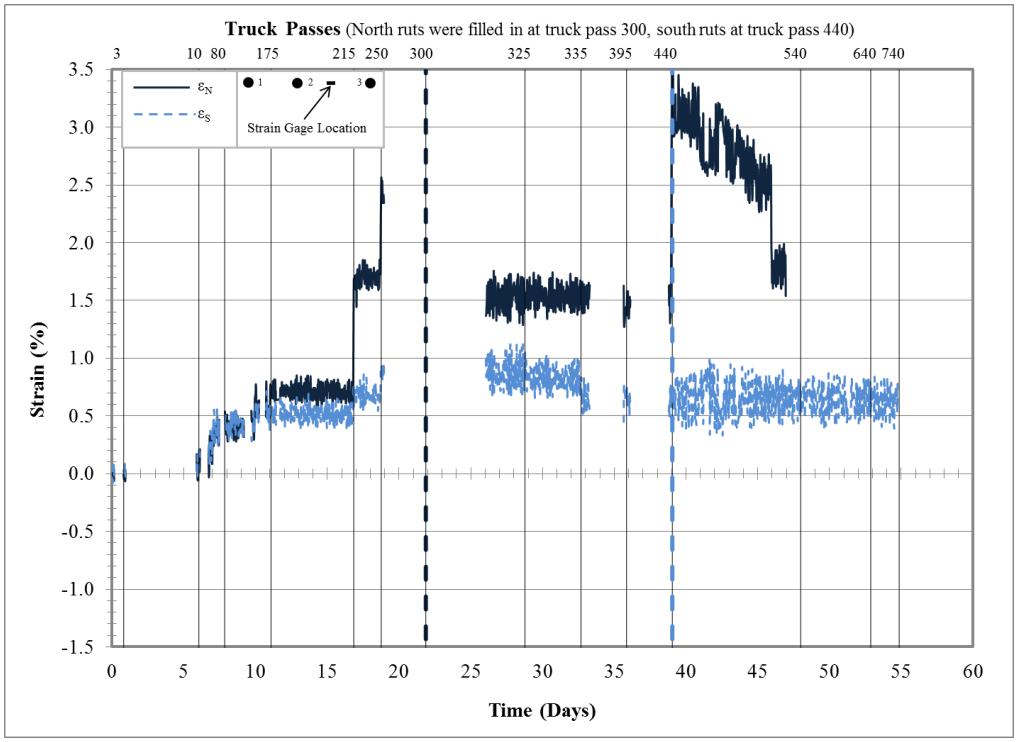


Figure K-11: Tensar TX 140.

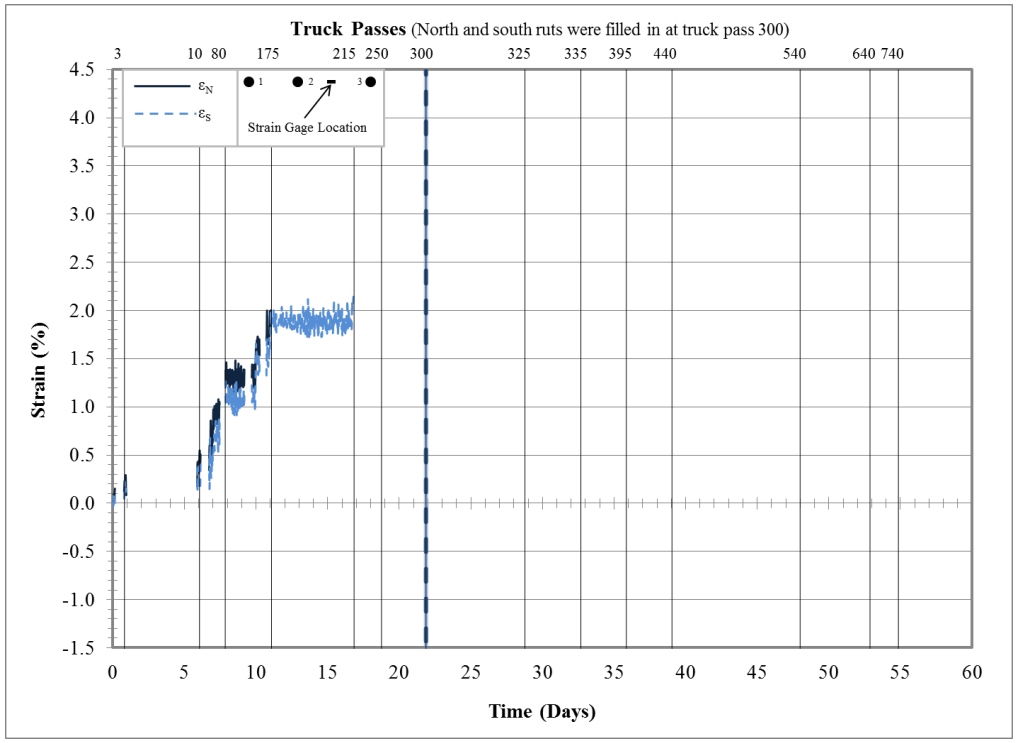


Figure K-12: Tensar TX 160.

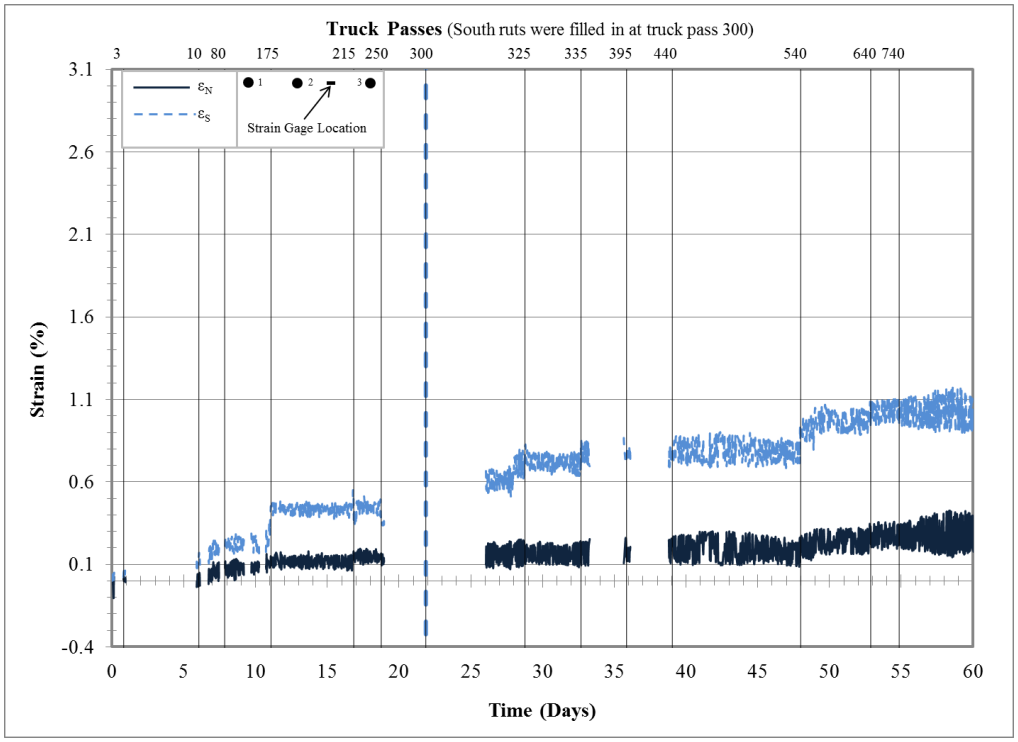


Figure K-13: TenCate Mirafi RS580i.

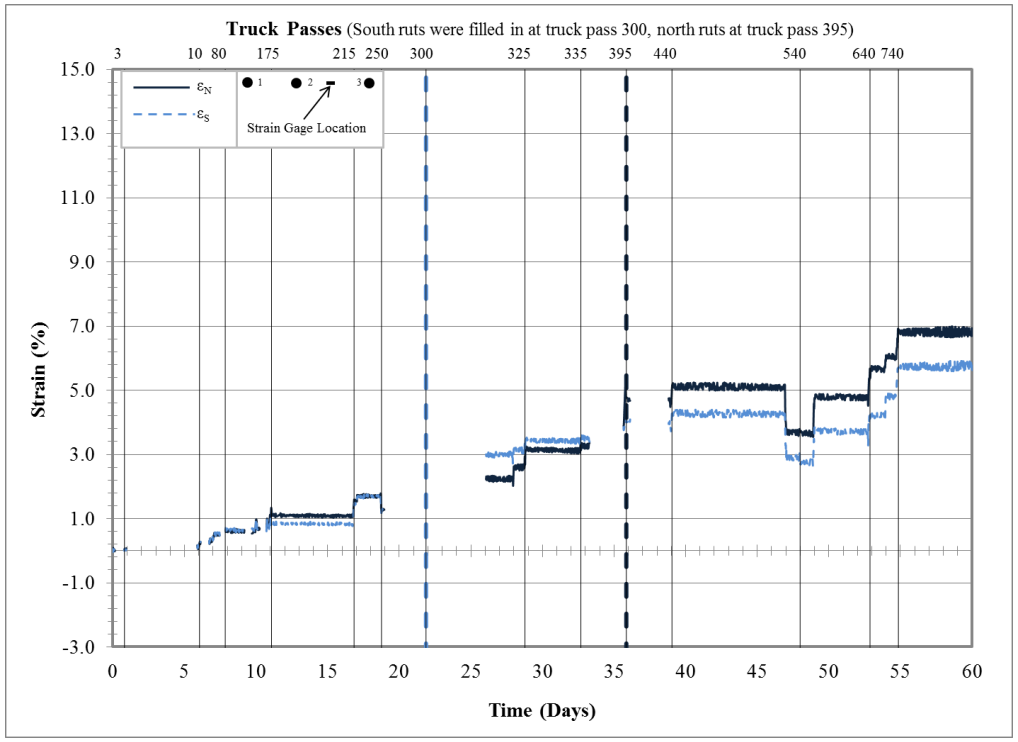


Figure K-14: Propex Geotex 801.

APPENDIX L:

LVDT DYNAMIC DISPLACEMENT PLOTS

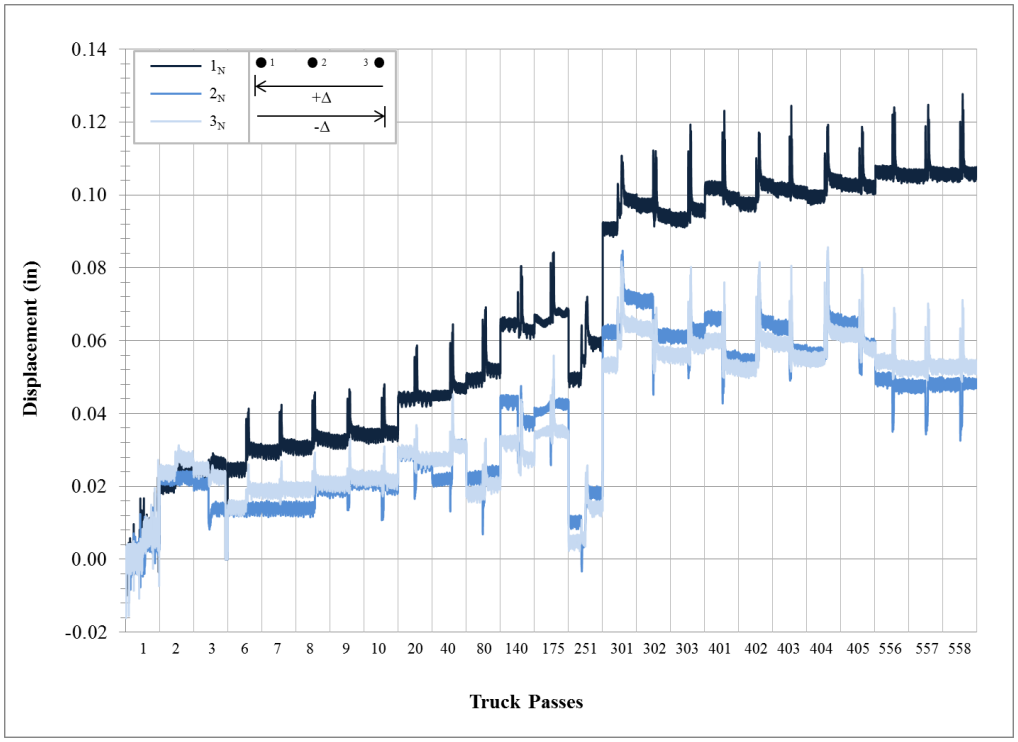


Figure L-1: Tensar BX Type 2 (1-North) (CBR = 2.15).

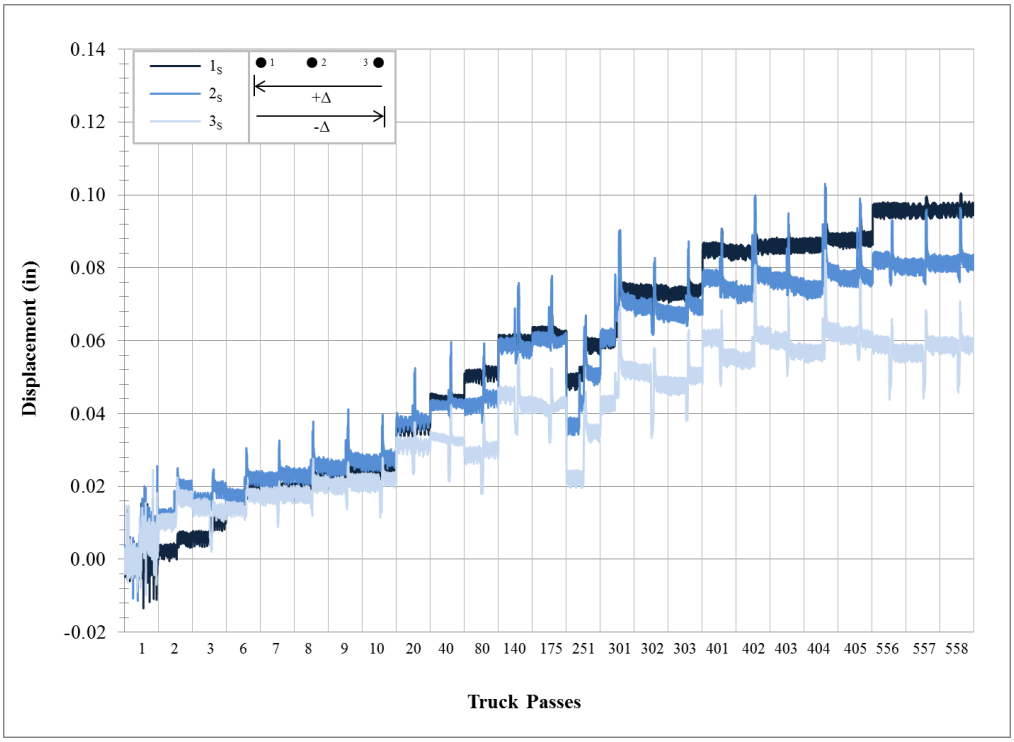


Figure L-2: Tensar BX Type 2 (1-South) (CBR = 2.15).

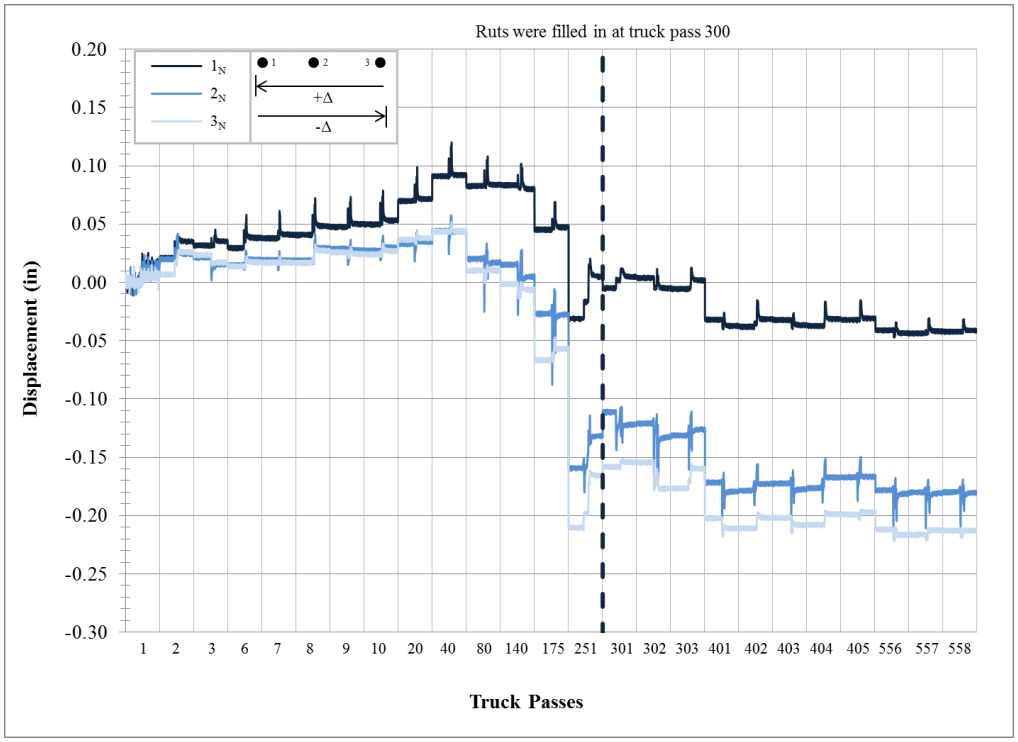


Figure L-3: Tensar BX Type 2 (2-North) (CBR = 1.61).

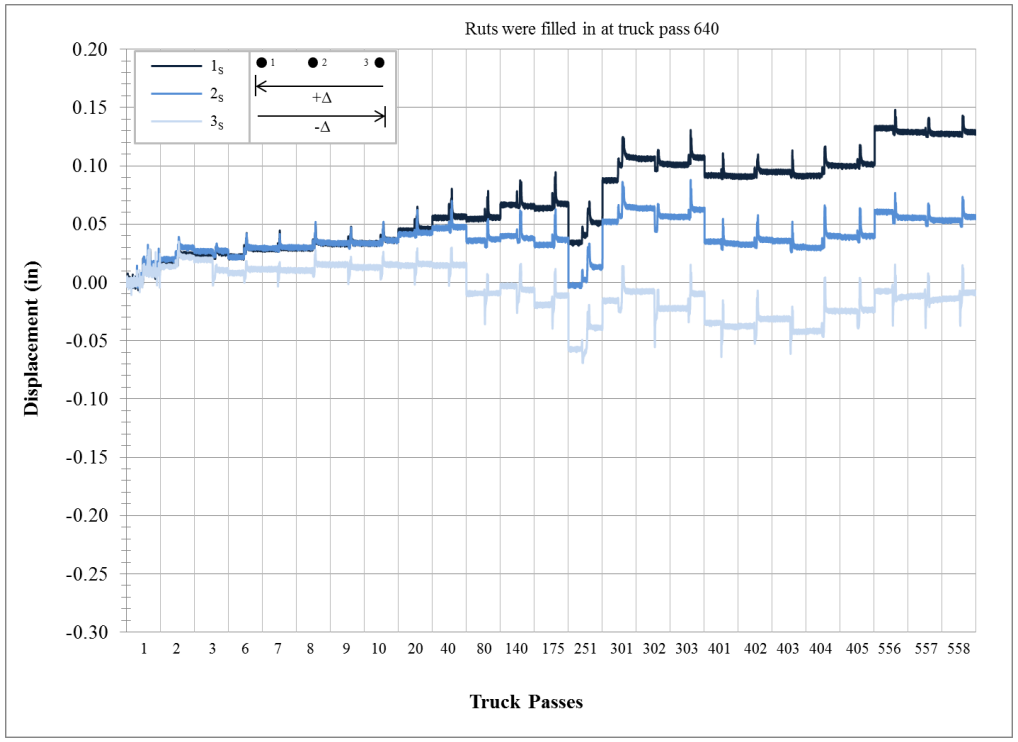


Figure L-4: Tensar BX Type 2 (2-South) (CBR = 1.61).

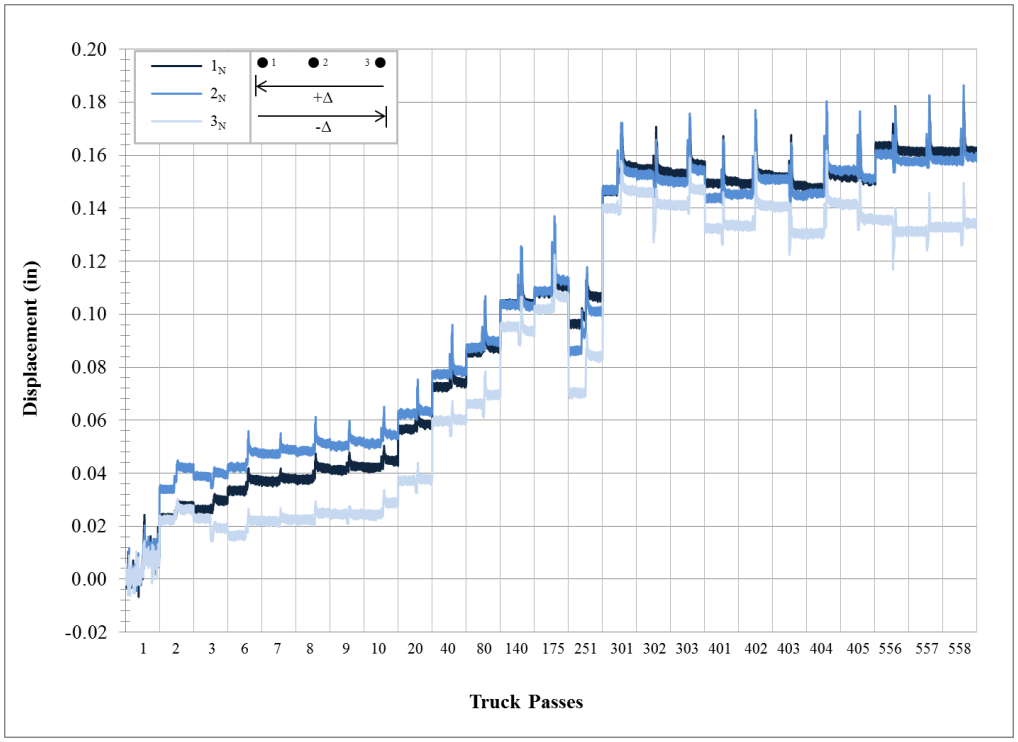


Figure L-5: Tensar BX Type 2 (3-North) (CBR = 1.78).

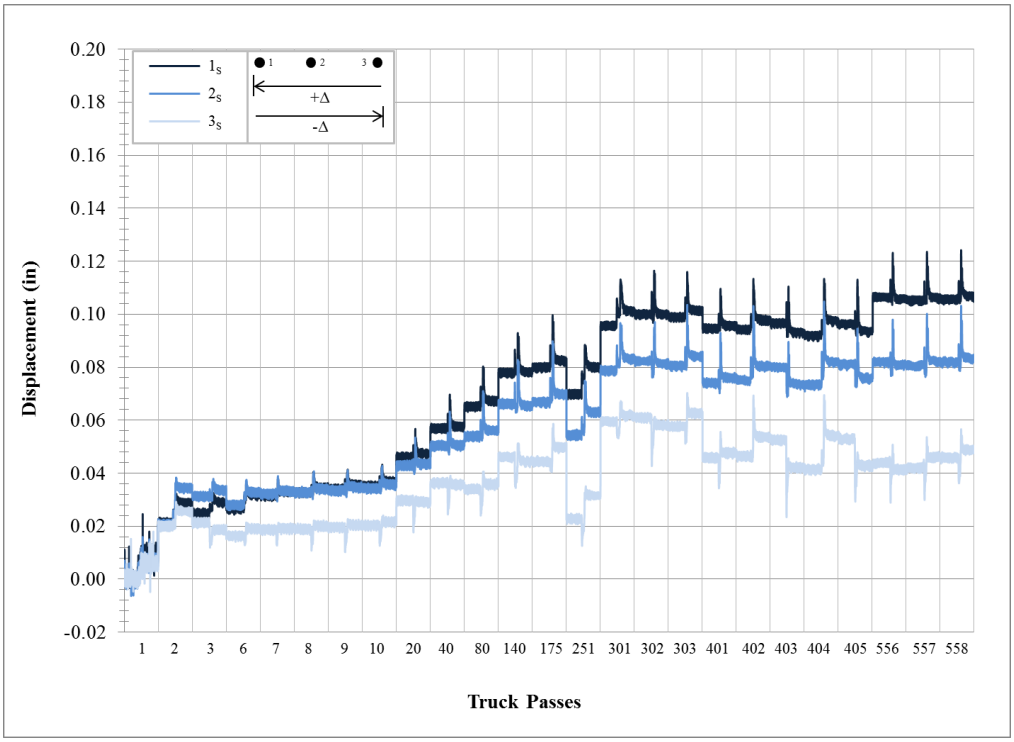


Figure L-6: Tensar BX Type 2 (3-South) (CBR = 1.78).

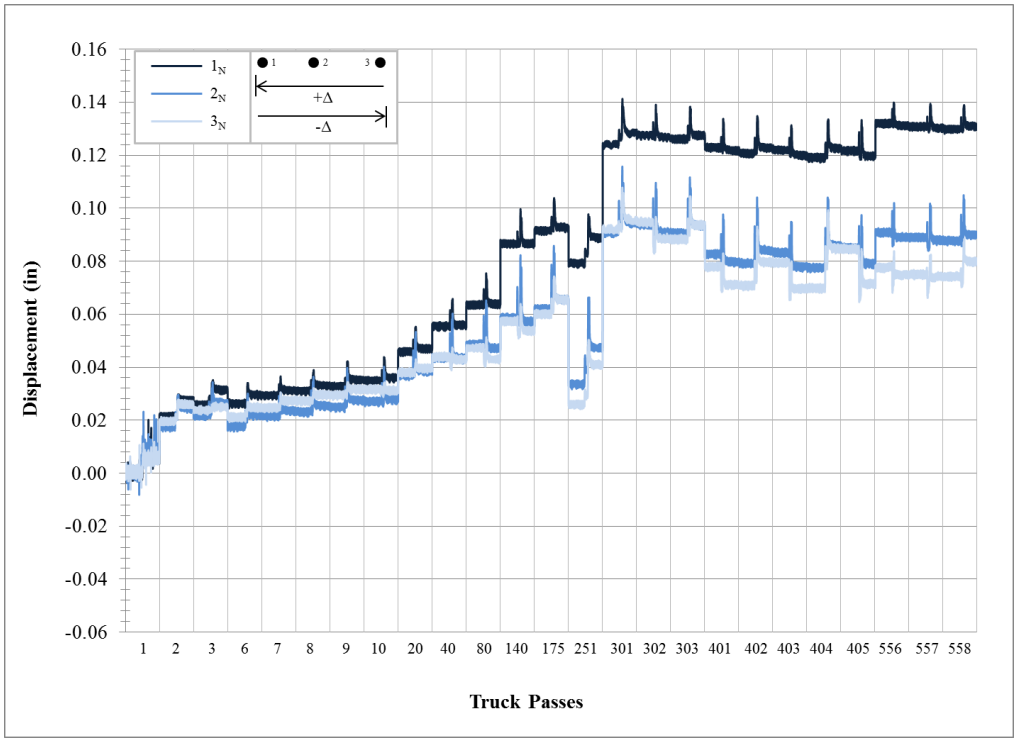


Figure L-7: NAUE Secugrid 30/30 Q1 (4-North).

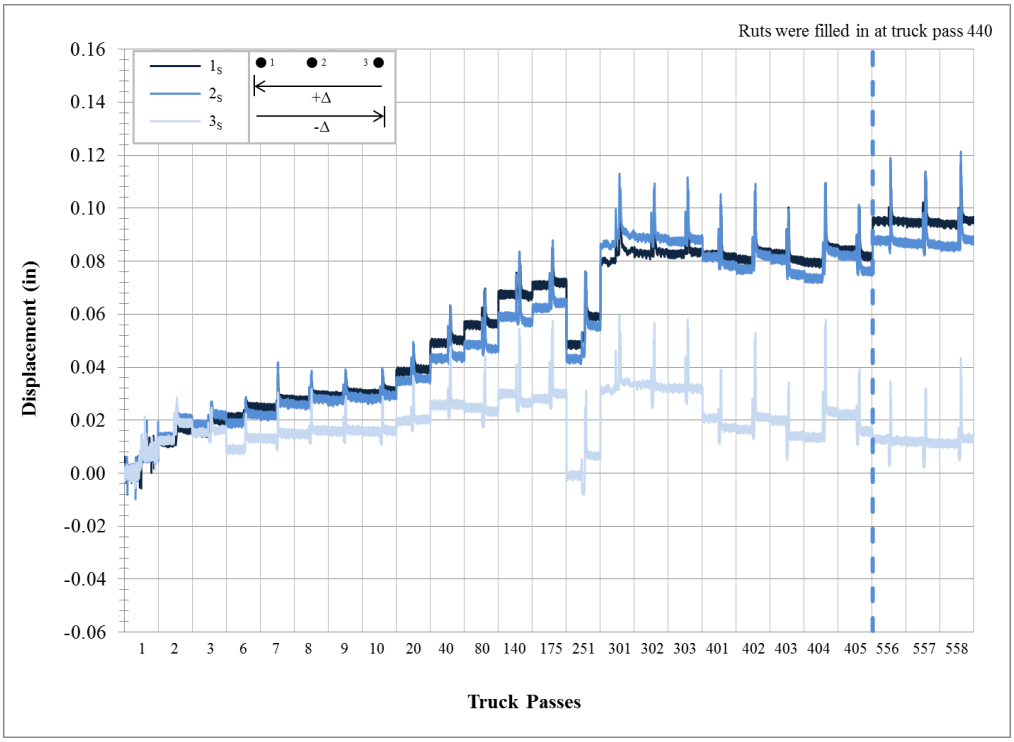


Figure L-8: NAUE Secugrid 30/30 Q1 (4-South).

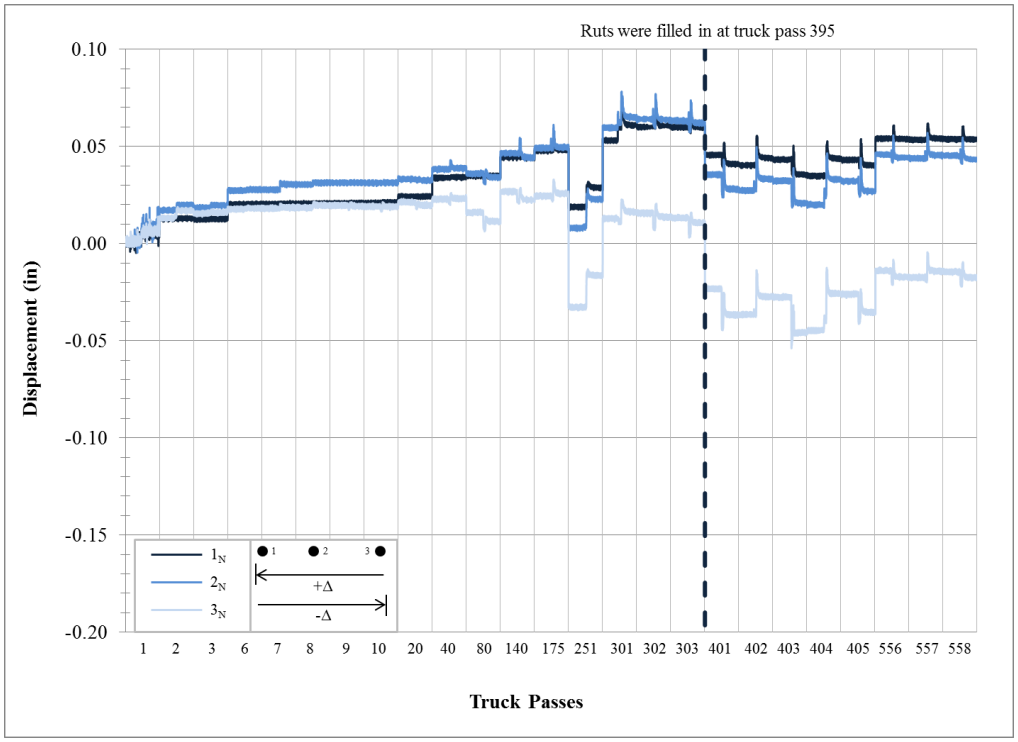


Figure L-9: Colbond Enkagrid Max 30 (5-North).

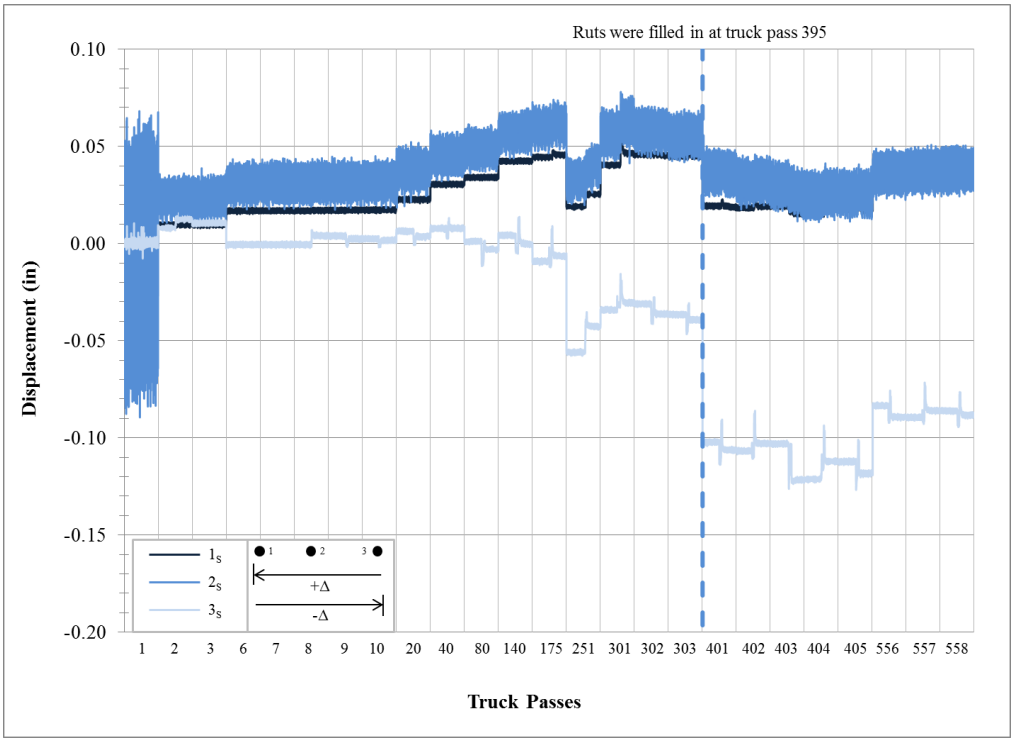


Figure L-10: Colbond Enkagrid Max 30 (5-South).

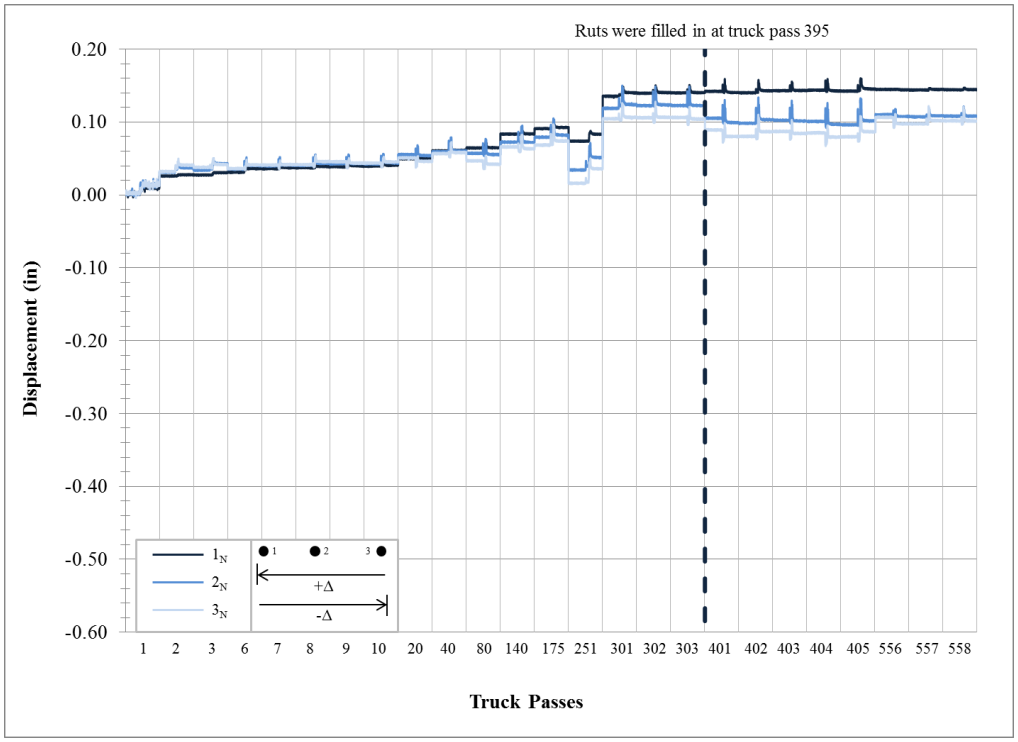


Figure L-11: Synteen SF 11 (6-North).

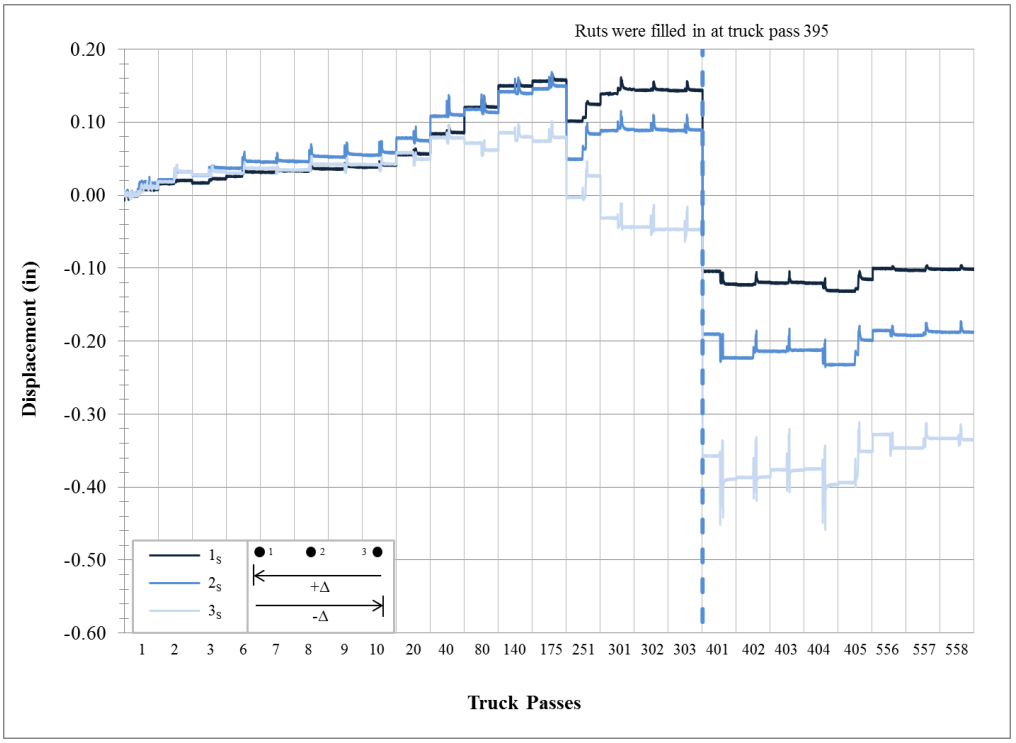


Figure L-12: Synteen SF 11 (6-South).

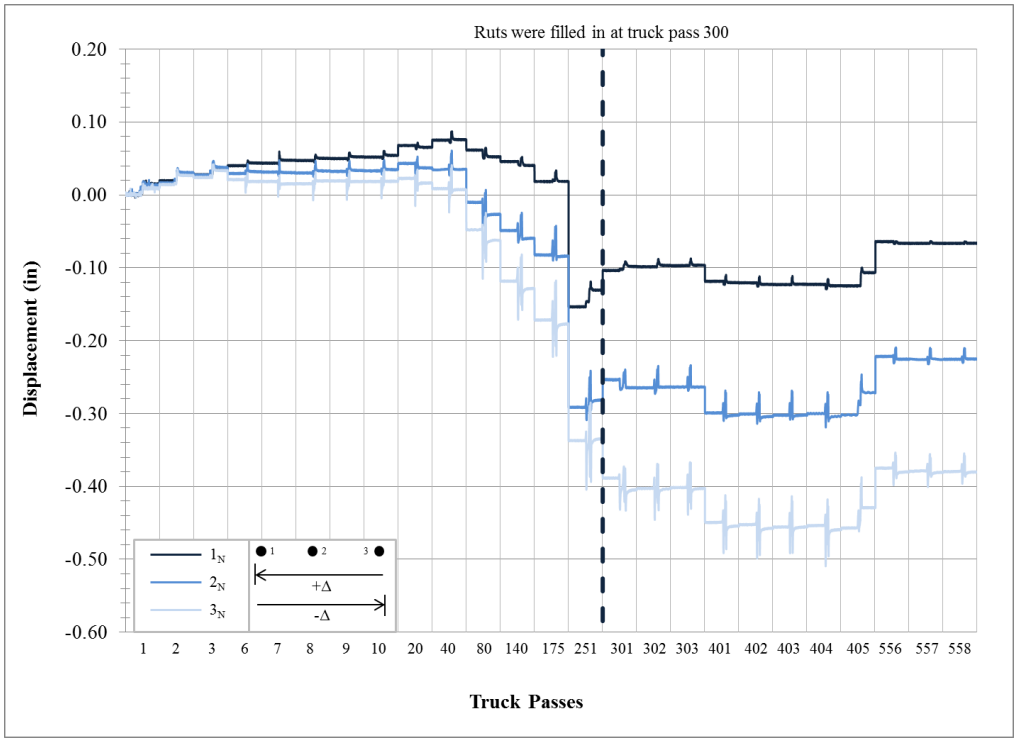


Figure L-13: Synteen SF 12 (7-North).

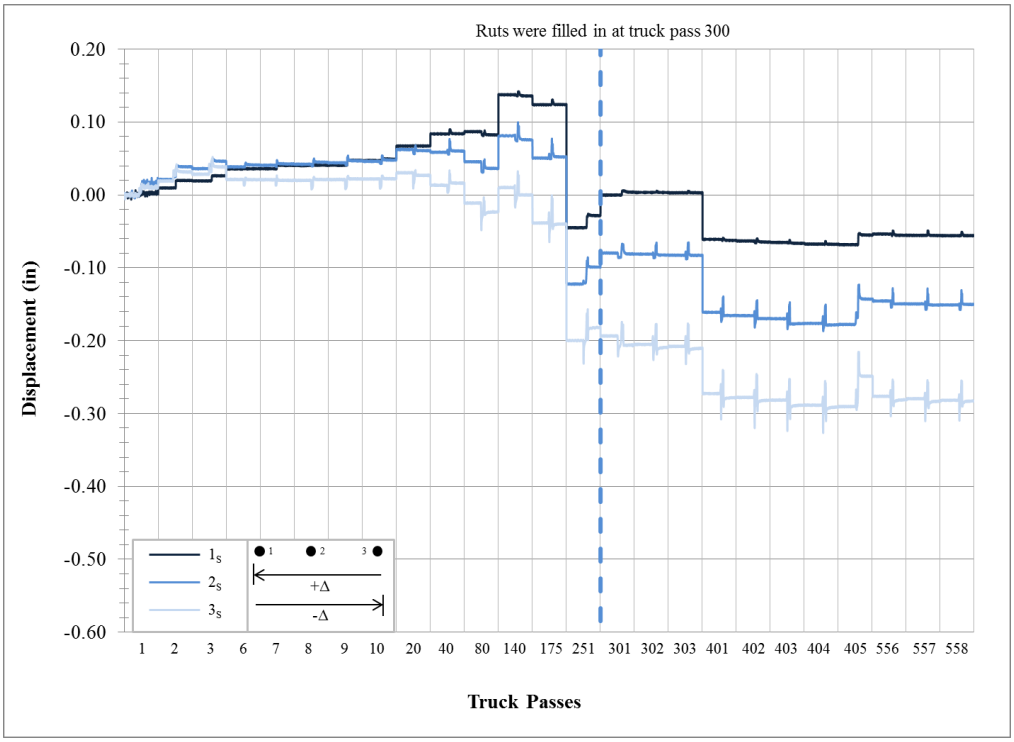


Figure L-14: Synteen SF 12 (7-South).

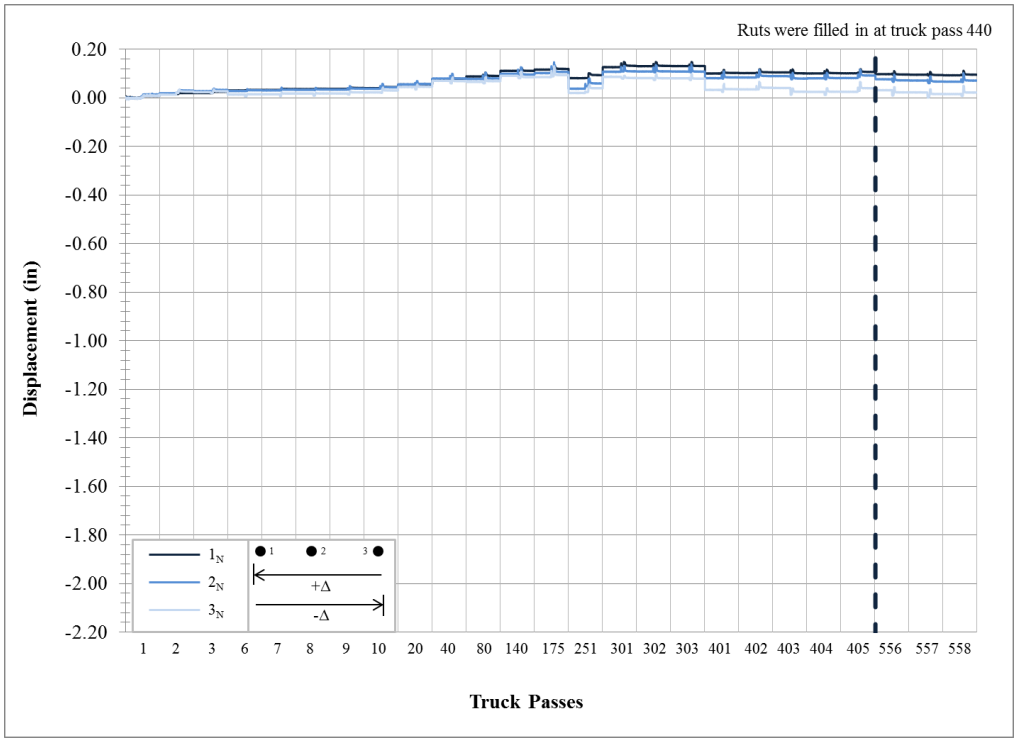


Figure L-15: TenCate Mirafi BXG 11 (8-North).

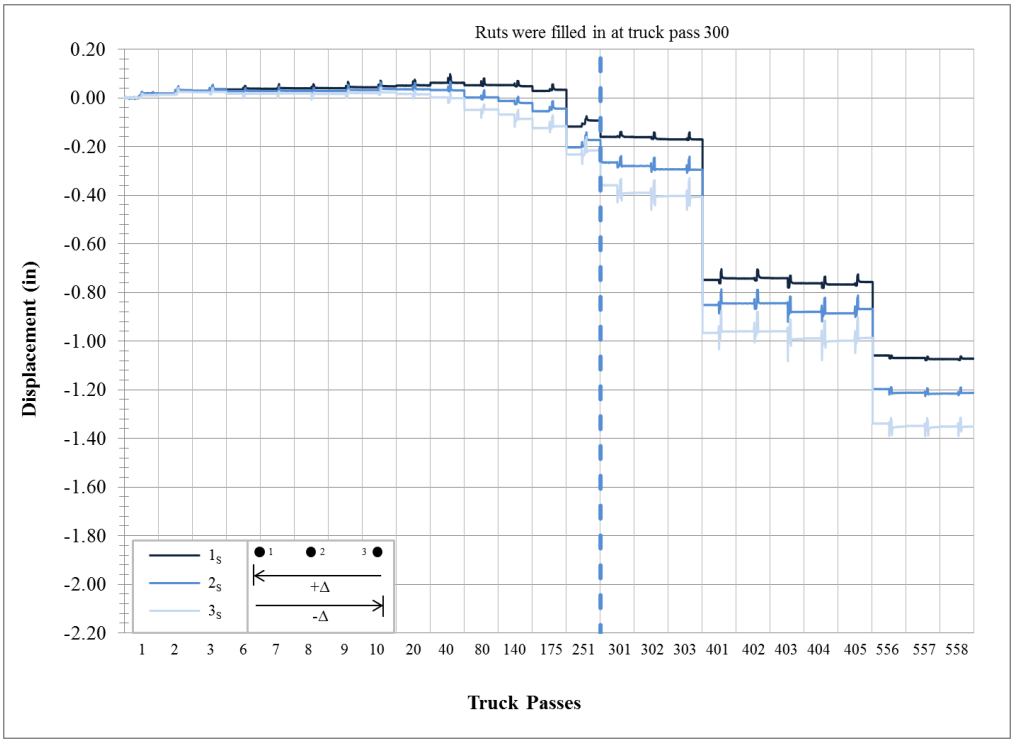


Figure L-16: TenCate Mirafi BXG 11 (8-South).

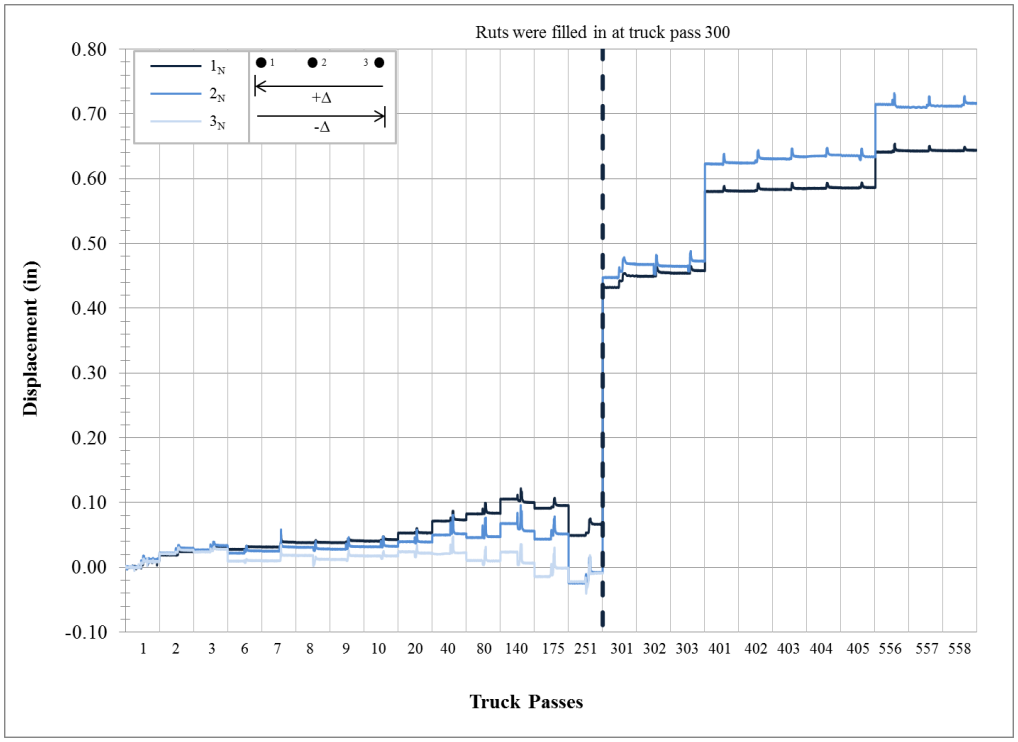


Figure L-17: Huesker Fornit 30 (9-North).

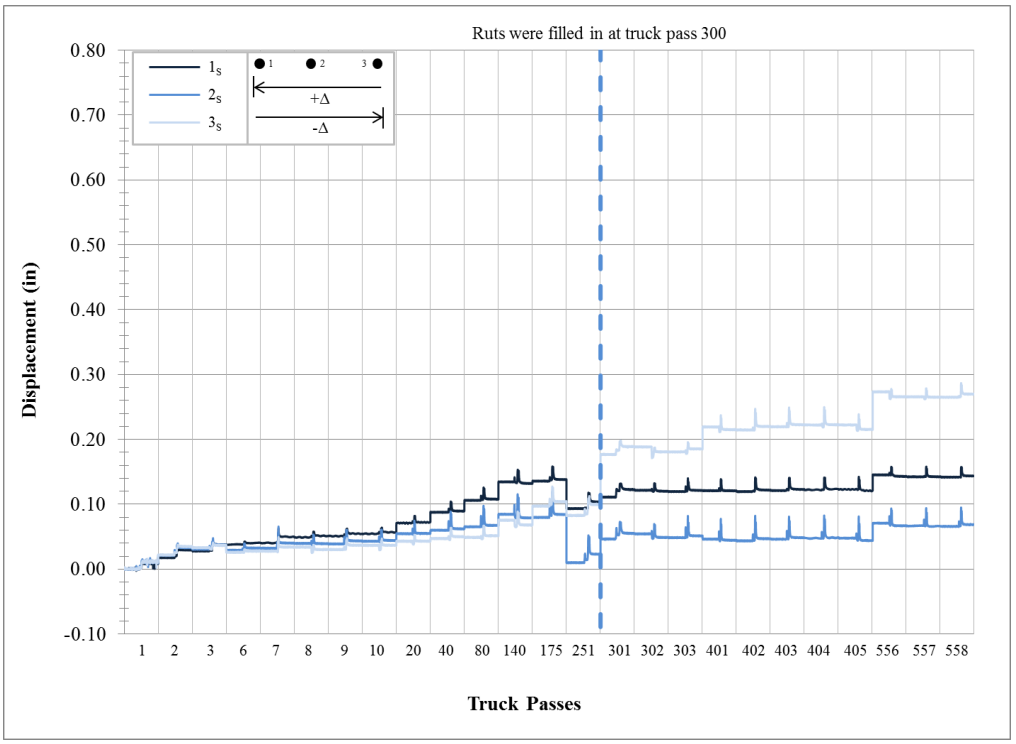


Figure L-18: Huesker Fornit 30 (9-South).

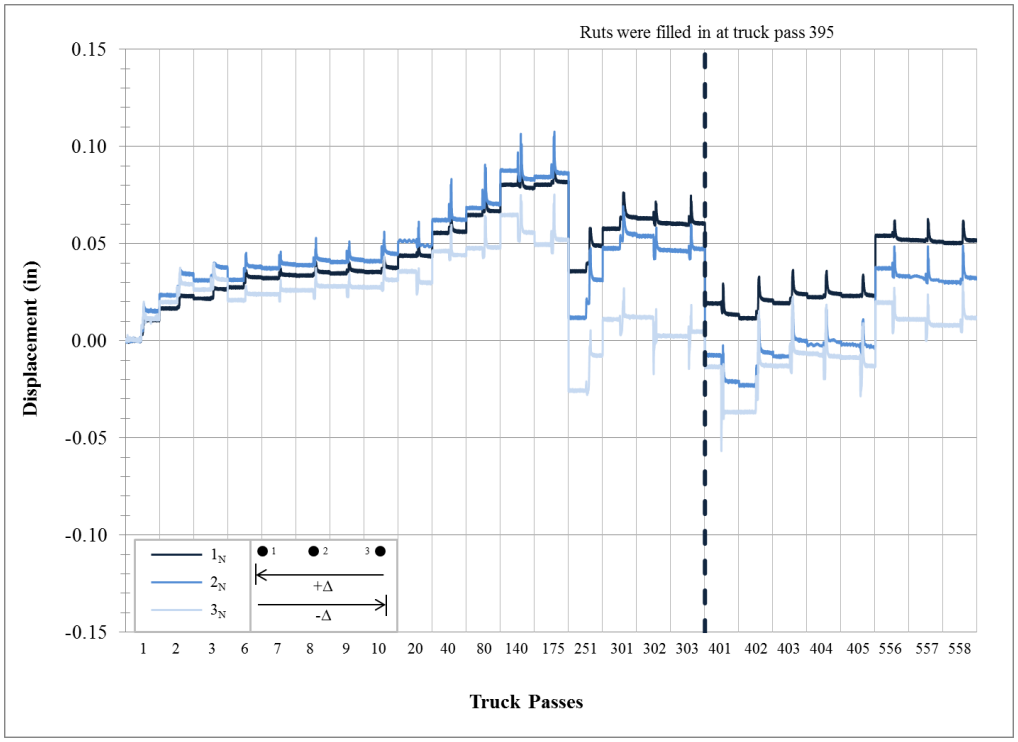


Figure L-19: SynTec Tenax MS330 (10-North).

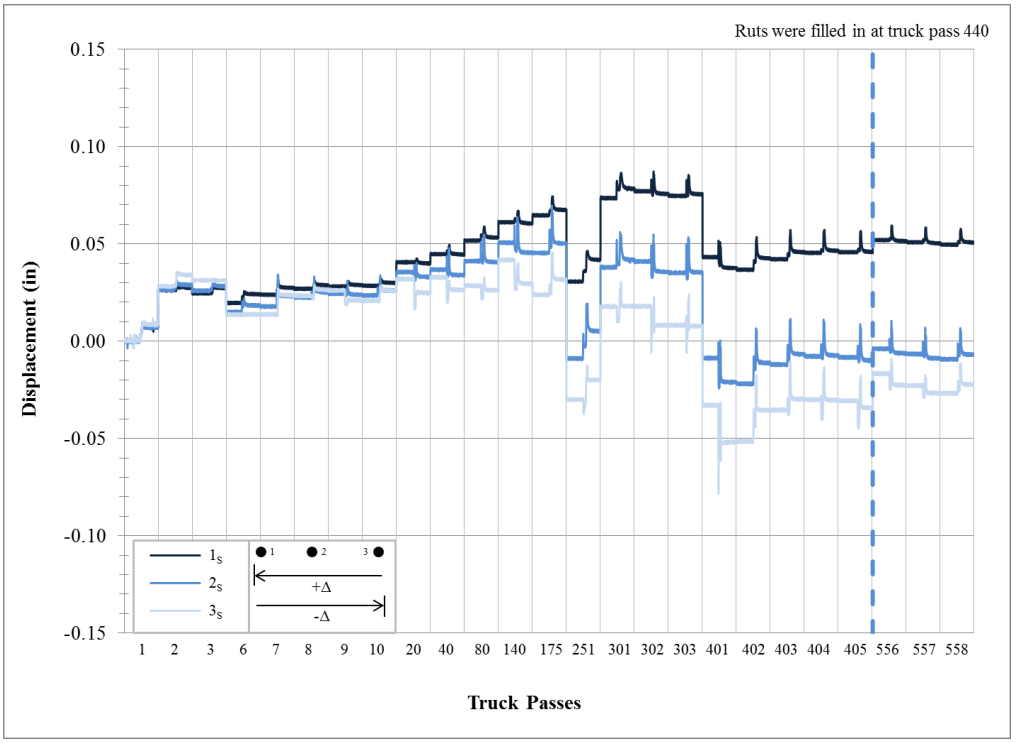


Figure L-20: SynTec Tenax MS330 (10-South).

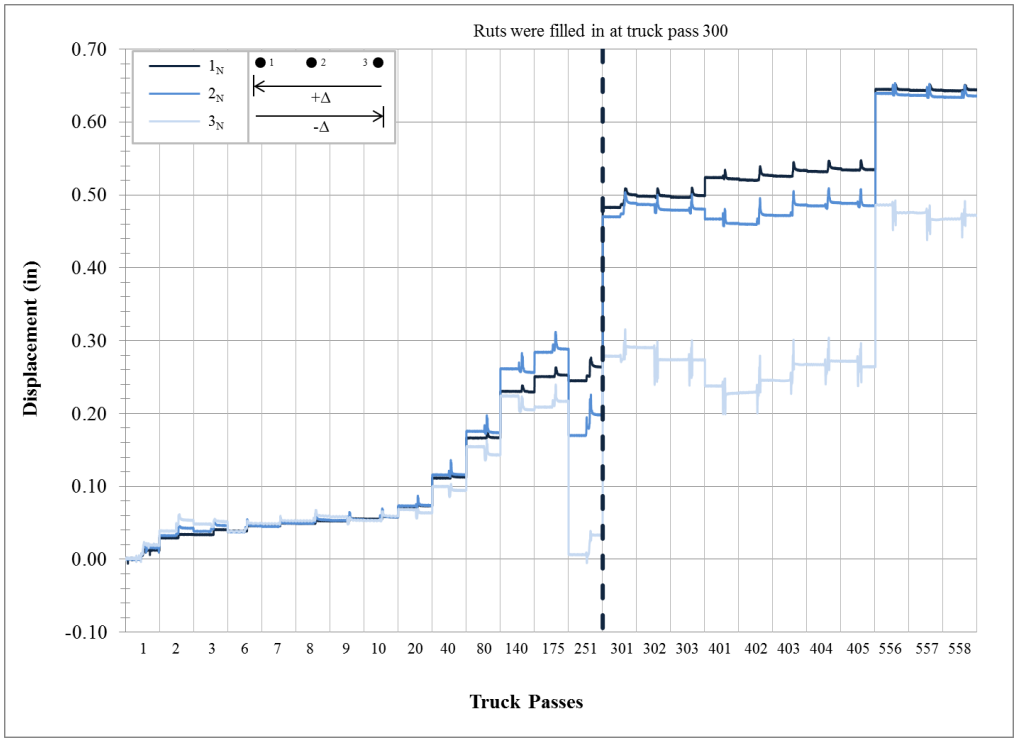


Figure L-21: Tensar TX 140 (11-North).

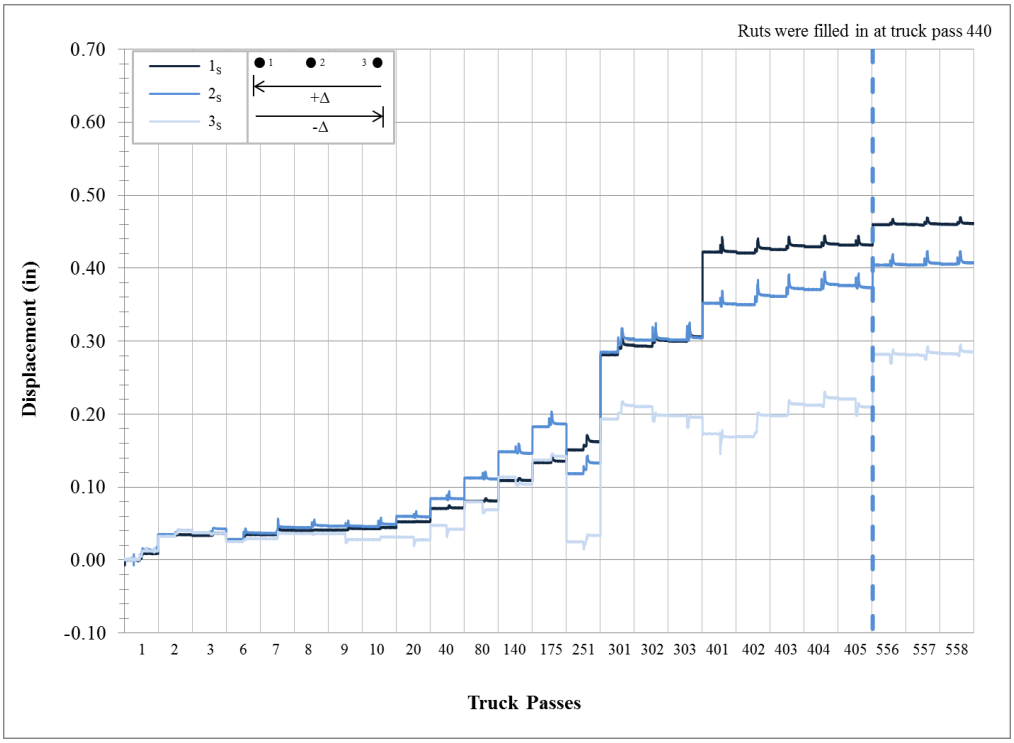


Figure L-22: Tensar TX 140 (11-South).

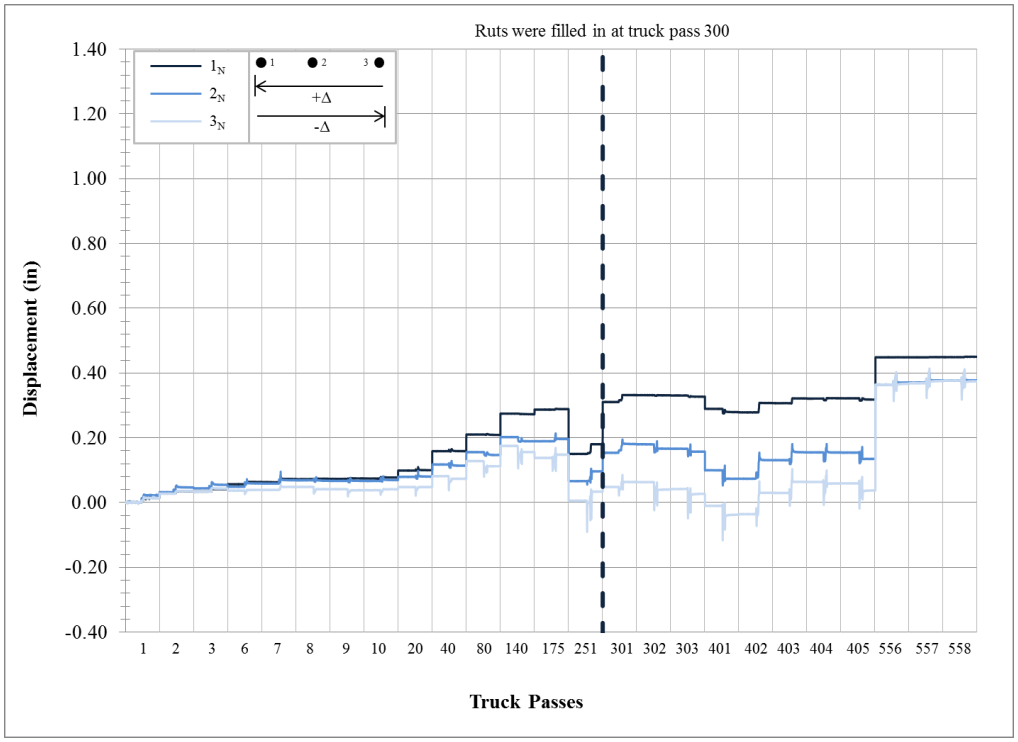


Figure L-23: Tensar TX 160 (12-North).

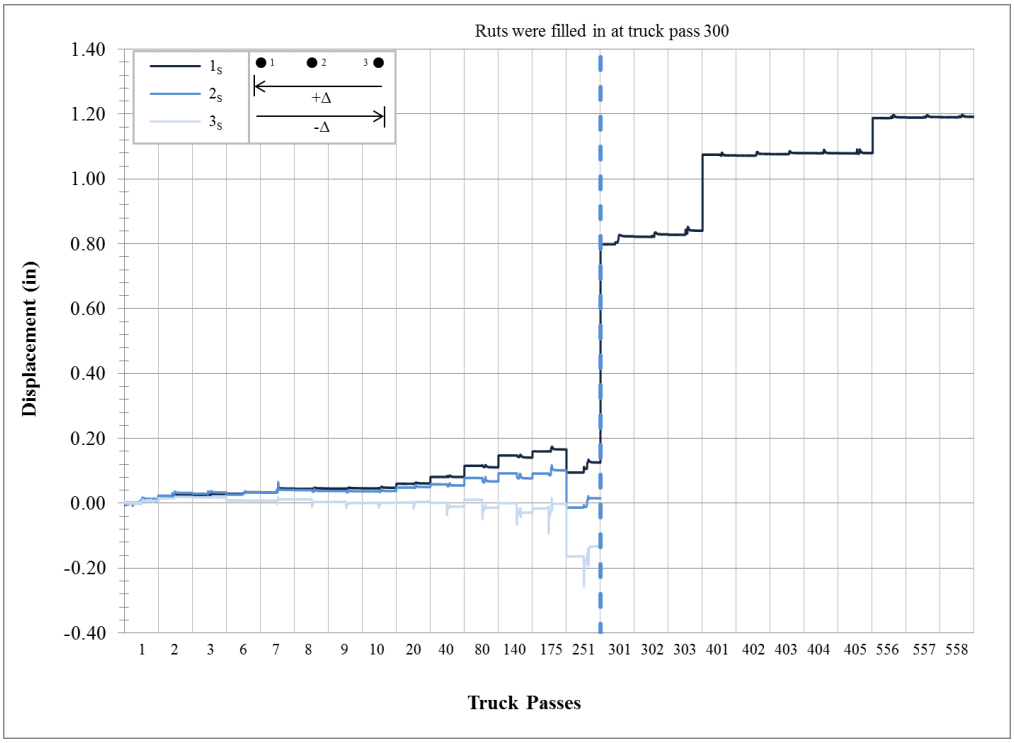


Figure L-24: Tensar TX 160 (12-South).

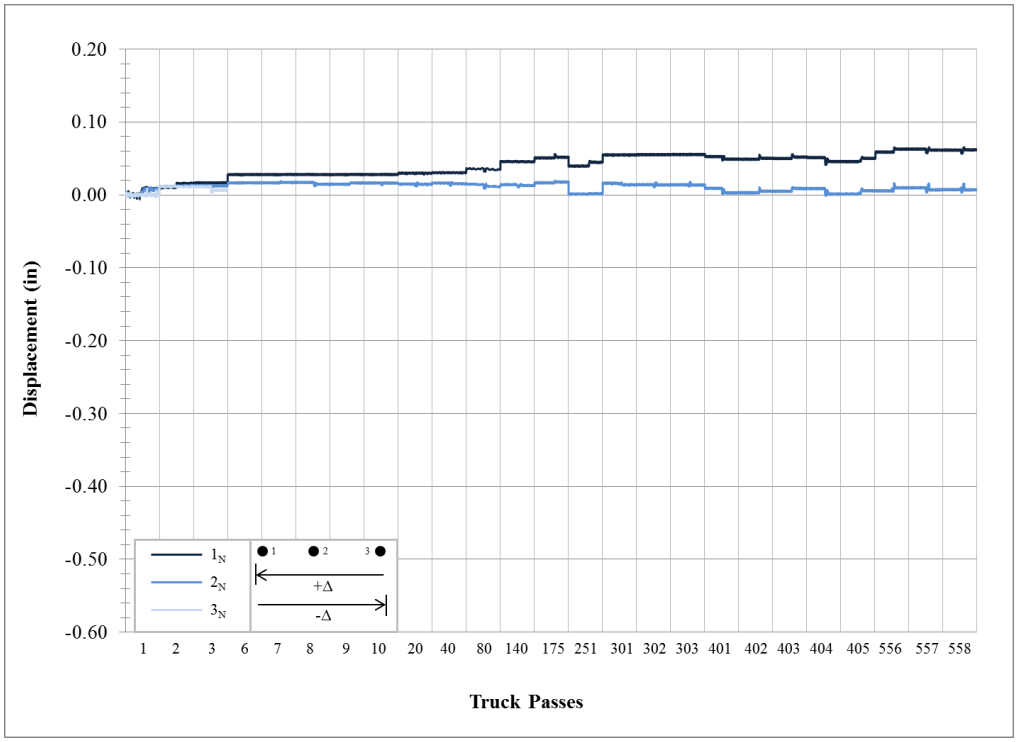


Figure L-25: TenCate Mirafi RS580i (13-North).

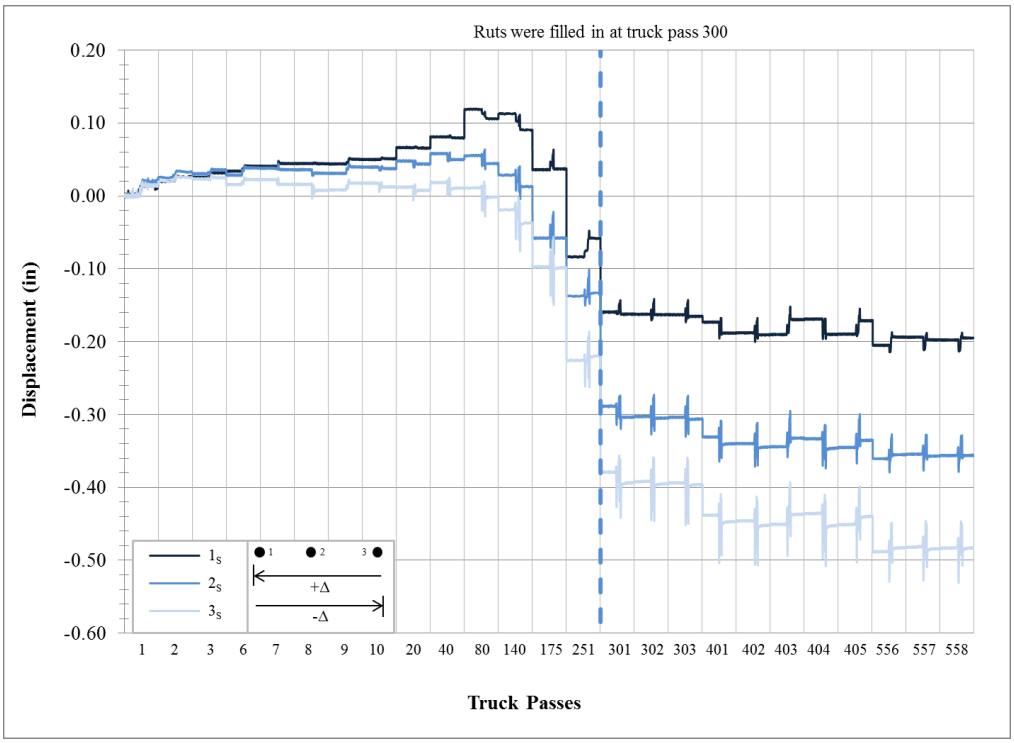


Figure L-26: TenCate Mirafi RS580i (13-South).

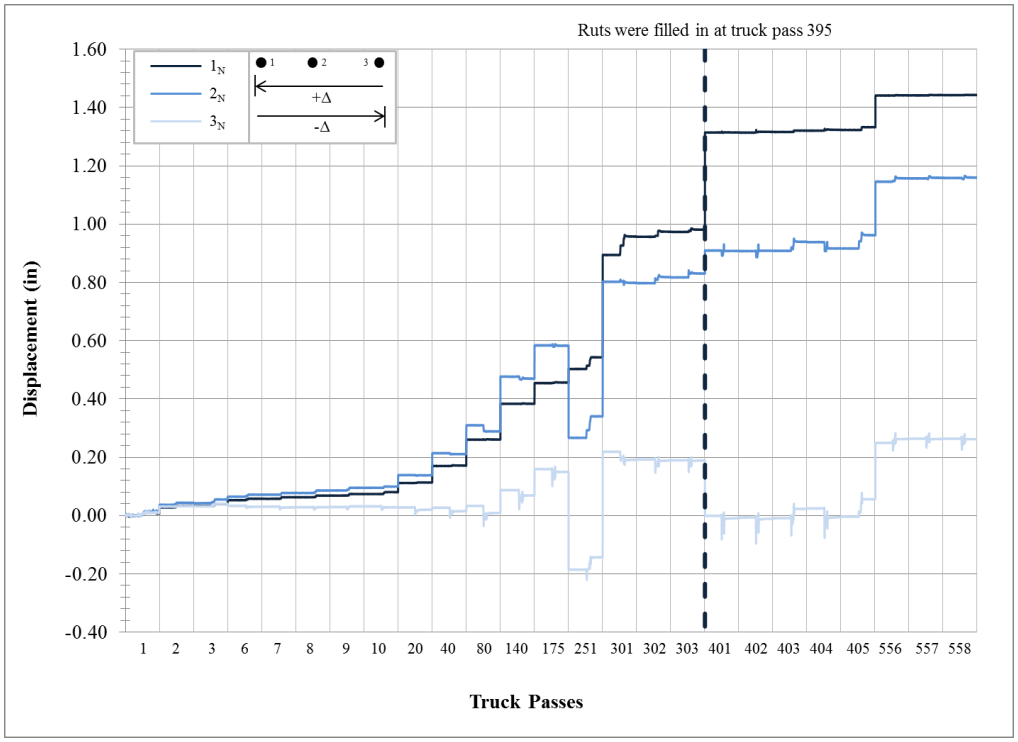


Figure L-27: Propex Geotex 801 (14-North).

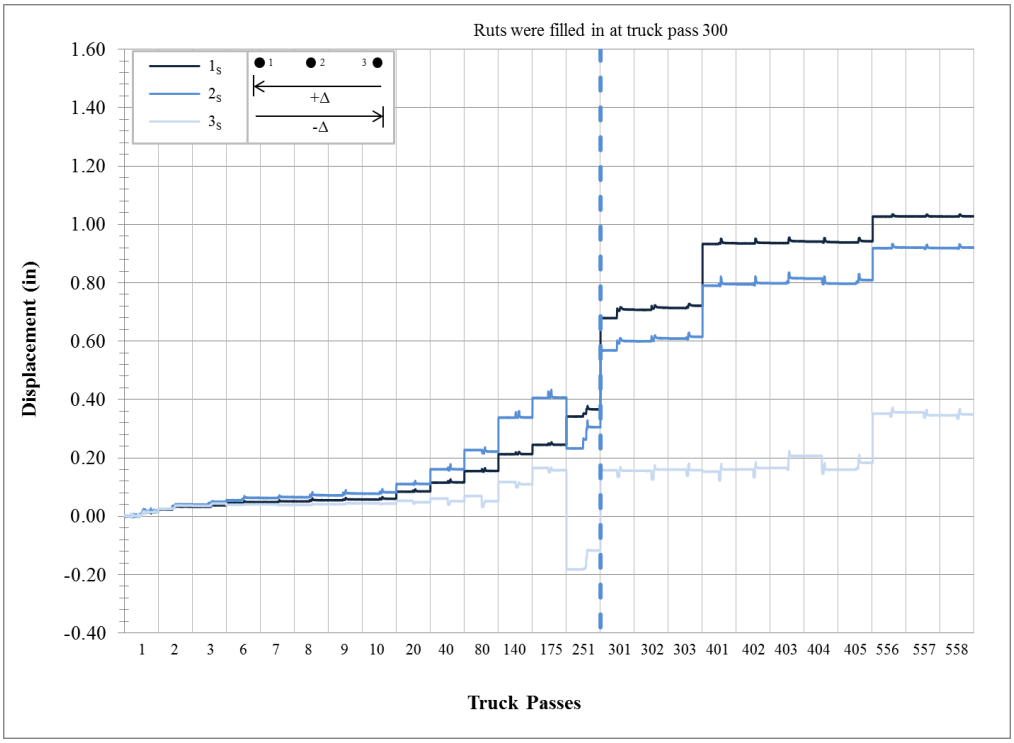


Figure L-28: Propex Geotex 801 (14-South).

APPENDIX M:

LVDT STATIC DISPLACEMENT PLOTS

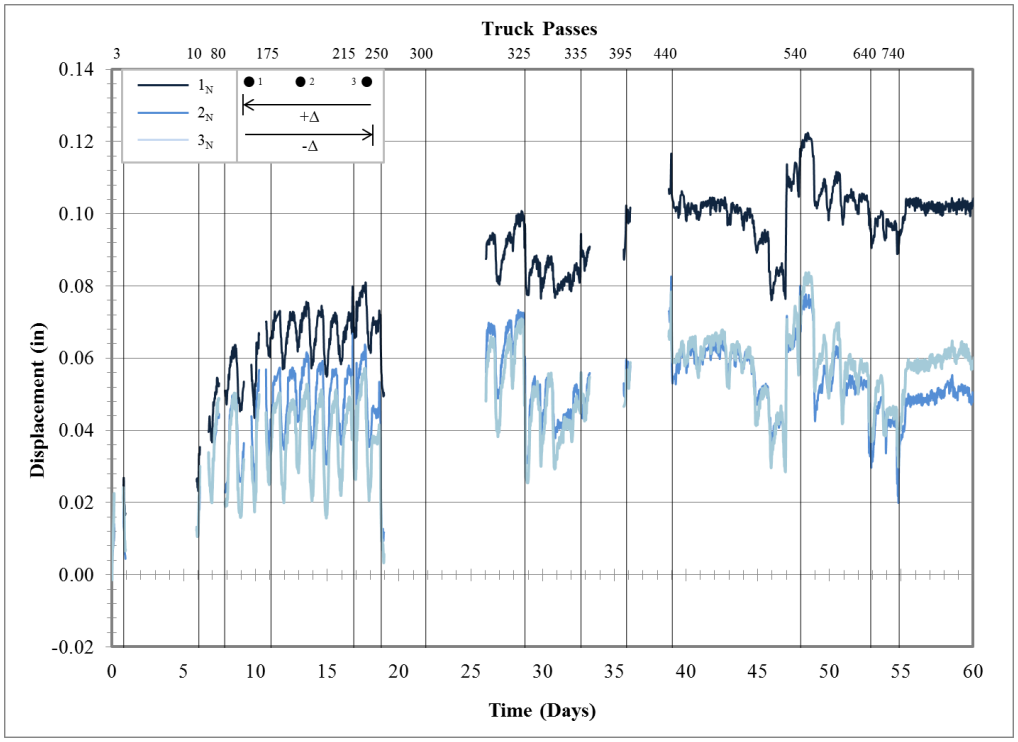


Figure M-1: Tensar BX Type 2 (1-North) (CBR = 2.15).

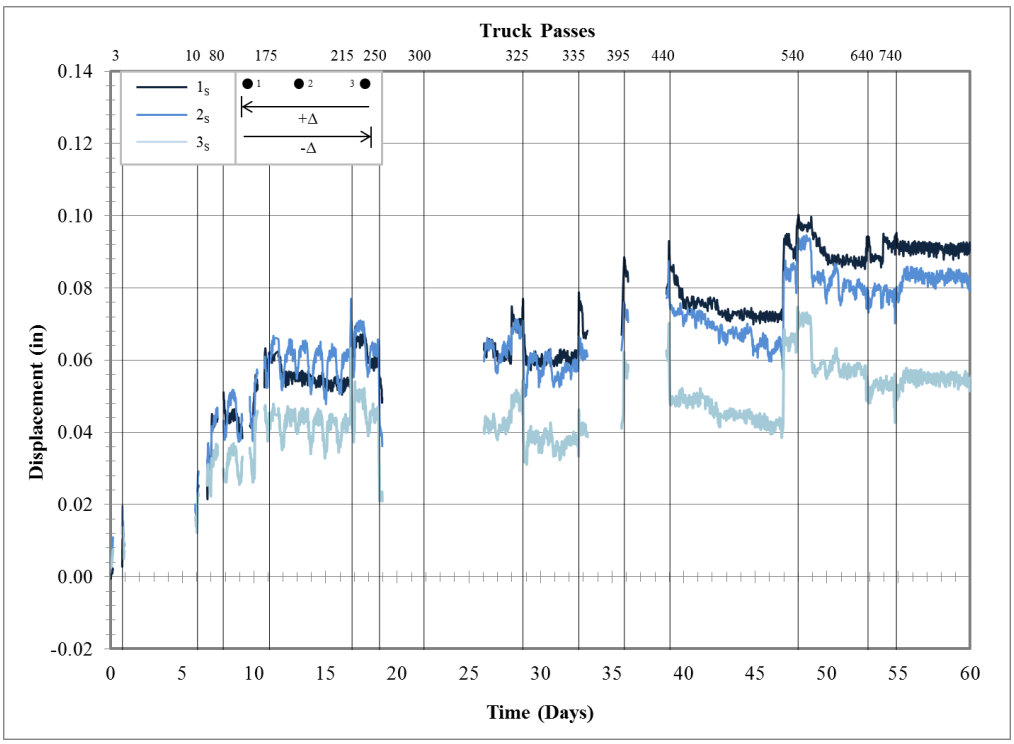


Figure M-2: Tensar BX Type 2 (1-South) (CBR = 2.15).

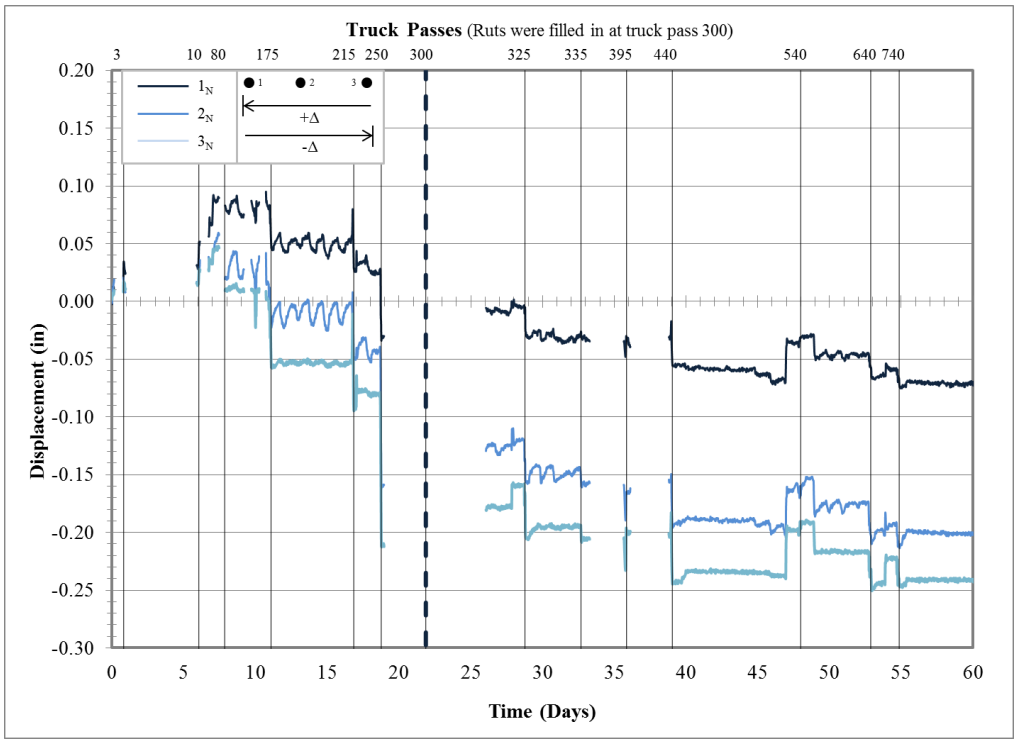


Figure M-3: Tensar BX Type 2 (2-North) (CBR = 1.61).

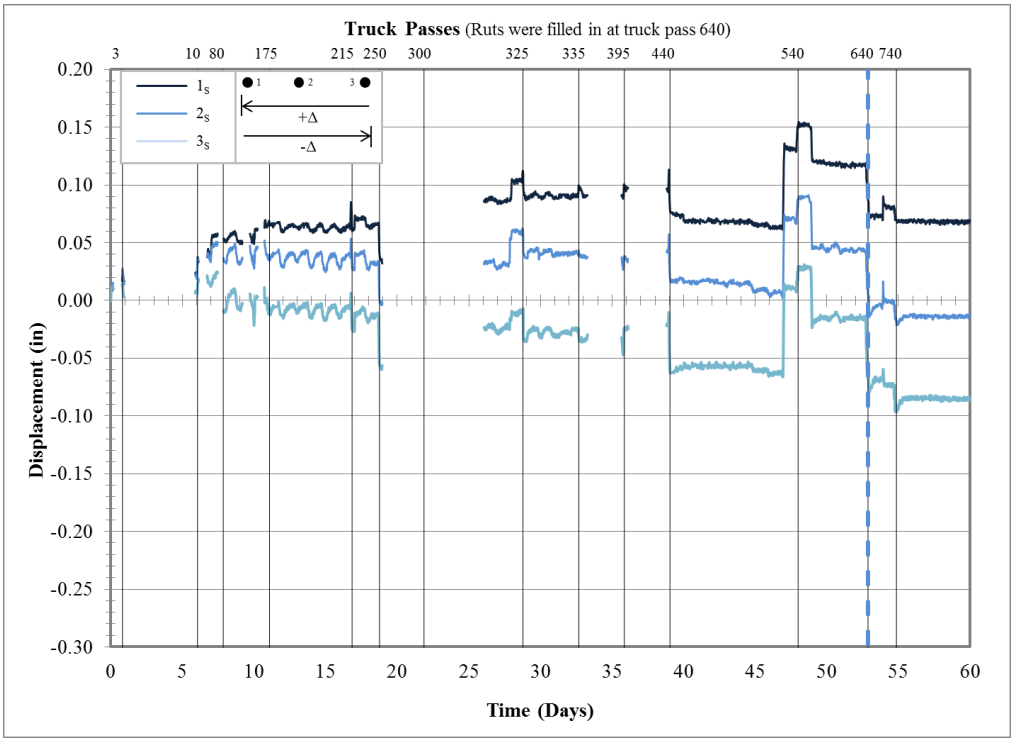


Figure M-4: Tensar BX Type 2 (2-South) (CBR = 1.61).

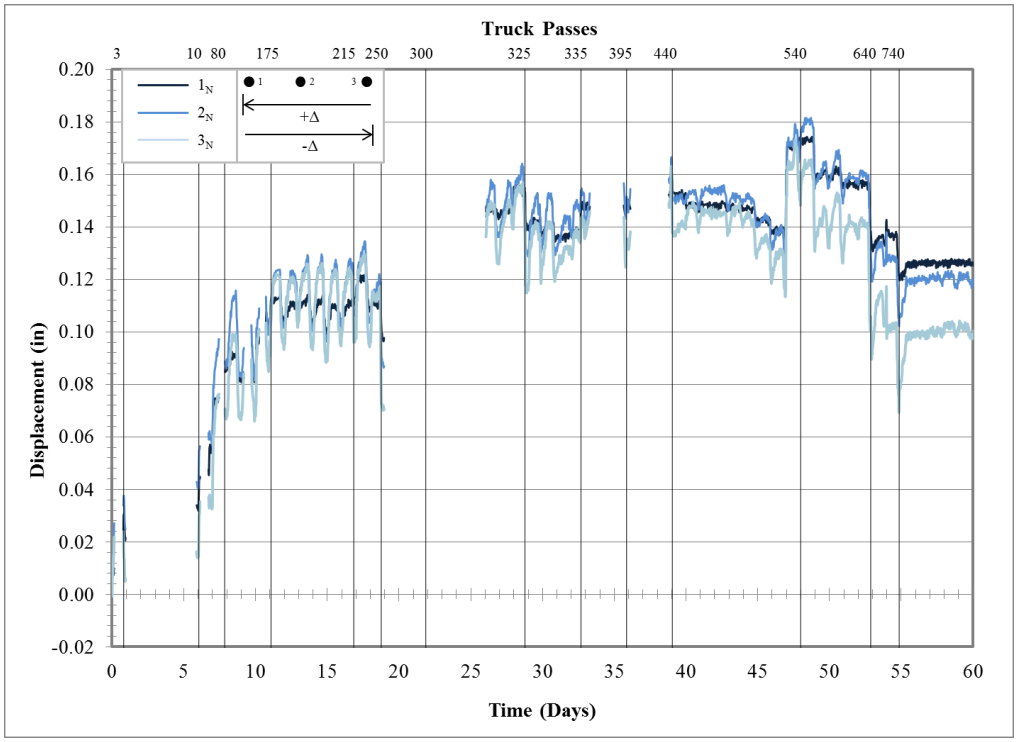


Figure M-5: Tensar BX Type 2 (3-North) (CBR = 1.78).

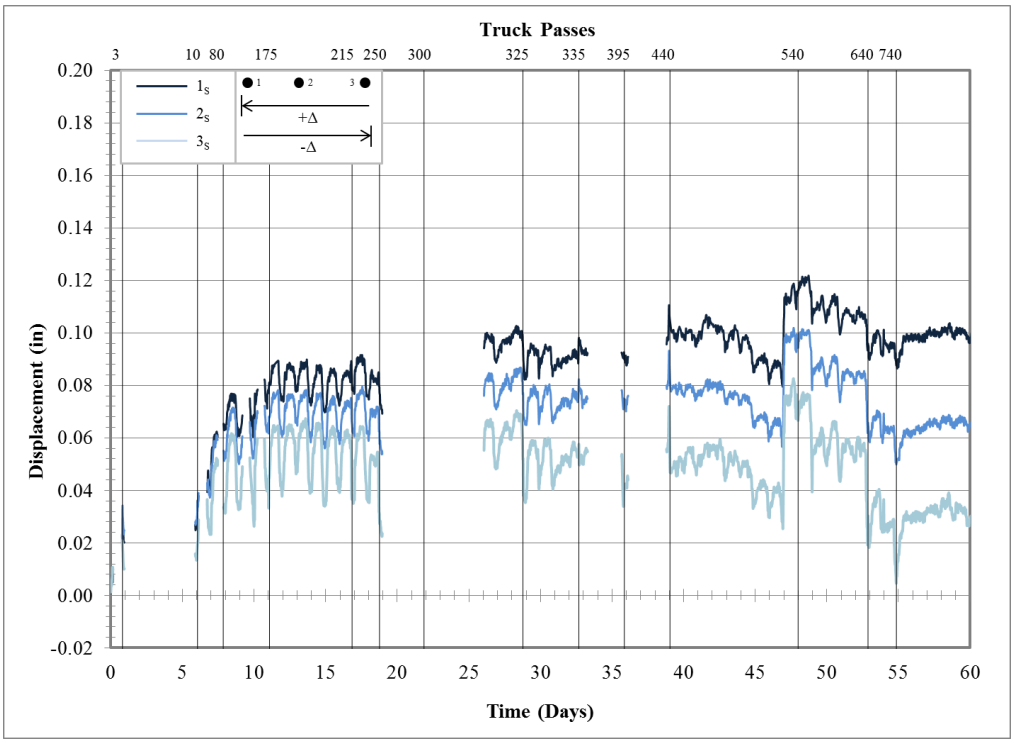


Figure M-6: Tensar BX Type 2 (3-South) (CBR = 1.78).

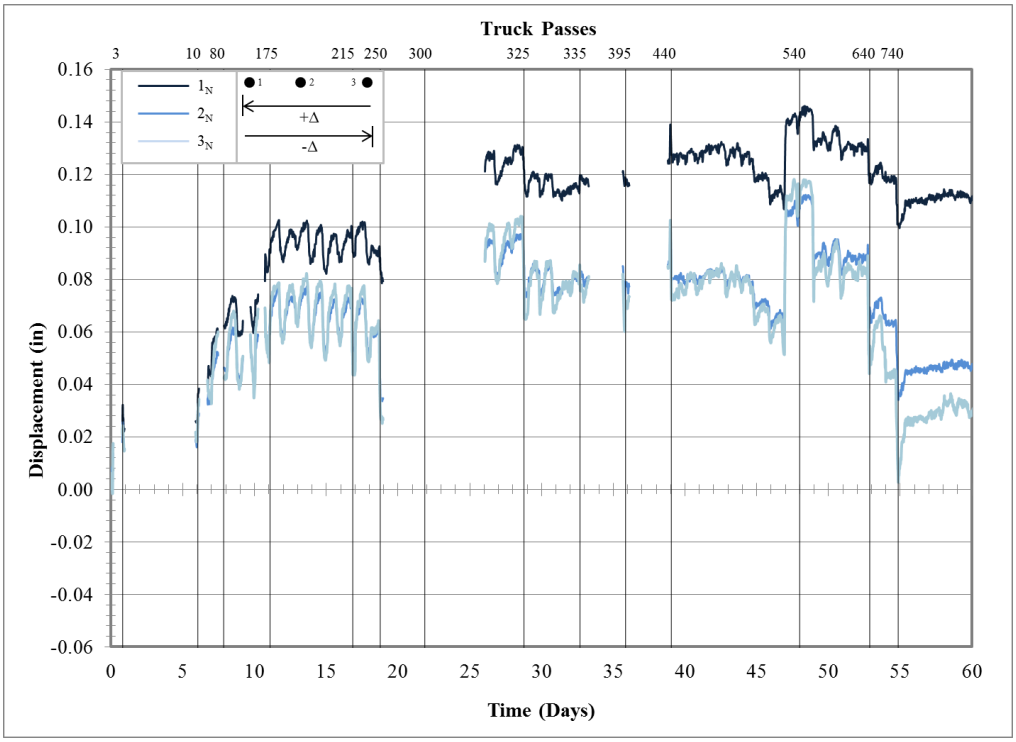


Figure M-7: NAUE Secugrid 30/30 Q1 (4-North).

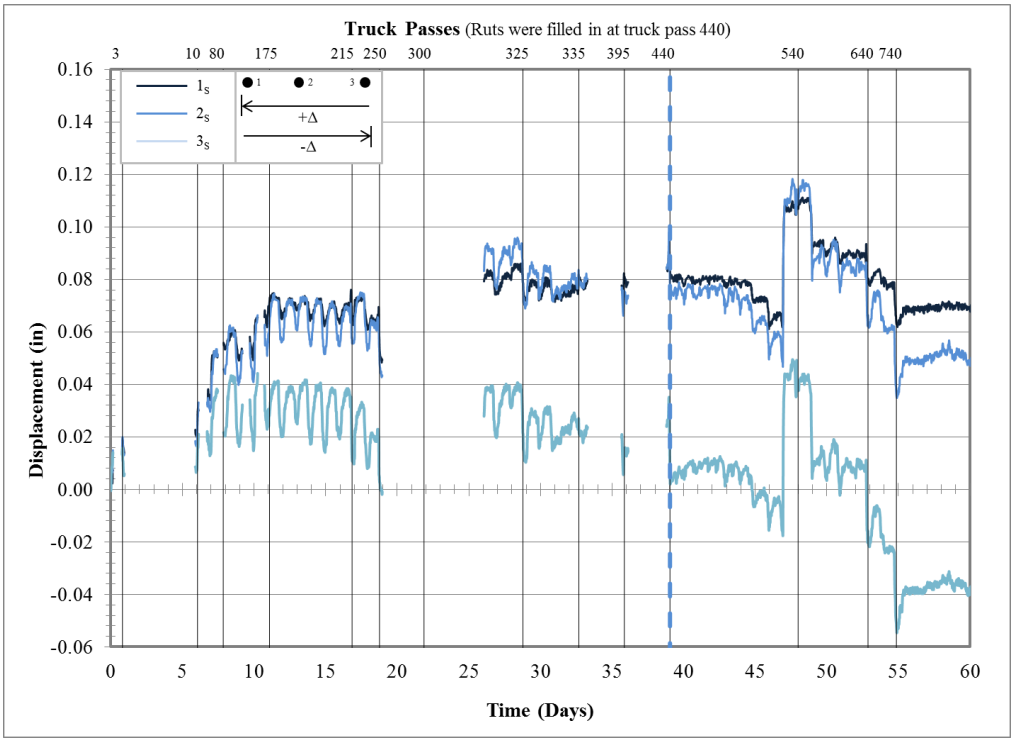


Figure M-8: NAUE Secugrid 30/30 Q1 (4-South).

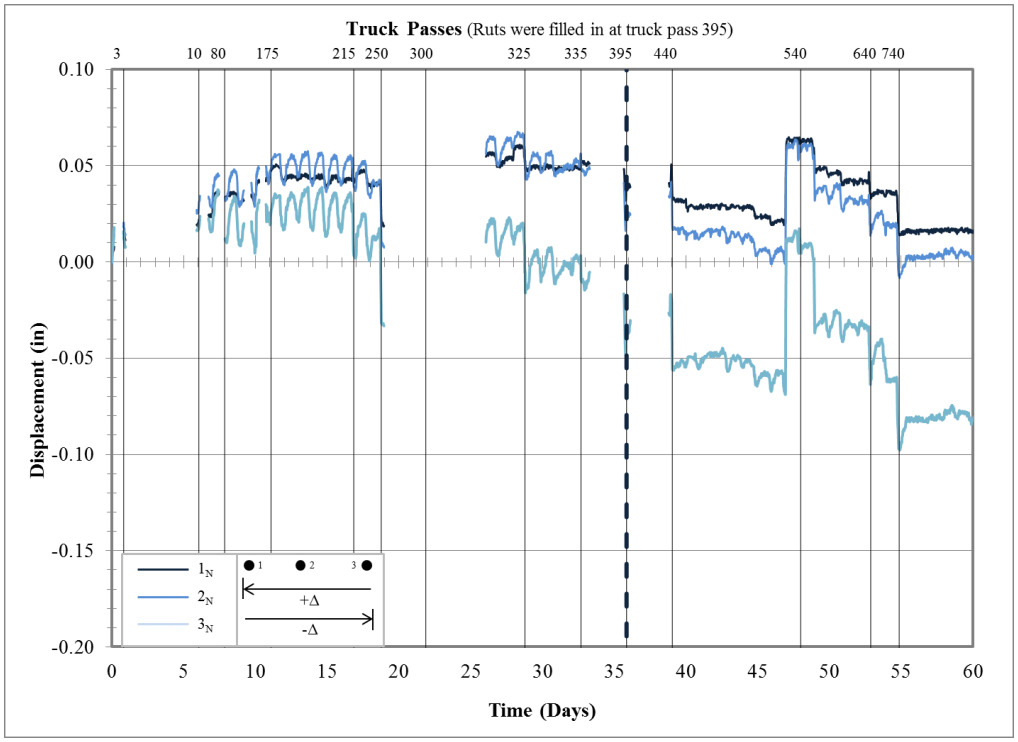


Figure M-9: Colbond Enkagrid Max 30 (5-North).

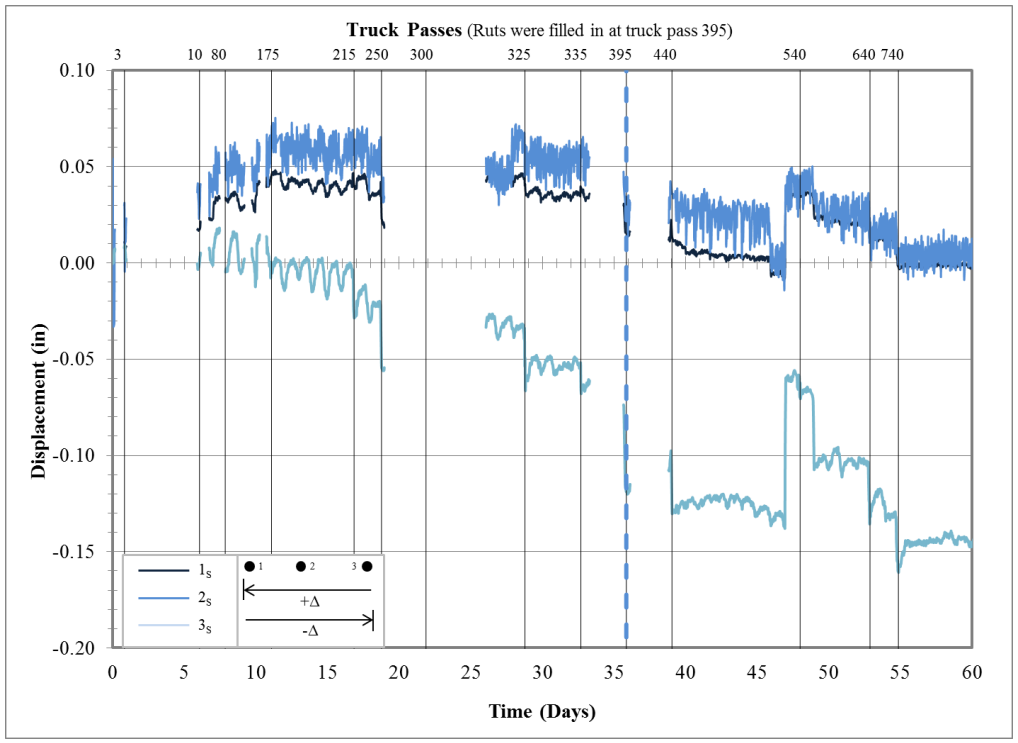


Figure M-10: Colbond Enkagrid Max 30 (5-South).

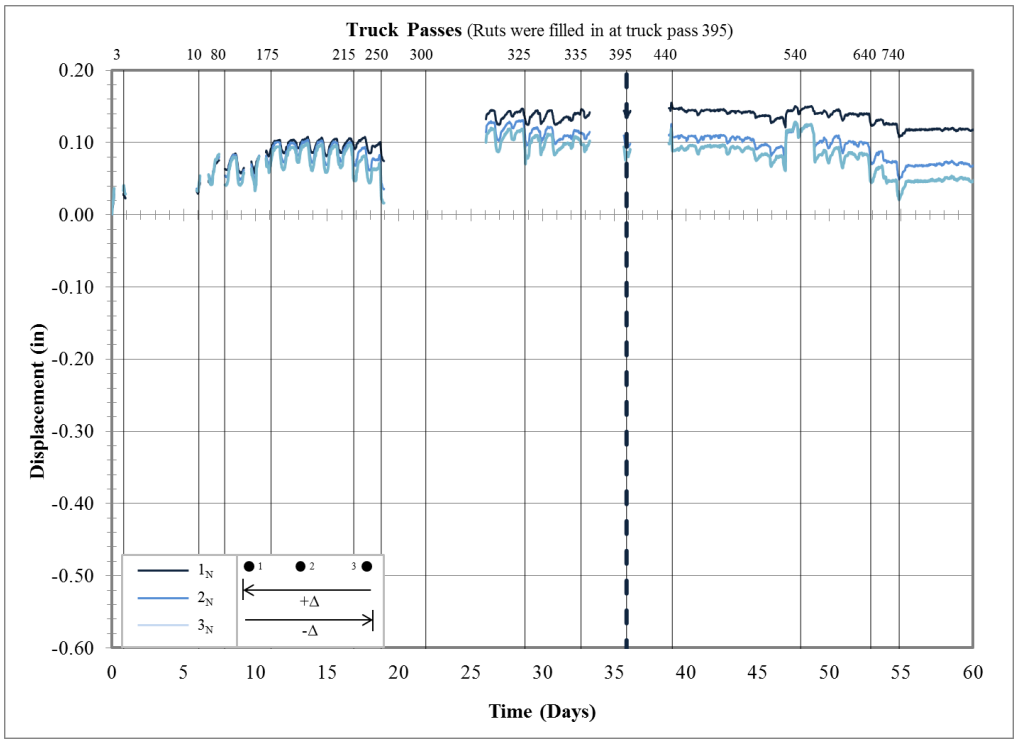


Figure M-11: Synteen SF 11 (6-North).

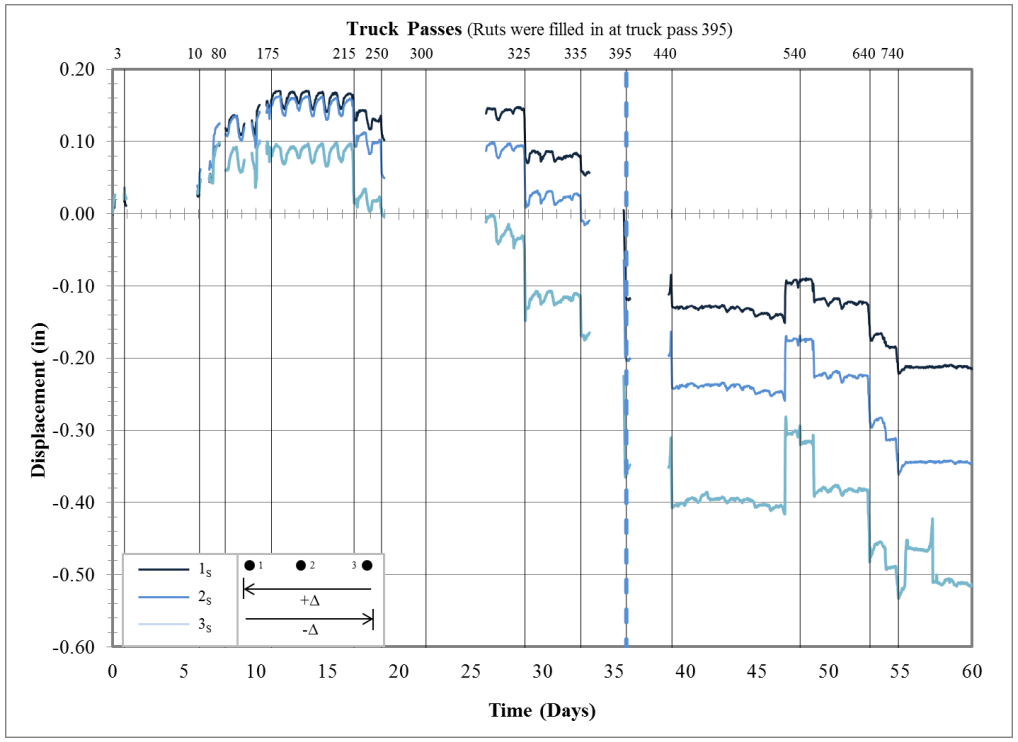


Figure M-12: Synteen SF 11 (6-South).

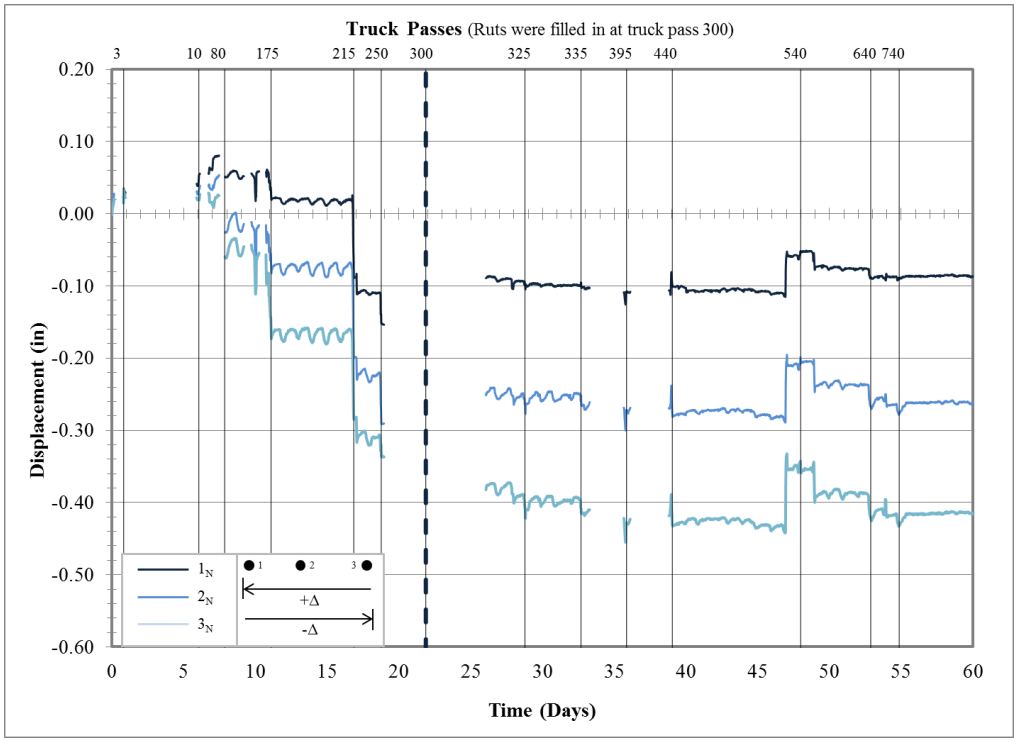


Figure M-13: Synteen SF 12 (7-North).

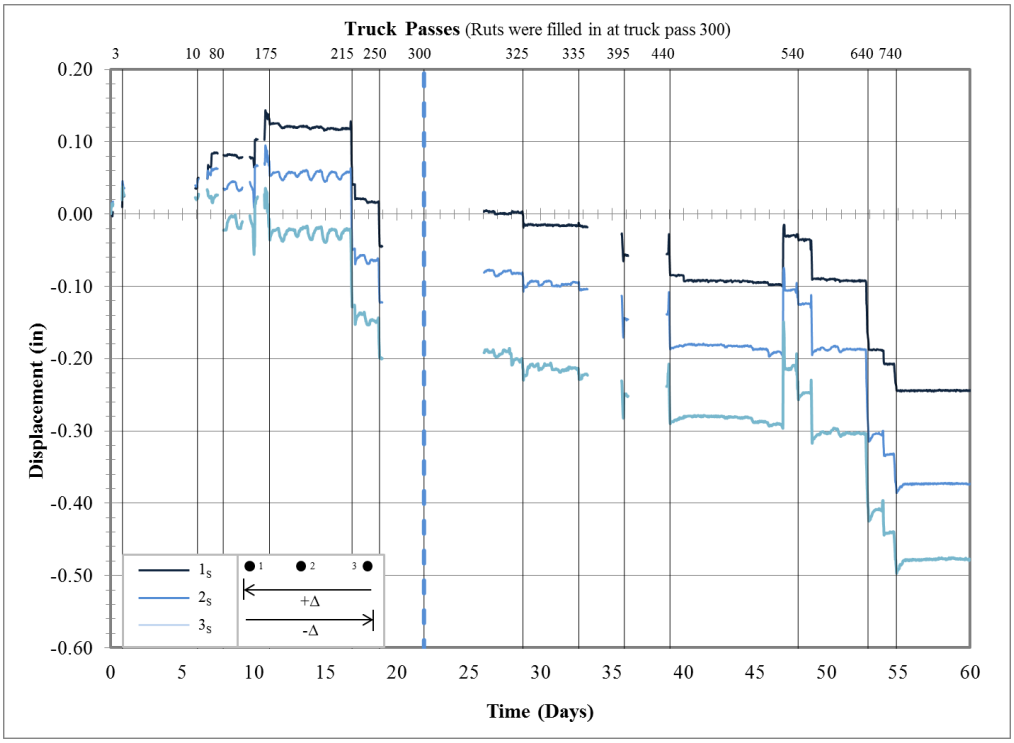


Figure M-14: Synteen SF 12 (7-South).

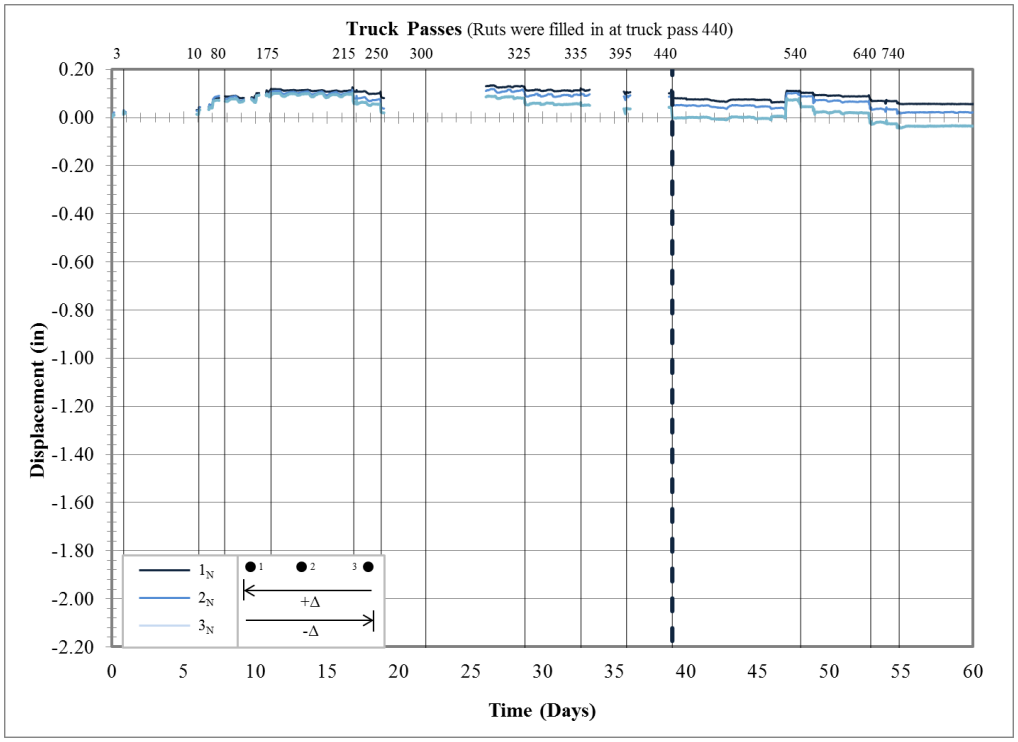


Figure M-15: TenCate Mirafi BXG 11 (8-North).

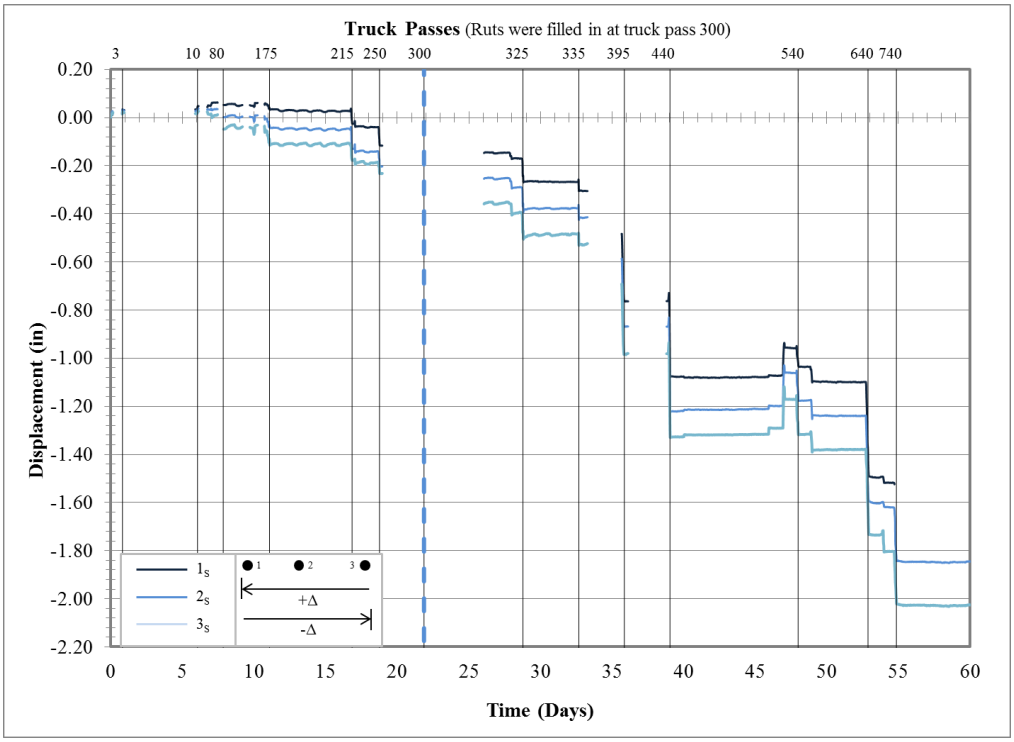


Figure M-16: TenCate Mirafi BXG 11 (8-South).

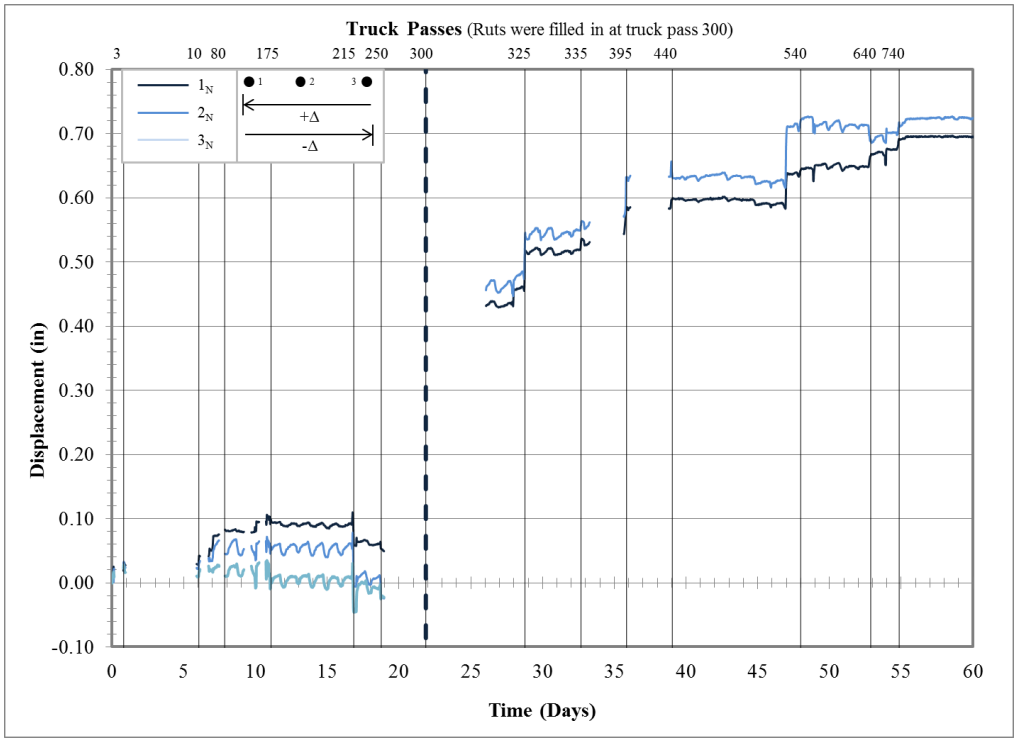


Figure M-17: Huesker Fornit 30 (9-North).

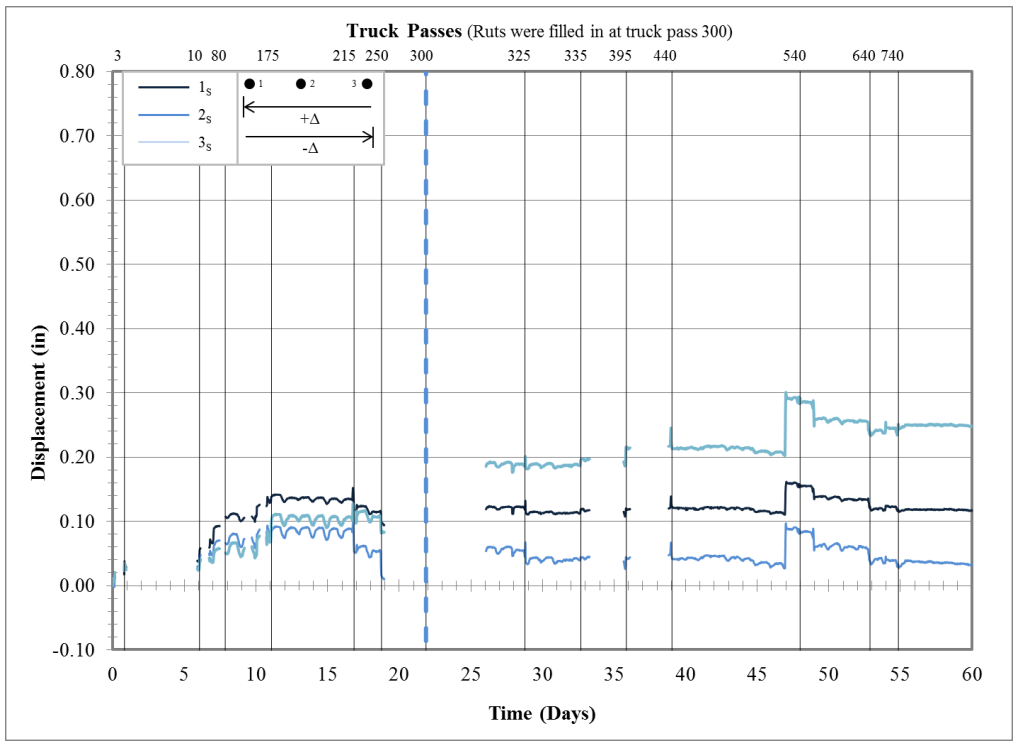


Figure M-18: Huesker Fornit 30 (9-South).

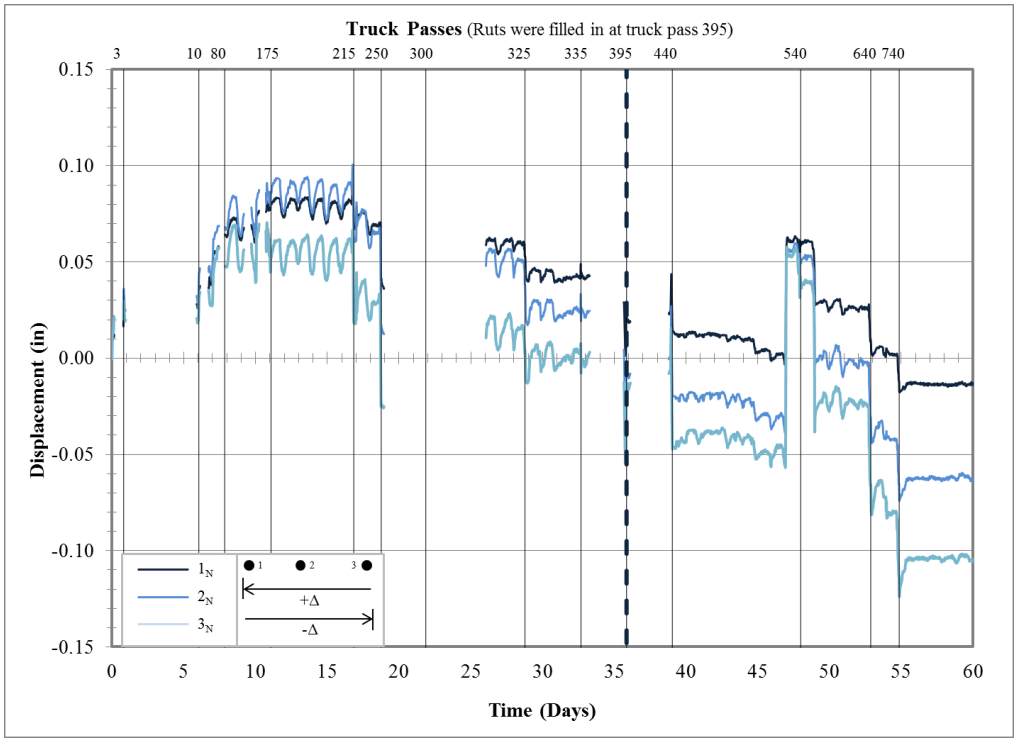


Figure M-19: SynTec Tenax MS330 (10-North).

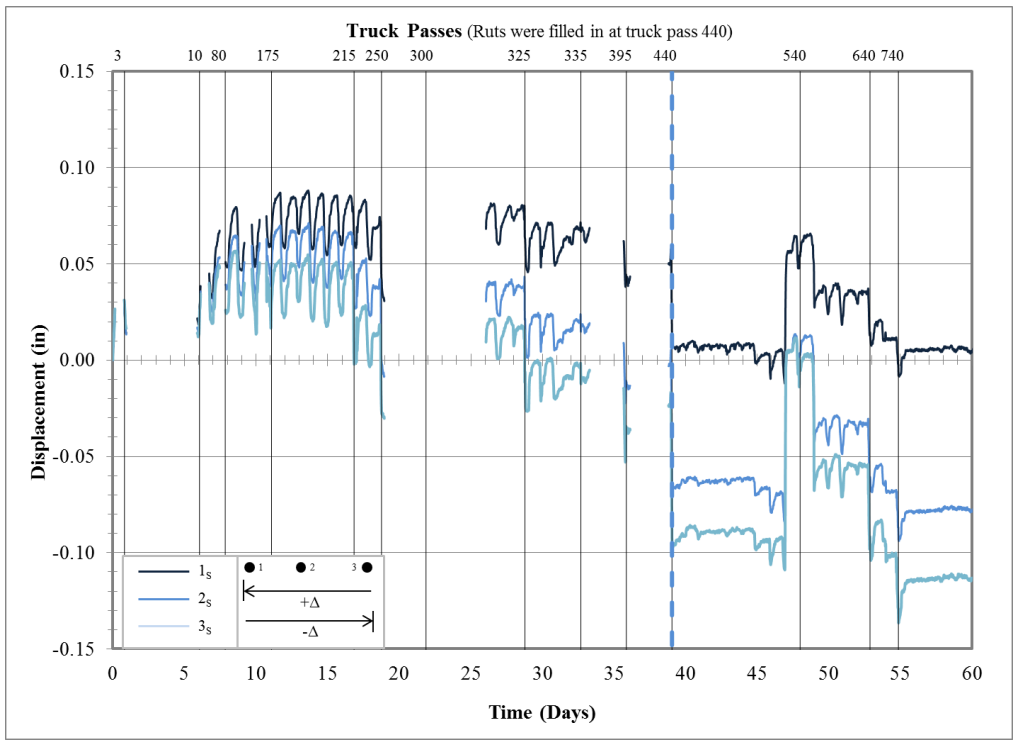


Figure M-20: SynTec Tenax MS330 (10-South).

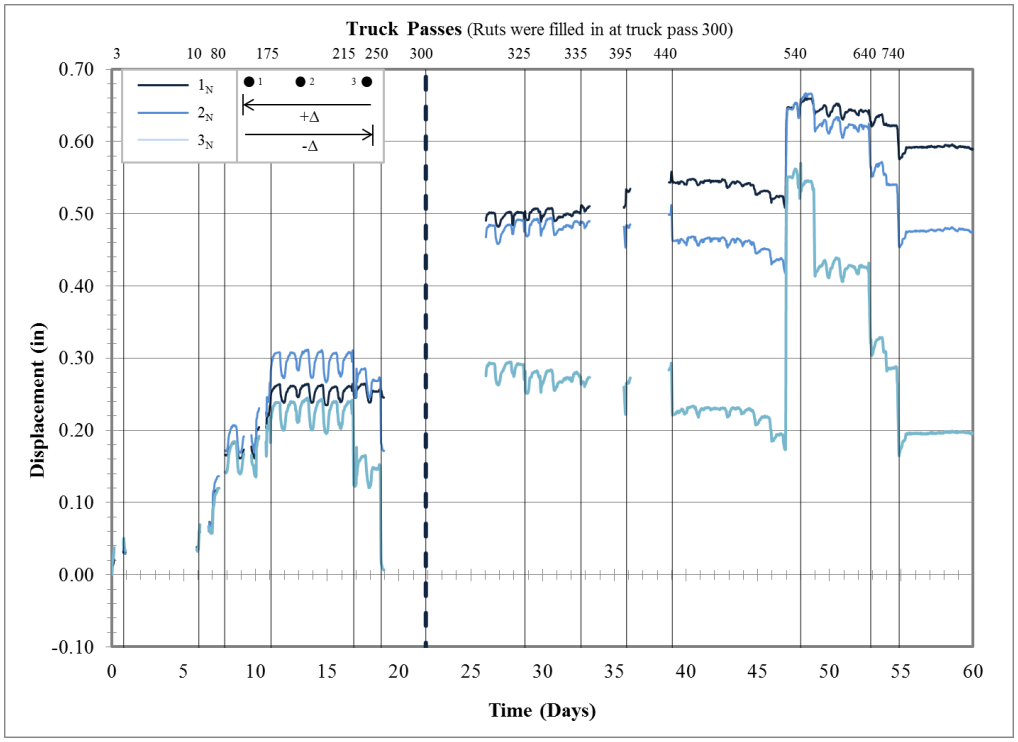


Figure M-21: Tensar TX 140 (11-North).

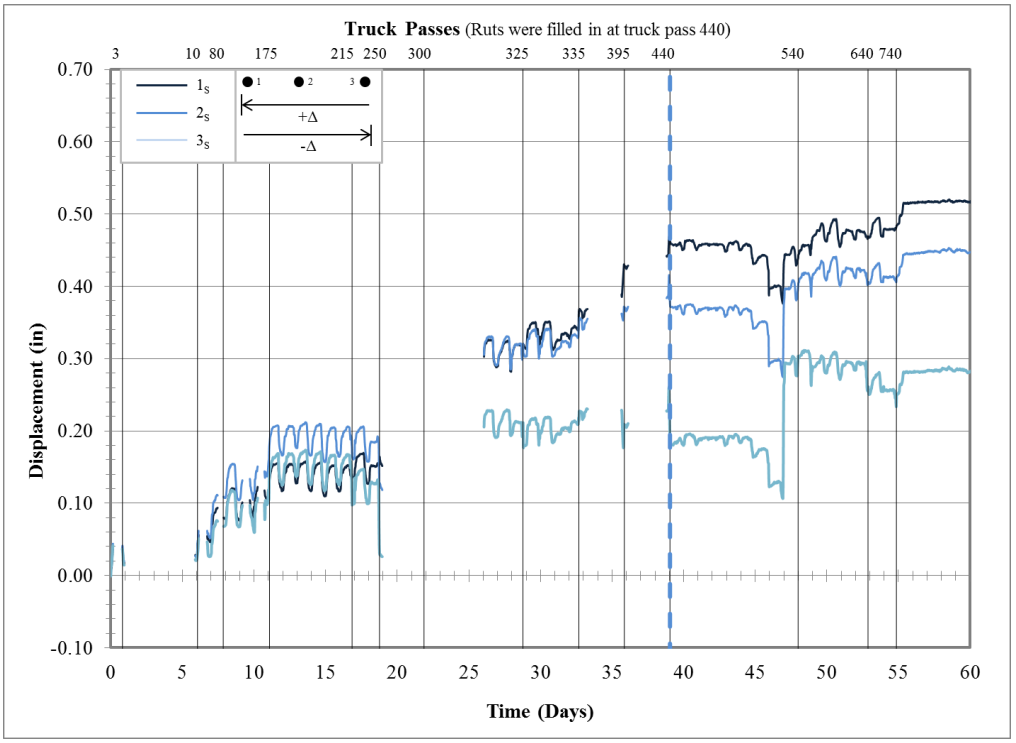


Figure M-22: Tensar TX 140 (11-South).

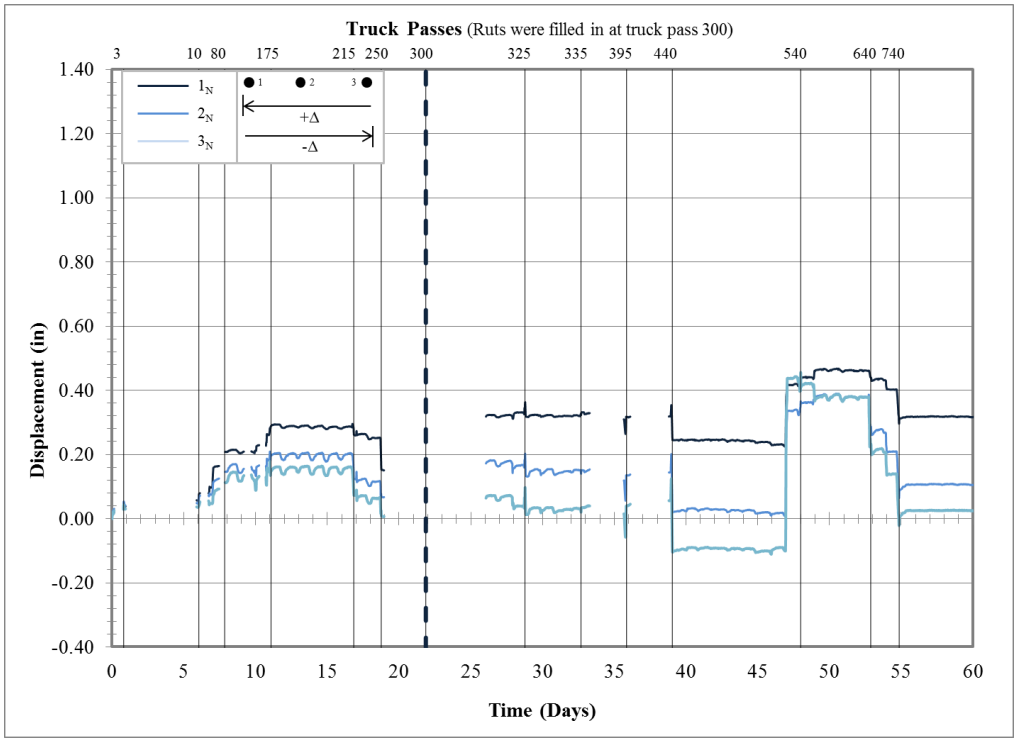


Figure M-23: Tensar TX 160 (12-North).

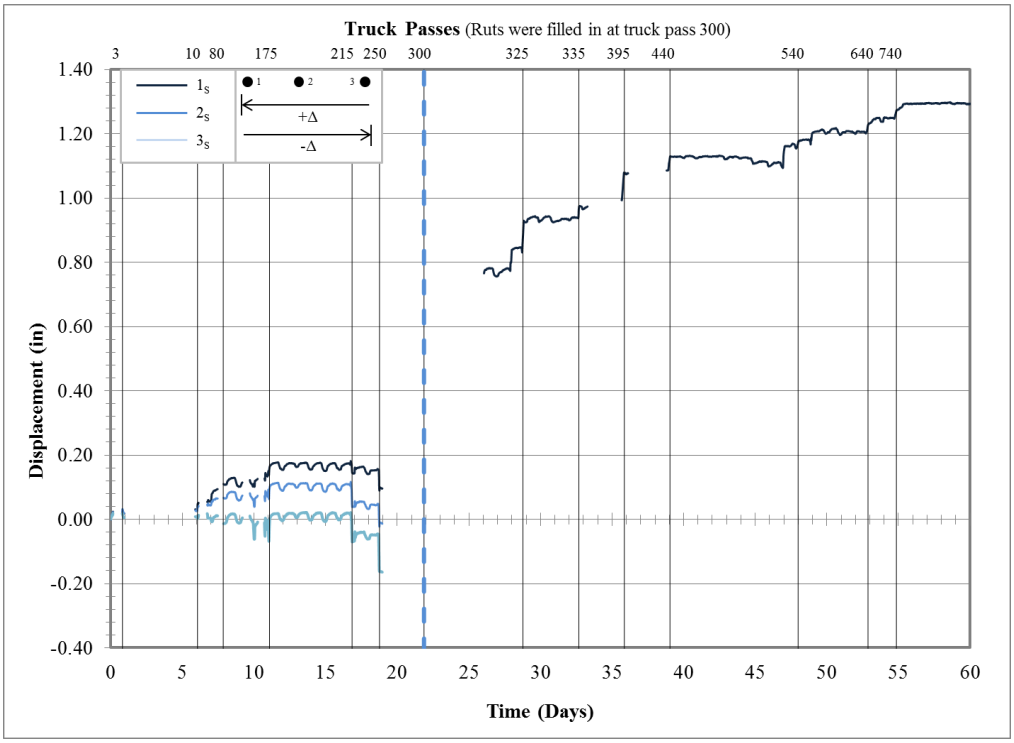


Figure M-24: Tensar TX 160 (12-South).

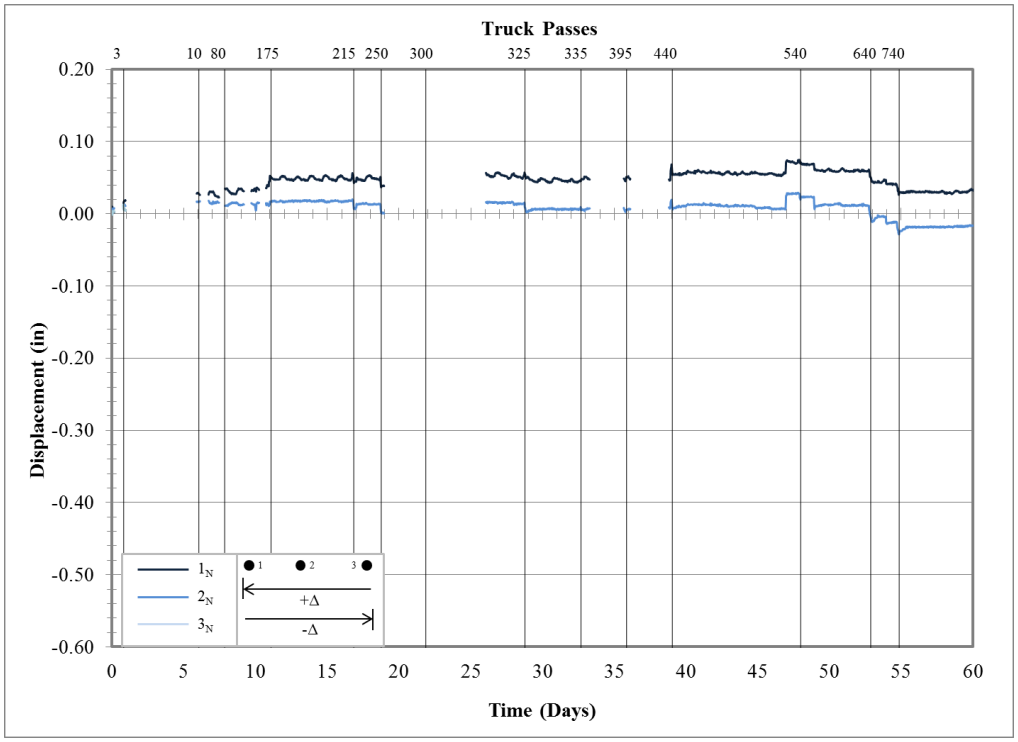


Figure M-25: TenCate Mirafi RS580i (13-North).

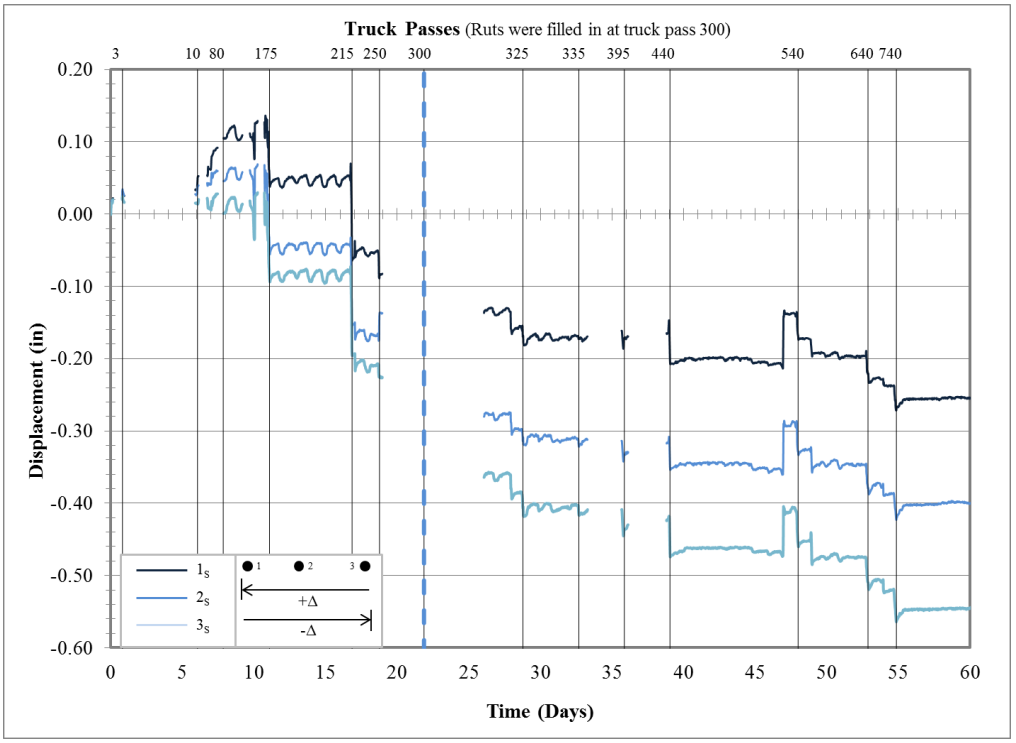


Figure M-26: TenCate Mirafi RS580i (13-South).

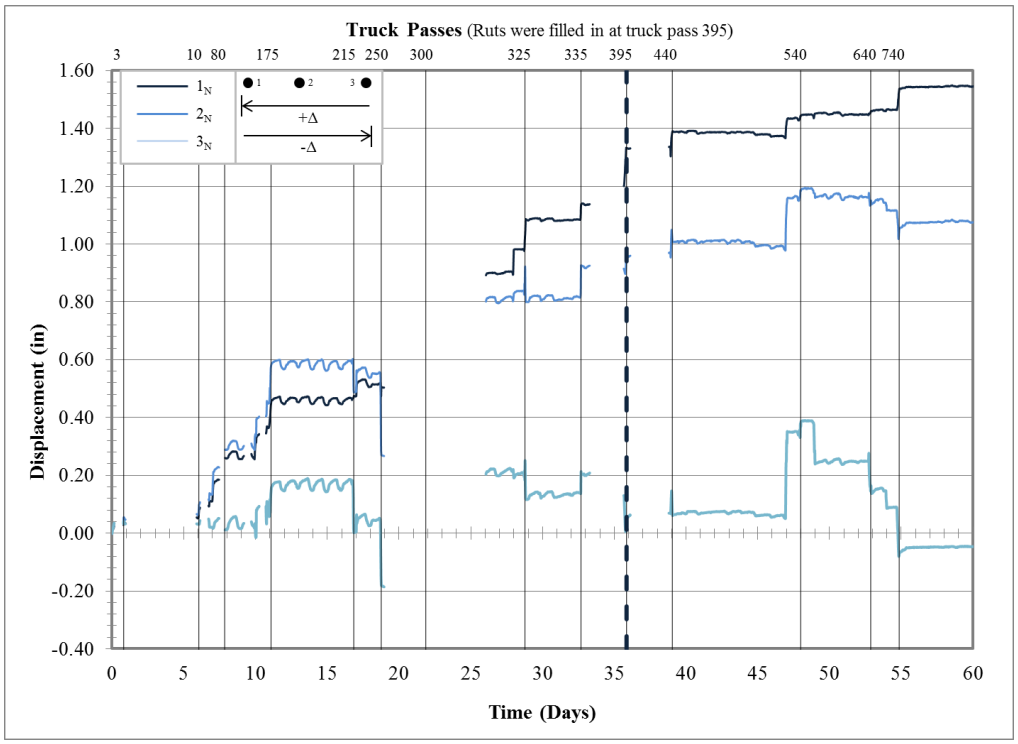


Figure M-27: Propex Geotex 801 (14-North).

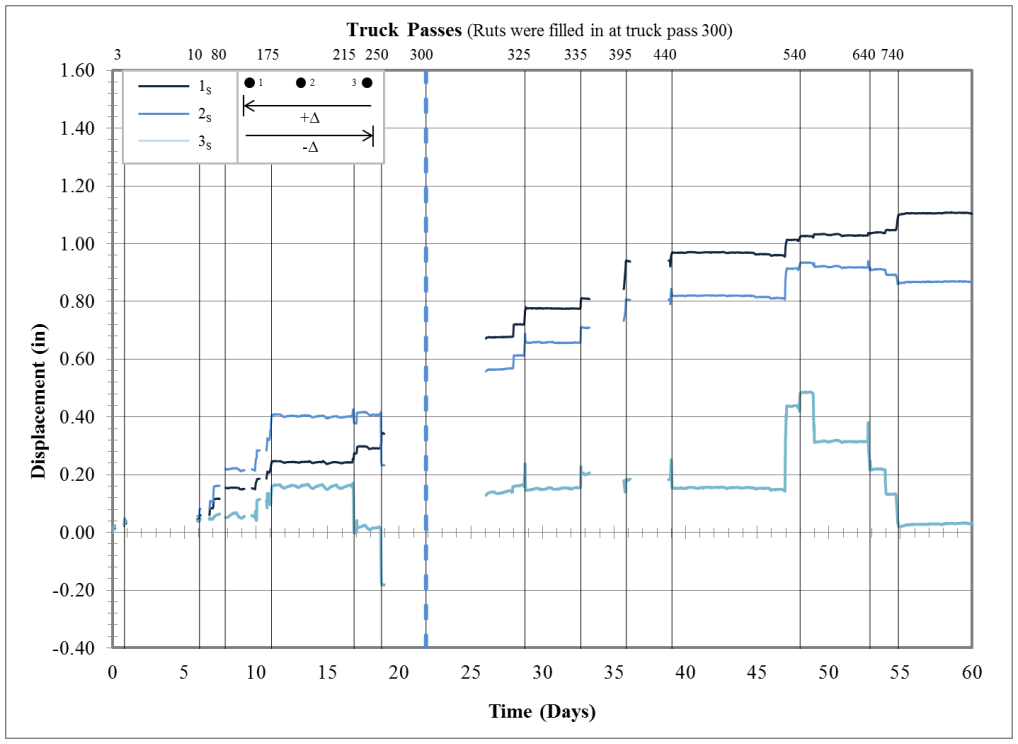


Figure M-28: Propex Geotex 801 (14-South).

APPENDIX N:

LVDT DYNAMIC STRAIN PLOTS

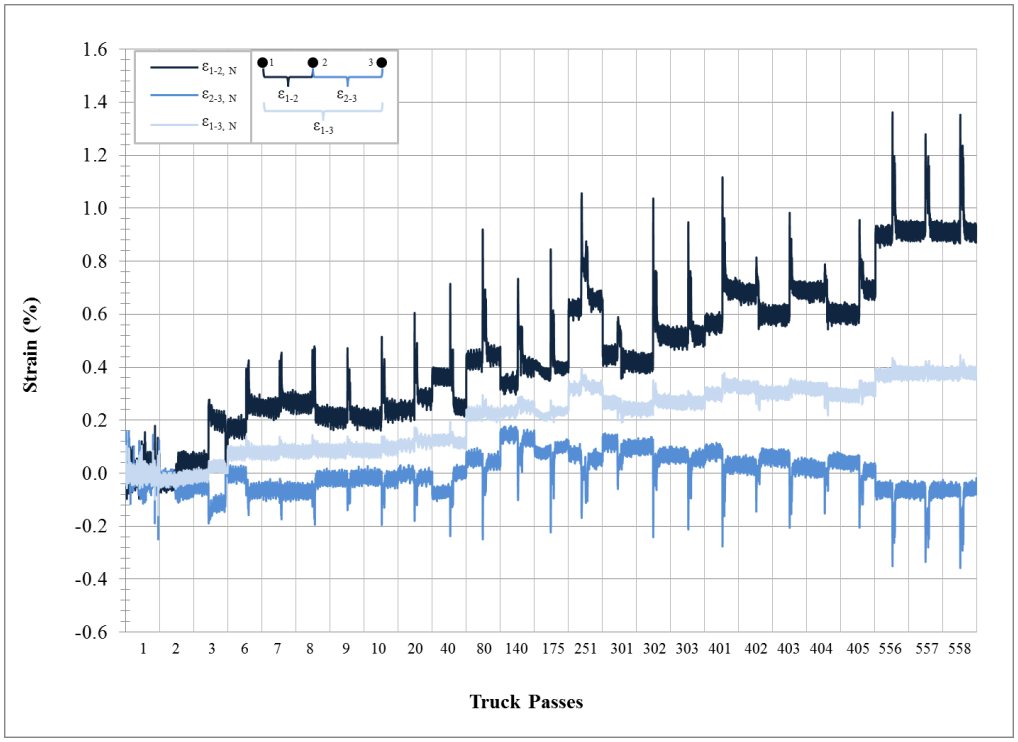


Figure N-1: Tensar BX Type 2 (1-North) (CBR = 2.15).

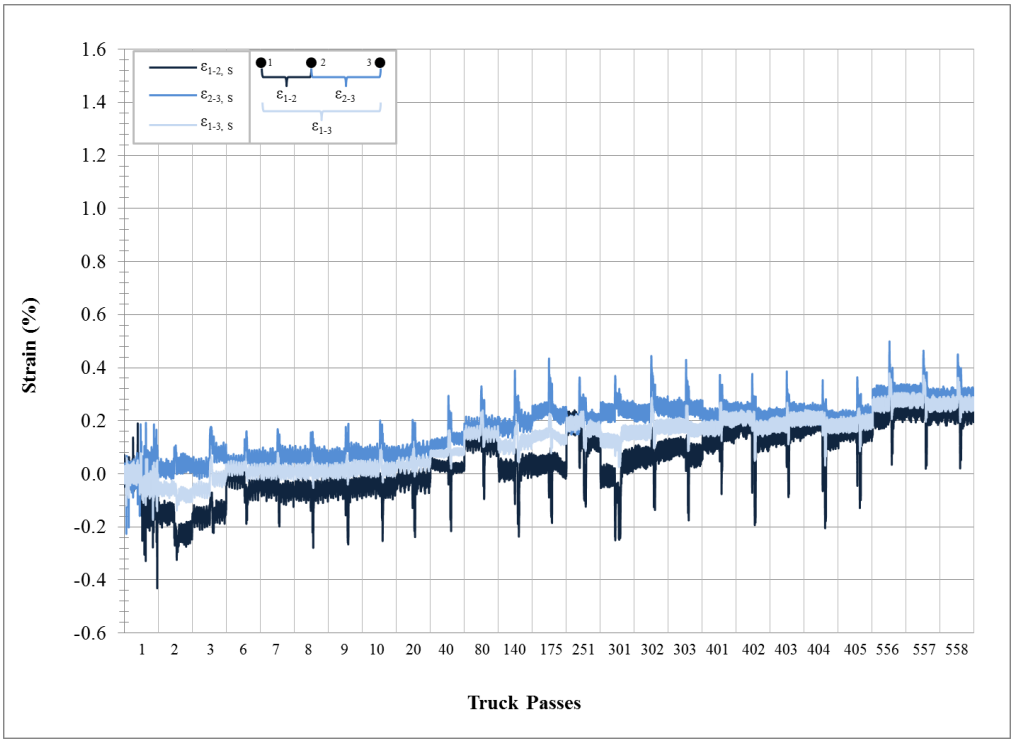


Figure N-2: Tensar BX Type 2 (1-South) (CBR = 2.15).

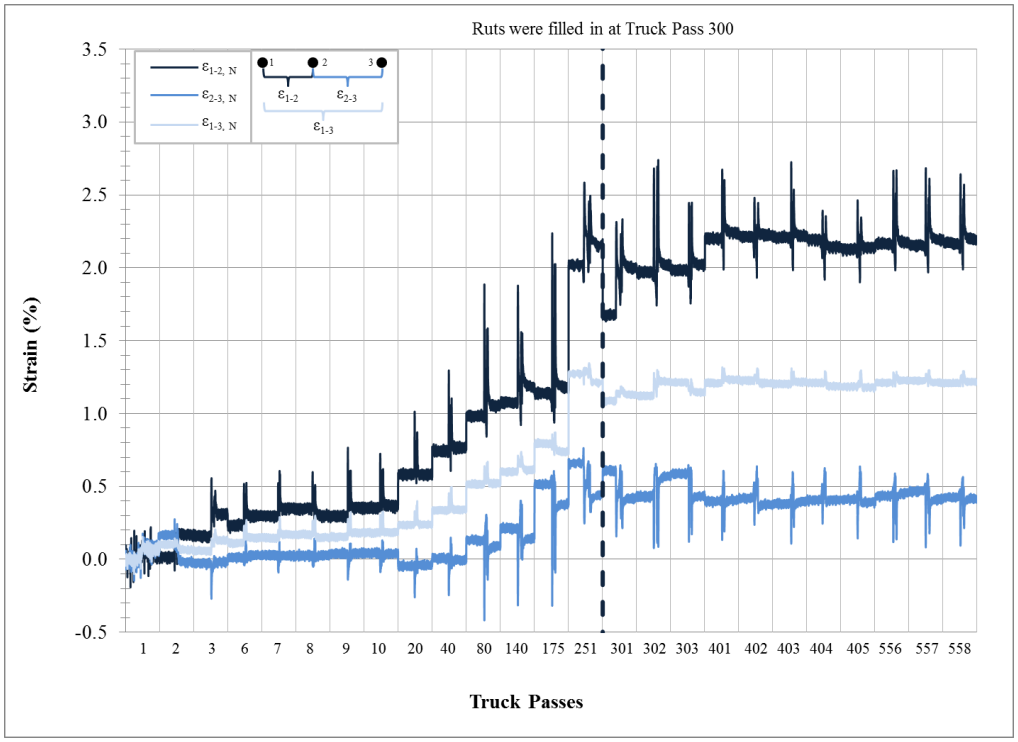


Figure N-3: Tensar BX Type 2 (2-North) (CBR = 1.61).

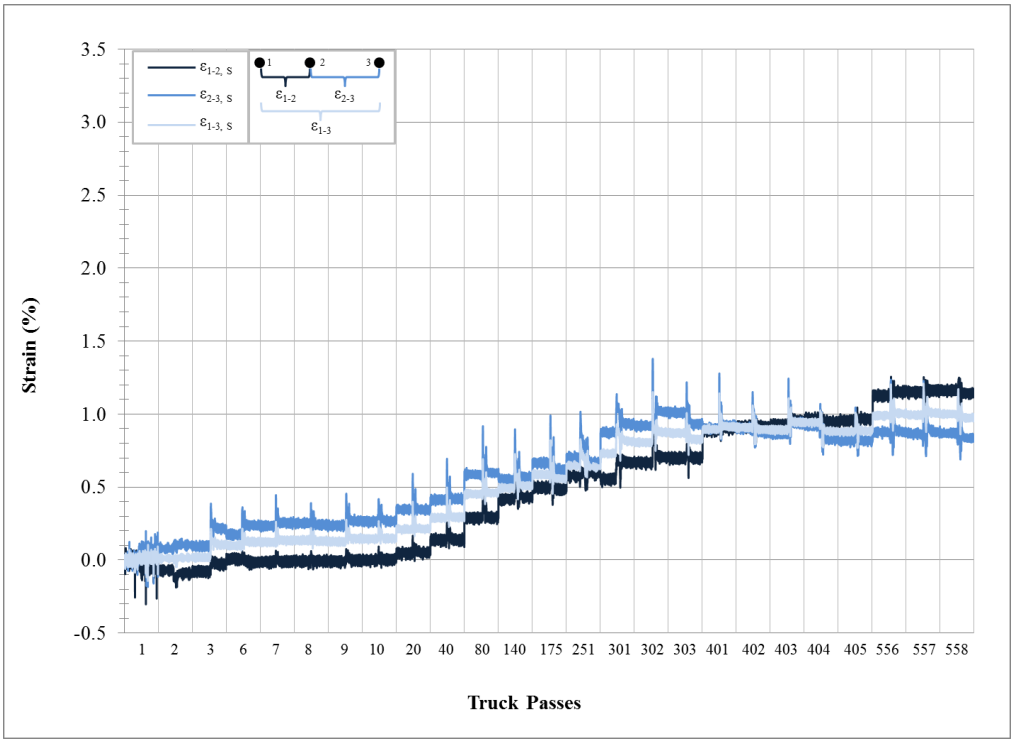


Figure N-4: Tensar BX Type 2 (2-South) (CBR = 1.61).

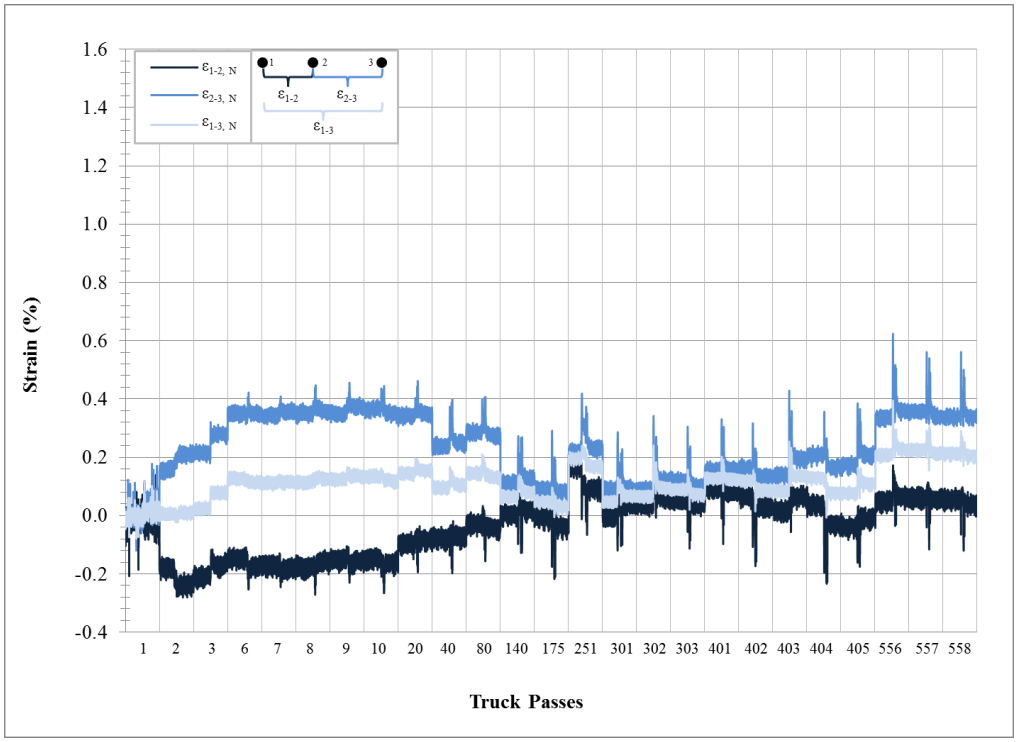


Figure N-5: Tensar BX Type 2 (3-North) (CBR = 1.78).

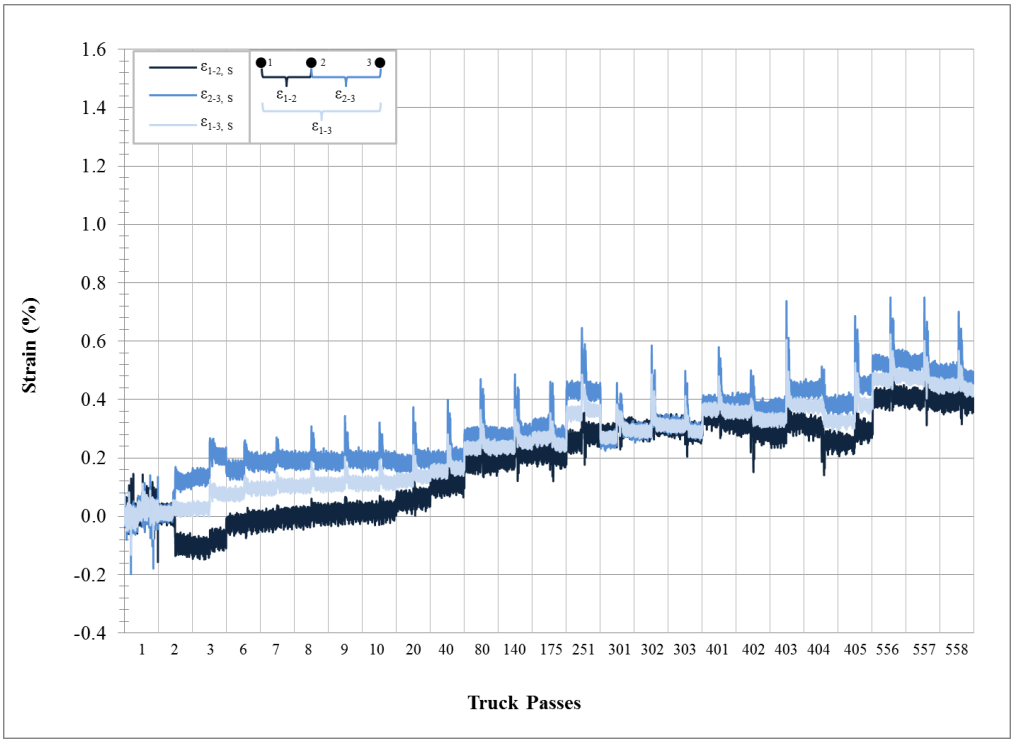


Figure N-6: Tensar BX Type 2 (3-South) (CBR = 1.78).

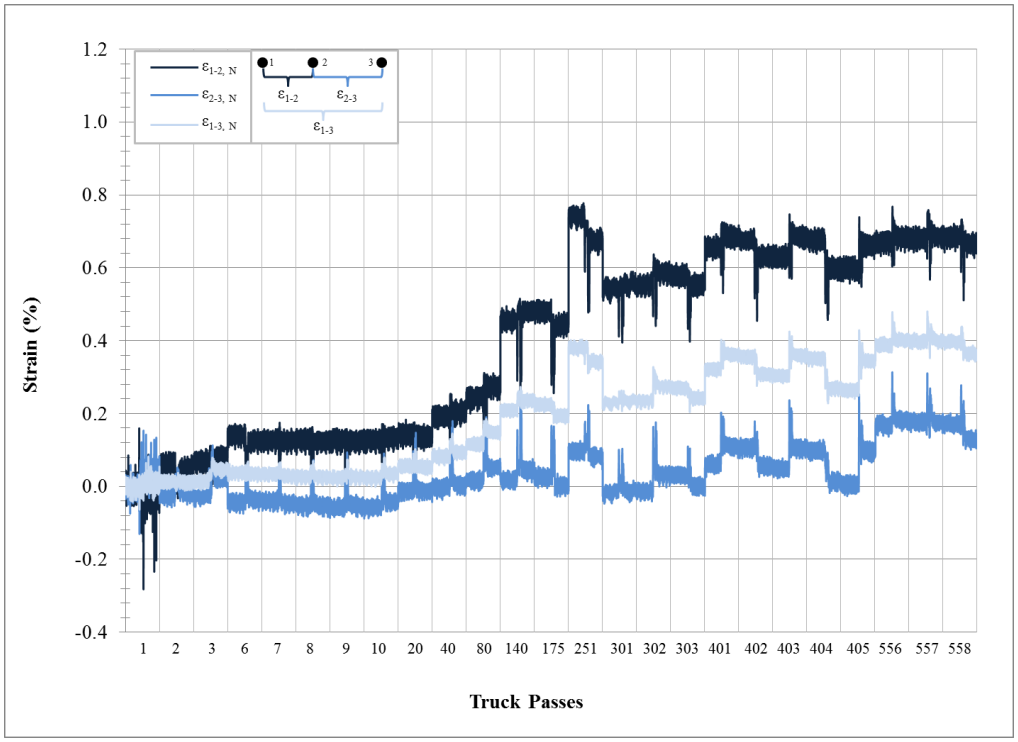


Figure N-7: NAUE Secugrid 30/30 Q1 (4-North).

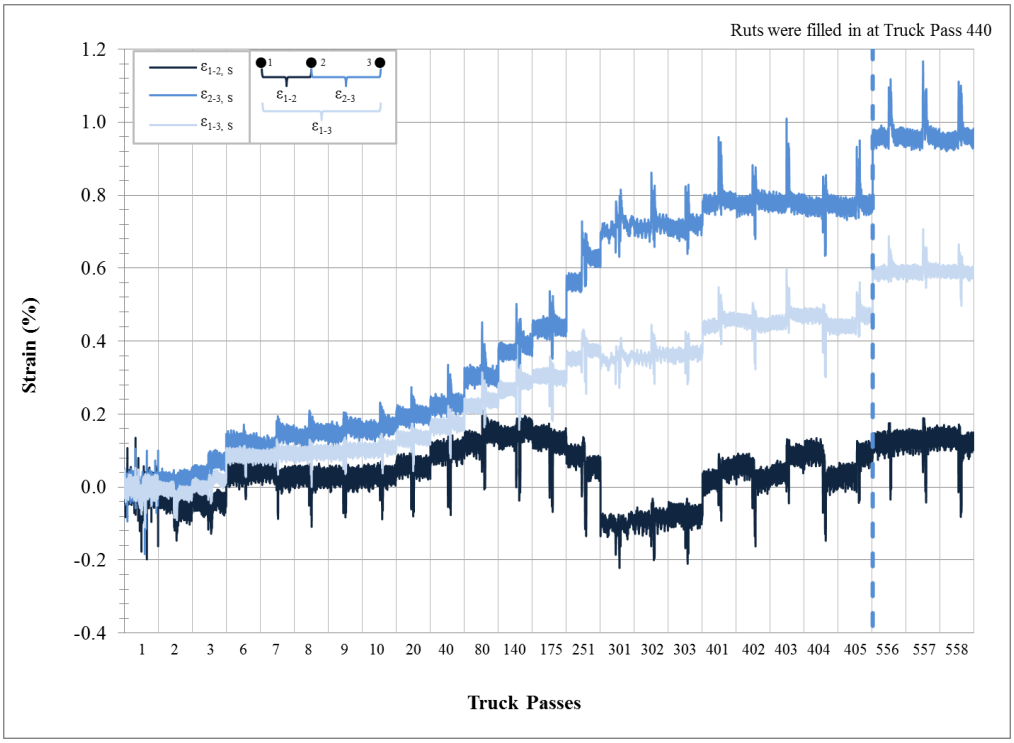


Figure N-8: NAUE Secugrid 30/30 Q1 (4-South).

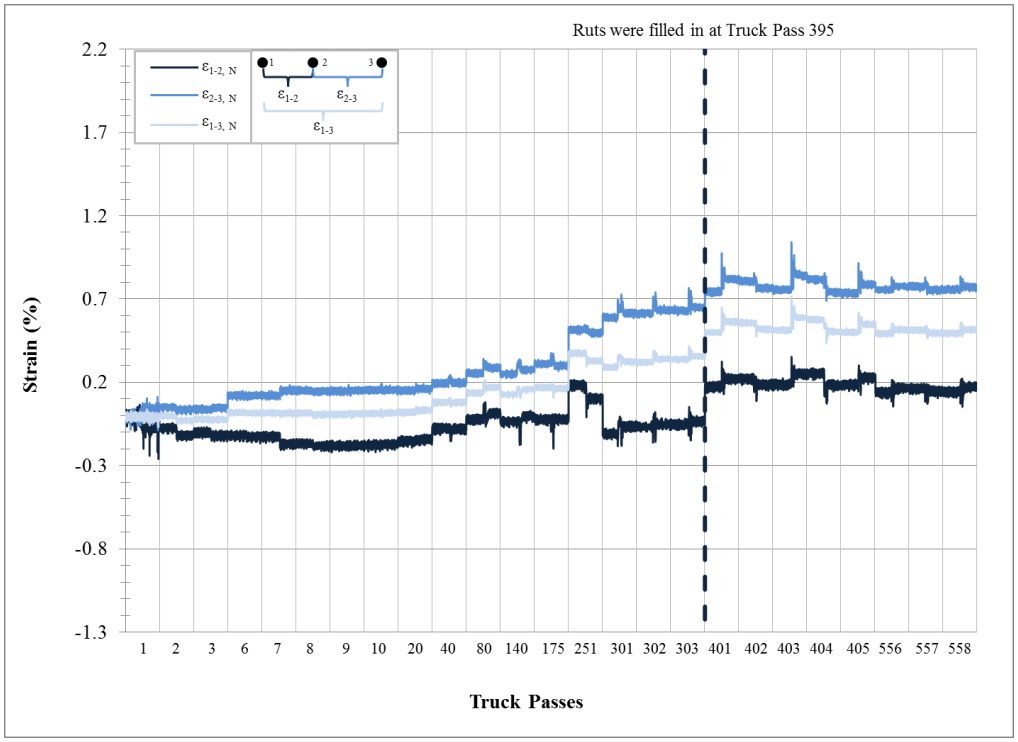


Figure N-9: Colbond Enkagrid Max 30 (5-North).

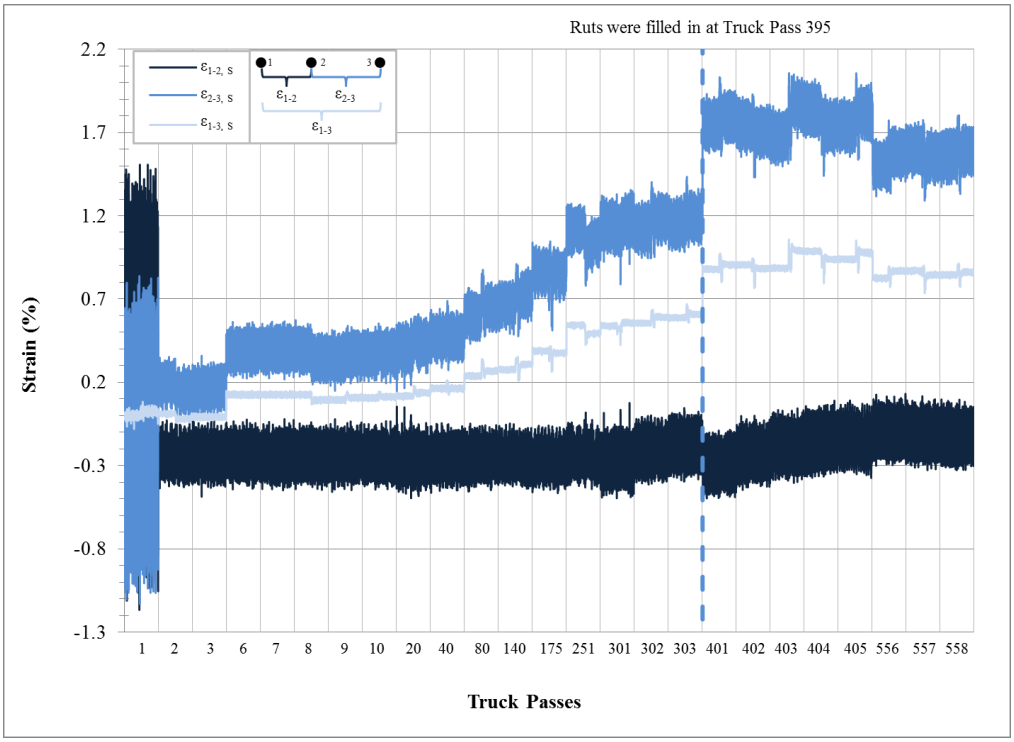


Figure N-10: Colbond Enkagrid Max 30 (5-South).

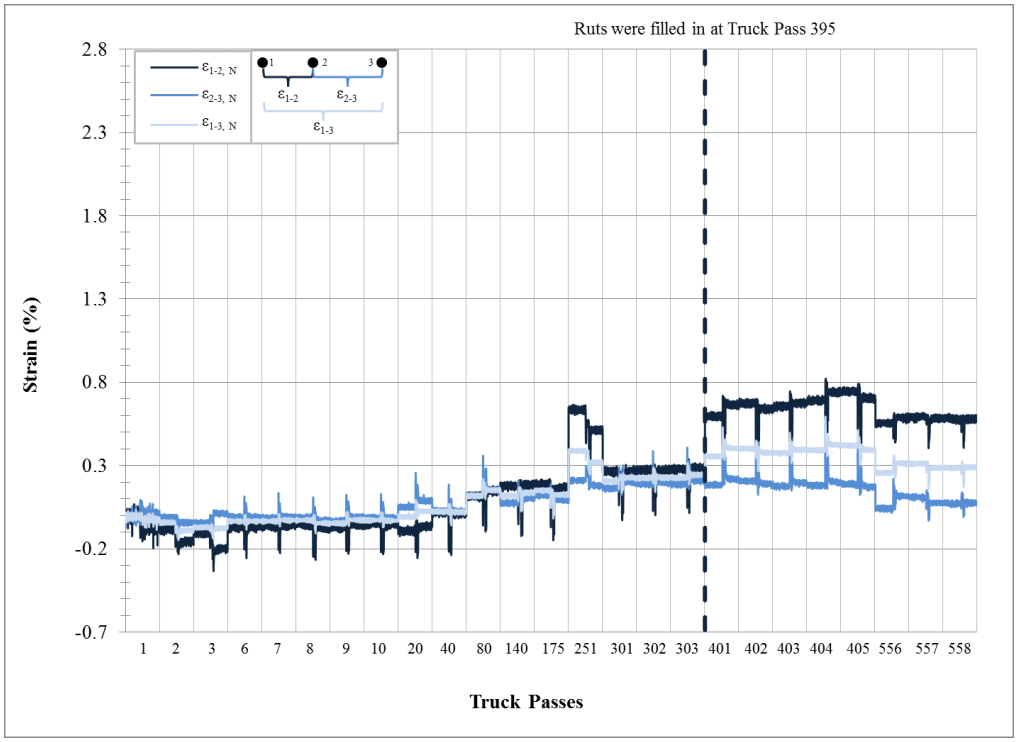


Figure N-11: Synteen SF 11 (6-North).

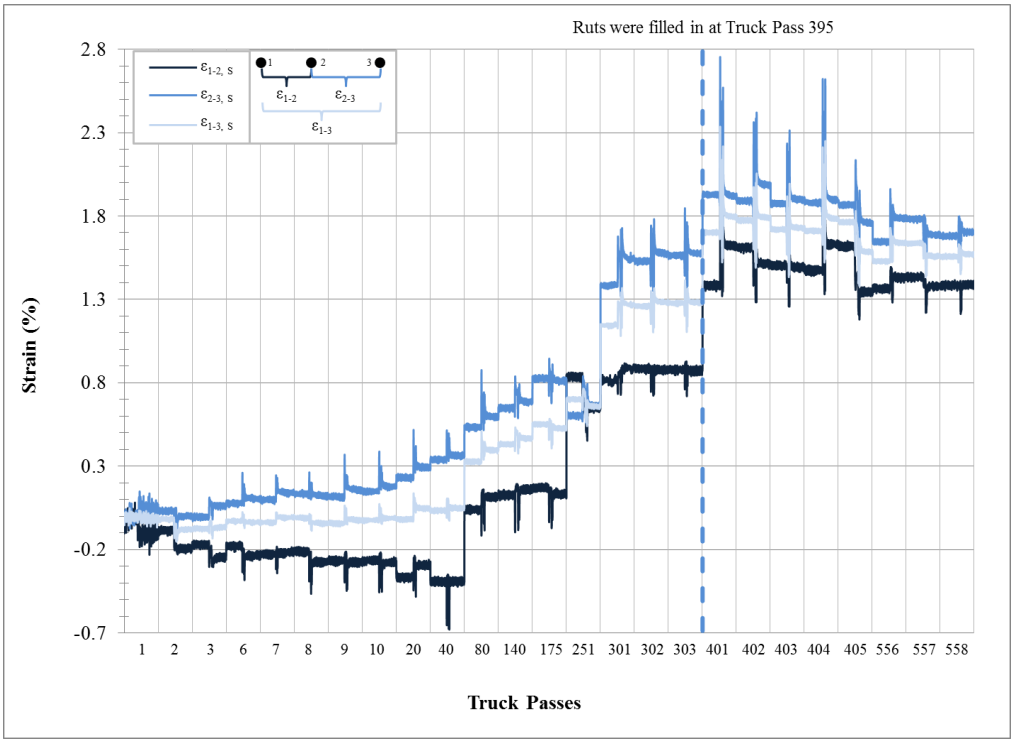


Figure N-12: Synteen SF 11 (6-South).

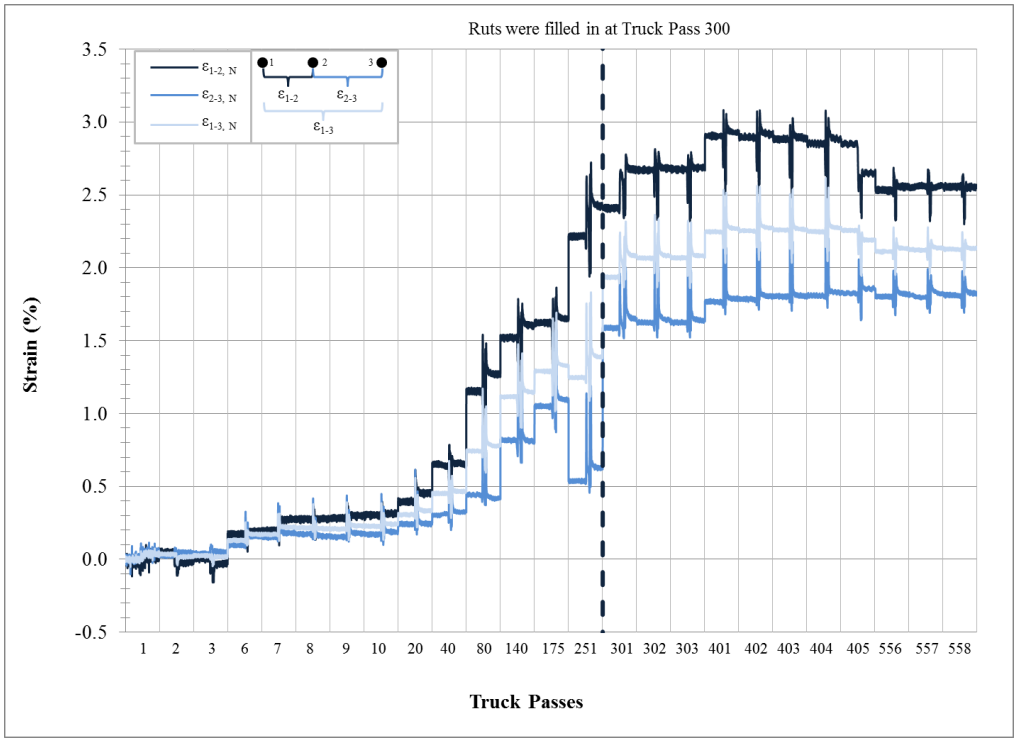


Figure N-13: Synteen SF 12 (7-North).

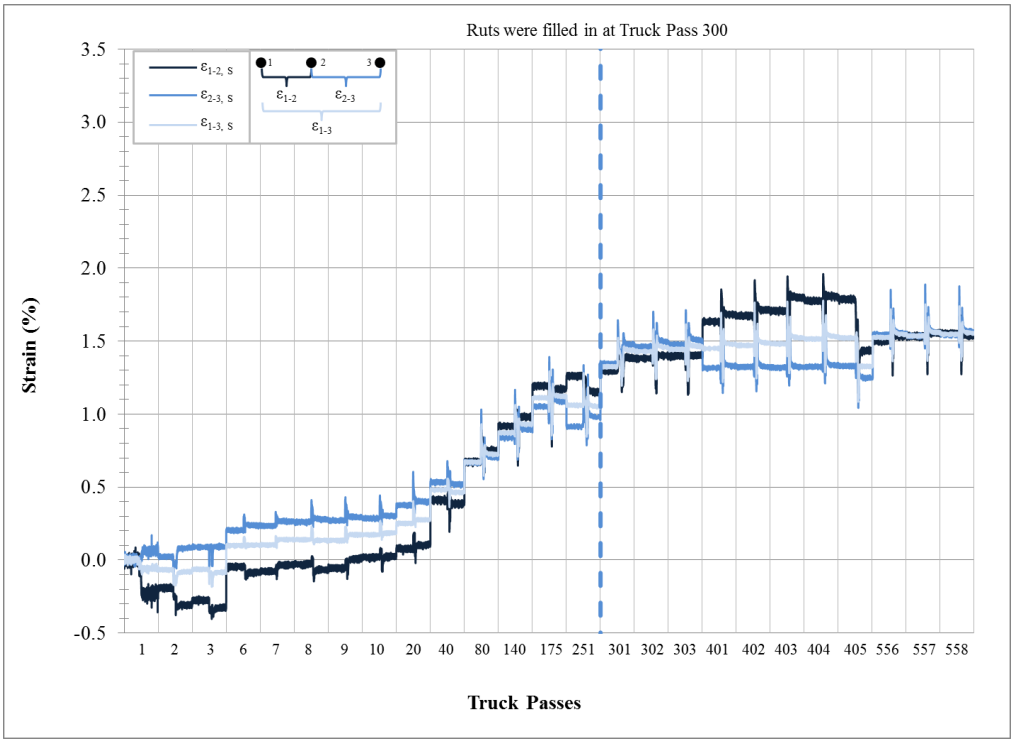


Figure N-14: Synteen SF 12 (7-South).

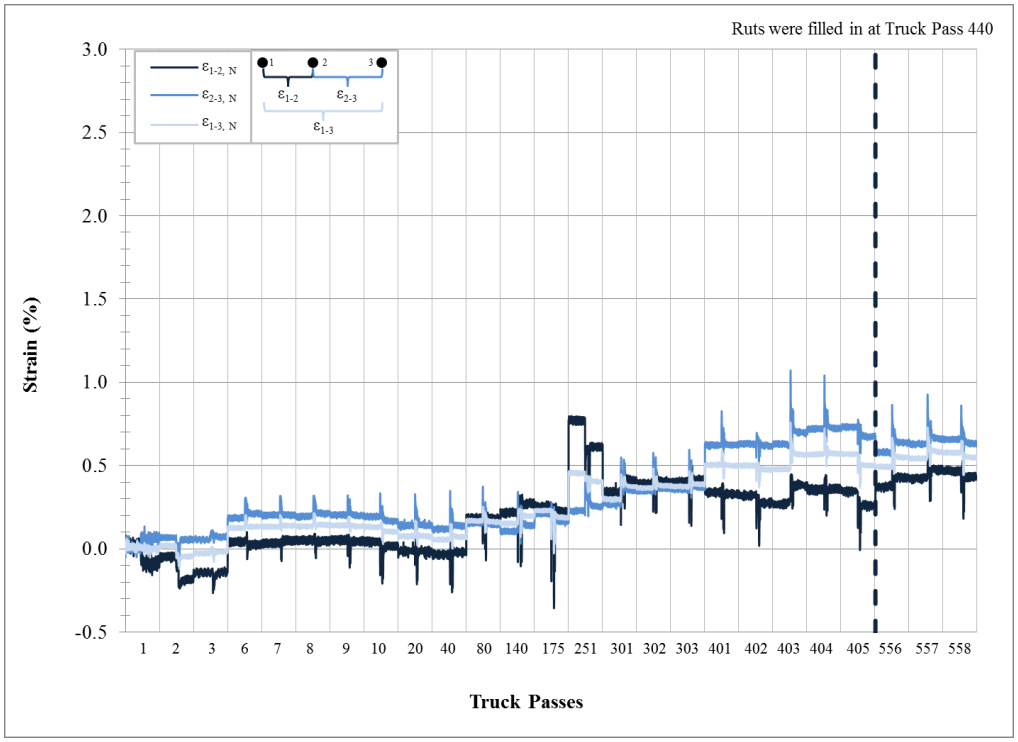


Figure N-15: TenCate Mirafi BXG 11 (8-North).

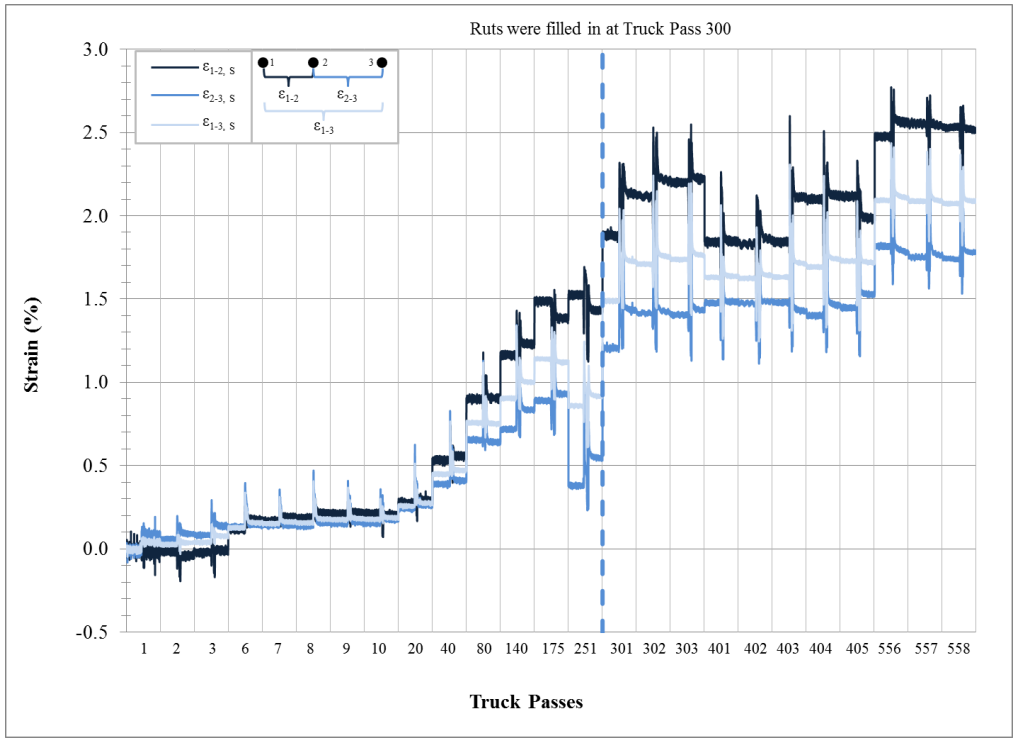


Figure N-16: TenCate Mirafi BXG 11 (8-South).

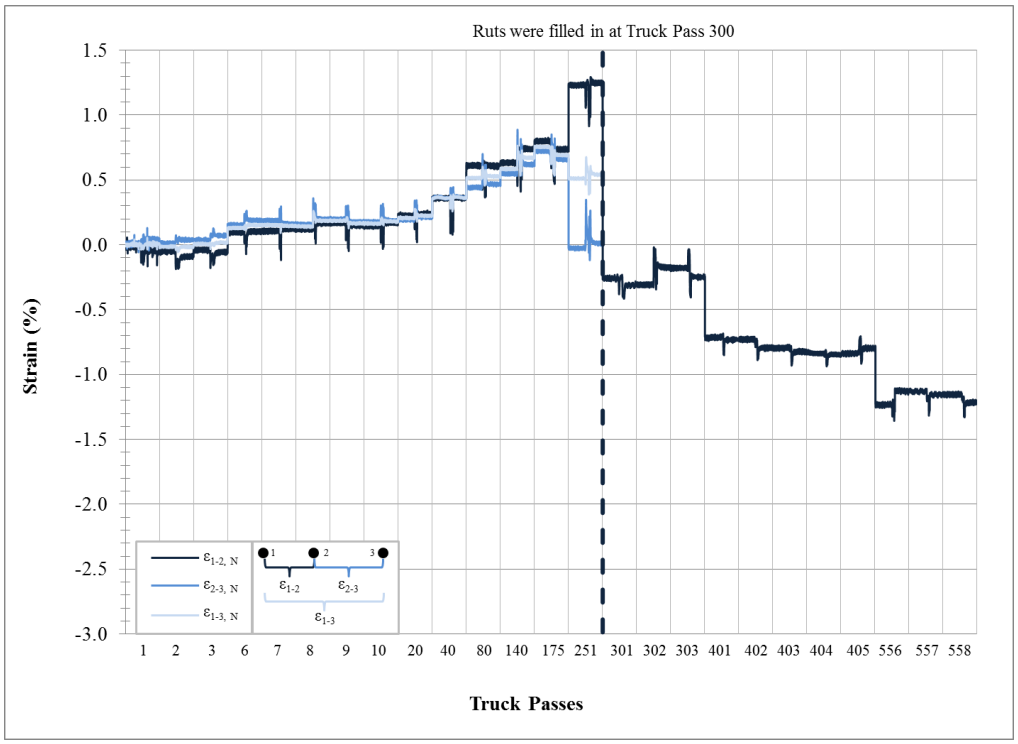


Figure N-17: Huesker Fornit 30 (9-North).

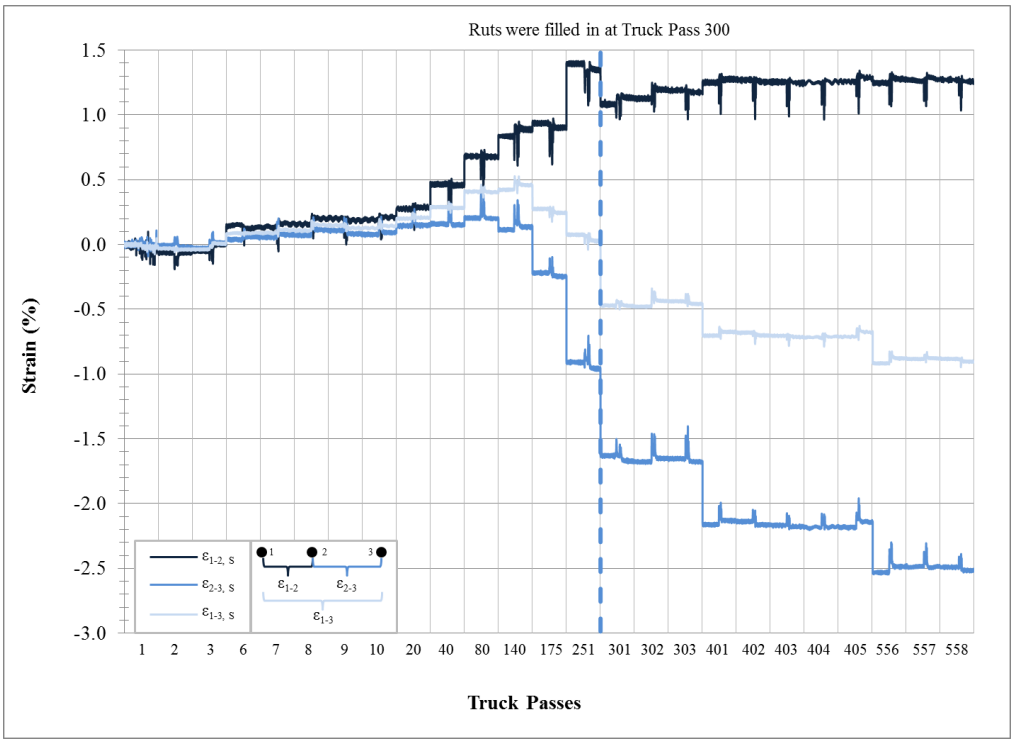


Figure N-18: Huesker Fornit 30 (9-South).

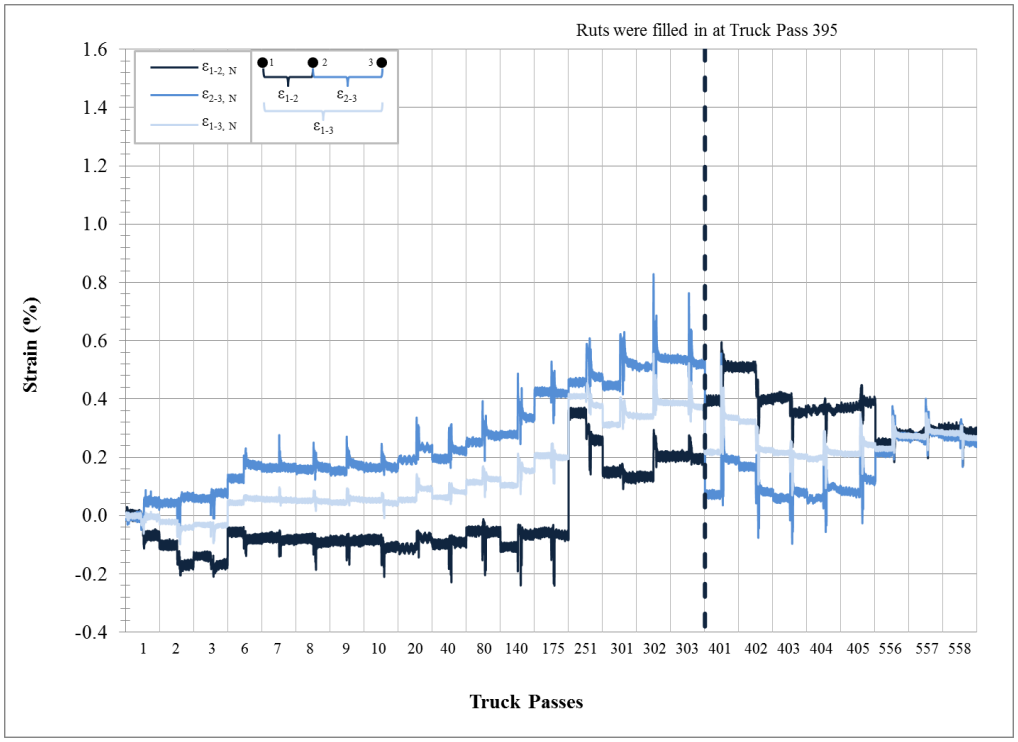


Figure N-19: SynTec Tenax MS330 (10-North).

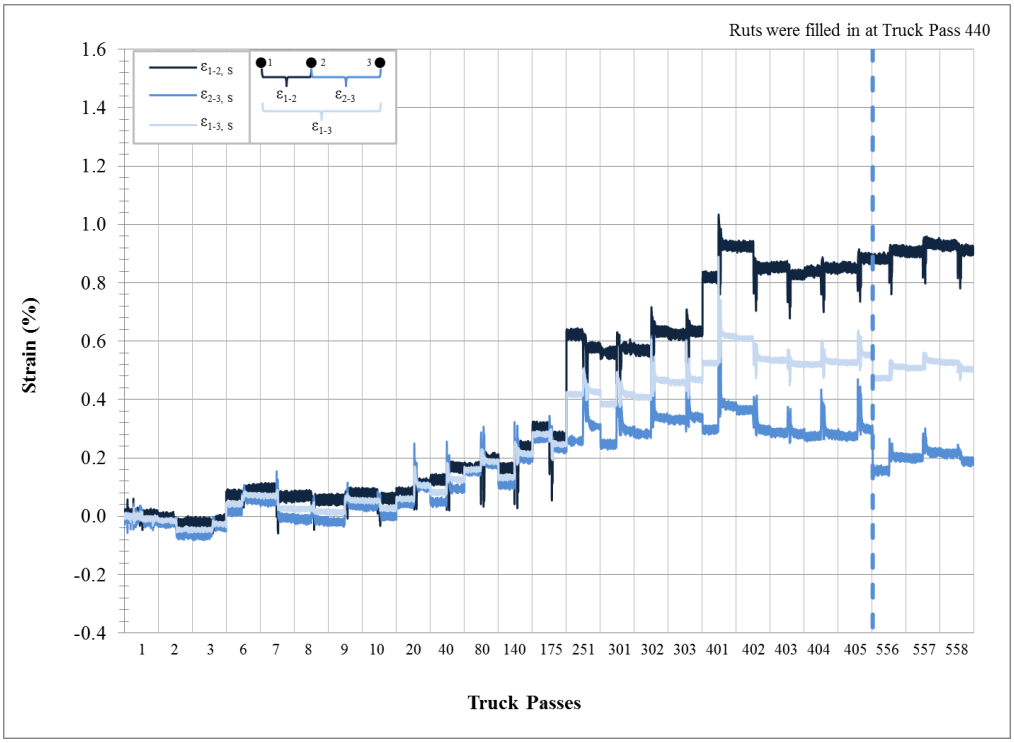


Figure N-20: SynTec Tenax MS330 (10-South).

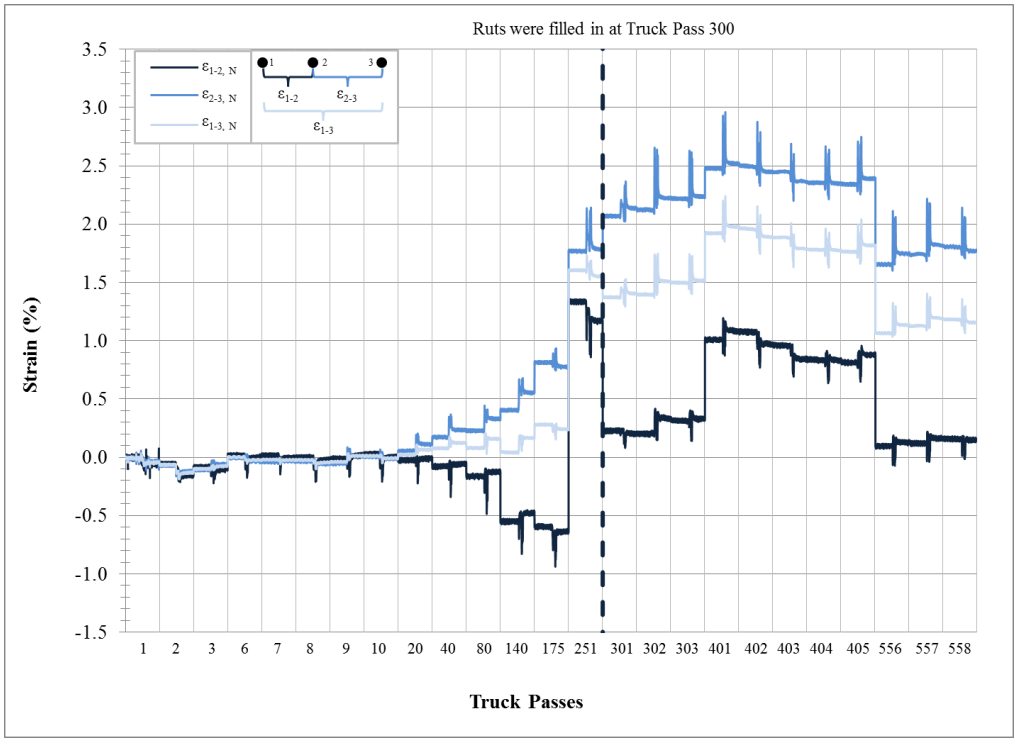


Figure N-21: Tensar TX 140 (11-North).

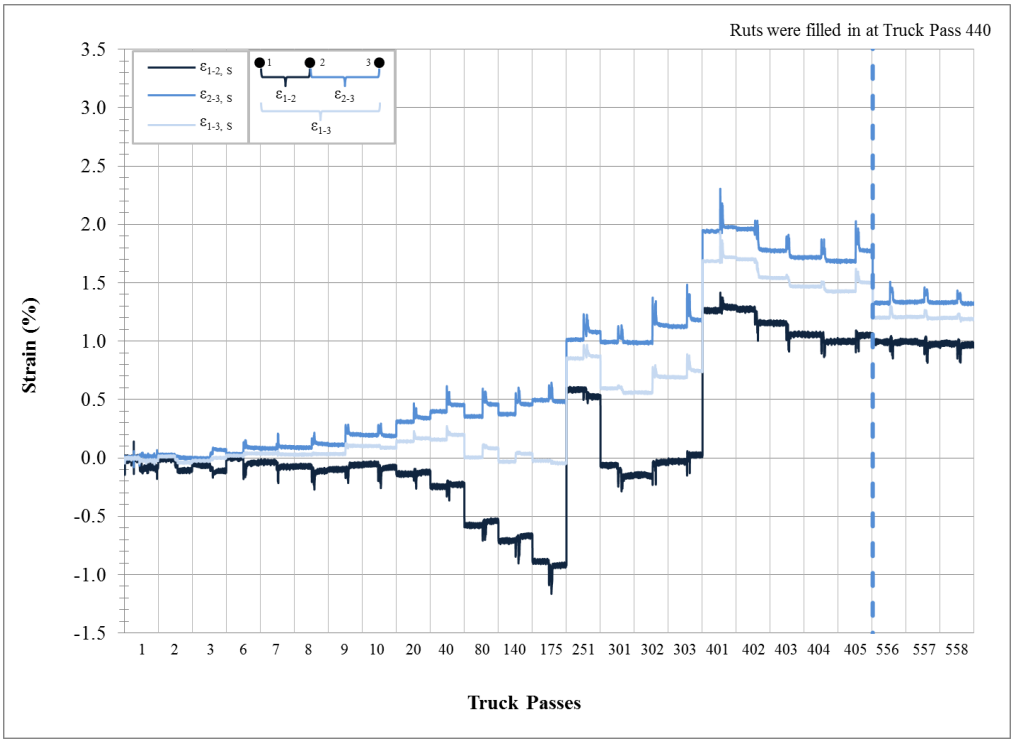


Figure N-22: Tensar TX 140 (11-South).

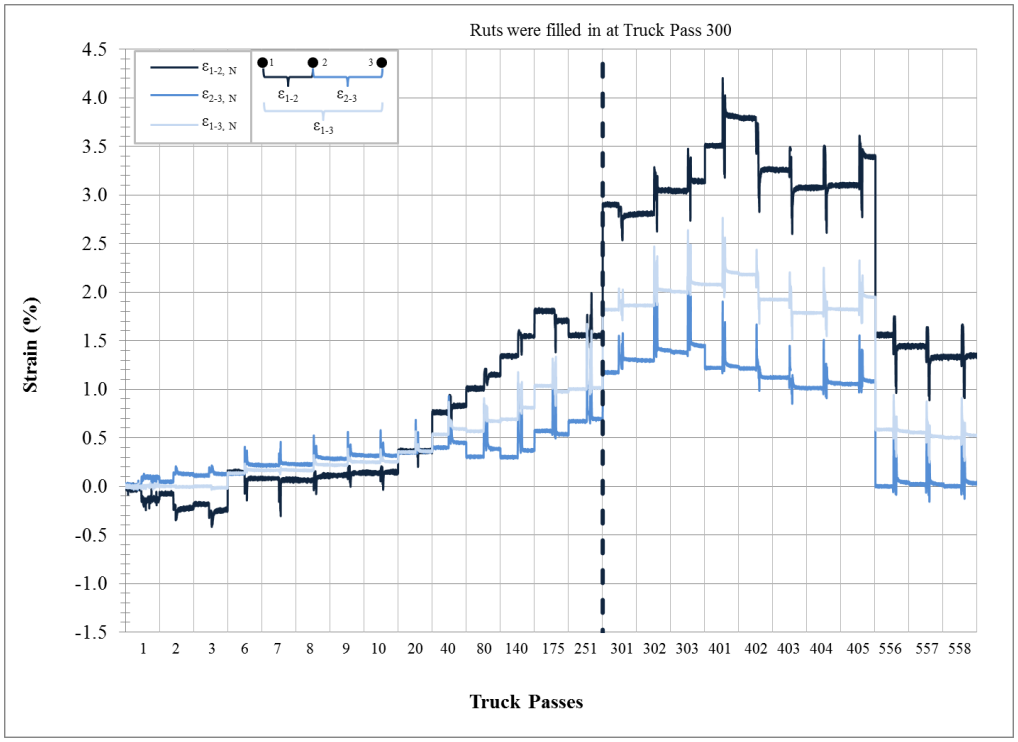


Figure N-23: Tensar TX 160 (12-North).

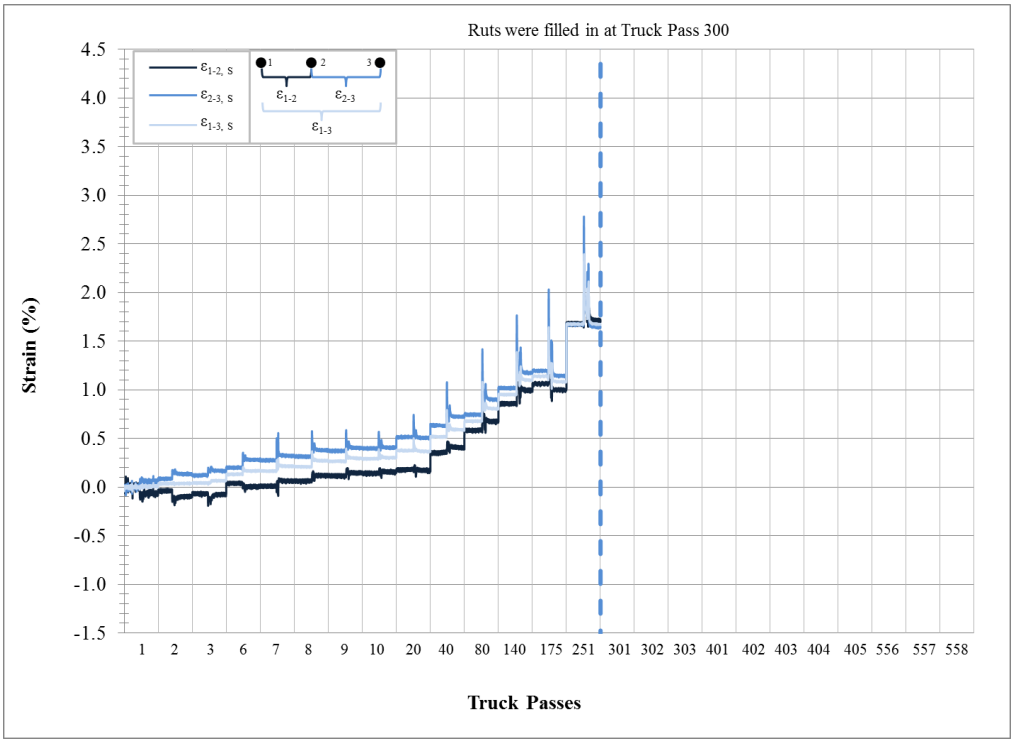


Figure N-24: Tensar TX 160 (12-South).

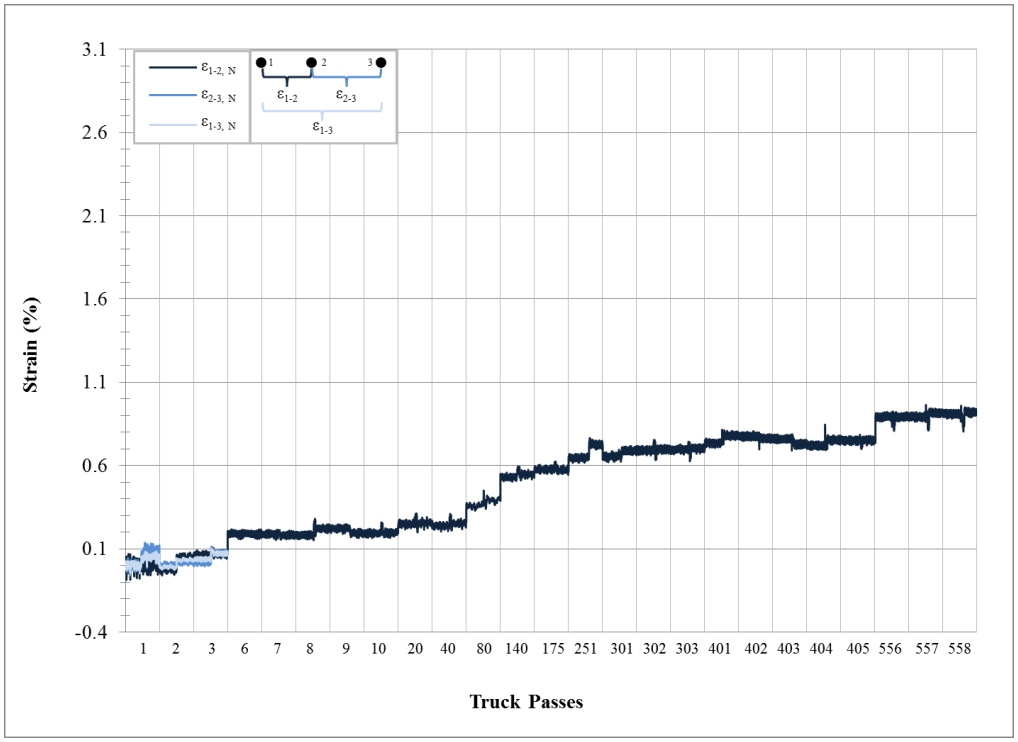


Figure N-25: TenCate Mirafi RS580i (13-North).

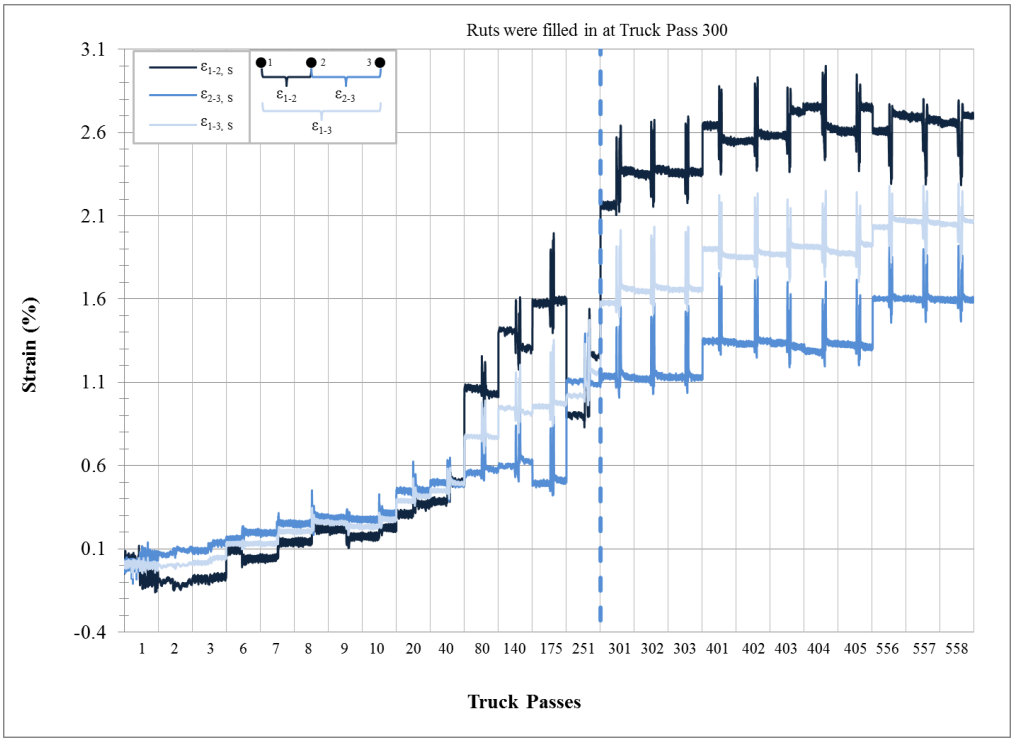


Figure N-26: TenCate Mirafi RS580i (13-South).

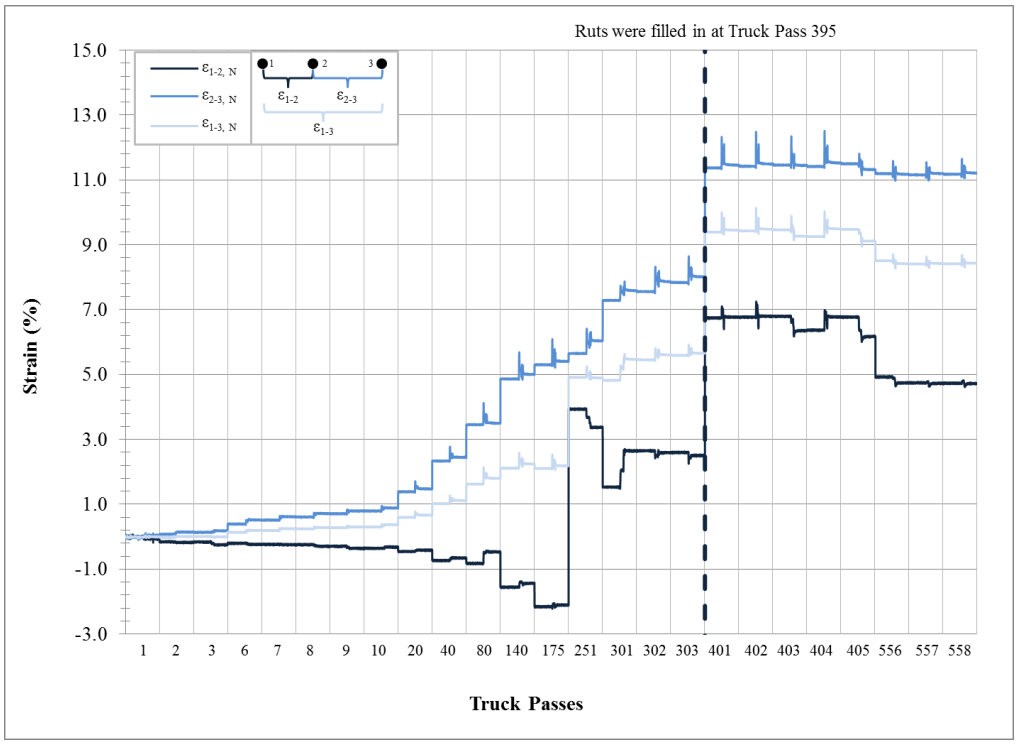


Figure N-27: Propex Geotex 801 (14-North).

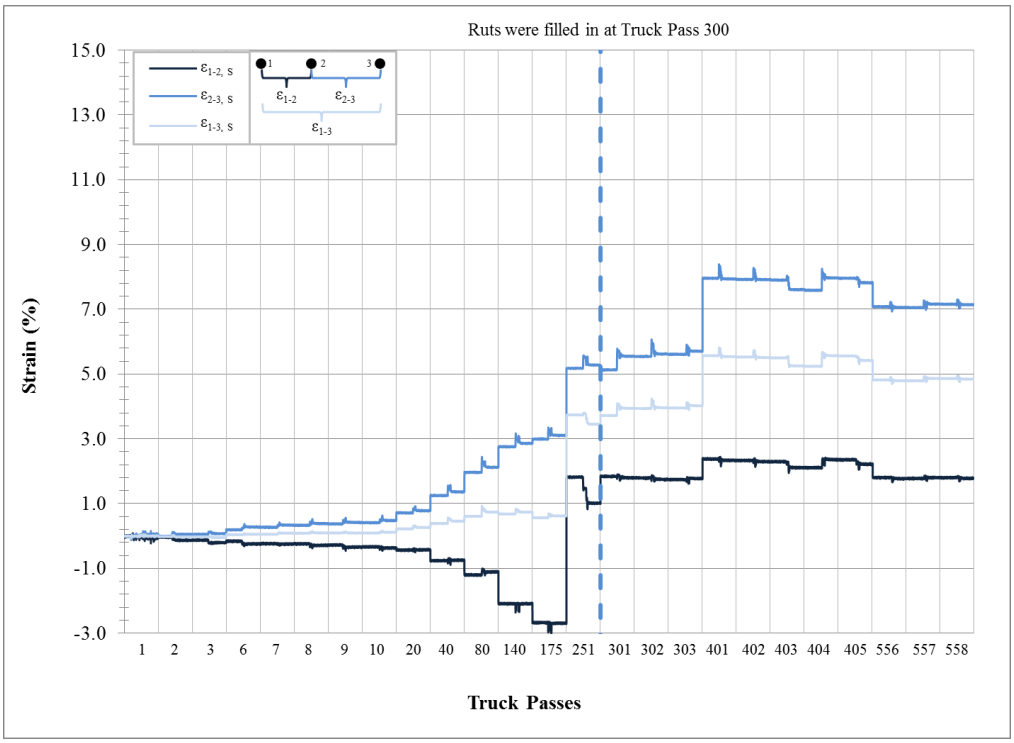


Figure N-28: Propex Geotex 801 (14-South).

APPENDIX O:

LVDT STATIC STRAIN PLOTS

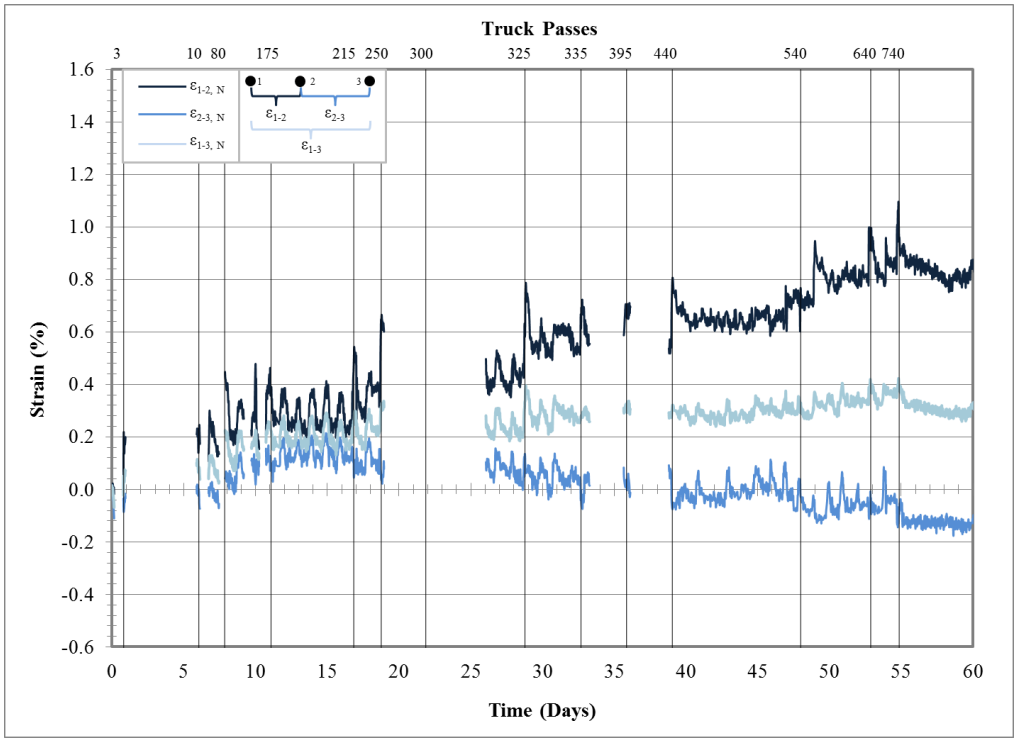


Figure O-1: Tensar BX Type 2 (1-North) (CBR = 2.15).

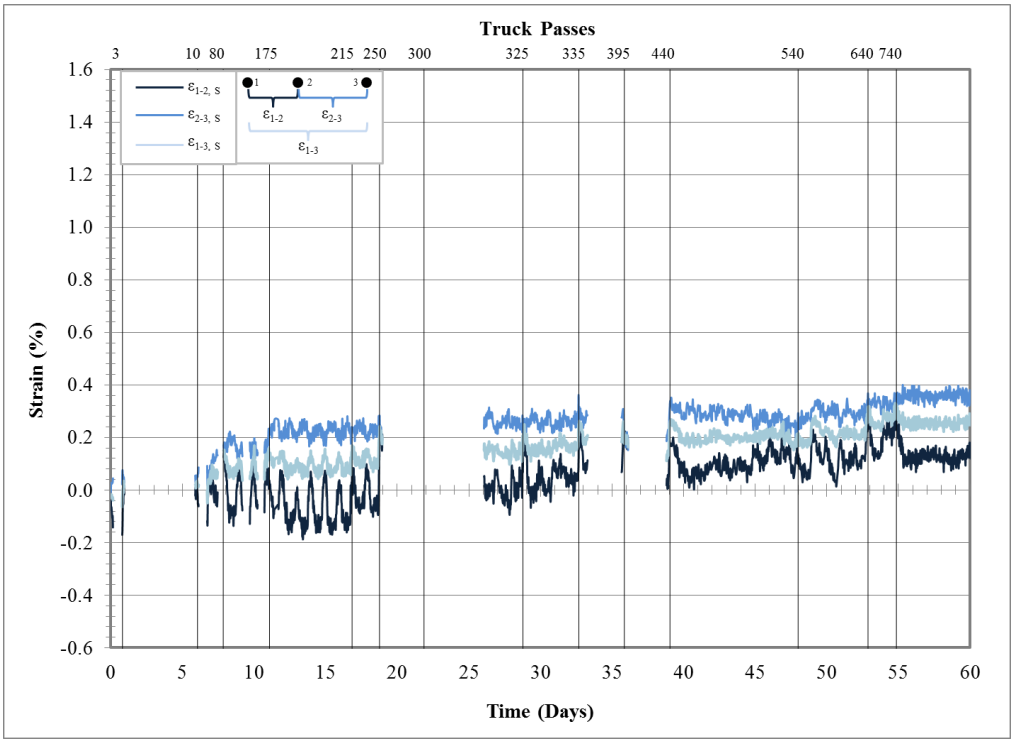


Figure O-2: Tensar BX Type 2 (1-South) (CBR = 2.15).

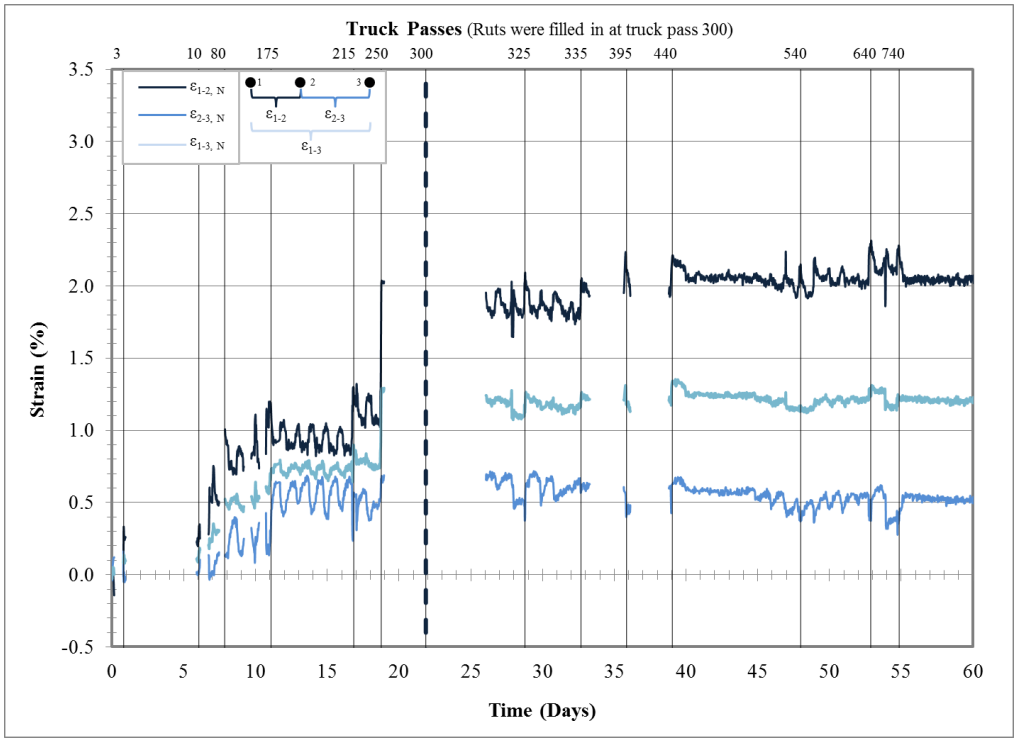


Figure O-3: Tensar BX Type 2 (2-North) (CBR = 1.61).

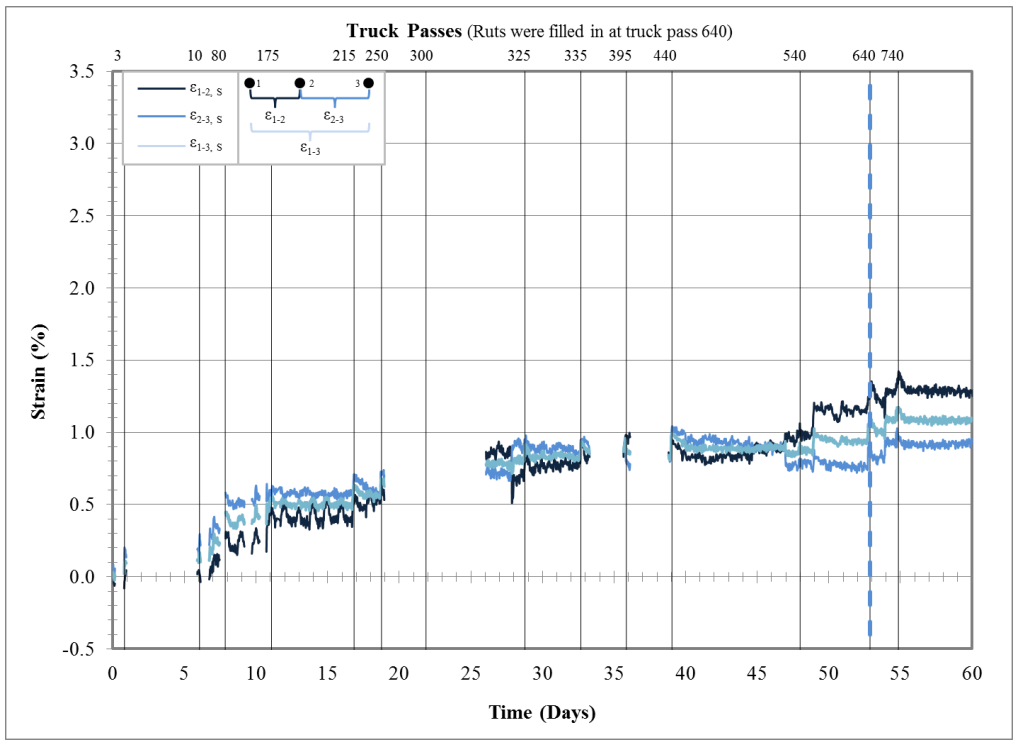


Figure O-4: Tensar BX Type 2 (2-South) (CBR = 1.61).

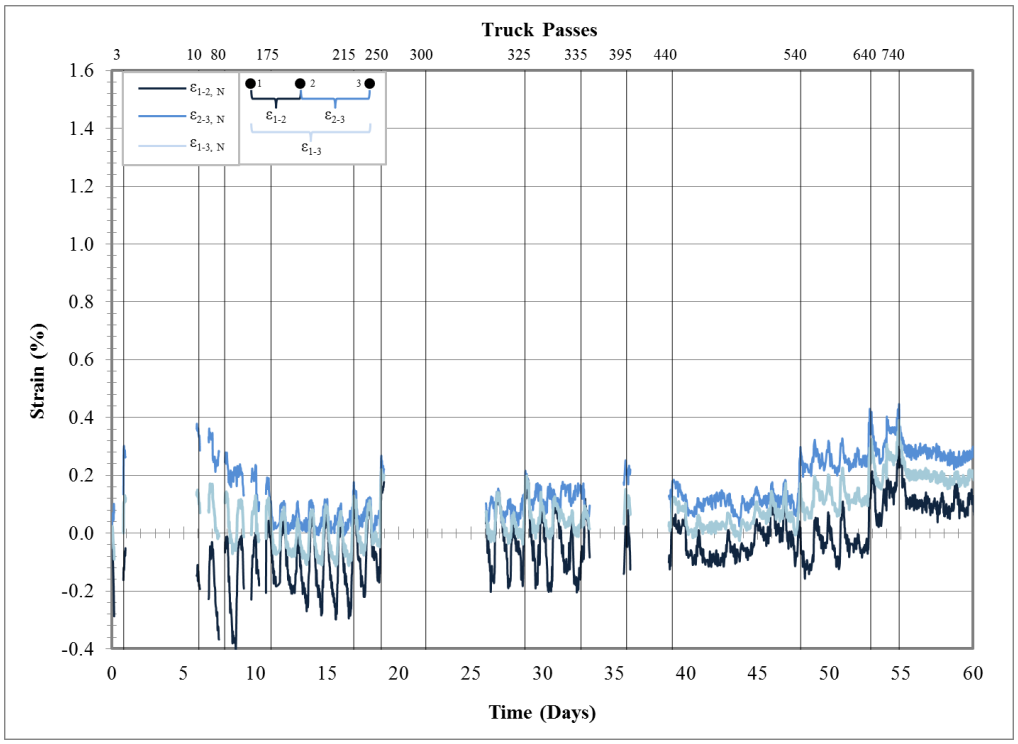


Figure O-5: Tensar BX Type 2 (3-North) (CBR = 1.78).

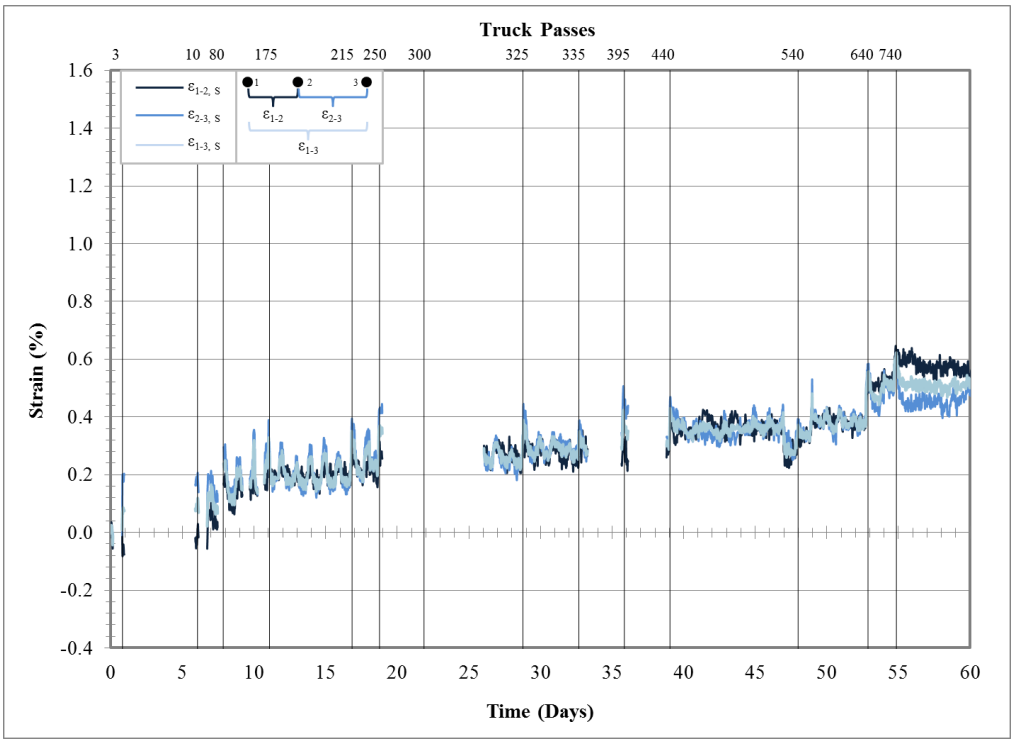


Figure O-6: Tensar BX Type 2 (3-South) (CBR = 1.78).

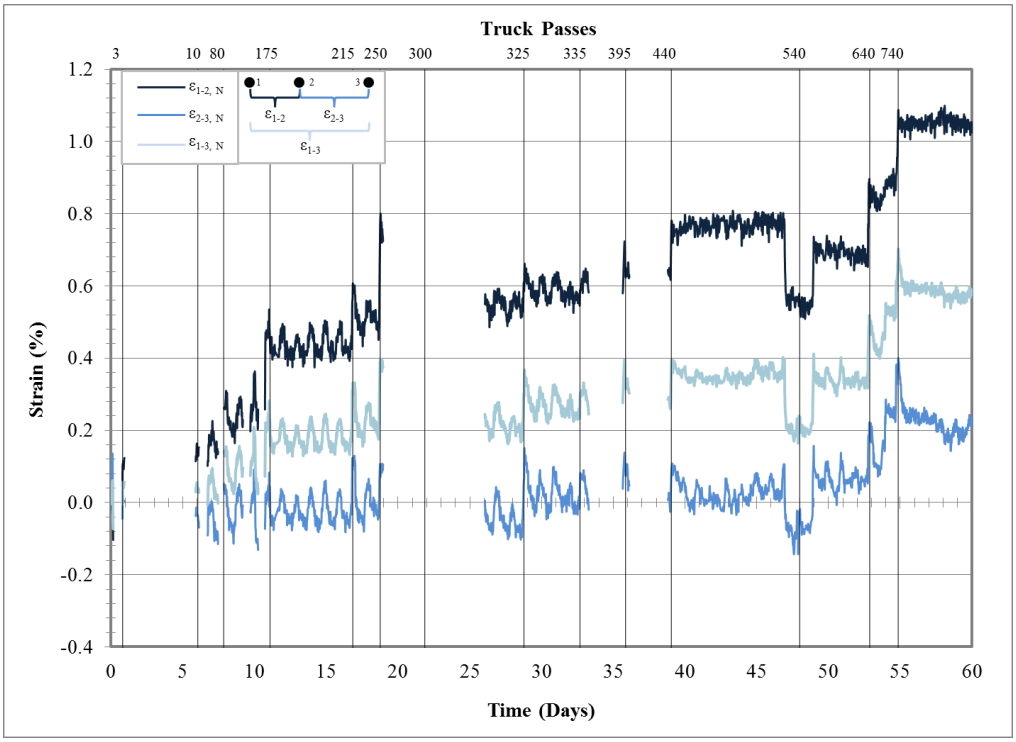


Figure O-7: NAUE Secugrid 30/30 Q1 (4-North).

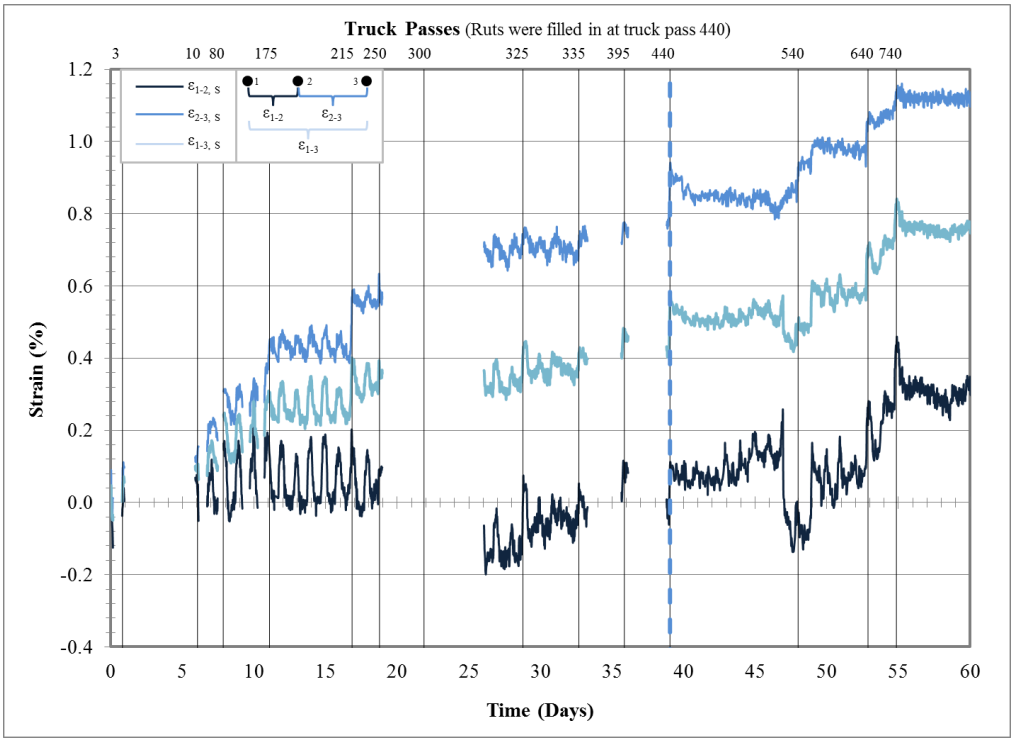


Figure O-8: NAUE Secugrid 30/30 Q1 (4-South).

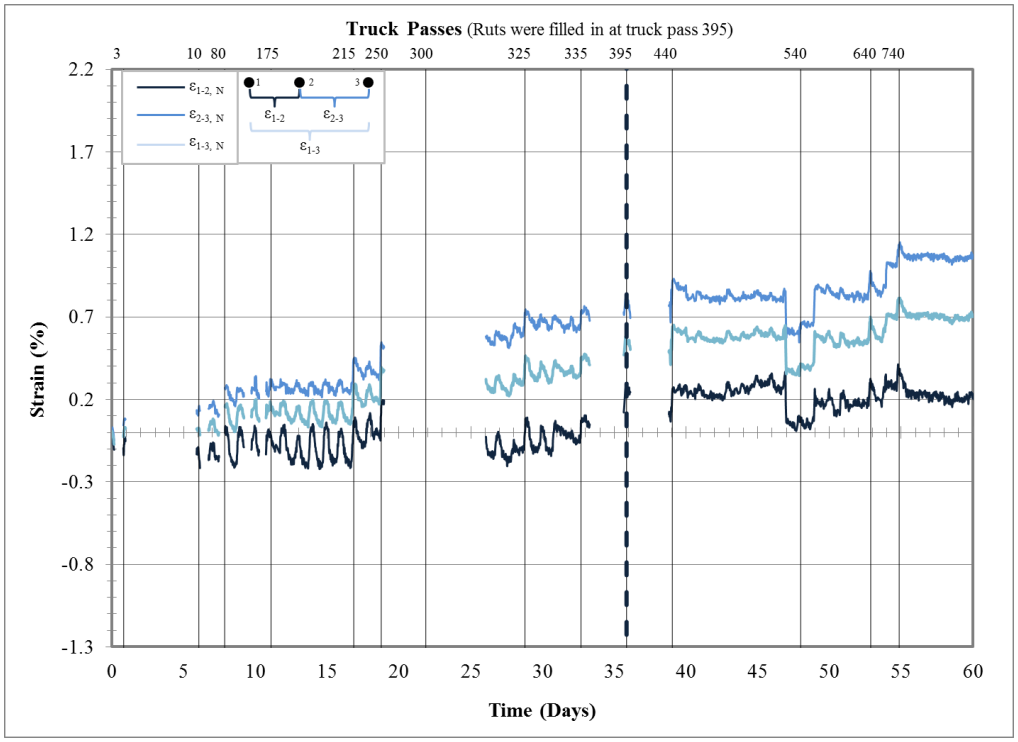


Figure O-9: Colbond Enkagrid Max 30 (5-North).

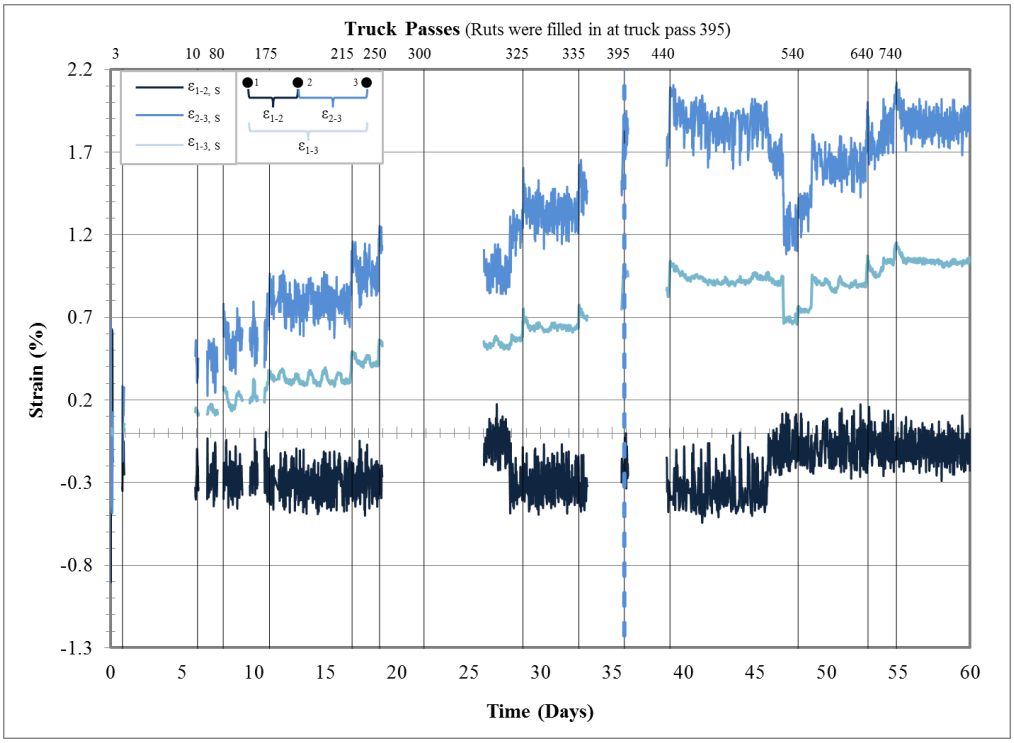


Figure O-10: Colbond Enkagrid Max 30 (5-South).

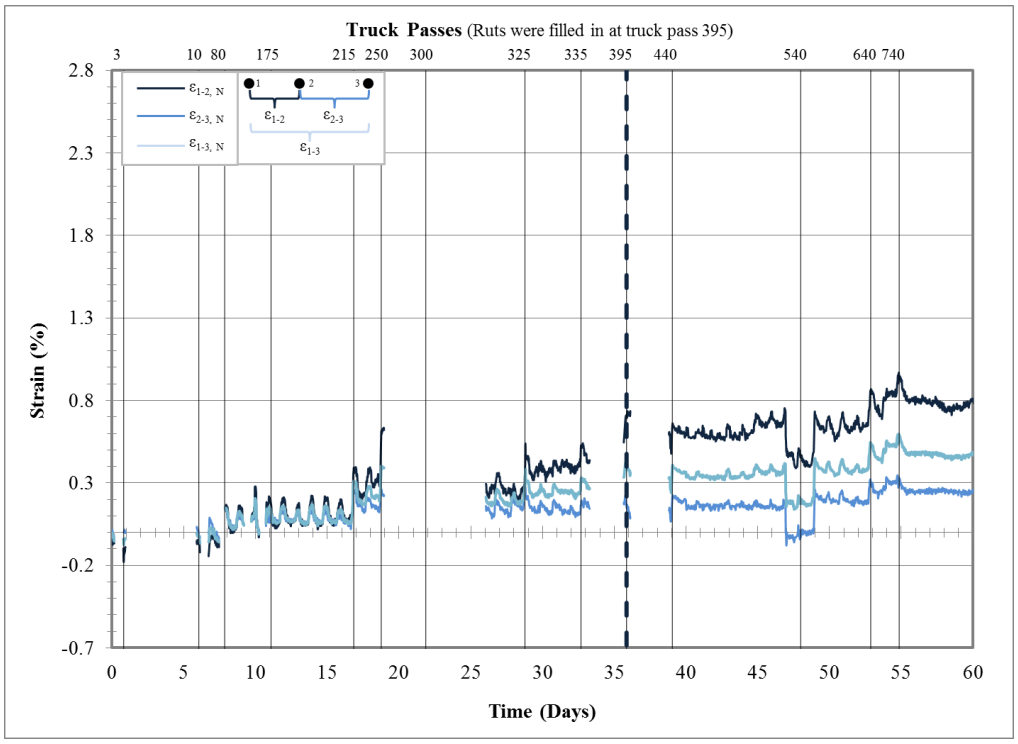


Figure O-11: Synteen SF 11 (6-North).

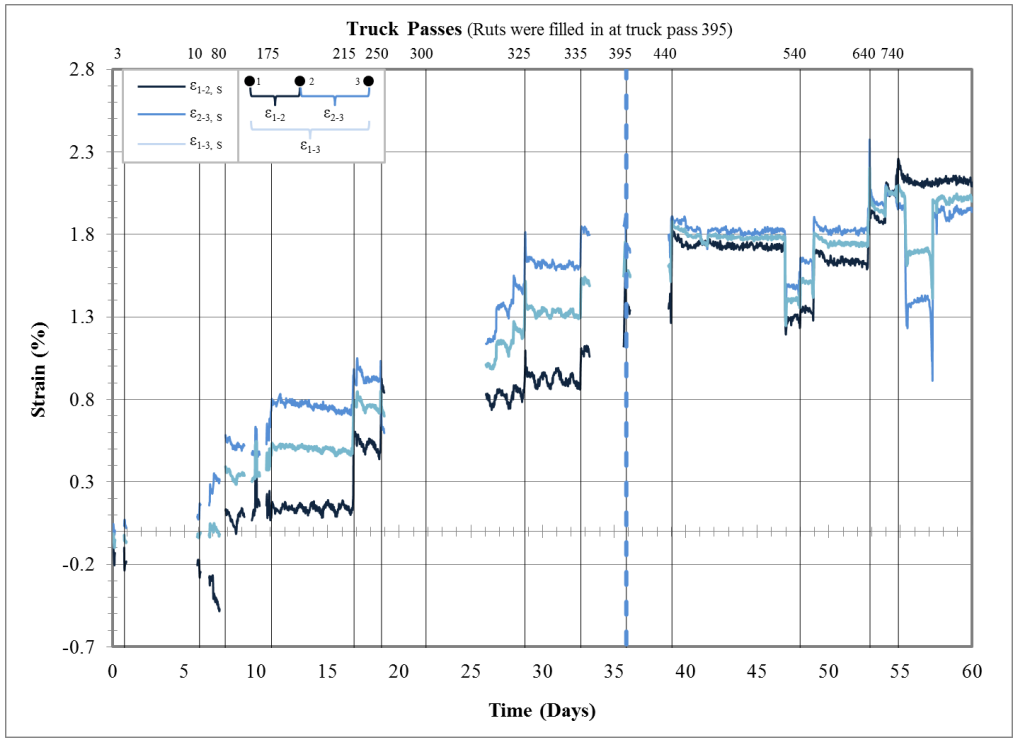


Figure O-12: Synteen SF 11 (6-South).

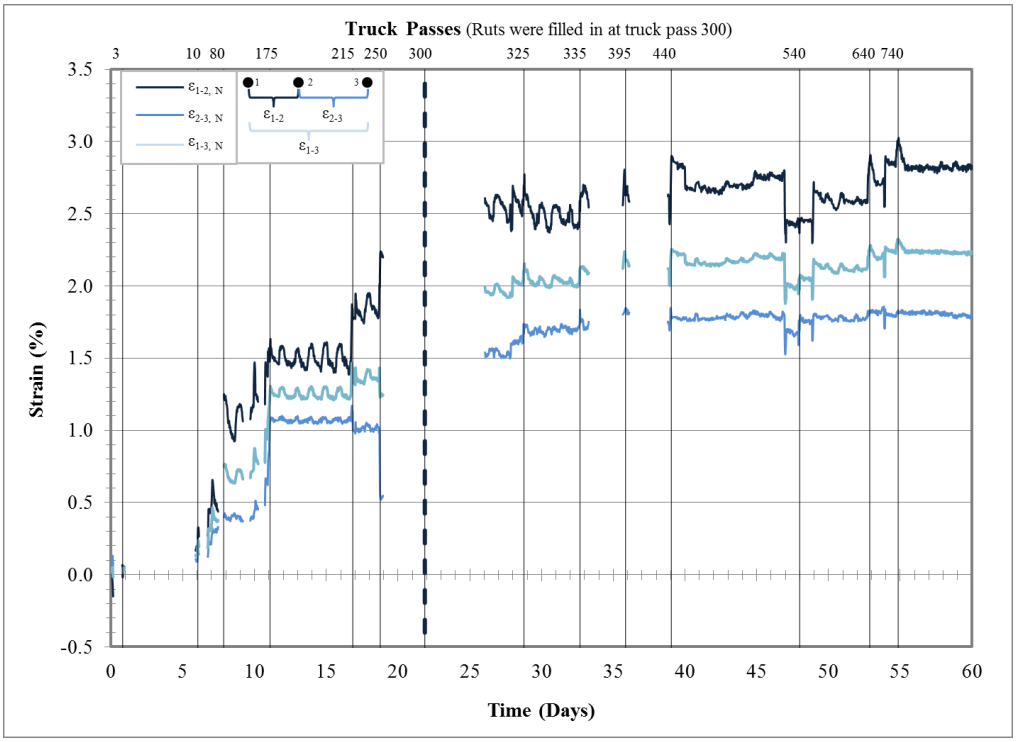


Figure O-13: Synteen SF 12 (7-North).

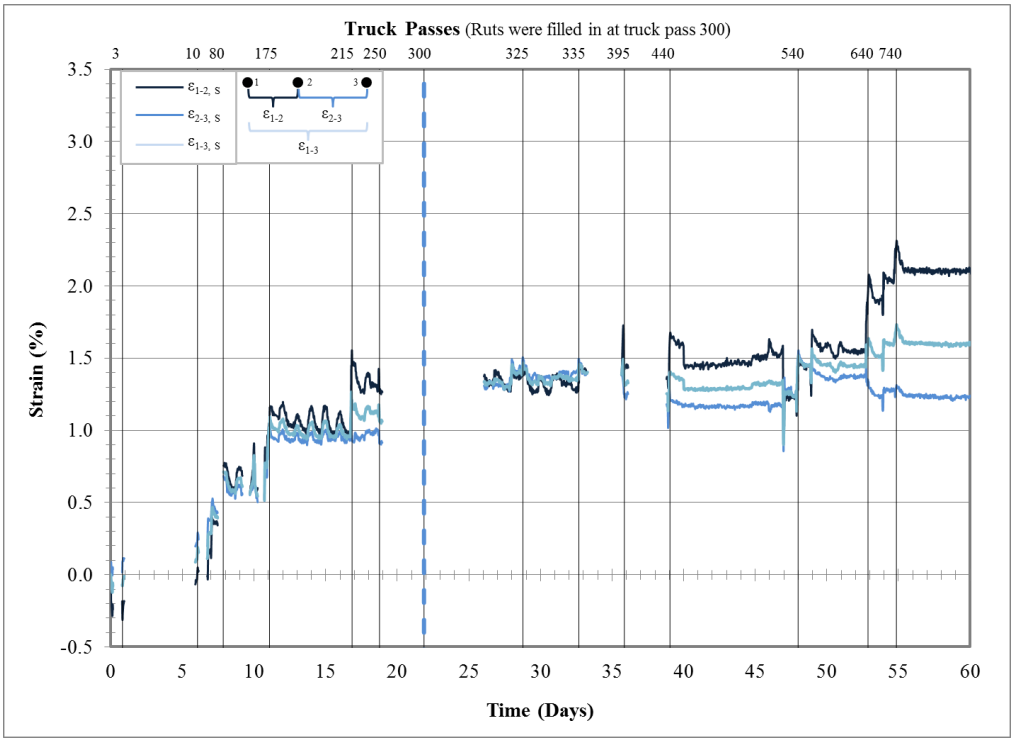


Figure O-14: Synteen SF 12 (7-South).

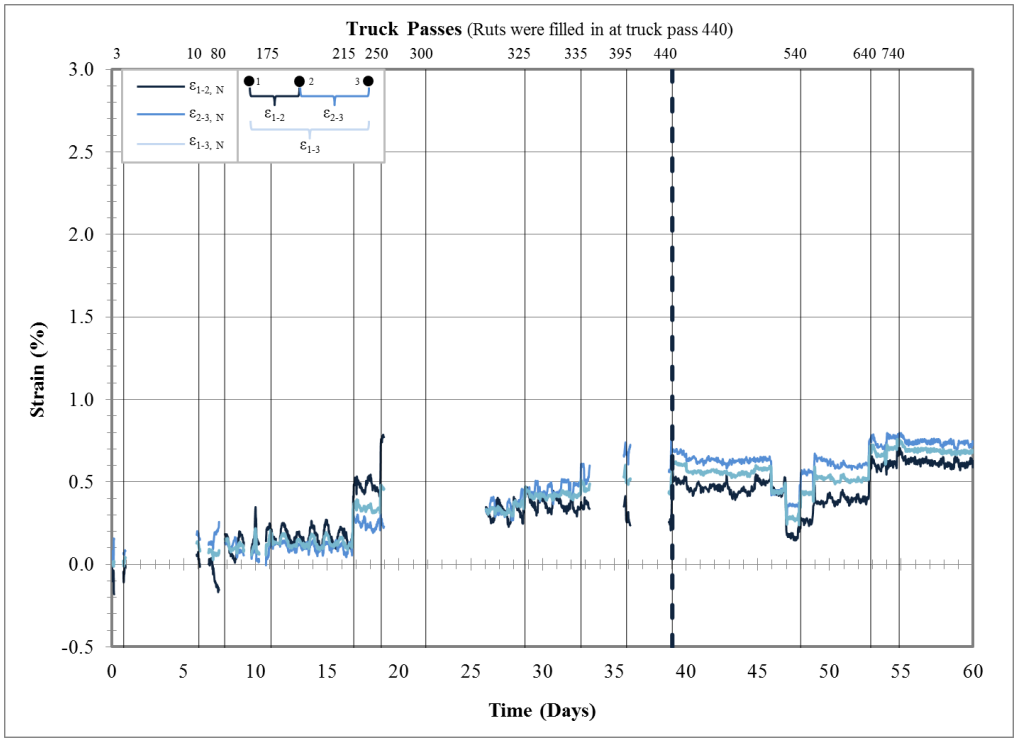


Figure O-15: TenCate Mirafi BXG 11 (8-North).

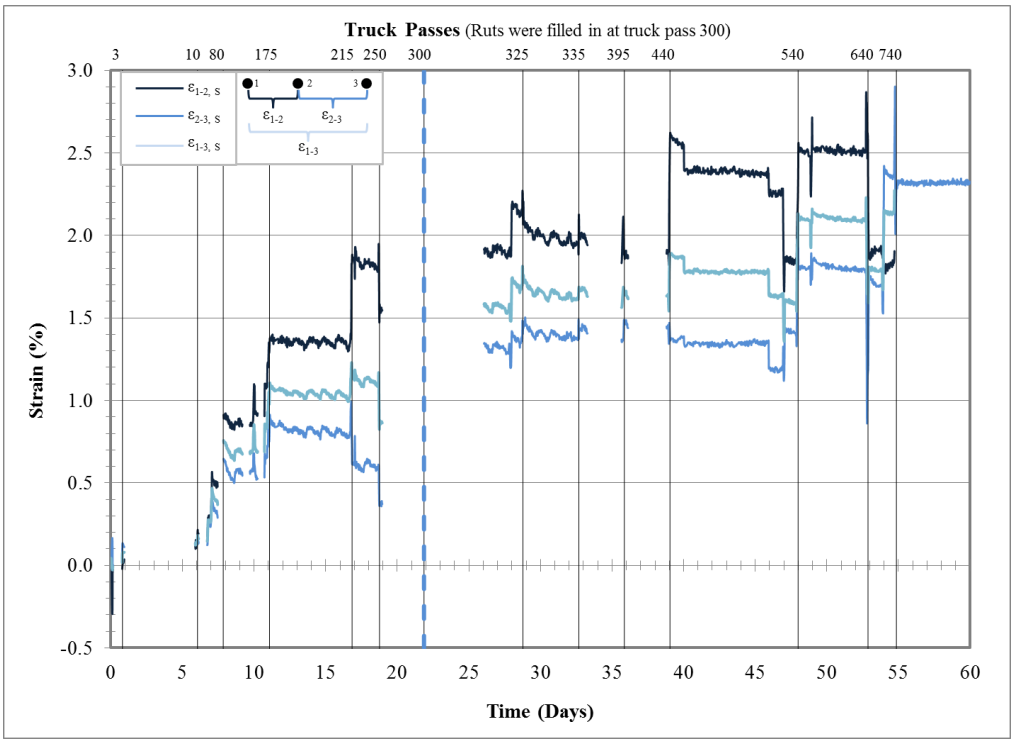


Figure O-16: TenCate Mirafi BXG 11 (8-South).

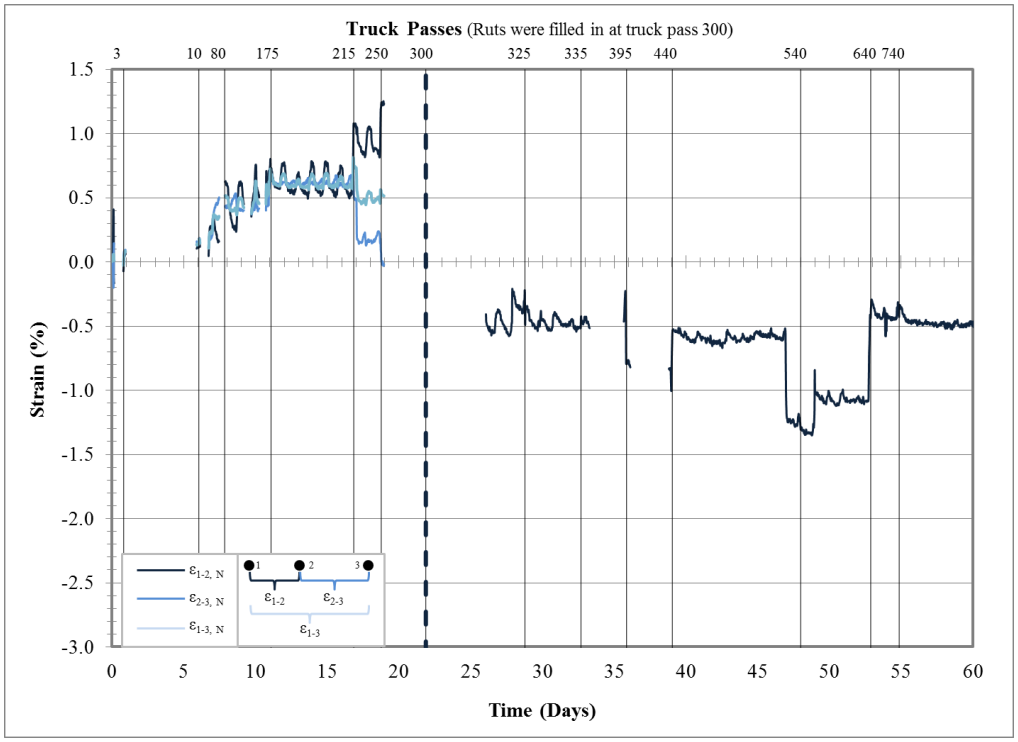


Figure O-17: Huesker Fornit 30 (9-North).

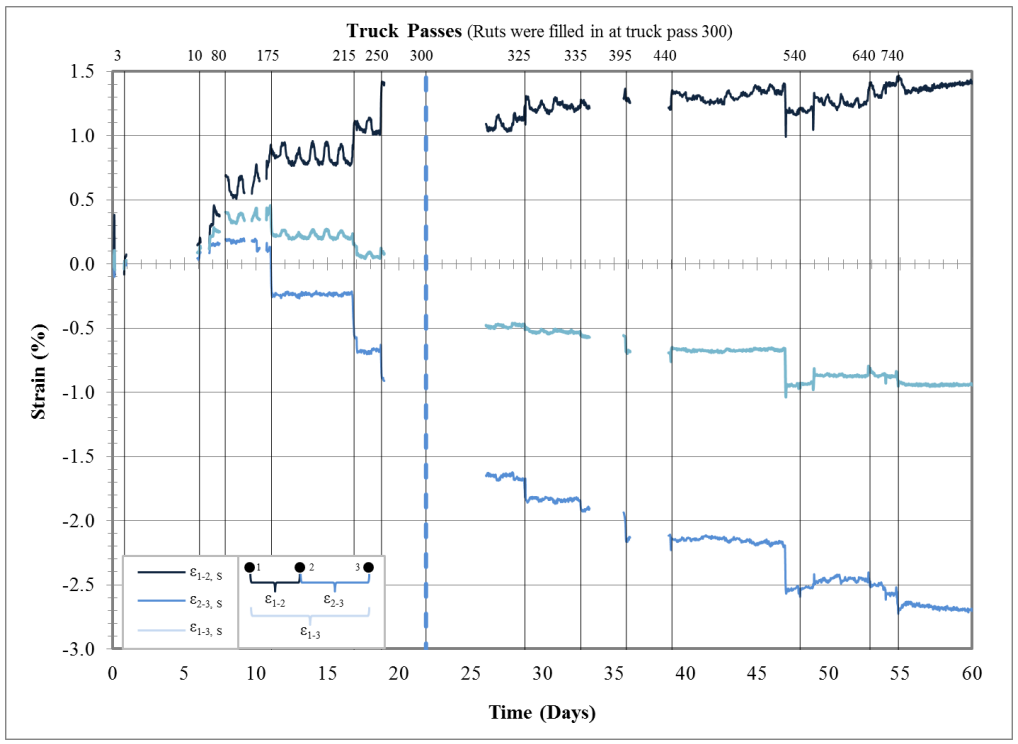


Figure O-18: Huesker Fornit 30 (9-South).

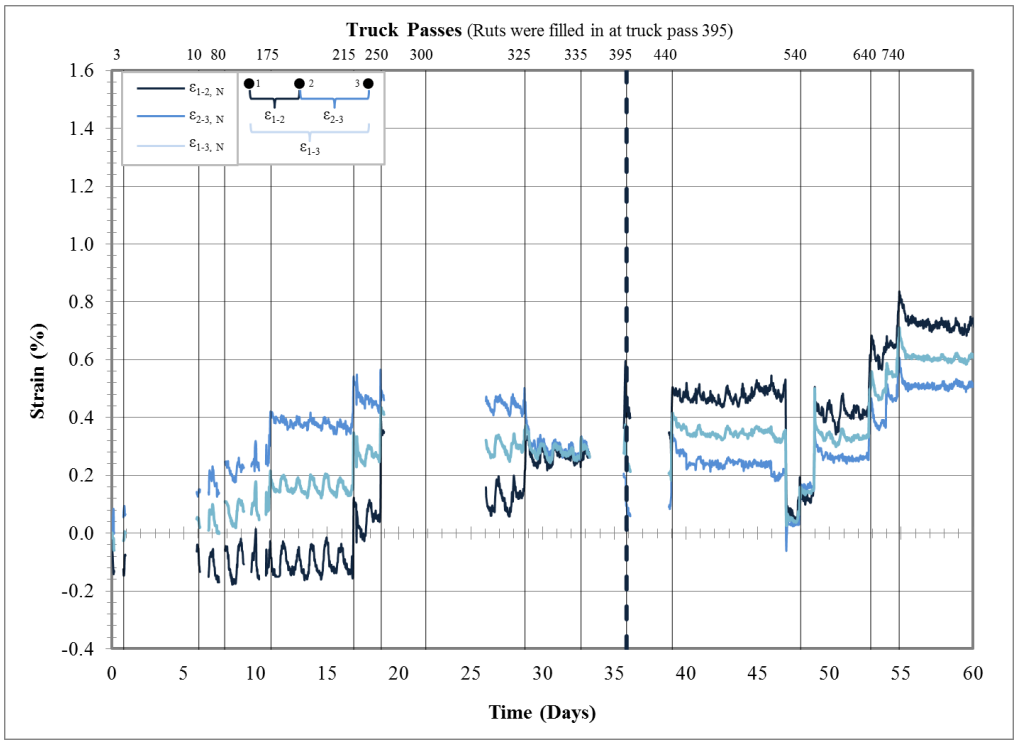


Figure O-19: SynTec Tenax MS330 (10-North).

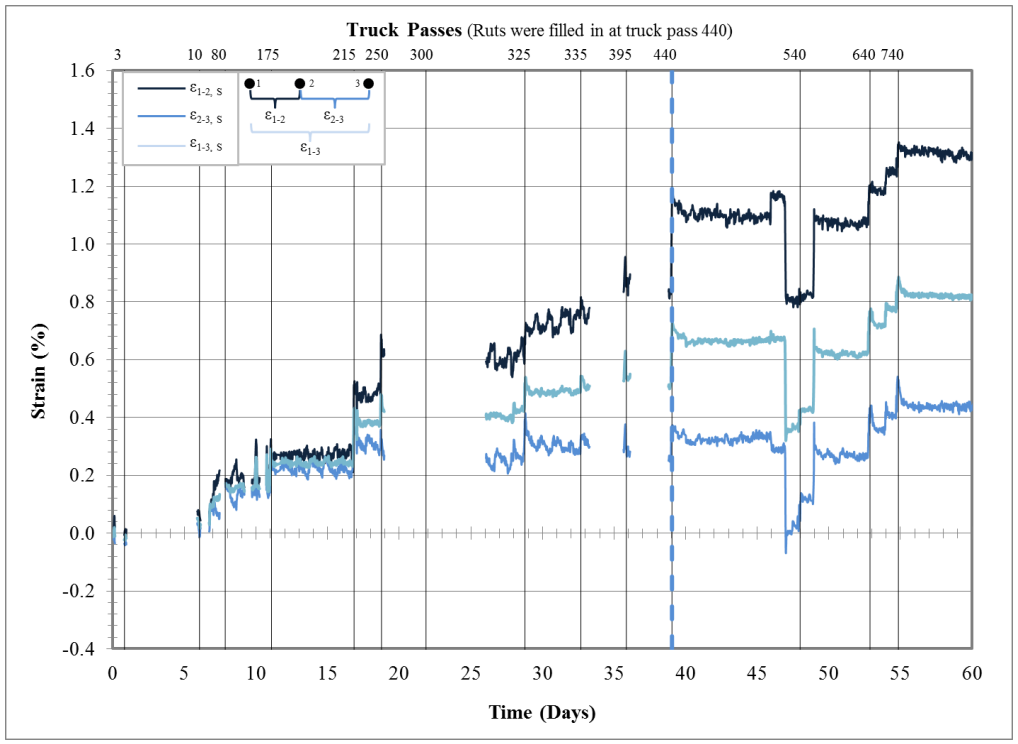


Figure O-20: SynTec Tenax MS330 (10-South).

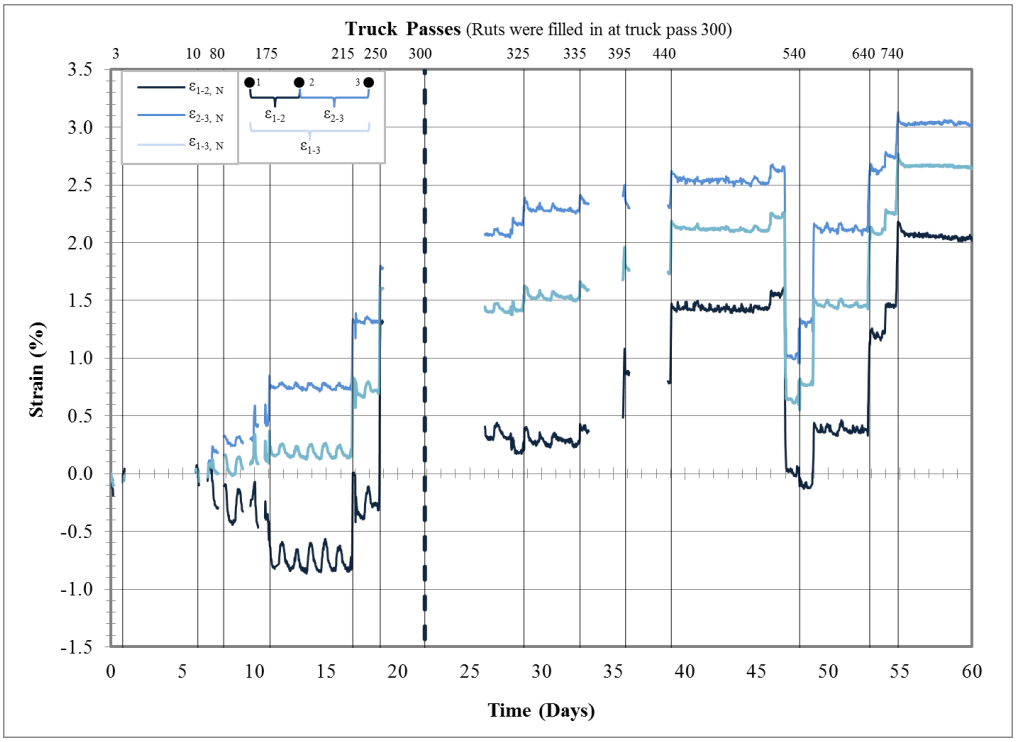


Figure O-21: Tensar TX 140 (11-North).

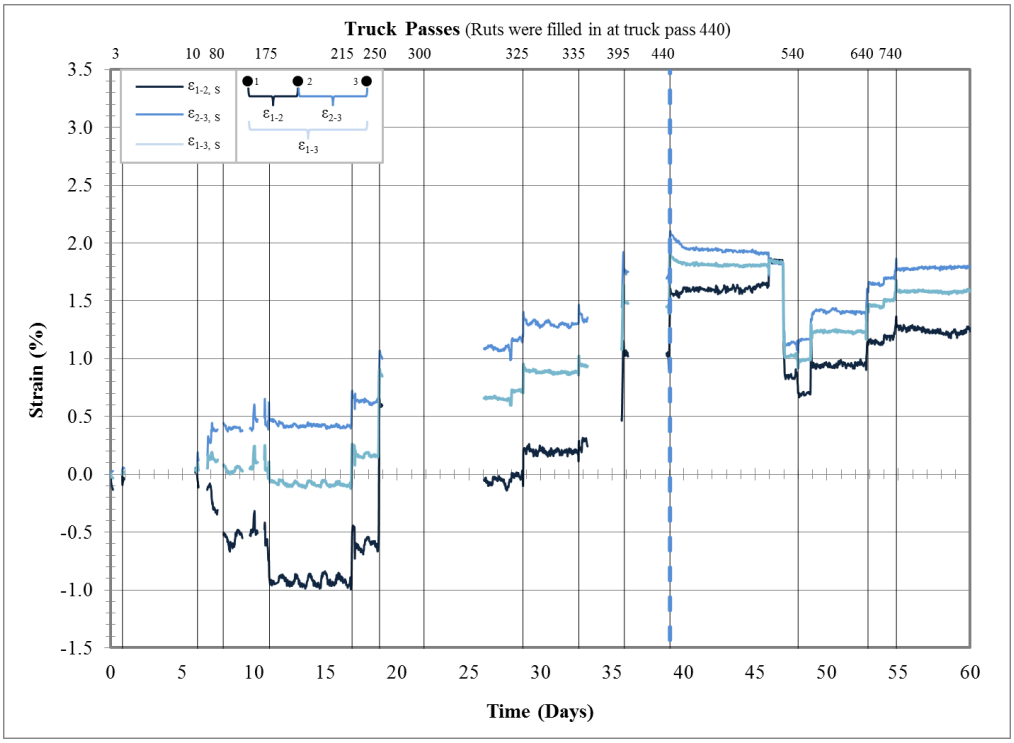


Figure O-22: Tensar TX 140 (11-South).

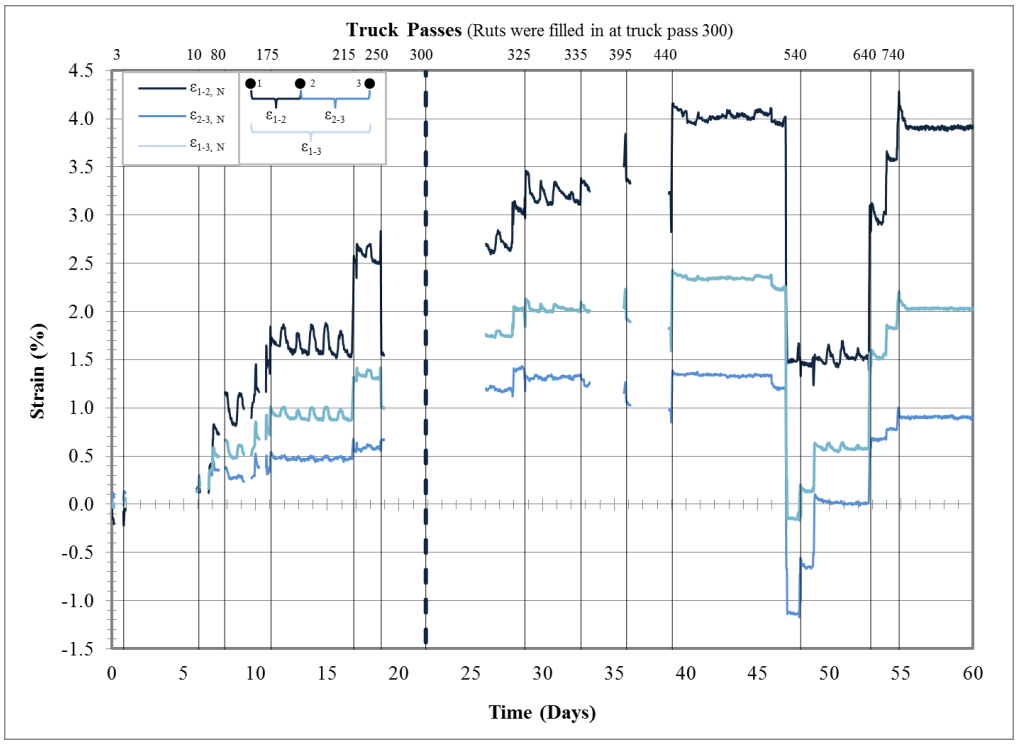


Figure O-23: Tensar TX 160 (12-North).

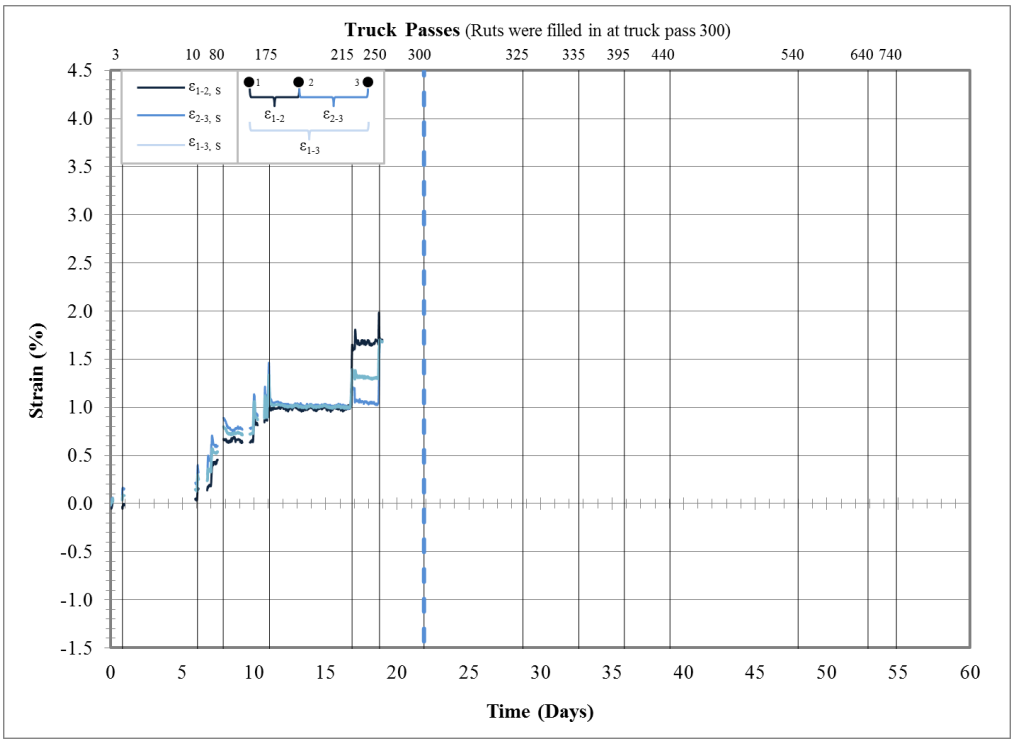


Figure O-24: Tensar TX 160 (12-South).

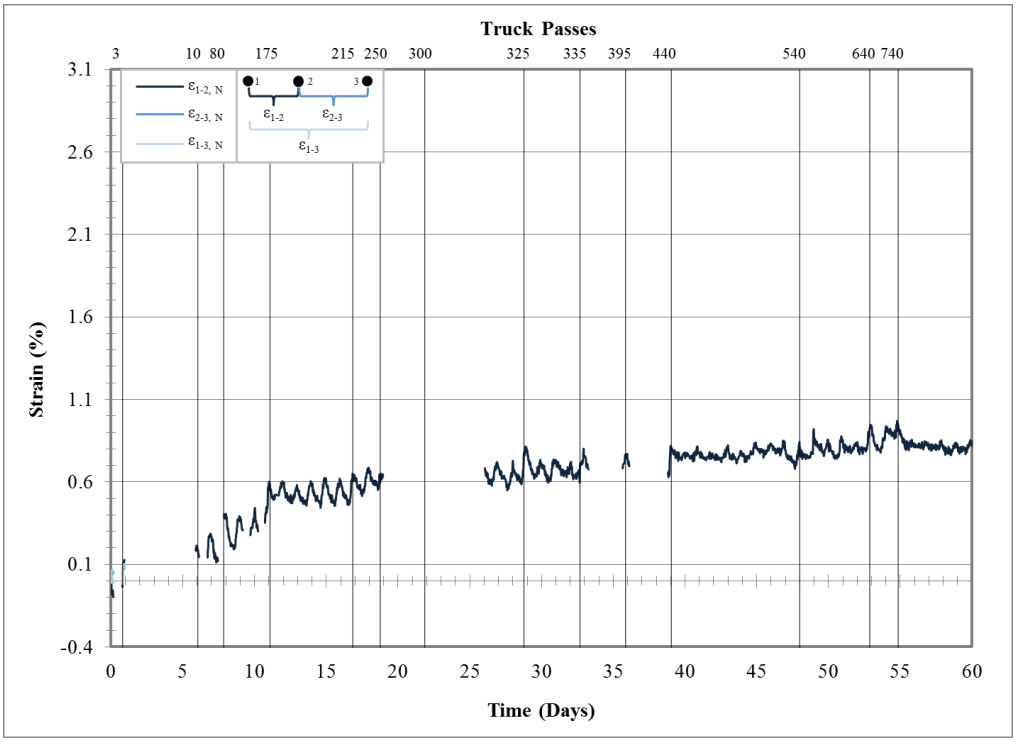


Figure O-25: TenCate Mirafi RS580i (13-North).

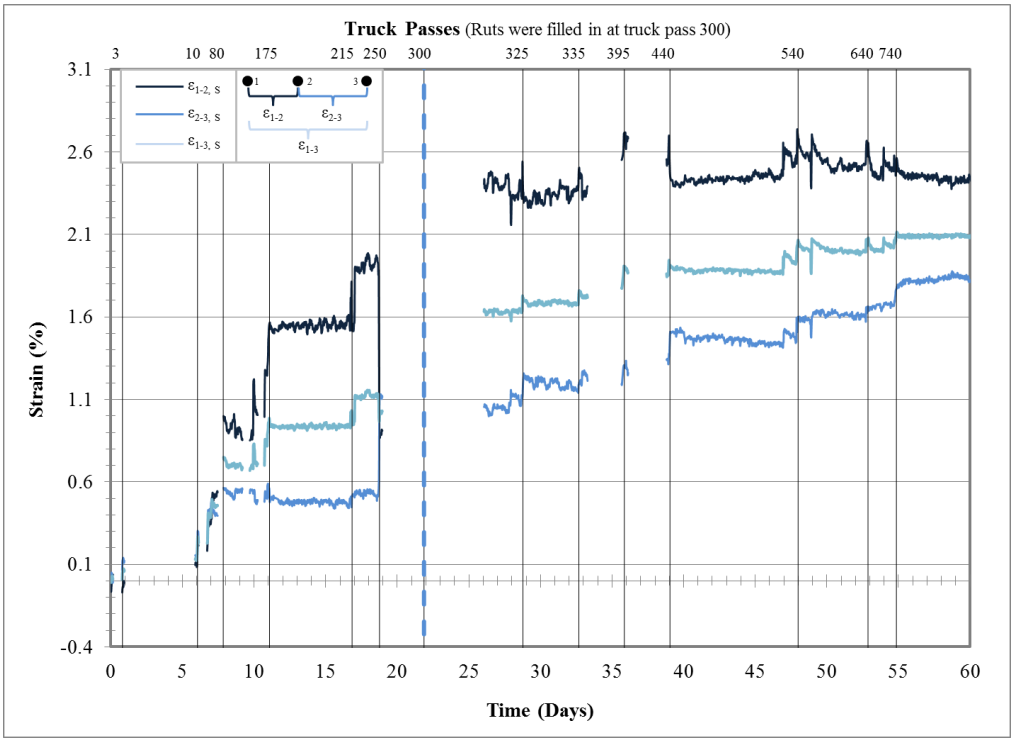


Figure O-26: TenCate Mirafi RS580i (13-South).

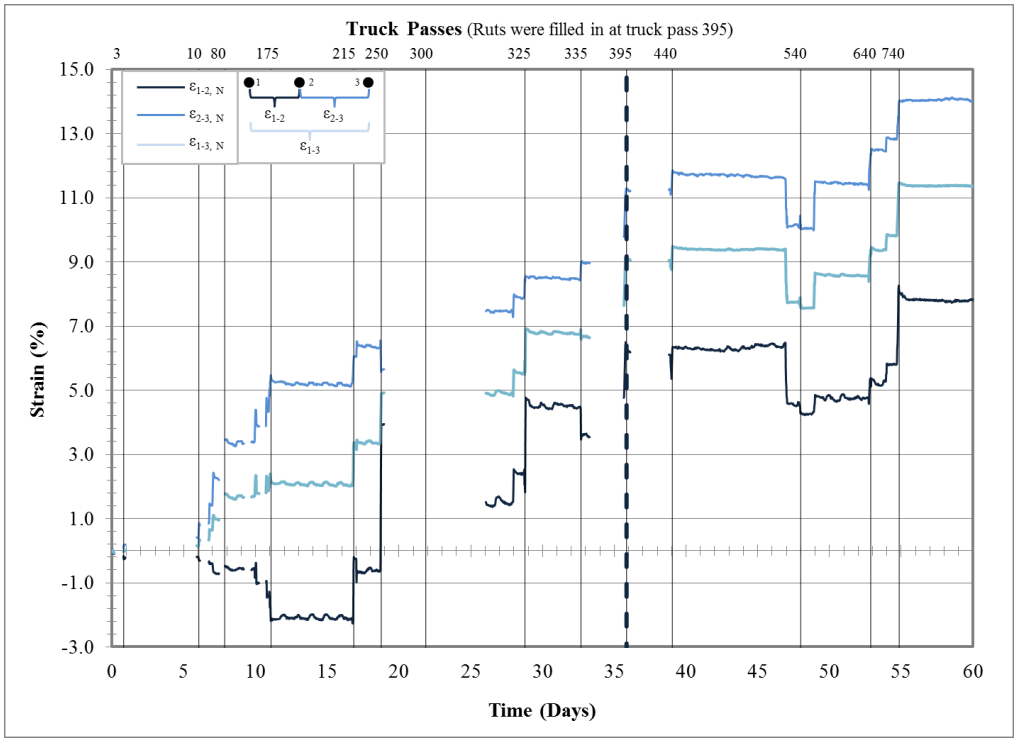


Figure O-27: Propex Geotex 801 (14-North).

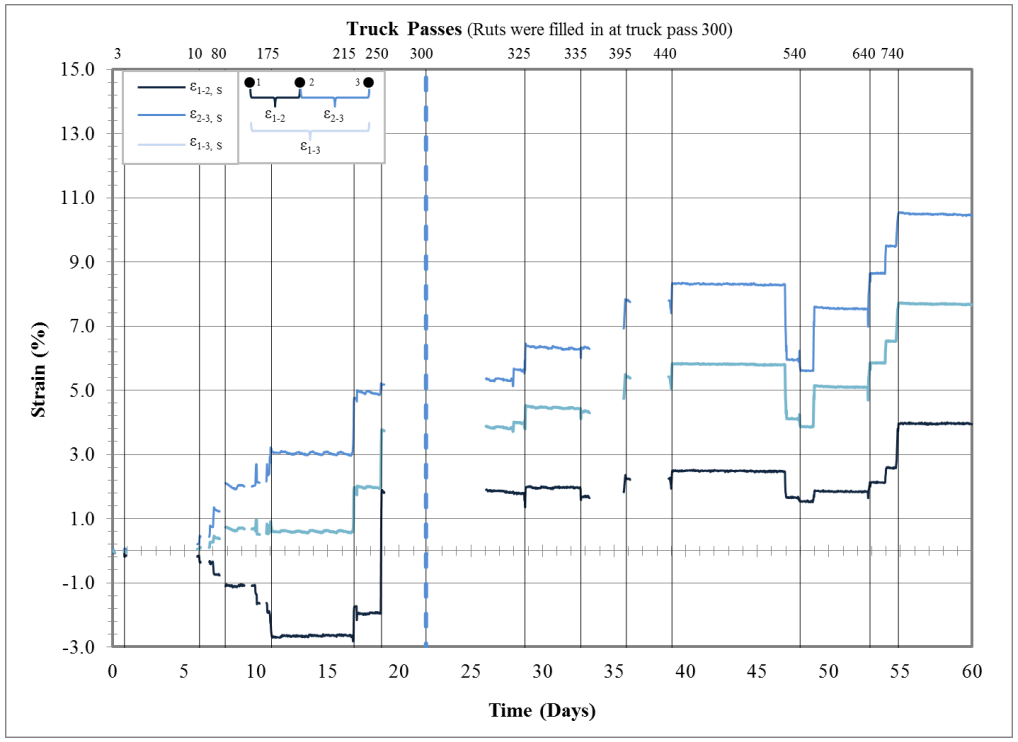


Figure O-28: Propex Geotex 801 (14-South).